

LONG-RANGE DEPENDENT PROCESSES: THEORY AND APPLICATIONS

EDITED BY: Ming Li and Carlo Cattani
PUBLISHED IN: Frontiers in Physics



frontiers

Frontiers eBook Copyright Statement

The copyright in the text of individual articles in this eBook is the property of their respective authors or their respective institutions or funders. The copyright in graphics and images within each article may be subject to copyright of other parties. In both cases this is subject to a license granted to Frontiers.

The compilation of articles constituting this eBook is the property of Frontiers.

Each article within this eBook, and the eBook itself, are published under the most recent version of the Creative Commons CC-BY licence.

The version current at the date of publication of this eBook is CC-BY 4.0. If the CC-BY licence is updated, the licence granted by Frontiers is automatically updated to the new version.

When exercising any right under the CC-BY licence, Frontiers must be attributed as the original publisher of the article or eBook, as applicable.

Authors have the responsibility of ensuring that any graphics or other materials which are the property of others may be included in the CC-BY licence, but this should be checked before relying on the CC-BY licence to reproduce those materials. Any copyright notices relating to those materials must be complied with.

Copyright and source acknowledgement notices may not be removed and must be displayed in any copy, derivative work or partial copy which includes the elements in question.

All copyright, and all rights therein, are protected by national and international copyright laws. The above represents a summary only. For further information please read Frontiers' Conditions for Website Use and Copyright Statement, and the applicable CC-BY licence.

ISSN 1664-8714

ISBN 978-2-83250-850-3

DOI 10.3389/978-2-83250-850-3

About Frontiers

Frontiers is more than just an open-access publisher of scholarly articles: it is a pioneering approach to the world of academia, radically improving the way scholarly research is managed. The grand vision of Frontiers is a world where all people have an equal opportunity to seek, share and generate knowledge. Frontiers provides immediate and permanent online open access to all its publications, but this alone is not enough to realize our grand goals.

Frontiers Journal Series

The Frontiers Journal Series is a multi-tier and interdisciplinary set of open-access, online journals, promising a paradigm shift from the current review, selection and dissemination processes in academic publishing. All Frontiers journals are driven by researchers for researchers; therefore, they constitute a service to the scholarly community. At the same time, the Frontiers Journal Series operates on a revolutionary invention, the tiered publishing system, initially addressing specific communities of scholars, and gradually climbing up to broader public understanding, thus serving the interests of the lay society, too.

Dedication to Quality

Each Frontiers article is a landmark of the highest quality, thanks to genuinely collaborative interactions between authors and review editors, who include some of the world's best academicians. Research must be certified by peers before entering a stream of knowledge that may eventually reach the public - and shape society; therefore, Frontiers only applies the most rigorous and unbiased reviews.

Frontiers revolutionizes research publishing by freely delivering the most outstanding research, evaluated with no bias from both the academic and social point of view. By applying the most advanced information technologies, Frontiers is catapulting scholarly publishing into a new generation.

What are Frontiers Research Topics?

Frontiers Research Topics are very popular trademarks of the Frontiers Journals Series: they are collections of at least ten articles, all centered on a particular subject. With their unique mix of varied contributions from Original Research to Review Articles, Frontiers Research Topics unify the most influential researchers, the latest key findings and historical advances in a hot research area! Find out more on how to host your own Frontiers Research Topic or contribute to one as an author by contacting the Frontiers Editorial Office: frontiersin.org/about/contact

LONG-RANGE DEPENDENT PROCESSES: THEORY AND APPLICATIONS

Topic Editors:

Ming Li, Zhejiang University, China

Carlo Cattani, University of Tuscia, Italy

Citation: Li, M., Cattani, C., eds. (2022). Long-Range Dependent Processes: Theory and Applications. Lausanne: Frontiers Media SA.
doi: 10.3389/978-2-83250-850-3

Table of Contents

| | |
|-----|--|
| 04 | <i>Application of Generalized Cauchy Process on Modeling the Long-Range Dependence and Self-Similarity of Sea Surface Chlorophyll Using 23 years of Remote Sensing Data</i> |
| | Junyu He |
| 13 | <i>Stability of Hybrid SDEs Driven by fBm</i> |
| | Wenyi Pei and Zhenzhong Zhang |
| 22 | <i>Almost Periodic Solutions to Impulsive Stochastic Delay Differential Equations Driven by Fractional Brownian Motion With $1/2 < H < 1$</i> |
| | Lili Gao and Xichao Sun |
| 31 | <i>Global Mean Sea Level. Time Trends and Persistence with Long Range Dependent Data</i> |
| | Luis Alberiko Gil-Alana |
| 34 | <i>A Novel Clock Skew Estimator and Its Performance for the IEEE 1588v2 (PTP) Case in Fractional Gaussian Noise/Generalized Fractional Gaussian Noise Environment</i> |
| | Yehonatan Avraham and Monika Pinchas |
| 55 | <i>Confidence Regions for Parameters in Stationary Time Series Models With Gaussian Noise</i> |
| | Xiuzhen Zhang, Riquan Zhang and Zhiping Lu |
| 65 | <i>Large Time Behavior on the Linear Self-Interacting Diffusion Driven by Sub-Fractional Brownian Motion With Hurst Index Large Than 0.5 I: Self-Repelling Case</i> |
| | Han Gao, Rui Guo, Yang Jin and Litan Yan |
| 77 | <i>Large Time Behavior on the Linear Self-Interacting Diffusion Driven by Sub-Fractional Brownian Motion II: Self-Attracting Case</i> |
| | Rui Guo, Han Gao, Yang Jin and Litan Yan |
| 90 | <i>Early Warning Signals for Critical Transitions in Sandpile Cellular Automata</i> |
| | Andrey Dmitriev, Vasily Kornilov, Victor Dmitriev and Nadezda Abbas |
| 99 | <i>Dehazing Based on Long-Range Dependence of Foggy Images</i> |
| | Hong Xu Yuan, Zhiwu Liao, Rui Xin Wang, Xinceng Dong, Tao Liu, Wu Dan Long, Qing Jin Wei, Ya Jie Xu, Yong Yu, Peng Chen and Rong Hou |
| 107 | <i>Characteristic Sequence Analysis of Giant Panda Voiceprint</i> |
| | Shaoxiang Hu, Zhiwu Liao, Rong Hou and Peng Chen |
| 114 | <i>Giant Panda Video Image Sequence and Application in 3D Reconstruction</i> |
| | Shaoxiang Hu, Zhiwu Liao, Rong Hou and Peng Chen |
| 124 | <i>Dependence Research on Multi-Layer Convolutions of Images</i> |
| | Zhiwu Liao, Yong Yu and Shaoxiang Hu |
| 128 | <i>Two Novel One-Way Delay Clock Skew Estimators and Their Performances for the Fractional Gaussian Noise/Generalized Fractional Gaussian Noise Environment Applicable for the IEEE 1588v2 (PTP) Case</i> |
| | Yehonatan Avraham and Monika Pinchas |
| 147 | <i>On the Fractional Weibull Process</i> |
| | Wujin Deng, Wanqing Song, Carlo Cattani, Jianxue Chen and Xiaolong Chen |



Application of Generalized Cauchy Process on Modeling the Long-Range Dependence and Self-Similarity of Sea Surface Chlorophyll Using 23 years of Remote Sensing Data

Junyu He^{1,2*}

¹Ocean Academy, Zhejiang University, Zhoushan, China, ²Ocean College, Zhejiang University, Zhoushan, China

OPEN ACCESS

Edited by:

Carlo Cattani,
University of Tuscia, Italy

Reviewed by:

Manuel Cobos Budia,
University of Granada, Spain
Mohammad Hossein Heydari,
Shiraz University of Technology, Iran

*Correspondence:

Junyu He
jxgzhejunyu@163.com

Specialty section:

This article was submitted to
Interdisciplinary Physics,
a section of the journal
Frontiers in Physics

Received: 30 July 2021

Accepted: 08 September 2021

Published: 28 September 2021

Citation:

He J (2021) Application of Generalized Cauchy Process on Modeling the Long-Range Dependence and Self-Similarity of Sea Surface Chlorophyll Using 23 years of Remote Sensing Data.
Front. Phys. 9:750347.
doi: 10.3389/fphy.2021.750347

Understanding the temporal characteristics of sea surface chlorophyll (SSC) is helpful for marine environmental management. This study chose 10 time series of remote daily sea surface chlorophyll products from the European Space Agency during the period from July 29, 1998 to December 31, 2020. A generalized Cauchy model was employed to capture the local and global behaviors of sea surface chlorophyll from a fractal perspective; the fractal dimension D measures the local similarity while the Hurst parameter H measures the global long-range dependence. The generalized Cauchy model was fitted to the empirical autocorrelation function values of each SSC series. The results showed that the sea surface chlorophyll was multi-fractal in both space and time with the D values ranging from 1.0000 to 1.7964 and H values ranging from 0.6757 to 0.8431. Specifically, regarding the local behavior, 9 of the 10 series had low D values (<1.5), representing weak self-similarity; on the other hand, regarding the global behavior, high H values represent strong long-range dependence that may be a general phenomenon of daily sea surface chlorophyll.

Keywords: long-range dependence, local self-similarity, generalized cauchy model, remote sensing, sea surface chlorophyll, autocorrelation function, Gulf of California

INTRODUCTION

Sea surface chlorophyll (SSC) is an important bio-indicator, representing the biomass of the phytoplankton in the surface layer of the ocean [1–3]. On one hand, phytoplankton have made significant contributions to capture greenhouse gas from the atmosphere and balance the carbon cycle globally [4,5]; on the other hand, under a suitable living environment condition (such as temperature, nutrients, etc.), the phytoplankton will grow rapidly and cause blooms, leading to the degradation of the water environment and ecosystem corruption [6–8]. Therefore, understanding the evolution and pattern of SSC is of great significance to ocean environmental management.

With the development of remote sensing technology, the sensors equipped on satellites can provide long-term SSC products at a global scale, which is conducive to the studies of SSC. For example, the pattern of global ocean primary production can be investigated at a large scale [9–12]. Likewise, the regional SSC variations were studied using remote sensing data. Yamada et al. [13] employed the Ocean Color and Temperature Scanner (OCTS) and the Sea-Viewing Wide Field of View Sensor (SeaWiFS) remote sensing data to study the SSC variation in the East China Sea and the Sea of Japan and found the interannual variability of the spring bloom and the weak temporal

transition of the fall bloom. In the Bohai Sea and the North Yellow Sea of China, Zhai et al. [14] found the SSC exhibited a spatially coherent increasing trend over 2003–2011 and a decreasing trend over 2012–2018 by using Moderate Resolution Imaging Spectroradiometer (MODIS) data; specifically, the decreasing trend was more obvious than the increasing trend. Further, the Ocean Colour Climate Change Initiative (OC-CCI) standard products with locally modified SSC was also used to detect four types of SSC annual cycle in the East China Sea, i.e., the summer bloom, spring and autumn bloom, early spring bloom, and low SSC [15]. In summary, the studies mentioned above only focused on the trends and made simple statistics for exploring the space-time SSC patterns.

Recently, specific SSC variation modeling has been implemented in several studies. He et al. [16] chose the optimal theoretical model (such as Exponential model, Spherical model, Gaussian model, and their combinations) to fit the spatial covariance of the SSC distribution in the Gulf of St. Lawrence, and found that the highest SSC variability occurred in November while it changed a lot during the period from August to November. Despite this, few studies have modeled the temporal variance or pattern of SSC. The long-range correlation (or dependence) of SSC was detected in the South China Sea with time scales ranging from a few weeks to 2 years [17]. However, the long-term mathematical modeling of the long-range dependence (LRD) and self-similarity of SSC is still lacking.

In general, several important parameters are used to characterize the complex behavior and dynamics of a time series, such as the Hurst parameter and the fractal dimension/index. Further, some methodologies have been developed to estimate these two parameters separately. Traditionally, the fractal dimension or index can be estimated by counting the number of level crossings, using increments, or the relationship between power variations and the fractal dimension [18–20]; besides this, some other fractal dimensions, such as number-based fragmentation fractal dimension and mass fractal dimension for soil properties can be calculated as shown in other studies [21–23]. Regarding the Hurst parameter, the variance-plot with various block sizes were fitted to obtain the slope β and the Hurst parameter can be calculated subsequently by $\beta = 2H - 1$; Kettani and Gubner [24] developed a variogram-based method to calculate the Hurst parameter and found the new method was superior to the wavelet method; Li [25] used the generalized fractional Gaussian noise to fit the autocorrelation function (ACF) of the traffic and further obtain the Hurst parameter; moreover, modified multifractal Gaussian noise theory was also developed to calculate the Hurst parameter of the sea level across the study period [26]. Given that the two parameters denote various fractal characteristics of the time series, it is important to seek ways to simultaneously obtain the fractal dimension and Hurst parameter. Luckily, the generalized Cauchy model provides a potential way to achieve this goal. It can be used to model the ACF of the studied time series, and it proves that the two parameters were independent of each other [27]. In the past few decades, the generalized Cauchy process has been successfully applied to model the sea-level fluctuations, teletraffic, and network traffic [27,28].

Given the above considerations, the objective of this work is to use the generalized Cauchy process to model the ACF of remote SSC data and explore the fractal characteristics of SSC, which will benefit local SSC monitoring, controlling, and policy-making.

METHODS AND MATERIALS

Data Collection

The long-term daily SSC data was collected from the European Space Agency (ESA). It merged remote sensing reflectance (Rrs) from several satellites, including SeaWiFS, MERIS (Medium Resolution Imaging Spectrometer), Aqua-MODIS, VIIRS (Visible and Infrared Imager/Radiometer Suite), and OLCI (Ocean and Land Color Instrument) [29]. Then, the SSC products are generated using Algorithm Theoretical Baseline Document (Optical Classification and Algorithm Blending) [30]. In the present study, the daily SSC products with spatial resolution $1^\circ \times 1^\circ$ were integrated during the period from July 29, 1998 to December 31, 2020 (8,192 days in total), and 10 locations were selected for further analysis, see **Figure 1**. Of the 10 locations, 7 are located in the Gulf of California (**Figure 1B**), with 2 and 1 located in the western coastal regions of Madagascar and South Africa, respectively.

Basic Theories

Long-Range Dependence

Let $x(t)$ and $r(\tau)$ denote the time series of the studied natural attribute and its ACF, i.e., $r(\tau) = E[x(t)x(t+\tau)]$, where E represents the expectation operator. Thus, LRD or long memory is used to depict the situation that the ACF decays slowly with the characteristic as $\int_{-\infty}^{+\infty} r(\tau)d\tau = \infty$ [31–33], i.e., the values of the studied natural attribute with large temporal lag show a strong correlation. Further, the asymptotic form of ACF with LRD can be expressed as **Eq. 1** with the help of the Hurst parameter [34].

$$\begin{cases} r(\tau) \sim c\tau^\beta (\tau \rightarrow \infty) \\ \beta = 2H - 2 \end{cases} \quad (1a-1b)$$

Where the Hurst parameter H ranges from 0.5 to 1 under the LRD condition, representing the global property of the time series $x(t)$, a larger value of H implies that the LRD is stronger.

Self-Similarity

The ACF is self-similar when it remains the same through aggregating the sub-series of $x(t)$ with nonoverlapping blocks [35], i.e., part of the time series is locally approximately similar to the entire time series. According to the literature [36,37], the fractal index (α) was employed to measure the local self-similarity, as follows:

$$\begin{cases} r(0) - r(\tau) \sim c|\tau|^\alpha \\ D = 2 - \frac{1}{2}\alpha \end{cases} \quad (2a-2b)$$

where $c > 0$ and $0 < \alpha \leq 2$. The fractal dimension, D , belongs to $[1, 2)$. A larger value of D means that the local self-similarity of the studied time series is stronger [27].

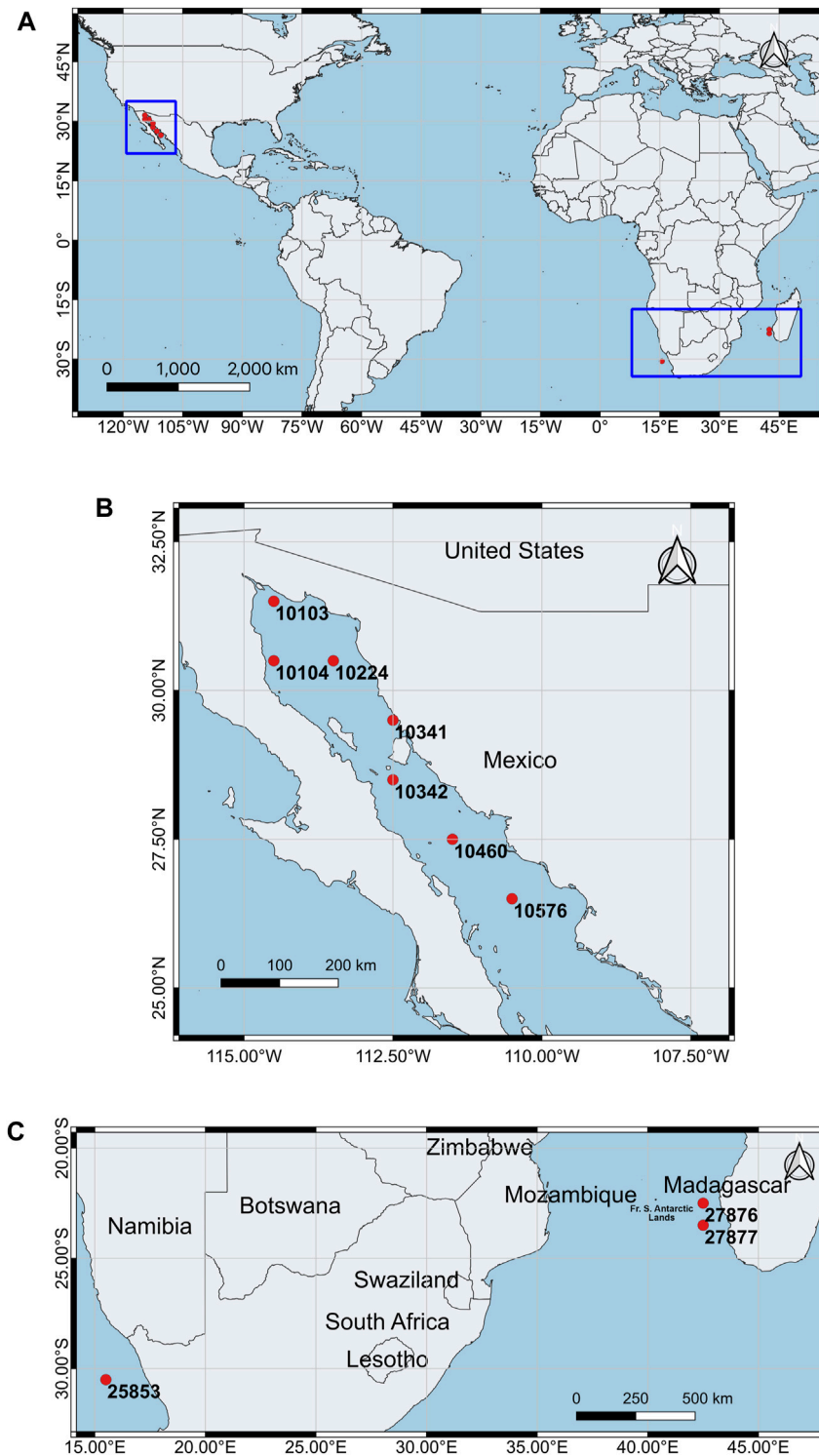


FIGURE 1 | 10 sea surface chlorophyll data locations. **(A)** shows the distribution of the 10 data locations at a global scale, while the zoom-in views of the two rectangles are shown in **(B)** and **(C)**. The number represents the identity of each data location.

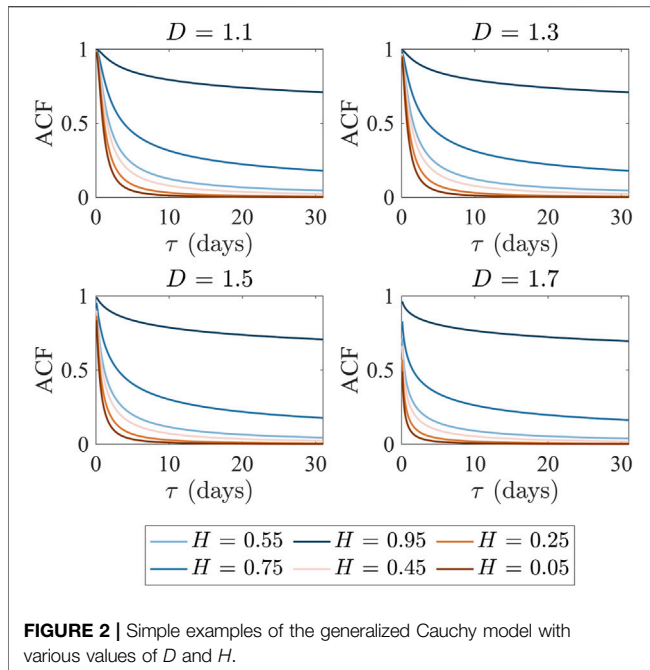


FIGURE 2 | Simple examples of the generalized Cauchy model with various values of D and H .

Generalized Cauchy Process

The generalized Cauchy process is applied when the time series $x(t)$ and its ACF are of the form of the following equation, subject to $1 < \alpha \leq 2$ and $\beta \geq 0$ [28,38]:

$$C(\tau) = \psi^2 (1 + |\tau|^\alpha)^{-\frac{\beta}{\alpha}} \quad (3)$$

where ψ^2 is the intensity of $x(t)$. The following comments discuss features of the two parameters in Eq. 3. Regarding the parameter β , it defines the dependence of $x(t)$ by setting $\tau \rightarrow \infty$: (a) if $0 \leq \beta < 1$, $\int_{-\infty}^{+\infty} [\lim_{\tau \rightarrow \infty} C(\tau)] d\tau = \int_{-\infty}^{+\infty} \psi^2 |\tau|^{-\beta} d\tau = \infty$, i.e., it represents the LRD with respect to β ; (b) if $\beta > 1$, $\int_{-\infty}^{+\infty} (1 + |\tau|^\alpha)^{-\frac{\beta}{\alpha}} d\tau = \frac{2}{\alpha} B(\frac{1}{\alpha}, \frac{\beta-\alpha}{\alpha}) < \infty$, where B is the beta function, i.e., it represents short-range dependence (SRD). Regarding the parameter α , it defines the self-similarity of $x(t)$ by setting $\tau \rightarrow 0$, thus $\lim_{\tau \rightarrow 0} C(\tau) = \psi^2 |\tau|^\alpha$ with respect to α . In short, the LRD and self-similarity of $x(t)$ only rely on the parameters β and α , respectively. In this case, with the definition of Eq. 1b and Eq. 2b, the generalized Cauchy process can be written as

$$C(\tau) = \psi^2 (1 + |\tau|^{4-2D})^{-\frac{1-H}{2-D}} \quad (4)$$

For modeling purpose, the intensity ψ^2 can be set to 1, and Eq. 4 becomes

$$C(\tau) = (1 + |\tau|^{4-2D})^{-\frac{1-H}{2-D}} \quad (5)$$

In this case, the generalized Cauchy process can simultaneously depict the LRD (global property) and self-similarity (local property) of $x(t)$ by using the two parameters H and D , respectively. Regarding the Hurst parameter H , if $0 \leq \beta < 1$, i.e., $0.5 < H < 1$, it represents LRD, and the values of ACF remain high even over large temporal

lag; whereas if $\beta > 1$, i.e., $0 < H < 0.5$, it represents SRD, and the value of ACF usually decays quickly, e.g., the value of ACF may decline to zero over a lag of several days. With various values of H and D , the ACFs were plotted in Figure 2. It was found that the ACF value of the generalized Cauchy process decreases as the temporal lag τ increases. Moreover, the ACF value increases when the value of H increases and the value of D is fixed, while the ACF value decreases a little when the value of D increases and the value of H is fixed. Among the six lines shown in the sub-figures, the three blue represent the LRD cases, and three red lines represent the SRD cases. Specifically, when the temporal lag, H value, and D value are equal to 7.2 days, 0.05, and 1.7 respectively, the value of ACF declines to 0.01, representing SRD characteristics; see the dark red line of the bottom right sub-figure in Figure 2. On the other hand, when the temporal lag, H value, and D value are equal to 31 days, 0.75, and 1.1 respectively, the value of ACF is still greater than 0.179, representing LRD characteristics; see the middle blue line of the top left sub-figure in Figure 2.

Autocorrelation Function Fitting Process

The original time series of SSC at each location was divided equally into 16 sub-series with no overlapping cases, each containing 512 data points. Considering that the value of the autocorrelation function may decay to zero with a 1-month temporal lag in some parts of the world [39,40], the theoretical autocorrelation function values for temporal lags between 0 and 32 was calculated by averaging the 16 autocorrelation functions of each sub-series. Then, the generalized Cauchy model (Eq. 5) was employed to fit each of the theoretical autocorrelation function values using the “lsqnonlin” function embedded in MATLAB software. Then, the fractal dimension D and the Hurst parameter H were estimated. The fitting performance of the generalized Cauchy model was evaluated by R^2 , MAE, and RMSE, as follows:

$$R^2 = 1 - \frac{SS_{res}}{SS_{tot}} = 1 - \frac{\sum [Y(\tau) - \hat{Y}(\tau)]^2}{\sum [Y(\tau) - \bar{Y}]^2} \quad (6)$$

$$MAE = \frac{1}{n} \sum_{\tau=1}^n |Y(\tau) - \hat{Y}(\tau)| \quad (7)$$

$$RMSE = \sqrt{\frac{\sum_{\tau=1}^n [Y(\tau) - \hat{Y}(\tau)]^2}{n}} \quad (8)$$

where $Y(\tau)$ and $\hat{Y}(\tau)$ represent the empirical ACF value and fitted ACF value at temporal lag τ respectively, \bar{Y} represents the mean value of the ACF series, n represents the length of the series, and SS_{res} and SS_{tot} represents the sum of squared residuals and the sum of squares of deviation from mean respectively.

RESULTS

Descriptive Statistics

The proportion of missing daily SSC data from ESA at the 10 locations ranges from 8.02 to 11.56% over the entire period. Given that the missing values were discretely distributed in

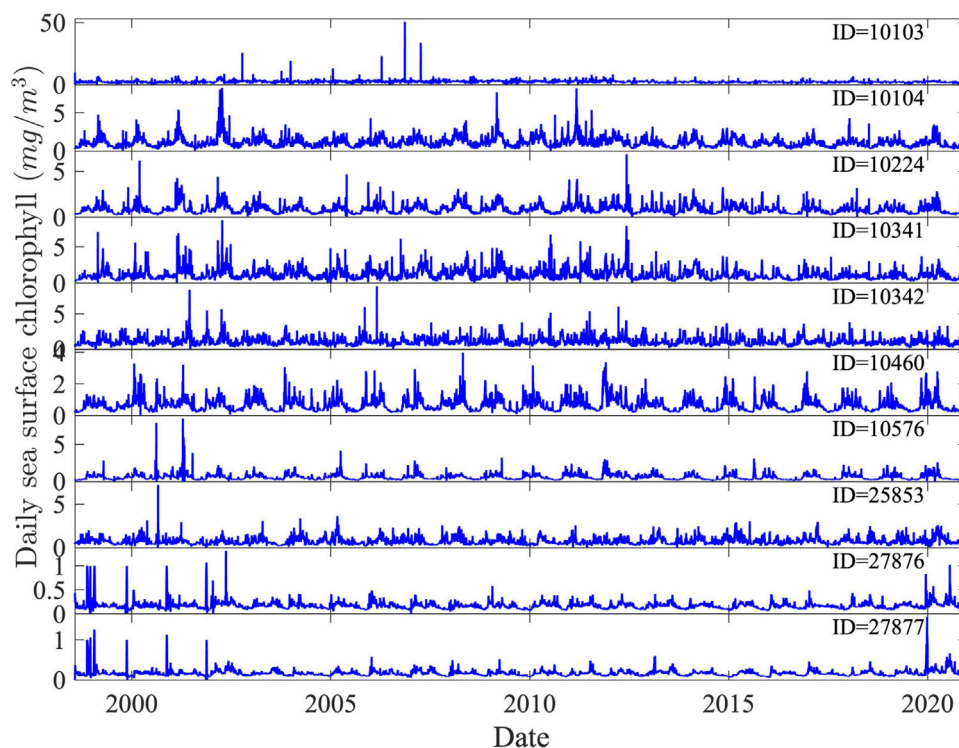


FIGURE 3 | Sea surface chlorophyll time series at the 10 chosen locations.

TABLE 1 | Descriptive statistics of the considered 10 time series of SSC.

| ID | Min | Max | Mean | Standard Deviation | Coefficient of variation |
|--------|--------|---------|--------|--------------------|--------------------------|
| 10,103 | 0.3129 | 50.6148 | 2.5001 | 1.1656 | 0.4662 |
| 10,104 | 0.1701 | 8.2633 | 1.1285 | 0.6692 | 0.5931 |
| 10,224 | 0.1979 | 6.8945 | 0.8643 | 0.4989 | 0.5773 |
| 10,341 | 0.2039 | 8.6791 | 1.1917 | 0.7225 | 0.6063 |
| 10,342 | 0.1570 | 8.8930 | 1.1009 | 0.5583 | 0.5072 |
| 10,460 | 0.1311 | 3.9872 | 0.6632 | 0.4025 | 0.6069 |
| 10,576 | 0.0753 | 8.4703 | 0.5909 | 0.4155 | 0.7032 |
| 25,853 | 0.0536 | 7.2255 | 0.7518 | 0.4039 | 0.5372 |
| 27,876 | 0.0522 | 1.3131 | 0.1697 | 0.0720 | 0.4244 |
| 27,877 | 0.0542 | 1.5799 | 0.1665 | 0.0763 | 0.4586 |

each SSC time series, they were interpolated by using the “spline” function in MATLAB software for further analysis. The SSC time series with full length (including 8192 SSC data) at the considered 10 locations are plotted in **Figure 3** and the corresponding descriptive statistical results are presented in **Table 1**. The statistical results indicate that the SSC has the highest range (i.e., from 0.3129 to 50.6148 mg/m³) in the location with ID 10103 during the studied period; while the values of SSC at the other six locations around the Mexico offshore regions range from 0.0753 to 8.8930 mg/m³. On the other hand, similar ranges (i.e., from 0.0522 to 1.5799 mg/m³) are found in the two locations around the offshore of Madagascar. The values of

SSC at the last location with ID 25853 range from 0.0536 to 7.2255 mg/m³.

Generalized Cauchy Process Fitting Results

Figure 4 shows the theoretical autocorrelation values and the corresponding fitted generalized Cauchy model with the fitting performance at each of the 10 daily SSC series. Our findings are as follows: 1) The autocorrelation functions of SSC can be well fitted by the generalized Cauchy model with R^2 ranging from 0.9469 to 0.9875, MAE ranging from 0.0143 to 0.0358, and $RMSE$ ranging from 0.0187 to 0.0434. 2) The values of the fractal dimension D and the Hurst parameter H vary at different locations. 3) A high value for the fractal dimension D (1.7964) with strong self-similarity was only found at the location with ID = 10,103, while the D values at other locations are lower than 1.5 and 5 of the 10 locations have D values approximately equal to 1. This shows that most of the 10 daily SSC series have weak self-similarity. 4) The values of the Hurst parameter H of the 10 daily SSC series range from 0.6757 to 0.8431, indicating that the daily SSC series at the 10 locations have strong long-range dependence.

DISCUSSION

The present work employed the generalized Cauchy process to model the ACF of daily remote SSC data during a 23-year period

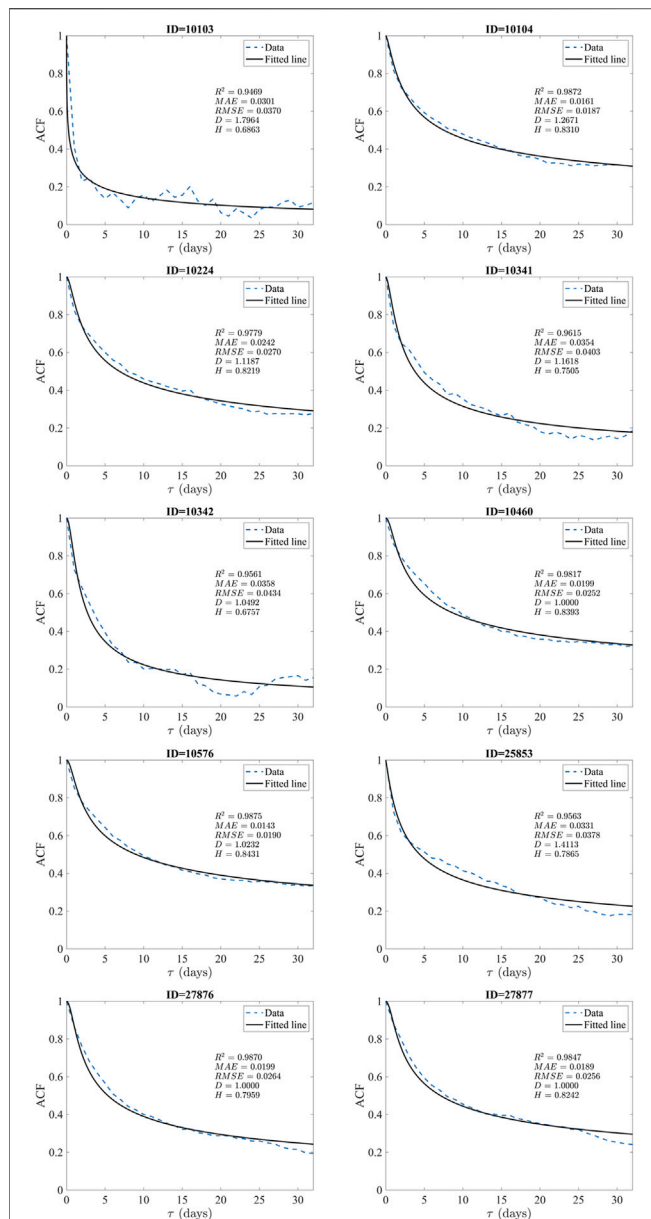


FIGURE 4 | The empirical autocorrelation function values (dash blue line) and the fitted generalized Cauchy model (black line) for each of the 10 data points.

and good performance of the fitting was obtained, indicating that the SSC in the 10 chosen locations follows a heavy-tailed distribution [41]. Compared to the generalized Gaussian noise model, the outstanding ability of the generalized Cauchy model is that it can simultaneously estimate both independent variables (Hurst parameter and fractal dimension). This means that it can describe the global correlation and local self-similarity of the considered natural attribute [27,42], such as the SSC in the present work. To the best of my knowledge, the present effort is one of the earliest studies in obtaining the LRD and self-similarity of the SSC in view of fractal statistics.

Impacts of Environmental Factors on the Fractal Characteristics of Sea Surface Chlorophyll

Relatively low self-similarity and high LRD of the SSC series at the 10 locations can be summarized. A rather different case was found in a lake study, i.e., the chlorophyll-a was autocorrelated over lags of five or 6 days [43], indicating SRD. The nutrients and aquatic environment (light, temperature, salinity, etc.) impact the algae growth and further influence the SSC variability [44–48]. With the continuous variation of these factors, the variation of SSC across time is also smooth according to the algae growth, causing the weak irregularity characteristics with low values of the fractal dimension and strong LRD with high values of the Hurst parameter. This phenomenon leads to the empirical values of ACF (blue dash line shown in **Figure 4**) being slightly higher than the theoretical values of ACF (black line shown in **Figure 4**) with the temporal lags between 2 and 10 days at most locations. However, with the temporal lag increasing from 10 to 25 days, the empirical values become smaller than the theoretical values, because the SSC may be influenced by the global climatic dynamics, such as the Southern Pacific Oscillation Index [49], which is different from algae's own growth condition. Moreover, there may be another situation that algae blooms with enough nutrient inputs [50], leading to extremely high SSC values, e.g., the SSC value increases rapidly and peaks for one or 2 days (as some peaks shown in **Figure 3**); and that may be the reason that the value of the fractal dimension is the highest among the 10 series, i.e., $D = 1.7964$ with the highest maximum SSC value and standard deviation across the study period. On the other hand, the values of the fractal dimension and Hurst parameter varied at various locations, indicating that the environmental conditions are rather different from each other. Moreover, various species of algae may exist at various locations and their growth response to the environmental conditions are rather different [51,52]. Compared to the values of the fractal dimension (varies from 1.7244 to 1.7838) of SSC in the Chesapeake Bay [45], the values of the fractal dimension obtained in the current study are rather low; this may due to the fact that the river discharge and the nutrients it carries are not as large as the rivers (e.g., Susquehanna River and Potomac River) that run into the Chesapeake Bay. However, the values of the Hurst parameters in the current study are greater than that in the Chesapeake Bay study with LRD characteristics, indicating that a large nutrient load in the Chesapeake Bay may lead to weak LRD. Therefore, the LRD may be a general feature of SSC variations in oceans.

Besides this, the aquatic environment will also influence the behavior of the zooplankton, e.g., warm waters will favor the consumption of the zooplankton, causing the reduction of SSC [53–55]. On the other hand, the upwelling system and surface currents around the coastal areas play important roles in shaping the distribution of zooplankton and further influence the variation of SSC [56]. The upwelling system on the California coast shows seasonal variabilities and can be summarized into four types: “Winter Storms” season (Dec-Jan-Feb), “Upwelling Transition” period (Mar and Jun), “Peak Upwelling” season (Apr-May), “Upwelling Relaxation” season (Jul-Aug-Sep), and “Winter Transition” season (Oct-Nov), so the impacts of upwelling system on the SSC are also seasonally continuous. That may be one of the reasons that SSC has LRD characteristic [57].

Long-Range Dependence of Sea Surface Chlorophyll at the Studied Locations

The present study employed ACF to describe the fractal characteristics (especially the long-range dependence) of SSC with temporal lags of 32 days. The empirical values of the ACF at the 10 studied locations range from 0.1160 to 0.3351, and the mean and standard deviation of the empirical values are 0.2319 and 0.0764, respectively. These results show that strong long-range dependence can be detected within a temporal lag of 1 month. Robles-Tamayo et al. [49] detected seasonal, semi-annual, and annual cycles of SSC in the Gulf of California using the Level 3 products of MODIS remote sensing data. In other words, the SSC variation may experience peak and valley values in a season (3 months). Moreover, the SSC values of the four seasons vary a lot with high values of the standard deviation. Regarding the seasonal variation, Escalante-Almazán [58] found that the mean values of SSC in the central gulf were 1.09, 1.20, 0.44, and 0.60 mg/m³ for winter, spring, summer, and autumn, respectively. The large variation between seasons suggests that the SSC may not have long-range dependence at an annual or semi-annual scale. On the other hand, in the warm period the mean \pm standard deviation values of SSC in the south, central midriff islands, and north sub-regions of the Gulf of California are 0.79 ± 0.89 , 0.55 ± 0.37 , 1.19 ± 0.83 , and 0.63 ± 0.39 mg/m³ respectively, and in the cold period, the values are 2.05 ± 1.20 , 1.84 ± 0.73 , 2.80 ± 1.40 , and 1.50 ± 0.61 mg/m³ respectively [49]. The large standard deviations represent large variations of SSC, indicating that the SSC may not have large LRD at a semi-annual or annual scale. To test the LRD of SSC at a seasonal scale, the empirical values of ACF at the 10 studied locations were calculated with a temporal lag of 128 days. The results show that the value of empirical ACF at the 10 locations first reached 0 at the temporal lags of 49, 75, 89, 59, 47, 85, 89, 69, 70, and 67 days, respectively. Otherwise, with large temporal lags, the values of ACF will fluctuate around zero. Hence, long-range dependence at a seasonal scale (i.e., with temporal lag larger than 90 days) is relatively weak compared to the monthly scale.

Comparisons to Previous Works

Comparisons between the current study and previous studies were conducted as follows. Some ACFs of teletraffic was rather high, above 0.98 with even 128 days lag [27], but the ACF value of SSC in the current study fall below 0.5 with 31 days lag. This may be the reason why very high values of the Hurst parameter (larger than 0.99) were detected with teletraffic rather than SSC. In addition, the values of the fractal dimension of teletraffic were much larger than that of SSC, demonstrating that stronger self-similarity was found in teletraffic series than SSC. This may be due to the fact that values for teletraffic are more random in occurrence while the values for SSC are more like a continuous series associated with several environmental factors mentioned above. In another study [28], the generalized Cauchy process was used to model the ACF of sea level fluctuations with a temporal resolution of 1 h, and found that the value of the fractal dimension was approximately equal to 1 at several locations while the most of them were larger than 1.8; the values of Hurst parameter were larger than 0.98. Interestingly, the locations with low fractal dimension values are located in the Gulf of Mexico, which is similar to the seven locations studied in the current study, i.e., the weak self-similarity may occur in a stable environment.

Limitations and Future Work

Certain limitations of the current study should be acknowledged: 1) Although there may be a relationship between the fractal characteristics of SSC and the living environment, rigorous proof and statistical analysis was not conducted in the current study due to lack of data. Therefore, future work can focus on quantitatively exploring the impacts of nutrients and temperature on the fractal dimension or Hurst parameters of SSC. 2) Even SSC products with high spatiotemporal coverage were used in the current study, there still exist missing values from other locations. Hence, spatiotemporal interpolation methods should be employed to obtain a more complete remote SSC dataset for mapping the global fractal dimension or Hurst parameter of SSC, such as the Bayesian maximum entropy approach [59–61], so that the spatial pattern of the fractal dimension and Hurst parameter can be further studied. 3) Taking into consideration the stochastic differential equations, the evolution pattern (or law) of SSC can be further explored, such as the fractional Brownian motion pattern [62,63].

CONCLUSION

The present study applied a novel generalized Cauchy model to depict the variations of SSC and good performance was obtained. The fractal characteristics of the SSC vary at different locations in terms of the fractal dimension and Hurst parameter; weak self-similarity was found in most locations with low values of the fractal dimension while strong LRD was detected across all locations with reactively high value of the Hurst parameter.

DATA AVAILABILITY STATEMENT

The original contributions presented in the study are included in the article/Supplementary Material, further inquiries can be directed to the corresponding author.

AUTHOR CONTRIBUTIONS

JH contributed to conception and design of the study, organized the database, performed the statistical analysis, wrote the first draft of the manuscript. The author contributed to manuscript revision, read, and approved the submitted version.

FUNDING

This work is supported by the China Postdoctoral Science Foundation (2020M681825) and National Natural Science Foundation of China (No. 42171398).

ACKNOWLEDGMENTS

I would like to thank Prof. Ming Li for his guidance in modeling the generalized Cauchy process and Chen, Bairu for his assistant in improving the manuscript.

REFERENCES

- Hayashida H, Matear RJ, and Strutton PG. Background Nutrient Concentration Determines Phytoplankton Bloom Response to Marine Heatwaves. *Glob Change Biol* (2020) 26:4800–11. doi:10.1111/gcb.15255
- Liu C, Sun Q, Xing Q, Wang S, Tang D, Zhu D, et al. Variability in Phytoplankton Biomass and Effects of Sea Surface Temperature Based on Satellite Data From the Yellow Sea, China. *Plos One* (2019) 14:e0220058. doi:10.1371/journal.pone.0220058
- Shafeeque M, Sathyendranath S, George G, Balchand AN, and Platt T. Comparison of Seasonal Cycles of Phytoplankton Chlorophyll, Aerosols, Winds and Sea-Surface Temperature off Somalia. *Front Mar Sci* (2017) 4: 386. doi:10.3389/fmars.2017.00386
- Chu S. Carbon Capture and Sequestration. *Science* (2009) 325:1599. doi:10.1126/science.1181637
- Nair A, Sathyendranath S, Platt T, Morales J, Stuart V, Forget M-H, et al. Remote Sensing of Phytoplankton Functional Types. *Remote Sensing Environ* (2008) 112:3366–75. doi:10.1016/j.rse.2008.01.021
- Brooks BW, Lazorchak JM, Howard MDA, Johnson M-VV, Morton SL, Perkins DAK, et al. Are Harmful Algal Blooms Becoming the Greatest Inland Water Quality Threat to Public Health and Aquatic Ecosystems? *Environ Toxicol Chem* (2016) 35:6–13. doi:10.1002/etc.3220
- Riebesell U, Aberle-Malzahn N, Achterberg EP, Algueró-Muñoz M, Alvarez-Fernandez S, Aristegui J, et al. Toxic Algal Bloom Induced by Ocean Acidification Disrupts the Pelagic Food Web. *Nat Clim Change* (2018) 8: 1082–6. doi:10.1038/s41558-018-0344-1
- Watson SB, Whittom BA, Higgins SN, Paerl HW, Brooks BW, and Wehr JD. Harmful Algal Blooms. In: JD Wehr, RG Sheath, and JP Kociolek, editors. *Freshwater Algae of North America (Second Edition), Aquatic Ecology*. Boston: Academic Press (2015) p. 873–920. doi:10.1016/B978-0-12-385876-4.00020-7
- Eppey RW, Stewart E, Abbott MR, and Heyman U. Estimating Ocean Primary Production From Satellite Chlorophyll. Introduction to Regional Differences and Statistics for the Southern California Bight. *J Plankton Res* (1985) 7:57–70. doi:10.1093/plankt/7.1.57
- Gregg WW, and Rouseaux CS. Global Ocean Primary Production Trends in the Modern Ocean Color Satellite Record (1998–2015). *Environ Res Lett* (2019) 14:124011. doi:10.1088/1748-9326/ab4667
- Longhurst A, Sathyendranath S, Platt T, and Caverhill C. An Estimate of Global Primary Production in the Ocean From Satellite Radiometer Data. *J Plankton Res* (1995) 17:1245–71. doi:10.1093/plankt/17.6.1245
- Platt T, and Sathyendranath S. Oceanic Primary Production: Estimation by Remote Sensing at Local and Regional Scales. *Science* (1988) 241:1613–20. doi:10.1126/science.241.4873.1613
- Yamada K, Ishizaka J, and Nagata H. Spatial and Temporal Variability of Satellite Primary Production in the Japan Sea From 1998 to 2002. *J Oceanogr* (2005) 61:857–69. doi:10.1007/s10872-006-0005-2
- Zhai F, Wu W, Gu Y, Li P, Song X, Liu P, et al. Interannual-Decadal Variation in Satellite-Derived Surface Chlorophyll-A Concentration in the Bohai Sea Over the Past 16 Years. *J Mar Syst* (2021) 215:103496. doi:10.1016/j.jmarsys.2020.103496
- Hao Q, Chai F, Xiu P, Bai Y, Chen J, Liu C, et al. Spatial and Temporal Variation in Chlorophyll a Concentration in the Eastern China Seas Based on a Locally Modified Satellite Dataset. *Estuarine, Coastal Shelf Sci* (2019) 220: 220–31. doi:10.1016/j.ecss.2019.01.004
- He J, Chen Y, Wu J, Stow DA, and Christakos G. Space-Time Chlorophyll-A Retrieval in Optically Complex Waters that Accounts for Remote Sensing and Modeling Uncertainties and Improves Remote Estimation Accuracy. *Water Res* (2020) 171:115403. doi:10.1016/j.watres.2019.115403
- Zhan H, Shi P, Mao Q, and Zhang T. Long-Range Correlations in Remotely Sensed Chlorophyll in the South China Sea. *Chin Sci Bull* (2006) 51:45–9. doi:10.1007/s11434-006-9045-7
- Feuerverger A, Hall P, and Wood ATA. Estimation of Fractal Index and Fractal Dimension of a Gaussian Process by Counting the Number of Level Crossings. *J Time Ser Anal* (1994) 15:587–606. doi:10.1111/j.1467-9892.1994.tb00214.x
- Gneiting T, Ševčíková H, and Percival DB. Estimators of Fractal Dimension: Assessing the Roughness of Time Series and Spatial Data. *Stat Sci* (2012) 27: 247–77. doi:10.1214/11-sts370
- Kent JT, and Wood ATA. Estimating the Fractal Dimension of a Locally Self-Similar Gaussian Process by Using Increments. *J R Stat Soc Ser B Methodol* (1997) 59:679–99. Available at: <https://www.jstor.org/stable/2346018>
- Rieu M, and Sposito G. Fractal Fragmentation, Soil Porosity, and Soil Water Properties: I. Theory. *Soil Sci Soc America J* (1991) 55:1231–8. doi:10.2136/sssaj1991.03615995005500050006x
- Tyler SW, and Wheatcraft SW. Fractal Scaling of Soil Particle-Size Distributions: Analysis and Limitations. *Soil Sci Soc America J* (1992) 56: 362–9. doi:10.2136/sssaj1992.03615995005600020005x
- Young IM, and Crawford JW. The Fractal Structure of Soil Aggregates: its Measurement and Interpretation. *J Soil Sci* (1991) 42:187–92. doi:10.1111/j.1365-2389.1991.tb00400.x
- Kettani H, and Gubner JA. A Novel Approach to the Estimation of the Hurst Parameter in Self-Similar Traffic. In: 27th Annual IEEE Conference on Local Computer Networks, 2002. Proceedings. LCN 2002. Presented at the 27th Annual IEEE Conference on Local Computer Networks, 2002. Proceedings. Piscataway: LCN 2002. (2002). p. 160–5.
- Li M. Generalized Fractional Gaussian Noise and its Application to Traffic Modeling. *Physica A: Stat Mech its Appl* (2021) 579:126138. doi:10.1016/j.physa.2021.126138
- Li M. Modified Multifractional Gaussian Noise and its Application. *Phys Scr* (2021) 96:125002. doi:10.1088/1402-4896/ac1cf6
- Li M. Long-Range Dependence and Self-Similarity of Teletraffic With Different Protocols at the Large Time Scale of Day in the Duration of 12 years: Autocorrelation Modeling. *Phys Scr* (2020) 95:065222. doi:10.1088/1402-4896/ab82c4
- Li M, and Li J-Y. Generalized Cauchy Model of Sea Level Fluctuations With Long-Range Dependence. *Physica A: Stat Mech its Appl* (2017) 484:309–35. doi:10.1016/j.physa.2017.04.130
- ESA. *Alfred» D4.2 - Product User Guide for v5.0 dataset.Pdf*. Plymouth: Eur. Space Agency (2020). Available from <https://docs.pml.space/share/s/okB2fOuPT7Cj2r4C5sppDg> (Accessed June 26, 2021).
- ESA. *Alfred» OC-CCl_D2.1_ATBC_OCAB_v1.0.Pdf*. Plymouth: Eur. Space Agency (2020). Available from <https://docs.pml.space/share/s/fpEzM3HNR6CmdicAnDtrA> (accessed June 26, 2021).
- Beran J. *Statistics for Long-Memory Processes*. Boca Raton: Routledge (2017). doi:10.1201/9780203738481
- Beran J. Statistical Methods for Data With Long-Range Dependence. *Stat Sci* (1992) 7:404–16. doi:10.1214/ss/1177011122
- Beran J, Feng Y, Ghosh S, and Kulik R. *Long-memory Processes*. Berlin, Heidelberg: Springer Berlin Heidelberg (2013) doi:10.1007/978-3-642-35512-7
- Hurst HE. Long-Term Storage Capacity of Reservoirs. *T Am Soc Civ Eng* (1951) 116:770–99. doi:10.1061/taceat.0006518
- Crovella ME, and Bestavros A. Self-Similarity in World Wide Web Traffic: Evidence and Possible Causes. *Ieee/acm Trans Networking* (1997) 5:835–46. doi:10.1109/90.650143
- Hall P. On the Effect of Measuring a Self-Similar Process. *SIAM J Appl Math* (1995) 55:800–8. doi:10.1137/s0036139992236566
- Hall P, and Wood A. On the Performance of Box-Counting Estimators of Fractal Dimension. *Biometrika* (1993) 80:246–51. doi:10.1093/biomet/80.1.246
- Li M. Multi-Fractional Generalized Cauchy Process and its Application to Teletraffic. *Physica A: Stat Mech its Appl* (2020) 550:123982. doi:10.1016/j.physa.2019.123982
- Uz B, and Yoder J. High Frequency and Mesoscale Variability in SeaWiFS Chlorophyll Imagery and its Relation to Other Remotely Sensed Oceanographic Variables. *Deep Sea Res Part Topical Stud Oceanography* (2004) 51:1001–17. doi:10.1016/s0967-0645(04)00097-9
- Feng J, Durant JM, Stige LC, Hessen DO, Hjermann DØ, Zhu L, et al. Contrasting Correlation Patterns Between Environmental Factors and Chlorophyll Levels in the Global Ocean. *Glob Biogeochem. Cycles* (2015) 29:2095–107. doi:10.1002/2015gb005216
- Li M. Fractal Time Series-A Tutorial Review. *Math Probl Eng* (2010) 2010: 1–26. doi:10.1155/2010/157264
- Liu H, Song W, and Zio E. Generalized Cauchy Difference Iterative Forecasting Model for Wind Speed Based on Fractal Time Series. *Nonlinear Dyn* (2021) 103:759–73. doi:10.1007/s11071-020-06150-z

43. Malkin SY, Silsbe GM, Smith REH, and Howell ET. A Deep Chlorophyll Maximum Nourishes Benthic Filter Feeders in the Coastal Zone of a Large Clear lake. *Limnol Oceanogr* (2012) 57:735–48. doi:10.4319/lo.2012.57.3.0735
44. Dodds WK. Nutrients and the “Dead Zone”: the Link Between Nutrient Ratios and Dissolved Oxygen in the Northern Gulf of Mexico. *Front Ecol Environ* (2006) 4:211–7. doi:10.1890/1540-9295(2006)004[0211:natdzt]2.0.co;2
45. He J, Christakos G, Wu J, Li M, and Leng J. Spatiotemporal BME Characterization and Mapping of Sea Surface Chlorophyll in Chesapeake Bay (USA) Using Auxiliary Sea Surface Temperature Data. *Sci Total Environ* (2021) 794:148670. doi:10.1016/j.scitotenv.2021.148670
46. Lee HS, and Lee JHW. Continuous Monitoring of Short Term Dissolved Oxygen and Algal Dynamics. *Water Res* (1995) 29:2789–96. doi:10.1016/0043-1354(95)00126-6
47. Rhee G-Y. Effects of N:P Atomic Ratios and Nitrate Limitation on Algal Growth, Cell Composition, and Nitrate Uptake 1. *Limnol Oceanogr* (1978) 23: 10–25. doi:10.4319/lo.1978.23.1.0010
48. Singh SP, and Singh P. Effect of Temperature and Light on the Growth of Algae Species: A Review. *Renew Sustainable Energ Rev* (2015) 50:431–44. doi:10.1016/j.rser.2015.05.024
49. Robles-Tamayo CM, García-Morales R, Valdez-Holguín JE, Figueroa-Preciado G, Herrera-Cervantes H, López-Martínez J, et al. Chlorophyll a Concentration Distribution on the Mainland Coast of the Gulf of California, Mexico. *Remote Sensing* (2020) 12:1335. doi:10.3390/rs12081335
50. Damar A, Prismayanti AD, Rudianto BY, Ramli A, and Kurniawan F. Algae Bloom Phenomenon in Jakarta Bay as Symptoms of Severe Eutrophication: Monitoring Results of 2014–2016. *IOP Conf Ser Earth Environ Sci* (2021) 744: 012009. doi:10.1088/1755-1315/744/1/012009
51. Butterwick C, Heaney SI, and Talling JF. Diversity in the Influence of Temperature on the Growth Rates of Freshwater Algae, and its Ecological Relevance. *Freshw Biol* (2005) 50:291–300. doi:10.1111/j.1365-2427.2004.01317.x
52. Righetti D, Vogt M, Gruber N, Psomas A, and Zimmermann NE. Global Pattern of Phytoplankton Diversity Driven by Temperature and Environmental Variability. *Sci Adv* (2019) 5:eau6253. doi:10.1126/sciadv.aau6253
53. Chou W-R, Fang L-S, Wang W-H, and Tew KS. Environmental Influence on Coastal Phytoplankton and Zooplankton Diversity: a Multivariate Statistical Model Analysis. *Environ Monit Assess* (2012) 184:5679–88. doi:10.1007/s10661-011-2373-3
54. Fernandes LDd. A, Quintanilha J, Monteiro-Ribas W, Gonzalez-Rodriguez E, and Coutinho R. Seasonal and Interannual Coupling Between Sea Surface Temperature, Phytoplankton and Meroplankton in the Subtropical South-Western Atlantic Ocean. *J Plankton Res* (2012) 34:236–44. doi:10.1093/plankt/fbr106
55. George JA, Lonsdale DJ, Merlo LR, and Gobler CJ. The Interactive Roles of Temperature, Nutrients, and Zooplankton Grazing in Controlling the winter-spring Phytoplankton Bloom in a Temperate, Coastal Ecosystem, Long Island Sound. *Limnol Oceanogr* (2015) 60:110–26. doi:10.1002/lno.10020
56. Messié M, and Chavez FP. Nutrient Supply, Surface Currents, and Plankton Dynamics Predict Zooplankton Hotspots in Coastal Upwelling Systems. *Geophys Res Lett* (2017) 44:8979–86. doi:10.1002/2017gl074322
57. Walter RK, Armenta KJ, Shearer B, Robbins I, and Steinbeck J. Coastal Upwelling Seasonality and Variability of Temperature and Chlorophyll in a Small Coastal Embayment. *Continental Shelf Res* (2018) 154:9–18. doi:10.1016/j.csr.2018.01.002
58. Escalante-Almazán F. Temporal and Spatial Variation of Sea Surface Temperature, Chlorophyll a, and Primary Productivity in the Gulf of California. *CiencMar* (2013) 39:203–15. doi:10.7773/cm.v39i2.2233
59. Christakos G. *Spatiotemporal Random fields: Theory and Applications*. Amsterdam: Elsevier (2017).
60. He J, and Kolovos A. Bayesian Maximum Entropy Approach and its Applications: a Review. *Stoch Environ Res Risk Assess* (2018) 32:859–77. doi:10.1007/s00477-017-1419-7
61. Wu J, He J, and Christakos G. *Quantitative Analysis and Modeling of Earth and Environmental Data*. Amsterdam: Elsevier (2021). In press.
62. Heydari MH, Mahmoudi MR, Shakiba A, and Avazzadeh Z. Chebyshev Cardinal Wavelets and Their Application in Solving Nonlinear Stochastic Differential Equations With Fractional Brownian Motion. *Commun Nonlinear Sci Numer Simulation* (2018) 64:98–121. doi:10.1016/j.cnsns.2018.04.018
63. Heydari MH, Avazzadeh Z, and Mahmoudi MR. Chebyshev Cardinal Wavelets for Nonlinear Stochastic Differential Equations Driven With Variable-Order Fractional Brownian Motion. *Chaos, Solitons & Fractals* (2019) 124:105–24. doi:10.1016/j.chaos.2019.04.040

Conflict of Interest: The author declares that the research was conducted in the absence of any commercial or financial relationships that could be construed as a potential conflict of interest.

Publisher’s Note: All claims expressed in this article are solely those of the authors and do not necessarily represent those of their affiliated organizations, or those of the publisher, the editors and the reviewers. Any product that may be evaluated in this article, or claim that may be made by its manufacturer, is not guaranteed or endorsed by the publisher.

Copyright © 2021 He. This is an open-access article distributed under the terms of the Creative Commons Attribution License (CC BY). The use, distribution or reproduction in other forums is permitted, provided the original author(s) and the copyright owner(s) are credited and that the original publication in this journal is cited, in accordance with accepted academic practice. No use, distribution or reproduction is permitted which does not comply with these terms.



Stability of Hybrid SDEs Driven by fBm

Wenyi Pei^{1,2,3*} and Zhenzhong Zhang⁴

¹School of Statistics and Mathematics, Zhejiang Gongshang University, Hangzhou, China, ²Collaborative Innovation Center of Statistical Data Engineering, Technology and Application, Zhejiang Gongshang University, Hangzhou, China, ³College of Information Science and Technology, Donghua University, Shanghai, China, ⁴Department of Statistics, Donghua University, Shanghai, China

In this paper, the exponential stability of stochastic differential equations driven by multiplicative fractional Brownian motion (fBm) with Markovian switching is investigated. The quasi-linear cases with the Hurst parameter $H \in (1/2, 1)$ and linear cases with $H \in (0, 1/2)$ and $H \in (1/2, 1)$ are all studied in this work. An example is presented as a demonstration.

Keywords: stochastic differential equation (SDEs), stability, fractional brownian motion, markovian switching, hybrid system

1 INTRODUCTION

In the natural world, it is a common phenomena that many practical systems may face random abrupt changes in their structures and parameters, such as environmental variance, changing of subsystem interconnections and so on. To deal with these abrupt changes, Markovian switching systems, a particular class of hybrid systems, are investigated and widely used [1, 2]. Especially in signal processing, financial engineering, queueing networks, wireless communications and so on (see, e.g. [1, 3]).

In recent years, much attention has been paid to the stability of stochastic hybrid systems. For example, Mao [4] considers the exponential stability of general nonlinear stochastic hybrid systems. In [5], the criteria of moment exponential stability are obtained for stochastic hybrid delayed systems with Lévy noise in mean square. Zhou [6] investigates the p th moment exponential stability of the same systems. Some sufficient conditions for asymptotic stability in distribution of SDEs with Markovian switching are reported in [7]. See also [8, 9] for more results about Markovian switching.

On the other hand, it is generally known that if $H \in (0, 1/2)$ and $H \in (1/2, 1)$, $\{B_t^H\}_{t \geq 0}$ has a long range dependence, which means if we put

$$r(n) = \text{cov}(B_1^H, (B_{n+1}^H - B_n^H)),$$

then $\sum_{n=1}^{\infty} r(n) = \infty$. Besides, the process $\{B_t^H\}_{t \geq 0}$ is also self-similar for any $H \in (0, 1)$. Since the pioneering work of Hurst [10, 11] and Mandelbrot [12], the fractional Brownian motion has been suggested as a useful tool in many fields such as mathematical finance [13, 14] and weather derivatives [15]. Even though fractional Brownian motion is not a semimartingale, more and more financial models have been extended to fBm (see, e.g. [16, 17]). Therefore, in this paper, the risk assets are described by hybrid stochastic systems driven by multiplicative fBm. Then it is a natural and interesting question that under what conditions, this stochastic systems have some exponential stability. For the sake of clarity, we only consider the one dimensional cases. For more details about fractional noise, we refer the reader to [18–21].

The main purpose of this paper is to discuss the exponential stability of a risky asset, with price dynamics:

$$\begin{cases} dX_t = f(X_t, t, r_t)dt + g(X_t, t, r_t)dB_t^H, \\ X_0 = x_0 > 0, \end{cases} \quad (1)$$

where $g(X_t, t, r_t) = \sigma(t, r_t)X_t$, $\{r_t\}_{t \geq 0}$ is a Markov chain taking values in $\mathbb{S} = \{1, 2, \dots, N\}$, $\{B_t^H\}_{t \geq 0}$ is a standard fractional Brownian motion. Moreover, $f(x, t, r_t): \mathbb{R} \times \mathbb{R}_+ \times \mathbb{S} \rightarrow \mathbb{R}$ and $\sigma(t, r_t): \mathbb{R}_+ \times \mathbb{S} \rightarrow \mathbb{R}$.

OPEN ACCESS

Edited by:

Ming Li,
Zhejiang University, China

Reviewed by:

Xichao Sun,
Bengbu University, China
Yaosheng Hu,
University of Alberta, Canada

*Correspondence:

Wenyi Pei
peiwenyi@163.com

Specialty section:

This article was submitted to
Interdisciplinary Physics,
a section of the journal
Frontiers in Physics

Received: 26 September 2021

Accepted: 13 October 2021

Published: 02 November 2021

Citation:

Pei W and Zhang Z (2021) Stability of
Hybrid SDEs Driven by fBm.
Front. Phys. 9:783434.
doi: 10.3389/fphy.2021.783434

In this paper, the initial value x_0 is assumed to be deterministic, otherwise more calculations about Wick product are required.

Equation 1 can be regarded as the result of the following N fractional stochastic differential equations:

$$\begin{cases} dX_t = f(X_t, t, i)dt + g(X_t, t, i)dB_t^H, & 1 \leq i \leq N, \\ X_0 = x_0 > 0, \end{cases}$$

switching from one to another according to the movement of $\{r_t\}_{t \geq 0}$.

Throughout this paper, unless otherwise specified, we let C denote a general constant and p denote a non-negative constant. Let $C^{2,1}(\mathbb{R} \times \mathbb{R}_+ \times \mathbb{S}; \mathbb{R})$ denote the family of all real value functions on $\mathbb{R} \times \mathbb{R}_+ \times \mathbb{S}$ which are continuously twice differentiable with respect to the first variables and once differentiable with respect to the second variables.

This paper is organized as follows. For the convenience of the reader, we briefly recall some of the basic results in **Section 2**. In **Section 3**, we investigate the solution and an extended Itô's Formula for the general hybrid fractional stochastic differential **Equation 1**. **Section 3** is devoted to the linear cases. In this section the moment exponential stability and almost sure exponential stability are discussed respectively. In **Section 4**, some useful criteria for the exponential stability with respect to quasi-linear cases are presented. Finally, a numerical example and graphical illustration are presented in **Section 6**.

2 PRELIMINARIES

2.1 Markov Chain

Let $\{r_t\}_{t \geq 0}$ be a right-continuous Markov chain taking values in a finite state space $\mathbb{S} = \{1, 2, \dots, N\}$. The generator $Q = (q_{ij})_{N \times N}$ is given by

$$\mathbb{P}\{r_{t+\Delta} = j \mid r_t = i\} = \begin{cases} q_{ij}\Delta + o(\Delta), & \text{if } i \neq j, \\ 1 + q_{ii}\Delta + o(\Delta), & \text{if } i = j, \end{cases}$$

where $\Delta > 0$.

Here q_{ij} is the transition rate from i to j if $i \neq j$. According to [22, 23], a continuous-time Markov chain $\{r_t\}_{t \geq 0}$ with generator $Q = (q_{ij})_{N \times N}$ can be represented as a stochastic integral with respect to a Poisson random measure. Then we have

$$dr_t = \int_{\mathbb{R}} h(r_{t-}, y) \nu(dt \times dy),$$

with initial condition $r_0 = i_0$, where $\nu(dt \times dy)$ is a Poisson random measure with intensity $dt \times m(dy)$. Here $m(\cdot)$ is the Lebesgue measure on \mathbb{R} .

Throughout this paper, unless otherwise specified, the Markov chain $\{r_t\}_{t \geq 0}$ has the invariant probability measure $\mu = (\mu_i)_{i \in \mathbb{S}}$ and is assumed to be independent of $\{B_t^H\}_{t \geq 0}$. Almost every sample path of the Markov chain $\{r_t\}_{t \geq 0}$ is assumed to be a right-continuous step function with a finite number of simple jumps in any finite time interval $[0, T]$. The generator $Q = (q_{ij})_{N \times N}$ is assumed to be irreducible and conservative, i.e., $q_i := -q_{ii} = \sum_{i \neq j} q_{ij} < \infty$. For more details about Markovian switching we further refer the reader to [24–26].

2.2 Fractional Brownian Motion and Wick Product

We recall some of the basic results of fBm briefly, which will be needed throughout this paper. For more details about fBm we refer the reader to [16, 17, 27, 28]. If $H \in (0, 1/2) \cup (1/2, 1)$, then the (standard) fractional Brownian motion with Hurst parameter H is a continuous centered Gaussian process $\{B_t^H\}_{t \geq 0}$ with $\mathbb{E}(B_t^H) = 0$ and covariance function:

$$\mathbb{R}^H(s, t) = \mathbb{E}(B_s^H B_t^H) = \frac{1}{2}(|s|^{2H} + |t|^{2H} - |s - t|^{2H}), \quad s, t \geq 0.$$

To simplify the representation, it is always assumed that $B_0^H = 0$.

Besides, $\{B_t^H\}_{t \geq 0}$ has the following Wiener integral representation:

$$B_t^H = \int_0^t K^H(t, s) dW_s,$$

where $\{W_t\}_{t \geq 0}$ is a Wiener process and $K^H(t, s)$ is the kernel function defined by

$$K_H(t, s) = c_H s^{\frac{1}{2}-H} \int_0^t (u - s)^{H-\frac{3}{2}} u^{H-\frac{1}{2}} du,$$

in which $c_H = (\frac{H(2H-1)}{B(2-2H, H-\frac{1}{2})})^{\frac{1}{2}}$, where $B(\cdot, \cdot)$ is the Beta function, and $s < t$. In this paper, $\{B_t^H\}_{t \geq 0}$ generates a filtration $\{\mathcal{F}_t, t \geq 0\}$ with $\mathcal{F}_t = \sigma\{B_s^H, s \leq t\}$. Denote $(\Omega, \mathcal{F}, P, \mathcal{F}_t)$ the complete probability space, with the filtration described above.

Let \mathcal{I} be the set of all finite multi-indices $\alpha = (\alpha_1, \dots, \alpha_n)$ for some $n \geq 1$ of non-negative integers. Denote $|\alpha| = \alpha_1 + \dots + \alpha_n$ and $\alpha! = \alpha_1! \cdots \alpha_n!$.

Define the Hermite polynomials:

$$h_n(x) = (-1)^n e^{x^2} \frac{d^n}{dx^n} (e^{-x^2}), \quad n \geq 0,$$

and Hermite functions:

$$\tilde{h}_n(x) = \pi^{-\frac{1}{4}} (n!)^{-\frac{1}{2}} h_n(x) e^{-\frac{x^2}{2}}, \quad n \geq 0.$$

Let $S(\mathbb{R})$ denote the Schwartz space of rapidly decreasing infinitely differentiable \mathbb{R} -valued functions. Denote the dual space of $S(\mathbb{R})$ by $S'(\mathbb{R})$. Define

$$\mathcal{H}_\alpha(\omega) = \prod_{i=1}^n h_{\alpha_i}(\langle \tilde{h}_i(x), \omega \rangle),$$

the product of Hermite polynomials. Consider a square integrable random variable

$$F = F(\omega) \in L^2(S'(\mathbb{R}), \mathcal{F}, P).$$

According to [17, 29], every $F(\omega)$ has a unique representation:

$$F(\omega) = \sum_{\alpha \in \mathcal{I}} c_\alpha \mathcal{H}_\alpha(\omega),$$

besides,

$$\|F\|_{L^2(\omega)}^2 = \sum_{\alpha \in \mathcal{I}} \alpha! c_\alpha^2 < \infty.$$

Definition 2.1. (Wick Product) For $F, G \in L^2(S'(\mathbb{R}), \mathcal{F}, P)$, set $F(\omega) = \sum_{\alpha \in \mathcal{I}} c_\alpha \mathcal{H}_\alpha(\omega)$ and $G(\omega) = \sum_{\beta \in \mathcal{I}} d_\beta \mathcal{H}_\beta(\omega)$. Their Wick product is defined by

$$\begin{aligned} F \diamond G(\omega) &= \sum_{\alpha, \beta \in \mathcal{I}} a_\alpha b_\beta \mathcal{H}_{\alpha+\beta}(\omega) \\ &= \sum_{\gamma \in \mathcal{I}} \left(\sum_{\alpha+\beta=\gamma} a_\alpha b_\beta \right) \mathcal{H}_\gamma(\omega). \end{aligned}$$

2.3 Malliavin Derivative

Let $L^p := L^p(\Omega, \mathcal{F}, P)$ be the space of all random variables $\Omega \rightarrow \mathbb{R}$, such that

$$\|F\|_p = \mathbb{E}(|F|^p)^{1/p} < \infty,$$

and let

$$L^2_\phi(\mathbb{R}_+) = \left\{ f | f: \mathbb{R}_+ \rightarrow \mathbb{R}, |f|_\phi^2 := \int_0^\infty \int_0^\infty f(s) f(t) \phi(s, t) ds dt < \infty \right\},$$

where $\phi(s, t) = H(2H - 1)|s - t|^{2H-2}$.

Definition 2.2. The ϕ -derivative of $F \in L^p$ in the direction of Φ_g is defined by

$$D_{\Phi_g} F(\omega) = \lim_{\delta \rightarrow 0} \frac{1}{\delta} \left\{ F\left(\omega + \delta \int_0^\infty (\Phi_g)(u) du\right) - F(\omega) \right\},$$

if the limit exists in L^p . Moreover if there exists a process $(D_s^\phi F_s, s \geq 0)$ such that

$$D_{\Phi_g} F = \int_0^\infty D_s^\phi F_s g_s ds \quad a.s.,$$

for all $g \in L^2_\phi$, then F is said to be ϕ -differentiable.

According to [16, 30], let $\mathcal{A}(0, T)$ be the family of stochastic process on $[0, T]$ such that $F \in \mathcal{A}(0, T)$ if $\mathbb{E}|F|_\phi^2 < \infty$ and F is ϕ -differentiable, the trace of $(D_s^\phi F_t, 0 \leq s \leq T, 0 \leq t \leq T)$ exists and $\mathbb{E} \int_0^T (D_s^\phi F_s)^2 ds < \infty$, and for each sequence of partitions $\pi_n, n \in \mathbb{N}$ such that $|\pi_n| \rightarrow 0$, as $n \rightarrow \infty$. Moreover

$$\sum_{i=0}^{n-1} \mathbb{E} \left\{ \int_{t_i^{(n)}}^{t_{i+1}^{(n)}} |D_s^\phi F_{t_i^{(n)}}^\pi - D_s^\phi F_s| ds \right\}^2 \rightarrow 0,$$

and

$$\mathbb{E}|F^\pi - F|_\phi^2 \rightarrow 0,$$

as $n \rightarrow \infty$. Here $\pi_n: 0 = t_0^{(n)} < t_1^{(n)} < \dots < t_n^{(n)} = T$, and $|\pi_n| = \max_{i \in \{0, 1, \dots, n-1\}} \{t_{i+1}^{(n)} - t_i^{(n)}\}$.

Now we define the B_t^H -integral considered in [16].

Definition 2.3. Let $\{F_t\}_{t \geq 0}$ be a stochastic process such that $F \in \mathcal{A}(0, T)$. Define $\int_0^T F_s dB_s^H$ by

$$\int_0^T F_s dB_s^H = \lim_{|\pi| \rightarrow 0} \sum_{i=0}^{n-1} F_{t_i}^\pi \diamond (B_{t_{i+1}}^H - B_{t_i}^H),$$

where $|\pi| = \max_{i \in \{0, 1, \dots, n-1\}} \{t_{i+1} - t_i\}$.

Remark 2.1. : According to Theorem 3.6.1 in [16], if $F_s \in \mathcal{A}(0, T)$, then the stochastic integral satisfies $\mathbb{E} \int_0^T F_s dB_s^H = 0$, and

$$\mathbb{E} \left| \int_0^T F_s dB_s^H \right|^2 = \mathbb{E} \left[\left(\int_0^T D_s^\phi F_s ds \right)^2 + |1_{[0, T]} F|_\phi^2 \right]$$

What's more, according to Definition 3.4.1 in [16], the stochastic integral can be extended by

$$\int_{\mathbb{R}} F_t dB_t^H := \int_{\mathbb{R}} F_t \diamond W^H(t) dt,$$

where $F: \mathbb{R} \rightarrow (S)_H^*$ is a given function such that $F_t \diamond W^H(t)$ is dt -integrable in $(S)_H^*$. Here $(S)_H^*$ is the fractional Hida distribution space defined by Definition 3.1.11 in [16]. In particular, the integral on $[0, T]$ can be defined by

$$\int_0^T F_t dB_t^H = \int_{\mathbb{R}} F_t I_{[0, T]}(t) dB_t^H.$$

3 HYBRID FRACTIONAL SYSTEMS

In this section, firstly, we consider the existence and uniqueness of solution for Eq. 1. Then, an extended Itô's Formula is presented.

3.1 Existence and Uniqueness

To ensure the existence and uniqueness, we impose the following assumptions.

Assumption 3.1. Let $f = f(x, t, i): \mathbb{R} \times \mathbb{R}_+ \times \mathbb{S} \rightarrow \mathbb{R}$ satisfy the hypotheses:

- 1) For each fixed $i \in \mathbb{S}$, $f(x, t, i)$ is measurable in all the arguments.
- 2) For each fixed $i \in \mathbb{S}$, there exists a constant $C > 0$, such that $|f(x, t, i) - f(y, t, i)| \leq C|x - y|$, $\forall x, y \in \mathbb{R}$, $\forall t \in \mathbb{R}_+$.
- 3) For each fixed $i \in \mathbb{S}$, there exists a constant $C > 0$, such that

$$|f(x, t, i)| \leq C(1 + |x|), \quad \forall (x, t) \in \mathbb{R} \times \mathbb{R}_+.$$

Assumption 3.2. Let $\sigma = \sigma(t, i): \mathbb{R}_+ \times \mathbb{S} \rightarrow \mathbb{R}$ satisfy the hypotheses:

- 1) For each fixed $i \in \mathbb{S}$, $\sigma(t, i)$ is nonrandom;
- 2) For each fixed $i \in \mathbb{S}$, $\sigma(t, i) \in L^{\frac{1}{H}}(\mathbb{R}_+)$.

Lemma 3.1. : Let Assumptions 3.1, 3.2 hold. Then Eq. 1 has a unique solution.

Proof: The existence and uniqueness can be proved similar to that for Theorem 2.6 in [31], so we omit it here.

3.2 The Itô Formula

Next, we first review the results in [16, 30] on the Itô formula with respect to fBm. Then we extend it to SDEs driven by fBm with Markovian switching.

Lemma 3.2. [16] (The Itô Formula) Let $(F_u, 0 \leq u \leq T)$ be a stochastic process in $\mathcal{A}(0, T)$. Assume that there exists an $\alpha > 1 - H$ and $C > 0$ such that

$$\mathbb{E}|F_u - F_v|^2 \leq C|u - v|^{2\alpha},$$

where $|u - v| \leq \delta$ for some $\delta > 0$ and

$$\lim_{0 \leq u, v \leq t, |u-v| \rightarrow 0} \mathbb{E}|D_u^\phi(F_u - F_v)|^2 = 0.$$

Let $\sup_{0 \leq s \leq T} |G_s| < \infty$ and $\tilde{g} = \tilde{g}(x, t) \in C^{2,1}(\mathbb{R} \times \mathbb{R}_+; \mathbb{R})$ with bounded derivatives. Moreover, for $\eta_t = \int_0^t F_u dB_u^H$, it is assumed that $\mathbb{E} \int_0^T |F_s D_s^\phi \eta_s| ds < \infty$ and $(\frac{\partial \tilde{g}}{\partial x}(s, \eta_s) F_s, s \in [0, T])$ is in $\mathcal{A}(0, T)$. Denote $x_t = x_0 + \int_0^t G_u du + \int_0^t F_u dB_u^H$, $x_0 \in \mathbb{R}$ for $t \in [0, T]$. Let $(\frac{\partial \tilde{g}}{\partial x}(x_s, s) F_s, s \in [0, T]) \in \mathcal{A}(0, T)$, $\mathbb{E}[\sup_{0 \leq s \leq t} |G_s|] < \infty$. Then for $t \in [0, T]$,

$$\begin{aligned} \tilde{g}(x_t, t) &= \tilde{g}(x_0, 0) + \int_0^t \frac{\partial \tilde{g}}{\partial s}(x_s, s) ds + \int_0^t \frac{\partial \tilde{g}}{\partial x}(x_s, s) G_s ds \\ &\quad + \int_0^t \frac{\partial \tilde{g}}{\partial x}(x_s, s) F_s dB_s^H + \int_0^t \frac{\partial^2 \tilde{g}}{\partial x^2}(x_s, s) F_s D_s^\phi x_s ds. \end{aligned}$$

Here $D_s^\phi x_s$ is the Malliavin derivative defined in **Definition 2.2**.

In particular, for the process $X_t^{(i)} = X_0^{(i)} + \int_0^t f(X_s^{(i)}, s, i) ds + \int_0^t g(X_s^{(i)}, s, i) dB_s^H$, with each fixed $i \in \mathbb{S}$, we have that

$$\begin{aligned} F(X_t^{(i)}, t, i) &= F(X_0^{(i)}, 0, i) + \int_0^t \frac{\partial F}{\partial s}(X_s^{(i)}, s, i) ds \\ &\quad + \int_0^t \frac{\partial F}{\partial x}(X_s^{(i)}, s, i) f(X_s^{(i)}, s, i) ds + \int_0^t \frac{\partial F}{\partial x}(X_s^{(i)}, s, i) g(X_s^{(i)}, s, i) dB_s^H \\ &\quad + \int_0^t \frac{\partial^2 F}{\partial x^2}(X_s^{(i)}, s, i) g(X_s^{(i)}, s, i) D_s^\phi X_s^{(i)} ds, \end{aligned} \quad (2)$$

Formally,

$$\begin{aligned} dF(X_t^{(i)}, t, i) &= F_t(X_t^{(i)}, t, i) dt + F_{xx}(X_t^{(i)}, t, i) g(X_t^{(i)}, t, i) D_s^\phi X_s^{(i)} dt \\ &\quad + F_x(X_t^{(i)}, t, i) f(X_t^{(i)}, t, i) dt + F_x(X_t^{(i)}, t, i) g(X_t^{(i)}, t, i) dB_t^H, \end{aligned}$$

Let

$$\begin{aligned} \mathcal{L}^{(i)} F(X_t^{(i)}, t, i) &= F_t(X_t^{(i)}, t, i) + F_x(X_t^{(i)}, t, i) f(X_t^{(i)}, t, i) \\ &\quad + F_{xx}(X_t^{(i)}, t, i) g(X_t^{(i)}, t, i) D_s^\phi X_s^{(i)}. \end{aligned} \quad (3)$$

Substituting **Eq. 3** into **Eq. 2**, we get

$$\begin{aligned} F(X_t^{(i)}, t, i) &= F(X_0^{(i)}, 0, i) + \int_0^t \mathcal{L}^{(i)} F(X_s^{(i)}, s, i) ds \\ &\quad + \int_0^t F_x(X_s^{(i)}, s, i) g(X_s^{(i)}, s, i) dB_s^H. \end{aligned} \quad (4)$$

In the sequel of this paper, unless otherwise specified, we let the coefficients of **Eq. 1** satisfy the conditions in **Lemma 3.2**, for each fixed $i \in \mathbb{S}$. Set $V(X_t, t, r_t) \in C^{2,1}(\mathbb{R} \times \mathbb{R}_+ \times \mathbb{S}; \mathbb{R}_+)$. Next we consider the Itô formula which reveals how V maps (X_t, t, r_t) into a new process $V(X_t, t, r_t)$, where $\{X_t\}_{t \geq 0}$ is a stochastic process with the stochastic differential **Eq. 1**.

Lemma 3.3. If $V(X_t, t, r_t) \in C^{2,1}(\mathbb{R} \times \mathbb{R}_+ \times \mathbb{S}; \mathbb{R}_+)$, then for any $0 \leq s < t$,

$$\begin{aligned} \mathbb{E}V(X_t, t, r_t) &= \mathbb{E}V(X_s, s, r_s) + \mathbb{E} \int_s^t \mathcal{A}V(X_u, u, r_u) du \\ &\quad + \mathbb{E} \int_s^t V_x(X_u, u, r_u) g(X_u, u, r_u) dB_u^H \end{aligned} \quad (5)$$

where $\mathcal{A}V$ is defined by

$$\mathcal{A}V(x, t, i) = \mathcal{L}^{(i)} V(x, t, i) + \sum_{j=1}^N \gamma_{ij} V(x, t, j).$$

Proof: This result can be obtained similarly to that in [31] and we therefore omit it. For further details we also refer to [2, 23].

4 LINEAR HYBRID FRACTIONAL SYSTEMS

There are many models for financial markets with fBm (see, e.g. [16]). The simplest nontrivial type of market is the fBm version of the classical Black Scholes market, in which linear fractional SDEs is used. Thus, we would like to give some new criteria for switching linear fractional SDEs with $H \in (0, \frac{1}{2})$ or $H \in (\frac{1}{2}, 1)$. At first, we present a definition and a useful lemma.

Definition 4.1. Let $H \in (0, 1)$. The operator M is defined on functions $f \in S(\mathbb{R})$ by

$$Mf(x) = -\frac{d}{dx} \frac{C_H}{(H-1/2)} \int_{\mathbb{R}} (t-s)|t-x|^{H-\frac{3}{2}} f(t) dt \quad (6)$$

where

$$\begin{aligned} C_H &= \left\{ 2\Gamma\left(H - \frac{1}{2}\right) \cos\left[\frac{\pi}{2}\left(H - \frac{1}{2}\right)\right] \right\}^{-1} \\ &\quad [\Gamma(2H+1) \sin(\pi H)]^{\frac{1}{2}}. \end{aligned}$$

Here $\Gamma(\cdot)$ denotes the classical Gamma function.

According to [16], **Eq. 6** can be restated as follows.

For $H \in (0, 1/2)$, we have

$$Mf(x) = C_H \int_{\mathbb{R}} \frac{f(x-t) - f(x)}{|t|^{3/2-H}} dt.$$

For $H = 1/2$, we have

$$Mf(x) = f(x).$$

For $H \in (1/2, 1)$, we have

$$Mf(x) = C_H \int_{\mathbb{R}} \frac{f(t)}{|t-x|^{3/2-H}} dt.$$

Lemma 4.1. Let $\{r_t\}_{t \geq 0}$ be a right-continuous Markov chain which takes values in a finite state space $\mathbb{S} = \{1, 2, \dots, N\}$. Assume that it is irreducible and positive recurrent with invariant measure μ . If $\alpha(\cdot): \mathbb{S} \rightarrow \mathbb{R}$ is a function verifying

$$\alpha := \sum_{i \in \mathbb{S}} \mu(i) \alpha(i) > 0.$$

Then there exists constants $C, c > 0$ such that:

$$ce^{-\alpha t} \leq \mathbb{E} \left[e^{-\int_0^t \alpha(r_s) ds} \right] \leq Ce^{-\alpha t},$$

for any initial condition r_0 and every $t \geq 0$.

Proof: It is a consequence of Perron-Frobenius theorem and the study of eigenvalues. See Proposition 4.1 in [25], Proposition 4.2 in [25], and Lemma 2.7 in [26], for further details.

In **Eq. 1**, let us consider the case $g(x, t, r_t) = \sigma(t, r_t)x = t^h b(r_t)x$, $f(x, t, r_t) = \alpha(r_t)x$, where $\alpha(i)$ and $b(i)$ are constants for each $i \in \mathbb{S}$. This means that we are considering the following linear equation:

$$\begin{cases} dX_t = \alpha(r_t)X_t dt + \sigma(t, r_t)X_t dB_t^H, \\ X_0 = x_0. \end{cases} \quad (7)$$

Set $\bar{b} = \max\{|b(i)|, i \in \mathbb{S}\}$ and $\underline{b} = \min\{|b(i)|, i \in \mathbb{S}\}$. x_0 is the deterministic initial value. For the sake of clarity, we firstly set $h = 1/2 - H$.

4.1 p th Moment Exponential Stability

Theorem 4.1. Let $\{X_t\}_{t \geq 0}$ be the solution of **Eq. 7** with $H \in (1/2, 1)$, $h = 1/2 - H$.

- 1) If $\sum_{i \in \mathbb{S}} \mu_i \alpha(i) - \frac{(1-p)\bar{b}^2}{2} < 0$, then $\limsup_{t \rightarrow \infty} \frac{1}{t} \log(\mathbb{E}|X_t|^p) < 0$.
- 2) If $\sum_{i \in \mathbb{S}} \mu_i \alpha(i) - \frac{(1-p)\bar{b}^2}{2} > 0$, then $\lim_{t \rightarrow \infty} \mathbb{E}|X_t|^p = \infty$.

Proof. According to [16], without too many calculations, we obtain that $\{X_t\}_{t \geq 0}$ has the following form:

$$X_t = x_0 \exp \left[\int_0^t \sigma(r_s) dB_s^H + \int_0^t \alpha(r_s) ds - \frac{1}{2} \int_{\mathbb{R}} (M_s(\sigma(t, r_s) I_{[0,t]}(s)))^2 ds \right], \quad (8)$$

where M_s is the operator M acting on the variable s . Let $x_0 \neq 0$. It follows from **Eq. 8** that

$$\begin{aligned} \mathbb{E}|X_t|^p &= \mathbb{E} \left(|x_0|^p \exp \left[\int_0^t \sigma(t, r_s) dB_s^H + \int_0^t \alpha(r_s) ds - \frac{1}{2} \int_{\mathbb{R}} (M_s(\sigma(t, r_s) I_{[0,t]}(s)))^2 ds \right] \right)^p \\ &= \mathbb{E} \left(|x_0|^p \exp \left[\int_0^t \sigma(t, r_s) dB_s^H + \int_0^t \alpha(r_s) ds - \frac{1}{2} \int_{\mathbb{R}} (M_s(\sigma(t, r_s) I_{[0,t]}(s)))^2 ds \right] \right)^p \end{aligned} \quad (9)$$

We then see from **Eq. 9** that

$$\mathbb{E}|X_t|^p = \mathbb{E} \left(\exp \left(p \left[\int_0^t \alpha(r_s) ds - \frac{1-p}{2} \int_{\mathbb{R}} (M_s(\sigma(t, r_s) I_{[0,t]}(s)))^2 ds \right] \right) \right) \zeta_t, \quad (10)$$

where

$$\begin{aligned} \zeta_t &= |x_0|^p \exp \int_0^t p \sigma(s, r_s) dB_s^H - \frac{p^2}{2} \\ &\quad \int_{\mathbb{R}} (M_s(\sigma(t, r_s) I_{[0,t]}(s)))^2 ds. \end{aligned}$$

Noting that ζ_t is the solution to the equation

$$d\zeta_t = p\sigma(t, r_t)\zeta_t dB_t^H,$$

with initial value $\zeta_0 = |x_0|^p$. Thus

$$\zeta_t = |x_0|^p + \int_0^t p\sigma(t, r_s) dB_s^H,$$

which yields

$$\mathbb{E}\zeta_t = \mathbb{E} \left[|x_0|^p + \int_0^t p\sigma(t, r_s) dB_s^H \right] = |x_0|^p. \quad (11)$$

Substituting **Eq. 11** into **Eq. 10** gives

$$\mathbb{E}|X_t|^p = \mathbb{E} \exp \left(p \left[\int_0^t \alpha(r_s) ds - \frac{1-p}{2} \int_{\mathbb{R}} (M_s(\sigma(t, r_s) I_{[0,t]}(s)))^2 ds \right] \right) |x_0|^p. \quad (12)$$

Note that

$$\begin{aligned} \int_{\mathbb{R}} (M_s(\underline{b} s^h I_{[0,t]}(s)))^2 ds &\leq \int_{\mathbb{R}} (M_s(\sigma(t, r_s) I_{[0,t]}(s)))^2 ds \\ &\leq \int_{\mathbb{R}} (M_s(\bar{b} s^h I_{[0,t]}(s)))^2 ds. \end{aligned}$$

Consequently, by **Definition 4.1** and [16], one has

$$\underline{b}^2 t \leq \int_{\mathbb{R}} (M_s(\sigma(t, r_s) I_{[0,t]}(s)))^2 ds \leq \bar{b}^2 t. \quad (13)$$

Making use of **Eqs 12, 13**, we obtain that

$$\begin{aligned} \mathbb{E} \exp \left(p \left[\int_0^t \alpha(r_s) ds - \frac{1-p}{2} \bar{b}^2 t \right] \right) |x_0|^p &\leq \mathbb{E}|X_t|^p \\ &\leq \mathbb{E} \exp \left(p \left[\int_0^t \alpha(r_s) ds - \frac{1-p}{2} \underline{b}^2 t \right] \right) |x_0|^p. \end{aligned}$$

Therefore, by **Lemma 4.1** and **Eq. 12**, the required assertions follow. The proof is complete.

Theorem 4.2. Let $\{X_t\}_{t \geq 0}$ be the solution of **Eq. 7** with $H \in (0, 1/2)$, $h = 1/2 - H$.

- 1) If $\sum_{i \in \mathbb{S}} \mu_i \alpha(i) < \frac{(1-p)\bar{b}^2}{2}$, then $\limsup_{t \rightarrow \infty} \frac{1}{t} \log(\mathbb{E}|X_t|^p) < 0$.
- 2) If $\sum_{i \in \mathbb{S}} \mu_i \alpha(i) > \frac{(1-p)\bar{b}^2}{2}$, then $\lim_{t \rightarrow \infty} \mathbb{E}|X_t|^p = \infty$.

Proof: Similar to **Theorem 4.1**, we write the solution as follows.

$$\mathbb{E}|X_t|^p = \mathbb{E} \exp \left(p \left[\int_0^t \alpha(r_s) ds + \frac{p-1}{2} \int_{\mathbb{R}} (M_s(\sigma(t, r_s) I_{[0,t]}(s)))^2 ds \right] \right) |x_0|^p. \quad (14)$$

Note that M_s is the operator M acting on the variable s , where

$$Mf(x) = C_H \int_{\mathbb{R}} \frac{f(x-t) - f(x)}{|t|^{3/2-H}} dt.$$

According to [16], we also have that

$$\underline{b}^2 t \leq \int_{\mathbb{R}} (M_s(\sigma(t, r_s) I_{[0,t]}(s)))^2 ds \leq \bar{b}^2 t. \quad (15)$$

Consequently, by **Lemma 4.1**, the result follows. The proof is complete.

Remark 4.1. In the above **Theorems 4.1, 4.2**, the parameter h is supposed to be $H - 1/2$. Noting that by **Eqs 13, 15** and together with the **Definition 4.1**, the stability of solution for

Eq. 7 with $h < 1/2 - H$ or $h > 1/2 - H$ can be deduced respectively without too many difficulties.

Remark 4.2. Take $H = 1/2$. It's easy to show that if $\sum_{i \in \mathbb{S}} \mu_i \alpha(i) = \alpha < \frac{(1-p)\sigma^2}{2}$, then $\limsup_{t \rightarrow \infty} \frac{1}{t} \log(\mathbb{E}|X_t|^p) < 0$, and if $\sum_{i \in \mathbb{S}} \mu_i \alpha(i) = \alpha > \frac{(1-p)\sigma^2}{2}$, then $\lim_{t \rightarrow \infty} \mathbb{E}|X_t|^p = \infty$, which coincide with the results of SDEs driven by Brownian motion in [4, 32].

4.2 Almost Sure Exponential Stability

To proceed, we need to introduce the definition of almost sure stability and a useful lemma.

Definition 4.2. The equilibrium point $x = 0$ is said to be almost surely exponential stable if

$$\limsup_{t \rightarrow \infty} \frac{1}{t} \log|X_t| < 0 \quad a.s.$$

for any $x_0 \in \mathbb{R}$.

Lemma 4.2. (Law of the iterated logarithm) For a standard fBm $\{B_t^H\}_{t \geq 0}$, we have that

$$\limsup_{t \rightarrow \infty} \frac{B_t^H}{t^H \sqrt{\log \log t}} = C_H, \quad (16)$$

where $C_H > 0$ is a suitable constant.

Proof: By [33], we have

$$\limsup_{t \rightarrow 0^+} \frac{B_t^H}{t^H \sqrt{\log \log t^{-1}}} = c_H,$$

where c_H is a suitable constant. Then the thesis follows by the self-similarity of fBm and a change of variable $t \rightarrow 1/t$.

For the sake of clarity, we firstly set $h = 0$. Namely, let us consider

$$\begin{cases} dX_t = \alpha(r_t)X_t dt + b(r_t)X_t dB_t^H, \\ X_0 = x_0. \end{cases} \quad (17)$$

Noting that **Eq. 17** is exactly the geometry fBm with Markovian Switching. We proceed to discuss the almost sure exponential stability about it.

Theorem 4.3. 1) If $0 < H < 1/2$, the equilibrium point $x = 0$ of the system **Eq. 17** is almost surely exponential stable when $\sum_{i \in \mathbb{S}} \mu_i \alpha(i) < 0$, but unstable when $\sum_{i \in \mathbb{S}} \mu_i \alpha(i) > 0$; 2) If $H = 1/2$, the equilibrium point $x = 0$ of the system **Eq. 17** is almost surely exponential stable when $\sum_{i \in \mathbb{S}} \mu_i \alpha(i) < \frac{1}{2}b^2$, but unstable when $\sum_{i \in \mathbb{S}} \mu_i \alpha(i) > \frac{1}{2}b^2$; 3) If $1/2 < H < 1$, the equilibrium point $x = 0$ of the system **Eq. 17** is almost surely exponential stable for all parameters $\alpha(i)$ and $\sigma(i)$, $i \in \mathbb{S}$.

Proof: Define

$$\lambda = \limsup_{t \rightarrow \infty} \frac{1}{t} \log|X_t|.$$

From **Eqs 8, 16**, we have

$$\begin{aligned} \lambda &= \limsup_{t \rightarrow \infty} \frac{1}{t} \log|X_t| \\ &= \limsup_{t \rightarrow \infty} \frac{1}{t} \log \left| x_0 \exp \left[\int_0^t \sigma(r_s) dB_s^H + \int_0^t \alpha(r_s) ds - \frac{1}{2} \int_{\mathbb{R}} (M_s(\sigma(r_s)I_{[0,t]}(s)))^2 ds \right] \right| \\ &= \lim_{t \rightarrow \infty} \left(\sum_{i \in \mathbb{S}} \mu_i \alpha(i) - \frac{1}{2t} \int_{\mathbb{R}} (M_s(\sigma(r_s)I_{[0,t]}(s)))^2 ds \right). \end{aligned}$$

By **Definition 4.1** and [16], one has

$$\underline{b}^2 t^{2H} \leq \int_{\mathbb{R}} (M_s(b(r_s)I_{[0,t]}(s)))^2 ds \leq \bar{b}^2 t^{2H}. \quad (18)$$

Making use of **Eq. 18**, we get

$$\lambda = \begin{cases} \sum_{i \in \mathbb{S}} \mu_i \alpha(i), & 0 < H < 1/2; \\ -\infty, & 1/2 < H < 1. \end{cases}$$

Especially, when $H = 1/2$, we have that

$$\sum_{i \in \mathbb{S}} \mu_i \alpha(i) - \frac{1}{2} \bar{b}^2 \leq \lambda \leq \sum_{i \in \mathbb{S}} \mu_i \alpha(i) - \frac{1}{2} \underline{b}^2.$$

Therefore, the required results follows. The proof is complete.

Remark 4.3. Making use of **Eq. 18**, one can discuss the almost sure exponential stability for **Eq. 7** with $h \neq 0$. The proofs are similar to **Theorem 4.3** and are omitted.

5 QUASI-LINEAR HYBRID FRACTIONAL SYSTEMS

We now apply the extended Itô Formula in **Section 3** to discuss the stability for quasi-linear fractional SDEs with Markovian switching.

Theorem 5.1. : Let **Assumptions 3.1, 3.2** hold. If there exists a function $V \in C^{2,1}(\mathbb{R} \times \mathbb{R}_+ \times \mathbb{S}; \mathbb{R}_+)$ and positive constants a_1, a_2, b and $p \geq 1$, such that

$$a_1 |X_t|^p \leq |V(X_t, t, i)| \leq a_2 |X_t|^p, \quad (19)$$

$$\mathcal{L}^{(i)} V(X_t, t, i) \leq -b |X_t|^p, \quad (20)$$

for all $X_t \in \mathbb{R}$, $t \geq t_0$, $i \in \mathbb{S}$.

Then the solution of **Eq. 1** is p th moment exponential stable. More precisely,

$$\limsup_{t \rightarrow \infty} \frac{1}{t} \log(\mathbb{E}|X_t|^p) < 0.$$

Proof: According to **Lemma 3.1**, **Eq. 1** has a unique solution. Denote it $\{X_t\}_{t \geq 0}$. Set

$$U(X_t, t, i) = e^{\lambda t} V(X_t, t, i),$$

where $\lambda \in (\eta, \frac{b}{a_2})$, $\eta > 0$. Making use of **Definition 2.3** and **Lemma 3.2**, one has $\mathcal{A}U = e^{\lambda t} (\lambda V + \mathcal{A}V)$ and $(U_x g, s \in [0, T]) \in \mathcal{A}(0, T)$.

Applying the conditions **Eq. 19, 20**, together with the generalized ItôEq. 5 and **Remark 2.1**, we obtain that for any $t \in [0, T]$

$$\begin{aligned} a_1 e^{\eta t} \mathbb{E}|X_t|^p &\leq \mathbb{E}U(X_t, t, i) = \mathbb{E}V(X_0, 0, r_0) + \mathbb{E} \int_0^t \mathcal{A}U ds \\ &\quad + \mathbb{E} \int_0^t U_x g B_s^H = \mathbb{E}V(X_0, 0, r_0) + \mathbb{E} \int_0^t \mathcal{L}^{(r_s)} U ds \\ &= \mathbb{E}V(X_0, 0, r_0) + \mathbb{E} \int_0^t e^{\lambda s} (\lambda V + \mathcal{A}V) ds \leq \mathbb{E}V(X_0, 0, r_0) \\ &\quad + \mathbb{E} \int_0^t e^{\lambda s} (\lambda a_2 - b) |X_t|^p ds. \end{aligned}$$

Thus we obtain that

$$a_1 e^{\eta t} \mathbb{E}|X_t|^p \leq \mathbb{E}V(X_0, 0, r_0) + \mathbb{E} \int_0^t e^{\lambda s} (\lambda a_2 - b) |X_t|^p ds. \quad (21)$$

Dividing both sides of **Eq. 21** by $a_1 e^{\eta t}$, noting that $\lambda a_2 - b < 0$, we get

$$\begin{aligned} \mathbb{E}|X_t|^p &\leq \frac{e^{-\eta t}}{a_1} \mathbb{E}V(X_0, 0, r_0) + \frac{e^{-\eta t}}{a_1} \mathbb{E} \int_0^t e^{\lambda s} (\lambda a_2 - b) |X_t|^p ds \\ &\leq \frac{e^{-\eta t}}{a_1} \mathbb{E}V(X_0, 0, r_0). \end{aligned}$$

Consequently,

$$\sup_{t \in [0, T]} a_1 e^{\eta t} \mathbb{E}|X_t|^p \leq \mathbb{E}V(X_0, 0, r_0).$$

Letting $T \rightarrow \infty$ gives

$$\sup_{t \geq 0} \mathbb{E}|X_t|^p \leq \frac{e^{-\eta t}}{a_1} \mathbb{E}V(X_0, 0, r_0),$$

and the required assertion follows. The proof is complete.

In the sequel of this section, we give another useful criterion and prove it briefly.

Theorem 5.2. Assume that **Eq. 1** has a unique solution and there exist a function $V \in C^{2,1}(\mathbb{R} \times \mathbb{R}_+ \times \mathbb{S}; \mathbb{R}_+)$ and positive constants $b_1, b_2, p \geq 1$ and $\beta_i \in \mathbb{R}$ such that for all $x \in \mathbb{R}, t \geq t_0, i \in \mathbb{S}$,

$$\begin{aligned} b_1 |x|^p &\leq |V(x, t, i)| \leq b_2 |x|^p, \\ \mathcal{L}^{(i)} V(x, t, i) &\leq \beta_i V(x, t, i), \end{aligned}$$

and

$$\sum_{i \in \mathbb{S}} \mu_i \beta_i < 0$$

Then **Eq. 1** is p th moment exponential stable.

Proof: Set $\bar{\beta}_i = \frac{1}{\theta} \beta_i$, where $\theta \in (0, 1)$. Let $\delta = -\sum_{i \in \mathbb{S}} \mu_i \bar{\beta}_i = -\mu \bar{\beta}$. Let $\mathbf{1}$ denote the vector which all elements are 1. Then,

$$\mu(\bar{\beta} + \delta \mathbf{1}) = \mu \bar{\beta} + \delta = -\delta + \delta = 0. \quad (22)$$

By [1], **Eq. 22** implies the Poisson equation:

$$Qc = \bar{\beta} + \delta \mathbf{1}. \quad (23)$$

Note that **Eq. 23** has the solution $c = (c_1, \dots, c_N)^T$. Hence,

$$-\delta = \bar{\beta}_i - \sum_{j=1}^N q_{ij} c_j, \quad i \in \mathbb{S}. \quad (24)$$

For each $i \in \mathbb{S}$, set $U(x, t, i) = (1 - \theta c_i) V(x, t, i)$, where $\theta \in (0, 1)$ is already defined and sufficiently small satisfying $1 - \theta c_i > 0$.

Then, for any $t \in [0, T]$ we get

$$\begin{aligned} \mathcal{A}U(x, t, i) &= (1 - \theta c_i) \mathcal{L}^{(i)} V(x, t, i) + \sum_{j \neq i} q_{ij} (U(x, t, j) - U(x, t, i)) \\ &= (1 - \theta c_i) \mathcal{L}^{(i)} V(x, t, i) - \theta V(x, t, i) \sum_{j \neq i} q_{ij} (c_j - c_i) \\ &\leq (1 - \theta c_i) \theta V(x, t, i) \left[\bar{\beta}_i - \sum_{j \neq i} q_{ij} \frac{c_j - c_i}{(1 - \theta c_i)} \right]. \end{aligned} \quad (25)$$

According to [1, 31], one has

$$\begin{aligned} \sum_{j \neq i} q_{ij} \frac{c_j - c_i}{(1 - \theta c_i)} &= \sum_{j \neq i} q_{ij} c_j + \sum_{j \neq i} q_{ij} \frac{\theta c_i c_j - c_i}{1 - \theta c_i} \\ &= \sum_{j=1}^N q_{ij} c_j + \sum_{j \neq i} q_{ij} \frac{c_i (c_j - c_i)}{1 - \theta c_i} \theta = \sum_{j=1}^N q_{ij} c_j + o(\theta). \end{aligned} \quad (26)$$

Making use of **Eqs 25, 26**, we obtain that

$$\mathcal{A}U(x, t, i) \leq (1 - \theta c_i) \theta V(x, t, i) \left[\bar{\beta}_i - \sum_{j=1}^N q_{ij} c_j + o(\theta) \right]. \quad (27)$$

Substituting **Eq. 24** into **Eq. 27**, we get

$$\mathcal{A}U(x, t, i) \leq (1 - \theta c_i) \theta V(x, t, i) [o(\theta) - \delta] = \kappa U(x, t, i),$$

where $\kappa < 0$. Making use of **Theorem 5.1**, the desired criterion follows.

On the other hand, we can prove it in another way. Set $\eta > 0$ and $\lambda \in (\eta, -\kappa)$. Define

$$\bar{U}(X_t, t, i) = \frac{e^{\lambda t}}{1 - \theta c_i} U(X_t, t, i).$$

Compute

$$\begin{aligned} b_1 e^{\eta t} \mathbb{E}|X_t|^p &\leq \mathbb{E} \bar{U}(X_t, t, i) = \mathbb{E}U(X_0, 0, i_0) + \mathbb{E} \int_0^t \mathcal{A} \bar{U} ds + \mathbb{E} \int_0^t \bar{U}_x g dB_s^H \\ &= \mathbb{E}U(X_0, 0, i_0) + \mathbb{E} \int_0^t e^{\lambda s} (\lambda U + \mathcal{A}U) ds \leq \mathbb{E}U(X_0, 0, i_0) + \mathbb{E} \int_0^t e^{\lambda s} (\lambda + \kappa) U ds \\ &= \mathbb{E}V(X_0, 0, i_0) + \mathbb{E} \int_0^t e^{\lambda s} (\lambda + \kappa) V ds \\ &\leq \mathbb{E}V(X_0, 0, i_0) + \mathbb{E} \int_0^t e^{\lambda s} (\lambda + \kappa) b_2 |X_t|^p ds. \end{aligned}$$

Thus we obtain that

$$b_1 e^{\eta t} \mathbb{E}|X_t|^p \leq V(X_0, 0, i_0) + \mathbb{E} \int_0^t e^{\lambda s} b_2 (\lambda + \kappa) |X_t|^p ds, \quad (28)$$

Dividing both sides of **Eq. 28** by $b_1 e^{\eta t}$, noting that $b_2(\lambda + \kappa) < 0$, we get

$$\begin{aligned} \mathbb{E}|X_t|^p &\leq \frac{e^{-\eta t}}{b_1} \mathbb{E}V(X_0, 0, r_0) + \frac{e^{-\eta t}}{b_1} \mathbb{E} \int_0^t e^{\lambda s} b_2 (\lambda + \kappa) |X_t|^p ds \\ &\leq \frac{e^{-\eta t}}{b_1} \mathbb{E}V(X_0, 0, r_0). \end{aligned}$$

Therefore, we obtain the required assertion

$$\limsup_{t \rightarrow \infty} \frac{1}{t} \log(\mathbb{E}|X_t|^p) < 0.$$

The proof is complete.

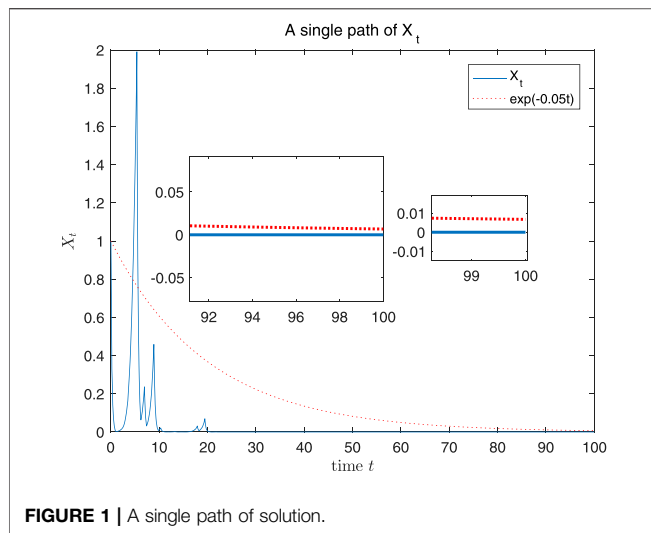


FIGURE 1 | A single path of solution.

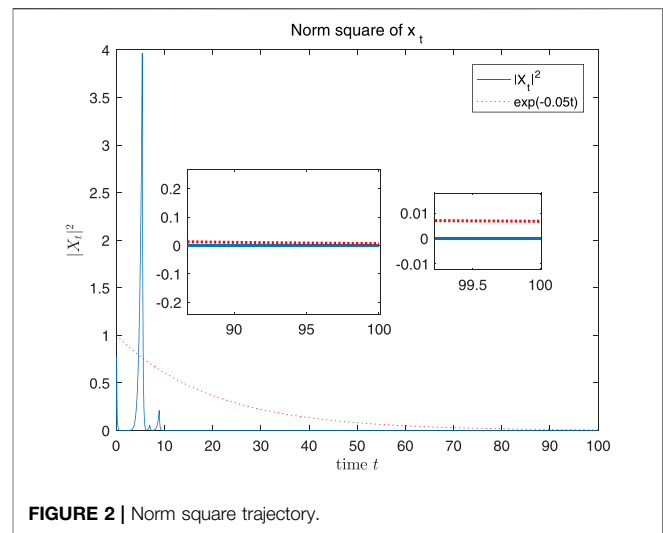


FIGURE 2 | Norm square trajectory.

6 EXAMPLE

In this section we give a numerical example to illustrate our results.

Example 1. Let $\{r_t\}_{t \geq 0}$ be a right-continuous Markov chain taking values in $\mathbb{S} = \{1, 2\}$ with invariant probability measure $\mu_1 = \mu_2 = \frac{1}{2}$.

Consider a risky asset, with the price dynamics:

$$\begin{cases} dX_t = f(X_t, t, r_t)dt + \sigma(t, r_t)X_t dB_t^H, \\ X_0 = 1, \end{cases} \quad (29)$$

on $t \geq 0$. Here we take $H = 0.7$ and

$$\begin{cases} f(x, t, i) = -4x, \quad \sigma(t, i) = \frac{1}{t+1}, \quad \text{if } i = 1, \\ f(x, t, i) = [2 - \sin(x)]x, \quad \sigma(t, i) = e^{-t}, \quad \text{if } i = 2. \end{cases}$$

Note that for all $i \in \mathbb{S}$, $dX_t = f(X_t, t, i)dt + \sigma(t, i)X_t dB_t^H$ satisfy the hypotheses (i)-(v). Then, by **Lemma 3.1**, it is easy to show that **Eq. 29** has a unique solution $\{X_t\}_{t \geq 0}$ as well. Set $V(x, t, i) = x^2$, for $i = 1, 2$.

Noting that for some $t_0 > 0$ sufficiently large and all $t > t_0$, we have

$$\begin{aligned} \mathcal{L}^{(1)}V(x, t, 1) &= V_x(x, t, 1)f(X_t, t, 1) + V_{xx}(x, t, 1)\frac{1}{t+1}x D_s^\phi x \\ &\leq -8x^2 + 2\frac{1}{t+1}x[xHt^{2H-1}] \\ &= -8x^2 + o(1)x^2 := \beta_1 x^2, \end{aligned}$$

and

$$\begin{aligned} \mathcal{L}^{(2)}V(x, t, 2) &= V_x(x, t, 2)f(X_t, t, 2) + V_{xx}(x, t, 2)e^{-t}x D_s^\phi x \\ &= 2x^2[2 - \sin(x)] + o(1)x^2 \\ &\leq 6x^2 + o(1)x^2 := \beta_2 x^2. \end{aligned}$$

Compute

$$\sum_{i \in \mathbb{S}} \mu_i \beta_i = \frac{1}{2}(-8 + 6) + o(1) < 0.$$

By **Theorem 5.2**, it's clear that the solution of **Eq. 29** is second moment exponential stable. **Figures 1, 2** show a single path of the solution and the solution's norm square, respectively.

DATA AVAILABILITY STATEMENT

The original contributions presented in the study are included in the article/Supplementary Material, further inquiries can be directed to the corresponding author.

AUTHOR CONTRIBUTIONS

WP contributed to conception and design of the study. WP wrote the first draft of the manuscript. ZZ and WP wrote sections of the manuscript. All authors contributed to manuscript revision, read, and approved the submitted version.

FUNDING

The research of WP was supported by the Characteristic and Preponderant Discipline of Key Construction Universities in Zhejiang Province (Zhejiang Gongshang University-Statistics).

ACKNOWLEDGMENTS

The authors are grateful to thank the reviewers for careful reading of the paper and for helpful comments that led to improvement of the first version of this paper.

REFERENCES

- Yin GG, and Zhu C. *Hybrid switching diffusions: Properties and applications*, *Stoch. Model. Appl. Probab.* New York: Springer (2010).
- Mao XR, and Yuan CG. *Stochastic differential equations with Markovian switching*. South Kensington: Imperial College Process (2006).
- Hamilton JD. A new approach to the economic analysis of nonstationary time series and the business cycle. *Econometrica* (1989) 57:357–84. doi:10.2307/1912559
- Mao X. Stability of stochastic differential equations with Markovian switching. *Stochastic Process their Appl* (1999) 79:45–67. doi:10.1016/s0304-4149(98)00070-2
- Yuan C, and Mao X. Stability of stochastic delay hybrid systems with jumps. *Eur J Control* (2010) 16:595–608. doi:10.3166/ejc.16.595-608
- Zhou W, Yang J, Yang X, Dai A, Liu H, and Fang JA. pth Moment exponential stability of stochastic delayed hybrid systems with Lévy noise. *Appl Math Model* (2015) 39:5650–8. doi:10.1016/j.apm.2015.01.025
- Yuan C, and Mao X. Asymptotic stability in distribution of stochastic differential equations with Markovian switching. *Stochastic Process their Appl* (2003) 103:277–91. doi:10.1016/s0304-4149(02)00230-2
- Li X, and Mao X. A note on almost sure asymptotic stability of neutral stochastic delay differential equations with Markovian switching. *Automatica* (2012) 48:2329–34. doi:10.1016/j.automatica.2012.06.045
- Wu H, and Sun J. p-Moment stability of stochastic differential equations with impulsive jump and Markovian switching. *Automatica* (2006) 42:1753–9. doi:10.1016/j.automatica.2006.05.009
- Hurst HE. Long-term storage capacity in reservoirs. *Trans Amer Soc Civil Eng* (1951) 116:400–10. doi:10.1061/taceat.0006518
- Hurst HE. Methods of using long-term storage in reservoirs. *Proc Inst Civil Eng* (1956) 5:519–43. doi:10.1680/iicep.1956.11503
- Mandelbrot BB. *The Fractal Geometry of Nature*. San Francisco, CA: Freeman (1983).
- Mandelbrot BB. *Fractals and Scaling in Finance: Discontinuity, Concentration, Risk*. Berlin: Springer-Verlag (1997).
- Hu Y, and Øksendal B. Fractional white noise calculus and applications to finance. *Infin Dimens Anal Quan Probab. Relat. Top.* (2003) 06:1–32. doi:10.1142/s0219025703001110
- Brody DC, Syroka J, and Zervos M. Dynamical pricing of weather derivatives. *Quantitative Finance* (2002) 2:189–98. doi:10.1088/1469-7688/2/3/302
- Biagini F, Hu YZ, Øksendal B, and Zhang TS. *Stochastic calculus for fractional Brownian motion and applications*. London: Springer-Verlag (2008).
- Mishura YS. *Stochastic calculus for Fractional Brownian Motion and related process*. Berlin: Springer-Verlag (2008).
- Li M. Modified multifractional Gaussian noise and its application. *Phys Scr* (2021) 96:125002. doi:10.1088/1402-4896/ac1cf6
- Li M. Generalized fractional Gaussian noise and its application to traffic modeling. *Physica A* (2021) 579:1236137. doi:10.1016/j.physa.2021.126138
- Li M. Multi-fractional generalized Cauchy process and its application to teletraffic. *Physica A: Stat Mech its Appl* (2020) 550:123982. doi:10.1016/j.physa.2019.123982
- Li M. Fractal time series a tutorial review. *Math Probl Eng* (2010) 2010:157264. doi:10.1155/2010/157264
- Ghosh MK, Arapostathis A, and Marcus SI. Ergodic control of switching diffusions. *SIAM J Control Optim* (1997) 35:1952–88. doi:10.1137/s0363012996299302
- Skorohod AV. *Asymptotic Methods in the Theory of Stochastic Differential Equations*. US: American Mathematical Society (1989).
- Anderson WJ. *Continuous-time Markov chain*. New York: Springer (1991).
- Bardet JB, Gurin H, and Malrieu F. Long time behavior of diffusions with Markov switching. *ALEA Lat Am J Probab Math Stat* (2010) 7:151–70.
- Cloez B, and Hairer M. Exponential ergodicity for Markov processes with random switching. *Bernoulli* (2015) 21:505–36. doi:10.3150/13-bej577
- Alos E, Mazet O, and Nualart D. Stochastic calculus with respect to Gaussian processes. *Ann Probab* (1999) 29:766–801.
- Nualart D, and Răşcanu A. Differential equations driven by fractional Brownian motion. *Collect Math* (2000) 53:55–81.
- Holdeb H, Øksendal B, Ubøe J, and Zhang T. *Stochastic partial differential equations*. Boston: Birkhäuser (1996).
- Duncan TE, Hu Y, and Pasik-Duncan B. Stochastic Calculus for Fractional Brownian Motion I. Theory. *SIAM J Control Optim* (2000) 38:582–612. doi:10.1137/s036301299834171x
- Yan L, Pei WY, Pei W, and Zhang Z. Exponential stability of SDEs driven by fBm with Markovian switching. *Discrete Cont Dyn-a* (2019) 39:6467–83. doi:10.3934/dcds.2019280
- Mao XR. *Stochastic differential equations and applications*. New York: Horwood (1997).
- Arcones MA. On the law of the iterated logarithm for gaussian processes. *J Theor Probab* (1995) 8:877–903. doi:10.1007/bf02410116

Conflict of Interest: The authors declare that the research was conducted in the absence of any commercial or financial relationships that could be construed as a potential conflict of interest.

Publisher's Note: All claims expressed in this article are solely those of the authors and do not necessarily represent those of their affiliated organizations, or those of the publisher, the editors and the reviewers. Any product that may be evaluated in this article, or claim that may be made by its manufacturer, is not guaranteed or endorsed by the publisher.

Copyright © 2021 Pei and Zhang. This is an open-access article distributed under the terms of the Creative Commons Attribution License (CC BY). The use, distribution or reproduction in other forums is permitted, provided the original author(s) and the copyright owner(s) are credited and that the original publication in this journal is cited, in accordance with accepted academic practice. No use, distribution or reproduction is permitted which does not comply with these terms.



Almost Periodic Solutions to Impulsive Stochastic Delay Differential Equations Driven by Fractional Brownian Motion With $\frac{1}{2} < H < 1$

Lili Gao and Xichao Sun*

Department of Mathematics and Physics, Bengbu University, Bengbu, China

In this article, we study the existence and uniqueness of square-mean piecewise almost periodic solutions to a class of impulsive stochastic functional differential equations driven by fractional Brownian motion. Moreover, the stability of the mild solution is obtained. To illustrate the results obtained in the paper, an impulsive stochastic functional differential equation driven by fractional Brownian motion is considered.

Keywords: fractional Brownian motion, square-mean piecewise almost periodic solution, impulsive systems, stochastic functional differential equation, stability

OPEN ACCESS

Edited by:

Ming Li,
Zhejiang University, China

Reviewed by:

Mohammad Hossein Heydari,
Shiraz University of Technology, Iran

Yong Ren,
Anhui Normal University, China
Yaozhong Hu,
University of Alberta, Canada

*Correspondence:

Xichao Sun
sunxichao626@126.com

Specialty section:

This article was submitted to
Interdisciplinary Physics,
a section of the journal
Frontiers in Physics

Received: 25 September 2021

Accepted: 14 October 2021

Published: 22 November 2021

Citation:

Gao L and Sun X (2021) Almost
Periodic Solutions to Impulsive
Stochastic Delay Differential Equations
Driven by Fractional Brownian Motion
With $\frac{1}{2} < H < 1$.
Front. Phys. 9:783125.
doi: 10.3389/fphy.2021.783125

1 INTRODUCTION

Impulsive systems arise naturally in a wide variety of evolutionary processes in which states are changed abruptly at certain moments of time. Impulsive stochastic modeling has come to play an important role in many branches of science where more and more people have encountered impulsive stochastic differential equations. For example, a stochastic model for drug distribution in a biological system was described by Tsokos and Padgett [1] as a closed system with a simplified heart, one organ, or capillary bed, and recirculation of blood with a constant rate of flow, where the heart is considered as a mixing chamber of constant volume. Recently, there has been a significant development in impulsive stochastic differential equations (ISDEs). The existence and stability of ISDEs were investigated in [2–11] and the references therein.

On the other hand, in recent years, there has been considerable interest in studying fractional Brownian motions (fBMs) due to their compact properties and applications in various scientific areas, including telecommunications [12, 13], turbulence [14], image processing [15], and finance [16]. Stochastic differential equations (SDEs) driven by fBMs attract the interest of researchers [2, 3, 17–21]. Taking the time delay into account, the theory of stochastic differential equations has been generalized to stochastic functional differential equations; it makes the dynamics more complex and the system may lose stability and show almost periodicity. Arthi et al. [2] considered the existence and exponential stability for neutral stochastic integrodifferential equations with impulses driven by fractional Brownian motion (fBm), and Caraballo [3] studied the existence of mild solutions to stochastic delay evolution equations with fBm and impulses.

In this paper, we are concerned with the existence and stability of almost periodic mild solutions to the following impulsive stochastic functional differential system driven by fBm with Hurst index $H \in (1/2, 1)$:

$$\begin{cases} dx(t) = [Ax(t) + b(t, x_t)]dt + \sigma(t)dB^H(t), & t \neq t_i, \quad i \in \mathbb{Z}, \\ \Delta x(t_i) = x(t_i^+) - x(t_i^-) = I_i(x(t_i)), & i \in \mathbb{Z}, \\ x_{t_0} = \xi = \{\xi(t) : -\theta \leq t \leq 0\}, \end{cases} \quad (1)$$

where \mathbb{Z} is the set of integer, for any $i, k \in \mathbb{Z}$, and the sequence $\{t_i\}$ is such that the derived sequence $\{t_i^k = t_{i+k} - t_i\}$ is equipotentially almost periodic. Moreover, $A: D(A) \subset \mathbb{H} \rightarrow \mathbb{H}$ is a linear bounded operator, $\rho(A)$ is the resolvent set of A , and for $\lambda \in \rho(A)$, $R(\lambda, A)$ is the resolvent of A . In addition, b , σ , and I_t are appropriate functions, $x_t(\cdot): [-\theta, 0] \rightarrow \mathbb{H}$ is given by $x_t(s) = x(t + s)$, for any $s \in [-\theta, 0]$, and $\xi \in \mathcal{C}_\theta$ is an \mathcal{F}_{t_0} -measurable random variable such that $E\|\xi\|^2 < \infty$. Let $\theta > 0$ be a given constant and let

$\mathcal{C}_\theta = \{\phi: [-\theta, 0] \times \Omega \rightarrow \mathbb{H}, \phi \text{ be continuous everywhere except for a finite number of points } s \text{ at which } \phi(s^-) \text{ and } \phi(s^+) \text{ exist and satisfy } \phi(s^-) = \phi(s^+), \text{ endowed with the norm}$

$$\|\phi\|_{\mathcal{C}_\theta} = \sup_{-\theta \leq s \leq 0} (E\|\phi(s)\|^2)^{\frac{1}{2}},$$

such that $\phi(s, \cdot)$ is \mathcal{F}_0 -measurable for each $s \in [-\theta, 0]$ and $\sup_{s \in [-\theta, 0]} E\|\phi(s)\|^2 < \infty$.

There are several difficulties with our problems. First, there is the delay for the impulsive stochastic differential equations. Second, about the stochastic differential equations driven by fractional Brownian motion, the classical stochastic integral failed for lack of the martingale property. Third, there is no strong solution for stochastic partial delay differential equations driven by fractional Brownian motion. The lifting space method, mild solutions, fixed point theorem, and semigroup theory will be used to overcome these difficulties.

The paper is organized as follows. In **Section 2**, we introduce some notations and necessary preliminaries. **Section 3** is devoted to stating the existence and uniqueness of the mild square-mean piecewise almost periodic solution to (1). In **Section 4**, we show the stability of the mild square-mean piecewise almost periodic solution. An example is provided to illustrate the effectiveness of the results.

2 PRELIMINARIES

Let $(\mathbb{H}, \|\cdot\|_{\mathbb{H}}, (\cdot, \cdot)_{\mathbb{H}})$ and $(\mathbb{K}, \|\cdot\|_{\mathbb{K}}, (\cdot, \cdot)_{\mathbb{K}})$ denote two real separable Hilbert spaces. We denote by $\mathbb{L}(\mathbb{H}, \mathbb{K})$ the set of all linear bounded operators from \mathbb{H} into \mathbb{K} , equipped with the usual operator norm $\|\cdot\|$ and use $|\cdot|$ to denote the Euclidean norm of a vector. In this article, we use the symbol $\|\cdot\|$ to denote the norms of operators regardless of the spaces involved when no confusion possibly arises. Let $(\Omega, \mathcal{F}, \{\mathcal{F}_t\}_{t \geq 0}, P)$ be a filtered complete probability space satisfying the usual condition.

2.1 Fractional Brownian Motion

In this subsection, we briefly introduce some useful results about fBm and the corresponding stochastic integral taking values in a Hilbert space. For more details, refer to Hu [22], Mishura [23], Nualart [24], and references therein.

A real standard fractional Brownian motion $\{\beta^H(t), t \in \mathbb{R}\}$ with Hurst parameter $H \in (0, 1)$ is a Gaussian process with continuous sample paths such that $E[\beta^H(t)] = 0$ and

$$E[\beta^H(t)\beta^H(s)] = \frac{1}{2}(|t|^{2H} + |s|^{2H} - |t-s|^{2H}),$$

for all $s, t \geq 0$. It is known that fBm $\{\beta^H(t), t \geq 0\}$ with $H > \frac{1}{2}$ admits the following Wiener integral representation:

$$\beta^H(t) = \int_0^t K_H(t, s) dW(s),$$

where W is a standard Brownian motion and the kernel $K_H(t, s)$ is given by

$$K_H(t, s) = c_H \int_s^t (u-s)^{H-\frac{3}{2}} \left(\frac{u}{s}\right)^{H-\frac{1}{2}} du, \quad s < t,$$

where $c_H > 0$ is a constant satisfying $E(\beta_1^H)^2 = 1$. For any function $\sigma \in L^2(0, T)$, the Wiener integral of σ with respect to β^H is defined by

$$\int_0^T \sigma(s) d\beta^H(s) = \int_0^T K_H^* \sigma(s) dW(s),$$

for any $T > 0$, where $K_H^* \sigma(s) = \int_s^T \frac{\partial K_H}{\partial r}(r, s) dr$. A \mathbb{K} -valued, \mathcal{F}_t -adapted fBm B^H with Hurst index H can be defined by

$$B^H(t) = \sum_{n=1}^{\infty} \sqrt{\lambda_n} e_n \beta_n^H(t),$$

where $\beta_n^H, n = 1, 2, \dots$ are independent fBms with the same Hurst parameter $H \in (\frac{1}{2}, 1)$, $\{e_n, n \in \mathbb{N}\}$, which is a complete orthonormal basis in \mathbb{K} , $\{\lambda_n, n \in \mathbb{N}\}$ that is a bounded sequence of non-negative real numbers satisfying $Qe_n = \lambda_n e_n$, and Q is non-negative self-adjoint trace class operator with $\text{Tr} Q = \sum_{n=1}^{\infty} \lambda_n < +\infty$.

Let $\mathbb{L}_2^0(\mathbb{H}, \mathbb{K})$ denote the space of all $\sigma \in \mathbb{L}(\mathbb{H}, \mathbb{K})$ such that $\sigma Q^{\frac{1}{2}}$ is a Hilbert-Schmidt operator. The norm is defined by $\|\sigma\|_{\mathbb{L}_2^0}^2 = \sum_{n=1}^{\infty} \|\sqrt{\lambda_n} \sigma e_n\|^2$. Generally, σ is called a Q -Hilbert-Schmidt operator from \mathbb{H} to \mathbb{K} .

Definition 2.1. Let $\sigma: [0, T] \rightarrow \mathbb{L}_2^0(\mathbb{H}, \mathbb{K})$ such that

$$\sum_{n=1}^{\infty} \|K_H^* (\sigma e_n)\|_{\mathbb{L}_2^0}^2 < \infty,$$

then the stochastic integral of σ with respect to fBm B^H is defined by

$$\begin{aligned} \int_0^t \sigma(s) dB^H(s) &:= \sum_{n=1}^{\infty} \int_0^t \sigma(s) Q^{\frac{1}{2}} e_n d\beta_n^H(s) \\ &= \sum_{n=1}^{\infty} \int_0^t (K_H^* (\sigma(s) Q^{\frac{1}{2}} e_n))(s) dW(s). \end{aligned}$$

Remark. If $\{\lambda_n\}_{n \in \mathbb{N}}$ is a bounded sequence of non-negative real numbers such that the nuclear operator Q satisfies $Qe_n = \lambda_n e_n$ assuming that there exists a positive constant K_σ such that $\|\sigma\|_{\mathbb{L}_2^0}^2 \leq K_\sigma$ uniformly in $[0, T]$, then it is obvious that $\sum_{n=1}^{\infty} \|\sigma Q^{\frac{1}{2}} e_n\|^2$ is uniformly convergent for $t \in [0, T]$.

2.2 Piecewise Almost Periodic Stochastic Processes

In this subsection, we recall some notations about the square-mean piecewise almost periodic stochastic process and introduce

some lemmas. For further details, we refer to Takens and Teissier [25] and Liu [26].

Recall that a stochastic process $X: \mathbb{R} \rightarrow L^2(\Omega; \mathbb{H})$ is said to be continuous if

$$\lim_{t \rightarrow s} E\|X(t) - X(s)\|^2 = 0,$$

for all $s \in \mathbb{R}$, and it is said to be bounded if there exists $N > 0$, such that $E\|X(t)\|^2 \leq N$ for all $t \in \mathbb{R}$. For convenience, we list the following concepts and notations:

- $L^2(\Omega, \mathbb{H})$ is Banach space when it is equipped with norm $\|\cdot\|_{L^2(\Omega, \mathbb{H})}$.
- Let \mathcal{T} be the set consisting of all real sequences $\{t_i\}_{i \in \mathbb{Z}}$ such that $\alpha = \inf_{i \in \mathbb{Z}} (t_{i+1} - t_i) > 0$, and $\lim_{i \rightarrow -\infty} t_i = -\infty$, $\lim_{i \rightarrow \infty} t_i = \infty$, $x(t_i^-)$ and $x(t_i^+)$ represent the left and right limits of $x(t)$ at the point t_i , $i \in \mathbb{Z}$, respectively.
- Let $PC(\mathbb{R}, L^2(\Omega, \mathbb{H}))$ be the space consisting of all stochastically bounded functions $b: \mathbb{R} \rightarrow L^2(\Omega, \mathbb{H})$ such that $b(\cdot)$ is stochastically continuous at t for any $t \notin \{t_i\}_{i \in \mathbb{Z}}$, and $b(t_i) = b(t_i^-)$ for all $i \in \mathbb{Z}$, $\{t_i\}_{i \in \mathbb{Z}} \in \mathcal{T}$.
- Let $PC(\mathbb{R} \times C_\theta, L^2(\Omega, \mathbb{H}))$ be the space of all piecewise stochastic process $b: \mathbb{R} \times C_\theta \rightarrow L^2(\Omega, \mathbb{H})$ such that
- for any $\phi \in C_\theta$, $b(\cdot, \phi)$ is stochastically continuous at point t for any $t \notin \{t_i\}_{i \in \mathbb{Z}}$ and $b(t_i, \phi) = b(t_i^-, \phi)$ for all $i \in \mathbb{Z}$; and $b(t, \cdot)$ is stochastically continuous at $\phi \in C_\theta$, for $t \in \mathbb{R}$.
- For $k < i$, $t - t_k = t - t_i + t_i - t_k \geq t - t_i + (i - k)\alpha$, if $\{t_i\}_{i \in \mathbb{Z}} \in \mathcal{T}$, and $t_i < t \leq t_{i+1}$ (see [27]).

Definition 2.2. ([28]). The family of the sequence $\{t_i^k = t_{i+k} - t_i\}_{i \in \mathbb{Z}, k \in \mathbb{Z}}$ will be called equipotentially almost periodic if for any $\varepsilon > 0$; there exists a relatively dense set \mathbb{Q}_ε of \mathbb{R} and an integer $q \in \mathbb{Z}$ such that the inequality

$$|t_{i+q} - t_i - \tau| < \varepsilon, \quad (2)$$

holds for each $\tau \in \mathbb{Q}_\varepsilon$ and $i \in \mathbb{Z}$.

Definition 2.3. A function $\{b(t), t \geq 0\}$ is said to be square-mean piecewise almost periodic if the following conditions are fulfilled:

- For any $\varepsilon > 0$, there exists a positive number $\delta = \delta(\varepsilon)$ such that if the points t' and t'' belong to the same interval of continuity and $|t' - t''| < \delta$, then $E\|b(t') - b(t'')\|^2 < \varepsilon$.
- For any $\varepsilon > 0$, there exists $l(\varepsilon) > 0$, such that every interval of length $l(\varepsilon)$ contains a number τ with the property

$$\sup_{t \in \mathbb{R}} E\|b(t + \tau) - b(t)\|^2 < \varepsilon,$$

which satisfies the condition $|t - t_i| > \varepsilon, i \in \mathbb{Z}$.

Let $\mathcal{AP}_T(\mathbb{R}, L^2(\Omega; \mathbb{H}))$ denote the space of all square-mean piecewise almost periodic functions. Obviously $\mathcal{AP}_T(\mathbb{R}, L^2(\Omega; \mathbb{H}))$ endowed with the supremum norm is a Banach space. Let $\mathcal{UPC}(\mathbb{R}; L^2(\Omega; \mathbb{H}))$ be the space of all functions $b \in PC(\mathbb{R}, L^2(\Omega; \mathbb{H}))$ such that b satisfies the condition (a) in Definition 2.3. It is easy to check that $\mathcal{UPC}(\mathbb{R}; L^2(\Omega; \mathbb{H}))$ is a Banach space with the norm

$$\|X\|_\infty = \sup_{t \in \mathbb{R}} (E\|X(t)\|^2)^{\frac{1}{2}},$$

for each $X \in \mathcal{UPC}(\mathbb{R}; L^2(\Omega; \mathbb{H}))$.

Definition 2.4. (compare with [28]). A sequence $\{x_i\}: \mathbb{Z} \rightarrow L^2(\Omega, \mathbb{H})$ is called square-mean almost periodic if for any $\varepsilon > 0$, there exists a natural number $N = N(\varepsilon)$ such that, for each $k \in \mathbb{Z}$, there is at least one integer p in the segment $[k, k + N]$, for which inequality

$$E\|x_{i+p} - x_i\|^2 < \varepsilon,$$

holds for all $i \in \mathbb{Z}$.

Definition 2.5. The function $b(t, \varphi) \in PC(\mathbb{R} \times C_\theta, L^2(\Omega, \mathbb{H}))$ is said to be square-mean piecewise almost periodic in $t \in \mathbb{R}$ uniformly in $\varphi \in \Lambda$, where $\Lambda \subseteq C_\theta$ is compact if for any $\varepsilon > 0$, there exists $l(\varepsilon, \Lambda) > 0$ such that any interval of length $l(\varepsilon, \Lambda)$ contains at least a number τ for which

$$\sup_{t \in \mathbb{R}} E\|b(t + \tau, x) - b(t, x)\|^2 < \varepsilon,$$

for each $x \in \Lambda$, $t \in \mathbb{R}$, satisfying $|t - t_i| > \varepsilon$. The collection of all such processes is denoted by $\mathcal{AP}_T(\mathbb{R} \times C_\theta, L^2(\Omega, \mathbb{H}))$.

Lemma 2.1. Let the function $f: \mathbb{R} \times C_\theta \rightarrow L^2(\Omega; \mathbb{H})$ be square-mean piecewise almost periodic in $t \in \mathbb{R}$ uniformly for $y \in C_\theta$, where $\Lambda \subset C_\theta$ is compact. If f is a Lipschitz function in the following sense,

$$E\|f(t, y) - f(t, \tilde{y})\| < M_2(\|y - \tilde{y}\|_{C_\theta}), \quad (3)$$

for all $y, \tilde{y} \in C_\theta$, $t \in \mathbb{R}$, and a constant $M_2 > 0$, then for any $\phi(\cdot) \in \mathcal{AP}_T(\mathbb{R}, L^2(\Omega; \mathbb{H}))$, $f(\cdot, \phi) \in \mathcal{AP}_T(\mathbb{R}, L^2(\Omega; \mathbb{H}))$.

Proof. Noting that $\phi(t): \mathbb{R} \rightarrow L^2(\Omega; \mathbb{H})$ is square-mean almost periodic, we can conclude that $\phi_t = \{\phi(t + s), -\theta \leq s \leq 0, \theta > 0\}$ is square-mean almost periodic by Theorem 1.2.7 of [29]. Thus, for each $\varepsilon > 0$, there exists a constant $l(\varepsilon) > 0$ such that every interval with the length $l(\varepsilon)$ contains a number τ satisfying

$$E\|\phi_{t+\tau} - \phi_t\|_{C_\theta}^2 \leq \frac{\varepsilon}{4M^2}, \forall t \in \mathbb{R}. \quad (4)$$

Noting that $f: \mathbb{R} \times C_\theta \rightarrow L^2(\Omega; \mathbb{H})$ is square-mean piecewise almost periodic, we can see that for any $\varepsilon > 0$, there exists $l(\varepsilon, \Lambda) > 0$ such that each interval with length $l(\varepsilon, \Lambda)$ contains at least a number τ satisfying

$$E\|f(t + \tau, \phi_t) - f(t, \phi_t)\|^2 \leq \frac{\varepsilon}{4}, \forall t \in \mathbb{R}, \quad (5)$$

for any $x \in \Lambda (\subseteq C_\theta)$, $t \in \mathbb{R}$ with $|t - t_i| > \varepsilon$. Using the elementary inequality $|a + b|^2 \leq 2(|a|^2 + |b|^2)$ and condition (3), we have

$$\begin{aligned} & E\|f(t + \tau, \phi_{t+\tau}) - f(t, \phi_t)\|^2 \\ & \leq 2E\|f(t + \tau, \phi_{t+\tau}) - f(t, \phi_{t+\tau})\|^2 + 2E\|f(t, \phi_{t+\tau}) - f(t, \phi_t)\|^2 \\ & \leq 2E\|f(t + \tau, \phi_{t+\tau}) - f(t, \phi_{t+\tau})\|^2 + 2M_2^2 E\|\phi_{t+\tau} - \phi_t\|_{C_\theta}^2, \end{aligned}$$

for all $t \in \mathbb{R}$. Combining (4) and (5), one can show that

$$\sup_{t \in \mathbb{R}} E \|f(t + \tau, \phi_{t+\tau}) - f(t, \phi_t)\|^2 \leq 2 \cdot \frac{\varepsilon}{4} + 2M^2 \cdot \frac{\varepsilon}{4M^2} \leq \varepsilon,$$

which implies that $f(t, \phi_t)$ is square-mean piecewise almost periodic.

3 EXISTENCE OF SQUARE-MEAN PIECEWISE ALMOST PERIODIC SOLUTION

In this section, we study the existence of the square-mean piecewise almost periodic solution to (1). We first present some assumptions as follows:

(H1) Let the bounded linear operator A be an infinitesimal generator of an analytic semigroup $\{S(t), t \geq 0\}$ such that

$$\|S(t)\| \leq M e^{-\gamma t}, \quad t \geq 0 \quad (6)$$

for some $\gamma > 0, M > 0$. Moreover, $R(\lambda, A)$ is almost periodic, where $\lambda \in \rho(A)$.

(H2) Let $b \in \mathcal{AP}_{\mathcal{T}}(\mathbb{R} \times \mathcal{C}_{\theta}, L^2(\Omega, \mathbb{H}))$. Moreover, there exists a positive constant M_b such that

$$E \|b(t, x) - b(t, \tilde{x})\|^2 \leq M_b \|x - \tilde{x}\|_{\mathcal{C}_{\theta}}^2,$$

for any $x, \tilde{x} \in \mathcal{C}_{\theta}$.

(H3) Let $\sigma \in \mathcal{AP}_{\mathcal{T}}(\mathbb{R} L_2^0(\Omega, L^2(\Omega, \mathbb{H})))$ and let $\{I_i x(t_i), i \in \mathbb{Z}\}$ be a square-mean piecewise almost periodic sequence satisfying

$$E \|I_i(x) - I_i(y)\|^2 \leq M_I E \|x - y\|^2.$$

for some positive constant M_I .

Recall the notion of a mild solution for Eq. 1.

Definition 3.1. An \mathcal{F}_t -progressive process $\{x(t)\}_{t \in \mathbb{R}}$ is called a mild solution of the system (1) on \mathbb{R} if it satisfies the corresponding stochastic integral equation

$$\begin{aligned} x(t) = & S(t)x_0 + \int_{t_0}^t S(t-s)b(s, x_s)ds \\ & + \int_{t_0}^t S(t-s)\sigma(s)dB^H(s) \\ & + \sum_{t_0 < t_i < t} S(t-t_i)I_i(x(t_i)), \end{aligned} \quad (7)$$

for all $t \geq t_0$ and for each $t_0 \in \mathbb{R}$.

Theorem 3.1. Let (H1) – (H3) be satisfied. Then, (1) has a unique square-mean piecewise almost periodic mild solution whenever

$$\Theta := \frac{M^2 M_b}{\gamma^2} + \frac{M^2 M_I}{(1 - e^{-\gamma\alpha})^2} < 1. \quad (8)$$

Consider the following equation:

$$\begin{aligned} x(t) = & \int_{-\infty}^t S(t-s)b(s, x_s)ds + \int_{-\infty}^t S(t-s)\sigma(s)dB^H(s) \\ & + \sum_{t_i < t} S(t-t_i)I_i(x(t_i)), \end{aligned}$$

with $t \geq t_0$. It is easy to verify that the above equation is equivalent to (7). Define the operator \mathcal{L} on $\mathcal{AP}_{\mathcal{T}}(\mathbb{R}, L^2(\Omega, \mathbb{H}))$ by

$$\begin{aligned} \mathcal{L}x(t) = & \int_{-\infty}^t S(t-s)b(s, x_s)ds \\ & + \int_{-\infty}^t S(t-s)\sigma(s)dB^H(s) + \sum_{t_i < t} S(t-t_i)I_i(x(t_i)) \\ \equiv & \Phi_1(t) + \Phi_2(t) + \Phi_3(t), \end{aligned}$$

for all $t \in \mathbb{R}$. To prove the theorem, it is sufficient to show that the next statements hold:

- I) $\mathcal{L}x(t)$ is square-mean piecewise almost periodic.
- II) \mathcal{L} admits a unique fixed point.

Proof of Statement (I) This will be done in two steps.

Step 1. We claim that $\mathcal{L}x(t) \in \mathcal{UPC}$.

Let $i \in \mathbb{Z}$. By the uniform continuity of $S(t)$, we can see that, for any $\varepsilon > 0$, there exists a number $\delta > 0$ between 0 and $\min\{\sqrt{\frac{\varepsilon}{b}}, \frac{2^H\sqrt{\varepsilon}}{\sqrt{\sigma}}\}$ such that

$$\|S(t'' - t') - I\|^2 \leq \min\left\{\frac{\gamma^2 \varepsilon}{\tilde{b}}, \frac{\gamma^{2H} \varepsilon}{H^{2H} \tilde{\sigma}}, \frac{(1 - e^{-\gamma\alpha})^2 \varepsilon}{\tilde{I}}\right\}, \quad (9)$$

for all $t', t'' \in (t_i, t_{i+1})$, $t' < t''$ as $0 < t'' - t' < \delta$, where $\tilde{b} = 36M^2\|b\|_{\infty}^2$, $\tilde{\sigma} = 36H(2H-1)M^2\|\sigma\|_{\infty}^2$, $\tilde{I} = 9M^2\|I\|_{\infty}^2$. It follows from the inequality $|a + b + c|^3 \leq 3(a^2 + b^2 + c^2)$ that

$$\begin{aligned} E\|\mathcal{L}x(t') - \mathcal{L}x(t'')\|^2 \leq & 3E\|\Phi_1(t') - \Phi_1(t'')\|^2 \\ & + 3E\|\Phi_2(t') - \Phi_2(t'')\|^2 + 3E\|\Phi_3(t') - \Phi_3(t'')\|^2, \end{aligned}$$

for all $t', t'' \in (t_i, t_{i+1})$, $t' < t''$. By the assumptions (H1), (H2), and (H3), we have that

$$\begin{aligned} E\left\|\int_{t'}^{t''} S(t''-s)b(s, x_s)ds\right\|^2 \leq & M^2 \int_{t'}^{t''} e^{-\gamma(t''-s)} \\ & ds \int_{t'}^{t''} e^{-\gamma(t''-r)} E\|b(s, x_r)\|^2 dr \\ \leq & M^2 (t'' - t')^2 \sup_{t \in \mathbb{R}} E\|b(t, x_t)\|^2, \end{aligned} \quad (10)$$

and

$$\begin{aligned} E\left\|\int_{t'}^{t''} S(t''-s)\sigma(s)dB^H(s)\right\|^2 \leq & H(2H-1)M^2\|\sigma\|_{\infty}^2 \left(\int_{t'}^{t''} e^{-\frac{\gamma(t''-s)}{H}} ds\right)^{2H} \\ \leq & M^2 (t'' - t')^{2H} \sup_{t \in \mathbb{R}} E\|b(t, x_t)\|^2, \end{aligned} \quad (11)$$

for all $t', t'' \in (t_i, t_{i+1})$, $t' < t''$. Moreover, we also have that

$$\begin{aligned}
& E \left\| \int_{-\infty}^{t'} [S(t' - s) - S(t'' - s)] b(s, x_s) ds \right\|^2 \\
&= E \left\| \int_{-\infty}^{t'} [I - S(t'' - t')] S(t' - s) b(s, x_s) ds \right\|^2 \\
&\leq M^2 \|I - S(t'' - t')\|^2 \int_{-\infty}^{t'} e^{-\gamma(t' - s)} ds \int_{-\infty}^{t'} e^{-\gamma(t' - r)} E \|b(s, x_r)\|^2 dr \\
&\leq M^2 \|I - S(t'' - t')\|^2 \gamma^{-2} \sup_{t \in \mathbb{R}} E \|b(t, x_t)\|^2,
\end{aligned} \tag{12}$$

and

$$\begin{aligned}
& E \left\| \int_{-\infty}^{t'} [S(t' - s) - S(t'' - s)] \sigma(s) dB^H(s) \right\|^2 \\
&\leq H(2H - 1) M^2 \|I - S(t'' - t')\|^2 \\
&\quad \left(\int_{-\infty}^{t'} e^{-\frac{\gamma(t' - s)}{H}} \|\sigma(s)\|_{L_0^2}^{\frac{1}{H}} ds \right)^{2H} \\
&\leq H(2H - 1) M^2 \|I - S(t'' - t')\|^2 \|\sigma\|_{\infty}^2 \left(\frac{H}{\gamma} \right)^{2H},
\end{aligned} \tag{13}$$

for all $t', t'' \in (t_i, t_{i+1})$, $t' < t''$. Combining these with Hölder's inequality and (9), we get that

$$E \|\Phi_1(t') - \Phi_1(t'')\|^2 \leq \frac{2M^2}{\gamma^2} \frac{\gamma^2 \varepsilon}{b} \|b\|_{\infty}^2 + 2\delta^2 M^2 \|b\|_{\infty}^2 \leq \frac{\varepsilon}{9},$$

and

$$\begin{aligned}
& E \|\Phi_2(t') - \Phi_2(t'')\|^2 \\
&\leq 2H(2H - 1) M^2 \left(\|I - S(t'' - t')\|^2 \|\sigma\|_{\infty}^2 \left(\frac{H}{\gamma} \right)^{2H} \right. \\
&\quad \left. + \|\sigma\|_{\infty}^2 (t'' - t')^{2H} \right) \leq \frac{\varepsilon}{9},
\end{aligned}$$

for all $t', t'' \in (t_i, t_{i+1})$, $t' < t''$ provided $|t'' - t'| < \delta$. Similarly, by the assumptions (H1) and (H3) and (9), one can see that

$$\begin{aligned}
& E \|\Phi_3(t') - \Phi_3(t'')\|^2 \leq E \left\| \sum_{t_i < t'} S(t' - t_i) I_i(x(t_i)) \right. \\
&\quad \left. - \sum_{t_i < t''} S(t'' - t_i) I_i(x(t_i)) \right\|^2 \\
&\leq E \left\| \sum_{t_i < t''} [S(t' - t_i) I_i(x(t_i)) - S(t'' - t_i) I_i(x(t_i))] \right\|^2 \\
&\leq M^2 \|I - S(t'' - t')\|^2 \left(\sum_{t_i < t'} e^{-\gamma(t' - t_i)} \right) \\
&\quad \left(\sum_{t_i < t'} e^{-\gamma(t' - t_i)} E \|I_i(x(t_i))\|^2 \right) \\
&\leq M^2 \|I - S(t'' - t')\|^2 \left(\sum_{t_i < t'} e^{-\gamma(t' - t_i)} \right)^2 \|I\|_{\infty}^2 \\
&\leq M^2 \|I - S(t'' - t')\|^2 \left(\frac{1}{1 - e^{-\gamma\alpha}} \right)^2 \|I\|_{\infty}^2 \leq \frac{\varepsilon}{9},
\end{aligned}$$

for all $t', t'' \in (t_i, t_{i+1})$, $t' < t''$ provided $|t'' - t'| < \delta$. Thus, we have shown that the estimate

$$E \|\mathcal{L}x(t') - \mathcal{L}x(t'')\|^2 < \varepsilon,$$

holds for all $t', t'' \in (t_i, t_{i+1})$, $t' < t''$ provided $|t'' - t'| < \delta$, which means $\mathcal{L}x(t) \in \mathcal{UPC}$.

Step 2. We prove the almost periodicity of $\mathcal{L}x(t)$.

For $\Phi_1(t)$, let $t_i < t < t_{i+1}$; by (H1), (H2), and Hölder's inequality, we have that

$$\begin{aligned}
& E \|\Phi_1(t + \tau) - \Phi_1(t)\|^2 \\
&= E \left\| \int_{-\infty}^{t+\tau} S(t + \tau - s) b(s, x_s) ds - \int_{-\infty}^t S(t - s) b(s, x_s) ds \right\|^2 \\
&= E \left\| \int_{-\infty}^t S(t - s) [b(s + \tau, x_{s+\tau}) - b(s, x_s)] ds \right\|^2 \\
&\leq E \left(\int_{-\infty}^t M e^{-\gamma(t-s)} \|b(s + \tau, x_{s+\tau}) - b(s, x_s)\| ds \right)^2 \\
&\leq \frac{M^2}{\gamma} \left(\sum_{j=-\infty}^{i-1} \int_{t_j+\eta}^{t_{j+1}-\eta} e^{-\gamma(t-s)} E \|b(s + \tau, x_{s+\tau}) - b(s, x_s)\|^2 ds \right. \\
&\quad + \sum_{j=-\infty}^{i-1} \int_{t_j}^{t_{j+1}-\eta} e^{-\gamma(t-s)} E \|b(s + \tau, x_{s+\tau}) - b(s, x_s)\|^2 ds \\
&\quad + \sum_{j=-\infty}^{i-1} \int_{t_{j+1}-\eta}^{t_{j+1}} e^{-\gamma(t-s)} E \|b(s + \tau, x_{s+\tau}) - b(s, x_s)\|^2 ds \\
&\quad \left. + \int_{t_i}^{t_{i+1}-\eta} e^{-\gamma(t-s)} E \|b(s + \tau, x_{s+\tau}) - b(s, x_s)\|^2 ds \right),
\end{aligned}$$

where $\eta = \min\{\varepsilon, \frac{\alpha}{2}\}$. By Lemma 2.1 and (H2), we find that for any $\varepsilon > 0$ and $i \in \mathbb{Z}$, there exists a real number $l(\varepsilon, \Lambda) > 0$ such that every interval of length $l(\varepsilon, \Lambda)$ contains at least a constant τ and

$$E \|b(t + \tau, x_{t+\tau}) - b(t, x_t)\|^2 < \varepsilon, \quad \forall t \in \mathbb{R},$$

for each $x \in \Lambda$, $|t - t_i| > \varepsilon$, since $b \in \mathcal{AP}_{\mathcal{T}}(\mathbb{R}, L^2(\Omega, \mathbb{H}))$, where $\Lambda \subset \mathcal{C}_{\theta}$ is compact.

For $s \in [t_j + \eta, t_{j+1} - \eta]$, $j \in \mathbb{Z}$, $j \leq i$, $t - s \geq t - t_i + t_i - (t_{j+1} - \eta) \geq t - t_i + \alpha(i + j - 1) + \eta$, we have

$$\begin{aligned}
& \sum_{j=-\infty}^{i-1} \int_{t_j+\eta}^{t_{j+1}-\eta} e^{-\gamma(t-s)} E \|b(s + \tau, x_{s+\tau}) - b(s, x_s)\|^2 ds \\
&\leq \varepsilon \sum_{j=-\infty}^{i-1} \int_{t_j+\eta}^{t_{j+1}-\eta} e^{-\gamma(t-s)} ds \leq \frac{\varepsilon}{\gamma} \sum_{j=-\infty}^{i-1} e^{-\gamma(t-t_{j+1}+\eta)} \\
&\leq \frac{\varepsilon}{\gamma} \sum_{j=-\infty}^{i-1} e^{-\gamma\alpha(i-j+1)} \leq \frac{\varepsilon}{\gamma(1 - e^{-\gamma\alpha})}.
\end{aligned}$$

For $s \in [t_j, t_j + \eta]$, $j \in \mathbb{Z}$, $j \leq i$, by the mean value theorem of integral, we get that

$$\begin{aligned} & \sum_{j=-\infty}^{i-1} \int_{t_j}^{t_{j+\eta}} e^{-\gamma(t-s)} E \|b(s+\tau, x_{s+\tau}) - b(s, x_s)\|^2 ds \\ & \leq 2 \sup_{s \in \mathbb{R}} E \|b(s, x_s)\|^2 \sum_{j=-\infty}^{i-1} \int_{t_j}^{t_{j+\eta}} e^{-\gamma(t-s)} ds \leq 2 \|b\|_{\infty}^2 \varepsilon e^{\gamma\eta} \\ & \quad \sum_{j=-\infty}^{i-1} e^{-\gamma(t-t_j)} \\ & \leq 2 \|b\|_{\infty}^2 \varepsilon e^{\gamma\eta} e^{\gamma(t-t_i)} \sum_{j=-\infty}^{i-1} e^{-\gamma\alpha(i-j)} \leq \frac{2 \|b\|_{\infty}^2 e^{\frac{\gamma}{2}}}{1 - e^{-\gamma\alpha}} \varepsilon. \end{aligned}$$

Similarly, we can show that

$$\begin{aligned} & \sum_{j=-\infty}^{i-1} \int_{t_{j+1-\eta}}^{t_{j+1}} e^{-\gamma(t-s)} E \|b(s+\tau, x_{s+\tau}) - b(s, x_s)\|^2 ds \leq C_1 \varepsilon, \\ & \int_{t_i}^{t_{i+\eta}} e^{-\gamma(t-s)} E \|b(s+\tau, x_{s+\tau}) - b(s, x_s)\|^2 ds \leq C_2 \varepsilon, \end{aligned}$$

where C_1, C_2 are two positive constants. Thus, we have introduced the next estimate:

$$E \|\Phi_1(t+\tau) - \Phi_1(t)\|^2 < N_1 \varepsilon,$$

where N_1 is a positive constant, which implies that $\Phi_1(t)$ is square-mean piecewise almost periodic.

We now show that $\Phi_2(t)$ is square-mean piecewise almost periodic. Recall that $t \mapsto \sigma(t)$ is piecewise almost periodic if for each $\varepsilon > 0$ there exists a real number $l(\varepsilon) > 0$ such that the estimate

$$\|\sigma(s+\tau) - \sigma(s)\|^2 < \varepsilon, \forall t \in \mathbb{R}, |t - t_i| > \varepsilon, i \in \mathbb{Z} \quad (14)$$

holds for every interval of length $l(\varepsilon)$ containing a number τ . By using (H1) and the computation of fBm, we have

$$\begin{aligned} & E \|\Phi_2(t+\tau) - \Phi_2(t)\|^2 \\ & = E \left\| \int_{-\infty}^{t+\tau} S(t+\tau-s) \sigma(s) dB^H(s) - \int_{-\infty}^t S(t-s) \sigma(s) dB^H(s) \right\|^2 \\ & = E \left\| \int_{-\infty}^t S(t-s) \sigma(s+\tau) dB^H(s+\tau) - \int_{-\infty}^t S(t-s) \sigma(s) dB^H(s) \right\|^2 \\ & = E \left\| \int_{-\infty}^t S(t-s) [\sigma(s+\tau) - \sigma(s)] d\tilde{B}^H(s) \right\|^2 \\ & = H(2H-1) \sum_{n=1}^{\infty} \int_{-\infty}^t \int_{-\infty}^t \|S(t-u) [\sigma(u+\tau) - \sigma(u)] Q^{\frac{1}{2}} e_n\| \\ & \quad \times \|S(t-v) [\sigma(v+\tau) - \sigma(v)] Q^{\frac{1}{2}} e_n\| \cdot |u-v|^{2H-2} dudv \\ & \leq H(2H-1) M^2 \sum_{n=1}^{\infty} \int_{-\infty}^t \int_{-\infty}^t e^{-\gamma(t-u)} \|\sigma(u+\tau) - \sigma(u)\| Q^{\frac{1}{2}} e_n\| \\ & \quad \times e^{-\gamma(t-v)} \|\sigma(v+\tau) - \sigma(v)\| Q^{\frac{1}{2}} e_n\| \cdot |u-v|^{2H-2} dudv \\ & \leq H(2H-1) M^2 \left(\int_{-\infty}^t (e^{-\gamma(t-s)} \|\sigma(s+\tau) - \sigma(s)\|_{L_2^0})^{\frac{1}{H}} ds \right)^{2H}. \end{aligned}$$

Furthermore, by Hölder's inequality, we have

$$\begin{aligned} & E \|\Phi_2(t+\tau) - \Phi_2(t)\|^2 \\ & \leq H(2H-1) M^2 \left(\int_{-\infty}^t e^{\frac{-\gamma(t-s)}{2H-1}} ds \right)^{\frac{2H-1}{2H}} \\ & \quad \left(\int_{-\infty}^t e^{-\gamma(t-s)} \|\sigma(s+\tau) - \sigma(s)\|_{L_2^0}^2 ds \right) \\ & \leq H(2H-1) M^2 \left(\frac{2H-1}{\gamma} \right)^{\frac{2H-1}{2H}} \\ & \quad \left(\sum_{j=-\infty}^{i-1} \int_{t_{j+1-\eta}}^{t_{j+1}} e^{-\gamma(t-s)} \|\sigma(s+\tau) - \sigma(s)\|_{L_2^0}^2 ds \right. \\ & \quad + \sum_{j=-\infty}^{i-1} \int_{t_j}^{t_{j+\eta}} e^{-\gamma(t-s)} \|\sigma(s+\tau) - \sigma(s)\|_{L_2^0}^2 ds \\ & \quad + \sum_{j=-\infty}^{i-1} \int_{t_{j+1-\eta}}^{t_{j+1}} e^{-\gamma(t-s)} \|\sigma(s+\tau) - \sigma(s)\|_{L_2^0}^2 ds \\ & \quad \left. + \int_{t_i}^{t_{i+\eta}} e^{-\gamma(t-s)} \|\sigma(s+\tau) - \sigma(s)\|_{L_2^0}^2 ds \right), \end{aligned}$$

where $\eta = \min\{\varepsilon, \frac{\alpha}{2}\}$. In the same way as that of handling $\Phi_1(t)$, one can introduce the estimate

$$E \|\Phi_2(t+\tau) - \Phi_2(t)\|^2 < N_2 \varepsilon,$$

where N_2 is a positive constant, and hence $\Phi_2(t)$ is piecewise square-mean almost periodic.

For $\Phi_3(t) = \sum_{t_i < t} S(t-t_i) I_i(x(t_i))$, $i \in \mathbb{Z}$, let $\beta_i = I_i(x(t_i))$. For $t_i < t \leq t_{i+1}$, $|t - t_i| > \varepsilon$, $|t - t_{i+1}| > \varepsilon$, $i \in \mathbb{Z}$, by (2), one has $t_{i+q+1} > t + \tau > t_{i+q}$. From (H3), it follows that β_i is a square-mean almost periodic sequence, for any $\varepsilon > 0$; there exists such a natural number $N = N(\varepsilon)$ that, for an arbitrary $k \in \mathbb{Z}$, there is at least one integer $p > 0$ in the segment $[k, k+N]$ such that the inequality

$$E \|\beta_{i+p} - \beta_i\|^2 < \varepsilon,$$

holds for all $i \in \mathbb{Z}$. We get

$$\begin{aligned} & E \|\Phi_3(t+\tau) - \Phi_3(t)\|^2 \\ & = E \left\| \sum_{t_i < t+\tau} S(t+\tau-t_i) \beta_i - \sum_{t_i < t} S(t-t_i) \beta_i \right\|^2 \\ & \leq E \|S(t-t_i) (\beta_{i+q} - \beta_i)\|^2 \\ & \leq M^2 \sum_{t_i < t} e^{-\gamma(t-t_i)} \sum_{t_i < t} e^{-\gamma(t-t_i)} E \|\beta_{i+q} - \beta_i\|^2 \\ & \leq \frac{M^2 \varepsilon}{(1 - e^{-\gamma\alpha})^2}, \end{aligned}$$

which implies that $\Phi_3(t) \in \mathcal{AP}_{\mathcal{T}}(\mathbb{R}, L^2(\Omega, \mathbb{H}))$. Thus, we have proved that $\mathcal{L}x(t) \in \mathcal{AP}_{\mathcal{T}}(\mathbb{R}, L^2(\Omega, \mathbb{H}))$ and $\mathcal{L}x(t)$ is square-mean piecewise almost periodic.

Proof of Statement (II). Given $B = \{u \in \mathcal{AP}_{\mathcal{T}}(\mathbb{R}, L^2(\Omega, \mathbb{H}))\}$ and assuming that $x(t), y(t) \in B$ are both almost periodic solutions of (1) and $x(t) \neq y(t)$, then we have

$$\begin{aligned}
& E\|\mathcal{L}x(t) - \mathcal{L}y(t)\|^2 \\
&= E\left\|\int_{-\infty}^t S(t-s)[b(s, x_s) - b(s, y_s)]ds\right. \\
&\quad \left. + \sum_{t_i < t} S(t-t_i)[I_i(x(t_i)) - I_i(y(t_i))]\right\|^2 \\
&\leq 2\left(E\left\|\int_{-\infty}^t S(t-s)[b(s, x_s) - b(s, y_s)]ds\right\|^2\right. \\
&\quad \left.+ E\left\|\sum_{t_i < t} S(t-t_i)[I_i(x(t_i)) - I_i(y(t_i))]\right\|^2\right) \\
&\equiv 2(A_1 + A_2).
\end{aligned}$$

From (H1), (H2), (H3) and the Cauchy-Schwarz inequality, we have that

$$\begin{aligned}
A_1 &\leq E\left(\int_{-\infty}^t M^2 e^{-2\gamma(t-s)} \|b(s, x_s) - b(s, y_s)\| ds\right)^2 \\
&\leq \left(\int_{-\infty}^t M^2 e^{-\gamma(t-s)} ds\right) \left(\int_{-\infty}^t e^{-\gamma(t-s)} E\|b(s, x_s) - b(s, y_s)\|^2 ds\right) \\
&\leq \frac{M^2}{\gamma} \int_{-\infty}^t e^{-\gamma(t-s)} M_b E\|x_s - y_s\|_{C_b}^2 ds \\
&\leq \frac{M^2}{\gamma^2} M_b \sup_{r \in \mathbb{R}} E\|x(r) - y(r)\|^2 = \frac{M^2 M_b}{\gamma^2} \|x - y\|_{\infty}^2,
\end{aligned}$$

and

$$\begin{aligned}
A_2 &\leq E\left\|\sum_{t_i < t} M^2 e^{-2\gamma(t-t_i)} [I_i(x(t_i)) - I_i(y(t_i))]\right\|^2 \\
&\leq \left(\sum_{t_i < t} M^2 e^{-\gamma(t-t_i)}\right) \left(\sum_{t_i < t} e^{-\gamma(t-t_i)} E\|I_i(x(t_i)) - I_i(y(t_i))\|^2\right) \\
&\leq \frac{M^2}{1 - e^{-\gamma\alpha}} \left(\sum_{t_i < t} e^{-\gamma(t-t_i)} M_I E\|x(t_i) - y(t_i)\|^2\right) \\
&\leq \frac{M^2 M_I}{(1 - e^{-\gamma\alpha})^2} \sup_{r \in \mathbb{R}} E\|x(r) - y(r)\|^2 = \frac{M^2 M_I}{(1 - e^{-\gamma\alpha})^2} \|x - y\|_{\infty}^2.
\end{aligned}$$

It follows that

$$E\|\mathcal{L}x(t) - \mathcal{L}y(t)\|^2 \leq \Theta \|x - y\|_{\infty}^2,$$

for each $t \in \mathbb{R}$, which implies that

$$\|\mathcal{L}x(t) - \mathcal{L}y(t)\|_{\infty} \leq \sqrt[2]{\Theta} \|x - y\|_{\infty}.$$

This means that \mathcal{L} is a contraction when (8) holds and statement (II) follows.

4 ASYMPTOTIC STABILITY

In this section, we are interested in the asymptotical stability of the almost periodic mild solution to (1) with $t_0 = 0$. For convenience, we rewrite the equation as follows:

$$\begin{cases} dx(t) = [Ax(t) + b(t, x_t)]dt + \sigma(t)dB^H(t), & t \in [t_0, \infty), \quad t \neq \pm t_i \quad i \in \mathbb{Z}, \\ \Delta x(t_i) = x(t_i^+) - x(t_i^-) = I_i(x(t_i)), & i \in \mathbb{Z}, \\ x_{t_0} = \xi = \{\xi(t) : -\theta \leq t \leq 0\}. \end{cases} \quad (15)$$

Lemma 4.1. ([30]). Let a nonnegative piecewise continuous function $t \mapsto v(t)$ satisfy the inequality

$$v(t) \leq C + \int_{t_0}^t u(\sigma)v(\sigma)d\sigma + \sum_{t_0 < \sigma_i < t} \alpha_i v(\sigma_i),$$

for $t \geq t_0$, where $C \geq 0$, $u(\sigma) > 0$, $\alpha_i \geq 0$, $i \in \mathbb{Z}$, and σ_i , $i \in \mathbb{Z}$ are the first kind discontinuity points of the function v . Then, the following estimate holds:

$$v(t) \leq C \prod_{t_0 < \sigma_i < t} (1 + \alpha_i) e^{\int_{t_0}^t u(\sigma)d\sigma}.$$

Theorem 4.1. Assume that (H1) – (H3) hold. The almost periodic solutions to (15) are asymptotically stable in the square-mean sense if

$$\frac{1}{\alpha} \ln\left(1 + \frac{3M^2 M_I}{1 - e^{-\gamma\alpha}}\right) - \gamma + \frac{3M^2 M_b}{\gamma} < 0, \quad (16)$$

Proof. Let $x(t)$ and $x^*(t)$ be two square-mean piecewise almost periodic mild solutions of (15); we then have that

$$\begin{aligned}
E\|x(t) - x^*(t)\|^2 &= E\left\|S(t)[\xi - \xi^*] + \int_0^t S(t-s)[b(s, x_s) - b(s, x_s^*)]ds\right. \\
&\quad \left.+ \sum_{0 < t_i < t} S(t-t_i)[I_i(x(t_i)) - I_i(x^*(t_i))]\right\|^2,
\end{aligned}$$

for all $t \geq 0$. By using Cauchy-Schwartz's inequality, Fubini's theorem, and assumptions (H1) – (H3), we deduce that

$$\begin{aligned}
E\|x(t) - x^*(t)\|^2 &\leq 3E\|S(t)[\xi - \xi^*]\|^2 + 3E\left\|\int_0^t S(t-s)[b(s, x_s) - b(s, x_s^*)]ds\right\|^2 \\
&\quad + 3E\left\|\sum_{0 < t_i < t} S(t-t_i)[I_i(x(t_i)) - I_i(x^*(t_i))]\right\|^2 \\
&\leq 3M^2 e^{-2\gamma t} \|\xi - \xi^*\|^2 + 3E\left(\int_0^t M e^{-\gamma(t-s)} \|b(s, x_s) - b(s, x_s^*)\| ds\right)^2 \\
&\quad + 3E\left\|\sum_{0 < t_i < t} M e^{-\gamma(t-t_i)} [I_i(x(t_i)) - I_i(x^*(t_i))]\right\|^2 \\
&\leq 3M^2 e^{-\gamma t} \|\xi - \xi^*\|^2 + 3 \int_0^t M^2 e^{-\gamma(t-s)} ds \int_0^t e^{-\gamma(t-s)} E\|b(s, x_s) - b(s, x_s^*)\|^2 ds \\
&\quad + 3\left(\sum_{0 < t_i < t} M^2 e^{-\gamma(t-t_i)}\right) \left(\sum_{0 < t_i < t} e^{-\gamma(t-t_i)} E\|I_i(x(t_i)) - I_i(x^*(t_i))\|^2\right) \\
&\leq 3M^2 e^{-\gamma t} \|\xi - \xi^*\|^2 + \frac{3M^2}{\gamma} M_b \int_0^t e^{-\gamma(t-s)} \|x_s - x_s^*\|_{C_b}^2 ds \\
&\quad + \frac{3M^2}{1 - e^{-\gamma\alpha}} M_I \left(\sum_{0 < t_i < t} e^{-\gamma(t-t_i)} E\|x(t_i) - x^*(t_i)\|^2\right) \\
&\leq 3M^2 e^{-\gamma t} \|\xi - \xi^*\|^2 + \frac{3M^2}{\gamma} M_b \int_0^t e^{-\gamma(t-s)} \left(\sup_{0 \leq r \leq s} E\|x(r) - x^*(r)\|^2\right) ds \\
&\quad + \frac{3M^2}{1 - e^{-\gamma\alpha}} M_I \left(\sum_{0 < t_i < t} e^{-\gamma(t-t_i)} E\|x(t_i) - x^*(t_i)\|^2\right),
\end{aligned}$$

for $t \geq 0$. Multiplying both sides of the above inequality by $e^{\gamma t}$, we get

$$\begin{aligned}
e^{\gamma t} E\|x(t) - x^*(t)\|^2 &\leq 3M^2 \|\xi - \xi^*\|^2 \\
&\quad + \frac{3M^2}{\gamma} M_b \int_0^t e^{\gamma s} \left(\sup_{0 \leq r \leq s} E\|x(r) - x^*(r)\|^2\right) ds \\
&\quad + \frac{3M^2}{1 - e^{-\gamma\alpha}} M_I \left(\sum_{0 < t_i < t} e^{\gamma t_i} E\|x(t_i) - x^*(t_i)\|^2\right),
\end{aligned}$$

for $t \geq 0$, which implies that

$$\begin{aligned} \sup_{0 \leq s \leq t} e^{\gamma s} E \|x(s) - x^*(s)\|^2 &\leq 3M^2 \|\xi - \xi^*\|^2 + \frac{3M^2}{\gamma} M_b \int_0^t \\ &\times \sup_{0 \leq r \leq s} e^{\gamma r} E \|x(r) - x^*(r)\|^2 ds \\ &+ \frac{3M^2}{1 - e^{-\gamma\alpha}} M_I \left(\sum_{0 < t_i < t} \sup_{0 \leq r \leq t_i} e^{\gamma r} E \|x(r) - x^*(r)\|^2 \right), \end{aligned}$$

for $t \geq 0$. Combining this with Lemma 4.1, we get that

$$\begin{aligned} \sup_{0 \leq s \leq t} e^{\gamma s} E \|x(s) - x^*(s)\|^2 &\leq 3M^2 \|\xi - \xi^*\|^2 \prod_{0 < t_i < t} \left(1 + \frac{3M^2}{1 - e^{-\gamma\alpha}} M_I \right) e^{\int_0^t \frac{3M^2}{\gamma} M_b d\sigma} \\ &\leq 3M^2 \|\xi - \xi^*\|^2 \left(1 + \frac{3M^2}{1 - e^{-\gamma\alpha}} M_I \right)^{\frac{t}{\alpha}} e^{\frac{3M^2}{\gamma} M_b t}, \end{aligned}$$

for $t \geq 0$. So,

$$e^{\gamma t} E \|x(t) - x^*(t)\|^2 \leq 3M^2 \|\xi - \xi^*\|^2 \left(1 + \frac{3M^2}{1 - e^{-\gamma\alpha}} M_I \right)^{\frac{t}{\alpha}} e^{\frac{3M^2}{\gamma} M_b t},$$

for $t \geq 0$. Thus, we get the desired estimate

$$\begin{aligned} E \|x(t) - x^*(t)\|^2 &\leq 3M^2 \|\xi - \xi^*\|^2 \left(1 + \frac{3M^2}{1 - e^{-\gamma\alpha}} M_I \right)^{\frac{t}{\alpha}} e^{\frac{3M^2}{\gamma} M_b t} e^{-\gamma t} \\ &\leq 3M^2 \|\xi - \xi^*\|^2 e^{\left[\frac{1}{\alpha} \ln \left(1 + \frac{3M^2 M_I}{1 - e^{-\gamma\alpha}} \right) - \gamma + \frac{3M^2 M_b}{\gamma} \right] t}, \end{aligned}$$

and the square-mean piecewise almost periodic solution of (15) is asymptotically stable in the square-mean sense because of (16). This completes the proof.

5 AN EXAMPLE

Consider the semilinear impulsive stochastic partial functional differential equations of the following form:

$$\begin{cases} dv(t, x) = \left[\frac{\partial^2}{\partial x^2} v(t, x) + 2a \sin(x(t-r)) \sin t \right] dt \\ \quad + \cos t dB^H(t), \quad t \neq \pm t_i \quad i \in \mathbb{Z}, \\ \Delta x(t_i) = x(t_i^+) - x(t_i^-) = 2a \cos(x(t_i)), \quad i \in \mathbb{Z}, \\ v(t, 0) = v(t, \pi) = 0, \\ x_{t_0} = \xi = \{\xi(s) : -\theta \leq s \leq 0\}, \end{cases} \quad (17)$$

where r is a constant and $B^H(t)$ is a fractional Brownian motion. Denote $X = L^2(\Omega, L^2([0, \pi]))$ and define $A: D(A) \subseteq X \rightarrow X$ given by $A = \frac{\partial^2}{\partial x^2}$ with the following domain:

$$D(A) = \{v(\cdot) \in X : v'' \in X, v' \in X \text{ are absolutely continuous on } [0, \pi]\}.$$

It is well known that a strongly continuous semigroup $\{S(t)\}_{t \geq 0}$ generated by the operator A satisfies $\|S(t)\| \leq e^{-t}$, for $t \geq 0$. Take

$$b(t, x_t) = 2a \sin(x_t) \sin t,$$

and

$$I_i(x(t_i)) = 2a \cos(x(t_i)).$$

Thus, one has

$$E \|b(t, x_t) - b(t, y_t)\|^2 \leq 4a^2 \|x_t - y_t\|_{C_\theta}^2,$$

and

$$\|I_i(x) - I_i(y)\|^2 \leq 4a^2 \|x - y\|^2.$$

Let $\alpha = 1$. Then, (17) has a square-mean piecewise almost periodic mild solution, provided that $0 < a^2 < \frac{1}{16}$ by Theorem 3.1, and moreover the solution of (17) is asymptotically stable in the square-mean sense provided that $0 < a^2 < \frac{1}{36}$ by Theorem 4.1.

6 CONCLUSION

In this article, we have investigated the existence and asymptotic stability of square-mean piecewise almost periodic mild solutions for a class of impulsive stochastic delay differential equations driven by fractional Brownian motion with the Hurst parameter $H \in (\frac{1}{2}, 1)$ in a Hilbert space. An example is presented to illustrate our theoretical results. Fractional Brownian motion B^H with $H \in (0, \frac{1}{2})$ admits different Wiener integral representation from fractional Brownian motion with $H \in (\frac{1}{2}, 1)$. It is difficult to get the square-mean piecewise almost periodic mild solutions of ISDEs driven by fractional Brownian motion with $H \in (0, \frac{1}{2})$ in a Hilbert space properly due to estimation without moment.

DATA AVAILABILITY STATEMENT

The raw data supporting the conclusion of this article will be made available by the authors, without undue reservation.

AUTHOR CONTRIBUTIONS

LG and XS carried out the mathematical studies, participated in the sequence alignment, drafted the manuscript and participated in the design of the study and performed proof of results. All authors read and approved the submitted version.

FUNDING

This work was supported by the National Natural Science Foundation of China, No. 11971101; Natural Science Foundation of Anhui Province, No.1808085MA02; and Natural Science Foundation of Bengbu University, Nos. 2020ZR04zd and BBXY2020KYQD05.

ACKNOWLEDGMENTS

The authors are indebted to Professor Litan Yan for his encouragement and helpful discussion. The authors are grateful to the referees and the associate editor for valuable comments and suggestions to improve this article.

REFERENCES

1. Tsokos CP, Padgett WJ. *Random Integral Equations with Applications to Life Sciences and Engineering*. New York: Academic Press (1974).
2. Arthi G, Park JH, Jung HY. Existence and Exponential Stability for Neutral Stochastic Integrodifferential Equations with Impulses Driven by a Fractional Brownian Motion. *Commun Nonlinear Sci Numer Simulation* (2016) 32: 145–57. doi:10.1016/j.cnsns.2015.08.014
3. Caraballo T. Existence of Mild Solutions to Stochastic Delay Evolution Equations with a Fractional Brownian Motion and Impulses. *Stoch Anal Appl* (2015) 33:244–58. doi:10.1080/07362994.2014.981641
4. Cheng L, Hu L, Ren Y. Perturbed Impulsive Neutral Stochastic Functional Differential Equations. *Qual Theor Dyn Syst*. (2021) 20:27. doi:10.1007/s12346-021-00469-7
5. Shi J, Li C, Sun J. Stability of Impulsive Stochastic Differential Delay Systems and its Application to Impulsive Stochastic Neural Networks. *Nonlinear Anal* (2011) 74:3099–111. doi:10.1016/j.na.2011.01.026
6. Liu X, Liu J, Xie W. Existence and Uniqueness Results for Impulsive Hybrid Stochastic Delay Systems. *Appl Nonlinear Anal* (2010) 17:37–53. doi:10.1016/j.nahs.2009.11.004
7. Sakthivel R, Luo J. Asymptotic Stability of Nonlinear Impulsive Stochastic Differential Equations. *Stat Probab Lett* (2009) 79:1219–23. doi:10.1016/j.spl.2009.01.011
8. Wu X, Yan L, Zhang W, Chen L. Exponential Stability of Impulsive Stochastic Delay Differential Systems. *Discrete Dyn Nat Soc* (2012) 2012:1–15. doi:10.1155/2012/296136
9. Chen H, Xiao S. Existence and Exponential Stability for Impulsive Stochastic Partial Functional Differential Equations. *J Math Phys* (2017) 58:032701. doi:10.1063/1.4976727
10. Ma S, Kang Y. Periodic Averaging Method for Impulsive Stochastic Differential Equations with Lévy Noise. *Appl Maths Lett* (2019) 93:91–7. doi:10.1016/j.aml.2019.01.040
11. Guo Y, Zhu Q, Wang F. Stability Analysis of Impulsive Stochastic Functional Differential Equations. *Commun Nonlinear Sci Numer Simulation* (2020) 82: 105013. doi:10.1016/j.cnsns.2019.105013
12. Li M. Multi-fractional Generalized Cauchy Process and its Application to Teletraffic. *Physica A: Stat Mech its Appl* (2020) 550:123982. doi:10.1016/j.physa.2019.123982
13. Li M. Generalized Fractional Gaussian Noise and its Application to Traffic Modeling. *Physica A* (2020) 579:12638. doi:10.1016/j.physa.2021.126138
14. Li M. Modified Multifractional Gaussian Noise and its Application. *Phys Scr* (2021) 96:125002. doi:10.1088/1402-4896/ac1cf6
15. Zachevsky I, Zeevi YY. Single-Image Superresolution of Natural Stochastic Textures Based on Fractional Brownian Motion. *IEEE Trans Image Process* (2014) 23:2096–108. doi:10.1109/TIP.2014.2312284
16. Ksendal B. *Fractional Brownian Motion in Finance*. London: Springer (2008).
17. Heydari MH, Mahmoudi MR, Shakiba A, Avazzadeh Z. Chebyshev Cardinal Wavelets and Their Application in Solving Nonlinear Stochastic Differential Equations with Fractional Brownian Motion. *Commun Nonlinear Sci Numer Simulation* (2018) 64:98–121. doi:10.1016/j.cnsns.2018.04.018
18. Heydari MH, Avazzadeh Z, Mahmoudi MR. Chebyshev Cardinal Wavelets for Nonlinear Stochastic Differential Equations Driven with Variable-Order Fractional Brownian Motion. *Chaos, Solitons & Fractals* (2019) 124:105–24. doi:10.1016/j.chaos.2019.04.040
19. Li Z, Xu L, Zhou J. Viability for Coupled SDEs Driven by Fractional Brownian Motion. *Appl Maths Optimization* (2021) 84:55C98. doi:10.1007/s00245-021-09761-z
20. Cui J, Yan L. Controllability of Neutral Stochastic Evolution Equations Driven by Fractional Brownian Motion. *Acta Mathematica Scientia* (2017) 37:108–18. doi:10.1016/s0252-9602(16)30119-9
21. Biagini F, Hu Y, Øksendal B, Zhang T. *Stochastic Calculus for Fractional Brownian Motion and Applications*. New York: Springer (2008).
22. Hu Y. Integral Transformations and Anticipative Calculus for Fractional Brownian Motions. *Mem AMS* (2005) 175:825. doi:10.1090/memo/0825
23. Mishura Y. *Stochastic Calculus for Fractional Brownian Motion and Related*. New York: Springer (2008).
24. Nurlart D. *The Malliavin Calculus and Related Topics*. New York: Springer (2006).
25. Stamov GT. *Almost Periodic Solutions of Impulsive Differential Equations*. New York: Springer (2012).
26. Liu J, Zhang C. Existence and Stability of Almost Periodic Solutions to Impulsive Stochastic Differential Equations. *CUBO* (2013) 15:77–96. doi:10.4067/s0719-06462013000100005
27. Henríquez HR, De Andrade B, Rabelo M. Existence of Almost Periodic Solutions for a Class of Abstract Impulsive Differential Equations. *ISRN Math Anal* (2011) 2011:1–21. doi:10.5402/2011/632687
28. Samoilenko AM, Perestyuk NA. *Impulsive Differential Equations*. Singapore: World Scientific (1995).
29. Yoshizawa T. *Stability Theory and Existence of Periodic Solutions and Almost Periodic Solutions*. New York: Springer (1975).
30. Wang Y, Liu Z. Almost Periodic Solutions for Stochastic Differential Equations with Lévy Noise. *Nonlinearity* (2012) 25:2803–21. doi:10.1088/0951-7715/25/10/2803

Conflict of Interest: The authors declare that the research was conducted in the absence of any commercial or financial relationships that could be construed as a potential conflict of interest.

Publisher's Note: All claims expressed in this article are solely those of the authors and do not necessarily represent those of their affiliated organizations, or those of the publisher, the editors and the reviewers. Any product that may be evaluated in this article, or claim that may be made by its manufacturer, is not guaranteed or endorsed by the publisher.

Copyright © 2021 Gao and Sun. This is an open-access article distributed under the terms of the Creative Commons Attribution License (CC BY). The use, distribution or reproduction in other forums is permitted, provided the original author(s) and the copyright owner(s) are credited and that the original publication in this journal is cited, in accordance with accepted academic practice. No use, distribution or reproduction is permitted which does not comply with these terms.



Global Mean Sea Level. Time Trends and Persistence with Long Range Dependent Data

Luis Alberiko Gil-Alana^{1,2*}

¹Faculty of Economics and NCID-ICS, University of Navarra, Pamplona, Spain, ²Facultad de Ciencias Jurídicas y Empresariales, Universidad Francisco de Vitoria, Madrid, Spain

Global mean sea level data are examined in this work by looking at the presence of time trends in the context of long memory or long range dependent processes. By looking at both seasonal signals retained and seasonal signals removed data from 1992 to 2020, the results show that the two series display significant time trend coefficients and high levels of persistence.

Keywords: sea level, time trend, fractional integration, long memory JEL classification: C12, K32, Q54, nonstationarity

1 INTRODUCTION

The evidence shows that global mean sea level (GMSL) has risen during the 20th century [1], and this rise has been larger than that observed during the previous two centuries [2]. In line with this, GMSL data are examined in this work by using a long memory or long range dependent model. The idea is to estimate a linear time trend in the data under the assumption that the errors in the regression model might be fractionally integrated, which is a particular model within the long memory class. The reason for this is that this property (long memory) has been widely observed in the majority of geophysical and climatological series (see, e.g., [3–5]; etc.) and therefore it should also be expected in the sea level data (see also [6]).

The model examined in the empirical section is the following one:

$$y_t = \gamma_0 + \gamma_1 \beta t + x_t, \quad (1 - B)^d x_t = u_t, \quad (1)$$

where y_t is the sea level data; γ_0 and γ_1 are unknown parameters referring to an intercept and a (linear) time trend, and x_t is the regression error that is assumed to be integrated of order d or $I(d)$ where d can be any real value, and thus, potentially fractional. In this context, B is the backshift operator, i.e., $B^k x_t = x_{t-k}$, and the d -differenced process u_t in (1) is supposed to be integrated of order 0, or $I(0)$, defined as a covariance stationary process where its spectral density function is positive and bounded at all frequencies. It includes the case of a white noise process but also stationary and invertible AutoRegressive Moving Average (ARMA) models. Thus, if u_t is ARMA(p, q), x_t is said to be AutoRegressive Fractionally Integrated Moving Average (ARFIMA(p, d, q)) model. In this paper, however, we will deal with the autocorrelation by using a non-parametric method [7] widely used in the context of $I(d)$ models. In this context, evidence of significantly positive values of γ_1 in (1) will indicate that the sea level data reflect increases over time, and we do the estimation without imposing the strong assumption that the x_t in (1) are $I(0)$ but $I(d)$ with d freely estimated from the data.

2 METHODOLOGY

As it has been mentioned in the previous section, the methodology used in this work is based on long memory, which is a feature observed in many time series of different disciplines including among

OPEN ACCESS

Edited by:

Ming Li,
Zhejiang University, China

Reviewed by:

Manuel Monge,
Universidad Francisco de Vitoria,
Spain
Junyu He,
Zhejiang University, China

*Correspondence:

Luis Alberiko Gil-Alana
alana@unav.es

Specialty section:

This article was submitted to
Interdisciplinary Physics,
a section of the journal
Frontiers in Physics

Received: 18 October 2021

Accepted: 22 November 2021

Published: 13 December 2021

Citation:

Gil-Alana LA (2021) Global Mean Sea
Level. Time Trends and Persistence
with Long Range Dependent Data.
Front. Phys. 9:797402.
doi: 10.3389/fphy.2021.797402

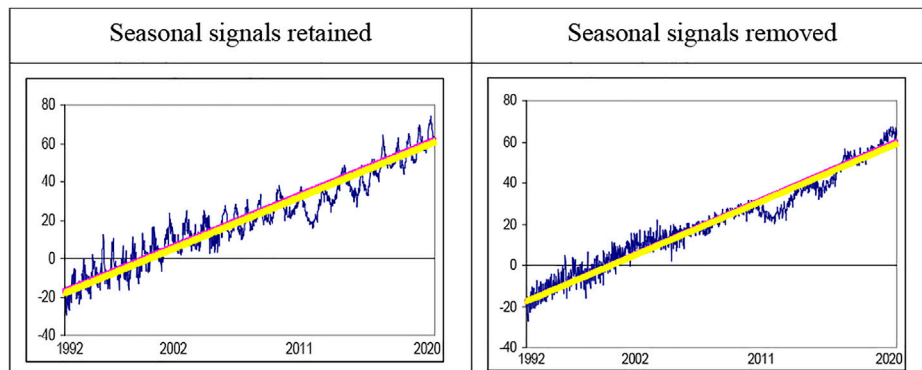


FIGURE 1 | Time series plots. Seasonal signals retained. Seasonal signals removed.

TABLE 1 | Estimated coefficients I: White noise errors.

| Series | d | | |
|-------------------|-------------------|------------------|---------------|
| Seasonal retained | 0.73 (0.69, 0.78) | -17.3955 (-5.86) | 0.0639 (3.95) |
| Seasonal removed | 0.73 (0.69, 0.78) | -17.3955 (-5.86) | 0.0639 (3.95) |

In parenthesis in column 2: 95% confidence band of values of d . In columns 3 and 4, t -values.

TABLE 2 | Estimated coefficients imposing $d = 0$.

| Series | d (diff. par.) | γ_0 | γ_1 |
|-------------------|------------------|-------------------|-----------------|
| Seasonal retained | 0.00 | -15.6869 (-42.89) | 0.0591 (115.36) |
| Seasonal removed | 0.00 | -15.5863 (-83.52) | 0.0590 (225.60) |

others climatological and meteorological data. Long memory processes are characterized because the spectral density function of the data (which is the Fourier transform of the autocovariances) displays values that explode at the smallest (zero) frequency, which is usually consistent with first differentiation of the data. However, in many cases, the spectral density function of the first differenced data shows values close to zero at the zero frequency, which is consistent with over-differentiation. This was the origin of fractional differentiation [8], which is a particular model satisfying the long memory property, and that is described by the second equation presented in (1).

The differencing parameter d is important from various viewpoints. Thus, if $d = 0$, the series is said to be short memory or $I(0)$, unlike what happens with positive d that implies long memory or long range dependence, so-named because of the strong degree of association between the observations even if they are far distant in time; also, from a statistical viewpoint, the value 0.5 is important. Thus, if $d < 0.5$ the series is still covariance stationary, while $d \geq 0.5$ implies nonstationarity; finally, if $d < 1$ the series is said to be mean reverting with the effect of the shocks disappearing in the long run, contrary to what happens with $d \geq 1$ with shocks persisting forever.

We estimate the parameter d by using the Whittle function expressed in the frequency domain, employing a version of the tests of Robinson [9] widely used in empirical applications (see, e.g. [10]). Note, however, that the fractional integration approach employed in this work is merely one of the numerous formulations for long range

dependence that include among others the generalized Cauchy processes, the generalized fractional Gaussian noise models and the modified multifractional fractional Gaussian noise model (see, e.g., [11, 12]). These methods may also be considered as flexible tools to investigate long range dependence in time series, including sea level data ([13, 14], etc.).

3 DATASET

We use data which are estimates of sea level based on measurements from satellite radar altimeters. They are available for TOPEX/Poseidon (T/P), Jason-1, Jason-2, and Jason-3, which have been monitored. Only altimetry measurements between 66°S and 66°N have been processed. An inverted barometer has been applied to the time series.

Two time series are examined (see Figure 1) referring to the global mean sea level data, with seasonal signals retained and removed.

The data are provided by the NOAA Laboratory for Satellite Altimetry from the NOAA (<http://www.star.nesdis.noaa.gov/sod/lsa/SeaLevelRise/>) and Radar Altimeter Database System (<http://www.deos.tudelft.nl/altim/rads/>).

4 RESULTS

Table 1 displays the estimated coefficients of the model given by Eq. 1 under the assumption that the error term u_t is a white noise process. We observe that the estimated value of d is 0.73 for the seasonal signals retained data and 0.45 for the seasonal signals removed data, and in both cases, the confidence intervals reject the null of $d = 1$ in favour of $d < 1$, implying mean reversion in its behaviour. Thus, shocks will have a transitory effect in the series, disappearing by themselves in the long run, and faster in the case of the seasonal signals removed data. The time trend coefficient is significantly positive in the two series, being slightly higher with the seasonal signals retained data.

Very similar results are obtained under the assumption of autocorrelated (Bloomfield)¹ errors. The estimates of d are now

¹The model of Bloomfield [7] is a non-parametric approach that produces errors with the autocorrelation function decaying exponentially fast as in the ARMA case. (see [17], for its implementation in the context of fractional integration).

TABLE 3 | Estimated coefficients II: Weakly autocorrelated (Bloomfield) errors.

| Series | d (diff. par.) | γ_0 | γ_1 |
|-------------------|-------------------|-------------------|----------------|
| Seasonal retained | 0.66 (0.59, 0.75) | -17.7419 (-6.52) | 0.0637 (6.65) |
| Seasonal removed | 0.38 (0.34, 0.42) | -17.4462 (-15.31) | 0.0622 (37.23) |

In parenthesis in column 2: 95% confidence band of values of d. In columns 3 and 4, t-values.

slightly smaller (0.66 for the seasonal retained data and 0.38 for the seasonal removed data), and the slope coefficients are again significant, 0.0637 in the first case (seasonal retained) and 0.0622 in the seasonal signals removed data. The estimated time trends are displayed in **Figure 1**.

Finally, in **Table 2**, we display the coefficients under the assumption that x_t in **Eq. 1** is I (0). Thus, the long memory feature is not taken into account. We observe that the slope coefficient, though significant, is slightly smaller than under the I (d) specification. Note, however, that this hypothesis is decisively rejected according to the results in **Tables 1, 3** where d was found to be significantly positive. Thus, the fact that the long memory is not considered here produces a bias reducing the amount of the global sea level rise.

5 CONCLUSION

We have examined data corresponding to the global mean sea level for the time period from 1992 to 2020, using a long range dependent model based on fractional integration and testing for the presence of time trends. Our results show first that long range dependence is a

feature of these data, consistent with works such as Ercan et al. [6] and others, since the degree of differentiation is in the interval (0, 1) in the two series examined. Moreover, the slope coefficient is highly significantly positive and slightly higher than the one observed under the wrong assumption that the errors are I (0).

Further work with these series should investigate other alternative approaches for trends in the data such as LOWESS, piece-wise-linear trends, or the presence of non-linear trends, using, for example, either segmented trends based on structural breaks or, alternatively, using non-linear polynomials in time, like those based on Chebyshev polynomials [15], in both cases using still long memory and fractional integration. Data disaggregated by areas should also be examined. Finally, it would also be of interest to link the inter-annual fluctuations with ENSO as suggested by authors such as Cazenave et al. [16]. Work in these directions is now in progress.

DATA AVAILABILITY STATEMENT

The raw data supporting the conclusion of this article will be made available by the authors, without undue reservation.

AUTHOR CONTRIBUTIONS

LG-A is the only contributor of the manuscript.

REFERENCES

- Oppenheimer M, Glavovic BC, Hinkel J, van de Wal R, Magnan AK, AbdElgawad A, et al. Sea Level Rise and Implications for Low-Lying Islands, Coasts and Communities. In: *IPCC Special Report on the Ocean and Cryosphere in a Changing Climate*. Springer (2019). p. 321–446.
- Warrick RA, Oerlemans J. Sea Level Rise. In: JT Houghton, GJ Jenkins, JJ Ephraim, editors. *Climate Change: The IPCC Scientific Assessment*. Cambridge, United Kingdom, and New York, NY, USA: Cambridge University Press (1990). p. 260–81.
- Bunde A. Long-term Memory in Climate: Detection, Extreme Events and Significance of Trends. In: CLE Franzke T O'Kane, editors. *Chapter 11 in Nonlinear and Stochastic Climate Dynamics*. Cambridge University Press (2017).
- Gil-Alana LA, Sauci L. Temperatures across Europe: Evidence of Time Trends. *Climatic Change* (2019) 157:355–64. doi:10.1007/s10584-019-02568-6
- Yuan N, Huang Y, Duan J, Zhu C, Xoplaki E, Luterbacher J. On Climate Prediction: How Much Can We Expect from Climate Memory? *Clim Dyn* (2019) 52:855–64. doi:10.1007/s00382-018-4168-5
- Ercan A, Kavvas ML, Abbasov RK. Introduction. In: *Long-range Dependence and Sea Level Forecasting*. Springer International Publishing. Springer Briefs in Statistics (2013). p. 1–5. doi:10.1007/978-3-319-01505-7_1
- Bloomfield P. An Exponential Model for the Spectrum of a Scalar Time Series. *Biometrika* (1973) 60:217–26. doi:10.1093/biomet/60.2.217
- Granger CWJ. Long Memory Relationships and the Aggregation of Dynamic Models. *J Econom* (1980) 14:227–38. doi:10.1016/0304-4076(80)90092-5
- Robinson PM. Efficient Tests of Nonstationary Hypotheses. *J Am Stat Assoc* (1994) 89:1420–37. doi:10.1080/01621459.1994.10476881
- Gil-Alana LA, Robinson PM. Testing of Unit Root and Other Nonstationary Hypotheses in Macroeconomic Time Series. *J Econom* (1997) 80(2):241–68. doi:10.1016/s0304-4076(97)00038-9
- Beran J. Statistical Methods for Data with Long-Range Dependence. *Stat Sci* (1992) 7(4):404–16. doi:10.1214/ss/1177011122
- Li M. Generalized Fractional Gaussian Noise and its Application to Traffic Modelling. *Physica A* (2021) 579:123613722. doi:10.1016/j.physa.2021.126138
- Li M, Li J-Y. Generalized Cauchy Model of Sea Level Fluctuations with Long-Range Dependence. *Physica A: Stat Mech its Appl* (2017) 484:309–35. doi:10.1016/j.physa.2017.04.130
- Li M. Modified Multifractional Gaussian Noise and its Application. *Phys Scr* (2021) 96(12):12500212. doi:10.1088/1402-4896/ac1cf6
- Cuestas JC, Gil-Alana LA. Testing for Long Memory in the Presence of Non-linear Deterministic Trends with Chebyshev Polynomials. *Stud Nonlinear Dyn Econom* (2016) 20:57–74. doi:10.1515/snde-2014-0005
- Cazenave A, Dieng H-B, Meyssignac B, von Schuckmann K, Decharme B, Berthier E. The Rate of Sea-Level Rise. *Nat Clim Change* (2014) 4:358–61. doi:10.1038/nclimate2159
- Gil-Alana LA. The Use of the bloomfield Model as an Approximation to ARMA Processes in the Context of Fractional Integration. *Math Comp Model* (2004) 39:429–36. doi:10.1016/s0895-7177(04)90515-8

Conflict of Interest: The author declares that the research was conducted in the absence of any commercial or financial relationships that could be construed as a potential conflict of interest.

Publisher's Note: All claims expressed in this article are solely those of the authors and do not necessarily represent those of their affiliated organizations, or those of the publisher, the editors, and the reviewers. Any product that may be evaluated in this article, or claim that may be made by its manufacturer, is not guaranteed or endorsed by the publisher.

Copyright © 2021 Gil-Alana. This is an open-access article distributed under the terms of the Creative Commons Attribution License (CC BY). The use, distribution or reproduction in other forums is permitted, provided the original author(s) and the copyright owner(s) are credited and that the original publication in this journal is cited, in accordance with accepted academic practice. No use, distribution or reproduction is permitted which does not comply with these terms.



A Novel Clock Skew Estimator and Its Performance for the IEEE 1588v2 (PTP) Case in Fractional Gaussian Noise/Generalized Fractional Gaussian Noise Environment

Yehonatan Avraham and Monika Pinchas *

Department of Electrical and Electronic Engineering, Ariel University, Ariel, Israel

OPEN ACCESS

Edited by:

Ming Li,
Zhejiang University, China

Reviewed by:

Jianyong Chen,
Shenzhen University, China
Zhiwu Liao,
Sichuan Normal University, China

*Correspondence:

Monika Pinchas
monika.pinchas@gmail.com

Specialty section:

This article was submitted to
Interdisciplinary Physics,
a section of the journal
Frontiers in Physics

Received: 17 October 2021

Accepted: 10 November 2021

Published: 22 December 2021

Citation:

Avraham Y and Pinchas M (2021) A
Novel Clock Skew Estimator and Its
Performance for the IEEE 1588v2
(PTP) Case in Fractional Gaussian
Noise/Generalized Fractional Gaussian
Noise Environment.
Front. Phys. 9:796811.
doi: 10.3389/fphy.2021.796811

Papers in the literature dealing with the Ethernet network characterize packet delay variation (PDV) as a long-range dependence (LRD) process. Fractional Gaussian noise (fGn) or generalized fraction Gaussian noise (gfGn) belong to the LRD process. This paper proposes a novel clock skew estimator for the IEEE1588v2 applicable for the white-Gaussian, fGn, or gfGn environment. The clock skew estimator does not depend on the unknown asymmetry between the fixed delays in the forward and reverse paths nor on the clock offset between the Master and Slave. In addition, we supply a closed-form-approximated expression for the mean square error (MSE) related to our new proposed clock skew estimator. This expression is a function of the Hurst exponent H , as a function of the parameter a for the gfGn case, as a function of the total sent Sync messages, as a function of the Sync period, and as a function of the PDV variances of the forward and reverse paths. Simulation results confirm that our closed-form-approximated expression for the MSE indeed supplies the performance of our new proposed clock skew estimator efficiently for various values of the Hurst exponent, for the parameter a in gfGn case, for different Sync periods, for various values for the number of Sync periods and for various values for the PDV variances of the forward and reverse paths. Simulation results also show the advantage in the performance of our new proposed clock skew estimator compared to the literature known ML-like estimator (MLLE) that maximizes the likelihood function obtained based on a reduced subset of observations (the first and last timing stamps). This paper also presents designing graphs for the system designer that show the number of the Sync periods needed to get the required clock skew performance ($MSE = 10^{-12}$). Thus, the system designer can approximately know in advance the total delay or the time the system has to wait until getting the required system's performance from the MSE point of view.

Keywords: PTP, PDV, LRD, fGn, gfGn

1 INTRODUCTION

Clock synchronization is an essential process in computer networks. This process has to achieve frequency (clock skew) and time (offset or phase) synchronization to ensure that all the components function accurately. There are three significant protocols for time and frequency distribution over the Network: global positioning system (GPS), network time protocol (NTP), and Precision Time Protocol (PTP) Pinchas [1]; Levy and Pinchas [2]; Karthik and Blum [3]. GPS offers frequency and time synchronization accuracy in the sub-microsecond range Levy and Pinchas [2]. However, it requires expensive equipment and routine maintenance Guruswamy et al. [4]. Furthermore, we have a limitation in placing the equipment that communicates with the satellites in certain places Shan et al. [5]; Karthik and Blum [3]. According to Vyas et al. [6]; Peng et al. [7] the GPS also suffers from a weak indoor GPS signal. The NTP is not designed for local area networks (LANs) and has slow response and software clock implementations Levy and Pinchas [2]. Therefore, it can not achieve accurate results compared to the PTP protocol Pinchas [1]. The PTP is defined by the standard IEEE 1588v2 Arnold [8]. It requires minimal Network, computing, and hardware resources Fubin et al. [9]. According to Arnold [8], the PTP is based on a two-way message exchange scheme between the Master and the Slave. By using the two-way message exchange, frequency and time synchronization can be approximately estimated by applying some assumptions. The synchronous Ethernet (SyncE) is a protocol defined by the ITU ITU-T Recommendation [10,11]. It distributes a reference timing signal, where this signal can be extracted, processed, and frequency can be recovered from this signal by the Ethernet equipment clock (EEC) ITU-T Recommendation [10,11]. It should be pointed out that according to Levy and Pinchas [2], the EEC is not available in every system. Generally, the GPS or the SyncE are applied for frequency synchronization, where the PTP protocol and the GPS can be also applied for time or frequency synchronization as well unlike SyncE. The use of PTP for time synchronization is an important step for operations such as managing, securing, planning, and debugging when it is needed to determine the time that events happen Pinchas [1]. The use of PTP for time and frequency synchronization is required in electrical grid networks, cellular base station synchronization, industrial control, communication in financial markets Guruswamy et al. [4]; Karthik and Blum [12] and in Industrial Internet of things (IIoT) Puttnies et al. [13]. The PTP has three different synchronization issues: a.) phase synchronization only, where the PTP protocol is applied for estimating the constant offset. In this scenario, frequency synchronization already exists between the Master and the Slave. b.) Frequency synchronization only, where the PTP is applied for this purpose, while the time (offset) synchronization is not needed here. c.) Time and frequency synchronization is carried out with the PTP protocol. Please note that the offset between the Master and the Slave increases when no frequency synchronization exists between the Master and the Slave.

The PTP uses hardware timestamps traveling between the Master and the Slave nodes Arnold [8], where the path is through

several switches and routers. The traveling time in those components determines the duration of the delay in this path. According to Karthik and Blum [12,14,15]; Guruswamy et al. [16] there are two types of delay: a.) the fixed delay, a deterministic propagation delay along the network path, and b.) the random delay, also named as PDV. The PDV is defined as a random variable due to the routers, or the switches behavior ITU-T Recommendation [11]. As mentioned in Karthik and Blum [12] the primary source of the PDV is the output queuing delay, caused when a message arrives at a switch or router and has to wait in a queue due to other traffic that blocked the exit port. The PDV has a major impact on the accuracy obtained with the PTP Sathis Kumar and Kemparaj [17]. Theoretically, PTP can achieve precision of the order of nanoseconds, but, in practice, the PDV causes lower accuracy Puttnies et al. [13]. The queuing delay depends on the load in the network Levy and Pinchas [2]. As the load in the network increases, the PDV may increase accordingly, meaning a higher load may lead to a lower synchronization (time and frequency) accuracy Pinchas [1]. In order to estimate the offset or the clock skew in that scenario, the PTP usually needs more message exchanges between the Master and the Slave, as will be also seen in the simulation results.

The presence of the fixed delay and the PDV cause a problem in estimating the clock skew (frequency) and the offset (time). Due to the behavior of the random delay (PDV), this problem is modeled as a statistical estimation problem Guruswamy et al. [4]. This estimation task is an open issue because we have more unknown variables than number of equations. In order to overcome this problem, the symmetric path between the Master and the Slave is assumed in some algorithms (please refer to **Table 1**). However, the assumption of a symmetric path may lead to an inaccuracy in the clock skew and offset estimation task, since in practice, this assumption is not valid.

According to Mizrahi [18]; Mizrahi and Moses [19], a correlation exists between network latency measurements taken at adjacent times. Therefore, the network latency can not be characterized as white noise. In Li and Limb [20]; Peng et al. [21]; Jusak and Harris [22] the PDV is characterized as a Long-Range Dependence (LRD) process. This process can be modeled as a fractional Gaussian noise (fGn) Li and Zhao [23]; Pinchas [1]; Levy and Pinchas [2]; Paxson [24]; Ledesma and Liu [25] or as a generalized fractional Gaussian noise (gfGn) Li [26] (where fGn is a special case of gfGn). Those models (fGn, gfGn) are with Hurst exponent in the range of $0.5 \leq H < 1$, where for $H = 0.5$ we have the white Gaussian noise. It should be pointed out that we have also the modified multifractional Gaussian noise (mmfGn) Li [27] and the multi-fractional generalized Cauchy process Li [28] for representing a LRD process. But, in this paper we focus on the fGn/gfGn case. The traffic model has a significant impact on the estimation accuracy. Therefore, network traffic models such as the Gaussian or Exponential models may not accurately describe a real network traffic.

On one hand, the PTP is applied for the offset synchronization task only as is done in Pinchas [1], Mizrahi [18,29], Karthik and Blum [14]; Guruswamy et al. [4]; Anand Guruswamy et al. [30]. On the other hand, we may find other algorithms estimating the clock skew and the offset as is done in Levy and Pinchas [2]; Chin

TABLE 1 | Clock skew estimators.

| The algorithm | References | Forward/Reverse paths | PDF models (of the PDV) | Closed form of the clock skew variance |
|-------------------------|--------------------------|-----------------------|-------------------------|--|
| Linear programming | Puttnies et al. [13] | Symmetric | Gaussian | No |
| ML estimator | Chaudhari et al. [32] | Symmetric | Exponential | No |
| ML estimator | Li and Jeske [33] | Symmetric | Exponential | No |
| ML estimator | Noh et al. [34] | known | Gaussian/Exponential | Yes |
| ML estimator | Noh et al. [34] | Asymmetric | Gaussian/Exponential | No |
| ML estimator | Levy and Pinchas [2] | Asymmetric | fGn | Yes |
| KF estimator | Giorgi and Narduzzi [35] | Asymmetric | Gaussian | — |
| KF estimator | Chaloupka et al. [36] | OWD (forward) | — | — |
| KF and SMC estimator | Shan et al. [5] | Symmetric | Gaussian | — |
| SAGE estimator | Karthik and Blum [12] | Asymmetric | GMM | No |
| Our new proposed method | | Asymmetric | fGn, gfGn | Yes |

and Chen [31], Puttnies et al. [13], Chaudhari et al. [32]; Li and Jeske [33], Noh et al. [34], Guruswamy et al. [4]; Karthik and Blum [12,14,15], Giorgi and Narduzzi [35]. In addition, we may find in the literature algorithms that estimate only the clock skew as is done in Shan et al. [5]; Chaloupka et al. [36]. In this paper, we focus on the clock skew algorithms. In the literature, we can find several approaches estimating the clock skew: 1) The Maximum Likelihood (ML) estimator Levy and Pinchas [2], Karthik and Blum [12]; Guruswamy et al. [4], Chaudhari et al. [32]; Li and Jeske [33]; Noh et al. [34]; Karthik and Blum [11,14]. 2) The Linear Programming estimator Puttnies et al. [13]. 3) The Kalman Filter (KF) estimator Chaloupka et al. [36]; Shan et al. [5]; Giorgi and Narduzzi [35]. Please note that each algorithm used different assumptions, which may also lead to inaccuracy of the clock skew estimator. The authors in Puttnies et al. [13] presented a linear programming estimator that can decrease the influence of the PDV on the synchronization accuracy. However, they assumed that the PDV is Gaussian and that the fixed delay is symmetric between the forward (Master to Slave) and the reverse (Slave to Master) paths. In Chaudhari et al. [32]; Li and Jeske [33] the authors presented an ML estimator where an Exponential model was applied describing the PDV. In addition, they assumed the symmetric path assumption between the forward and reverse paths. In Noh et al. [34] the author suggested first an ML estimator for estimating the clock skew by using the Gaussian and Exponential model for the PDV case. The fixed delay was assumed to be known in this algorithm, which is often an unknown parameter. Therefore, the author presented another algorithm that does not depend on the knowledge of the fixed delay. Still, these algorithms presented in Noh et al. [34] are suitable only for the Gaussian or for the Exponential case. In Levy and Pinchas [2] the authors proposed an ML estimator for estimating the clock skew and the offset in the presence of asymmetric paths and where the PDV was modeled as fGn. This method Levy and Pinchas [2] is based on the dual slave clocks in a slave presented by Chin and Chen [31]. However, Kim [37] demonstrated that the algorithm in Chin and Chen [31] is unusable in practical cases. In Giorgi and Narduzzi [35] the authors presented KF equations with symmetrical paths assumption. The measurement uncertainty in Kalman's

equations gives the solution to the asymmetric forward and the reverse paths. According to Giorgi and Narduzzi [35], the uncertainty was taken in a range of 0.1–100 micro seconds. However, in practice, the asymmetry between the paths can be greater than the given range, so that the clock skew simulation results may be less accurate for that scenario. In addition, this algorithm Giorgi and Narduzzi [35] applies the Gaussian model for the PDV. In Chaloupka et al. [36] the authors used the One Way Mode (OWM) to avoid the asymmetric path problem. Based on simulation results demonstrated in Chaloupka et al. [36], the clock skew estimator achieves relative accurate results only after we wait for a relative long time which in practical cases we can not always afford. The authors in Shan et al. [5] applied KF combined with Sliding Mode Controller (SMC) in order to get better accuracy. Also here, the algorithm assumes symmetrical paths and a Gaussian model for describing the PDV. In Karthik and Blum [12,15]; Guruswamy et al. [4] the authors presented an innovative estimator for the clock skew and for the offset between the Master and the Slave. In Guruswamy et al. [4] the authors presented first their joint estimator, the MINIMAX algorithm, that minimizes the maximum mean squared error of all the unknown parameters. This algorithm assumes that the fixed delays from the Master to Slave and Slave to Master are known, or at least, the difference between them is known. In Karthik and Blum [15] the authors assumed complete knowledge of the statistical information describing the PDV. Recently Karthik and Blum [12], an algorithm was proposed for estimating both the offset and the clock skew in the presence of unknown asymmetric paths, named as the Space Alternating Generalized Expectation-Maximization (SAGE) algorithm. This algorithm assumed a Gaussian Mixture Model (GMM) for the PDV. In estimating the clock skew and the offset according to Karthik and Blum [12], the assumption of having more than only one Master-Slave path was applied (assumption of having multiple Masters). In addition, half of the paths have to be symmetric. Please note that this method Karthik and Blum [12] may be overqualified for applications requiring only clock skew estimation, since Karthik and Blum [12] needs the calculation of the offset estimator for carrying

out the clock skew estimator. Thus, the offset estimator can not be shut down when calculating the clock skew estimator. The authors in Karthik and Blum [12] also presented an expression for the Cramer-Rao lower bound (CRLB). This expression (CRLB) is based on the knowledge of which of the multiple masters to the slave paths are considered as asymmetric (where the fixed delays in the Master-Slave and Slave-Master are asymmetric) and on the knowledge of the probability density function (PDF) of the random queuing delays of those paths. Please refer to **Table 1** that summarizes the different clock skew algorithms (described earlier in this section), with their assumptions.

In this paper, we propose a novel clock skew estimator based on PTP in an fGn/gfGn environment with Hurst exponent in the range of $0.5 \leq H < 1$ that does not depend on the unknown asymmetry between the fixed path delays in the forward and reverse directions nor on the clock offset between the Master and Slave. We supply a closed-form-approximated expression for the performance (MSE) related to our new proposed clock skew estimator. This closed-form-approximated expression is a function of the Hurst exponent H , as a function of the parameter a for gfGn, as a function of the number of total PTP messages exchanges used in the system for synchronization, as a function of the period between the messages and as a function of the PDV variances in the forward and reverse directions. In addition, we supply designing graphs for the system designer that show the number of PTP messages exchanges needed in the network to get the required clock skew performance as a function of the network parameters (Hurst exponent, parameter a in gfGn and variances of the forward and reverse directions PDV), for the rates of PTP messages exchanges of 64 packets/sec, 16 packets/sec and 8 packets/sec. Simulation results confirm that our closed-form-approximated expression for the MSE related to our new proposed clock skew estimator indeed supplies efficiently the performance of our new proposed estimator for various values of the Hurst exponent, for the parameter a in gfGn, for different periods between the messages, for various values for the number of PTP messages exchanges and for various values for the variances of the PDV in the forward and reverse directions. Simulation results also show the advantage in performance of our new proposed clock skew estimator for various values of the Hurst exponent compared to the literature known ML-like estimator (MLLE) Noh et al. [34] that maximizes the likelihood function obtained based on a reduced subset of observations (the first and last timing stamps). In addition, simulation results will also show the advantage in performance of our new proposed clock skew estimator compared to the maximum likelihood clock skew estimator proposed by Levy and Pinchas [2] and compared to the Kalman clock skew estimator given by Chaloupka et al. [36].

The paper is organized as follows. In **Section 2**, we briefly introduce the system under consideration and the assumptions we applied for our algorithm. **Section 3** proposes the new clock skew estimator and the closed-form approximated expression for the MSE related to our new clock skew estimator. In **Section 4**, we

propose some designing graphs while in **Section 5**, we present simulation results. **Section 6**, is our conclusion.

2 SYSTEM DESCRIPTION

The IEEE 1588v2 is based on the Master-Slave architecture. This protocol distributes information from a Master to its Slave by exchanging messages with timestamps (please refer to **Figure 1**). The following sequence of steps are performed by the two-way message exchange:

- 1) The Master initiates the exchange by sending a SYNC message to the Slave at timestamp t_1 .
- 2) The Slave receives the SYNC message and keeps the arrival time at timestamp t_2 .
- 3) The Master sends the FOLLOW UP message to the Slave with the timestamp t_1 .
- 4) The Slave sends back to the Master DELAY REQ message at timestamp t_3 .
- 5) The Master receives the DELAY REQ message and keeps the arrival time at timestamp t_4 .
- 6) The Master sends the timestamp t_4 to the Slave with the DELAY RESP message.

Based on Karthik and Blum [12,14,15] we may write:

$$t_1[j] + d_{ms} + \omega_1[j] = t_2[j](1 + \alpha) + Q \quad (1)$$

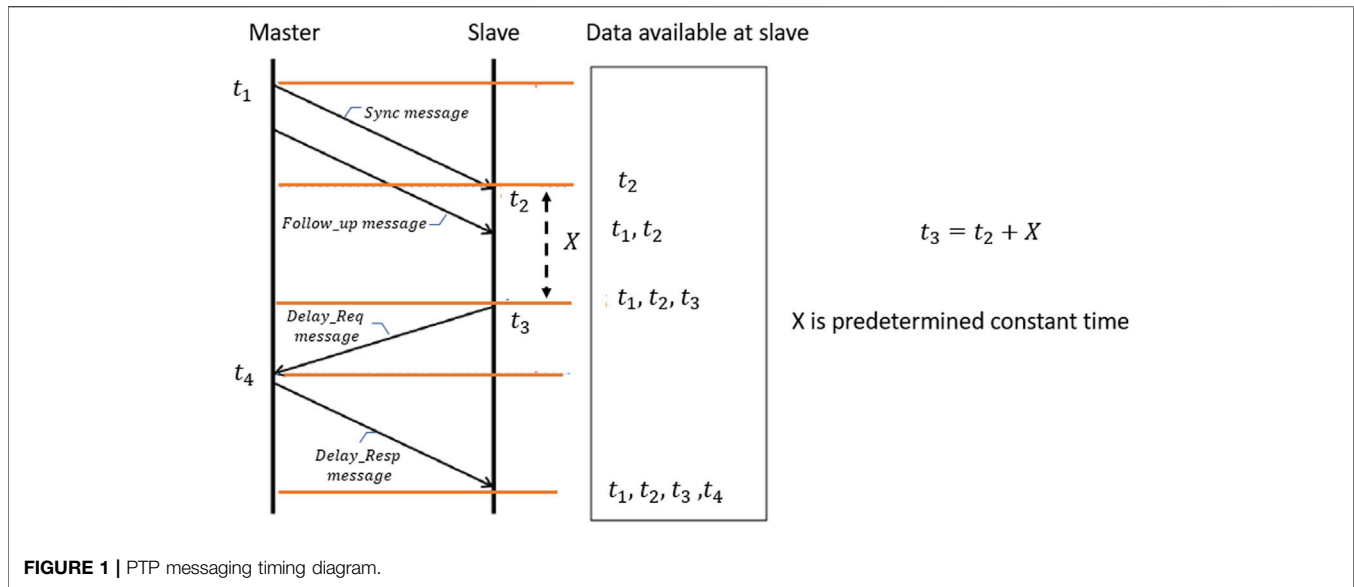
$$t_4[j] - d_{sm} - \omega_2[j] = t_3[j](1 + \alpha) + Q \quad (2)$$

where Q is the time difference between the Master and the Slave clocks (offset) and α is the clock skew. The forward and the reverse fixed delays are denoted as d_{ms} , d_{sm} respectively and the forward and the reverse PDV are denoted as $\omega_1[j]$, $\omega_2[j]$ respectively. The total number of the Sync messages periods is denoted as J , where $j = 1, 2, 3, \dots, J$.

We consider three different models for the PDV:

- 1) The PDV is modeled as a white-Gaussian noise with zero mean and the variance $E[\omega_n[j], \omega_n[m]]$ is $\sigma_{\omega_n}^2$ when $j = m$ and zero when $j \neq m$ where $E[\cdot]$ denotes the expectation operator on (\cdot) and $n = 1, 2$.
- 2) The PDV is modeled as an fGn process with zero mean. Based on Li and Zhao [23]; Peng et al. [21] we have:
 - a. When $j = m$: $E[\omega_n[j], \omega_n[m]] = \sigma_{\omega_n}^2$.
 - b. When $j \neq m$: $E[\omega_n[j], \omega_n[m]] = \frac{\sigma_{\omega_n}^2}{2} [|j - m| - 1]^{2H} - 2(|j - m|)^{2H} + (|j - m| + 1)^{2H}$.
- 3) The PDV is modeled as an gfGn process with zero mean. Based on Li [26] we have:
 - a. When $j = m$: $E[\omega_n[j], \omega_n[m]] = \sigma_{\omega_n}^2$.
 - b. When $j \neq m$: $E[\omega_n[j], \omega_n[m]] = \frac{\sigma_{\omega_n}^2}{2} [|j - m|^a - 1]^{2H} - 2|(j - m)^a|^{2H} + (|(j - m)^a| + 1)^{2H}$.

In this paper we assume that the forward and reverse PDVs are independent. This assumption is consistent with real systems. Thus, we can write: $E[\omega_1[j], \omega_2[m]] = 0 \quad \forall \quad j, m$.



3 THE CLOCK SKEW ESTIMATOR AND ITS PERFORMANCE

In this section we present our new clock skew estimator and the closed-form-approximated expression for the MSE related to our new clock skew estimator for three PDV cases: 1. The PDV is a white-Gaussian process, 2. The PDV is an fGn process, 3. The PDV is an gfGn process. At first, we present our new proposed clock skew estimator in Theorem 1. Theorem 2 presents a general closed-form approximated expression for the MSE related to our new clock skew estimator involving the expectation operator on the PDVs. Since the PDV can be one of three cases (a white-Gaussian process, an fGn process and an gfGn process), the MSE from Theorem 2 is further developed for each case. Namely, Theorem 3, Theorem 4 and Theorem 5 are the closed-form approximated expressions for the MSE related to our new clock skew estimator for the white-Gaussian case, fGn case and gfGn case respectively.

3.1 Theorem 1

For the case of $t_3[j] - t_2[j] = X$, where X is a constant. The clock skew estimator can be defined as:

$$\hat{\alpha} = \frac{1}{J(J-1)} \sum_{i=1}^{J-1} \sum_{j=1}^{J-i} \left(\frac{T_{1,j}(i) + T_{4,j}(i)}{T_{2,j}(i)} \right) - 1 \quad (3)$$

where

$$\begin{aligned} T_{1,j}(i) &= t_1[j+i] - t_1[j], & T_{2,j}(i) &= t_2[j+i] - t_2[j], \\ T_{4,j}(i) &= t_4[j+i] - t_4[j] \end{aligned} \quad (4)$$

3.1.1 Proof of Theorem 1

In order to avoid the fixed delay, we can subtract between two timestamps from different Sync periods. Based on Eqs 1, 2 we have:

$$T_{1,j}(i) + \Omega_{1,j}(i) = (1 + \alpha_{j,i}) T_{2,j}(i) \quad (5)$$

$$T_{4,j}(i) - \Omega_{2,j}(i) = (1 + \alpha_{j,i}) T_{3,j}(i) \quad (6)$$

where

$$\begin{aligned} T_{3,j}(i) &= t_3[j+i] - t_3[j], & \Omega_{1,j}(i) &= \omega_1[j+i] - \omega_1[j], \\ \Omega_{2,j}(i) &= \omega_2[j+i] - \omega_2[j] \end{aligned} \quad (7)$$

and $\alpha_{j,i}$ is the clock skew between the $(j+i)$ -th and i th Sync period.

Based on the summation of Eqs. 5, 6, we can define:

$$\frac{T_{1,j}(i) + \Omega_{1,j}(i)}{T_{2,j}(i)} + \frac{T_{4,j}(i) - \Omega_{2,j}(i)}{T_{3,j}(i)} = 2 \left(1 + \alpha_{j,i} \right) \quad (8)$$

Please note that $T_{3,j}(i) = t_3[j+i] - t_3[j]$ is also $T_{3,j}(i) = t_2[j+i] + X - (t_2[j] + X)$, meaning that $T_{3,j}(i) = T_{2,j}(i)$. Therefore, $\alpha_{j,i}$ is:

$$\alpha_{j,i} = \frac{1}{2} \left(\left(\frac{T_{1,j}(i) + T_{4,j}(i)}{T_{2,j}(i)} \right) + \left(\frac{\Omega_{1,j}(i) - \Omega_{2,j}(i)}{T_{2,j}(i)} \right) \right) - 1 \quad (9)$$

Thus the clock skew can be defined as:

$$\alpha = \frac{2}{J(J-1)} \sum_{i=1}^{J-1} \sum_{j=1}^{J-i} \alpha_{j,i} \quad (10)$$

By putting Eq. 9 into Eq. 10 we have:

$$\alpha = \frac{1}{J(J-1)} \sum_{i=1}^{J-1} \sum_{j=1}^{J-i} \left(\left(\frac{T_{1,j}(i) + T_{4,j}(i)}{T_{2,j}(i)} \right) + \left(\frac{\Omega_{1,j}(i) - \Omega_{2,j}(i)}{T_{2,j}(i)} \right) \right) - 1 \quad (11)$$

Now, we can write **Eq. 11** as:

$$\begin{aligned}\alpha &= \frac{1}{J(J-1)} \left(\sum_{i=1}^{J-1} \sum_{j=1}^{J-i} \left(\frac{T_{1,j}(i) + T_{4,j}(i)}{T_{2,j}(i)} \right) - 1 + \sum_{i=1}^{J-1} \sum_{j=1}^{J-i} \left(\frac{\Omega_{1,j}(i) - \Omega_{2,j}(i)}{T_{2,j}(i)} \right) \right) \\ &= \hat{\alpha} + \frac{1}{J(J-1)} \sum_{i=1}^{J-1} \sum_{j=1}^{J-i} \left(\frac{\Omega_{1,j}(i) - \Omega_{2,j}(i)}{T_{2,j}(i)} \right)\end{aligned}\quad (12)$$

Based on **Eq. 12** the clock skew estimator is as defined in **Eq. 3** and this completes our proof.

3.2 Theorem 2

For the case where $|\frac{\Omega_{n,j}(i)}{T_{1,j}(i)}| \ll 1$ [$n = 1, 2$ and where $|\cdot|$ is the absolute value of (\cdot)], the general expression for the approximated MSE related to our new clock skew estimator is:

$$\begin{aligned}E[e^2] &\approx \left(\frac{1+\alpha}{(J(J-1))T_{syn}} \right)^2 \sum_{i=1}^{J-1} \sum_{j=1}^{J-i} \sum_{k=1}^{J-i} \sum_{m=1}^{J-k} \\ &\quad \left[\frac{E[\Omega_{1,j}(i)\Omega_{1,m}(k)]}{ik} + \frac{E[\Omega_{2,j}(i)\Omega_{2,m}(k)]}{ik} + \frac{1}{T_{syn}^2} \frac{E[\Omega_{1,j}^2(i)\Omega_{1,m}^2(k)]}{(ik)^2} \right]\end{aligned}\quad (13)$$

3.2.1 Proof of Theorem 2

Based on **Eq. 12** the error is defined as:

$$e = \alpha - \hat{\alpha} = \frac{1}{J(J-1)} \sum_{i=1}^{J-1} \sum_{j=1}^{J-i} \left(\frac{\Omega_{1,j}(i) - \Omega_{2,j}(i)}{T_{2,j}(i)} \right) \quad (14)$$

According to **Eq. 5** we have:

$$T_{2,j}(i) = \frac{T_{1,j}(i) + \Omega_{1,j}(i)}{(1+\alpha)} \quad (15)$$

Based on **Eq. 15** we may write the expectation of **Eq. 14** as:

$$E[e] = \frac{(1+\alpha)}{(J(J-1))} \sum_{i=1}^{J-1} \sum_{j=1}^{J-i} E \left[\frac{a_{j,i}}{(1+a_{j,i})} - \frac{b_{j,i}}{(1+a_{j,i})} \right] \quad (16)$$

where $a_{j,i}$ and $b_{j,i}$ are defined as:

$$a_{j,i} = \frac{\Omega_{1,j}(i)}{T_{1,j}(i)}; \quad b_{j,i} = \frac{\Omega_{2,j}(i)}{T_{1,j}(i)} \quad (17)$$

For $|\frac{\Omega_{n,j}(i)}{T_{1,j}(i)}| \ll 1$ and based on Spiegel et al. [38] we can rewrite **Eq. 16**:

$$E[e] \approx \frac{(1+\alpha)}{(J(J-1))} \sum_{i=1}^{J-1} \sum_{j=1}^{J-i} [E[a_{j,i}(1-a_{j,i})] - E[b_{j,i}(1-a_{j,i})]] \quad (18)$$

Based on the assumption made in **Section 2**, we may write **Eq. 18** as:

$$E[e] \approx \frac{(1+\alpha)}{(J(J-1))} \sum_{i=1}^{J-1} \sum_{j=1}^{J-i} [E[a_{j,i} - a_{j,i}^2] - E[b_{j,i}]] \quad (19)$$

Now, based on **Eq. 19** the approximated MSE related to our new proposed clock skew estimator can be written as:

$$\begin{aligned}E[e^2] &\approx \frac{(1+\alpha)^2}{(J(J-1))^2} \sum_{i=1}^{J-1} \sum_{j=1}^{J-i} \sum_{k=1}^{J-i} \sum_{m=1}^{J-k} \\ &\quad [E[a_{j,i}a_{m,k}] - E[a_{j,i}^2a_{m,k}] - E[a_{j,i}a_{m,k}^2] + E[a_{j,i}^2a_{m,k}^2] + E[b_{j,i}b_{m,k}]]\end{aligned}\quad (20)$$

Next, by recalling the definitions of $T_{1,j}(i)$ and $T_{1,m}(k)$, we can write:

$$\begin{aligned}T_{1,j}(i) &= t_1[j+i] - t_1[j] = iT_{syn} \\ T_{1,m}(k) &= t_1[m+k] - t_1[m] = kT_{syn}\end{aligned}\quad (21)$$

where T_{syn} is denoted as the Sync message period.

Based on **Eq. 21** we can simplify the expressions in **Eq. 20**:

$$E[a_{j,i}a_{m,k}] = E \left[\frac{\Omega_{1,j}(i)}{T_{1,j}(i)} \frac{\Omega_{1,m}(k)}{T_{1,m}(k)} \right] = \frac{E[\Omega_{1,j}(i)\Omega_{1,m}(k)]}{ikT_{syn}^2} \quad (22)$$

$$E[a_{j,i}^2a_{m,k}] = E \left[\frac{\Omega_{1,j}^2(i)}{T_{1,j}^2(i)} \frac{\Omega_{1,m}(k)}{T_{1,m}(k)} \right] = \frac{E[\Omega_{1,j}^2(i)\Omega_{1,m}(k)]}{i^2kT_{syn}^3} \quad (23)$$

$$E[a_{j,i}a_{m,k}^2] = E \left[\frac{\Omega_{1,j}(i)}{T_{1,j}(i)} \frac{\Omega_{1,m}^2(k)}{T_{1,m}^2(k)} \right] = \frac{E[\Omega_{1,j}(i)\Omega_{1,m}^2(k)]}{ik^2T_{syn}^3} \quad (24)$$

$$E[a_{j,i}^2a_{m,k}^2] = E \left[\frac{\Omega_{1,j}^2(i)}{T_{1,j}^2(i)} \frac{\Omega_{1,m}^2(k)}{T_{1,m}^2(k)} \right] = \frac{E[\Omega_{1,j}^2(i)\Omega_{1,m}^2(k)]}{i^2k^2T_{syn}^4} \quad (25)$$

$$E[b_{j,i}b_{m,k}] = E \left[\frac{\Omega_{2,j}(i)}{T_{1,j}(i)} \frac{\Omega_{2,m}(k)}{T_{1,m}(k)} \right] = \frac{E[\Omega_{2,j}(i)\Omega_{2,m}(k)]}{ikT_{syn}^2} \quad (26)$$

Since the PDV has zero mean (please refer to **Section 2**), **Eqs 23, 24** can be set to zero.

Now, by putting **Eqs 22, 25, 26** into **Eq. 20** we obtain the expression in **Eq. 13** and this completes our proof.

In the following, we will calculate the approximated expression for the MSE related to our new proposed clock skew estimator for three different cases:

1) The white-Gaussian case, 2) The fGn case, 3) The gfGn case.

3.3 Theorem 3

The approximate MSE for the white-Gaussian case is:

$$E[e^2] \approx \left(\frac{1}{(J(J-1))} \right)^2 \left(\frac{\sigma_{\omega_1}^2 + \sigma_{\omega_2}^2}{T_{syn}^2} A \right) \left(1 + \frac{1}{P} \right) \quad (27)$$

where P is defined as:

$$P = \frac{A}{B} \left(\frac{\sigma_{\omega_1}^2 + \sigma_{\omega_2}^2}{\sigma_{\omega_1}^4} \right) T_{syn}^2 \quad (28)$$

and A and B are given by:

$$A = \left(2 \sum_{i=1}^{J-1} \frac{J-i}{i^2} + \sum_{i=1}^{J-1} \sum_{j=1}^{J-i} \sum_{k=1}^{J-i} \sum_{\substack{m=1 \\ k \neq i}}^{J-i} \sum_{\substack{m=j \\ m=j+i-k}}^{J-k} \frac{1}{ik} - \sum_{i=1}^{J-1} \sum_{j=1}^{J-i} \sum_{k=1}^{J-i} \sum_{\substack{m=1 \\ m=j+i \\ m=j-k}}^{J-k} \frac{1}{ik} \right) \quad (29)$$

$$B = \left(12 \sum_{i=1}^{J-1} \frac{J-i}{i^4} + 6 \sum_{i=1}^{J-1} \sum_{j=1}^{J-i} \sum_{k=1}^{J-i} \sum_{\substack{m=1 \\ k \neq i}}^{J-i} \sum_{\substack{m=j \\ m=j+i-k \\ m=j-i}}^{J-k} \frac{1}{(ik)^2} + 4 \sum_{i=1}^{J-1} \sum_{j=1}^{J-i} \sum_{k=1}^{J-i} \sum_{\substack{m=1 \\ m=j+i \\ m=j-i \\ m \neq j+i}}^{J-k} \frac{1}{(ik)^2} \right) \quad (30)$$

3.3.1 Proof of Theorem 3

In the following, we calculate separately the three different parts in Eq. 13. We start with the first part in Eq. 13. Based on Eq. 7 we can write:

$$\frac{\sum_{i=1}^{J-1} \sum_{j=1}^{J-i} \sum_{k=1}^{J-i} \sum_{m=1}^{J-k} \frac{E[\Omega_{1,j}(i)\Omega_{1,m}(k)]}{ik} = \sum_{i=1}^{J-1} \sum_{j=1}^{J-i} \sum_{k=1}^{J-i} \sum_{m=1}^{J-k} \frac{E[\omega_1[j+i]\omega_1[m+k] - \omega_1[j+i]\omega_1[m] - \omega_1[j]\omega_1[m+k] + \omega_1[j]\omega_1[m]]}{ik} \quad (31)$$

For calculating Eq. 31 we have to consider only five non-zero cases.

The first case is when $i = k$ and $m = j$. For this case Eq. 31 is:

$$\sum_{i=1}^{J-1} \sum_{j=1}^{J-i} \sum_{k=1}^{J-i} \sum_{\substack{m=1 \\ k \neq i}}^{J-k} \frac{E[\omega_1[j+i]\omega_1[m+k] + \omega_1[j]\omega_1[m]]}{ik} = \sum_{i=1}^{J-1} \sum_{j=1}^{J-i} \frac{E[\omega_1[j+i]\omega_1[j+i] + \omega_1[j]\omega_1[j]]}{i^2} = 2\sigma_{\omega_1}^2 \sum_{i=1}^{J-1} \frac{J-i}{i^2} \quad (32)$$

The second case is when $i \neq k$ and $m = j$. For this case Eq. 31 is:

$$\sum_{i=1}^{J-1} \sum_{j=1}^{J-i} \sum_{k=1}^{J-i} \sum_{\substack{m=1 \\ k \neq i}}^{J-k} \frac{E[\omega_1[j]\omega_1[m]]}{ik} = \sum_{i=1}^{J-1} \sum_{j=1}^{J-i} \sum_{k=1}^{J-i} \sum_{\substack{m=1 \\ k \neq i}}^{J-k} \frac{E[\omega_1[j]\omega_1[j]]}{ik} = \sigma_{\omega_1}^2 \sum_{i=1}^{J-1} \sum_{j=1}^{J-i} \sum_{k=1}^{J-i} \sum_{\substack{m=1 \\ k \neq i}}^{J-k} \frac{1}{ik} \quad (33)$$

The third case is when $m = j + i$. For this case Eq. 31 is:

$$\sum_{i=1}^{J-1} \sum_{j=1}^{J-i} \sum_{k=1}^{J-i} \sum_{\substack{m=1 \\ m=j+i}}^{J-k} \frac{E[\omega_1[j+i]\omega_1[m]]}{ik} = \sum_{i=1}^{J-1} \sum_{j=1}^{J-i} \sum_{k=1}^{J-i} \sum_{\substack{m=1 \\ m=j+i}}^{J-k} \frac{E[\omega_1[j+i]\omega_1[j+i]]}{ik} = -\sigma_{\omega_1}^2 \sum_{i=1}^{J-1} \sum_{j=1}^{J-i} \sum_{k=1}^{J-i} \sum_{\substack{m=1 \\ m=j+i}}^{J-k} \frac{1}{ik} \quad (34)$$

The fourth case is when $m = j - k$. For this case Eq. 31 is:

$$\sum_{i=1}^{J-1} \sum_{j=1}^{J-i} \sum_{k=1}^{J-i} \sum_{\substack{m=1 \\ m=j-k}}^{J-k} \frac{E[\omega_1[j]\omega_1[m+k]]}{ik} = \sum_{i=1}^{J-1} \sum_{j=1}^{J-i} \sum_{k=1}^{J-i} \sum_{\substack{m=1 \\ m=j-k}}^{J-k} \frac{E[\omega_1[j]\omega_1[j]]}{ik} = -\sigma_{\omega_1}^2 \sum_{i=1}^{J-1} \sum_{j=1}^{J-i} \sum_{k=1}^{J-i} \sum_{\substack{m=1 \\ m=j-k}}^{J-k} \frac{1}{ik} \quad (35)$$

The fifth case is when $i \neq k$ and $m = j + i - k$. For this case Eq. 31 is:

$$\sum_{i=1}^{J-1} \sum_{j=1}^{J-i} \sum_{k=1}^{J-i} \sum_{\substack{m=1 \\ m=j+i-k}}^{J-k} \frac{E[\omega_1[j+i]\omega_1[m+k]]}{ik} = \sum_{i=1}^{J-1} \sum_{j=1}^{J-i} \sum_{k=1}^{J-i} \sum_{\substack{m=1 \\ m=j+i-k}}^{J-k} \frac{E[\omega_1[j+i]\omega_1[j+i]]}{ik} = \sigma_{\omega_1}^2 \sum_{i=1}^{J-1} \sum_{j=1}^{J-i} \sum_{k=1}^{J-i} \sum_{\substack{m=1 \\ m=j+i-k}}^{J-k} \frac{1}{ik} \quad (36)$$

Based on Eqs 32–36, we may write Eq. 31 as:

$$\sum_{i=1}^{J-1} \sum_{j=1}^{J-i} \sum_{k=1}^{J-i} \sum_{m=1}^{J-k} \frac{E[\Omega_{1,j}(i)\Omega_{1,m}(k)]}{ik} = \sigma_{\omega_1}^2 \left(2 \sum_{i=1}^{J-1} \frac{J-i}{i^2} + \sum_{i=1}^{J-1} \sum_{j=1}^{J-i} \sum_{k=1}^{J-i} \sum_{\substack{m=1 \\ k \neq i}}^{J-k} \frac{1}{ik} - \sum_{i=1}^{J-1} \sum_{j=1}^{J-i} \sum_{k=1}^{J-i} \sum_{\substack{m=1 \\ m=j+i \\ m=j-k}}^{J-k} \frac{1}{ik} \right) \quad (37)$$

Based on Eq. 7 the second part in Eq. 13 can be given as:

$$\sum_{i=1}^{J-1} \sum_{j=1}^{J-i} \sum_{k=1}^{J-i} \sum_{m=1}^{J-k} \frac{E[\Omega_{2,j}(i)\Omega_{2,m}(k)]}{ik} = \sum_{i=1}^{J-1} \sum_{j=1}^{J-i} \sum_{k=1}^{J-i} \sum_{m=1}^{J-k} \frac{E[\omega_2[j+i]\omega_2[m+k] - \omega_2[j+i]\omega_2[m] - \omega_2[j]\omega_2[m+k] + \omega_2[j]\omega_2[m]]}{ik} \quad (38)$$

The only change in Eq. 38 concerning Eq. 31 is the PDV. Therefore, we can use the calculations we made for the first part. Based on Eq. 37, we can write Eq. 38 as:

$$\sum_{i=1}^{J-1} \sum_{j=1}^{J-i} \sum_{k=1}^{J-i} \sum_{m=1}^{J-k} \frac{E[\Omega_{2,j}(i)\Omega_{2,m}(k)]}{ik} = \sigma_{\omega_2}^2 \left(2 \sum_{i=1}^{J-1} \frac{J-i}{i^2} + \sum_{i=1}^{J-1} \sum_{j=1}^{J-i} \sum_{k=1}^{J-i} \sum_{\substack{m=1 \\ k \neq i}}^{J-k} \frac{1}{ik} - \sum_{i=1}^{J-1} \sum_{j=1}^{J-i} \sum_{k=1}^{J-i} \sum_{\substack{m=1 \\ m=j+i \\ m=j-k}}^{J-k} \frac{1}{ik} \right) \quad (39)$$

The third part in Eq. 13 is:

$$\begin{aligned} \frac{1}{T_{syn}^2} \sum_{i=1}^{J-1} \sum_{j=1}^{J-i} \sum_{k=1}^{J-i-j} \sum_{m=1}^{J-k} \frac{E[\Omega_{1,j}^2(i) \Omega_{1,m}^2(k)]}{(ik)^2} &= \frac{1}{T_{syn}^2} \sum_{i=1}^{J-1} \sum_{j=1}^{J-i} \sum_{k=1}^{J-i-j} \sum_{m=1}^{J-k} \\ &\left(\frac{E[\omega_1^2[j+i] \omega_1^2[m+k] + \omega_1^2[j+i] \omega_1^2[m] + \omega_1^2[j] \omega_1^2[m+k] + \omega_1^2[j] \omega_1^2[m]]}{(ik)^2} \right. \\ &- 2 \frac{E[\omega_1^2[j+i] \omega_1[m+k] \omega_1[m] + \omega_1^2[j] \omega_1[m+k] \omega_1[m]]}{(ik)^2} \\ &- 2 \frac{E[\omega_1[j+i] \omega_1[j] \omega_1^2[m+k] + \omega_1[j+i] \omega_1[j] \omega_1^2[m]]}{(ik)^2} \\ &\left. + 4 \frac{E[\omega_1[j+i] \omega_1[j] \omega_1[m+k] \omega_1[m]]}{(ik)^2} \right) \end{aligned} \quad (40)$$

In order to calculate Eq. 40 we have to consider only six non-zero cases.

The first case is when $i = k$ and $m = j$. For this case Eq. 40 is:

$$\begin{aligned} \frac{1}{T_{syn}^2} \sum_{i=1}^{J-1} \sum_{j=1}^{J-i} \sum_{k=1}^{J-i-j} \sum_{m=1}^{J-k} \\ \left(\frac{E[\omega_1^2[j+i] \omega_1^2[j+i] + \omega_1^2[j+i] \omega_1^2[j] + \omega_1^2[j] \omega_1^2[j+i] + \omega_1^2[j] \omega_1^2[j]]}{i^4} \right. \\ \left. + 4 \frac{E[\omega_1[j+i] \omega_1[j] \omega_1[j+i] \omega_1[j]]}{i^4} \right) = \frac{2(3\sigma_{\omega_1}^4) + 6(\sigma_{\omega_1}^2 \sigma_{\omega_1}^2)}{T_{syn}^2} \sum_{i=1}^{J-1} \frac{J-i}{i^4} \end{aligned} \quad (41)$$

The second case is when $i \neq k$ and $m = j$. For this case Eq. 40 is:

$$\begin{aligned} \frac{1}{T_{syn}^2} \sum_{i=1}^{J-1} \sum_{j=1}^{J-i} \sum_{k=1}^{J-i-j} \sum_{m=1}^{J-k} \\ \frac{E[\omega_1^2[j+i] \omega_1^2[j+k] + \omega_1^2[j+i] \omega_1^2[j] + \omega_1^2[j] \omega_1^2[j+k] + \omega_1^2[j] \omega_1^2[j]]}{(ik)^2} \\ = \frac{(3\sigma_{\omega_1}^4) + 3(\sigma_{\omega_1}^2 \sigma_{\omega_1}^2)}{T_{syn}^2} \sum_{i=1}^{J-1} \sum_{j=1}^{J-i} \sum_{k=1}^{J-i-j} \sum_{m=1}^{J-k} \frac{1}{(ik)^2} \end{aligned} \quad (42)$$

The third case is when $m = j + i$. For this case Eq. 40 is:

$$\begin{aligned} \frac{1}{T_{syn}^2} \sum_{i=1}^{J-1} \sum_{j=1}^{J-i} \sum_{k=1}^{J-i-j} \sum_{m=1}^{J-k} \\ \frac{E[\omega_1^2[j+i] \omega_1^2[j+i+k] + \omega_1^2[j+i] \omega_1^2[j+i] + \omega_1^2[j] \omega_1^2[j+i+k] + \omega_1^2[j] \omega_1^2[j+i]]}{(ik)^2} \\ = \frac{(3\sigma_{\omega_1}^4) + 3(\sigma_{\omega_1}^2 \sigma_{\omega_1}^2)}{T_{syn}^2} \sum_{i=1}^{J-1} \sum_{j=1}^{J-i} \sum_{k=1}^{J-i-j} \sum_{m=1}^{J-k} \frac{1}{(ik)^2} \end{aligned} \quad (43)$$

The fourth case is when $m = j - k$. For this case Eq. 40 is:

$$\begin{aligned} \frac{1}{T_{syn}^2} \sum_{i=1}^{J-1} \sum_{j=1}^{J-i} \sum_{k=1}^{J-i-j} \sum_{m=1}^{J-k} \\ \frac{E[\omega_1^2[j+i] \omega_1^2[j] + \omega_1^2[j+i] \omega_1^2[j-k] + \omega_1^2[j] \omega_1^2[j] + \omega_1^2[j] \omega_1^2[j-k]]}{(ik)^2} \\ = \frac{(3\sigma_{\omega_1}^4) + 3(\sigma_{\omega_1}^2 \sigma_{\omega_1}^2)}{T_{syn}^2} \sum_{i=1}^{J-1} \sum_{j=1}^{J-i} \sum_{k=1}^{J-i-j} \sum_{m=1}^{J-k} \frac{1}{(ik)^2} \end{aligned} \quad (44)$$

The fifth case is when $i \neq k$ and $m = j + i - k$. For this case Eq. 40 is:

$$\begin{aligned} \frac{1}{T_{syn}^2} \sum_{i=1}^{J-1} \sum_{j=1}^{J-i} \sum_{k=1}^{J-i-j} \sum_{m=1}^{J-k} \\ \frac{E[\omega_1^2[j+i] \omega_1^2[j+i] + \omega_1^2[j+i] \omega_1^2[j+i-k] + \omega_1^2[j] \omega_1^2[j+i] + \omega_1^2[j] \omega_1^2[j+i-k]]}{(ik)^2} \\ = \frac{(3\sigma_{\omega_1}^4) + 3(\sigma_{\omega_1}^2 \sigma_{\omega_1}^2)}{T_{syn}^2} \sum_{i=1}^{J-1} \sum_{j=1}^{J-i} \sum_{k=1}^{J-i-j} \sum_{m=1}^{J-k} \frac{1}{(ik)^2} \end{aligned} \quad (45)$$

The sixth case is when $m \neq j$ and $m \neq j + i$ and $m \neq j - k$ and $m + k \neq j + i$. For this case Eq. 40 is:

$$\begin{aligned} \frac{1}{T_{syn}^2} \sum_{i=1}^{J-1} \sum_{j=1}^{J-i} \sum_{k=1}^{J-i-j} \sum_{\substack{m=1 \\ m \neq j \\ m \neq j+i-k \\ m \neq j+i \\ m \neq j-i}}^{J-k} \frac{E[\omega_1^2[j+i] \omega_1^2[m+k] + \omega_1^2[j+i] \omega_1^2[m]]}{(ik)^2} \\ + \frac{E[\omega_1^2[j] \omega_1^2[m+k] + \omega_1^2[j] \omega_1^2[m]]}{(ik)^2} = \frac{4(\sigma_{\omega_1}^2 \sigma_{\omega_1}^2)}{T_{syn}^2} \sum_{i=1}^{J-1} \sum_{j=1}^{J-i} \sum_{k=1}^{J-i-j} \sum_{\substack{m=1 \\ m \neq j \\ m \neq j+i-k \\ m \neq j+i \\ m \neq j-i}}^{J-k} \frac{1}{(ik)^2} \end{aligned} \quad (46)$$

Based on Eqs 41–46, we can write Eq. 40 as:

$$\begin{aligned} \frac{1}{T_{syn}^2} \sum_{i=1}^{J-1} \sum_{j=1}^{J-i} \sum_{k=1}^{J-i-j} \sum_{m=1}^{J-k} \frac{E[\Omega_{1,j}^2(i) \Omega_{1,m}^2(k)]}{(ik)^2} &= \frac{\sigma_{\omega_1}^4}{T_{syn}^2} \left(12 \sum_{i=1}^{J-1} \frac{J-i}{i^4} \right. \\ &+ 6 \sum_{i=1}^{J-1} \sum_{j=1}^{J-i} \sum_{k=1}^{J-i-j} \sum_{\substack{m=1 \\ m \neq j \\ m \neq j+i \\ m \neq j-k \\ m \neq j+i-k}}^{J-k} \frac{1}{(ik)^2} + 4 \sum_{i=1}^{J-1} \sum_{j=1}^{J-i} \sum_{k=1}^{J-i-j} \sum_{\substack{m=1 \\ m \neq j \\ m \neq j+i-k \\ m \neq j+i \\ m \neq j-i}}^{J-k} \frac{1}{(ik)^2} \left. \right) \end{aligned} \quad (47)$$

Now, based on Eqs 37, 39, 47 we may write the approximated MSE related to our new proposed clock skew estimator for the white-Gaussian case as:

$$\begin{aligned} E[e^2] &\approx \left(\frac{1+\alpha}{(J(J-1))} \right)^2 \left[\frac{(\sigma_{\omega_1}^2 + \sigma_{\omega_2}^2)}{T_{syn}^2} \left(2 \sum_{i=1}^{J-1} \frac{J-i}{i^2} + \sum_{i=1}^{J-1} \sum_{j=1}^{J-i} \sum_{k=1}^{J-i-j} \sum_{m=1}^{J-k} \frac{1}{ik} \right. \right. \\ &- \sum_{i=1}^{J-1} \sum_{j=1}^{J-i} \sum_{k=1}^{J-i-j} \sum_{\substack{m=1 \\ m \neq j+i \\ m \neq j-k}}^{J-k} \frac{1}{ik} \left. \right) + \frac{\sigma_{\omega_1}^4}{T_{syn}^4} \left(12 \sum_{i=1}^{J-1} \frac{J-i}{i^4} \right. \\ &\left. + 6 \sum_{i=1}^{J-1} \sum_{j=1}^{J-i} \sum_{k=1}^{J-i-j} \sum_{\substack{m=1 \\ m \neq j \\ m \neq j+i-k \\ m \neq j+i \\ m \neq j-k}}^{J-k} \frac{1}{(ik)^2} + 4 \sum_{i=1}^{J-1} \sum_{j=1}^{J-i} \sum_{k=1}^{J-i-j} \sum_{\substack{m=1 \\ m \neq j \\ m \neq j+i-k \\ m \neq j+i \\ m \neq j-i}}^{J-k} \frac{1}{(ik)^2} \right) \left. \right] \end{aligned} \quad (48)$$

In order to calculate the approximated MSE related to our new proposed clock skew estimator, it can be assumed that $(1 + \alpha) \approx 1$, because in practical systems, the two clocks (Master and Slave) operate at almost the same frequency. Therefore, **Eq. 48** can be rewritten as:

$$E[e^2] \approx \left(\frac{1}{(J(J-1))} \right)^2 \left[\frac{(\sigma_{\omega_1}^2 + \sigma_{\omega_2}^2)}{T_{syn}^2} A + \frac{\sigma_{\omega_1}^4}{T_{syn}^4} B \right] \quad (49)$$

where A and B are defined in **Eqs 29, 30** respectively.

Next, we define the correction factor P . This correction factor helps us to calculate the expression for the approximated MSE related to our new proposed clock skew estimator in the fGn and gfGn cases, as will be shown later on.

In the following, we define P as:

$$\frac{\sigma_{\omega_1}^2 + \sigma_{\omega_2}^2}{T_{syn}^2} A = \left(\frac{\sigma_{\omega_1}^4}{T_{syn}^4} B \right) P \rightarrow P = \frac{A}{B} \left(\frac{\sigma_{\omega_1}^2 + \sigma_{\omega_2}^2}{\sigma_{\omega_1}^4} \right) T_{syn}^2 \quad (50)$$

We can write **Eq. 49** as:

$$E[e^2] \approx \left(\frac{1}{(J(J-1))} \right)^2 \frac{(\sigma_{\omega_1}^2 + \sigma_{\omega_2}^2)}{T_{syn}^2} A \left[1 + \frac{B}{A} \left(\frac{\sigma_{\omega_1}^4}{\sigma_{\omega_1}^2 + \sigma_{\omega_2}^2} \right) \frac{1}{T_{syn}^2} \right] \quad (51)$$

Now, by putting **Eq. 50** into **Eq. 51** we can write the closed-form approximated expression for the approximated MSE related to our new proposed clock skew estimator as is defined in **Eq. 27** and this completes our proof.

3.4 Theorem 4

For the case where the PDV is defined as an fGn process with $0.5 \leq H < 1$, the closed-form approximated expression for the approximated MSE related to our new proposed clock skew estimator is approximately given by:

$$E[e^2] \approx \left(\frac{1}{(J(J-1))} \right)^2 \left(\frac{\sigma_{\omega_1}^2 + \sigma_{\omega_2}^2}{T_{syn}^2} \right) \left(\left(1 + \frac{1}{P} \right) C + D \right) \quad (52)$$

where C and D are given by:

$$C = \sum_{i=1}^{J-1} \sum_{j=1}^{J-i} \frac{1}{i^2} (2 - fG_H(i, H)) + \sum_{i=1}^{J-1} \sum_{j=1}^{J-i} \sum_{k=1}^{J-i-j} \sum_{m=1}^{J-i-j-k} \frac{1}{ik} \left(1 + \frac{1}{2} (fG_H(i-k, H) - fG_H(i, H) - fG_H(k, H)) \right) - \sum_{i=1}^{J-1} \sum_{j=1}^{J-i} \sum_{k=1}^{J-i-j} \sum_{m=1}^{J-i-j-k} \frac{1}{ik} \left(1 - \frac{1}{2} (fG_H(i, H) - fG_H(k, H) + fG_H(i+k, H)) \right) \quad (53)$$

$$D = \sum_{i=1}^{J-1} \sum_{j=1}^{J-i} \sum_{k=1}^{J-i-j} \sum_{m=1}^{J-i-j-k} \frac{1}{2ik} (fG_H(j-m, H) - fG_H(j+i-m, H) - fG_H(j-m-k, H) + fG_H(j+i-m-k, H)) \quad (54)$$

and the function $fG_H(\cdot)$ is:

$$fG_H(x, H) = [|x| - 1]^{2H} - 2(|x|)^{2H} + (|x| + 1)^{2H} \quad (55)$$

3.4.1 Proof of Theorem 4

Based on **Eq. 7** the two first parts in **Eq. 13** can be written as:

$$\sum_{i=1}^{J-1} \sum_{j=1}^{J-i} \sum_{k=1}^{J-i-j} \sum_{m=1}^{J-i-j-k} \frac{E[\Omega_{1,j}(i)\Omega_{1,m}(k) + \Omega_{2,j}(i)\Omega_{2,m}(k)]}{ik} = \sum_{i=1}^{J-1} \sum_{j=1}^{J-i} \sum_{k=1}^{J-i-j} \sum_{m=1}^{J-i-j-k} \left(\frac{E[\omega_1[j+i]\omega_1[m+k] - \omega_1[j+i]\omega_1[m] - \omega_1[j]\omega_1[m+k] + \omega_1[j]\omega_1[m]]}{ik} + \frac{E[\omega_2[j+i]\omega_2[m+k] - \omega_2[j+i]\omega_2[m] - \omega_2[j]\omega_2[m+k] + \omega_2[j]\omega_2[m]]}{ik} \right) \quad (56)$$

For calculating **Eq. 56** we have to consider only six non-zero cases.

The two parts in **Eq. 56** have the same calculations. Therefore, we present our calculations for the first part that is given by:

$$\sum_{i=1}^{J-1} \sum_{j=1}^{J-i} \sum_{k=1}^{J-i-j} \sum_{m=1}^{J-i-j-k} \frac{E[\Omega_{1,j}(i)\Omega_{1,m}(k)]}{ik} = \sum_{i=1}^{J-1} \sum_{j=1}^{J-i} \sum_{k=1}^{J-i-j} \sum_{m=1}^{J-i-j-k} \left(\frac{E[\omega_1[j+i]\omega_1[m+k] - \omega_1[j+i]\omega_1[m] - \omega_1[j]\omega_1[m+k] + \omega_1[j]\omega_1[m]]}{ik} \right) \quad (57)$$

The first case is when $i = k$ and $m = j$. For this case **Eq. 57** is:

$$\sum_{i=1}^{J-1} \sum_{j=1}^{J-i} \sum_{k=1}^{J-i-j} \sum_{m=1}^{J-i-j-k} \frac{E[\Omega_{1,j}(i)\Omega_{1,m}(k)]}{ik} = \sum_{i=1}^{J-1} \sum_{j=1}^{J-i} \sum_{k=1}^{J-i-j} \sum_{m=1}^{J-i-j-k} \left(\frac{E[\omega_1[j+i]\omega_1[j+i] - \omega_1[j+i]\omega_1[j] - \omega_1[j]\omega_1[j+i] + \omega_1[j]\omega_1[j]]}{i^2} \right) \quad (58)$$

which can be written also as:

$$\sum_{i=1}^{J-1} \sum_{j=1}^{J-i} \sum_{k=1}^{J-i-j} \sum_{m=1}^{J-i-j-k} \frac{E[\Omega_{1,j}(i)\Omega_{1,m}(k)]}{ik} = 2\sigma_{\omega_1}^2 \sum_{i=1}^{J-1} \sum_{j=1}^{J-i} \frac{1}{i^2} - 2 \left(\frac{\sigma_{\omega_1}^2}{2} \right) \sum_{i=1}^{J-1} \sum_{j=1}^{J-i} \frac{1}{i^2} (|j - (j+i)| - 1)^{2H} - 2(|j - (j+i)|)^{2H} + (|j - (j+i)| + 1)^{2H} \quad (59)$$

after rearranging **Eq. 59**:

$$\sum_{i=1}^{J-1} \sum_{j=1}^{J-i} \sum_{k=1}^{J-i-j} \sum_{m=1}^{J-i-j-k} \frac{E[\Omega_{1,j}(i)\Omega_{1,m}(k)]}{ik} = \sigma_{\omega_1}^2 \left(\sum_{i=1}^{J-1} \frac{1}{i^2} (2 - (|i-1|^{2H} - 2(i)^{2H} + (i+1)^{2H})) \right) \quad (60)$$

The second case is when $i \neq k$ and $m = j$. For this case **Eq. 57** is:

$$\sum_{i=1}^{J-1} \sum_{j=1}^{J-i} \sum_{k=1}^{J-i-j} \sum_{m=1}^{J-i-j-k} \frac{E[\Omega_{1,j}(i)\Omega_{1,m}(k)]}{ik} = \sum_{i=1}^{J-1} \sum_{j=1}^{J-i} \sum_{k=1}^{J-i-j} \sum_{m=1}^{J-i-j-k} \left(\frac{E[\omega_1[j+i]\omega_1[j+k] - \omega_1[j+i]\omega_1[j] - \omega_1[j]\omega_1[j+k] + \omega_1[j]\omega_1[j]]}{ik} \right) \quad (61)$$

which can be written also as:

$$\sum_{i=1}^{l-1} \sum_{j=1}^{l-i} \sum_{k=1}^{l-i} \sum_{m=1}^{l-k} \frac{E[\Omega_{1,j}(i)\Omega_{1,m}(k)]}{ik} = \sigma_{\omega_1}^2 \sum_{i=1}^{l-1} \sum_{j=1}^{l-i} \sum_{k=1}^{l-i} \sum_{m=1}^{l-k} \frac{1}{ik}$$

$$\left(1 + \frac{1}{2} \left(-\left[\|j+i-j|-1 \right|^{2H} - 2(l+j-i-j)^{2H} + (l+j-i-j+1)^{2H} \right] \right. \\ \left. - \left[\|j-j-k|-1 \right|^{2H} - 2(l-j-j-k)^{2H} + (l-j-j-k+1)^{2H} \right] + \right. \\ \left. \left[\|j+i-j-k|-1 \right|^{2H} - 2(l+j-i-j-k)^{2H} + (l+j-i-j-k+1)^{2H} \right] \right) \quad (62)$$

after rearranging Eq. 62:

$$\sum_{i=1}^{l-1} \sum_{j=1}^{l-i} \sum_{k=1}^{l-i} \sum_{m=1}^{l-k} \frac{E[\Omega_{1,j}(i)\Omega_{1,m}(k)]}{ik} = \sigma_{\omega_1}^2 \sum_{i=1}^{l-1} \sum_{j=1}^{l-i} \sum_{k=1}^{l-i} \sum_{m=1}^{l-k} \frac{1}{ik}$$

$$\left(1 + \frac{1}{2} \left(\left[(l-k-1)^{2H} - 2(l-k)^{2H} + (l-k+1)^{2H} \right] \right. \right. \\ \left. \left. - \left[(l-1)^{2H} - 2(l)^{2H} + (l+1)^{2H} \right] + \left[(l-k-1)^{2H} - 2(l-k)^{2H} + (l-k+1)^{2H} \right] \right) \right) \quad (63)$$

The third case is when $m = j + i$. For this case Eq. 57 is:

$$\sum_{i=1}^{l-1} \sum_{j=1}^{l-i} \sum_{k=1}^{l-i} \sum_{m=j+i}^{l-k} \frac{E[\Omega_{1,j}(i)\Omega_{1,m}(k)]}{ik} = \sum_{i=1}^{l-1} \sum_{j=1}^{l-i} \sum_{k=1}^{l-i} \sum_{m=j+i}^{l-k} \frac{1}{ik}$$

$$\left(\frac{E[\omega_1[j+i]\omega_1[j+i+k] - \omega_1[j+i]\omega_1[j+i] - \omega_1[j]\omega_1[j+i+k] + \omega_1[j]\omega_1[j+i]]}{ik} \right) \quad (64)$$

which can be written also as:

$$\sum_{i=1}^{l-1} \sum_{j=1}^{l-i} \sum_{k=1}^{l-i} \sum_{m=j+i}^{l-k} \frac{E[\Omega_{1,j}(i)\Omega_{1,m}(k)]}{ik} = \sigma_{\omega_1}^2 \sum_{i=1}^{l-1} \sum_{j=1}^{l-i} \sum_{k=1}^{l-i} \sum_{m=j+i}^{l-k} \frac{1}{ik}$$

$$\left(-1 + \frac{1}{2} \left(\left[\|j-j-i|-1 \right|^{2H} - 2(l-j-j-i)^{2H} + (l-j-j-i+1)^{2H} \right] \right. \\ \left. - \left[\|j-j-i-k|-1 \right|^{2H} - 2(l-j-j-i-k)^{2H} + (l-j-j-i-k+1)^{2H} \right] \right. \\ \left. + \left[\|j+i-j-i-k|-1 \right|^{2H} - 2(l+j-i-j-i-k)^{2H} + (l+j-i-j-i-k+1)^{2H} \right] \right) \quad (65)$$

after rearranging Eq. 65:

$$\sum_{i=1}^{l-1} \sum_{j=1}^{l-i} \sum_{k=1}^{l-i} \sum_{m=j+i}^{l-k} \frac{E[\Omega_{1,j}(i)\Omega_{1,m}(k)]}{ik} = \sigma_{\omega_1}^2 \sum_{i=1}^{l-1} \sum_{j=1}^{l-i} \sum_{k=1}^{l-i} \sum_{m=j+i}^{l-k} \frac{1}{ik}$$

$$\left(-1 + \frac{1}{2} \left(\left[(l-k-1)^{2H} - 2(l-k)^{2H} + (l-k+1)^{2H} \right] + \left[(l-1)^{2H} - 2(l)^{2H} + (l+1)^{2H} \right] \right. \right. \\ \left. \left. - \left[(l-k-1)^{2H} - 2(l-k)^{2H} + (l-k+1)^{2H} \right] \right) \right) \quad (66)$$

The fourth case is when $m = j - k$. For this case Eq. 57 is:

$$\sum_{i=1}^{l-1} \sum_{j=1}^{l-i} \sum_{k=1}^{l-i} \sum_{m=j-k}^{l-k} \frac{E[\Omega_{1,j}(i)\Omega_{1,m}(k)]}{ik} = \sum_{i=1}^{l-1} \sum_{j=1}^{l-i} \sum_{k=1}^{l-i} \sum_{m=j-k}^{l-k} \frac{1}{ik}$$

$$\left(\frac{E[\omega_1[j+i]\omega_1[j] - \omega_1[j+i]\omega_1[j-k] - \omega_1[j]\omega_1[j] + \omega_1[j]\omega_1[j-k]]}{ik} \right) \quad (67)$$

which can be written also as:

$$\sum_{i=1}^{l-1} \sum_{j=1}^{l-i} \sum_{k=1}^{l-i} \sum_{m=j-k}^{l-k} \frac{E[\Omega_{1,j}(i)\Omega_{1,m}(k)]}{ik} = \sigma_{\omega_1}^2 \sum_{i=1}^{l-1} \sum_{j=1}^{l-i} \sum_{k=1}^{l-i} \sum_{m=j-k}^{l-k} \frac{1}{ik}$$

$$\left(-1 + \frac{1}{2} \left(\left[\|j+i-j|-1 \right|^{2H} - 2(l+j-i-j)^{2H} + (l+j-i-j+1)^{2H} \right] \right. \\ \left. - \left[\|j+i-j+k|-1 \right|^{2H} - 2(l+j-i-j+k)^{2H} + (l+j-i-j+k+1)^{2H} \right] \right. \\ \left. + \left[\|j-j+k|-1 \right|^{2H} - 2(l-j-j+k)^{2H} + (l-j-j+k+1)^{2H} \right] \right) \quad (68)$$

after rearranging Eq. 68:

$$\sum_{i=1}^{l-1} \sum_{j=1}^{l-i} \sum_{k=1}^{l-i} \sum_{m=j-k}^{l-k} \frac{E[\Omega_{1,j}(i)\Omega_{1,m}(k)]}{ik} = \sigma_{\omega_1}^2 \sum_{i=1}^{l-1} \sum_{j=1}^{l-i} \sum_{k=1}^{l-i} \sum_{m=j-k}^{l-k} \frac{1}{ik}$$

$$\left(-1 + \frac{1}{2} \left(-\left[(l+k-1)^{2H} - 2(l+k)^{2H} + (l+k+1)^{2H} \right] \right. \right. \\ \left. \left. + \left[(l-1)^{2H} - 2(l)^{2H} + (l+1)^{2H} \right] + \left[(l-k-1)^{2H} - 2(l-k)^{2H} + (l-k+1)^{2H} \right] \right) \right) \quad (69)$$

The fifth case is when $i \neq k$ and $m = j + i - k$. For this case Eq. 57 is:

$$\sum_{i=1}^{l-1} \sum_{j=1}^{l-i} \sum_{k=1}^{l-i} \sum_{m=j+i-k}^{l-k} \frac{E[\Omega_{1,j}(i)\Omega_{1,m}(k)]}{ik} = \sum_{i=1}^{l-1} \sum_{j=1}^{l-i} \sum_{k=1}^{l-i} \sum_{m=j+i-k}^{l-k} \frac{1}{ik}$$

$$\left(\frac{E[\omega_1[j+i]\omega_1[j+i] - \omega_1[j+i]\omega_1[j+i-k] - \omega_1[j]\omega_1[j+i] + \omega_1[j]\omega_1[j+i-k]]}{ik} \right) \quad (70)$$

which can be written also as:

$$\sum_{i=1}^{l-1} \sum_{j=1}^{l-i} \sum_{k=1}^{l-i} \sum_{m=j+i-k}^{l-k} \frac{E[\Omega_{1,j}(i)\Omega_{1,m}(k)]}{ik} = \sigma_{\omega_1}^2 \sum_{i=1}^{l-1} \sum_{j=1}^{l-i} \sum_{k=1}^{l-i} \sum_{m=j+i-k}^{l-k} \frac{1}{ik}$$

$$\left(1 + \frac{1}{2} \left(\left[\|j-j-i+k|-1 \right|^{2H} - 2(l-j-j-i+k)^{2H} + (l-j-j-i+k+1)^{2H} \right] \right. \\ \left. - \left[\|j+i-j-i+k|-1 \right|^{2H} - 2(l+j-i-j-i+k)^{2H} + (l+j-i-j-i+k+1)^{2H} \right] \right. \\ \left. - \left[\|j-j-i|-1 \right|^{2H} - 2(l-j-j-i)^{2H} + (l-j-j-i+1)^{2H} \right] \right) \quad (71)$$

after rearranging Eq. 71:

$$\sum_{i=1}^{l-1} \sum_{j=1}^{l-i} \sum_{k=1}^{l-i} \sum_{m=j+i-k}^{l-k} \frac{E[\Omega_{1,j}(i)\Omega_{1,m}(k)]}{ik} = \sigma_{\omega_1}^2 \sum_{i=1}^{l-1} \sum_{j=1}^{l-i} \sum_{k=1}^{l-i} \sum_{m=j+i-k}^{l-k} \frac{1}{ik}$$

$$\left(1 + \frac{1}{2} \left(\left[(l-k-1)^{2H} - 2(l-k)^{2H} + (l-k+1)^{2H} \right] \right. \right. \\ \left. \left. - \left[(l-k-1)^{2H} - 2(l-k)^{2H} + (l-k+1)^{2H} \right] - \left[(l-1)^{2H} - 2(l)^{2H} + (l+1)^{2H} \right] \right) \right) \quad (72)$$

The sixth case is when $m \neq j$ and $m \neq j + i$ and $m \neq j - k$ and $m + k \neq j + i$. For this case Eq. 57 is:

$$\sum_{i=1}^{l-1} \sum_{j=1}^{l-i} \sum_{k=1}^{l-i} \sum_{m=j}^{l-k} \frac{E[\Omega_{1,j}(i)\Omega_{1,m}(k)]}{ik} = \sum_{i=1}^{l-1} \sum_{j=1}^{l-i} \sum_{k=1}^{l-i} \sum_{m=j}^{l-k} \frac{1}{ik}$$

$$\left(\frac{E[\omega_1[j+i]\omega_1[m+k] - \omega_1[j+i]\omega_1[m] - \omega_1[j]\omega_1[m+k] + \omega_1[j]\omega_1[m]]}{ik} \right) \quad (73)$$

which can be written also as:

$$\sum_{i=1}^{J-1} \sum_{j=1}^{J-i} \sum_{k=1}^{J-i} \sum_{\substack{m=1 \\ m \neq j \\ m \neq j+i \\ m \neq j-k \\ m \neq j+i-k}}^{J-k} \frac{E[\Omega_{1,j}(i)\Omega_{1,m}(k)]}{ik} = \frac{\sigma_{\omega_1}^2}{2} \sum_{i=1}^{J-1} \sum_{j=1}^{J-i} \sum_{k=1}^{J-i} \sum_{\substack{m=1 \\ m \neq j \\ m \neq j+i \\ m \neq j-k \\ m \neq j+i-k}}^{J-k} \frac{1}{ik} \\ \left(\left[|j+i-m-k|-1 \right]^{2H} - 2(|j+i-m-k|)^{2H} + (|j+i-m-k|+1)^{2H} \right) \\ - \left[|j+i-m|-1 \right]^{2H} - 2(|j+i-m|)^{2H} + (|j+i-m|+1)^{2H} \\ - \left[|j-m-k|-1 \right]^{2H} - 2(|j-m-k|)^{2H} + (|j-m-k|+1)^{2H} \\ + \left[|j-m|-1 \right]^{2H} - 2(|j-m|)^{2H} + (|j-m|+1)^{2H} \right) \quad (74)$$

Please note that the summation of Eqs 60, 63, 66, 69, 72 can be written as $(\sigma_{\omega_1}^2 C)$, where C is defined in Eq. 53. The expression in Eq. 74 can be written as $(\sigma_{\omega_1}^2 D)$, where D is defined in Eq. 54.

Now, we can write Eq. 57 as:

$$\sum_{i=1}^{J-1} \sum_{j=1}^{J-i} \sum_{k=1}^{J-i} \sum_{m=1}^{J-k} \frac{E[\Omega_{1,j}(i)\Omega_{1,m}(k)]}{ik} = \sigma_{\omega_1}^2 (C + D) \quad (75)$$

Based on Eq. 75 we may write Eq. 56 as:

$$\sum_{i=1}^{J-1} \sum_{j=1}^{J-i} \sum_{k=1}^{J-i} \sum_{m=1}^{J-k} \left(\frac{E[\Omega_{1,j}(i)\Omega_{1,m}(k)]}{ik} + \frac{E[\Omega_{2,j}(i)\Omega_{2,m}(k)]}{ik} \right) \\ = (\sigma_{\omega_1}^2 + \sigma_{\omega_2}^2) (C + D) \quad (76)$$

The third part in Eq. 13 is quite difficult to carry out for the fGn case. Now, looking at Eq. 27 we notice that Eq. 27 consists actually on the sum of the two first parts of Eq. 13 multiplied by the factor $(1 + \frac{1}{P})$. Please note that P (28) is actually obtained by dividing the sum of the first two parts of Eq. 13 by the third part of Eq. 13 for the white-Gaussian noise.

In order to carry out the third part in Eq. 13 for the fGn case, we approximate it based on Eq. 27. In our approximation we simply multiply the expression of $C(\sigma_{\omega_1}^2 + \sigma_{\omega_2}^2)$ with the expression of $(1 + \frac{1}{P})$. The expression for D is not multiplied with the expression of $(1 + \frac{1}{P})$, since D is zero for $H = 0.5$.

This completes our proof.

3.5 Theorem 5

For the case where the PDV is defined as an gfGn process with $0.5 \leq H < 1$ and $0 < a \leq 1$ the closed-form approximated expression for the MSE related to our new proposed clock skew estimator is given by:

$$E[e^2] \approx \left(\frac{1}{J(J-1)} \right)^2 \left(\frac{\sigma_{\omega_1}^2 + \sigma_{\omega_2}^2}{T_{syn}^2} \right) \left(\left(1 + \frac{1}{P} \right) C^* + D^* \right) \quad (77)$$

where C^* and D^* are given by:

$$C^* = \sum_{i=1}^{J-1} \frac{J-i}{P^2} (2 - fG_H^*(i, H, a)) \\ + \sum_{i=1}^{J-1} \sum_{j=1}^{J-i} \sum_{k=1}^{J-i} \sum_{\substack{m=1 \\ m \neq j \\ m \neq j+i \\ m \neq j-k \\ m \neq j+i-k}}^{J-k} \frac{1}{ik} \left(1 + \frac{1}{2} (fG_H^*(i-k, H, a) - fG_H^*(i, H, a) - fG_H^*(k, H, a)) \right) \\ - \sum_{i=1}^{J-1} \sum_{j=1}^{J-i} \sum_{k=1}^{J-i} \sum_{\substack{m=1 \\ m \neq j \\ m \neq j+i \\ m \neq j-k \\ m \neq j+i-k}}^{J-k} \frac{1}{ik} \left(1 - \frac{1}{2} (fG_H^*(i, H, a) - fG_H^*(k, H, a) + fG_H^*(i+k, H, a)) \right) \quad (78)$$

$$D^* = \sum_{i=1}^{J-1} \sum_{j=1}^{J-i} \sum_{k=1}^{J-i} \sum_{\substack{m=1 \\ m \neq j \\ m \neq j+i \\ m \neq j-k \\ m \neq j+i-k}}^{J-k} \frac{1}{2ik} (fG_H^*(j-m, H, a) - fG_H^*(j+i-m, H, a) \\ - fG_H^*(j-m-k, H, a) + fG_H^*(j+i-m-k, H, a)) \quad (79)$$

and the function $fG_H^*(.)$ is:

$$fG_H^*(x, H, a) = \left[\|x^a\| - 1 \right]^{2H} - 2(\|x^a\|)^{2H} + (\|x^a\| + 1)^{2H} \quad (80)$$

3.5.1 Proof of Theorem 5

As already was shown in Section 2, we have for the fGn process Li and Zhao [23]; Peng et al. [21]:

$$\text{for } j = m \quad E[\omega_n[j], \omega_n[m]] = \sigma_{\omega_n}^2 \\ \text{for } j \neq m \quad E[\omega_n[j], \omega_n[m]] = \frac{\sigma_{\omega_n}^2}{2} \left[\|j-m\| - 1 \right]^{2H} - 2(\|j-m\|)^{2H} + (\|j-m\| + 1)^{2H} \quad (81)$$

where $n = 1, 2$.

On the other hand, we have for the gfGn process Li [26]:

$$\text{for } j = m \quad E[\omega_n[j], \omega_n[m]] = \sigma_{\omega_n}^2 \\ \text{for } j \neq m \quad E[\omega_n[j], \omega_n[m]] = \frac{\sigma_{\omega_n}^2}{2} \left[\|(j-m)^a\| - 1 \right]^{2H} - 2(\|(j-m)^a\|)^{2H} + (\|(j-m)^a\| + 1)^{2H} \quad (82)$$

Please note that the difference between Eqs 81, 82 is only by the a factor. Thus, we can use Eqs 52–55 for the gfGn case where the function $fG_H(.)$ defined in Eq. 55 and used in Eq. 53 to Eq. 54 is substituted by the function $fG_H^*(.)$ Eq. 80 and this completes our proof.

4 DESIGNING GRAPHS

In this section, we propose some designing graphs for the fGn and gfGn cases. Thus, the designing graphs for the fGn case will be based on Theorem 4 while the designing graph for the gfGn case will be based on Theorem 5. The closed-form approximated expression for the MSE (for the fGn process Eq. 52 and for the gfGn process Eq. 77) is a function of H , a function of T_{syn} , a function of the total sent Sync messages, and a function of the PDV variances. It could be very helpful for the system designer if he could approximately know the total sent Sync messages that the system needs in order to receive the system's requirement such as $MSE = 10^{-12}$.

Thus in the following, we will try to create some designing graphs that can help the system designer to achieve the system's requirement of $MSE = 10^{-12}$.

Based on Eqs 28, 52, 77 we can write the approximated MSE related to our new proposed clock skew estimator as:

$$E[e^2] \approx \frac{1}{(J(J-1))^2} \left(\left(\frac{\sigma_{\omega_1}^2 + \sigma_{\omega_2}^2}{T_{syn}^2} \right) (C^t + D^t) + \frac{\sigma_{\omega_1}^4}{T_{syn}^4} \left(\frac{B}{A} C^t \right) \right) \quad (83)$$

where A and B are defined in **Eqs 29, 30** respectively. For the fGn case $C^t = C$ **Eq. 53** and $D^t = D$ **Eq. 54**, and for the gfGn case $C^t = C^*$ **Eq. 78** and $D^t = D^*$ **Eq. 79**.

After arranging **Eq. 83** we have:

$$(\sigma_{\omega_1}^2 + \sigma_{\omega_2}^2) + \frac{\sigma_{\omega_1}^4}{T_{syn}^2} \left(\frac{B}{A} \frac{C^t}{C^t + D^t} \right) \approx E[e^2] T_{syn}^2 \frac{(J(J-1))^2}{(C^t + D^t)} \quad (84)$$

In order to simplify **Eq. 84** we use the following condition:

$$(\sigma_{\omega_1}^2 + \sigma_{\omega_2}^2) \gg \frac{\sigma_{\omega_1}^4}{T_{syn}^2} \left(\frac{B}{A} \frac{C^t}{C^t + D^t} \right) \quad (85)$$

Thus, for the fGn and gfGn cases, we may write based on **Eqs 84, 85**:

$$(\sigma_{\omega_1}^2 + \sigma_{\omega_2}^2) \approx E[e^2] T_{syn}^2 \frac{(J(J-1))^2}{(C^t + D^t)} \quad (86)$$

Based on **Eq. 86** we carry out some designing graphs (**Figures 2–5**) that were obtained for $MSE = 10^{-12}$ and for three different T_{syn} rates: $64 \frac{\text{packet}}{\text{sec}}$, $16 \frac{\text{packet}}{\text{sec}}$ and $8 \frac{\text{packet}}{\text{sec}}$. Please note that we have three designing graphs for the fGn case (**Figures 2–4**) where each designing graph was carried out for various values for H , and one designing graph for the gfGn case with $H = 0.95$ (**Figure 5**).

In order to see if **Eq. 85** can actually be ignored, we are going back to the obtained designing graph in **Figure 2** to check ourselves.

In the following, we assume that $\sigma_{\omega_1} = \sigma_{\omega_2}$ and for simplicity we denote the expression $\frac{B}{A} \frac{C^t}{C^t + D^t}$ as F .

According to **Figure 2**, where $T_{syn} = 15.6ms$ ($64 \frac{\text{packet}}{\text{sec}}$) and $H = 0.9$:

$$\begin{aligned} 1. \quad & \sigma_{\omega_1}^2 + \sigma_{\omega_2}^2 = 9.65e - 13 \Rightarrow J = 30 \\ & \Rightarrow F = 46.88 \Rightarrow \frac{\sigma_{\omega_1}^4}{T_{syn}^2} = 9.57e - 22 \\ & \Rightarrow \sigma_{\omega_1}^2 + \sigma_{\omega_2}^2 = 9.65e - 13 \gg F \frac{\sigma_{\omega_1}^4}{T_{syn}^2} = 4.49e - 20 \\ 2. \quad & \sigma_{\omega_1}^2 + \sigma_{\omega_2}^2 = 2.89e - 11 \Rightarrow J = 140 \Rightarrow F = 94.97 \\ & \Rightarrow \frac{\sigma_{\omega_1}^4}{T_{syn}^2} = 8.58e - 19 \\ & \Rightarrow \sigma_{\omega_1}^2 + \sigma_{\omega_2}^2 = 2.89e - 11 \gg F \frac{\sigma_{\omega_1}^4}{T_{syn}^2} = 8.15e - 17 \\ 3. \quad & \sigma_{\omega_1}^2 + \sigma_{\omega_2}^2 = 4.76e - 8 \Rightarrow J = 500 \\ & \Rightarrow F = 150.93 \Rightarrow \frac{\sigma_{\omega_1}^4}{T_{syn}^2} = 2.33e - 16 \\ & \Rightarrow \sigma_{\omega_1}^2 + \sigma_{\omega_2}^2 = 4.76e - 8 \gg F \frac{\sigma_{\omega_1}^4}{T_{syn}^2} = 3.52e - 14 \end{aligned}$$

According to **Figure 2**, where $T_{syn} = 15.6ms$ ($64 \frac{\text{packet}}{\text{sec}}$) and $H = 0.8$:

$$\begin{aligned} 1. \quad & \sigma_{\omega_1}^2 + \sigma_{\omega_2}^2 = 8.92e - 13 \Rightarrow J = 30 \Rightarrow F = 56.37 \\ & \Rightarrow \frac{\sigma_{\omega_1}^4}{T_{syn}^2} = 8.18e - 22 \\ & \Rightarrow \sigma_{\omega_1}^2 + \sigma_{\omega_2}^2 = 8.92e - 13 \gg F \frac{\sigma_{\omega_1}^4}{T_{syn}^2} = 4.61e - 20 \\ 2. \quad & \sigma_{\omega_1}^2 + \sigma_{\omega_2}^2 = 3.63e - 11 \Rightarrow J = 140 \Rightarrow F = 137.77 \\ & \Rightarrow \frac{\sigma_{\omega_1}^4}{T_{syn}^2} = 1.35e - 18 \\ & \Rightarrow \sigma_{\omega_1}^2 + \sigma_{\omega_2}^2 = 3.63e - 11 \gg F \frac{\sigma_{\omega_1}^4}{T_{syn}^2} = 1.86e - 16 \\ 3. \quad & \sigma_{\omega_1}^2 + \sigma_{\omega_2}^2 = 7.72e - 10 \Rightarrow J = 500 \Rightarrow F = 260.74 \\ & \Rightarrow \frac{\sigma_{\omega_1}^4}{T_{syn}^2} = 6.12e - 16 \end{aligned}$$

$$\Rightarrow \sigma_{\omega_1}^2 + \sigma_{\omega_2}^2 = 7.72e - 10 \gg F \frac{\sigma_{\omega_1}^4}{T_{syn}^2} = 1.59e - 13$$

According to **Figure 2**, where $T_{syn} = 15.6ms$ ($64 \frac{\text{packet}}{\text{sec}}$) and $H = 0.6$:

$$\begin{aligned} 1. \quad & \sigma_{\omega_1}^2 + \sigma_{\omega_2}^2 = 1.47e - 12 \Rightarrow J = 30 \\ & \Rightarrow F = 81.39 \Rightarrow \frac{\sigma_{\omega_1}^4}{T_{syn}^2} = 2.22e - 21 \\ & \Rightarrow \sigma_{\omega_1}^2 + \sigma_{\omega_2}^2 = 1.47e - 12 \gg F \frac{\sigma_{\omega_1}^4}{T_{syn}^2} = 1.81e - 19 \\ 2. \quad & \sigma_{\omega_1}^2 + \sigma_{\omega_2}^2 = 1.09e - 10 \Rightarrow J = 140 \\ & \Rightarrow F = 306.76 \Rightarrow \frac{\sigma_{\omega_1}^4}{T_{syn}^2} = 1.22e - 17 \\ & \Rightarrow \sigma_{\omega_1}^2 + \sigma_{\omega_2}^2 = 1.09e - 10 \gg F \frac{\sigma_{\omega_1}^4}{T_{syn}^2} = 3.75e - 15 \\ 3. \quad & \sigma_{\omega_1}^2 + \sigma_{\omega_2}^2 = 3.84e - 9 \Rightarrow J = 500 \\ & \Rightarrow F = 881.07 \Rightarrow \frac{\sigma_{\omega_1}^4}{T_{syn}^2} = 1.52e - 14 \\ & \Rightarrow \sigma_{\omega_1}^2 + \sigma_{\omega_2}^2 = 3.84e - 9 \gg F \frac{\sigma_{\omega_1}^4}{T_{syn}^2} = 1.34e - 11 \end{aligned}$$

According to the list from above, we can see that for $10 < J < 500$, **Eq. 86** is applicable.

5 SIMULATION RESULTS

In this section, we test our new proposed clock skew estimator **Eq. 3** and our closed-form-approximated expression for the MSE for the white-Gaussian **Eq. 27**, fGn **Eq. 52** and gfGn **Eq. 77** cases. At first, we show various simulation results in order to show the efficiency of our new proposed clock skew estimator **Eq. 3** compared to the ML-like estimator (MLLE) Noh et al. [34] that maximizes the likelihood function obtained based on a reduced subset of observations (the first and last timing stamps). According to Noh et al. [34] we have:

$$\hat{\beta} = \frac{T_{2,1}(J-1)^2 + T_{3,1}(J-1)^2}{T_{1,1}(J-1)T_{2,1}(J-1) + T_{3,1}(J-1)T_{4,1}(J-1)} - 1 \quad (87)$$

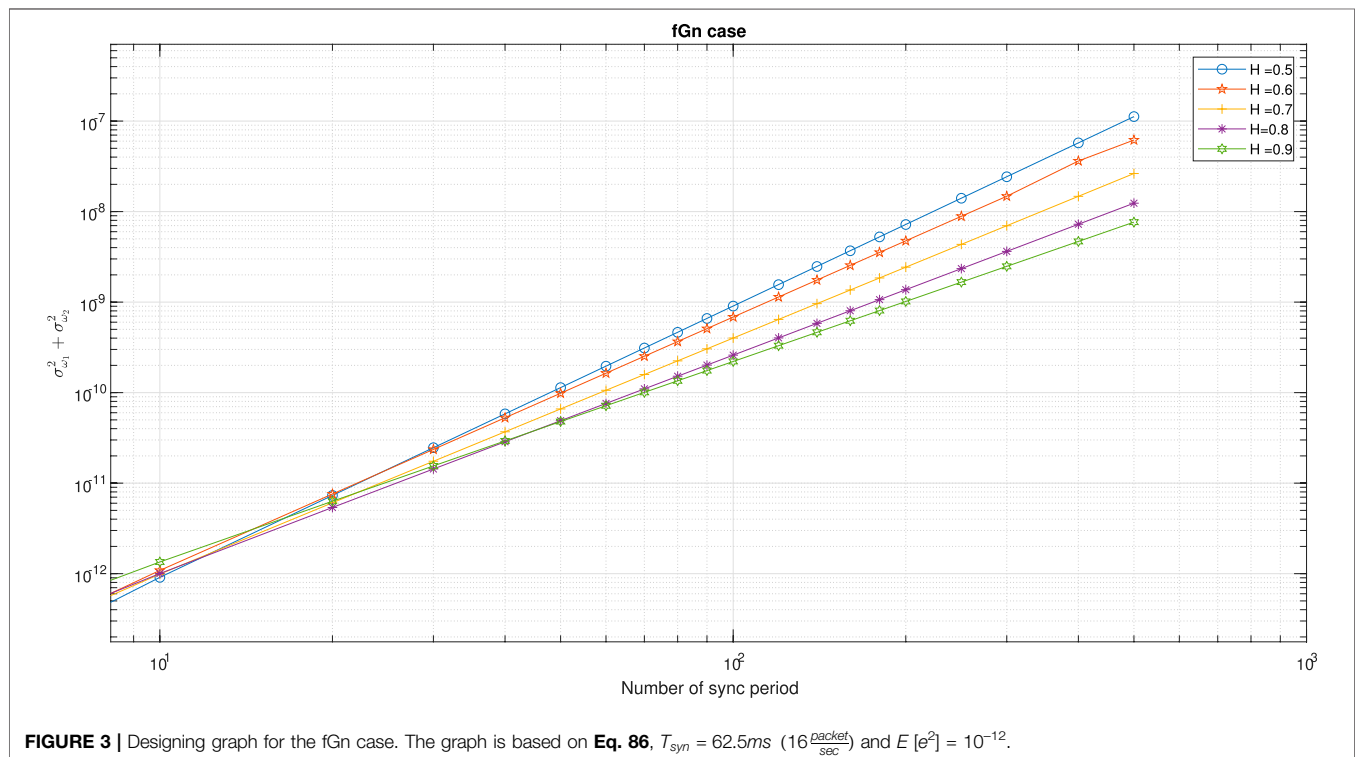
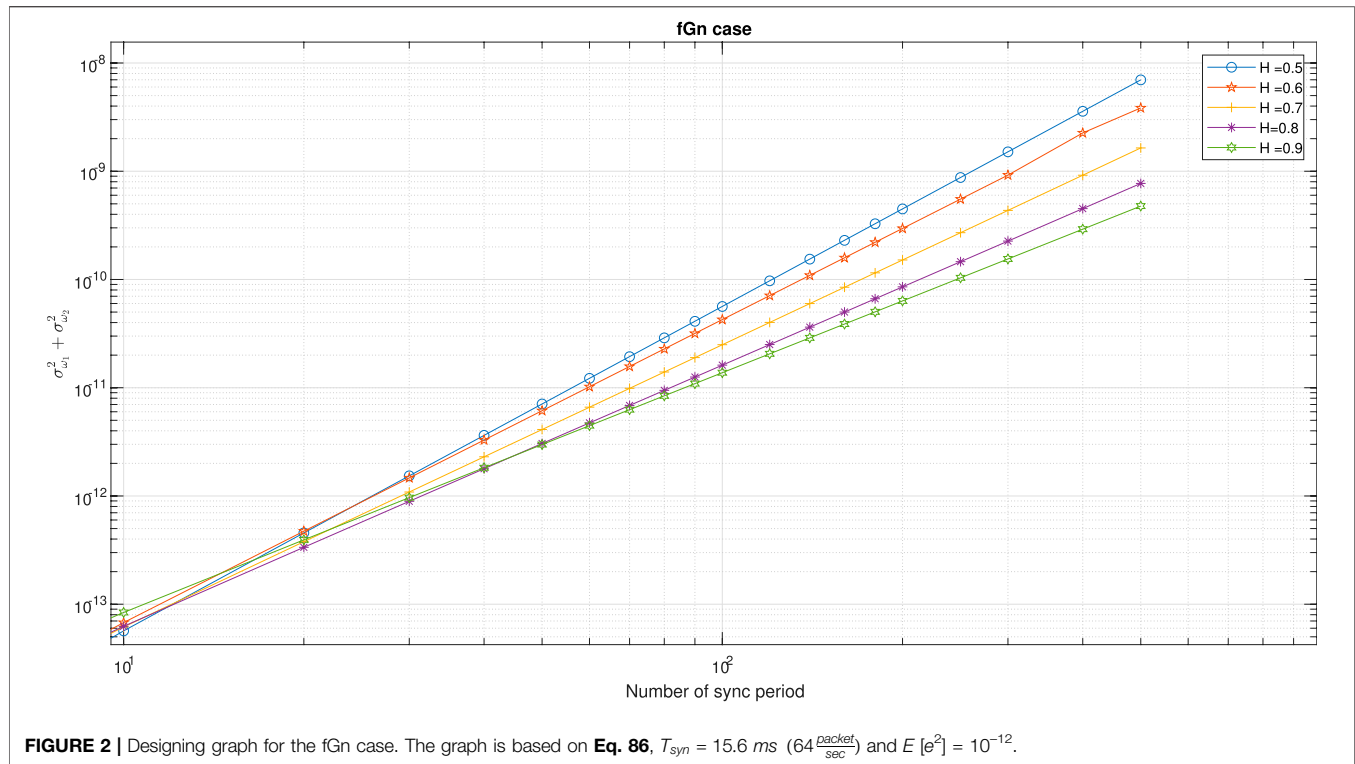
where

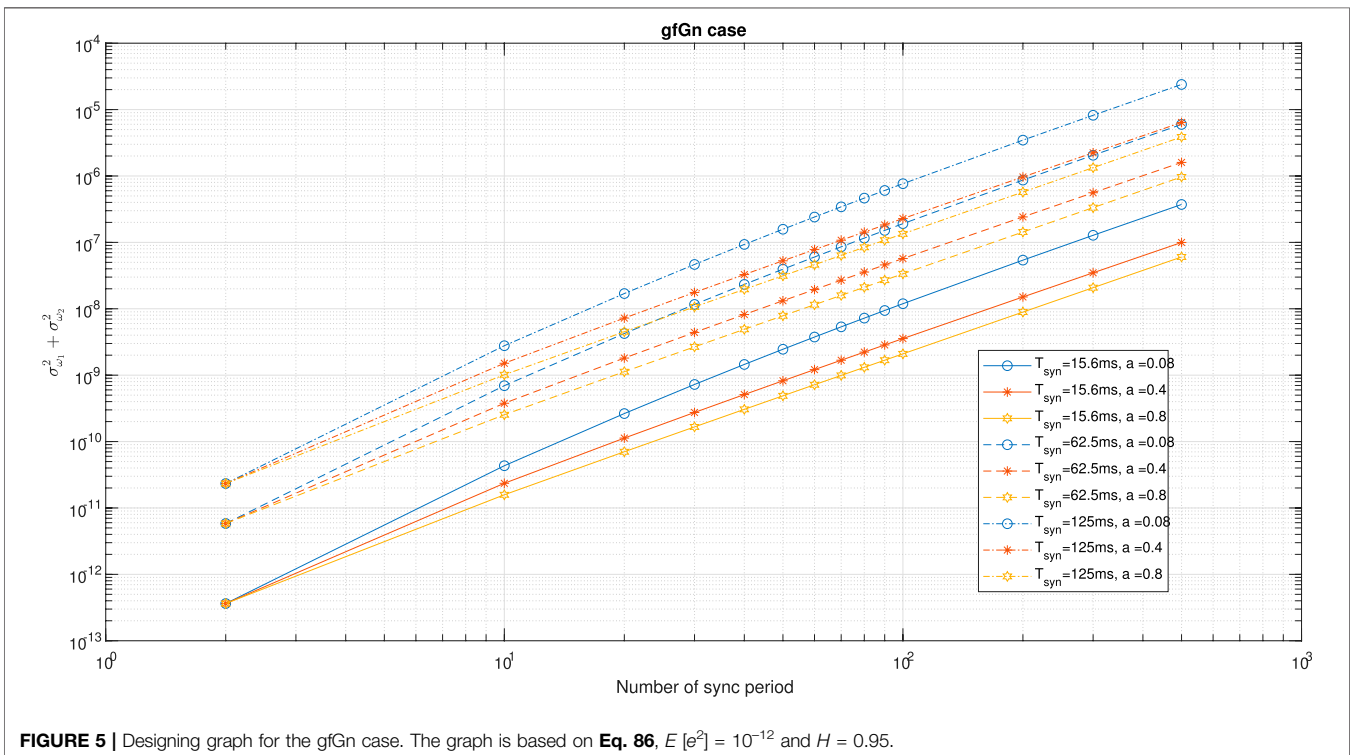
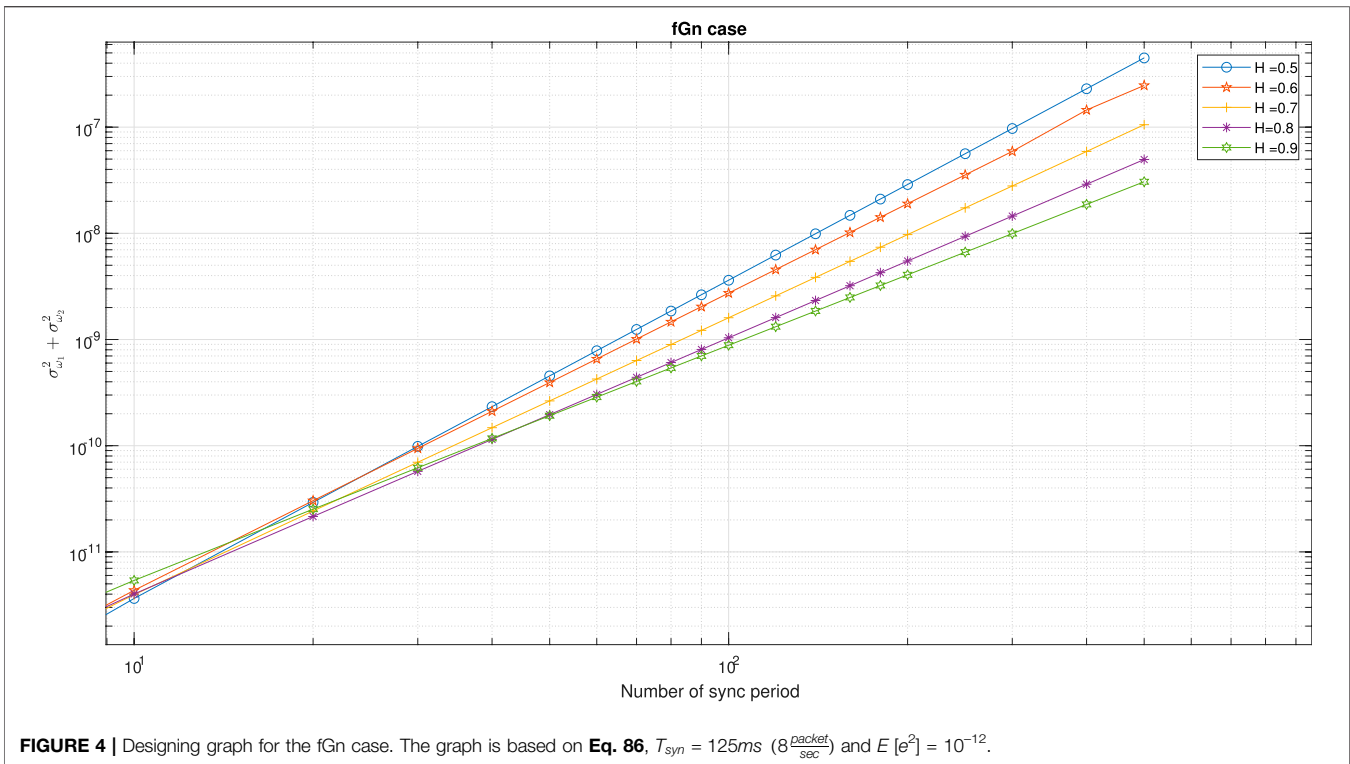
$$\hat{\beta} = \frac{1}{\alpha + 1} - 1 \quad (88)$$

$T_{2,1}(J-1) = t_2[J] - t_2[1]$, $T_{1,j}(i)$, $T_{2,j}(i)$, $T_{3,j}(i)$ and $T_{4,j}(i)$ are defined in **Eqs. 4, 7**.

Figure 6 shows the performance comparison between our new proposed clock skew estimator **Eq. 3** with the estimator obtained from Noh et al. [34] for the Gaussian case. The results in **Figure 6** were obtained for different values for the PDV variances. In addition, we also show there the performance of the new proposed closed-form-approximated expression for the MSE **Eq. 27** compared to the simulated one via **Eq. 3**. According to **Figure 6** our new clock skew estimator **Eq. 3** achieves a lower MSE compared to the clock skew estimator from Noh et al. [34] for the Gaussian case. In addition, we can clearly see from **Figure 6** that our new closed-form-approximated expression for the MSE **Eq. 27** supplies results that are very close to the simulated one.

Figure 7 shows the performance comparison between our new proposed clock skew estimator **Eq. 3** with the clock skew





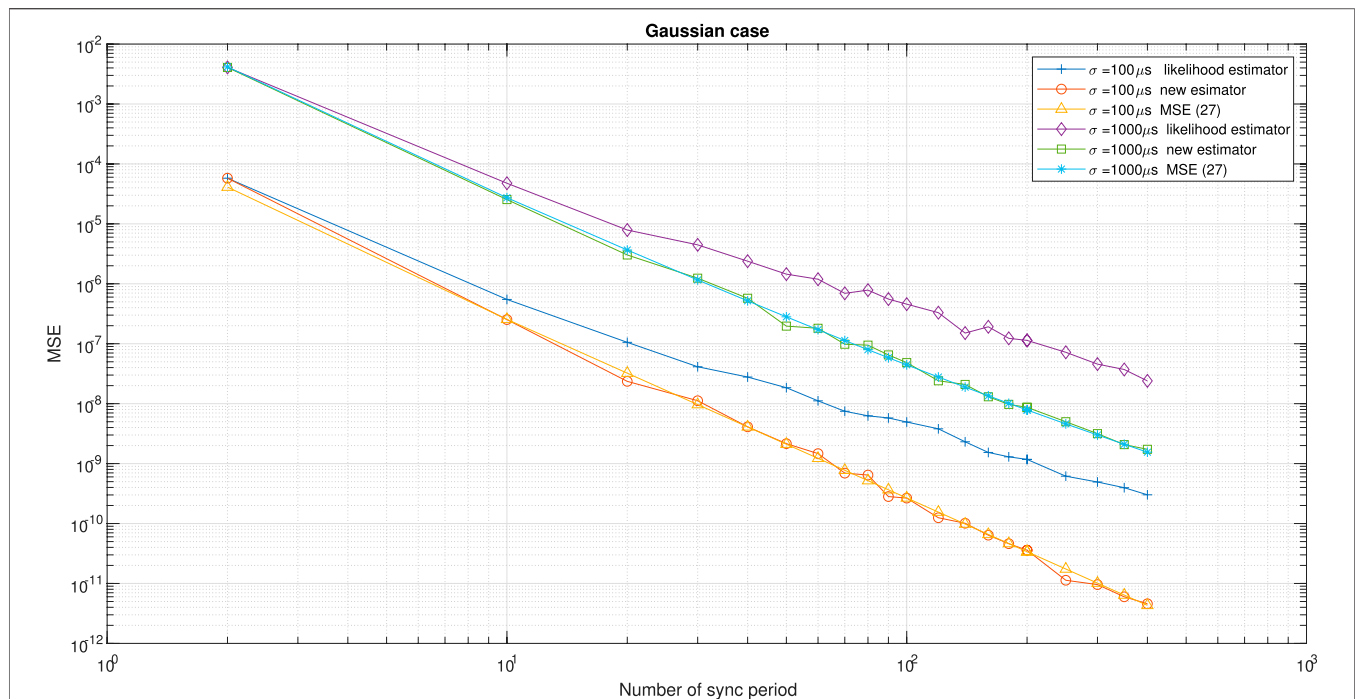


FIGURE 6 | Performance comparison between the new clock skew estimator **Eq. 3** with the clock skew estimator of Noh et al. [34] denoted here as the likelihood estimator. In addition, we have the simulated performance results for our new proposed expression for the MSE **Eq. 27** for the white-Gaussian case. $\alpha = 50 \text{ ppm}$, $Q = 5 \text{ ms}$, $T_{\text{syn}} = 15.6 \text{ ms}$ ($64 \frac{\text{packet}}{\text{sec}}$). For: $\sigma_{w1} = \sigma_{w2} = \sigma = 100 \mu\text{s}$ the delay $d_{\text{ms}} = 1 \text{ ms}$, $d_{\text{sm}} = 0.8 \text{ ms}$ For: $\sigma_{w1} = \sigma_{w2} = 1000 \mu\text{s}$, the delay $d_{\text{ms}} = 3.3 \text{ ms}$, $d_{\text{sm}} = 3 \text{ ms}$. The results were obtained for 100 Monte-Carlo trails.

estimator obtained from Noh et al. [34] for the fGn case with different values for H . **Figure 8** shows the performance comparison between our new proposed clock skew estimator **Eq. 3** with the clock skew estimator obtained from Noh et al. [34] for the fGn case with different values for the PDV variances. In addition, we also show in **Figures 7, 8** the performance of our new closed-form-approximated expression for the MSE **Eq. 52** compared to the simulated one. According to **Figures 7, 8** our new clock skew estimator achieves a lower MSE compared to the clock skew estimator from Noh et al. [34] for the fGn case. In addition, we can clearly see from **Figures 7, 8** that the performance of our new closed-form-approximated expression for the MSE **Eq. 52** is very close to the performance obtained by the simulated MSE.

Figure 9 shows the MSE obtained by the new proposed clock skew estimator **Eq. 3** compared with our closed-form-approximated expression for the MSE **Eq. 52** for the fGn case. The results in **Figure 9** were obtained for different forward and reverse PDV variances. According to **Figure 9** there is a high correlation between the performance of our closed-form-approximated expression for the MSE **Eq. 52** with the simulated MSE.

Figure 10 shows the performance comparison between our new proposed clock skew estimator **Eq. 3** with the clock skew estimator obtained from Noh et al. [34] for the fGn

case. The results in **Figure 10** were obtained for different values of a (please note that we set the values of H and a according to Li [26]). In addition, we also show in **Figure 10** the performance of our closed-form-approximated expression for the MSE **Eq. 77** compared to the simulated one. According to **Figure 10**, our new clock skew estimator achieves a lower MSE compared to the clock skew estimator from Noh et al. [34]. In addition, we can see from **Figure 10** that the performance of our closed-form-approximated expression for the MSE **Eq. 77** is high correlated with the simulated one.

It should be pointed out that the clock skew estimator from Noh et al. [34], does not depend on the unknown fixed delay paths nor on the clock offset between the Master and Slave. Thus, it is a good candidate for performance comparison with our new proposed clock skew estimator **Eq. 3**. Please note that in order to carry out a fair performance comparison, we can only take those clock skew estimators for the simulation performance comparison task, that do not rely on the symmetric assumption for the forward and reverse fixed delay paths as is the case in Puttnies et al. [13], Chaudhari et al. [32], Li and Jeske [33] and Shan et al. [5] (please refer to **Table 1**). In addition, those clock skew estimators should not rely on multiple Masters or on multiple paths between the Master and Slave as is the case in Karthik and Blum [12]. Thus, based

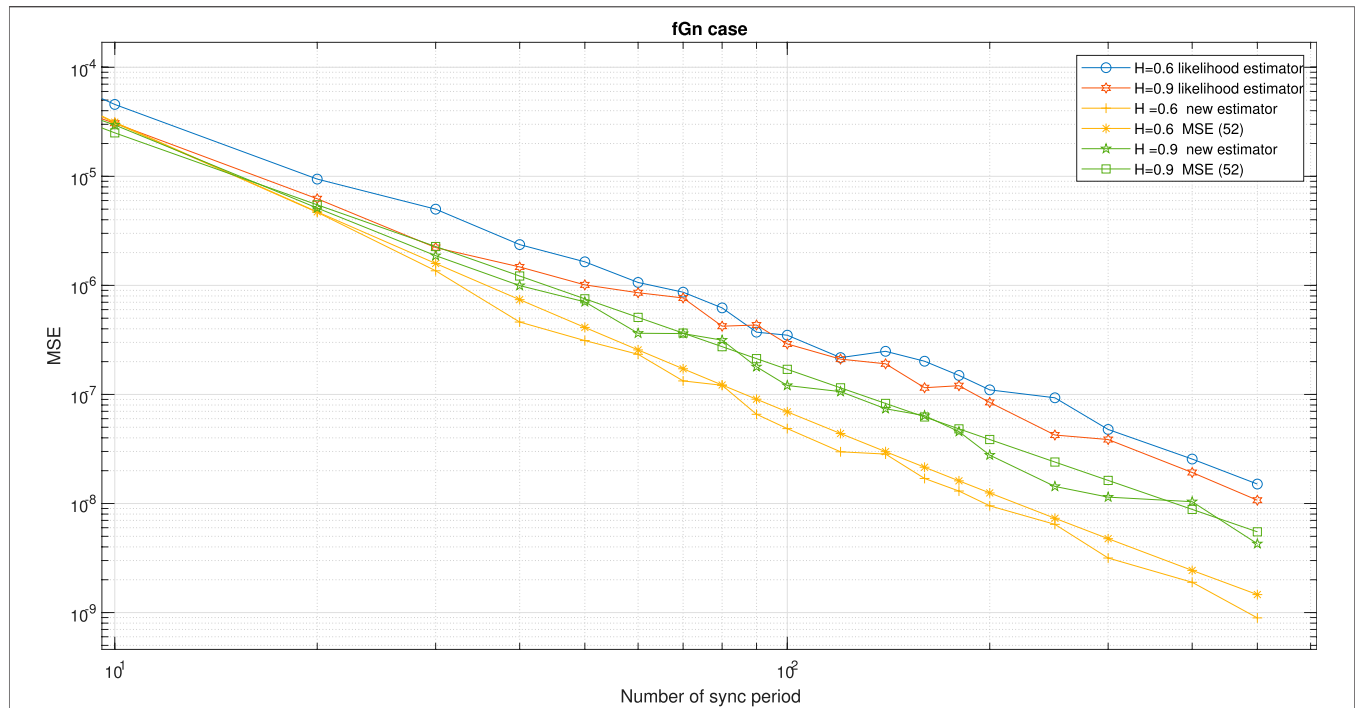


FIGURE 7 | Performance comparison between the new clock skew estimator **Eq. 3** with the clock skew estimator of Noh et al. [34] denoted here as the likelihood estimator. In addition, we have the simulated performance results for our new proposed expression for the MSE **Eq. 52** for the fGn case. $\alpha = 50 \text{ ppm}$, $Q = 5 \text{ ms}$. $T_{\text{syn}} = 15.6 \text{ ms}$ ($64 \frac{\text{packet}}{\text{sec}}$), $\sigma_{w_1} = \sigma_{w_2} = 1000 \mu\text{s}$, $d_{\text{ms}} = 5 \text{ ms}$, $d_{\text{sm}} = 5.5 \text{ ms}$. The results were obtained for 100 Monte-Carlo trails.

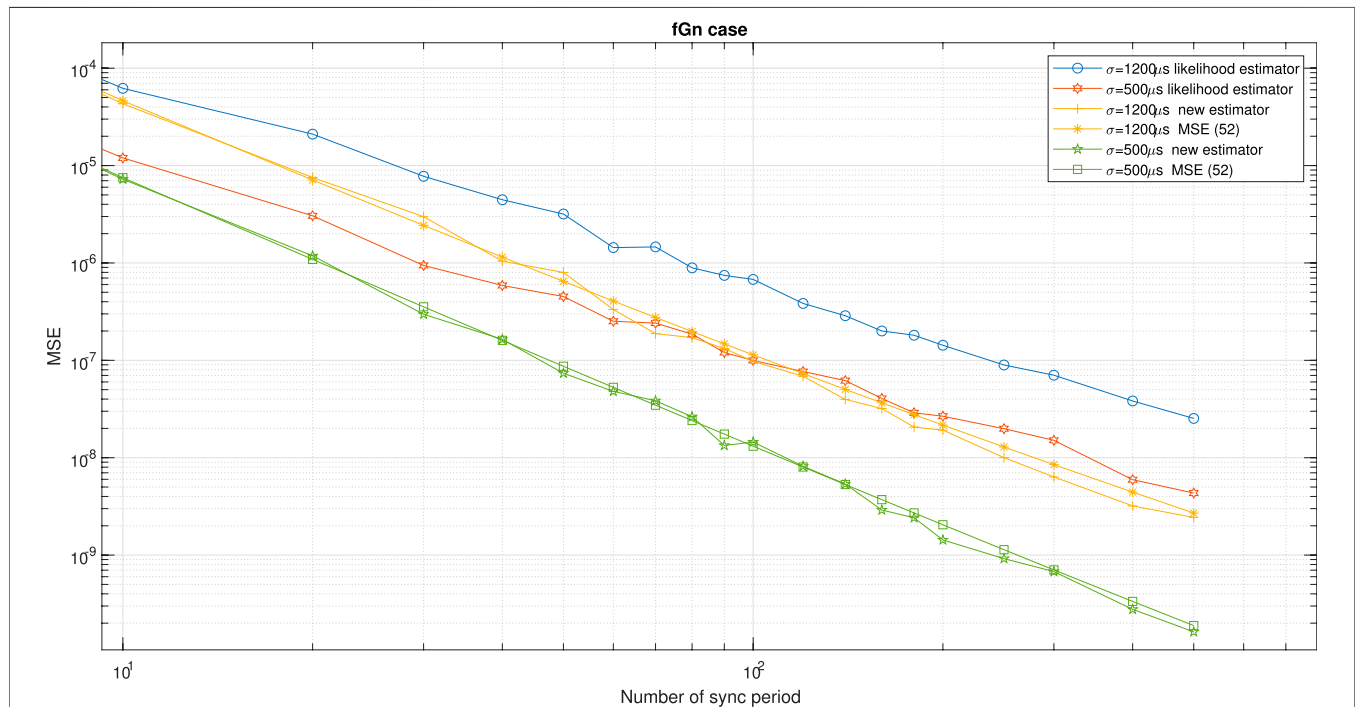
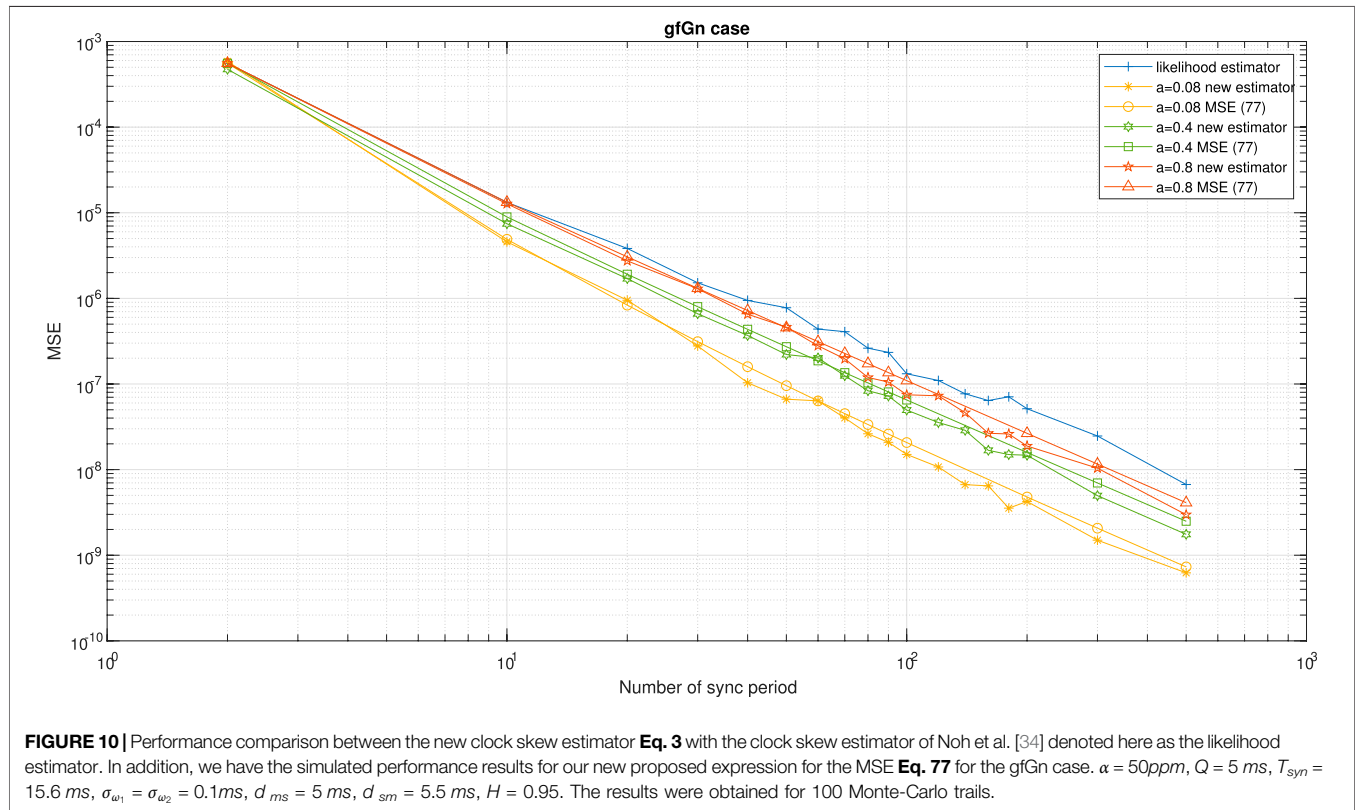
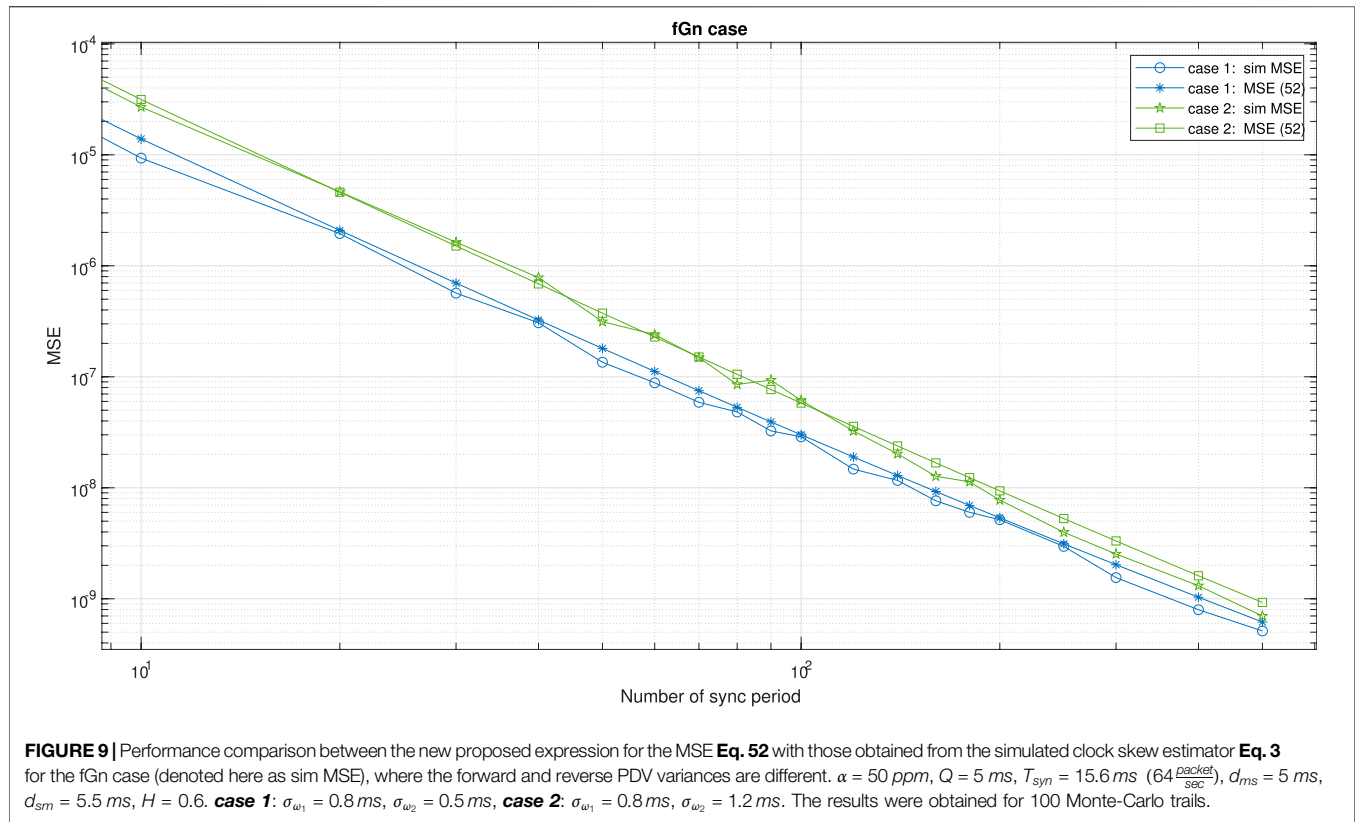
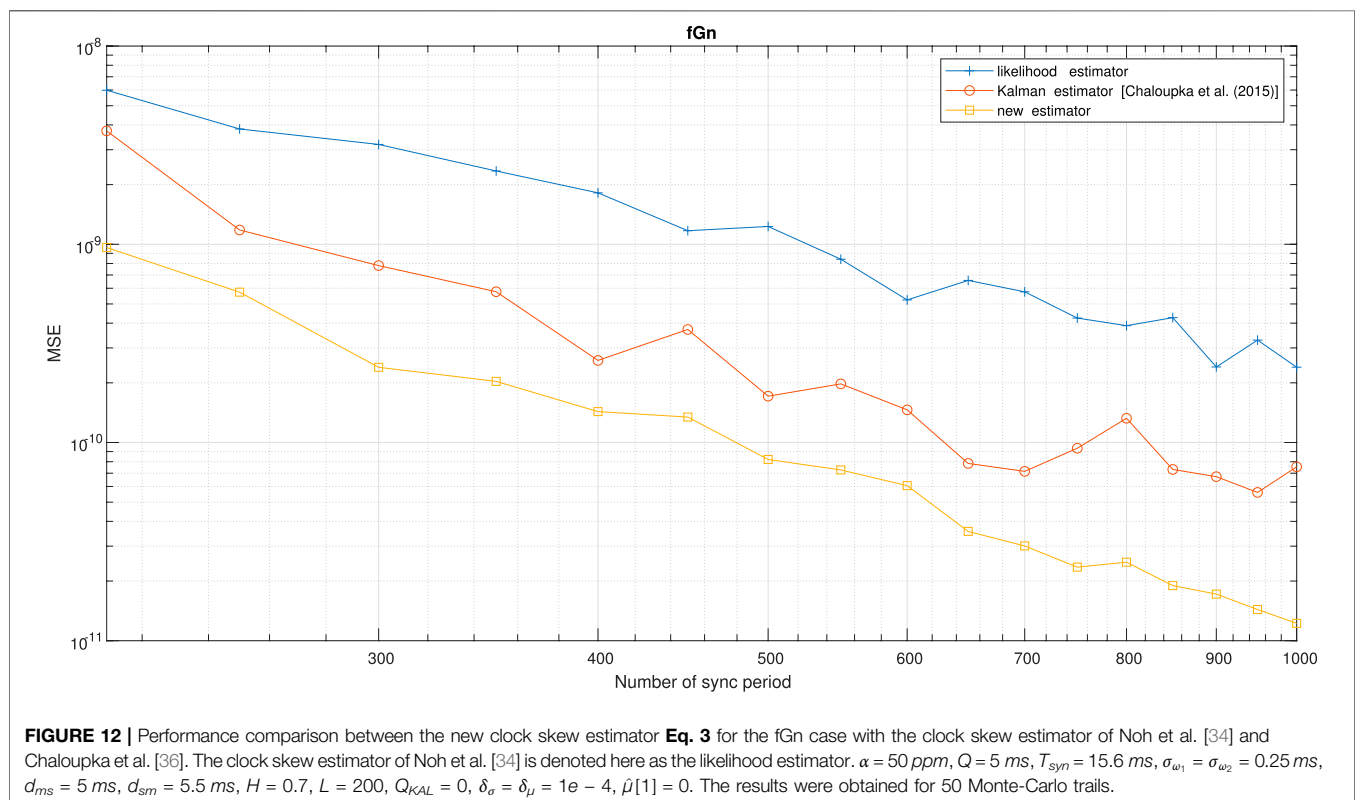
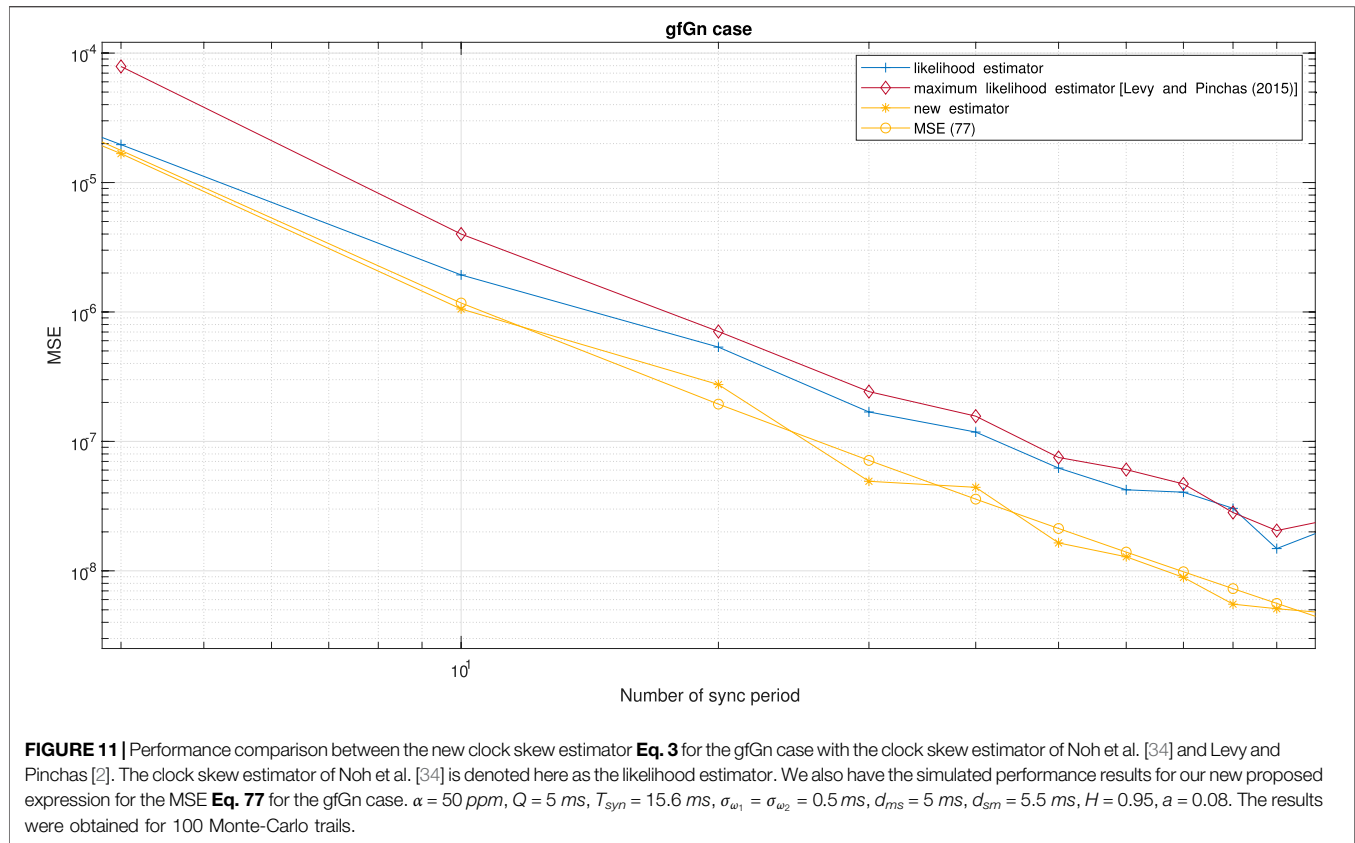


FIGURE 8 | Performance comparison between the new clock skew estimator **Eq. 3** with the clock skew estimator of Noh et al. [34] denoted here as the likelihood estimator. In addition, we have the simulated performance results for our new proposed expression for the MSE **Eq. 52** for the fGn case. $\alpha = 50 \text{ ppm}$, $Q = 5 \text{ ms}$, $T_{\text{syn}} = 15.6 \text{ ms}$ ($64 \frac{\text{packet}}{\text{sec}}$), $\sigma_{w_1} = \sigma_{w_2} = \sigma$, $d_{\text{ms}} = 5 \text{ ms}$, $d_{\text{sm}} = 5.5 \text{ ms}$, $H = 0.6$. The results were obtained for 100 Monte-Carlo trails.





on **Table 1**, we can use for the simulation performance comparison task also the recently proposed clock skew estimators proposed by Levy and Pinchas [2] and Chaloupka et al. [36]. But, as already was mentioned earlier in this paper, Levy and Pinchas [2] is based on the dual slave clocks in a slave presented by Chin and Chen [31] where Kim [37] demonstrated that the algorithm in Chin and Chen [31] is unusable in practical cases. The clock skew estimator proposed by Chaloupka et al. [36] depends on a predefined parameter L defining the sliding window's length in the algorithm which has an important role for reaching a low value for the MSE. But, this predefined parameter (L) depends also on the total number of sync periods available for the frequency synchronization task. In other words, the predefined parameter (L) can not be set too large, for example to a value of 1,000 if the available total number of sync periods is only 500. In addition, the noise measurement variance is estimated in Chaloupka et al. [36] involving two smoothing factors which must also be defined in advance.

According to Levy and Pinchas [2] we have:

$$\hat{\varepsilon} = \left(2 \sum_{i=1}^J \sum_{j=1}^J \sum_{k=1}^{\min(i,j)-1} [A_{\max}(J, i, j, k, H) (\Delta T_{s1,i} - \Delta T_{s2,i}) (\Delta T_{s1,j} - \Delta T_{s2,j})] \right) \left(\sum_{i=1}^J \sum_{j=1}^J \sum_{k=1}^{\min(i,j)-1} [A_{\max}(J, i, j, k, H) [\Delta T_{m,j} (\Delta T_{s1,i} - \Delta T_{s2,i}) + \Delta T_{m,i} (\Delta T_{s1,j} - \Delta T_{s2,j})]] \right)^{-1} - 1 \quad (89)$$

where $A_{\max}(J, i, j, k, H)$ is:

$$A_{\max}(J, i, j, k, H) = \left[\frac{\Gamma(J)}{\Gamma(-H+0.5)\Gamma(J-H+0.5)} \right]^2 (\Gamma(i-k-H+0.5) \Gamma(J-H+0.5-i+k) \Gamma(j-k-H+0.5) \Gamma(J-H+0.5-j+k)) \frac{(\Gamma(J-i+k) \Gamma(J-j+k) \Gamma(i-k) \Gamma(j-k))^{-1}}{\left[\frac{1}{(i-k)} \frac{1}{(j-k)} - \frac{1}{(J-i+k)} \frac{1}{(J-j+k)} \right]} \quad (90)$$

and $\hat{\varepsilon}$ is:

$$\hat{\varepsilon} = \frac{1}{\hat{\alpha} + 1} - 1 \quad (91)$$

$\Gamma(\cdot)$ denotes the Gamma function, Δ denotes the difference between two consecutive timestamps. $T_{m,i}$ is the timestamp in the i th period when the Master sends the Sync message. $T_{s1,i}$ is the timestamp in the i th period when the dual-Slave receives the Sync message. $T_{s2,i}$ is the timestamp in the i th period when the Slave receives the Sync message.

According to Chaloupka et al. [36] the Kalman's measurement equation is:

$$T_{1,j}(L) - T_{2,j}(L) = T_{2,j}(L) \alpha[j] + \Omega_{1,j}(L) \quad (92)$$

where L is the sliding window's length as defined in Chaloupka et al. [36].

The Kalman's state equation is:

$$\hat{\alpha}[j+1] = \hat{\alpha}[j] + u[j]. \quad (93)$$

where the variance of $u[j]$ is Q_{KAL} . The estimate of the noise measurement variance is given by Chaloupka et al. [36]:

$$\hat{R}[j] = (1 - \delta_\sigma) \hat{R}[j-1] + \delta_\sigma (x[j] - \hat{\mu}[j])^2 \quad (94)$$

where

$$\hat{\mu}[j] = (1 - \delta_\mu) \hat{\mu}[j-1] + \delta_\mu x[j]; \quad x[j] = T_{1,j}(L) - T_{2,j}(L) \quad (95)$$

δ_μ and δ_σ are smoothing factors which are between zero and one.

Figure 11 shows the performance comparison between our new proposed clock skew estimator **Eq. 3** with the clock skew estimator obtained from Noh et al. [34] and Levy and Pinchas [2] for the gfGn case. In addition, we also show in **Figure 11** the performance of our closed-form-approximated expression for the MSE **Eq. 77** compared to the simulated one. According to **Figure 11**, our new proposed clock skew estimator achieves a lower MSE compared to the clock skew estimators proposed by Noh et al. [34] and Levy and Pinchas [2].

Figure 12 shows the performance comparison between our new proposed clock skew estimator **Eq. 3** with the clock skew estimator obtained from Noh et al. [34] and Chaloupka et al. [36] for the fGn case. According to **Figure 12** our new proposed clock skew estimator achieves a lower MSE compared to the clock skew estimators proposed by Noh et al. [34] and Chaloupka et al. [36].

6 CONCLUSION

In this paper, we have developed a novel clock skew estimator (applicable for the PTP case) in the presence of asymmetric in the forward and reverse paths. This estimator does not depend on the unknown fixed paths nor on the clock offset between the Master and Slave. Our clock skew estimator does not need multiple Masters nor prior knowledge about the forward and the reverse paths. In addition, we proposed a closed-form approximated expression for the MSE related to our new proposed clock skew estimator. This closed-form approximated expression for the MSE is suitable for the white-Gaussian, fGn, or gfGn environment. Thus, the clock skew estimator and its performance (MSE) are applicable for the long-range dependence environment. It can be seen from the simulation results that the performance of our closed-form approximated expression for the MSE has a high correlation with the performance obtained via the new proposed clock skew estimator. This paper also supplies designing graphs for the system designer that may help the system designer to have approximately the total sent Sync messages to receive the system's requirement ($MSE = 10^{-12}$). For a requirement of MSE lower than 10^{-12} , new designing graphs can be easily obtained by **Eq. 86**. Thus, we have also a closed-form approximated expression **Eq. 86** that can help the system designer to figure out the total sent Sync messages needed to get the MSE of any value.

DATA AVAILABILITY STATEMENT

The original contributions presented in the study are included in the article/Supplementary Material, further inquiries can be directed to the corresponding author.

REFERENCES

- Pinchas M. Cooperative Multi PTP Slaves for Timing Improvement in an Fgn Environment. *IEEE Commun Lett* (2018) 22:1366–9. doi:10.1109/lcomm.2018.2830339
- Levy C, Pinchas M. Maximum Likelihood Estimation of Clock Skew in IEEE 1588 with Fractional Gaussian Noise. *Math Probl Eng* (2015) 2015:1–24. doi:10.1155/2015/174289
- Karthik AK, Blum RS. Estimation Theory-Based Robust Phase Offset Determination in Presence of Possible Path Asymmetries. *IEEE Trans Commun* (2018) 66:1624–35. doi:10.1109/tcomm.2017.2761879
- Guruswamy A, Blum RSR, Kishore S, Bordogna M. Minimax Optimum Estimators for Phase Synchronization in IEEE 1588. *IEEE Trans Commun* (2015) 63:3350–62. doi:10.1109/tcomm.2015.2455531
- Shan F, Yu J, Dong J, Chang X, Yu Z. In: Research on High-accuracy Clock Synchronization Based on IEEE 1588 Protocol; 19–20 Oct. 2019; Dalian, China (2019).
- Vyas A, Dwivedi S, Gunnarsson F (2018). Improved Precision Time Protocol with Relative Clock Phase Information. In 2018 IEEE International Symposium on Precision Clock Synchronization for Measurement, Control, and Communication (ISPCS). doi:10.1109/ispcs.2018.8543064
- Peng J, Zhang L, McLernon D. On the Clock Offset Estimation in an Improved IEEE 1588 Synchronization Scheme. In: European Wireless 2013; 19th European Wireless Conference (2013).
- [Dataset] Arnold D. In: 1588–2019 - IEEE Standard for a Precision Clock Synchronization Protocol for Networked Measurement and Control Systems. IEEE (2019). Available at: <https://standards.ieee.org/standard/1588-2019.html>.
- Fubin P, Yubol Y, Leil G, Liangliang S. The Accuracy of IEEE 1588 Time Synchronization Protocol and its Improvement. In: IEEE 12th International Conference on Electronic Measurement & Instruments (2015). p. 280–4. doi:10.1109/icemi.2015.7494173
- [Dataset] ITU-T Recommendation. G.8262 : Timing Characteristics of Synchronous Equipment Slave Clock (2018). Available at: <https://www.itu.int/rec/T-REC-G.8262> (Accessed October 8, 2020).
- [Dataset] ITU-T Recommendation. G.8261 : Timing and Synchronization Aspects in Packet Networks (2019). Available at: <https://www.itu.int/rec/T-REC-G.8261-201908-I/en> (Accessed November 26, 2020).
- Karthik AK, Blum RS. Robust Clock Skew and Offset Estimation for IEEE 1588 in the Presence of Unexpected Deterministic Path Delay Asymmetries. *Ieee Trans Commun* (2020) 68:5102–19. doi:10.1109/tcomm.2020.2991212
- Puttnies H, Danielisx P, Timmermann D. PTP-LP: Using Linear Programming to Increase the Delay Robustness of IEEE 1588 PTP. In: IEEE Global Communications Conference (2018). doi:10.1109/glocom.2018.8647777
- Karthik AK, Blum RS. Robust Phase Offset Estimation for IEEE 1588 PTP in Electrical Grid Networks. In: 2018 IEEE Power & Energy Society General Meeting (2018). doi:10.1109/pesgm.2018.8586488
- Karthik AK, Blum RS. Optimum Full Information, Unlimited Complexity, Invariant, and Minimax Clock Skew and Offset Estimators for IEEE 1588. *IEEE Trans Commun* (2019) 67:3264–637. doi:10.1109/tcomm.2019.2900317
- Guruswamy A, Blum RSR, Kishore S, Bordogna M. Performance Lower Bounds for Phase Offset Estimation in IEEE 1588 Synchronization. *IEEE Trans Commun* (2015) 63:243–53. doi:10.1109/tcomm.2014.2371028
- Sathis Kumar S, Kemparaj P (2019). Enhanced Algorithms for Clock Selection in a Packet Based Synchronization Method. In 2019 IEEE 9th Symposium on Computer Applications & Industrial Electronics (ISCAIE) .doi:10.1109/iscaie.2019.8743747
- Mizrahi T. Slave Diversity: Using Multiple Paths to Improve the Accuracy of Clock Synchronization Protocols. In: 2012 IEEE International Symposium on Precision Clock Synchronization for Measurement, Control and Communication Proceedings (2012). doi:10.1109/ISPCS.2012.6336621
- Mizrahi T, Moses Y. On the Behavior of Network Delay in the Cloud. In: 2016 IEEE Conference on Computer Communications Workshops (INFOCOM WKSHPS) (2016). doi:10.1109/infcomw.2016.7562201
- Li M, Lim SC. Modeling Network Traffic Using Generalized Cauchy Process. *Physica A: Stat Mech its Appl* (2008) 387:2584–94. doi:10.1016/j.physa.2008.01.026
- Peng J, Zhang L, McLernon D. Long-range Dependence and Heavy-Tail Modeling for Teletraffic Data. *IEEE Signal Process. Mag* (2002) 19: 14–27.
- Jusak J, Harris RJ. Study of Udp-Based Internet Traffic: Long-Range Dependence Characteristics. In: 2011 Australasian Telecommunication Networks and Applications Conference (ATNAC) (2011). doi:10.1109/ATNAC.2011.6096648
- Li M, Zhao W. On Bandlimitedness and Lag-Limitedness of Fractional Gaussian Noise. *Physica A: Stat Mech its Appl* (2013) 392:1955–61. doi:10.1016/j.physa.2012.12.035
- Paxson V. Fast, Approximate Synthesis of Fractional Gaussian Noise for Generating Self-Similar Network Traffic. *SIGCOMM Comput Commun Rev* (1997) 27:5–18. doi:10.1145/269790.269792
- Ledesma S, Liu D. Synthesis of Fractional Gaussian Noise Using Linear Approximation for Generating Self-Similar Network Traffic. *SIGCOMM Comput Commun Rev* (2000) 30:4–17. doi:10.1145/505680.505682
- Li M. Generalized Fractional Gaussian Noise and its Application to Traffic Modeling. *Physica A: Stat Mech its Appl* (2021) 579:126138. doi:10.1016/j.physa.2021.126138
- Li M. Modified Multifractional Gaussian Noise and its Application. *Physica Scripta* (2021) 96:125002. doi:10.1088/1402-4896/ac1c6f
- Li M. Multi-fractional Generalized Cauchy Process and its Application to Teletraffic. *Physica A* (2020) 550:123982. doi:10.1016/j.physa.2019.123982
- Mizrahi T. A Game Theoretic Analysis of Delay Attacks against Time Synchronization Protocols. In: 2012 IEEE International Symposium on Precision Clock Synchronization for Measurement, Control and Communication Proceedings (2012). doi:10.1109/ISPCS.2012.6336612
- Guruswamy A, Blum RS, Kishore S, Bordogna M. Performance Lower Bounds for Phase Offset Estimation in IEEE 1588 Synchronization. *IEEE Trans Commun* (2015) 63:243–53. doi:10.1109/tcomm.2014.2371028
- Wen-long Chin W-L, Sau-gee Chen S-G. IEEE 1588 Clock Synchronization Using Dual Slave Clocks in a Slave. *IEEE Commun Lett* (2009) 13:456–8. doi:10.1109/lcomm.2009.090308
- Chaudhari QM, Serpedin E, Qaraqe K. On Maximum Likelihood Estimation of Clock Offset and Skew Network with Exponential Delays. *IEEE Trans Signal Process* (2008) 56:1685–97. doi:10.1109/tsp.2007.910536
- Li J, Jeske DR. Maximum Likelihood Estimators of Clock Offset and Skew under Exponential Delays. *Appl Stochastic Models Bus Ind* (2009) 25:445–59. doi:10.1002/asmb.777
- Noh K-L, Chaudhari QM, Serpedin E, Suter BW. Novel Clock Phase Offset and Skew Estimation Using Two-Way Timing Message Exchanges for Wireless Sensor Networks. *IEEE Trans Commun* (2007) 55:766–77. doi:10.1109/TCOMM.2007.894102
- Giorgi G, Narduzzi C. Performance Analysis of Kalman-Filter-Based Clock Synchronization in IEEE 1588 Networks. *IEEE Trans Instrum Meas* (2011) 60: 2902–9. doi:10.1109/tim.2011.2113120

AUTHOR CONTRIBUTIONS

All authors listed have made a substantial, direct, and intellectual contribution to the work and approved it for publication.

36. Chaloupka Z, Alsindi N, Aweya J. Clock Skew Estimation Using Kalman Filter and IEEE 1588v2 PTP for Telecom Networks. *IEEE Commun Lett* (2015) 19:1181–4. doi:10.1109/lcomm.2015.2427158
37. Kim KS. Comments on “IEEE 1588 Clock Synchronization Using Dual Slave Clocks in a Slave”. *IEEE Commun Lett* (2014) 18:981–2. doi:10.1109/lcomm.2014.2317738
38. Spiegel MR, Lipschutz S, Liu J. *Mathematical Handbook of Formulas and Tables*. New York: McGraw Hill Education (2009).

Conflict of Interest: The authors declare that the research was conducted in the absence of any commercial or financial relationships that could be construed as a potential conflict of interest.

Publisher’s Note: All claims expressed in this article are solely those of the authors and do not necessarily represent those of their affiliated organizations, or those of the publisher, the editors and the reviewers. Any product that may be evaluated in this article, or claim that may be made by its manufacturer, is not guaranteed or endorsed by the publisher.

Copyright © 2021 Avraham and Pinchas. This is an open-access article distributed under the terms of the Creative Commons Attribution License (CC BY). The use, distribution or reproduction in other forums is permitted, provided the original author(s) and the copyright owner(s) are credited and that the original publication in this journal is cited, in accordance with accepted academic practice. No use, distribution or reproduction is permitted which does not comply with these terms.



Confidence Regions for Parameters in Stationary Time Series Models With Gaussian Noise

Xiuzhen Zhang^{1,2}, Riquan Zhang¹ and Zhiping Lu^{1*}

¹Key Laboratory of Advanced Theory and Application in Statistics and Data Science, MOE, School of Statistics, East China Normal University, Shanghai, China, ²School of Mathematics and Statistics, Shanxi Datong University, Datong, China

This article develops two new empirical likelihood methods for long-memory time series models based on adjusted empirical likelihood and mean empirical likelihood. By application of Whittle likelihood, one obtains a score function that can be viewed as the estimating equation of the parameters of the long-memory time series model. An empirical likelihood ratio is obtained which is shown to be asymptotically chi-square distributed. It can be used to construct confidence regions. By adding pseudo samples, we simultaneously eliminate the non-definition of the original empirical likelihood and enhance the coverage probability. Finite sample properties of the empirical likelihood confidence regions are explored through Monte Carlo simulation, and some real data applications are carried out.

OPEN ACCESS

Edited by:

Ming Li,
Zhejiang University, China

Reviewed by:

Fukang Zhu,
Jilin University, China
Wang Dehui,
Liaoning University, China

*Correspondence:

Zhiping Lu
zplu@sfs.ecnu.edu.cn

Specialty section:

This article was submitted to
Interdisciplinary Physics,
a section of the journal
Frontiers in Physics

Received: 25 October 2021

Accepted: 17 November 2021

Published: 07 January 2022

Citation:

Zhang X, Zhang R and Lu Z (2022)
Confidence Regions for Parameters in
Stationary Time Series Models With
Gaussian Noise.
Front. Phys. 9:801692.
doi: 10.3389/fphy.2021.801692

Keywords: confidence region, adjusted empirical likelihood, mean empirical likelihood, stationary time series, long memory

1 INTRODUCTION

The empirical likelihood (EL) method is originally designed to construct a confidence region only for independent data [1,2]. Nowadays, it is quite popular in the statistical inference of time series, (dependent data) thanks to the asymptotical independent property of the periodogram ordinates, see [3], [4], and [5]. EL received considerable **attention** because of its nice statistic properties. For example, it runs a low risk of a misspecified probability model by setting up a semi-parametric moment model; it is easy to construct a confidence region or interval under the chi-square approximation; there is no need to calculate the covariance estimates when it is used to construct confidence regions; and the shape of confidence region that is naturally driven by data.

In spite of nice properties of EL, it still does not work well for the case of small sample or high-dimensional data. Its main drawback is the large coverage error of the corresponding confidence region. One reason for the under-coverage is that the original EL ratio poorly approximates to the chi-square limiting distribution. This under-coverage issue can be alleviated to some extent by the Bartlett correction [6]. Another reason for the under-coverage is the non-definition problem of the EL ratio. When the sample size is small, the definition of the original EL ratio often does not exist. [7] proposed adjusted EL by adding pseudo points to ensure the original convex hull lie on the opposite of the origin, which not only eliminates the non-definition but also improves the accuracy of approximation with the conventional level of adjustment. [8] put forward the optimal adjustment level to improve the chi-square approximation with a high-order precision, but the problem is not solved. Afterward, [9] derived an adjustment factor from the Bartlett correction and proved by adding two pseudo observations; the new adjusted EL (AEL) has the same order of chi-square approximation as the Bartlett correction. Many research studies about choosing an optimal adjustment factor arose, such as [10], [11], [12], and [13]. In practice, when the dimension of the unknown parameter is large, it is difficult to calculate the Bartlett correction factor. Recently, the mean EL

TABLE 1 | Coverage probabilities (average length) of confidence intervals of $\theta = 0.2$ in MA (1).

| Level | T | EL | AEL | MEL | AEL* |
|-------|-----|---------------|---------------|---------------|---------------|
| | | CP(AL) | CP(AL) | CP(AL) | CP(AL) |
| 0.90 | 60 | 0.857 (0.428) | 0.884 (0.463) | 0.874 (0.452) | 0.895 (0.963) |
| | 100 | 0.866 (0.324) | 0.883 (0.339) | 0.878 (0.334) | 0.887 (0.607) |
| | 200 | 0.885 (0.227) | 0.893 (0.233) | 0.892 (0.231) | 0.896 (0.306) |
| 0.95 | 60 | 0.921 (0.520) | 0.938 (0.578) | 0.937 (0.560) | 0.946 (1.382) |
| | 100 | 0.928 (0.389) | 0.941 (0.409) | 0.939 (0.407) | 0.944 (0.874) |
| | 200 | 0.934 (0.271) | 0.940 (0.279) | 0.940 (0.279) | 0.942 (0.407) |
| 0.99 | 60 | 0.975 (0.715) | 0.987 (1.068) | 0.987 (0.806) | 0.988 (2.440) |
| | 100 | 0.981 (0.522) | 0.987 (0.561) | 0.989 (0.566) | 0.988 (1.652) |
| | 200 | 0.983 (0.359) | 0.986 (0.369) | 0.987 (0.376) | 0.987 (0.733) |

(MEL) was proposed to improve the precision of the EL-based confidence regions by constructing a new pseudo data point [14]. By greatly increasing the sample size, the MEL method leads to a more accurate chi-square approximation. Hence, the corresponding coverage error is reduced, and the coverage probability is enhanced.

For time series, EL inherits the undesirable problem of under-coverage. To the best of our knowledge, there have been some works applying AEL on the improvement of the precision of the EL-based confidence region, such as [15] and [16]. But under their proposed conventional adjustment level $\alpha = \max(1, \log(n)/2)$, the precision of chi-square approximation distribution of AEL is not obviously enhanced. In this article, we propose another adjustment level to construct new AEL for the parameters in stationary short- and long-memory time series models with Gaussian noise. Following the Liu & Chen's method, our proposed AEL possesses a high-order approximation to chi-square distribution by adding two pseudo observations. We also propose the MEL method for estimating the parameters of stationary time series models. By increasing the sample size, the MEL does enhance the confidence precision. The Monte Carlo simulation results indicate that our proposed AEL-based confidence regions benefit more accurate coverage probabilities than those of the original EL and the previous AEL. When the sample size is moderate, the coverage probability based on MEL is comparable to the previous AEL. There is no need to compute the Bartlett correction factor for MEL, which is a challenge when the dimension of the parameter vector is large.

The remainder of this article is organized as follows; in **Section 2**, we present the proposed AEL and MEL ratio statistics for parameters in stationary ARMA and ARFIMA processes and deduce their asymptotical chi-square properties. Monte Carlo simulation results are provided in **Section 3** to show the improved finite-sample performance of our methods. Real data examples are presented in **Section 4**. **Section 5** is the brief proof of the theorem.

2 METHODOLOGY

In this section, we derive the asymptotical chi-square properties of the new AEL and MEL ratio statistics for the parameters in

representative stationary short- and long-memory models, that is, ARMA and ARFIMA models. We begin with introducing the moment-estimating equations of parameters in these models.

2.1 Estimating Equations

Suppose, we have a time series $\{X_t\}_{t=1,\dots,T}$ satisfying the relationship

$$\Phi(B)(I-B)^d X_t = \Theta(B)\epsilon_t, t \in \mathbb{Z}, d \in [0, 0.5),$$

where $\Phi(B) = \sum_{i=0}^p \phi_i B^i$ and $\Theta(B) = \sum_{i=0}^q \theta_i B^i$ with $\phi_0 = \theta_0 = -1$ and B is the backward operator. The two polynomials have no common factor to avoid the parameter redundancy. All roots of their corresponding equations strictly lie out of the unit circle to make sure that the model is stationary and invertible, which is the most important setup for many time series studies. d is the constant memory parameter and ϵ_t is a Gaussian white noise with mean 0 and variance σ^2 . Then, when $d = 0$, it is the popular ARMA (p,q) (short-memory) model. When $d \in (0, 0.5)$, it is the widely used ARFIMA (p,d,q) (long-memory) model [17]. σ^2 is often considered as a nuisance parameter. Then, $\beta = (\phi_1, \dots, \phi_p, d, \theta_1, \dots, \theta_q)$ is the parameter vector of our interest with the dimension $m = p + q + 1$. Many important literatures come up with the application of the fractional long-memory model ([18], [19], and [20]).

By taking the derivative of Whittle likelihood [21], the estimating equations are derived as

$$\sum_{i=1}^N \psi_i(I(\omega_i), \beta) = \sum_{i=1}^N \left(\frac{I(\omega_i)}{f_i(\beta)} - 1 \right) \frac{\partial \ln\{f_i(\beta)\}}{\partial \beta} = 0,$$

where $N = [(T-1)/2]$ and $[x]$ is the integer part of x . The periodogram ordinates are denoted as

$$I(\omega_i) = \left\{ \left[\sum_{t=1}^T x_t \sin(\omega_i t) \right]^2 + \left[\sum_{t=1}^T x_t \cos(\omega_i t) \right]^2 \right\} / 2\pi T,$$

$$\omega_i = 2\pi i/T, i = 1, \dots, N,$$

and the spectral density function is

$$f_i(\beta) = \frac{\sigma^2}{2\pi} |1 - e^{-i\omega_i}|^{-2d} \frac{|\Theta(e^{-i\omega_i})|^2}{|\Phi(e^{-i\omega_i})|^2}.$$

2.2 AEL of β

It is well known that when the origin lies out of certain convex constraints $\Omega_\beta = \{\psi_i(I(\omega_i), \beta), i = 1, \dots, N\}$ involving the computation of EL, the solution of the optimization problem does not exist, which results in the no definition of EL and the under-coverage of the corresponding confidence region. In this section, we propose a new AEL in time series to ensure the well definedness of AEL and improvement of the coverage probability of confidence regions.

For simplicity, denote $\psi_i := \psi_i(I(\omega_i), \beta)$. Based on the original sample set $\Omega_\beta = \{\psi_i, i = 1, \dots, N\}$, for a given β , the empirical log-likelihood ratio is defined as

$$R(\beta) = -2 \sup \left\{ \sum_{i=1}^N \ln N p_i, p_i > 0, \sum_{i=1}^N p_i = 1, \sum_{i=1}^N p_i \psi_i = 0 \right\}.$$

TABLE 2 | Coverage probabilities of confidence intervals of d in ARFIMA (0,d,0).

| Level | T | EL | AEL | MEL | AEL * | EL | AEL | MEL | AEL * |
|-------|-----|----|-----|-----|-----------|-------|-------|-------|----------|
| 0.90 | | | | | $d = 0.1$ | | | | |
| | | | | | $d = 0.2$ | | | | |
| | | | | | 20 | 0.796 | 0.875 | 0.840 | 0.899 |
| | | | | | 30 | 0.815 | 0.874 | 0.850 | 0.905 |
| | | | | | 50 | 0.838 | 0.874 | 0.862 | 0.898 |
| | | | | | 100 | 0.848 | 0.866 | 0.859 | 0.889 |
| | | | | | $d = 0.3$ | | | | |
| | | | | | $d = 0.4$ | | | | |
| | | | | | 20 | 0.800 | 0.885 | 0.843 | 0.908 |
| | | | | | 30 | 0.813 | 0.865 | 0.843 | 0.905 |
| | | | | | 50 | 0.827 | 0.862 | 0.848 | 0.895 |
| | | | | | 100 | 0.848 | 0.866 | 0.859 | 0.891 |
| 0.95 | | | | | $d = 0.1$ | | | | |
| | | | | | $d = 0.2$ | | | | |
| | | | | | 20 | 0.868 | 0.953 | 0.951 | 0.948 |
| | | | | | 30 | 0.889 | 0.935 | 0.923 | 0.950 |
| | | | | | 50 | 0.899 | 0.929 | 0.920 | 0.944 |
| | | | | | 100 | 0.909 | 0.922 | 0.921 | 0.935 |
| | | | | | $d = 0.3$ | | | | |
| | | | | | $d = 0.4$ | | | | |
| | | | | | 20 | 0.860 | 0.954 | 0.949 | 0.947 |
| | | | | | 30 | 0.880 | 0.930 | 0.922 | 0.948 |
| | | | | | 50 | 0.898 | 0.926 | 0.919 | 0.944 |
| | | | | | 100 | 0.907 | 0.920 | 0.918 | 0.937 |
| 0.99 | | | | | $d = 0.1$ | | | | |
| | | | | | $d = 0.2$ | | | | |
| | | | | | 20 | 0.932 | 1 | 0.954 | 0.978 |
| | | | | | 30 | 0.956 | 0.991 | 0.975 | 0.984 |
| | | | | | 50 | 0.968 | 0.986 | 0.983 | 0.990 |
| | | | | | 100 | 0.974 | 0.981 | 0.982 | 0.985 |
| | | | | | $d = 0.3$ | | | | |
| | | | | | $d = 0.4$ | | | | |
| | | | | | 20 | 0.931 | 1 | 0.956 | 0.976 |
| | | | | | 30 | 0.955 | 0.991 | 0.972 | 0.986 |
| | | | | | 50 | 0.972 | 0.984 | 0.983 | 0.989 |
| | | | | | 100 | 0.972 | 0.980 | 0.980 | 0.983 |

TABLE 3 | Coverage probabilities of 95% confidence intervals of ϕ in AR (1).

| T | EL | AEL | MEL | AEL * | EL | AEL | MEL | AEL * |
|--------------|-------|-------|-------|----------|--------------|-------|-------|----------|
| $\phi = 0.2$ | | | | | $\phi = 0.5$ | | | |
| 20 | 0.876 | 0.953 | 0.913 | 0.950 | 0.874 | 0.926 | 0.906 | 0.936 |
| 30 | 0.900 | 0.943 | 0.927 | 0.956 | 0.876 | 0.928 | 0.910 | 0.934 |
| 50 | 0.913 | 0.936 | 0.932 | 0.946 | 0.903 | 0.929 | 0.921 | 0.936 |
| 100 | 0.927 | 0.939 | 0.937 | 0.943 | 0.910 | 0.925 | 0.920 | 0.930 |
| 200 | 0.941 | 0.947 | 0.948 | 0.948 | 0.920 | 0.928 | 0.929 | 0.934 |
| $\phi = 0.7$ | | | | | $\phi = 0.9$ | | | |
| 20 | 0.841 | 0.938 | 0.881 | 0.933 | 0.788 | 0.889 | 0.838 | 0.900 |
| 30 | 0.862 | 0.919 | 0.890 | 0.937 | 0.815 | 0.874 | 0.845 | 0.883 |
| 50 | 0.865 | 0.904 | 0.888 | 0.922 | 0.813 | 0.857 | 0.838 | 0.897 |
| 100 | 0.893 | 0.911 | 0.905 | 0.921 | 0.809 | 0.835 | 0.829 | 0.913 |
| 200 | 0.908 | 0.916 | 0.918 | 0.922 | 0.828 | 0.840 | 0.840 | 0.889 |

TABLE 4 | Coverage probabilities of 95% confidence regions of (ϕ_1, ϕ_2) in AR (2).

| (ϕ_1, ϕ_2) | EL | AEL | MEL | AEL | EL | AEL | MEL | AEL |
|--------------------|-------|-------|-------|-----------|-------|-------|-------|-------|
| $T = 20$ | | | | $T = 30$ | | | | |
| (0.3.0.2) | 0.743 | 0.816 | 0.810 | 0.871 | 0.830 | 0.869 | 0.887 | 0.933 |
| (0.1.0.7) | 0.649 | 0.753 | 0.725 | 0.856 | 0.724 | 0.782 | 0.785 | 0.906 |
| (0.7.0.2) | 0.639 | 0.723 | 0.718 | 0.840 | 0.759 | 0.799 | 0.819 | 0.918 |
| (0.4.0.5) | 0.629 | 0.714 | 0.702 | 0.849 | 0.711 | 0.760 | 0.779 | 0.900 |
| $T = 50$ | | | | $T = 100$ | | | | |
| (0.3.0.2) | 0.860 | 0.882 | 0.900 | 0.948 | 0.879 | 0.892 | 0.903 | 0.928 |
| (0.1.0.7) | 0.770 | 0.803 | 0.819 | 0.929 | 0.787 | 0.807 | 0.817 | 0.936 |
| (0.7.0.2) | 0.802 | 0.829 | 0.851 | 0.920 | 0.825 | 0.839 | 0.846 | 0.933 |
| (0.4.0.5) | 0.785 | 0.819 | 0.830 | 0.910 | 0.799 | 0.817 | 0.830 | 0.925 |

If the origin contains in the convex set Ω_β , by a simple Lagrange multiplier calculation, $p_i = 1/(1 + \lambda_\beta^\tau \psi_i)$ and the Lagrange multiplier λ_β is the solution to $\sum_{i=1}^N \psi_i / (1 + \lambda^\tau \psi_i) = 0$. Therefore, the level of the $1 - \alpha$ confidence region is constructed as

$$\{\beta: R(\beta) \leq \chi_{m,1-\alpha}^2\},$$

where $\chi_{m,1-\alpha}^2$ is the $1 - \alpha$ quantile of chi-square distribution with the degree m of freedom. Such EL-based confidence regions often suffer from the problem of under-coverage.

To overcome such drawback, we propose a new AEL following the Liu & Chen's method. By adding two pseudo observations, the AEL not only guarantees the likelihood ratio to be always well defined but also obviously improves the coverage probability of the confidence region in stationary time series. Set the two pseudo observations $\psi_{N+1} = -a_1 \bar{\psi}$ and $\psi_{N+2} = a_2 \bar{\psi}$, where a_1, a_2 are positive and $\bar{\psi} = (\sum_{i=1}^N \psi_i)/N$. Then, for each given β , the new AEL ratio statistic is defined as

$$R^A(\beta) = -2 \sup \left\{ \sum_{i=1}^{N+2} \ln(N+2)p_i, p_i > 0, \sum_{i=1}^{N+2} p_i = 1, \sum_{i=1}^{N+2} p_i \psi_i = 0 \right\}.$$

By the Lagrange method, we have

$$R^A(\beta) = 2 \sum_{i=1}^{N+2} \ln(1 + (\lambda_\beta^*)^\tau \psi_i), \quad (1)$$

where the Lagrange multiplier λ_β^* satisfies the equation

$$\sum_{i=1}^{N+2} \frac{\psi_i}{1 + \lambda_\beta^{*\tau} \psi_i} = 0. \quad (2)$$

[22] proved such AEL ratio statistic $R^A(\beta_0)$ approximated to chi-square distribution with order $O(n^{-2})$ for the independent sample when β_0 is the true value. Here, we assert that such result is preserved for the stationary time series model as the following theorem:

Theorem 2.1. Assume the characteristic function of ψ satisfies Cramér's condition,

$$\limsup_{\|\psi\| \rightarrow \infty} |E \exp\{it^T \psi\}| < 1.$$

Also $E\|\psi\|^{18} < \infty$ and $\text{var}(\psi)$ are positive definites. If β_0 is the true value, then

$$Pr(R^A(\beta_0) \leq x) = Pr(\chi_m^2 \leq x) + O_p(n^{-2}). \quad (3)$$

Consequently, the $1 - \alpha$ confidence region for β based on AEL is constructed as

$$\{\beta: R^A(\beta) \leq \chi_{m,1-\alpha}^2\},$$

whose coverage error is $O(n^{-2})$.

Remark 1. The proof of Theorem 2.1 is similar to that of Theorem 1 in [22], hence is omitted. The two positive adjustment factors a_1 and a_2 are also obtained following the way of [22]. That is, a_1 and a_2 originate from the Bartlett correction factor. It is the intrinsic relationship between the new AEL and the Bartlett-corrected EL that makes the precision of approximation to enhance obviously. In practice, a_1 and a_2 are replaced by their moment estimators, which do not affect the order of chi-square approximation. For more details, refer to [22].

2.3 MEL of β

When the dimension of the parameter vector $m \geq 3$, it is difficult to compute the Bartlett correction factor. To avoid the computation and to resolve the under-coverage problem, we derive the MEL method in this subsection. By greatly increasing the sample size, MEL is constructed on the pseudo sample set $\tilde{\Omega}_\beta = \{(\psi_i + \psi_j)/2; 1 \leq i \leq j \leq N\}$. For simplicity, we denote $\tilde{\Omega}_\beta = \{g_1, \dots, g_K\}$ with $g_k := (\psi_i + \psi_j)/2$ and $K = N(N+1)/2$.

Then, the MEL ratio for given β is defined as

$$R^M(\beta) = -2 \sup \left\{ \sum_{k=1}^K \log(K p_k): p_k \geq 0, \sum_{k=1}^K p_k = 1, \sum_{k=1}^K p_k g_k = 0 \right\}.$$

By a simple Lagrange calculation, we have

$$R^M(\beta) = 2 \sum_{k=1}^K \ln(1 + (\lambda_\beta^*)^\tau g_k) / (N+1), \quad (4)$$

TABLE 5 | Coverage probabilities of 95% confidence regions of (θ, ϕ) in ARMA (1,1).

| (θ, ϕ) | EL | AEL | MEL | AEL* | EL | AEL | MEL | AEL* |
|------------------|-------|-------|-------|-----------|-------|-------|-------|-------|
| $T = 20$ | | | | $T = 30$ | | | | |
| (0.1.0.2) | 0.761 | 0.825 | 0.825 | 0.914 | 0.844 | 0.879 | 0.894 | 0.957 |
| (0.1.0.7) | 0.736 | 0.803 | 0.798 | 0.890 | 0.802 | 0.840 | 0.856 | 0.941 |
| (0.6.0.2) | 0.732 | 0.802 | 0.792 | 0.878 | 0.808 | 0.851 | 0.867 | 0.947 |
| (0.5.0.7) | 0.708 | 0.789 | 0.779 | 0.882 | 0.728 | 0.823 | 0.840 | 0.938 |
| $T = 50$ | | | | $T = 100$ | | | | |
| (0.1.0.2) | 0.876 | 0.900 | 0.918 | 0.951 | 0.904 | 0.914 | 0.927 | 0.942 |
| (0.1.0.7) | 0.847 | 0.872 | 0.890 | 0.945 | 0.880 | 0.896 | 0.903 | 0.929 |
| (0.6.0.2) | 0.852 | 0.878 | 0.898 | 0.955 | 0.887 | 0.895 | 0.907 | 0.933 |
| (0.5.0.7) | 0.834 | 0.859 | 0.873 | 0.951 | 0.866 | 0.881 | 0.892 | 0.934 |

TABLE 6 | Coverage probabilities of 95% confidence regions of (d, θ) in ARFIMA (0,d,1).

| (d, θ) | EL | AEL | MEL | AEL* | EL | AEL | MEL | AEL* |
|---------------|-------|-------|-------|-----------|-------|-------|-------|-------|
| $T = 20$ | | | | $T = 30$ | | | | |
| (0.1.0.3) | 0.653 | 0.727 | 0.707 | 0.865 | 0.801 | 0.838 | 0.856 | 0.930 |
| (0.2.0.7) | 0.718 | 0.797 | 0.785 | 0.857 | 0.793 | 0.843 | 0.853 | 0.925 |
| (0.3.0.4) | 0.624 | 0.703 | 0.681 | 0.874 | 0.733 | 0.789 | 0.792 | 0.919 |
| (0.4.0.7) | 0.724 | 0.799 | 0.787 | 0.866 | 0.795 | 0.844 | 0.858 | 0.922 |
| (0.4.0.1) | 0.738 | 0.799 | 0.796 | 0.884 | 0.817 | 0.856 | 0.876 | 0.941 |
| $T = 50$ | | | | $T = 100$ | | | | |
| (0.1.0.3) | 0.837 | 0.862 | 0.880 | 0.954 | 0.868 | 0.875 | 0.886 | 0.946 |
| (0.2.0.7) | 0.832 | 0.858 | 0.875 | 0.948 | 0.875 | 0.886 | 0.897 | 0.942 |
| (0.3.0.4) | 0.818 | 0.844 | 0.860 | 0.953 | 0.846 | 0.859 | 0.871 | 0.954 |
| (0.4.0.7) | 0.846 | 0.862 | 0.879 | 0.949 | 0.874 | 0.885 | 0.895 | 0.941 |
| (0.4.0.1) | 0.853 | 0.876 | 0.893 | 0.953 | 0.874 | 0.887 | 0.898 | 0.938 |

TABLE 7 | Coverage probabilities of 95% confidence regions of (ϕ, d) in ARFIMA (1,d,0).

| (ϕ, d) | EL | AEL | MEL | AEL* | EL | AEL | MEL | AEL* |
|-------------|-------|-------|-------|-----------|-------|-------|-------|-------|
| $T = 20$ | | | | $T = 30$ | | | | |
| (0.3.0.1) | 0.667 | 0.739 | 0.726 | 0.875 | 0.793 | 0.833 | 0.851 | 0.928 |
| (0.7.0.2) | 0.696 | 0.780 | 0.767 | 0.879 | 0.770 | 0.821 | 0.832 | 0.933 |
| (0.4.0.3) | 0.616 | 0.700 | 0.679 | 0.882 | 0.720 | 0.769 | 0.774 | 0.917 |
| (0.6.0.4) | 0.692 | 0.791 | 0.771 | 0.896 | 0.748 | 0.808 | 0.822 | 0.925 |
| (0.1.0.4) | 0.740 | 0.807 | 0.806 | 0.889 | 0.799 | 0.841 | 0.857 | 0.942 |
| $T = 50$ | | | | $T = 100$ | | | | |
| (0.3.0.1) | 0.842 | 0.867 | 0.887 | 0.953 | 0.858 | 0.872 | 0.882 | 0.941 |
| (0.7.0.2) | 0.825 | 0.850 | 0.866 | 0.931 | 0.856 | 0.872 | 0.885 | 0.941 |
| (0.4.0.3) | 0.818 | 0.846 | 0.862 | 0.949 | 0.839 | 0.854 | 0.864 | 0.944 |
| (0.6.0.4) | 0.796 | 0.825 | 0.845 | 0.930 | 0.843 | 0.856 | 0.868 | 0.942 |
| (0.1.0.4) | 0.857 | 0.882 | 0.899 | 0.955 | 0.866 | 0.881 | 0.891 | 0.940 |

and the Lagrange multiplier λ_{β}^{**} is the solution to

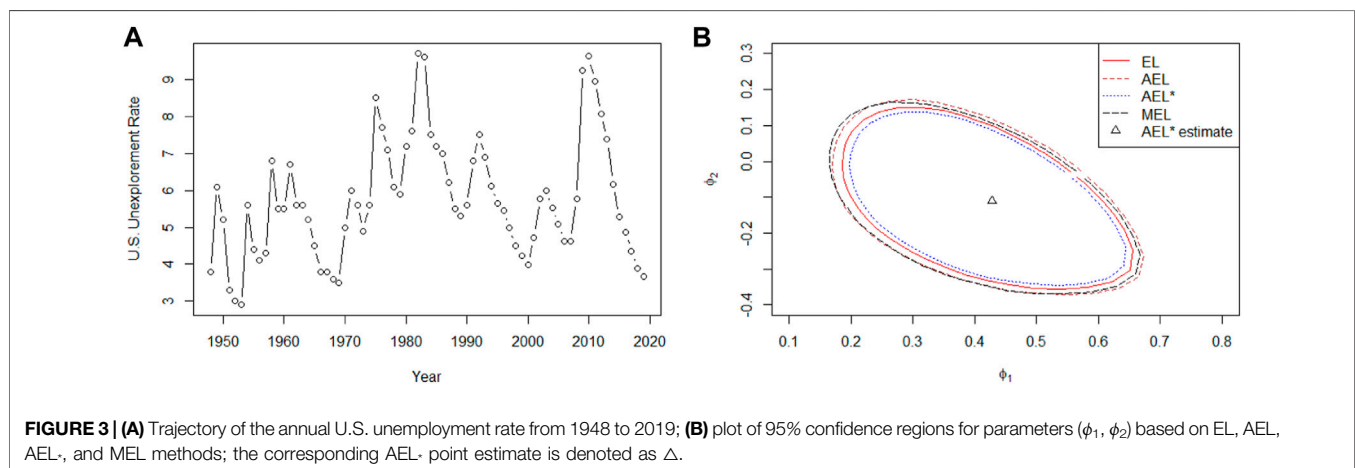
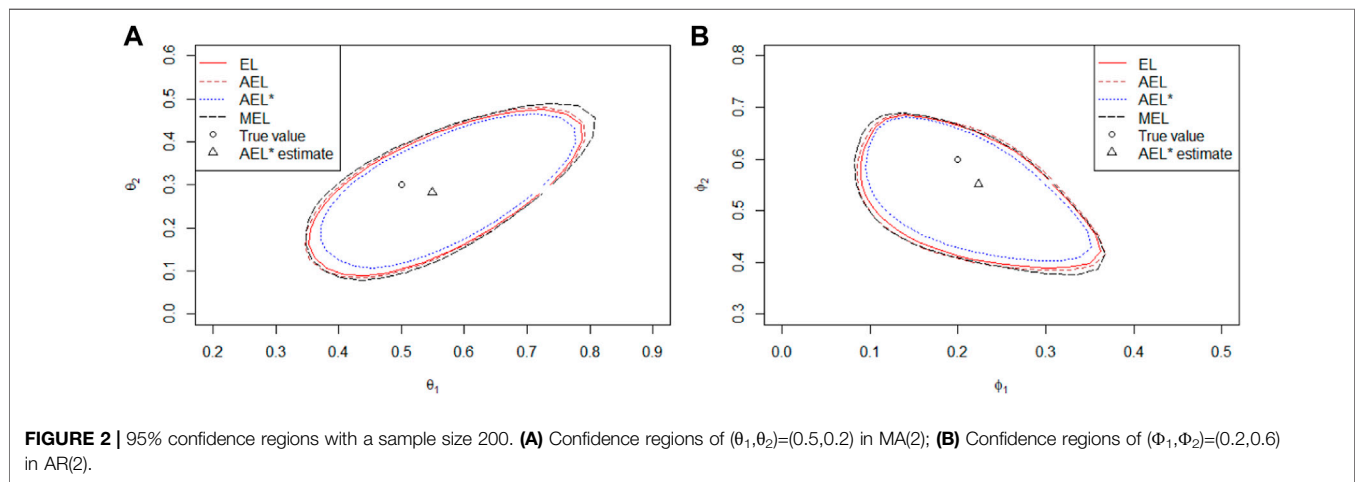
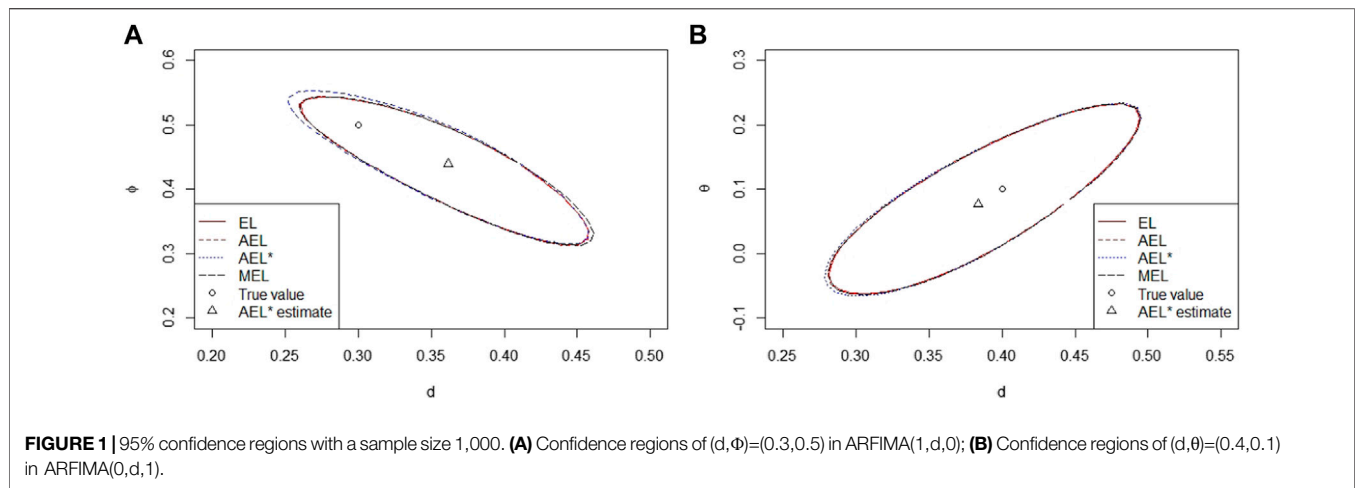
$$\sum_{k=1}^K \frac{g_k}{1 + \lambda^{\tau} g_k} = 0. \quad (5)$$

Theorem 2.2. Under the assumptions of A1–A4 [4], if β_0 is the true value, $R^M(\beta_0) \rightarrow \chi_m^2$ in distribution as $n \rightarrow \infty$.

Consequently, the MEL-based confidence region for β of level $1 - \alpha$ is

$$\{\beta: R^M(\beta) \leq \chi_m^2(1 - \alpha)\}.$$

In the next section, we will verify the accurate coverage probability of the confidence region under the finite sample by simulation study for different versions of EL.



3 SIMULATION

To investigate the finite-sample performance of our proposed AEL (the notation of our proposed AEL in the

following statements) and MEL, we carry out extensive Monte Carlo simulation studies of the ARMA (p, q) and ARFIMA (p, d, q) models in this section. **To emphasize that our proposed adjustment level is better than the**

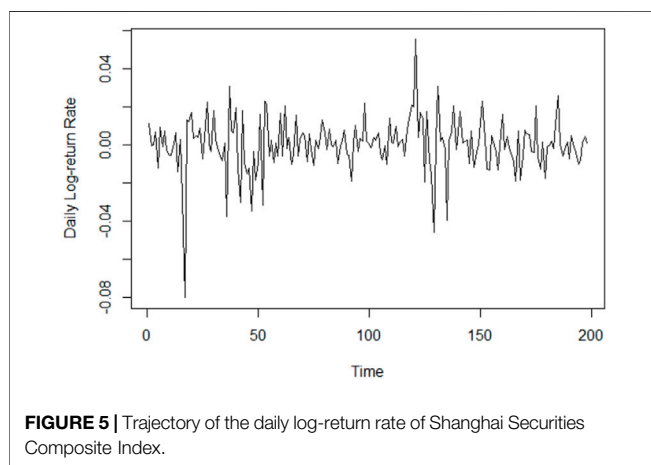
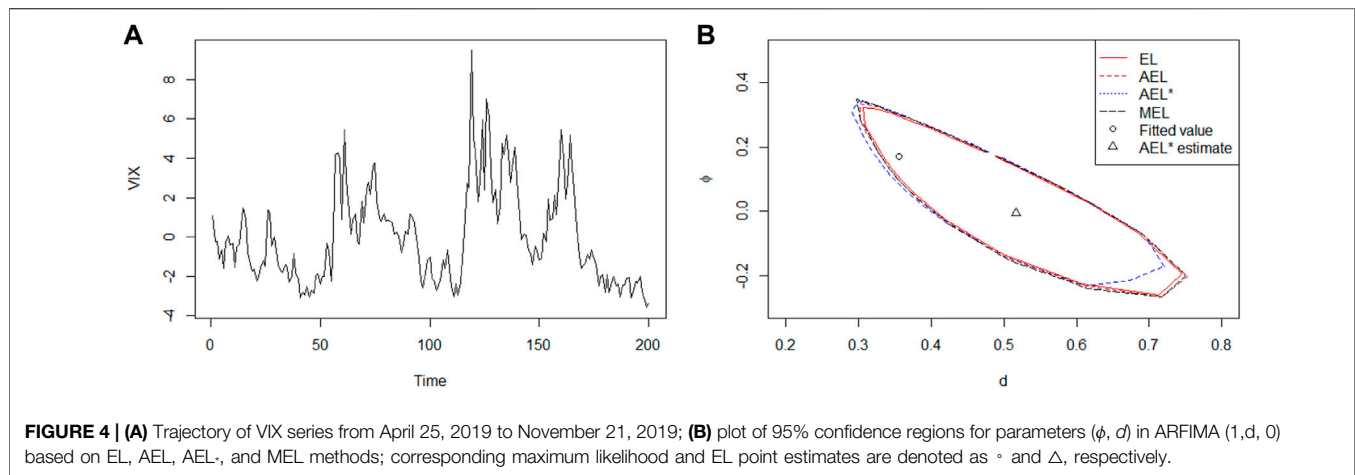


TABLE 8 | Point estimates and the length of 95% confidence interval of the Shanghai Securities Composite Index by fitting it as an ARFIMA (0,d,0) model.

| \hat{d} | \hat{d}_E | EL | AEL | MEL | AEL* |
|-----------|-------------|--------|--------|--------|--------|
| 0.0646 | 0.0306 | 5.3457 | 5.3822 | 6.0126 | 5.1740 |

conventional adjustment level $a = \max\{\log(N)/2, 1\}$ of AEL of [15] and [16], we also studied the unadjusted EL and their AEL. Furthermore, we studied the confidence region graphically.

| Parameter | Estimator |
|---|---|
| α^{rr} | $n\hat{\alpha}^{rr}/(n-1)$ |
| α^{st} | $n\hat{\alpha}^{st}/(n-3)$ |
| α^{rss} | $(n\hat{\alpha}^{rss} - 2\hat{\alpha}^{rr}\hat{\alpha}^{ss} - 4I(r=s)\hat{\alpha}^{rr}\hat{\alpha}^{rr})/(n-4)$ |
| $\alpha^{rr}\hat{\alpha}^{ss}$ | $\hat{\alpha}^{rr}\hat{\alpha}^{ss} - \hat{\alpha}^{rss}/n$ |
| $\alpha^{st}\hat{\alpha}^{st}$ | $\hat{\alpha}^{st}\hat{\alpha}^{st} - (\hat{\alpha}^{rssst} - \hat{\alpha}^{rst}\hat{\alpha}^{st})/n$ |
| $\alpha^{rr}\hat{\alpha}^{ss}\hat{\alpha}^{tt}$ | $\hat{\alpha}^{rr}\hat{\alpha}^{ss}\hat{\alpha}^{tt}$ |

3.1. Simulation Setup

We consider several ARMA (p,q) and ARFIMA (p,d,q) processes with different sample sizes and Gaussian noise with zero mean. In each case, 5,000 replications are generated to compute the coverage probability. **Nominal levels** are set to be $1 - \alpha = 0.90, 0.95, 0.99$, respectively. It is notable that although the series length is T , the sample size we use is only $N = [(T-1)/2]$. In the simulations, we use the consistent estimators \hat{a}_1 and \hat{a}_2 to replace the adjustment factors a_1 and a_2 , respectively. The computations \hat{a}_1 and \hat{a}_2 are completely similar to those of Section 3.3 in [22]. When the dimension of the parameter $m = 1$, we only add one pseudo observation with the adjustment level $\hat{a} = \hat{a}_1 - \hat{a}_2$. **Specifically,**

$$a_1 = \frac{1}{2m} \sum_r \left\{ \frac{\alpha^{rrrr}}{2(\alpha^{rr})^2} - \frac{(\alpha^{rrr})^2}{3(\alpha^{rr})^3} \right\} + \frac{1}{2m} \sum_{r < s} \left\{ \frac{\alpha^{rrss}}{\alpha^{rr}\alpha^{ss}} - \frac{(\alpha^{rss})^2}{\alpha^{rr}(\alpha^{ss})^2} \right\},$$

$$a_2 = \frac{1}{2m} \sum_{r < s} \frac{(\alpha^{rss})^2}{\alpha^{rr}(\alpha^{ss})^2} + \frac{1}{m} \sum_{r < s < t} \frac{(\alpha^{rst})^2}{\alpha^{rr}\alpha^{ss}\alpha^{tt}}$$

where $\alpha^{rs\dots t} = E(Y^r Y^s \dots Y^t)$, Y^t is the t th component of Y , $Y = P^T \psi_0$, $\psi_0 = \psi(I(\omega), \beta_0)$, and P is the orthogonal matrix such that $\text{Var}(\psi(I(\omega), \beta_0)) = P \text{diag}\{\xi_1, \dots, \xi_m\} P^T$. $\{\xi_i, i = 1, \dots, m\}$ are eigenvalues of $\text{Var}(\psi(I(\omega), \beta_0))$. Note $\hat{\alpha}^{rs\dots t} = n^{-1} \sum_i (Y_i^r Y_i^s \dots Y_i^t)$. Then, the consistent estimators \hat{a}_1 and \hat{a}_2 are obtained by replacing the components of a_1, a_2 with their corresponding consistent estimators, which are given in the following table:

3.2 Simulation Results

Tables 1–7 report the coverage probabilities of confidence regions based on four versions of EL. First, we find that our proposed AEL* performs better than other ELs in terms of the coverage probability for all cases and that the coverage probability of our proposed AEL* is the closest to the normal level. Second, when the sample size is very small, the coverage probability based on MEL is smaller than that based on AEL with the adjustment level $a = \max(\log(N)/2, 1)$. But, when the sample size is moderate, the coverage probability is comparable to that based on AEL method, which is because the improvement only relies on the increasing sample size in essence. So, MEL enhances the coverage probability at some expense of computational efficiency. Third, the coverage

probabilities based on AEL and AEL* are not always enhanced with the increasing sample size. Fourth, from **Table 1**, when the coverage probability increases, the corresponding average length of the confidence interval is getting large. Fifth, **Table 3** indicates that the coverage probabilities become small when the parameter approximates the critical value tending to non-stationarity. The confidence regions in **Figures 1, 2** are respectively depicted as the case with the series length 1,000 and 200. When the sample size is large, there is little difference in four kinds of the confidence region in **Figure 1**. In **Figure 2**, obviously, when the sample size is small, our proposed AEL*-based confidence region is the smallest among the four counterparts, and the MEL-based confidence contour contains others. It indicates that our proposed AEL* has not only high-coverage probabilities but also small confidence regions, and MEL has high-coverage probabilities and relative large confidence regions. The shape of the confidence region matches with the data-driven property of the EL method. That is, the shapes of confidence regions are completely determined by the data.

4 REAL EXAMPLES

In this section, we illustrate and compare the validity of our proposed EL methods described in previous sections by analyzing some real examples.

4.1 Annual U.S. Unemployment Rate

First, we take annual U.S. unemployment rate series as an example to investigate the confidence region of our proposed EL methods. The data are collected from 1948 to 2019 and available from <https://forecast-chart.com/forecast-unemployment-rate.html>. The trajectory of these data is displayed in **Figure 3A**. We consider it as a realization of a stationary process. By the sample autocovariance function (ACF) and partial autocovariance function (PACF) analysis, we fit the unemployment rate by an AR (2) model. The 95% confidence regions based on our proposed AEL* and MEL are displayed in **Figure 3B**. The shapes coincide with EL's data-driven property, and the size indicates our proposed methods are much better than the previous EL and AEL methods.

4.2 S&P 500 VIX

S&P 500 VIX is a forward-looking index. If it is extended to the price observations of the broader market level index, the investor

will get a peek into volatility of the larger market. So, it is meaningful to fit a proper model. Here, we collect the data from April 25, 2019 to November 21, 2019. The trajectory is displayed in **Figure 4A**. We fit the data by an ARFIMA (1,d, 0) model with maximum likelihood point estimates $(\hat{\phi}, \hat{d}) = (0.170, 0.356)$. Then, the confidence regions are exhibited in **Figure 4B**. Compared with the original EL and the previous AEL, our proposed AEL*-based confidence region is still the best, and the MEL-based confidence contour also contains the others.

4.3 Shanghai Securities Composite Index

Finally, we analyze the daily log-return rate of Shanghai Securities Composite Index. The data range from June 4, 2020 to March 26, 2021. **Figure 5A** displays the realization of the index. We fit it as an ARFIMA (0,d, 0) model. The maximum likelihood and the EL estimate are \hat{d} and \hat{d}_E , respectively, and the lengths of four kinds of the EL confidence interval are displayed in **Table 8**. We find that the confidence interval based on MEL is still the largest, and the one based on our proposed AEL* is still the smallest.

5 CONCLUSION

In this article, we introduce two new versions of EL to construct confidence regions for parameters in stationary short- and long-memory time series. Our proposed AEL* and MEL do enhance the approximation precision of chi-square limiting distribution, which determines the good performance of corresponding confidence regions. Simulations show that our proposed AEL* has the better coverage probability than that of the previous AEL and MEL.

DATA AVAILABILITY STATEMENT

The original contributions presented in the study are included in the article/Supplementary Material, further inquiries can be directed to the corresponding author.

AUTHOR CONTRIBUTIONS

ZL and XZ are responsible for the theoretical part. RZ is responsible for the simulation and application. ZLu and RZ are responsible for writing.

REFERENCES

- Owen AB Empirical Likelihood Ratio Confidence Intervals for a Single Functional. *Biometrika* (1988) 75:237–49. doi:10.1093/biomet/75.2.237
- Owen AB Empirical Likelihood Ratio Confidence Regions. *Ann Stat* (1990) 18: 90–120. doi:10.1214/aos/1176347494
- Monti A Empirical Likelihood Confidence Regions in Time Series Models. *Biometrika* (1997) 84:395–405. doi:10.1093/biomet/84.2.395
- Nordman DJ, Lahiri SN A Frequency Domain Empirical Likelihood for Short- and Long-Range Dependence. *Ann Stat* (2006) 34:3019–50. doi:10.1214/009053606000000902
- Yau CY Empirical Likelihood in Long-Memory Time Series Models. *J Time Ser Anal* (2012) 33:269–75. doi:10.1111/j.1467-9892.2011.00756.x
- DiCiccio TJ, Hall P, Romano JP Empirical Likelihood Is Bartlett Correctable. *Ann Stat* (1991) 19:1053–61. doi:10.1214/aos/1176348137
- Chen J, Variyath AM, Abraham B Adjusted Empirical Likelihood and its Properties. *J Comput Graphical Stat* (2008) 17:426–43. doi:10.1198/106186008x321068
- Emerson SC, Owen AB Calibration of the Empirical Likelihood Method for a Vector Mean. *Electron J Stat* (2009) 3:1161–92. doi:10.1214/09-ejs518
- Chan NH, Liu L Bartlett Correctability of Empirical Likelihood for Time Series. *Jjss* (2010) 40:221–38. doi:10.14490/jjss.40.221

10. Li X, Chen JH, Wu YH, Tu DS Constructing Nonparametric Likelihood Confidence Regions with High Order Precisions. *Stat Sinica* (2011) 21: 1767–83. doi:10.5705/ss.2009.117
11. Cheng C, Liu Y, Liu Z, Zhou W Balanced Augmented Jackknife Empirical Likelihood for Two Sample U-Statistics. *Sci China Math* (2018) 61(6):1129–38. doi:10.1007/s11425-016-9071-y
12. Dahlhaus R, Wefelmeyer W Asymptotically Optimal Estimation in Misspecified Time Series Models. *Ann Stat* (1996) 24:952–74. doi:10.1214/aos/1032526951
13. Jiang F, Wang L Adjusted Blockwise Empirical Likelihood for Long Memory Time Series Models. *Stat Methods Appl* (2018) 27:319–32. doi:10.1007/s10260-017-0403-1
14. Liang W, Dai H, He S Mean Empirical Likelihood. *Comput Stat Data Anal* (2019) 138:155–69. doi:10.1016/j.csda.2019.04.007
15. Piyadi Gamage RD, Ning W, Gupta AK Adjusted Empirical Likelihood for Long-Memory Time-Series Models. *J Stat Theor Pract* (2017) 11:220–33. doi:10.1080/15598608.2016.1271373
16. Piyadi Gamage RD, Ning W, Gupta AK Adjusted Empirical Likelihood for Time Series Models. *Sankhya B* (2017) 79:336–60. doi:10.1007/s13571-017-0137-y
17. Granger CWJ, Joyeux R An Introduction to Long-Memory Time Series Models and Fractional Differencing. *J Time Ser Anal* (1980) 1:15–29. doi:10.1111/j.1467-9892.1980.tb00297.x
18. Li M Multi-fractional Generalized Cauchy Process and its Application to Teletraffic. *Physica A: Stat Mech its Appl* (2020) 550:123982. doi:10.1016/j.physa.2019.123982
19. Li M Generalized Fractional Gaussian Noise and its Application to Traffic Modeling. *Physica A* (2021) 579:1236137. doi:10.1016/j.physa.2021.126138
20. Li M Modified Multifractional Gaussian Noise and its Application. *Phys Scr* (2021) 96:125002. doi:10.1088/1402-4896/ac1cf6
21. Whittle P Estimation and Information in Stationary Time Series. *Ark. Mat.r Matematik* (1953) 2:423–34. doi:10.1007/bf02590998
22. Liu YK, Chen JH Adjusted Empirical Likelihood with High-Order Precision. *Ann Stat* (2010) 38(3):1341–62. doi:10.1214/09-aos750

Conflict of Interest: The authors declare that the research was conducted in the absence of any commercial or financial relationships that could be construed as a potential conflict of interest.

Publisher's Note: All claims expressed in this article are solely those of the authors and do not necessarily represent those of their affiliated organizations, or those of the publisher, the editors, and the reviewers. Any product that may be evaluated in this article, or claim that may be made by its manufacturer, is not guaranteed or endorsed by the publisher.

Copyright © 2022 Zhang, Zhang and Lu. This is an open-access article distributed under the terms of the Creative Commons Attribution License (CC BY). The use, distribution or reproduction in other forums is permitted, provided the original author(s) and the copyright owner(s) are credited and that the original publication in this journal is cited, in accordance with accepted academic practice. No use, distribution or reproduction is permitted which does not comply with these terms.

APPENDIX

Proof of Theorem 2.2. For simplicity, denote $g_k := g_k(I(\omega_k), \beta)$, $\lambda := \lambda_{\beta}^{**}$, and $\rho := \rho_{\beta}$. Following [3], $\|\lambda\| = O_p(N^{-1/2})$ and $\frac{1}{N} \sum_{i=1}^N \psi_i = O_p(N^{-1/2})$. Hence,

$$\begin{aligned} \frac{1}{K} \sum_{k=1}^K g_k &= \frac{1}{K} \left(\sum_{1 \leq i \leq j \leq N} \frac{\psi_i + \psi_j}{2} \right) = \frac{1}{2K} \left(\sum_{i=1}^N \sum_{j=1}^N \frac{\psi_i + \psi_j}{2} + \sum_{i=1}^N \psi_i \right) \\ &= \frac{1}{N} \sum_{i=1}^N \psi_i = O_p(N^{-1/2}); \end{aligned}$$

$$\begin{aligned} \frac{1}{K} \sum_{k=1}^K g_k g_k^{\tau} &= \frac{1}{K} \sum_{1 \leq i \leq j \leq N} \left(\frac{\psi_i + \psi_j}{2} \right) \left(\frac{\psi_i + \psi_j}{2} \right)^{\tau} \\ &= \frac{1}{2K} \left(\sum_{i=1}^N \sum_{j=1}^N \left(\frac{\psi_i + \psi_j}{2} \right) \left(\frac{\psi_i + \psi_j}{2} \right)^{\tau} + \sum_{i=1}^N \psi_i \psi_i^{\tau} \right) \\ &= \frac{N+2}{4K} \sum_{i=1}^N \psi_i \psi_i^{\tau} + \frac{1}{4K} \sum_{i=1}^N \psi_i \sum_{j=1}^N \psi_j^{\tau} \\ &\rightarrow \frac{1}{2N} \sum_{i=1}^N \psi_i \psi_i^{\tau} + o_p(1). \end{aligned}$$

The Taylor expansion of equation (5) is

$$0 = \frac{1}{K} \sum_{k=1}^K \frac{g_k}{1 + \lambda^{\tau} g_k} = \frac{1}{K} \sum_{k=1}^K g_k - \frac{1}{K} \sum_{k=1}^K g_k g_k^{\tau} \lambda + o_p(1),$$

then $\lambda = (\frac{1}{K} \sum_{k=1}^K g_k g_k^{\tau})^{-1} (\frac{1}{K} \sum_{k=1}^K g_k) + o_p(1)$. Substituting λ into $R^M(\beta_0)$, we have

$$\begin{aligned} R^M(\beta_0) &= 2 \sum_{k=1}^K \ln(1 + \lambda^{\tau} g_k) / (N+1) \\ &= 2 \sum_{k=1}^K (\lambda^{\tau} g_k - (\lambda^{\tau} g_k)^2 / 2) / (N+1) + o_p(1); \\ &= \frac{N}{2} \left(\frac{1}{K} \sum_{k=1}^K g_k \right)^{\tau} \left(\frac{1}{K} \sum_{k=1}^K g_k g_k^{\tau} \right)^{-1} \left(\frac{1}{K} \sum_{k=1}^K g_k \right) + o_p(1) \\ &= N \left(\frac{1}{N} \sum_{i=1}^N \psi_i \right)^{\tau} \left(\frac{1}{N} \sum_{i=1}^N \psi_i \psi_i^{\tau} \right)^{-1} \left(\frac{1}{N} \sum_{i=1}^N \psi_i \right) + o_p(1). \end{aligned}$$

Combining Equations (4.4) and (4.5) of Monti (1997) with the proof of Theorem 1 of Yau (2012), we have $R^M(\beta_0) \xrightarrow{d} \chi_m^2$ as $n \rightarrow \infty$, where \xrightarrow{d} means convergence in distribution.



Large Time Behavior on the Linear Self-Interacting Diffusion Driven by Sub-Fractional Brownian Motion With Hurst Index Large Than 0.5 I: Self-Repelling Case

Han Gao^{1*}, Rui Guo², Yang Jin³ and Litan Yan³

¹College of Fashion and Art Design, Donghua University, Shanghai, China, ²College of Information Science and Technology, Donghua University, Shanghai, China, ³Department of Statistics, College of Science, Donghua University, Shanghai, China

Let S^H be a sub-fractional Brownian motion with index $\frac{1}{2} < H < 1$. In this paper, we consider the linear self-interacting diffusion driven by S^H , which is the solution to the equation

$$dX_t^H = dS_t^H - \theta \left(\int_0^t (X_s^H - X_t^H) ds \right) dt + \nu dt, \quad X_0^H = 0,$$

OPEN ACCESS

Edited by:

Ming Li,
Zhejiang University, China

Reviewed by:

Yu Sun,
Our Lady of the Lake University,
United States
Zhenxia Liu,
Linköping University, Sweden

*Correspondence:

Han Gao
1061760802@qq.com

Specialty section:

This article was submitted to
Interdisciplinary Physics,
a section of the journal
Frontiers in Physics

Received: 14 October 2021

Accepted: 05 November 2021

Published: 14 January 2022

Citation:

Gao H, Guo R, Jin Y and Yan L (2022)
Large Time Behavior on the Linear Self-
Interacting Diffusion Driven by Sub-
Fractional Brownian Motion With Hurst
Index Large Than 0.5 I: Self-
Repelling Case.
Front. Phys. 9:795210.
doi: 10.3389/fphy.2021.795210

where $\theta < 0$ and $\nu \in \mathbb{R}$ are two parameters. Such process X^H is called self-repelling and it is an analogue of the linear self-attracting diffusion [Cranston and Le Jan, *Math. Ann.* 303 (1995), 87–93]. Our main aim is to study the large time behaviors. We show the solution X^H diverges to infinity, as t tends to infinity, and obtain the speed at which the process X^H diverges to infinity as t tends to infinity.

Keywords: the self-repelling diffusion, asymptotic distribution, convergence, sub-fractional Brownian motion, stochastic integral

1 INTRODUCTION

In 1995, Cranston and Le Jan [1] introduced a linear self-attracting diffusion

$$X_t = B_t - \theta \int_0^t \int_0^s (X_s - X_u) du ds + \nu t, \quad t \geq 0 \quad (1.1)$$

with $\theta > 0$ and $X_0 = 0$, where B is a 1-dimensional standard Brownian motion. They showed that the process X_t converges in L^2 and almost surely, as t tends infinity. This is a special case of path dependent stochastic differential equations. Such path dependent stochastic differential equation was first developed by Durrett and Rogers [2] introduced in 1992 as a model for the shape of a growing polymer (Brownian polymer) as follows

$$X_t = X_0 + B_t + \int_0^t \int_0^s f(X_s - X_u) du ds, \quad (1.2)$$

where B is a d -dimensional standard Brownian motion and f is Lipschitz continuous. X_t corresponds to the location of the end of the polymer at time t . Under some conditions, they established asymptotic behavior of the solution of stochastic differential equation and gave some conjectures and questions. The model is a continuous analogue of the notion of edge (resp. vertex) self-interacting random walk. If $f(x) = g(x)x/\|x\|$ and $g(x) \geq 0$, X_t is a continuous analogue of a process introduced by

Diaconis and studied by Pemantle [3]. Let $\mathcal{L}^X(t, x)$ be the local time of the solution process X . Then, we have

$$X_t = X_0 + B_t + \int_0^t ds \int_{\mathbb{R}} f(-x) \mathcal{L}^X(s, X_s + x) dx$$

for all $t \geq 0$. This formulation makes it clear how the process X interacts with its own occupation density. We may call this solution a Brownian motion interacting with its own passed trajectory, i.e., a *self-interacting motion*. In general, the Eq. 1.2 defines a self-interacting diffusion without any assumption on f . If

$$x \cdot f(x) \geq 0 \quad (x \cdot f(x) \leq 0)$$

for all $x \in \mathbb{R}^d$, we call it self-repelling (resp. self-attracting). In 2002, Benaïm et al [4] also introduced a self-interacting diffusion with dependence on the (convolved) empirical measure. A great difference between these diffusions and Brownian polymers is that the drift term is divided by t . It is noteworthy that the interaction potential is attractive enough to compare the diffusion (a bit modified) to an Ornstein-Uhlenbeck process, in many case of f , which points out an access to its asymptotic behavior. More works can be found in Benaïm et al. [5], Cranston and Mountford [6], Gauthier [7], Herrmann and Roynette [8], Herrmann and Scheutzwow [9], Mountford and Tarr [10], Shen et al [11], Sun and Yan [12] and the references therein.

On the other hand, starting from the application of fractional Brownian motion in polymer modeling, Yan et al [13] considered an analogue of the linear self-interacting diffusion:

$$X_t^H = B_t^H - \theta \int_0^t \int_0^s (X_s^H - X_u^H) du ds + \nu t, \quad t \geq 0 \quad (1.3)$$

with $\theta \neq 0$ and $X_0^H = 0$, where B^H is a fractional Brownian motion (fBm, in short) with Hurst parameter $\frac{1}{2} \leq H < 1$. The solution of (1.3) is a Gaussian process. When $\theta > 0$, Yan et al [13] showed that the solution X^H of (1.3) converges in L^2 and almost surely, to the random variable

$$X_\infty^H = \int_0^\infty h_\theta(s) dB_s^H + \nu \int_0^\infty h_\theta(s) ds$$

where the function is defined as follows

$$h_\theta(s) = 1 - \theta s e^{\frac{1}{2}\theta s^2} \int_s^\infty e^{-\frac{1}{2}\theta u^2} du, \quad s \geq 0$$

with $\theta > 0$. Recently, Sun and Yan [14] considered the related parameter estimations with $\theta > 0$ and $\frac{1}{2} \leq H < 1$, and Gan and Yan [15] considered the parameter estimations with $\theta < 0$ and $\frac{1}{2} \leq H < 1$.

Motivated by these results, as a natural extension one can consider the following stochastic differential equation:

$$X_t = G_t - \theta \int_0^t \int_0^s (X_s - X_u) du ds + \nu t, \quad t \geq 0 \quad (1.4)$$

with $\theta > 0$ and $X_0 = 0$, where $G = \{G_t, t \geq 0\}$ is a Gaussian process with some suitable conditions which includes fractional Brownian motion and some related processes. However, for a (general) abstract Gaussian process it is difficult to find some

interesting fine estimates associated with the calculations. So, in this paper we consider the linear self-attracting diffusion driven by a sub-fractional Brownian motion (sub-fBm, in short). We choose this kind of Gaussian process because it is only the generalization of Brownian motion rather than the generalization of fractional Brownian motion. It only has some similar properties of fractional Brownian motion, such as long memory and self similarity, but it has no stationary increment. The so-called sub-fBm with index $H \in (0, 1)$ is a mean zero Gaussian process $S^H = \{S_t^H, t \geq 0\}$ with $S_0^H = 0$ and the covariance

$$R_H(t, s) \equiv E[S_t^H S_s^H] = s^{2H} + t^{2H} - \frac{1}{2} [(s+t)^{2H} + |t-s|^{2H}] \quad (1.5)$$

for all $s, t \geq 0$. For $H = 1/2$, S^H coincides with the standard Brownian motion B . S^H is neither a semimartingale nor a Markov process unless $H = 1/2$, so many of the powerful techniques from stochastic analysis are not available when dealing with S^H . As a Gaussian process, it is possible to construct a stochastic calculus of variations with respect to S^H (see, for example, Alós et al [16]). The sub-fBm has properties analogous to those of fBm and satisfies the following estimates:

$$\begin{aligned} [(2 - 2^{2H-1}) \wedge 1] (t-s)^{2H} &\leq E[(S_t^H - S_s^H)^2] \\ &\leq [(2 - 2^{2H-1}) \vee 1] (t-s)^{2H}. \end{aligned} \quad (1.6)$$

More works for sub-fBm and related processes can be found in Bojdecki et al. [17–20], Li [21–24], Shen and Yan [25, 26], Sun and Yan [27], Tudor [28–31], Ciprian A. Tudor [32] Yan et al [33–35] and the references therein.

In this present paper, we consider the linear self-interacting diffusion

$$X_t^H = S_t^H - \theta \int_0^t \int_0^s (X_s^H - X_u^H) du ds + \nu t, \quad t \geq 0 \quad (1.7)$$

with $\theta < 0$ and $X_0^H = 0$, where S^H is a sub-fBm with Hurst parameter $\frac{1}{2} \leq H < 1$. Our main aim is to show that the solution of (1.7) diverges to infinity and obtain the speed diverging to infinity, as t tends to infinity. The object of this paper is to expound and prove the following statements:

(I) For $\theta < 0$ and $\frac{1}{2} < H < 1$, the random variable

$$\xi_\infty^H = \int_0^\infty s e^{\frac{1}{2}\theta s^2} dS_s^H$$

exists as an element in L^2 .

(II) For $\theta < 0$ and $\frac{1}{2} < H < 1$, as $t \rightarrow \infty$, we have

$$J_0^H(t; \theta, \nu) := t e^{\frac{1}{2}\theta t^2} X_t^H \rightarrow \xi_\infty^H - \frac{\nu}{\theta}$$

in L^2 and almost surely.

(III) For $\theta < 0$ and $\frac{1}{2} < H < 1$, define the processes $J^H(n, \theta, \nu) = \{J_t^H(n, \theta, \nu), t \geq 0\}, n \geq 1$ by

$$J_n^H(t; \theta, \nu) := \theta t^2 \left(J_{n-1}^H(t; \theta, \nu) - (2n-3)!! \left(\xi_\infty^H - \frac{\nu}{\theta} \right) \right),$$

$$n = 1, 2, \dots,$$

for all $t \geq 0$, where $(-1)!! = 1$. We then have

$$J_n^H(t; \theta, \nu) \rightarrow (2n-1)!! \left(\xi_\infty^H - \frac{\nu}{\theta} \right)$$

holds in L^2 and almost surely for every $n \geq 1$, as $t \rightarrow \infty$.

This paper is organized as follows. In **Section 2** we present some preliminaries for sub-fBm and Malliavin calculus. In **Section 3**, we obtain some lemmas. In **Section 4**, we prove the main result. In **Section 5** we give some numerical results.

2 PRELIMINARIES

In this section, we briefly recall the definition and properties of stochastic integral with respect to sub-fBm. We refer to Alós et al [16], Nualart [36], and Tudor [31] for a complete description of stochastic calculus with respect to Gaussian processes. Throughout this paper we assume that $S^H = \{S_t^H, t \geq 0\}$ denotes a sub-fBm defined on the probability space (Ω, \mathcal{F}, P) with index H . As we pointed out before, the sub-fBm S^H is a rather special class of self-similar Gaussian processes such that $S_0^H = 0$, $E[S_t^H] = 0$ and

$$R^H(t, s) := E[S_t^H S_s^H] = s^{2H} + t^{2H} - \frac{1}{2} [(s+t)^{2H} + |t-s|^{2H}] \quad (2.1)$$

for all $s, t \geq 0$. For $H = 1/2$, S^H coincides with the standard Brownian motion B . S^H is neither a semimartingale nor a Markov process unless $H = 1/2$, so many of the powerful techniques from stochastic analysis are not available when dealing with S^H . As a Gaussian process, it is possible to construct a stochastic calculus of variations with respect to S^H . The sub-fBm appeared in Bojdecki et al [17] in a limit of occupation time fluctuations of a system of independent particles moving in \mathbb{R}^d according a symmetric α -stable Lévy process, and it also appears in Bojdecki et al [18] in a high-density limit of occupation time fluctuations of the above mentioned particle system, where the initial Poisson configuration has finite intensity measure.

The estimate (1.6) and normality imply that the sub-fBm $t \mapsto S_t^H$ admits almost surely a bounded $\frac{1}{H-\vartheta}$ -variation on any finite interval for any sufficiently small $\vartheta \in (0, H)$. That is, the paths of $t \mapsto S_t^H$ admits a bounded p_H -variation on any finite interval with $p_H > \frac{1}{H}$. As an immediate result, one can define the Young integral of a process $u = \{u_t, t \geq 0\}$ with respect to sub-fBm $B^{a,b}$

$$\int_0^t u_s dS_s^H$$

as the limit in probability of a Riemann sum. Clearly, the integral is well-defined and

$$u_t S_t^H = \int_0^t u_s dS_s^H + \int_0^t S_s^H du_s$$

for all $t \geq 0$, provided u is of bounded q_H -variation on any finite interval with $q_H > 1$ and $\frac{1}{p_H} + \frac{1}{q_H} > 1$ (see, for examples, Bertoin [37] and Föllmer [38]).

Let \mathcal{H} be the completion of the linear space \mathcal{E} generated by the indicator functions $1_{[0,t]}$, $t \in [0, T]$ with respect to the inner product

$$\langle 1_{[0,s]}, 1_{[0,t]} \rangle_{\mathcal{H}} = R^H(t, s)$$

for $s, t \in [0, T]$. When $\frac{1}{2} < H < 1$, we can show that

$$\begin{aligned} \|\varphi\|_{\mathcal{H}}^2 &= \int_0^T \int_0^T \varphi(t) \varphi(s) \frac{\partial^2}{\partial t \partial s} R^H(t, s) ds dt \\ &= \int_0^T \int_0^T \varphi(t) \varphi(s) \psi_H(t, s) ds dt, \quad \forall \varphi \in \mathcal{H}, \end{aligned}$$

where

$$\psi_H(t, s) = \frac{\partial^2}{\partial t \partial s} R^{a,b}(t, s) = H(2H-1)(|t-s|^{2H-2} - |t+s|^{2H-2})$$

for $s, t \in [0, T]$. Define the linear mapping $\mathcal{E} \ni \varphi \mapsto S^H(\varphi)$ by

$$1_{[0,t]} \mapsto S^H(1_{[0,t]}) = \int_0^T 1_{[0,t]}(s) dS_s^H \equiv S_t^H$$

for all $t \in [0, T]$ and it can be continuously extended to \mathcal{H} and we call the mapping Φ is called the Wiener integral with respect to S^H , denoted by

$$S^H(\varphi) = \int_0^T \varphi(s) dS_s^H$$

and

$$\|\varphi\|_{\mathcal{H}}^2 = E \left(\int_0^T \varphi(s) dS_s^H \right)^2 \quad (2.2)$$

for any $\varphi \in \mathcal{H}$.

For simplicity, in this paper we assume that $\frac{1}{2} < H < 1$. Thus, if for every $T > 0$, the integral

$$\int_0^T \varphi(s) dS_s^H$$

exists in L^2 and

$$\int_0^\infty \int_0^\infty \varphi(t) \varphi(s) \psi_H(t, s) ds dt < \infty,$$

we can define the integral

$$\int_0^\infty \varphi(s) dS_s^H$$

and

$$E \left(\int_0^\infty \varphi(s) dS_s^H \right)^2 = \int_0^\infty \int_0^\infty \varphi(t) \varphi(s) \psi_H(t, s) ds dt.$$

Denote by \mathcal{S} the set of smooth functionals of the form

$$F = f(S^H(\varphi_1), S^H(\varphi_2), \dots, S^H(\varphi_n)),$$

where $f \in C_b^\infty(\mathbb{R}^n)$ and $\varphi_i \in \mathcal{H}$. The Malliavin derivative D of a functional F as above is given by

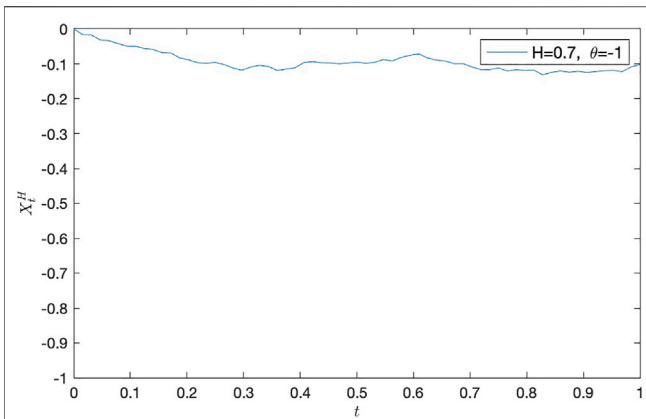


FIGURE 1 | A path of X_t^H with $\theta = -1$ and $H = 0.7$.

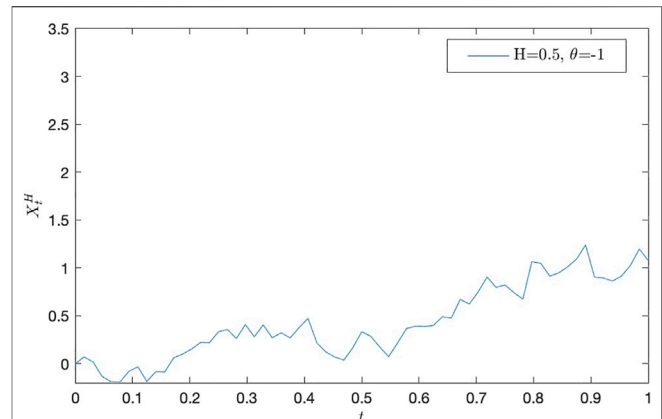


FIGURE 4 | A path of X_t^H with $\theta = -1$ and $H = 0.5$.

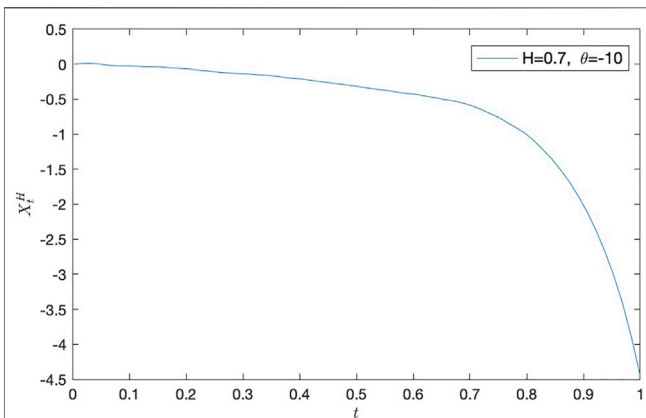


FIGURE 2 | A path of X_t^H with $\theta = -10$ and $H = 0.7$.

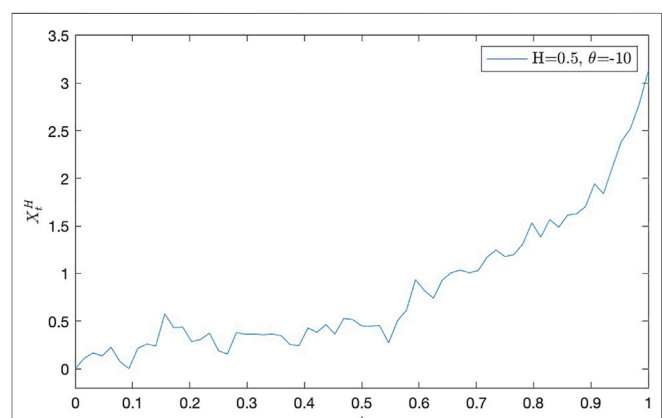


FIGURE 5 | A path of X_t^H with $\theta = -10$ and $H = 0.5$.

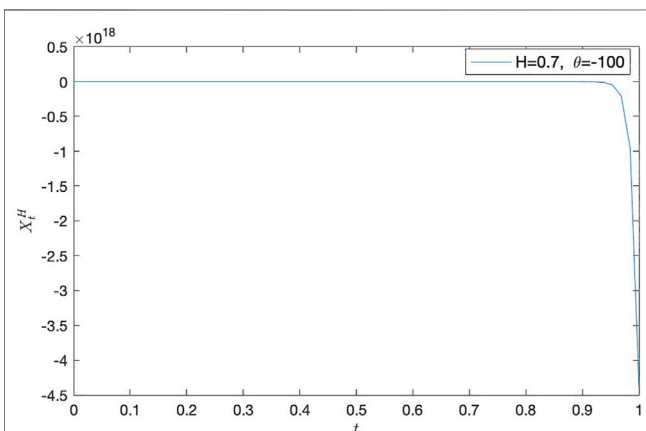


FIGURE 3 | A path of X_t^H with $\theta = -100$ and $H = 0.7$.

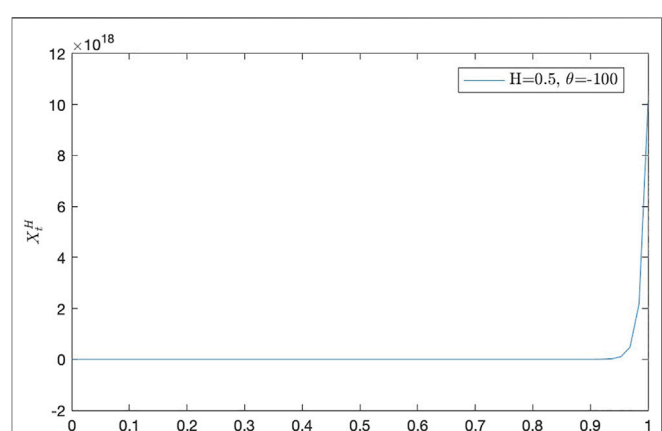


FIGURE 6 | A path of X_t^H with $\theta = -100$ and $H = 0.5$.

TABLE 1 | The data of X_t^H with $\theta = -1$ and $H = 0.7$.

| t | X_t^H | τ | X_t^H | t | X_t^H |
|--------|---------|--------|---------|--------|---------|
| 0.0000 | 0.0000 | 0.3438 | -0.1077 | 0.6875 | -0.0995 |
| 0.0156 | -0.0167 | 0.3594 | -0.1190 | 0.7031 | -0.1091 |
| 0.0313 | -0.0178 | 0.3750 | -0.1153 | 0.7188 | -0.1163 |
| 0.0469 | -0.0320 | 0.3906 | -0.1116 | 0.7344 | -0.1165 |
| 0.0625 | -0.0338 | 0.4063 | -0.0965 | 0.7500 | -0.1122 |
| 0.0781 | -0.0420 | 0.4219 | -0.0937 | 0.7656 | -0.1205 |
| 0.0938 | -0.0492 | 0.4375 | -0.0971 | 0.7813 | -0.1170 |
| 0.1094 | -0.0496 | 0.4531 | -0.0974 | 0.7969 | -0.1192 |
| 0.1250 | -0.0564 | 0.4688 | -0.0997 | 0.8125 | -0.1180 |
| 0.1406 | -0.0590 | 0.4844 | -0.0976 | 0.8281 | -0.1316 |
| 0.1563 | -0.0682 | 0.5000 | -0.0956 | 0.8438 | -0.1245 |
| 0.1719 | -0.0692 | 0.5156 | -0.0983 | 0.8594 | -0.1202 |
| 0.1875 | -0.0834 | 0.5313 | -0.0959 | 0.8750 | -0.1241 |
| 0.2031 | -0.0886 | 0.5469 | -0.0877 | 0.8906 | -0.1212 |
| 0.2188 | -0.0969 | 0.5625 | -0.0919 | 0.9063 | -0.1250 |
| 0.2344 | -0.0983 | 0.5781 | -0.0818 | 0.9219 | -0.1219 |
| 0.2500 | -0.0961 | 0.5938 | -0.0757 | 0.9375 | -0.1199 |
| 0.2656 | -0.1022 | 0.6094 | -0.0717 | 0.9531 | -0.1191 |
| 0.2813 | -0.1120 | 0.6250 | -0.0834 | 0.9688 | -0.1223 |
| 0.2969 | -0.1182 | 0.6406 | -0.0894 | 0.9844 | -0.1089 |
| 0.3125 | -0.1094 | 0.6563 | -0.0923 | 1.0000 | -0.1023 |
| 0.3281 | -0.1042 | 0.6719 | -0.0996 | — | — |

TABLE 3 | The data of X_t^H with $\theta = -100$ and $H = 0.7$.

| t | X_t^H | t | X_t^H | t | X_t^H |
|--------|---------|--------|-----------|--------|-----------|
| 0.0000 | 0.0000 | 0.3438 | -1.0056 | 0.6875 | -2.29E+07 |
| 0.0156 | 0.0132 | 0.3594 | -1.6439 | 0.7031 | -6.63E+07 |
| 0.0313 | 0.0093 | 0.3750 | -2.7733 | 0.7188 | -1.97E+08 |
| 0.0469 | 0.0070 | 0.3906 | -4.8028 | 0.7344 | -5.99E+08 |
| 0.0625 | 0.0103 | 0.4063 | -8.5377 | 0.7500 | -1.87E+09 |
| 0.0781 | 0.0116 | 0.4219 | -15.5941 | 0.7656 | -5.98E+09 |
| 0.0938 | 0.0092 | 0.4375 | -29.2598 | 0.7813 | -1.96E+10 |
| 0.1094 | 0.0066 | 0.4531 | -56.3669 | 0.7969 | -6.59E+10 |
| 0.1250 | 0.0081 | 0.4688 | -111.4786 | 0.8125 | -2.27E+11 |
| 0.1406 | 0.0049 | 0.4844 | -226.2866 | 0.8281 | -8.02E+11 |
| 0.1563 | 0.0094 | 0.5000 | -471.3711 | 0.8438 | -2.91E+12 |
| 0.1719 | -0.0029 | 0.5156 | -1.01E+03 | 0.8594 | -1.08E+13 |
| 0.1875 | -0.0114 | 0.5313 | -2.21E+03 | 0.8750 | -4.10E+13 |
| 0.2031 | -0.0279 | 0.5469 | -4.97E+03 | 0.8906 | -1.60E+14 |
| 0.2188 | -0.0484 | 0.5625 | -1.15E+04 | 0.9063 | -6.40E+14 |
| 0.2344 | -0.0557 | 0.5781 | -2.72E+04 | 0.9219 | -2.62E+15 |
| 0.2500 | -0.0837 | 0.5938 | -6.59E+04 | 0.9375 | -1.10E+16 |
| 0.2656 | -0.1240 | 0.6094 | -1.64E+05 | 0.9531 | -4.75E+16 |
| 0.2813 | -0.1834 | 0.6250 | -4.19E+05 | 0.9688 | -2.10E+17 |
| 0.2969 | -0.2706 | 0.6406 | -1.10E+06 | 0.9844 | -9.48E+17 |
| 0.3125 | -0.4085 | 0.6563 | -2.95E+06 | 1.0000 | -4.40E+18 |
| 0.3281 | -0.6332 | 0.6719 | -8.12E+06 | — | — |

TABLE 2 | The data of X_t^H with $\theta = -10$ and $H = 0.7$.

| t | X_t^H | t | X_t^H | t | X_t^H |
|--------|---------|--------|---------|--------|---------|
| 0.0000 | 0.0000 | 0.3438 | -0.1597 | 0.6875 | -0.5552 |
| 0.0156 | 0.0087 | 0.3594 | -0.1729 | 0.7031 | -0.5943 |
| 0.0313 | 0.0113 | 0.3750 | -0.1912 | 0.7188 | -0.6439 |
| 0.0469 | 0.0040 | 0.3906 | -0.2051 | 0.7344 | -0.7019 |
| 0.0625 | -0.0153 | 0.4063 | -0.2130 | 0.7500 | -0.7595 |
| 0.0781 | -0.0239 | 0.4219 | -0.2342 | 0.7656 | -0.8345 |
| 0.0938 | -0.0234 | 0.4375 | -0.2494 | 0.7813 | -0.9066 |
| 0.1094 | -0.0279 | 0.4531 | -0.2654 | 0.7969 | -0.9868 |
| 0.1250 | -0.0348 | 0.4688 | -0.2820 | 0.8125 | -1.0919 |
| 0.1406 | -0.0372 | 0.4844 | -0.2980 | 0.8281 | -1.2177 |
| 0.1563 | -0.0395 | 0.5000 | -0.3156 | 0.8438 | -1.3507 |
| 0.1719 | -0.0530 | 0.5156 | -0.3363 | 0.8594 | -1.5050 |
| 0.1875 | -0.0587 | 0.5313 | -0.3543 | 0.8750 | -1.6776 |
| 0.2031 | -0.0648 | 0.5469 | -0.3694 | 0.8906 | -1.8811 |
| 0.2188 | -0.0835 | 0.5625 | -0.3865 | 0.9063 | -2.1081 |
| 0.2344 | -0.0942 | 0.5781 | -0.4093 | 0.9219 | -2.3699 |
| 0.2500 | -0.1100 | 0.5938 | -0.4204 | 0.9375 | -2.6701 |
| 0.2656 | -0.1213 | 0.6094 | -0.4368 | 0.9531 | -3.0170 |
| 0.2813 | -0.1317 | 0.6250 | -0.4620 | 0.9688 | -3.4144 |
| 0.2969 | -0.1365 | 0.6406 | -0.4810 | 0.9844 | -3.8989 |
| 0.3125 | -0.1418 | 0.6563 | -0.5086 | 1.0000 | -4.4510 |
| 0.3281 | -0.1541 | 0.6719 | -0.5258 | — | — |

TABLE 4 | The data of X_t^H with $\theta = -1$ and $H = 0.5$.

| t | X_t^H | t | X_t^H | t | X_t^H |
|--------|---------|--------|---------|--------|---------|
| 0.0000 | 0.0000 | 0.3438 | 0.2713 | 0.6875 | 0.6225 |
| 0.0156 | 0.0711 | 0.3594 | 0.3234 | 0.7031 | 0.7483 |
| 0.0313 | 0.0168 | 0.3750 | 0.2698 | 0.7188 | 0.9047 |
| 0.0469 | -0.1326 | 0.3906 | 0.3765 | 0.7344 | 0.7963 |
| 0.0625 | -0.1887 | 0.4063 | 0.4725 | 0.7500 | 0.8221 |
| 0.0781 | -0.1911 | 0.4219 | 0.2156 | 0.7656 | 0.7416 |
| 0.0938 | -0.0792 | 0.4375 | 0.1224 | 0.7813 | 0.6743 |
| 0.1094 | -0.0320 | 0.4531 | 0.0691 | 0.7969 | 1.0655 |
| 0.1250 | -0.1853 | 0.4688 | 0.0377 | 0.8125 | 1.0480 |
| 0.1406 | -0.0827 | 0.4844 | 0.1668 | 0.8281 | 0.9146 |
| 0.1563 | -0.0861 | 0.5000 | 0.3344 | 0.8438 | 0.9478 |
| 0.1719 | 0.0616 | 0.5156 | 0.2866 | 0.8594 | 1.0125 |
| 0.1875 | 0.1014 | 0.5313 | 0.1759 | 0.8750 | 1.0931 |
| 0.2031 | 0.1542 | 0.5469 | 0.0739 | 0.8906 | 1.2403 |
| 0.2188 | 0.2224 | 0.5625 | 0.2168 | 0.9063 | 0.9036 |
| 0.2344 | 0.2205 | 0.5781 | 0.3676 | 0.9219 | 0.8949 |
| 0.2500 | 0.3345 | 0.5938 | 0.3904 | 0.9375 | 0.8626 |
| 0.2656 | 0.3581 | 0.6094 | 0.3878 | 0.9531 | 0.9140 |
| 0.2813 | 0.2635 | 0.6250 | 0.3985 | 0.9688 | 1.0247 |
| 0.2969 | 0.4084 | 0.6406 | 0.4900 | 0.9844 | 1.1976 |
| 0.3125 | 0.2820 | 0.6563 | 0.4769 | 1.0000 | 1.0780 |
| 0.3281 | 0.4043 | 0.6719 | 0.6713 | — | — |

$$DF = \sum_{j=1}^n \frac{\partial f}{\partial x_j} (S^H(\varphi_1), S^H(\varphi_2), \dots, S^H(\varphi_n)) \varphi_j.$$

The derivative operator D is then a closable operator from $L^2(\Omega)$ into $L^2(\Omega; \mathcal{H})$. We denote by $\mathbb{D}^{1,2}$ the closure of \mathcal{S} with respect to the norm

$$\|F\|_{1,2} := \sqrt{E|F|^2 + E\|DF\|_{\mathcal{H}}^2}.$$

The divergence integral δ is the adjoint of derivative operator D^H . That is, we say that a random variable u in $L^2(\Omega; \mathcal{H})$ belongs to the domain of the divergence operator δ , denoted by $\text{Dom}(\delta^S)$, if

$$E|\langle DF, u \rangle_{\mathcal{H}}| \leq c\|F\|_{L^2(\Omega)}$$

for every $F \in \mathbb{D}^{1,2}$, where c is a constant depending only on u . In this case $\delta(u)$ is defined by the duality relationship

$$E[F\delta(u)] = E\langle DF, u \rangle_{\mathcal{H}} \quad (2.3)$$

TABLE 5 | The data of X_t^H with $\theta = -10$ and $H = 0.5$.

| t | X_t^H | t | X_t^H | t | X_t^H |
|--------|---------|--------|---------|--------|---------|
| 0.0000 | 0.0000 | 0.3438 | 0.3643 | 0.6875 | 1.0084 |
| 0.0156 | 0.1112 | 0.3594 | 0.3489 | 0.7031 | 1.0312 |
| 0.0313 | 0.1668 | 0.3750 | 0.2532 | 0.7188 | 1.1722 |
| 0.0469 | 0.1353 | 0.3906 | 0.2453 | 0.7344 | 1.2474 |
| 0.0625 | 0.2259 | 0.4063 | 0.4297 | 0.7500 | 1.1783 |
| 0.0781 | 0.0764 | 0.4219 | 0.3837 | 0.7656 | 1.1997 |
| 0.0938 | 0.0025 | 0.4375 | 0.4639 | 0.7813 | 1.3114 |
| 0.1094 | 0.2166 | 0.4531 | 0.3663 | 0.7969 | 1.5335 |
| 0.1250 | 0.2593 | 0.4688 | 0.5287 | 0.8125 | 1.3820 |
| 0.1406 | 0.2412 | 0.4844 | 0.5164 | 0.8281 | 1.5679 |
| 0.1563 | 0.5773 | 0.5000 | 0.4502 | 0.8438 | 1.4858 |
| 0.1719 | 0.4322 | 0.5156 | 0.4488 | 0.8594 | 1.6145 |
| 0.1875 | 0.4384 | 0.5313 | 0.4538 | 0.8750 | 1.6282 |
| 0.2031 | 0.2872 | 0.5469 | 0.2729 | 0.8906 | 1.7043 |
| 0.2188 | 0.3078 | 0.5625 | 0.5069 | 0.9063 | 1.9432 |
| 0.2344 | 0.3761 | 0.5781 | 0.6164 | 0.9219 | 1.8384 |
| 0.2500 | 0.1896 | 0.5938 | 0.9359 | 0.9375 | 2.1171 |
| 0.2656 | 0.1558 | 0.6094 | 0.8222 | 0.9531 | 2.3878 |
| 0.2813 | 0.3807 | 0.6250 | 0.7422 | 0.9688 | 2.5204 |
| 0.2969 | 0.3637 | 0.6406 | 0.9326 | 0.9844 | 2.7823 |
| 0.3125 | 0.3641 | 0.6563 | 1.0095 | 1.0000 | 3.1237 |
| 0.3281 | 0.3580 | 0.6719 | 1.0371 | — | — |

TABLE 6 | The data of X_t^H with $\theta = -100$ and $H = 0.5$.

| t | X_t^H | t | X_t^H | t | X_t^H |
|--------|---------|--------|----------|--------|----------|
| 0.0000 | 0.0000 | 0.3438 | 2.1870 | 0.6875 | 5.26E+07 |
| 0.0156 | -0.1749 | 0.3594 | 3.5867 | 0.7031 | 1.52E+08 |
| 0.0313 | -0.3397 | 0.3750 | 6.3084 | 0.7188 | 4.52E+08 |
| 0.0469 | -0.4106 | 0.3906 | 11.0159 | 0.7344 | 1.37E+09 |
| 0.0625 | -0.3348 | 0.4063 | 19.5047 | 0.7500 | 4.29E+09 |
| 0.0781 | -0.3567 | 0.4219 | 35.6469 | 0.7656 | 1.37E+10 |
| 0.0938 | -0.3936 | 0.4375 | 66.9024 | 0.7813 | 4.50E+10 |
| 0.1094 | -0.3411 | 0.4531 | 129.1499 | 0.7969 | 1.51E+11 |
| 0.1250 | -0.2522 | 0.4688 | 255.5964 | 0.8125 | 5.21E+11 |
| 0.1406 | -0.1583 | 0.4844 | 518.9528 | 0.8281 | 1.84E+12 |
| 0.1563 | -0.1543 | 0.5000 | 1.08E+03 | 0.8438 | 6.66E+12 |
| 0.1719 | 0.0877 | 0.5156 | 2.31E+03 | 0.8594 | 2.47E+13 |
| 0.1875 | -0.1242 | 0.5313 | 5.07E+03 | 0.8750 | 9.42E+13 |
| 0.2031 | -0.0522 | 0.5469 | 1.14E+04 | 0.8906 | 3.67E+14 |
| 0.2188 | 0.1336 | 0.5625 | 2.63E+04 | 0.9063 | 1.47E+15 |
| 0.2344 | 0.0243 | 0.5781 | 6.23E+04 | 0.9219 | 6.02E+15 |
| 0.2500 | 0.1665 | 0.5938 | 1.51E+05 | 0.9375 | 2.53E+16 |
| 0.2656 | 0.2096 | 0.6094 | 3.77E+05 | 0.9531 | 1.09E+17 |
| 0.2813 | 0.4085 | 0.6250 | 9.62E+05 | 0.9688 | 4.81E+17 |
| 0.2969 | 0.5852 | 0.6406 | 2.52E+06 | 0.9844 | 2.18E+18 |
| 0.3125 | 0.8397 | 0.6563 | 6.76E+06 | 1.0000 | 1.01E+19 |
| 0.3281 | 1.3366 | 0.6719 | 1.86E+07 | — | — |

for any $F \in \mathbb{D}^{1,2}$. We have $\mathbb{D}^{1,2} \subset \text{Dom}(\delta)$ and for any $u \in \mathbb{D}^{1,2}$

$$\begin{aligned} E[\delta(u)^2] &= E\|u\|_{\mathcal{H}}^2 + E\langle Du, (Du)^* \rangle_{\mathcal{H} \otimes \mathcal{H}} \\ &= E\|u\|_{\mathcal{H}}^2 + E \int_{[0,T]^4} D_\xi u_r D_\eta u_s \phi_H(\eta, r) \phi_H(\xi, s) ds dr d\xi d\eta, \end{aligned}$$

where $(D^S u)^*$ is the adjoint of Du in the Hilbert space $\mathcal{H} \otimes \mathcal{H}$. We will denote

$$\delta(u) = \int_0^T u_s dS_s^H$$

for an adapted process u , and it is called Skorohod integral. Alós et al [16], we can obtain the relationship between the Skorohod and Young integral as follows

$$\int_0^T u_s dS_s^H = \int_0^T u_s \delta S_s^H + \int_0^T \int_0^T D_s u_t \psi(t, s) ds dt,$$

provided u has a bounded q -variation with $1 \leq q < \frac{1}{H}$ and $u \in \mathbb{D}^{1,2}(\mathcal{H})$ such that

$$\int_0^T \int_0^T D_s u_t \psi(t, s) ds dt < \infty.$$

Theorem 2.1. (Alós et al [16]). Let $0 < H < 1$ and let $f \in C^2(\mathbb{R})$ such that

$$\max\{|f(x)|, |f'(x)|, |f''(x)|\} \leq \kappa e^{\beta x^2}, \quad (2.4)$$

where κ and β are two positive constants with $\beta < \frac{1}{4}T^{-2H}$. Then we have

$$\begin{aligned} f(S_t^H) &= f(0) + \int_0^t f'(S_s^H) dS_s^H + H(2 - 2^{2H-1}) \\ &\quad \int_0^t f''(S_s^H) s^{2H-1} ds \end{aligned}$$

for all $t \in [0, T]$.

3 SOME BASIC ESTIMATES

Throughout this paper we assume that $\theta < 0$ and $\frac{1}{2} < H < 1$. Recall that the linear self-interacting diffusion with sub-fBm S^H defined by the stochastic differential equation

$$X_t^H = S_t^H - \theta \int_0^t \int_0^s (X_s^H - X_u^H) du ds + \nu t, \quad t \geq 0 \quad (3.1)$$

with $\theta < 0$. Define the kernel $(t, s) \mapsto h_\theta(t, s)$ as follows

$$h_\theta(t, s) = \begin{cases} 1 - \theta s e^{\frac{1}{2}\theta s^2} \int_s^t e^{-\frac{1}{2}\theta u^2} du, & t \geq s, \\ 0, & t < s \end{cases} \quad (3.2)$$

for $s, t \geq 0$. By the variation of constants method (see, Cranston and Le Jan [1]) or Itô's formula we may introduce the following representation:

$$X_t^H = \int_0^t h_\theta(t, s) dS_s^H + \nu \int_0^t h_\theta(t, s) ds \quad (3.3)$$

for $t \geq 0$.

The kernel function $(t, s) \mapsto h_\theta(t, s)$ with $\theta < 0$ admits the following properties (these properties are proved partly in Sun and Yan [12]):

- For all $s \geq 0$, the limit

$$\lim_{t \rightarrow \infty} (t e^{\frac{1}{2}\theta t^2} h_\theta(t, s)) = s e^{\frac{1}{2}\theta s^2} \quad (3.4)$$

for all $s \geq 0$.

- For all $t \geq s \geq 0$, we have

$$1 \leq h_\theta(t, s) \leq e^{-\frac{1}{2}\theta(t^2-s^2)}.$$

- For all $t \geq s, r \geq 0$, we have

$$h_\theta(t, 0) = h_\theta(t, t) = 1, \quad \int_s^t h_\theta(t, u) du = e^{\frac{1}{2}\theta s^2} \int_s^t e^{-\frac{1}{2}\theta u^2} du.$$

Lemma 3.1. Let $\theta < 0$ and define function

$$I_\theta(t) = -\theta t e^{\frac{1}{2}\theta t^2} \int_0^t e^{-\frac{1}{2}\theta u^2} du - 1.$$

We then have $\lim_{t \rightarrow \infty} t^2 I_\theta(t) = -\frac{1}{\theta}$ and

$$\lim_{t \rightarrow \infty} t^2 \left(1 + \theta t e^{-\frac{1}{2}\theta t^2} \int_t^\infty e^{\frac{1}{2}\theta u^2} du \right) = -\frac{1}{\theta}$$

Proof. This is simple calculus exercise.

Lemma 3.2. (Sun and Yan [12]). Let $\theta < 0$ and define the functions $t \mapsto I_\theta(t, n)$, $n = 1, 2, \dots$ as follows

$$I_\theta(t, 1) = -\theta t^2 I_\theta(t), \quad I_\theta(t, n+1) = -\theta t^2 [I_\theta(t, n) - (2n-1)!!].$$

Then we have

$$\lim_{t \rightarrow \infty} I_\theta(t, n) = (2n-1)!! \quad (3.5)$$

for every $n \geq 0$, where $(-1)! = 1$.

Lemma 3.3. Let $\theta < 0$. Then the integral

$$\Delta(H) = \int_0^\infty \int_0^\infty x y e^{\frac{1}{2}\theta(x^2+y^2)} \psi_H(x, y) dx dy \quad (3.6)$$

converges and as $t \rightarrow \infty$,

$$\lim_{t \rightarrow \infty} t^2 e^{-\theta t^2} E(X_t^H)^2 = \Delta(H).$$

Proof. An elementary may show that (3.6) converges for all $\theta < 0$. It follows from L'Hôpital's rule that

$$\begin{aligned} \lim_{t \rightarrow \infty} t^2 e^{\theta t^2} E(X_t^H)^2 &= \lim_{t \rightarrow \infty} t^2 e^{\theta t^2} \int_0^t \int_0^t h_\theta(t, x) h_\theta(t, y) \psi_H(x, y) dx dy \\ &= \lim_{t \rightarrow \infty} \frac{\theta^2}{t^{-2} e^{-\theta t^2}} \int_0^t dx \int_0^t x y e^{\frac{1}{2}\theta(x^2+y^2)} \psi_H(x, y) dy \int_x^t du \int_y^t e^{-\frac{1}{2}\theta(u^2+v^2)} dv \\ &= 2 \lim_{t \rightarrow \infty} \frac{\theta^2}{t^{-2} e^{-\theta t^2}} \int_0^t du \int_0^u dx \int_0^u dv \int_0^v d y x y e^{\frac{1}{2}\theta(x^2+y^2-u^2-v^2)} \psi_H(x, y) \\ &= \lim_{t \rightarrow \infty} \frac{-\theta}{t^{-1} e^{-\frac{1}{2}\theta t^2}} \int_0^t dx \int_0^t e^{-\frac{1}{2}\theta v^2} dv \int_0^v x y e^{\frac{1}{2}\theta(x^2+y^2)} \psi_H(x, y) dy \\ &= \lim_{t \rightarrow \infty} \frac{-\theta}{t^{-1} e^{-\frac{1}{2}\theta t^2}} \int_0^t e^{-\frac{1}{2}\theta v^2} dv \int_0^t dx \int_0^v x y e^{\frac{1}{2}\theta(x^2+y^2)} \psi_H(x, y) dy \\ &= \lim_{t \rightarrow \infty} \frac{-\theta}{t^{-1} e^{-\frac{1}{2}\theta t^2}} \int_0^t e^{-\frac{1}{2}\theta v^2} dv \int_0^v dx \int_0^v x y e^{\frac{1}{2}\theta(x^2+y^2)} \psi_H(x, y) dy \\ &= \int_0^\infty dx \int_0^\infty x y e^{\frac{1}{2}\theta(x^2+y^2)} \psi_H(x, y) dy, \end{aligned}$$

where we have used the following fact:

$$\begin{aligned} \lim_{t \rightarrow \infty} \frac{1}{t^{-1} e^{-\frac{1}{2}\theta t^2}} \int_0^t e^{-\frac{1}{2}\theta v^2} dv \int_v^t dx \int_0^v x y e^{\frac{1}{2}\theta(x^2+y^2)} \psi_H(x, y) dy \\ = \lim_{t \rightarrow \infty} \frac{1}{t^{-1} e^{-\frac{1}{2}\theta t^2}} \int_0^t dx \int_0^x e^{-\frac{1}{2}\theta v^2} dv \\ \int_0^v x y e^{\frac{1}{2}\theta(x^2+y^2)} \psi_H(x, y) dy = 0. \end{aligned}$$

This completes the proof.

Lemma 3.4. Let $\theta < 0$. Then, convergence

$$\begin{aligned} \lim_{t \rightarrow \infty} \frac{1}{t^{2-2H}} e^{-\theta t^2} \int_t^\infty \int_s^\infty s r e^{\frac{1}{2}\theta(s^2+r^2)} \psi_H(s, r) ds dr \\ = \frac{1}{4} (-\theta)^{-2H} \Gamma(2H+1). \end{aligned} \quad (3.7)$$

holds.

Proof. It follows from L'Hôpital's rule that

$$\begin{aligned} \lim_{t \rightarrow \infty} \frac{1}{t^{2-2H} e^{\theta t^2}} \int_t^\infty u e^{\frac{1}{2}\theta u^2} \left(\int_u^\infty v e^{\frac{1}{2}\theta v^2} \psi_H(u, v) dv \right) du \\ = -\frac{1}{2\theta} \lim_{t \rightarrow \infty} \frac{1}{t^{2-2H} e^{\frac{1}{2}\theta t^2}} \int_t^\infty v e^{\frac{1}{2}\theta v^2} \psi_H(t, v) dv \\ = -\lim_{t \rightarrow \infty} \frac{H(2H-1)}{2\theta t^{2-2H}} \int_t^\infty v e^{\frac{1}{2}\theta(v^2-t^2)} ((v-t)^{2H-2} - (v+t)^{2H-2}) dv \end{aligned}$$

for all $\theta < 0$ and $\frac{1}{2} < H < 1$. By making the change of variable $\frac{1}{2}\theta(v^2-t^2) = x$, we see that

$$\begin{aligned} \lim_{t \rightarrow \infty} \frac{1}{2\theta t^{2-2H}} \int_t^\infty v e^{\frac{1}{2}\theta(v^2-t^2)} ((v-t)^{2H-2} - (v+t)^{2H-2}) dv \\ = \lim_{t \rightarrow \infty} \frac{1}{2\theta^2 t^{2-2H}} \int_0^\infty e^{-x} \left\{ \left(\sqrt{t^2 + \frac{2x}{-\theta}} - t \right)^{2H-2} \right. \\ \left. - \left(\sqrt{t^2 + x} + t \right)^{2H-2} \right\} dx \\ = \lim_{t \rightarrow \infty} \frac{1}{2\theta^2 t^{2-2H}} \int_0^\infty e^{-x} \left(\frac{2x}{-\theta} \right)^{2H-2} \left(\sqrt{t^2 + \frac{2x}{-\theta}} + t \right)^{2-2H} dx \\ - \lim_{t \rightarrow \infty} \frac{1}{2\theta^2 t^{2-2H}} \int_0^\infty e^{-x} \left(\sqrt{t^2 + x} + t \right)^{2H-2} dx \\ = \frac{1}{2} (-\theta)^{-2H-1} \Gamma(2H-1) \end{aligned}$$

for all $\theta < 0$ and $\frac{1}{2} < H < 1$. This completes the proof.

Lemma 3.5. Let $\theta < 0$ and $0 \leq s < t \leq T$. We then have

$$c(t-s)^{2H} \leq E[(X_t^H - X_s^H)^2] \leq C(t-s)^{2H} \quad (3.8)$$

Proof. Given $0 \leq s < t \leq T$ and denote

$$\hat{X}_t^H = \int_0^t h_\theta(t, r) dS_r^H, \quad t \geq 0.$$

It follows that

$$\begin{aligned} E\left[\left(\hat{X}_t^H - \hat{X}_s^H\right)^2\right] &= E\left(\int_0^s [h_\theta(t, x) - h_\theta(s, x)] dS_x^H\right)^2 \\ &\quad + E\left(\int_s^t h_\theta(t, x) dS_x^H\right)^2 \\ &\quad + 2E\left(\int_s^t h_\theta(t, x) dS_y^H \int_0^s [h_\theta(t, x) - h_\theta(s, x)] dS_x^H\right). \end{aligned} \quad (3.9)$$

Now, we estimate the three terms. For the first term, we have

$$\begin{aligned} 0 &\leq E\left(\int_0^s [h_\theta(t, x) - h_\theta(s, x)] dS_x^H\right)^2 \\ &= \int_0^s \int_0^s (h_\theta(t, x) - h_\theta(s, x)) \\ &\quad (h_\theta(t, y) - h_\theta(s, y)) \psi_H(x, y) dx dy \\ &= \theta^2 \left(\int_s^t e^{-\frac{1}{2}\theta u^2} du\right)^2 \int_0^s \int_0^s x y e^{\frac{1}{2}\theta(x^2+y^2)} \psi_H(x, y) dx dy \\ &\leq \theta^2 s^2 (t-s)^2 e^{-\theta t^2} \int_0^s \int_0^s \psi_H(x, y) dx dy \\ &= \theta^2 s^2 (t-s)^2 e^{-\theta t^2} E(S_s^H)^2 \leq C_{H,T} (t-s)^2 \end{aligned}$$

for all $\theta < 0$ and $0 < s < t \leq T$. For the second term, we have

$$\begin{aligned} E\left(\int_s^t h_\theta(t, x) dS_x^H\right)^2 &= \int_s^t \int_s^t h_\theta(t, x) h_\theta(t, y) \psi_H(x, y) dx dy \\ &\leq e^{-\theta t^2} \int_s^t \int_s^t x y e^{\frac{1}{2}\theta(x^2+y^2)} \psi_H(x, y) dx dy \\ &\leq t^2 e^{-\theta t^2} \int_s^t \int_s^t \psi_H(x, y) dx dy \\ &\leq C_{H,T} (t-s)^{2H}. \end{aligned}$$

for all $\theta < 0$ and $0 < s < t \leq T$. Similarly, for the third term, we also prove

$$\begin{aligned} 0 &\leq E\left(\int_s^t h_\theta(t, y) dS_y^H \int_0^s [h_\theta(t, x) - h_\theta(s, x)] dS_x^H\right) \\ &= \int_s^t \int_0^s h_\theta(t, y) [h_\theta(t, x) - h_\theta(s, x)] \psi_H(x, y) dx dy \\ &\leq \theta^2 e^{-\frac{1}{2}\theta t^2} \left(\int_s^t e^{-\frac{1}{2}\theta u^2} du\right) \int_s^t y e^{\frac{1}{2}\theta y^2} dy \int_0^s x e^{\frac{1}{2}\theta x^2} \psi_H(x, y) dx \\ &\leq \theta^2 e^{-\theta t^2} (t-s) \int_s^t y e^{\frac{1}{2}\theta y^2} dy \int_0^s x e^{\frac{1}{2}\theta x^2} \psi_H(x, y) dx \\ &\leq C_{H,T} (t-s)^2 \end{aligned}$$

for all $\theta < 0$ and $0 < s < t \leq T$. Thus, we have obtained the following estimate:

$$E\left[\left(\hat{X}_t^H - \hat{X}_s^H\right)^2\right] \leq C_{H,T} |t-s|^{2H}$$

for all $\theta < 0$ and $0 < s < t \leq T$.

On the other hand, elementary calculations may show that

$$\int_0^s [h_\theta(t, r) - h_\theta(s, r)] dr = \theta \int_s^t e^{-\frac{1}{2}\theta u^2} du \int_0^s r e^{\frac{1}{2}\theta r^2} dr \leq C_{H,T} (t-s)$$

and

$$\int_s^t h_\theta(t, r) dr = e^{-\frac{1}{2}\theta s^2} \int_s^t e^{\frac{1}{2}\theta r^2} dr \leq C_{H,T} (t-s)$$

for all $\theta < 0$ and $0 < s < t \leq T$. It follows that

$$\begin{aligned} \left(\int_0^t h_\theta(t, r) dr - \int_0^s h_\theta(s, r) dr\right)^2 &= \left(\int_0^s [h_\theta(t, r) - h_\theta(s, r)] dr\right)^2 \\ &\quad + \left(\int_s^t h_\theta(t, r) dr\right)^2 + 2 \int_s^t h_\theta(t, r) dr \int_0^s [h_\theta(t, r) - h_\theta(s, r)] dr \\ &\leq C_{H,T} (t-s)^2 \end{aligned}$$

for all $\theta < 0$ and $0 < s < t \leq T$, which implies that

$$\begin{aligned} E\left[\left(X_t^{a,b} - X_s^{a,b}\right)^2\right] &= E\left[\left(\hat{X}_t^{a,b} - \hat{X}_s^{a,b}\right)^2\right] \\ &\quad + v^2 \left(\int_0^t h_\theta(t, r) dr - \int_0^s h_\theta(s, r) dr\right)^2 \\ &\leq C_{H,T} (t-s)^{2H} \end{aligned}$$

for all $\theta < 0$ and $0 < s < t \leq T$. Noting that the above calculations are invertible for all $\theta < 0$ and $0 < s < t \leq T$, one can obtain the left hand side in (3.8) and the lemma follows.

4 CONVERGENCE

In this section, we obtain the large time behaviors associated with the solution X^H to Eq. 3.1. From Lemma 3.5 and Guassinness, we find that the self-repelling diffusion $\{X_t^H, t \geq 0\}$ is H -Hölder continuous. So, the integral

$$\int_0^t s dX_s^H$$

exists with $t \geq 0$ as a Young integral and

$$tX_t^H = \int_0^t s dX_s^H + \int_0^t X_s^H ds$$

for all $t \geq 0$. Define the process $Y = \{Y_t, t \geq 0\}$ by

$$\begin{aligned} Y_t &:= \int_0^t (X_t^H - X_s^H) ds = tX_t^H - \int_0^t X_s^H ds = \int_0^t s dX_s^H \\ &= \int_0^t s dS_s^H - \int_0^t \theta s Y_s ds + \frac{1}{2} v t^2. \end{aligned}$$

By the variation of constants method, one can prove

$$Y_t = e^{-\frac{1}{2}\theta t^2} \int_0^t s e^{\frac{1}{2}\theta s^2} dS_s^H - \frac{v}{\theta} (e^{-\frac{1}{2}\theta t^2} - 1)$$

for all $t \geq 0$. Define Gaussian process $\xi^H = \{\xi_t^H, t \geq 0\}$ as follows

$$\xi_t^H := \int_0^t s e^{\frac{1}{2}\theta s^2} dS_s^H, \quad t \geq 0.$$

Lemma 4.1. Let $\theta < 0$ and $\frac{1}{2} < H < 1$. Then, the random variable

$$\xi_{\infty}^H := \int_0^{\infty} s e^{\frac{1}{2}\theta s^2} dS_s^H$$

exists as an element in L^2 . Moreover, ξ^H is H -Hölder continuous and $\xi_t^H \rightarrow \xi_{\infty}^H$ in L^2 and almost surely, as t tends to infinity.

Proof. This is simple calculus exercise. In fact, we have

$$\begin{aligned} E\left(\int_0^{\infty} x e^{\frac{1}{2}\theta x^2} dS_x^H\right)^2 &= \int_0^{\infty} \int_0^{\infty} x y e^{\frac{1}{2}\theta(x^2+y^2)} \psi_H(x, y) dx dy \\ &= 2 \int_0^{\infty} x e^{\frac{1}{2}\theta x^2} dx \int_0^x y e^{\frac{1}{2}\theta y^2} \psi_H(x, y) dy \\ &= 2H(2H-1) \int_0^{\infty} x e^{\frac{1}{2}\theta x^2} dx \\ &\quad \int_0^x y e^{\frac{1}{2}\theta y^2} ((x-y)^{2H-2} - (x+y)^{2H-2}) dy \\ &\leq 2H(2H-1) \int_0^{\infty} x e^{\frac{1}{2}\theta x^2} dx \\ &\quad \int_0^x ((x-y)^{2H-2} - (x+y)^{2H-2}) y dy \\ &= 2H(2H-1) C_H \int_0^{\infty} x^{2H+1} e^{\frac{1}{2}\theta x^2} dx \\ &= C_{\theta, H} \Gamma(2H+2) \end{aligned}$$

for all $\theta < 0$ and $\frac{1}{2} < H < 1$, which shows that the random variable ξ_{∞}^H exists as an element in L^2 .

Now, we show that the process $\xi^{a,b}$ is Hölder continuous. For all $0 < s < t$ by the inequality $e^{-x^2} x \leq C$ for all $x \geq 0$, we have

$$\begin{aligned} E(\xi_t^H - \xi_s^H)^2 &= E\left(\int_s^t x e^{\frac{1}{2}\theta x^2} dS_x^H\right)^2 \\ &= \int_s^t \int_s^t x y e^{\frac{1}{2}\theta(x^2+y^2)} \psi_H(x, y) dx dy \\ &= 2 \int_s^t x e^{\frac{1}{2}\theta x^2} dx \int_s^x y e^{\frac{1}{2}\theta y^2} \psi_H(x, y) dy \\ &= 2H(2H-1) \int_s^t x e^{\frac{1}{2}\theta x^2} dx \int_s^x y e^{\frac{1}{2}\theta y^2} ((x-y)^{2H-2} \\ &\quad - (x+y)^{2H-2}) dy \\ &\leq 2HC_{\theta}(2H-1) \int_s^t dx \int_s^x (x-y)^{2H-2} dy \\ &= C_{\theta, H} (t-s)^{2H}. \end{aligned}$$

Thus, the normality of ξ^H implies that

$$E(\xi_t^H - \xi_s^H)^{2n} \leq C_{\theta, H, n} (t-s)^{2nH}$$

for all $0 \leq s < t$, $\frac{1}{2} < H < 1$ and integer numbers $n \geq 1$, and the Hölder continuity follows.

Nextly, we check the $\xi_t^{a,b}$ converges to ξ_{∞}^H in L^2 . This follows from the next estimate:

$$\begin{aligned} E(\xi_t^H - \xi_{\infty}^H)^2 &= \int_t^{\infty} \int_t^{\infty} x y e^{\frac{1}{2}\theta(x^2+y^2)} \psi_H(x, y) dx dy \\ &= 2 \int_t^{\infty} \int_t^x x y e^{\frac{1}{2}\theta(x^2+y^2)} \psi_H(x, y) dx dy \\ &\leq 2e^{\frac{1}{2}\theta t^2} \int_t^{\infty} x e^{\frac{1}{2}\theta x^2} dx \int_t^x y \psi_H(x, y) dy \\ &\leq 2e^{\frac{1}{2}\theta t^2} \int_t^{\infty} x e^{\frac{1}{2}\theta x^2} dx \int_0^x y \psi_H(x, y) dy \\ &\leq 2H(2H-1) e^{\frac{1}{2}\theta t^2} \\ &\quad \cdot \int_t^{\infty} x e^{\frac{1}{2}\theta x^2} dx \int_0^x y ((x-y)^{2H-2} \\ &\quad - (x+y)^{2H-2}) dy \\ &\leq 2H(2H-1) e^{\frac{1}{2}\theta t^2} \cdot \int_t^{\infty} x e^{\frac{1}{2}\theta x^2} dx \int_0^x y (x-y)^{2H-2} dy \\ &= 2H(2H-1) \left(\int_0^1 u (1-u)^{2H-2} du \right) e^{\frac{1}{2}\theta t^2} \\ &\quad \int_t^{\infty} x^{2H+1} e^{\frac{1}{2}\theta x^2} dx \rightarrow 0, \end{aligned} \quad (4.1)$$

as t tends to infinity.

Finally, we check the $\xi_t^{a,b}$ converges to ξ_{∞}^H almost surely. By integration by parts we see that

$$\xi_t^H - \xi_{\infty}^H = \int_t^{\infty} s e^{\frac{1}{2}\theta s^2} dS_s^H = -t e^{\frac{1}{2}\theta t^2} S_t^H - \int_t^{\infty} (1 + \theta s^2) e^{\frac{1}{2}\theta s^2} S_s^H ds \quad (4.2)$$

for all $t \geq 0$. Elementary may check that the convergence

$$\eta_t^H := \int_t^{\infty} (1 + \theta s^2) e^{\frac{1}{2}\theta s^2} S_s^H ds \xrightarrow{a.s.} 0$$

holds almost surely, as t tends to infinity. In fact, by inequality

$$\int_t^{\infty} s^{\alpha} e^{\frac{1}{2}\theta s^2} ds \leq C t^{\alpha-1} e^{\frac{1}{2}\theta t^2}, \quad \alpha > -1,$$

with $t \geq 0$, we may show that

$$\begin{aligned} E\left(\sup_{n \leq t < n+1} |\eta_t^H|\right) &\leq \int_n^{\infty} \int_n^{\infty} (1 + \theta s^2) \\ &\quad (1 + \theta r^2) e^{\frac{1}{2}\theta(s^2+r^2)} E|S_s^H| |S_r^H| dr ds \\ &\leq C \left(\int_n^{\infty} s^{2+H} e^{\frac{1}{2}\theta s^2} ds \right)^2 \\ &\leq C n^{2+2H} e^{\theta n^2}, \end{aligned}$$

for all integer numbers $n \geq 1$, and hence

$$\sum_{n=0}^{\infty} P\left(\sup_{n \leq t < n+1} |\eta_t^H|^2 \geq \varepsilon\right) \leq C\varepsilon^{-2} \sum_{n=0}^{\infty} n^{2+2H} e^{\theta n^2} < \infty.$$

Thus, Borel-Cantelli's lemma implies that η_t^H converges to zero almost surely as t tends to infinity, and the lemma follows from (4.2).

Corollary 4.1. For all $\gamma > 0$, we have

$$t^\gamma (\xi_t^H - \xi_\infty^H) = t^\gamma \int_t^\infty s e^{\frac{1}{2}\theta s^2} dS_s^H \rightarrow 0,$$

in L^2 and almost surely, as t tends to infinity.

Lemma 4.2. Let $\theta < 0$ and $\frac{1}{2} < H < 1$. Then, we have

$$\Lambda_\gamma(t, \theta) := t^{\gamma+1} e^{\frac{1}{2}\theta t^2} \int_0^t e^{-\frac{1}{2}\theta u^2} (\xi_\infty^{a,b} - \xi_u^{a,b}) du \rightarrow 0$$

in L^2 and almost surely for every $\gamma \geq 0$, as t tends to infinity.

Proof. Given $0 < s \leq t$, $\theta < 0$ and denote

$$\begin{aligned} Y_\theta(s, t) &:= \int_0^t e^{-\frac{1}{2}\theta v^2} dv \int_v^\infty r e^{\frac{1}{2}\theta r^2} \psi_H(s, r) dr \\ &= \int_0^t r e^{\frac{1}{2}\theta r^2} \psi_H(s, r) dr \int_0^r e^{-\frac{1}{2}\theta v^2} dv \\ &\quad + \left(\int_0^t e^{-\frac{1}{2}\theta v^2} dv \right) \int_t^\infty r e^{\frac{1}{2}\theta r^2} \psi_H(s, r) dr \\ &\leq C \int_0^t r \psi_H(s, r) dr + \frac{C}{t} e^{-\frac{1}{2}\theta t^2} \int_t^\infty r e^{\frac{1}{2}\theta r^2} \psi_H(s, r) dr \\ &\leq C \left(\int_0^t r \psi_H(s, r) dr + (t-s)^{2H-2} t^{-1} \right), \end{aligned}$$

where we have used the fact

$$\int_0^x e^{-\frac{1}{2}\theta v^2} dv \leq \frac{C}{x} e^{-\frac{1}{2}\theta x^2}, \quad \forall x \geq 0$$

and estimates

$$\begin{aligned} \int_t^\infty r e^{\frac{1}{2}\theta r^2} \psi_H(s, r) dr &= H(2H-1) \int_t^\infty r ((r-s)^{2H-2} \\ &\quad - (s+r)^{2H-2}) e^{\frac{1}{2}\theta r^2} dr \\ &\leq H(2H-1) \int_t^\infty r (r-s)^{2H-2} e^{\frac{1}{2}\theta r^2} dr \\ &\leq H(2H-1) (t-s)^{2H-2} \int_t^\infty r e^{\frac{1}{2}\theta r^2} dr \\ &= \frac{H(2H-1)}{-\theta} (t-s)^{2H-2} e^{\frac{1}{2}\theta t^2}. \end{aligned}$$

It follows that

$$\begin{aligned} E|\Lambda_\gamma(t, \theta)|^2 &= t^{2\gamma+2} e^{\theta t^2} \int_0^t \int_0^t e^{-\frac{1}{2}\theta(u^2+v^2)} \\ &\quad \cdot E\left(\int_u^\infty s e^{\frac{1}{2}\theta s^2} dS_s^H\right) \left(\int_v^\infty r e^{\frac{1}{2}\theta r^2} dS_r^H\right) dudv \\ &= t^{2\gamma+2} e^{\theta t^2} \int_0^t \int_0^t e^{-\frac{1}{2}\theta(u^2+v^2)} dudv \\ &\quad \int_u^\infty \int_v^\infty r s e^{\frac{1}{2}\theta(r^2+s^2)} \psi_H(s, r) dr ds \\ &= t^{2\gamma+2} e^{\theta t^2} \int_0^t e^{-\frac{1}{2}\theta u^2} du \int_u^\infty s e^{\frac{1}{2}\theta s^2} Y_\theta(s, t) ds \\ &= t^{2\gamma+2} e^{\theta t^2} \int_0^t s e^{\frac{1}{2}\theta s^2} \psi_H(s, \theta) ds \int_0^s e^{-\frac{1}{2}\theta u^2} du \\ &\quad + t^{2\gamma+2} e^{\theta t^2} \int_t^\infty s e^{\frac{1}{2}\theta s^2} Y_\theta(s, t) ds \int_0^t e^{-\frac{1}{2}\theta u^2} du \\ &\leq t^{2\gamma+2} e^{\theta t^2} \int_0^t s^2 Y_\theta(s, t) ds \\ &\quad + t^{2\gamma+1} e^{\frac{1}{2}\theta t^2} \int_t^\infty s e^{\frac{1}{2}\theta s^2} Y_\theta(s, t) ds \\ &\rightarrow 0 \quad (t \rightarrow \infty), \end{aligned}$$

which shows that $\Lambda_\gamma(t, \theta)$ converges to zero in L^2 .

Now, we obtain the convergence with probability one. Noting that

$$\xi_\infty^H - \xi_u^H = \int_u^\infty s e^{\frac{1}{2}\theta s^2} dS_s^H$$

for all $u \geq 0$, we get

$$\begin{aligned} |\Lambda_\gamma(t, \theta)| &\leq t^{\gamma+1} e^{\frac{1}{2}\theta t^2} \int_0^t e^{-\frac{1}{2}\theta u^2} \left| \int_u^\infty s e^{\frac{1}{2}\theta s^2} dS_s^H \right| du \\ &\leq t^{\gamma+1} e^{\frac{1}{2}\theta t^2} \int_0^t e^{-\frac{1}{2}\theta u^2} \left(u |S_u^H| e^{\frac{1}{2}\theta u^2} + \int_u^\infty |S_s^H| (1-\theta s^2) |e^{\frac{1}{2}\theta s^2} ds \right) du \\ &= t^{\gamma+1} e^{\frac{1}{2}\theta t^2} \int_0^t u |S_u^H| du + t^{\gamma+1} e^{\frac{1}{2}\theta t^2} \int_0^t e^{-\frac{1}{2}\theta u^2} du \\ &\quad \int_u^\infty |S_s^H| (1-\theta s^2) |e^{\frac{1}{2}\theta s^2} ds \\ &= t^{\gamma+1} e^{\frac{1}{2}\theta t^2} \int_0^t u |S_u^H| du \\ &\quad + t^{\gamma+1} e^{\frac{1}{2}\theta t^2} \int_0^t |S_s^H| (1-\theta s^2) |e^{\frac{1}{2}\theta s^2} ds \int_0^s e^{-\frac{1}{2}\theta u^2} du \\ &\quad + t^{\gamma+1} e^{\frac{1}{2}\theta t^2} \int_t^\infty |S_s^H| (1-\theta s^2) |e^{\frac{1}{2}\theta s^2} ds \int_0^t e^{-\frac{1}{2}\theta u^2} du \\ &\leq t^{\gamma+1} e^{\frac{1}{2}\theta t^2} \int_0^t u |S_u^H| du + t^{\gamma+1} e^{\frac{1}{2}\theta t^2} \int_0^t |S_s^H| (1-\theta s^2) |s ds \\ &\quad + C_\theta t^\gamma \int_t^\infty |S_s^H| (1-\theta s^2) |e^{\frac{1}{2}\theta s^2} ds \\ &\rightarrow 0 \end{aligned}$$

almost surely for all $\gamma \geq 0$, $\theta < 0$ and $\frac{1}{2} < H < 1$, as t tends to infinity. This completes the proof.

The objects of this paper are to prove the following theorems which give the long time behaviors for X^H with $\frac{1}{2} < H < 1$.

Theorem 4.1. Let $\theta < 0$ and $\frac{1}{2} < H < 1$. Then, as $t \rightarrow \infty$, the convergence

$$J_0^H(t; \theta, \nu) := te^{\frac{1}{2}\theta t^2} X_t^H \rightarrow \xi_\infty^H - \frac{\nu}{\theta}$$

holds in L^2 and almost surely.

Proof. Given $t > 0$ and $\theta < 0$. Simple calculations may prove

$$\begin{aligned} J_0^H(t; \theta, \nu) &= te^{\frac{1}{2}\theta t^2} X_t^H \\ &= te^{\frac{1}{2}\theta t^2} \int_0^t h_\theta(t, s) dS_s^H + \nu te^{\frac{1}{2}\theta t^2} \int_0^t h_\theta(t, s) ds \\ &= te^{\frac{1}{2}\theta t^2} S_t^H - \theta t^2 e^{\frac{1}{2}\theta t^2} \int_0^t se^{\frac{1}{2}\theta s^2} \left(\int_s^t e^{-\frac{1}{2}\theta u^2} du \right) dS_s^H \\ &\quad + \nu te^{\frac{1}{2}\theta t^2} \int_0^t e^{-\frac{1}{2}\theta s^2} ds \\ &= te^{\frac{1}{2}\theta t^2} S_t^H - \theta te^{\frac{1}{2}\theta t^2} \int_0^t e^{-\frac{1}{2}\theta u^2} \left(\int_0^u se^{\frac{1}{2}\theta s^2} dS_s^H \right) du \\ &\quad + \nu te^{\frac{1}{2}\theta t^2} \int_0^t e^{-\frac{1}{2}\theta s^2} ds \\ &= te^{\frac{1}{2}\theta t^2} S_t^H - \theta te^{\frac{1}{2}\theta t^2} \int_0^t e^{-\frac{1}{2}\theta u^2} \xi_u^H du \\ &\quad + \nu te^{\frac{1}{2}\theta t^2} \int_0^t e^{-\frac{1}{2}\theta s^2} ds. \end{aligned} \quad (4.3)$$

It follows from Lemma 4.1, Corollary 4.1, and Lemma 4.2 that

$$\begin{aligned} J_0^H(t; \theta, \nu) - \left(\xi_\infty^H - \frac{\nu}{\theta} \right) &= te^{\frac{1}{2}\theta t^2} X_t^H - \left(\xi_\infty^H - \frac{\nu}{\theta} \right) \\ &= te^{\frac{1}{2}\theta t^2} S_t^H - \theta te^{\frac{1}{2}\theta t^2} \int_0^t e^{-\frac{1}{2}\theta u^2} (\xi_u^H - \xi_\infty^H) du \\ &\quad + \left(\xi_\infty^H - \frac{\nu}{\theta} \right) \left(-\theta te^{\frac{1}{2}\theta t^2} \int_0^t e^{-\frac{1}{2}\theta u^2} du - 1 \right) \rightarrow 0 \quad (t \rightarrow \infty) \end{aligned} \quad (4.4)$$

in L^2 and almost surely for all $\theta < 0$ and $\frac{1}{2} < H < 1$, as t tends to infinity.

Theorem 4.2. Define the processes $J^H(n, \theta, \nu) = \{J_t^H(n, \theta, \nu), t \geq 0\}$, $n \geq 1$ by

$$J_n^H(t; \theta, \nu) := \theta t^2 \left(J_{n-1}^H(t; \theta, \nu) - (2n-3)!! \left(\xi_\infty^H - \frac{\nu}{\theta} \right) \right),$$

$$n = 1, 2, \dots,$$

for all $t \geq 0$, where $(-1)!! = 1$. Then, the convergence

$$J_n^H(t; \theta, \nu) \rightarrow (2n-1)!! \left(\xi_\infty^H - \frac{\nu}{\theta} \right)$$

holds in L^2 and almost surely for every $n \geq 1$, as $t \rightarrow \infty$.

Proof. From the proof of Theorem 4.1, we find that the identities

$$\begin{aligned} J_0^H(t; \theta, \nu) - \left(\xi_\infty^H - \frac{\nu}{\theta} \right) &= te^{\frac{1}{2}\theta t^2} S_t^H + \theta te^{\frac{1}{2}\theta t^2} \int_0^t e^{-\frac{1}{2}\theta u^2} (\xi_u^H - \xi_\infty^H) du \\ &\quad + \left(\xi_\infty^H - \frac{\nu}{\theta} \right) \left(\theta te^{\frac{1}{2}\theta t^2} \int_0^t e^{-\frac{1}{2}\theta u^2} du - 1 \right), \\ J_n^H(t; \theta, \nu) &= \left(\xi_\infty^H - \frac{\nu}{\theta} \right) I_n(t, \theta) + t(\theta t^2)^n e^{-\frac{1}{2}\theta t^2} S_t^H \\ &\quad + \theta t(\theta t^2)^n e^{\frac{1}{2}\theta t^2} \int_0^t e^{\frac{1}{2}\theta u^2} (\xi_u^H - \xi_\infty^H) du. \end{aligned}$$

holds for all $t > 0$, $n \geq 1$ and $\theta < 0$, where $I_n(t, \theta)$ is given in Lemma 3.2. Thus, the theorem follows from Lemma 4.1, Corollary 4.1, Lemma 4.2 and Theorem 4.1.

5 SIMULATION

We have applied our results to the following linear self-repelling diffusion driven by a sub-fBm S^H with $\frac{1}{2} < H < 1$:

$$dX_t^H = dS_t^H - \theta \left(\int_0^t (X_t^H - X_s^H) ds \right) dt + \nu dt, \quad X_0^H = 0,$$

where $\theta < 0$ and $\nu \in \mathbb{R}$ are two parameters. We will simulate the process with $\nu = 0$ in the following cases:

- $H = 0.7$ and $\theta = -1$, $\theta = -10$, and $\theta = -100$, respectively (see, **Figure 1**, **Figure 2**, **Figure 3**, and **Table 1**, **Table 2**, **Table 3**);
- $H = 0.5$ and $\theta = -1$, $\theta = -10$, and $\theta = -100$, respectively (see, **Figure 4**, **Figure 5**, **Figure 6**, and **Table 4**, **Table 5**, **Table 6**);

Remark 1. From the following numerical results, we can find that it is important to study the estimates of parameters θ and ν .

DATA AVAILABILITY STATEMENT

The original contributions presented in the study are included in the article/Supplementary Material, further inquiries can be directed to the corresponding author.

AUTHOR CONTRIBUTIONS

All authors listed have made a substantial, direct, and intellectual contribution to the work and approved it for publication.

FUNDING

This study was funded by the National Natural Science Foundation of China (NSFC), grant no. 11971101.

REFERENCES

- Cranston M, Le Jan Y. Self Attracting Diffusions: Two Case Studies. *Math Ann* (1995) 303:87–93. doi:10.1007/bf01460980
- Durrett RT, Rogers LCG. Asymptotic Behavior of Brownian Polymers. *Probab Th Rel Fields* (1992) 92:337–49. doi:10.1007/bf01300560
- Pemantle R. Phase Transition in Reinforced Random Walk and RWRE on Trees. *Ann Probab* (1988) 16:1229–41. doi:10.1214/aop/1176991687
- Benaïm M, Ledoux M, Raimond O. Self-interacting Diffusions. *Probab Theor Relat Fields* (2002) 122:1–41. doi:10.1007/s004400100161
- Benaïm M, Ciotir I, Gauthier C-E. Self-repelling Diffusions via an Infinite Dimensional Approach. *Stoch Pde: Anal Comp* (2015) 3:506–30. doi:10.1007/s40072-015-0059-5
- Cranston M, Mountford TS. The strong Law of Large Numbers for a Brownian Polymer. *Ann Probab* (1996) 24:1300–23. doi:10.1214/aop/1065725183
- Gauthier C-E. Self Attracting Diffusions on a Sphere and Application to a Periodic Case. *Electron Commun Probab* (2016) 21(No. 53):1–12. doi:10.1214/16-ecp4547
- Herrmann S, Roynette B. Boundedness and Convergence of Some Self-Attracting Diffusions. *Mathematische Annalen* (2003) 325:81–96. doi:10.1007/s00208-002-0370-0
- Herrmann S, Scheutzw M. Rate of Convergence of Some Self-Attracting Diffusions. *Stochastic Process their Appl* (2004) 111:41–55. doi:10.1016/j.spa.2003.10.012
- Mountford T, Tarrés P. An Asymptotic Result for Brownian Polymers. *Ann Inst H Poincaré Probab Statist* (2008) 44:29–46. doi:10.1214/07-aihp113
- Shen L, Xia X, Yan L. Least Squares Estimation for the Linear Self-Repelling Diffusion Driven by α -stable Motions. *Appear Statist Probab Lett* (2021) 181: 109259. doi:10.1016/j.spl.2021.109259
- Sun X, Yan L. A Convergence on the Linear Self-Interacting Diffusion Driven by α -stable Motion. *Stochastics* 93(2021):1186–1208. doi:10.1080/17442508.2020.1869239
- Yan L, Sun Y, Lu Y. On the Linear Fractional Self-Attracting Diffusion. *J Theor Probab* (2008) 21:502–16. doi:10.1007/s10959-007-0113-y
- Sun X, Yan L. The Laws of Large Numbers Associated with the Linear Self-Attracting Diffusion Driven by Fractional Brownian Motion and Applications. *J Theoret Prob* (2021). [Epub of Print]. doi:10.1007/s10959-021-01126-0
- Gan Y, Yan L. Least Squares Estimation for the Linear Self-Repelling Diffusion Driven by Fractional Brownian Motion (In Chinese). *Sci CHINA Math* (2018) 48:1143–58. doi:10.1360/scm-2017-0387
- Alós E, Mazet O, Nualart D. Stochastic Calculus with Respect to Gaussian Processes. *Ann Prob* (2001) 29:766–801. doi:10.1214/aop/1008956692
- Bojdecki T, Gorostiza LG, Talarczyk A. Some Extensions of Fractional Brownian Motion and Sub-fractional Brownian Motion Related to Particle Systems. *Elect Comm Probab* (2007) 12:161–72. doi:10.1214/ecp.v12-1272
- Bojdecki T, Gorostiza LG, Talarczyk A. Sub-fractional Brownian Motion and its Relation to Occupation Times. *Stat Probab Lett* (2004) 69:405–19. doi:10.1016/j.spl.2004.06.035
- Bojdecki T, Gorostiza LG, Talarczyk A. Occupation Time Limits of Inhomogeneous Poisson Systems of Independent Particles. *Stochastic Process their Appl* (2008) 118:28–52. doi:10.1016/j.spa.2007.03.008
- Bojdecki T, Gorostiza LG, Talarczyk A. Self-Similar Stable Processes Arising from High-Density Limits of Occupation Times of Particle Systems. *Potential Anal* (2008) 28:71–103. doi:10.1007/s11118-007-9067-z
- Li M. Modified Multifractional Gaussian Noise and its Application. *Phys Scr* (2021) 96(1212):125002. doi:10.1088/1402-4896/ac1cf6
- Li M. Generalized Fractional Gaussian Noise and its Application to Traffic Modeling. *Physica A* 579(202122):1236137. doi:10.1016/j.physa.2021.126138
- Li M. Multi-fractional Generalized Cauchy Process and its Application to Teletraffic. *Physica A: Stat Mech its Appl* (2020) 550(14):123982. doi:10.1016/j.physa.2019.123982
- Li M. Fractal Time Series-A Tutorial Review. *Math Probl Eng* (2010) 2010:26. Article ID 157264. doi:10.1155/2010/157264
- Shen G, Yan L. An Approximation of Subfractional Brownian Motion. *Commun Stat - Theor Methods* (2014) 43:1873–86. doi:10.1080/03610926.2013.769598
- Shen G, Yan L. Estimators for the Drift of Subfractional Brownian Motion. *Commun Stat - Theor Methods* (2014) 43:1601–12. doi:10.1080/03610926.2012.697243
- Sun X, Yan L. A central Limit Theorem Associated with Sub-fractional Brownian Motion and an Application (In Chinese). *Sci Sin Math* (2017) 47:1055–1076. doi:10.1360/scm-2016-0748
- Tudor C. Some Properties of the Sub-fractional Brownian Motion. *Stochastics* (2007) 79:431–48. doi:10.1080/17442500601100331
- Tudor C. Inner Product Spaces of Integrands Associated to Subfractional Brownian Motion. *Stat Probab Lett* (2008) 78:2201–9. doi:10.1016/j.spl.2008.01.087
- Tudor C. On the Wiener Integral with Respect to a Sub-fractional Brownian Motion on an Interval. *J Math Anal Appl* (2009) 351:456–68. doi:10.1016/j.jmaa.2008.10.041
- Tudor C. Some Aspects of Stochastic Calculus for the Sub-fractional Brownian Motion. *Ann Univ Bucuresti Mathematica* (2008) 24:199–230.
- Ciprian A. Tudor, Analysis Of Variations For Self-Similar Processes. Heidelberg, New York: Springer (2013).
- Yan L, He K, Chen C. The Generalized Bouleau-Yor Identity for a Sub-fractional Brownian Motion. *Sci China Math* (2013) 56:2089–116. doi:10.1007/s11425-013-4604-2
- Yan L, Shen G. On the Collision Local Time of Sub-fractional Brownian Motions. *Stat Probab Lett* (2010) 80:296–308. doi:10.1016/j.spl.2009.11.003
- Yan L, Shen G, He K. Itô's Formula for the Sub-fractional Brownian Motion. *Comm Stochastic Anal* (2011) 5:135–59. doi:10.31390/cosa.5.1.09
- Nualart D. *Malliavin Calculus and Related Topics*. 2nd ed. New York: Springer (2006).
- Bertoin J. Sur une intégrale pour les processus α -variation borné. *Ann Probab* (1989) 17:1521–35. doi:10.1214/aop/1176991171
- Föllmer H, Calcul d'Itô Sans Probabilités, *Azéme and Yor : Sénaire de Probabilités XV, Lecture Notes in Math*, No 50. Springer-Verlag (1980). p. 143–5.

Conflict of Interest: The authors declare that the research was conducted in the absence of any commercial or financial relationships that could be construed as a potential conflict of interest.

Publisher's Note: All claims expressed in this article are solely those of the authors and do not necessarily represent those of their affiliated organizations, or those of the publisher, the editors and the reviewers. Any product that may be evaluated in this article, or claim that may be made by its manufacturer, is not guaranteed or endorsed by the publisher.

Copyright © 2022 Gao, Guo, Jin and Yan. This is an open-access article distributed under the terms of the Creative Commons Attribution License (CC BY). The use, distribution or reproduction in other forums is permitted, provided the original author(s) and the copyright owner(s) are credited and that the original publication in this journal is cited, in accordance with accepted academic practice. No use, distribution or reproduction is permitted which does not comply with these terms.



Large Time Behavior on the Linear Self-Interacting Diffusion Driven by Sub-Fractional Brownian Motion II: Self-Attracting Case

Rui Guo¹, Han Gao^{2*}, Yang Jin³ and Litan Yan³

¹College of Information Science and Technology, Donghua University, Shanghai, China, ²College of Fashion and Art Design, Donghua University, Shanghai, China, ³Department of Statistics, College of Science, Donghua University, Shanghai, China

In this study, as a continuation to the studies of the self-interaction diffusion driven by subfractional Brownian motion S^H , we analyze the asymptotic behavior of the linear self-attracting diffusion:

$$dX_t^H = dS_t^H - \theta \left(\int_0^t (X_s^H - X_t^H) ds \right) dt + \nu dt, \quad X_0^H = 0,$$

OPEN ACCESS

Edited by:

Ming Li,
Zhejiang University, China

Reviewed by:

Xiangfeng Yang,
Linköping University, Sweden
Yu Sun,
Our Lady of the Lake University,
United States

*Correspondence:

Han Gao
1061760802@qq.com

Specialty section:

This article was submitted to
Interdisciplinary Physics,
a section of the journal
Frontiers in Physics

Received: 09 October 2021

Accepted: 19 November 2021

Published: 25 January 2022

Citation:

Guo R, Gao H, Jin Y and Yan L (2022)
Large Time Behavior on the Linear Self-
Interacting Diffusion Driven by Sub-
Fractional Brownian Motion II: Self-
Attracting Case.
Front. Phys. 9:791858.
doi: 10.3389/fphy.2021.791858

where $\theta > 0$ and $\nu \in \mathbb{R}$ are two parameters. When $\theta < 0$, the solution of this equation is called self-repelling. Our main aim is to show the solution X^H converges to a normal random variable X_∞^H with mean zero as t tends to infinity and obtain the speed at which the process X^H converges to X_∞^H as t tends to infinity.

Keywords: subfractional Brownian motion, self-attracting diffusion, law of large numbers, Malliavin calculus, asymptotic distribution

1 INTRODUCTION

In a previous study (I) (see [12]), as an extension to classical result, we considered the linear self-interacting diffusion as follows:

$$X_t^H = S_t^H - \theta \int_0^t \int_0^s (X_s^H - X_u^H) du ds + \nu t, \quad t \geq 0, \quad (1)$$

with $\theta \neq 0$, where θ and ν are two real numbers, and S^H is a sub-fBm with the Hurst parameter $\frac{1}{2} \leq H < 1$. The solution of Eq. 1 is called self-repelling if $\theta < 0$ and is called self-attracting if $\theta > 0$. When $\theta < 0$, in a previous study (I), we showed that the solution X^H diverges to infinity as t tends to infinity and

$$J_0^H(t; \theta, \nu) := t e^{\frac{1}{2}\theta t^2} X_t^H \rightarrow \xi_\infty^H - \frac{\nu}{\theta}$$

and

$$J_n^H(t; \theta, \nu) := \theta t^2 \left(J_{n-1}^H(t; \theta, \nu) - (2n-3)!! \left(\xi_\infty^H - \frac{\nu}{\theta} \right) \right) \rightarrow (2n-1)!! \left(\xi_\infty^H - \frac{\nu}{\theta} \right)$$

in L^2 and almost surely, for all $n = 1, 2, \dots$, where $(-1)!! = 1$ and

$$\xi_{\infty}^H = \int_0^{\infty} s e^{\frac{1}{2}\theta s^2} dS_s^H.$$

In the present study, we consider the case $\theta > 0$ and study its large time behaviors.

Let us recall the main results concerning the system (Eq. 1). When $H = \frac{1}{2}$, as a special case of path-dependent stochastic differential equations, in 1995, Cranston and Le Jan [8] introduced a linear self-attracting diffusion (Eq. 1) with $\theta > 0$. They showed that the process X_t converges in L^2 and almost surely as t tends infinity. This path-dependent stochastic differential equation was first developed by Durrett and Rogers [10] introduced in 1992 as a model for the shape of a growing polymer (Brownian polymer). The general form of this kind of model can be expressed as follows:

$$X_t = X_0 + B_t + \int_0^t \int_0^s f(X_s - X_u) du ds, \quad (2)$$

where B is a d -dimensional standard Brownian motion and f is Lipschitz continuity. X_t corresponds to the location of the end of the polymer at time t . Under some conditions, they established asymptotic behavior of the solution of the stochastic differential equation. The model is a continuous analog of the notion of edge (respectively, vertex) self-interacting random walk (see, e.g., Pemantle [22]). By using the local time of the solution process X , we can make it clear how the process X interacts with its own occupation density. In general, Eq. 2 defines a self-interacting diffusion without any assumption on f . We call it self-repelling (respectively, self-attracting) if, for all $x \in \mathbb{R}^d$, $x \cdot f(x) \geq 0$ (respectively, ≤ 0). More examples can be found in Benaïm et al. [2, 3], Cranston and Mountford [9], Gan and Yan [11], Gauthier [13], Herrmann and Roynette [14], Herrmann and Scheutzow [15], Mountford and Tarr [20], Sun and Yan [26, 27], Yan et al [34], and the references therein.

In this present study, our main aim is to expound and prove the following statements:

(I) For $\theta > 0$ and $\frac{1}{2} < H < 1$, the random variable

$$X_{\infty}^H = \int_0^{\infty} h_{\theta}(s) dS_s^H + \nu \int_0^{\infty} h_{\theta}(s) ds$$

exists as an element in L^2 , where the function is defined as follows:

$$h_{\theta}(s) = 1 - \theta s e^{\frac{1}{2}\theta s^2} \int_s^{\infty} e^{-\frac{1}{2}\theta u^2} du, \quad s \geq 0$$

with $\theta > 0$.

(II) For $\theta > 0$ and $\frac{1}{2} < H < 1$, we have

$$X_t^H \rightarrow X_{\infty}^H$$

in L^2 and almost surely as $t \rightarrow \infty$.

(III) For $\theta > 0$ and $\frac{1}{2} < H < 1$, we have

$$\frac{t^H}{\sqrt{\lambda_{H,\theta}}} (X_t^H - X_{\infty}^H) \rightarrow N(0, 1)$$

in distribution as $t \rightarrow \infty$, where

$$\lambda_{H,\theta} = \frac{1}{2} \Gamma(2H+1) \theta^{-2H}.$$

(IV) For $\theta > 0$ and $\frac{1}{2} < H < 1$, we have

$$Y_t^H = \int_0^t (X_t^H - X_s^H) ds, \quad t \geq 0.$$

Then the convergence

$$\frac{1}{T^{3-2H}} \int_0^T (Y_t^H)^2 dt \rightarrow \frac{H}{3-2H} \theta^{-2H} \Gamma(2H)$$

holds in L^2 as T tends to infinity.

This article is organized as follows. In Section 2, we present some preliminaries for sub-fBm and Malliavin calculus. In Section 3, we obtain some lemmas. In Section 4, we prove the main results given as before. In Section 5, we give some numerical results.

2 PRELIMINARIES

In this section, we briefly recall the definition and properties of stochastic integral with respect to sub-fBm. We refer to Alós et al [1], Nualart [21], and Tudor [31] for a complete description of stochastic calculus with respect to Gaussian processes.

As we pointed out in the previous study (I) (see [12]), the sub-fBm S^H is a rather special class of self-similar Gaussian processes such that $S_0^H = 0$ and

$$R^H(t, s) := E[S_t^H S_s^H] = s^{2H} + t^{2H} - \frac{1}{2} [(s+t)^{2H} + |t-s|^{2H}] \quad (3)$$

for all $s, t \geq 0$. For $H = 1/2$, S^H coincides with the standard Brownian motion B . S^H is neither a semimartingale nor a Markov process unless $H = 1/2$, so many of the powerful techniques from stochastic analysis are not available when dealing with S^H . As a Gaussian process, it is possible to construct a stochastic calculus of variations with respect to S^H . The sub-fBm appeared in Bojdecki et al [4] in a limit of occupation time fluctuations of a system of independent particles moving in \mathbb{R}^d according a symmetric α -stable Lévy process. More examples for sub-fBm and related processes can be found in Bojdecki et al. [4–7], Li [16–19], Shen and Yan [23, 24], Sun and Yan [25], C. A. Tudor [32], Tudor [28–31], C. A. Tudor [33], Yan et al [33, 35, 36], and the references therein.

The normality and Hölder continuity of the sub-fBm S^H imply that $t \mapsto S_t^H$ admits a bounded p_H variation on any finite interval with $p_H > \frac{1}{H}$. As an immediate result, one can define the Young integral of a process $u = \{u_t, t \geq 0\}$ with respect to a sub-fBm S^H

$$\int_0^t u_s dS_s^H$$

as the limit in probability of a Riemann sum. Clearly, when u is of bounded q_H variation on any finite interval with $q_H > 1$ and $\frac{1}{p_H} + \frac{1}{q_H} > 1$, the integral is well-defined and

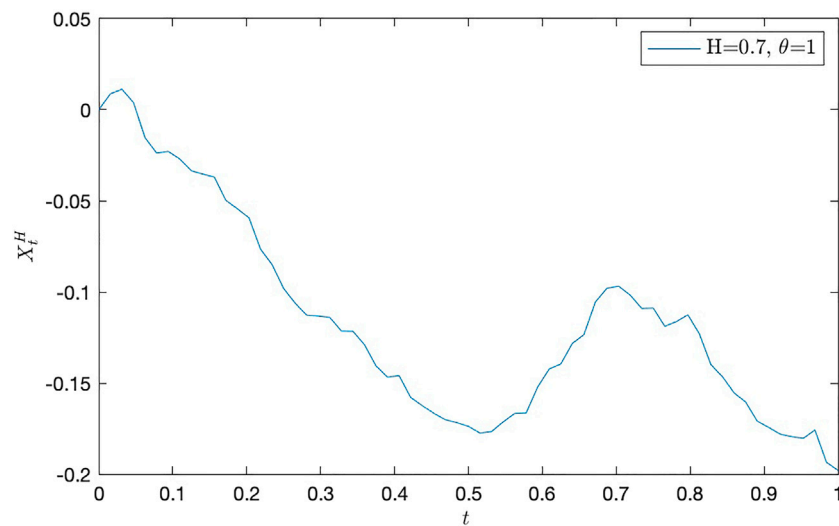


FIGURE 1 | Path of X_t^H with $\theta = 1$ and $H = 0.7$.

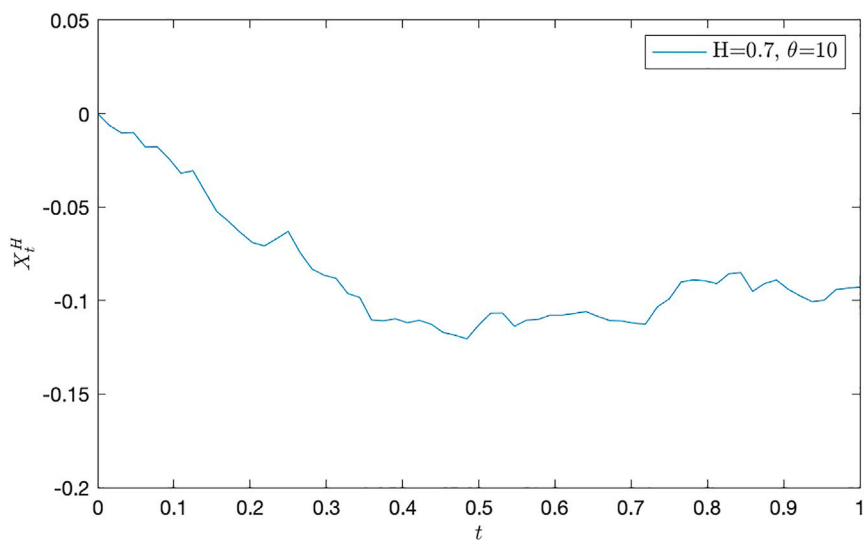


FIGURE 2 | Path of X_t^H with $\theta = 10$ and $H = 0.7$.

$$u_t S_t^H = \int_0^t u_s dS_s^H + \int_0^t S_s^H du_s$$

for all $t \geq 0$.

Let \mathcal{H} be the completion of the linear space \mathcal{E} generated by the indicator functions $1_{[0,t]}$, $t \in [0, T]$ with respect to the inner product:

$$\langle 1_{[0,s]}, 1_{[0,t]} \rangle_{\mathcal{H}} = R^H(t, s)$$

for $s, t \in [0, T]$. For every $\varphi \in \mathcal{H}$, we can define the Wiener integral with respect to S^H , denoted by

$$S^H(\varphi) = \int_0^T \varphi(s) dS_s^H$$

as a linear (isometric) mapping from \mathcal{H} onto \mathbb{S}^H by using the limit in probability of a *Riemann sum*, where \mathbb{S}^H is the Gaussian Hilbert space generating by S^H and

$$\|\varphi\|_{\mathcal{H}}^2 = E \left(\int_0^T \varphi(s) dS_s^H \right)^2 \quad (4)$$

for any $\varphi \in \mathcal{H}$. In particular, when $\frac{1}{2} < H < 1$, we can show that

$$\|\varphi\|_{\mathcal{H}}^2 = \int_0^T \int_0^T \varphi(t) \varphi(s) \psi_H(t, s) ds dt, \quad \forall \varphi \in \mathcal{H},$$

where

$$\psi_H(t, s) = \frac{\partial^2}{\partial t \partial s} R^H(t, s) = H(2H-1)(|t-s|^{2H-2} - |t+s|^{2H-2})$$

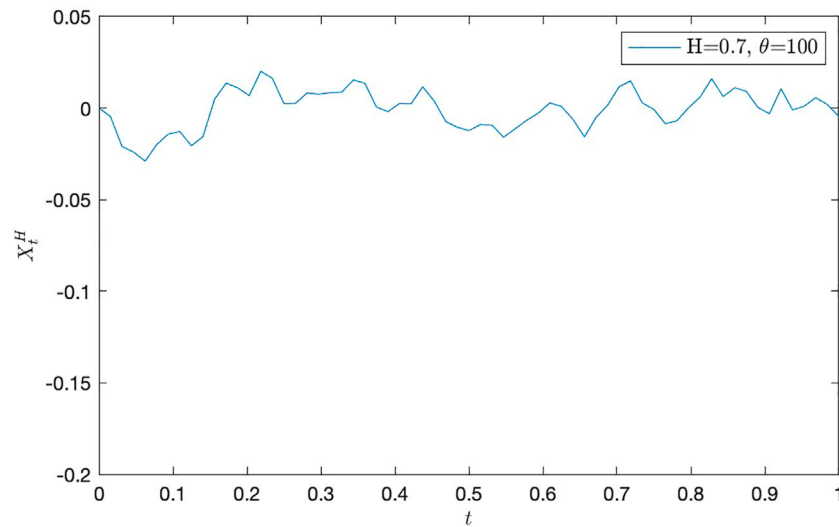


FIGURE 3 | Path of X_t^H with $\theta = 100$ and $H = 0.7$.

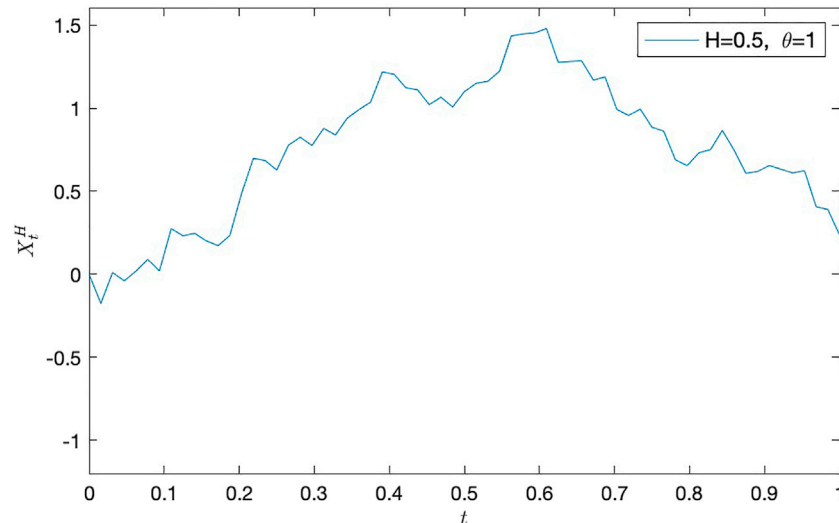


FIGURE 4 | Path of X_t^H with $\theta = 1$ and $H = 0.5$.

for $s, t \in [0, T]$. Thus, when $\frac{1}{2} < H < 1$ if for every $T > 0$, the integral $\int_0^T \varphi(s) dS_s^H$ exists in L^2 and

$$\int_0^\infty \int_0^\infty \varphi(t) \varphi(s) \psi_H(t, s) ds dt < \infty,$$

we can define the integral as follows:

$$\int_0^\infty \varphi(s) dS_s^H$$

and

$$E \left(\int_0^\infty \varphi(s) dS_s^H \right)^2 = \int_0^\infty \int_0^\infty \varphi(t) \varphi(s) \psi_H(t, s) ds dt.$$

Let now D and δ be the (Malliavin) derivative and divergence operators associated with the sub-fBm S^H . And let $\mathbb{D}^{1,2}$ denote the Hilbert space with respect to the norm as follows:

$$\|F\|_{1,2} := \sqrt{E|F|^2 + E\|DF\|_{\mathcal{H}}^2}.$$

Then the duality relationship

$$E[F\delta(u)] = E\langle DF, u \rangle_{\mathcal{H}} \quad (5)$$

holds for any $F \in \mathbb{D}^{1,2}$ and $\mathbb{D}^{1,2} \subset \text{Dom}(\delta)$. Moreover, for any $u \in \mathbb{D}^{1,2}$, we have

$$\begin{aligned} E[\delta(u)^2] &= E\|u\|_{\mathcal{H}}^2 + E\langle Du, (Du)^* \rangle_{\mathcal{H} \otimes \mathcal{H}} \\ &= E\|u\|_{\mathcal{H}}^2 + E \int_{[0,T]^4} D_\xi u_r D_\eta u_s \psi_H(\eta, r) \psi_H(\xi, s) ds dr d\xi d\eta, \end{aligned}$$

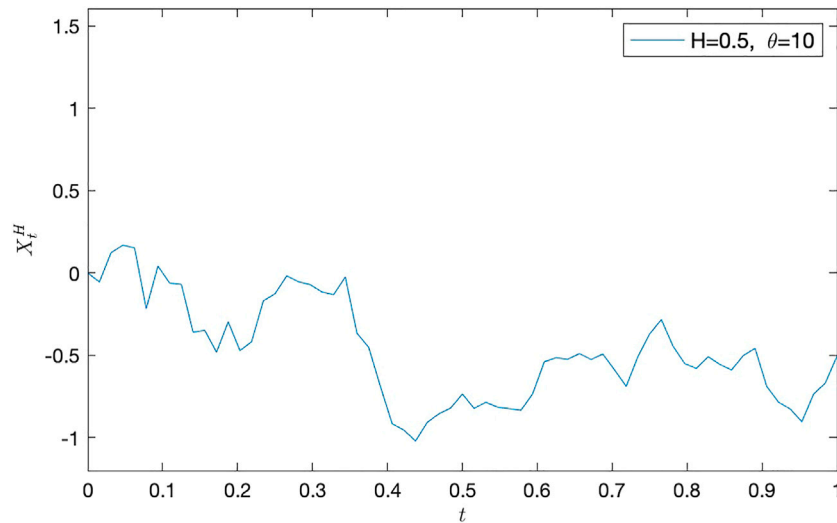


FIGURE 5 | Path of X^H with $\theta = 10$ and $H = 0.5$.

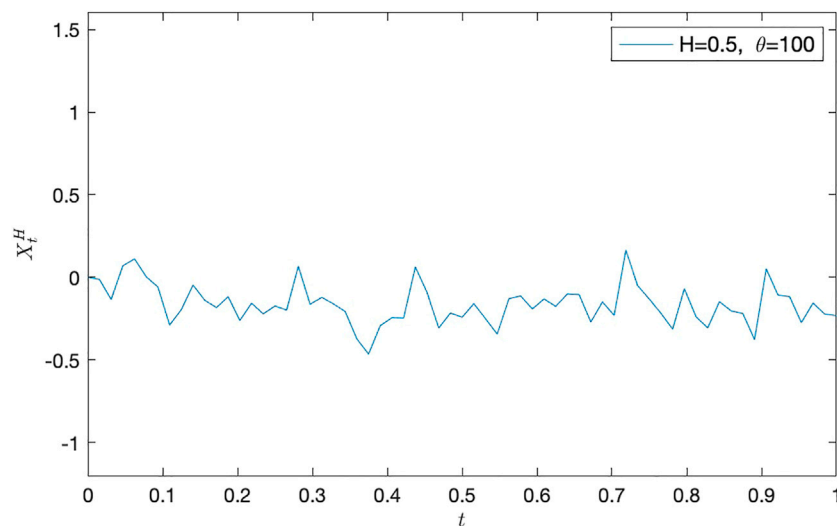


FIGURE 6 | Path of X^H with $\theta = 100$ and $H = 0.5$.

where $(Du)^*$ is the adjoint of Du in the Hilbert space given as follows: $\mathcal{H} \otimes \mathcal{H}$. We denote

$$\delta(u) = \int_0^T u_s \delta S_s^H$$

for an adapted process u , and it is called the Skorohod integral. By using Alós et al [1], we can obtain the relationship between the Skorohod and the Young integral as follows:

$$\int_0^T u_s dS_s^H = \int_0^T u_s \delta S_s^H + \int_0^T \int_0^T D_s u_t \psi_H(t, s) ds dt,$$

provided u has a bounded q variation with $1 \leq q < \frac{1}{H}$ and $u \in \mathbb{D}^{1,2}$ such that

$$\int_0^T \int_0^T D_s u_t \psi_H(t, s) ds dt < \infty.$$

3 SOME BASIC ESTIMATES

For simplicity, we throughout let C stand for a positive constant which depends only on its superscripts, and its value may be different in different appearances, and this assumption is also suitable to c . Recall that the linear self-attracting diffusion with sub-fBm S^H is defined by the following stochastic differential equation:

$$X_t^H = S_t^H - \theta \int_0^t \int_0^s (X_s^H - X_u^H) du ds + \nu t, \quad t \geq 0 \quad (6)$$

TABLE 1 | Data of X_t^H with $\theta = 1$ and $H = 0.7$

| t | X_t^H | t | X_t^H | t | X_t^H |
|--------|---------|--------|---------|--------|---------|
| 0.0000 | 0.0000 | 0.3438 | -0.1216 | 0.6875 | -0.0979 |
| 0.0156 | 0.0087 | 0.3594 | -0.1290 | 0.7031 | -0.0968 |
| 0.0313 | 0.0113 | 0.3750 | -0.1406 | 0.7188 | -0.1017 |
| 0.0469 | 0.0039 | 0.3906 | -0.1467 | 0.7344 | -0.1090 |
| 0.0625 | -0.0153 | 0.4063 | -0.1459 | 0.7500 | -0.1088 |
| 0.0781 | -0.0238 | 0.4219 | -0.1579 | 0.7656 | -0.1188 |
| 0.0938 | -0.0229 | 0.4375 | -0.1624 | 0.7813 | -0.1163 |
| 0.1094 | -0.0270 | 0.4531 | -0.1666 | 0.7969 | -0.1125 |
| 0.1250 | -0.0335 | 0.4688 | -0.1701 | 0.8125 | -0.1231 |
| 0.1406 | -0.0353 | 0.4844 | -0.1717 | 0.8281 | -0.1400 |
| 0.1563 | -0.0370 | 0.5000 | -0.1738 | 0.8438 | -0.1465 |
| 0.1719 | -0.0498 | 0.5156 | -0.1774 | 0.8594 | -0.1554 |
| 0.1875 | -0.0544 | 0.5313 | -0.1766 | 0.8750 | -0.1604 |
| 0.2031 | -0.0593 | 0.5469 | -0.1713 | 0.8906 | -0.1709 |
| 0.2188 | -0.0765 | 0.5625 | -0.1667 | 0.9063 | -0.1743 |
| 0.2344 | -0.0850 | 0.5781 | -0.1664 | 0.9219 | -0.1781 |
| 0.2500 | -0.0981 | 0.5938 | -0.1521 | 0.9375 | -0.1794 |
| 0.2656 | -0.1062 | 0.6094 | -0.1422 | 0.9531 | -0.1803 |
| 0.2813 | -0.1127 | 0.6250 | -0.1395 | 0.9688 | -0.1758 |
| 0.2969 | -0.1132 | 0.6406 | -0.1282 | 0.9844 | -0.1935 |
| 0.3125 | -0.1140 | 0.6563 | -0.1234 | 1.0000 | -0.1980 |
| 0.3281 | -0.1214 | 0.6719 | -0.1054 | | |

TABLE 3 | Data of X_t^H with $\theta = 100$ and $H = 0.7$

| t | X_t^H | t | X_t^H | t | X_t^H |
|--------|---------|--------|---------|--------|---------|
| 0.0000 | 0.0000 | 0.3438 | 0.0153 | 0.6875 | 0.0015 |
| 0.0156 | -0.0047 | 0.3594 | 0.0135 | 0.7031 | 0.0116 |
| 0.0313 | -0.0210 | 0.3750 | 0.0005 | 0.7188 | 0.0148 |
| 0.0469 | -0.0241 | 0.3906 | -0.0020 | 0.7344 | 0.0027 |
| 0.0625 | -0.0290 | 0.4063 | 0.0025 | 0.7500 | -0.0008 |
| 0.0781 | -0.0200 | 0.4219 | 0.0023 | 0.7656 | -0.0086 |
| 0.0938 | -0.0143 | 0.4375 | 0.0116 | 0.7813 | -0.0069 |
| 0.1094 | -0.0129 | 0.4531 | 0.0038 | 0.7969 | 0.0001 |
| 0.1250 | -0.0206 | 0.4688 | -0.0074 | 0.8125 | 0.0060 |
| 0.1406 | -0.0157 | 0.4844 | -0.0105 | 0.8281 | 0.0160 |
| 0.1563 | 0.0047 | 0.5000 | -0.0124 | 0.8438 | 0.0062 |
| 0.1719 | 0.0136 | 0.5156 | -0.0090 | 0.8594 | 0.0111 |
| 0.1875 | 0.0110 | 0.5313 | -0.0094 | 0.8750 | 0.0090 |
| 0.2031 | 0.0067 | 0.5469 | -0.0160 | 0.8906 | 0.0003 |
| 0.2188 | 0.0200 | 0.5625 | -0.0114 | 0.9063 | -0.0032 |
| 0.2344 | 0.0162 | 0.5781 | -0.0067 | 0.9219 | 0.0105 |
| 0.2500 | 0.0024 | 0.5938 | -0.0028 | 0.9375 | -0.0011 |
| 0.2656 | 0.0025 | 0.6094 | 0.0028 | 0.9531 | 0.0010 |
| 0.2813 | 0.0082 | 0.6250 | 0.0009 | 0.9688 | 0.0056 |
| 0.2969 | 0.0076 | 0.6406 | -0.0062 | 0.9844 | 0.0019 |
| 0.3125 | 0.0083 | 0.6563 | -0.0158 | 1.0000 | -0.0046 |
| 0.3281 | 0.0086 | 0.6719 | -0.0051 | | |

TABLE 2 | Data of X_t^H with $\theta = 10$ and $H = 0.7$

| t | X_t^H | t | X_t^H | t | X_t^H |
|--------|---------|--------|---------|--------|---------|
| 0.0000 | 0.0000 | 0.3438 | -0.0983 | 0.6875 | -0.1109 |
| 0.0156 | -0.0064 | 0.3594 | -0.1104 | 0.7031 | -0.1121 |
| 0.0313 | -0.0104 | 0.3750 | -0.1108 | 0.7188 | -0.1126 |
| 0.0469 | -0.0101 | 0.3906 | -0.1098 | 0.7344 | -0.1034 |
| 0.0625 | -0.0179 | 0.4063 | -0.1119 | 0.7500 | -0.0991 |
| 0.0781 | -0.0177 | 0.4219 | -0.1106 | 0.7656 | -0.0901 |
| 0.0938 | -0.0242 | 0.4375 | -0.1126 | 0.7813 | -0.0890 |
| 0.1094 | -0.0319 | 0.4531 | -0.1170 | 0.7969 | -0.0894 |
| 0.1250 | -0.0306 | 0.4688 | -0.1185 | 0.8125 | -0.0909 |
| 0.1406 | -0.0416 | 0.4844 | -0.1205 | 0.8281 | -0.0857 |
| 0.1563 | -0.0523 | 0.5000 | -0.1131 | 0.8438 | -0.0851 |
| 0.1719 | -0.0577 | 0.5156 | -0.1068 | 0.8594 | -0.0951 |
| 0.1875 | -0.0637 | 0.5313 | -0.1067 | 0.8750 | -0.0909 |
| 0.2031 | -0.0690 | 0.5469 | -0.1137 | 0.8906 | -0.0890 |
| 0.2188 | -0.0708 | 0.5625 | -0.1105 | 0.9063 | -0.0940 |
| 0.2344 | -0.0670 | 0.5781 | -0.1101 | 0.9219 | -0.0976 |
| 0.2500 | -0.0630 | 0.5938 | -0.1078 | 0.9375 | -0.1006 |
| 0.2656 | -0.0744 | 0.6094 | -0.1078 | 0.9531 | -0.0998 |
| 0.2813 | -0.0831 | 0.6250 | -0.1069 | 0.9688 | -0.0941 |
| 0.2969 | -0.0865 | 0.6406 | -0.1059 | 0.9844 | -0.0933 |
| 0.3125 | -0.0881 | 0.6563 | -0.1085 | 1.0000 | -0.0928 |
| 0.3281 | -0.0962 | 0.6719 | -0.1107 | | |

TABLE 4 | Data of X_t^H with $\theta = 1$ and $H = 0.5$

| t | X_t^H | t | X_t^H | t | X_t^H |
|--------|---------|--------|---------|--------|---------|
| 0.0000 | 0.0000 | 0.3438 | 0.9393 | 0.6875 | 1.1883 |
| 0.0156 | -0.1761 | 0.3594 | 0.9913 | 0.7031 | 0.9921 |
| 0.0313 | 0.0099 | 0.3750 | 1.0363 | 0.7188 | 0.9564 |
| 0.0469 | -0.0400 | 0.3906 | 1.2180 | 0.7344 | 0.9943 |
| 0.0625 | 0.0190 | 0.4063 | 1.2042 | 0.7500 | 0.8852 |
| 0.0781 | 0.0883 | 0.4219 | 1.1229 | 0.7656 | 0.8611 |
| 0.0938 | 0.0200 | 0.4375 | 1.1110 | 0.7813 | 0.6886 |
| 0.1094 | 0.2744 | 0.4531 | 1.0211 | 0.7969 | 0.6538 |
| 0.1250 | 0.2317 | 0.4688 | 1.0660 | 0.8125 | 0.7312 |
| 0.1406 | 0.2461 | 0.4844 | 1.0070 | 0.8281 | 0.7508 |
| 0.1563 | 0.2004 | 0.5000 | 1.0995 | 0.8438 | 0.8663 |
| 0.1719 | 0.1723 | 0.5156 | 1.1497 | 0.8594 | 0.7469 |
| 0.1875 | 0.2332 | 0.5313 | 1.1620 | 0.8750 | 0.6080 |
| 0.2031 | 0.4859 | 0.5469 | 1.2229 | 0.8906 | 0.6184 |
| 0.2188 | 0.6974 | 0.5625 | 1.4350 | 0.9063 | 0.6550 |
| 0.2344 | 0.6848 | 0.5781 | 1.4474 | 0.9219 | 0.6321 |
| 0.2500 | 0.6275 | 0.5938 | 1.4535 | 0.9375 | 0.6101 |
| 0.2656 | 0.7774 | 0.6094 | 1.4794 | 0.9531 | 0.6238 |
| 0.2813 | 0.8250 | 0.6250 | 1.2764 | 0.9688 | 0.4066 |
| 0.2969 | 0.7754 | 0.6406 | 1.2814 | 0.9844 | 0.3893 |
| 0.3125 | 0.8783 | 0.6563 | 1.2848 | 1.0000 | 0.2345 |
| 0.3281 | 0.8380 | 0.6719 | 1.1689 | | |

with $\theta > 0$. The kernel $(t, s) \mapsto h_\theta(t, s)$ is defined as follows:

$$h_\theta(t, s) = \begin{cases} 1 - \theta s e^{\frac{1}{2}\theta s^2} \int_s^t e^{-\frac{1}{2}\theta u^2} du, & t \geq s, \\ 0, & t < s \end{cases} \quad (7)$$

for $s, t \geq 0$. By the variation of constants method (see, Cranston and Le Jan [8]) or Itô's formula, we may introduce the following representation:

$$X_t^H = \int_0^t h_\theta(t, s) dS_s^H + \nu \int_0^t h_\theta(t, s) ds \quad (8)$$

for $t \geq 0$.

The kernel function $(t, s) \mapsto h_\theta(t, s)$ with $\theta > 0$ admits the following properties (these properties are proved partly in Cranston and Le Jan [8]):

- For all $s \geq 0$, the limit

TABLE 5 | Data of X_t^H with $\theta = 10$ and $H = 0.5$

| t | X_t^H | t | X_t^H | t | X_t^H |
|--------|---------|--------|---------|--------|---------|
| 0.0000 | 0.0000 | 0.3438 | -0.0247 | 0.6875 | -0.4927 |
| 0.0156 | -0.0548 | 0.3594 | -0.3666 | 0.7031 | -0.5894 |
| 0.0313 | 0.1227 | 0.3750 | -0.4522 | 0.7188 | -0.6890 |
| 0.0469 | 0.1679 | 0.3906 | -0.6907 | 0.7344 | -0.5079 |
| 0.0625 | 0.1515 | 0.4063 | -0.9154 | 0.7500 | -0.3703 |
| 0.0781 | -0.2177 | 0.4219 | -0.9541 | 0.7656 | -0.2832 |
| 0.0938 | 0.0411 | 0.4375 | -1.0205 | 0.7813 | -0.4455 |
| 0.1094 | -0.0617 | 0.4531 | -0.9069 | 0.7969 | -0.5515 |
| 0.1250 | -0.0697 | 0.4688 | -0.8553 | 0.8125 | -0.5799 |
| 0.1406 | -0.3592 | 0.4844 | -0.8201 | 0.8281 | -0.5093 |
| 0.1563 | -0.3489 | 0.5000 | -0.7357 | 0.8438 | -0.5561 |
| 0.1719 | -0.4818 | 0.5156 | -0.8220 | 0.8594 | -0.5892 |
| 0.1875 | -0.2966 | 0.5313 | -0.7852 | 0.8750 | -0.5017 |
| 0.2031 | -0.4717 | 0.5469 | -0.8146 | 0.8906 | -0.4580 |
| 0.2188 | -0.4175 | 0.5625 | -0.8239 | 0.9063 | -0.6895 |
| 0.2344 | -0.1693 | 0.5781 | -0.8337 | 0.9219 | -0.7846 |
| 0.2500 | -0.1265 | 0.5938 | -0.7353 | 0.9375 | -0.8257 |
| 0.2656 | -0.0178 | 0.6094 | -0.5397 | 0.9531 | -0.9034 |
| 0.2813 | -0.0536 | 0.6250 | -0.5152 | 0.9688 | -0.7364 |
| 0.2969 | -0.0714 | 0.6406 | -0.5245 | 0.9844 | -0.6692 |
| 0.3125 | -0.1158 | 0.6563 | -0.4899 | 1.0000 | -0.5061 |
| 0.3281 | -0.1322 | 0.6719 | -0.5258 | | |

TABLE 6 | Data of X_t^H with $\theta = 100$ and $H = 0.5$

| t | X_t^H | t | X_t^H | t | X_t^H |
|--------|---------|--------|---------|--------|---------|
| 0.0000 | 0.0000 | 0.3438 | -0.2074 | 0.6875 | -0.1493 |
| 0.0156 | -0.0129 | 0.3594 | -0.3732 | 0.7031 | -0.2308 |
| 0.0313 | -0.1348 | 0.3750 | -0.4649 | 0.7188 | 0.1644 |
| 0.0469 | 0.0697 | 0.3906 | -0.2925 | 0.7344 | -0.0500 |
| 0.0625 | 0.1115 | 0.4063 | -0.2445 | 0.7500 | -0.1317 |
| 0.0781 | 0.0029 | 0.4219 | -0.2467 | 0.7656 | -0.2182 |
| 0.0938 | -0.0589 | 0.4375 | 0.0628 | 0.7813 | -0.3137 |
| 0.1094 | -0.2888 | 0.4531 | -0.0917 | 0.7969 | -0.0691 |
| 0.1250 | -0.1956 | 0.4688 | -0.3072 | 0.8125 | -0.2391 |
| 0.1406 | -0.0469 | 0.4844 | -0.2162 | 0.8281 | -0.3062 |
| 0.1563 | -0.1391 | 0.5000 | -0.2418 | 0.8438 | -0.1478 |
| 0.1719 | -0.1833 | 0.5156 | -0.1593 | 0.8594 | -0.2034 |
| 0.1875 | -0.1175 | 0.5313 | -0.2509 | 0.8750 | -0.2193 |
| 0.2031 | -0.2616 | 0.5469 | -0.3442 | 0.8906 | -0.3769 |
| 0.2188 | -0.1568 | 0.5625 | -0.1295 | 0.9063 | 0.0515 |
| 0.2344 | -0.2215 | 0.5781 | -0.1130 | 0.9219 | -0.1076 |
| 0.2500 | -0.1736 | 0.5938 | -0.1915 | 0.9375 | -0.1173 |
| 0.2656 | -0.1985 | 0.6094 | -0.1313 | 0.9531 | -0.2746 |
| 0.2813 | 0.0674 | 0.6250 | -0.1758 | 0.9688 | -0.1556 |
| 0.2969 | -0.1633 | 0.6406 | -0.1008 | 0.9844 | -0.2232 |
| 0.3125 | -0.1219 | 0.6563 | -0.1049 | 1.0000 | -0.2320 |
| 0.3281 | -0.1610 | 0.6719 | -0.2703 | | |

$$h_\theta(s) := \lim_{t \rightarrow \infty} h_\theta(t, s) = 1 - \theta s e^{\frac{1}{2}\theta s^2} \int_s^\infty e^{-\frac{1}{2}\theta u^2} du \quad (9)$$

exists.

- For all $t \geq s \geq 0$, we have $h_\theta(s) \leq h_\theta(t, s)$, and

$$0 \leq h_\theta(s) \leq C_\theta \min\left\{1, \frac{1}{s^2}\right\}, \quad e^{-\frac{1}{2}\theta(t^2-s^2)} \leq h_\theta(t, s) \leq 1; \quad (10)$$

- For all $t \geq s, r \geq 0$ and $\theta \neq 0$, we have

$$h_\theta(t, 0) = h_\theta(t, t) = 1, \quad \int_s^t h_\theta(t, u) du = e^{\frac{1}{2}\theta s^2} \int_s^t e^{-\frac{1}{2}\theta u^2} du$$

and

$$|h_\theta(t, s) - h_\theta(s)| |h_\theta(t, r) - h_\theta(r)| \leq \frac{1}{t^2} s r e^{\frac{1}{2}\theta(s^2+r^2)} e^{-\theta t^2}; \quad (11)$$

- For all $t > 0$, we have

$$\left| \int_0^t [h_\theta(t, s) - h_\theta(s)] ds \right| \leq \frac{1}{\theta t}. \quad (12)$$

Lemma 3.1. Let $\frac{1}{2} < H < 1$ and $\theta > 0$. Then the random variable

$$X_\infty^H = \int_0^\infty h_\theta(s) dS_s^H + \nu \int_0^\infty h_\theta(s) ds$$

exists as an element in L^2 .

Proof. This is a simple calculus exercise. In fact, we have

$$\begin{aligned} E\left(\int_0^\infty h_\theta(s) dS_s^H\right)^2 &= \int_0^\infty \int_0^\infty h_\theta(s) h_\theta(r) \psi_H(s, r) ds dr \\ &= 2H(2H-1) \int_0^\infty \int_0^s h_\theta(s) h_\theta(r) ((s-r)^{2H-2} - (r+s)^{2H-2}) dr ds \\ &= 2H(2H-1) \int_0^1 \int_0^s h_\theta(s) h_\theta(r) ((s-r)^{2H-2} - (r+s)^{2H-2}) dr ds \\ &\quad + 2H(2H-1) \int_1^\infty \int_0^1 h_\theta(s) h_\theta(r) ((s-r)^{2H-2} - (r+s)^{2H-2}) dr ds \\ &\quad + 2H(2H-1) \int_1^\infty \int_1^s h_\theta(s) h_\theta(r) ((s-r)^{2H-2} - (r+s)^{2H-2}) dr ds \end{aligned}$$

for all $\theta > 0$ and $\frac{1}{2} < H < 1$. Clearly, **Eq. 10** implies that

$$\begin{aligned} &\int_0^1 \int_0^s h_\theta(s) h_\theta(r) ((s-r)^{2H-2} - (r+s)^{2H-2}) dr ds \\ &\leq (C_\theta)^2 \int_0^1 \int_0^s ((s-r)^{2H-2} - (r+s)^{2H-2}) dr ds \\ &= (C_\theta)^2 \int_0^1 \int_0^1 s^{2H-1} ((1-x)^{2H-2} - (1+x)^{2H-2}) dx ds < \infty, \end{aligned}$$

and

$$\begin{aligned} &\int_1^\infty \int_0^1 h_\theta(s) h_\theta(r) ((s-r)^{2H-2} - (r+s)^{2H-2}) dr ds \\ &\leq (C_\theta)^2 \int_1^\infty \int_0^1 s^{-2} ((s-r)^{2H-2} - (r+s)^{2H-2}) dr ds \\ &\leq (C_\theta)^2 \int_1^\infty s^{-2} ((s-1)^{2H-2} - s^{2H-2}) ds < \infty. \end{aligned}$$

and

$$\begin{aligned}
& \int_1^\infty \int_1^s h_\theta(s) h_\theta(r) \left((s-r)^{2H-2} - (r+s)^{2H-2} \right) dr ds \\
& \leq (C_\theta)^2 \int_1^\infty \int_1^s (rs)^{-2} \left((s-r)^{2H-2} - (r+s)^{2H-2} \right) dr ds \\
& \leq (C_\theta)^2 \int_1^\infty \int_r^\infty (rs)^{-2} \left((s-r)^{2H-2} - (r+s)^{2H-2} \right) dr ds \\
& = (C_\theta)^2 \int_1^\infty \int_1^\infty r^{2H-5} x^{-2} \left((x-1)^{2H-2} - (1+x)^{2H-2} \right) dx dr < \infty
\end{aligned}$$

for all $\theta > 0$ and $\frac{1}{2} < H < 1$. These show that the random variable X_∞^H exists as an element in L^2 .

Lemma 3.2. Let $\theta > 0$. We then have

$$\lim_{t \rightarrow \infty} t e^{\frac{1}{2}\theta t^2} \left(\int_0^t h_\theta(t, s) ds - \int_0^\infty h_\theta(s) ds \right) = -\frac{1}{\theta}. \quad (13)$$

Proof. This is a simple calculus exercise. In fact, we have

$$\begin{aligned}
& \int_0^t h_\theta(t, s) ds - \int_0^\infty h_\theta(s) ds = \int_0^t [h_\theta(t, s) - h_\theta(s)] ds - \int_t^\infty h_\theta(s) ds \\
& = \int_0^t \theta s e^{\frac{1}{2}\theta s^2} \left(\int_s^\infty e^{-\frac{1}{2}\theta u^2} du - \int_s^t e^{-\frac{1}{2}\theta u^2} du \right) ds - \int_t^\infty h_\theta(s) ds \\
& = (e^{\frac{1}{2}\theta t^2} - 1) \int_t^\infty e^{-\frac{1}{2}\theta u^2} du - \int_t^\infty h_\theta(s) ds.
\end{aligned}$$

for all $t \geq 0$ and $\theta > 0$. Noting that

$$\lim_{t \rightarrow \infty} t (e^{\frac{1}{2}\theta t^2} - 1) \int_t^\infty e^{-\frac{1}{2}\theta u^2} du = \lim_{t \rightarrow \infty} \frac{1}{t^{-1} e^{-\frac{1}{2}\theta t^2}} \int_t^\infty e^{-\frac{1}{2}\theta u^2} du = \frac{1}{\theta}$$

and

$$\begin{aligned}
& \lim_{t \rightarrow \infty} t \int_t^\infty h_\theta(s) ds = \lim_{t \rightarrow \infty} \frac{1}{t^{-1}} \int_t^\infty h_\theta(s) ds \\
& = \lim_{t \rightarrow \infty} t^2 h_\theta(t) = \lim_{t \rightarrow \infty} t^2 \left(1 - \theta t e^{\frac{1}{2}\theta t^2} \int_t^\infty e^{-\frac{1}{2}\theta u^2} du \right) = \frac{1}{\theta},
\end{aligned} \quad (14)$$

we see that

$$\begin{aligned}
& \lim_{t \rightarrow \infty} t e^{\frac{1}{2}\theta t^2} \left(\int_0^t h_\theta(t, s) ds - \int_0^\infty h_\theta(s) ds \right) \\
& = \lim_{t \rightarrow \infty} \frac{1}{t^{-1} e^{-\frac{1}{2}\theta t^2}} \left\{ (e^{\frac{1}{2}\theta t^2} - 1) \int_t^\infty e^{-\frac{1}{2}\theta u^2} du - \int_t^\infty h_\theta(s) ds \right\} = -\frac{1}{\theta}
\end{aligned}$$

by L'Hopital's rule.

Lemma 3.3. Let $\theta > 0$. We then have

$$\left| \frac{d}{dt} h_\theta(t) \right| \leq C_\theta \min \left\{ 1, \frac{1}{t^3} \right\} \quad (15)$$

for all $t \geq 0$.

Lemma 3.4. Let $\theta > 0$ and $\frac{1}{2} < H < 1$. We then have

$$\lim_{t \rightarrow \infty} \frac{1}{t^{2-2H}} e^{-\theta t^2} \int_0^t \int_0^s s r e^{\frac{1}{2}\theta(s^2+r^2)} \psi_H(s, r) ds dr = \frac{1}{4} \theta^{-2H} \Gamma(2H+1). \quad (16)$$

Proof. By L'Hopital's rule and the change of variable $\frac{1}{2}\theta(t^2 - r^2) = x$, it follows that

$$\begin{aligned}
& \lim_{t \rightarrow \infty} \frac{1}{t^{2-2H} e^{\theta t^2}} \int_0^t \int_0^s s r e^{\frac{1}{2}\theta(s^2+r^2)} \psi_H(s, r) ds dr \\
& = \lim_{t \rightarrow \infty} \frac{1}{2\theta t^{2-2H} e^{\frac{1}{2}\theta t^2}} \int_0^t e^{\frac{1}{2}\theta r^2} \psi_H(t, r) r dr \\
& = \lim_{t \rightarrow \infty} \frac{H(2H-1)}{2\theta t^{2-2H}} \int_0^t e^{-\frac{1}{2}\theta(t^2-r^2)} \left((t-r)^{2H-2} - (t+r)^{2H-2} \right) r dr \\
& = \lim_{t \rightarrow \infty} \frac{H(2H-1)}{2\theta^2 t^{2-2H}} \int_0^{\frac{1}{2}\theta t^2} e^{-x} \left(t - \sqrt{t^2 - \frac{2x}{\theta}} \right)^{2H-2} dx \\
& = \lim_{t \rightarrow \infty} \frac{H(2H-1)}{2\theta^2 t^{2-2H}} \int_0^{\frac{1}{2}\theta t^2} e^{-x} \left(\frac{2x}{\theta} \right)^{2H-2} \left(t + \sqrt{t^2 - \frac{2x}{\theta}} \right)^{2-2H} dx \\
& = \frac{1}{2} \theta^{-2H} H(2H-1) \Gamma(2H-1) = \frac{1}{4} \theta^{-2H} \Gamma(2H+1),
\end{aligned}$$

where we have used the equation

$$\lim_{t \rightarrow \infty} \frac{1}{t^{2-2H} e^{\frac{1}{2}\theta t^2}} \int_0^t e^{\frac{1}{2}\theta r^2} (t+r)^{2H-2} r dr = 0.$$

This completes the proof.

Lemma 3.5. Let $\theta > 0$ and $\frac{1}{2} < H < 1$. We then have

$$c(t-s)^{2H} \leq E[(X_t^H - X_s^H)^2] \leq C(t-s)^{2H} \quad (17)$$

for all $0 \leq s < t \leq T$, where C and c are two positive constants depending only on H , θ , ν and T .

Proof. The lemma is similar to Lemma 3.5 in the previous study (I).

Lemma 3.6. Let $\theta > 0$ and $\frac{1}{2} \leq H < 1$. Then the convergence

$$\int_t^\infty h_\theta(s) dS_s^H \rightarrow 0 \quad (18)$$

holds in L^2 and almost surely as t tends to infinity.

Proof. Convergence (18) in L^2 follows from Lemma (3.1). In fact, by Eq. 10, we have

$$\begin{aligned}
& E \left| \int_t^\infty h_\theta(s) dS_s^H \right|^2 \leq \int_t^\infty \int_t^\infty |h_\theta(s)| |h_\theta(r)| |\psi(s, r)| ds dr \\
& \leq C \int_t^\infty \int_t^\infty \min \left\{ 1, \frac{1}{s^2} \right\} \min \left\{ 1, \frac{1}{r^2} \right\} |\psi(s, r)| ds dr \\
& = CH(2H-1) \int_t^\infty \int_t^\infty (|s-r|^{2H-2} - |s+r|^{2H-2}) \frac{ds dr}{(sr)^2} \rightarrow 0,
\end{aligned}$$

as t tends to infinity.

On the other hand, by Lemma (3.5), 3.3 and the equation $\frac{S_t^H}{t} \rightarrow 0$ almost surely as t tends to infinity, we find that

$$\left| \int_t^\infty S_s^H dh_\theta(s) \right| \leq C_\theta \int_t^\infty |S_s^H| \frac{ds}{s^3} \rightarrow 0,$$

as t tends to infinity. It follows from the integration by parts that

$$\int_t^\infty h_\theta(s) dS_s^H = -h_\theta(t) S_t^H - \int_t^\infty S_s^H dh_\theta(s) \rightarrow 0$$

almost surely as t tends to infinity.

4 SOME LARGE TIME BEHAVIORS

In this section, we consider the long time behaviors for X^H with $\frac{1}{2} < H < 1$ and $\theta > 0$ and our objects are to prove the statements given in Section 1.

Theorem 4.1. Let $\theta > 0$ and $\frac{1}{2} \leq H < 1$. Then the convergence

$$X_t^H \xrightarrow{a.s.} X_\infty^H \quad (19)$$

holds in L^2 and almost surely as t tends to infinity.

Proof. When $H = \frac{1}{2}$, the convergence is obtained in Cranston-Le Jan [8]. Consider the decomposition

$$\begin{aligned} X_t^H - X_\infty^H &= \int_0^t [h_\theta(t, s) - h_\theta(s)] dS_s^H + \int_t^\infty h_\theta(s) dS_s^H \\ &\quad + \nu \left(\int_0^t h_\theta(t, s) ds - \int_0^\infty h_\theta(s) ds \right) \\ &\equiv Y_t^H + \int_t^\infty h_\theta(s) dS_s^H + \nu \Delta_t^H(\theta) \end{aligned} \quad (20)$$

for all $t \geq 0$.

We first check that Eq. 19 holds in L^2 . By Lemma 3.6 and Lemma 3.2, we only need to prove Y_t^H converges to zero in L^2 . It follows from the equation

$$\int_t^\infty e^{-\frac{1}{2}\theta u^2} du \sim \frac{1}{\theta t} e^{-\frac{1}{2}\theta t^2}$$

for all $\theta > 0$ as t tends to infinity and Lemma 3.4 that

$$\begin{aligned} E|Y_t^H|^2 &= \int_0^t \int_0^t |h_\theta(t, s) - h_\theta(s)| |h_\theta(t, r) - h_\theta(r)| \psi_H(s, r) ds dr \\ &= \left(\int_t^\infty e^{-\frac{1}{2}\theta u^2} du \right)^2 \int_0^t \int_0^t \theta^2 s r e^{\frac{\theta}{2}(s^2+r^2)} \psi_H(s, r) ds dr \\ &\sim \frac{1}{t^2} e^{-\theta t^2} \int_0^t \int_0^t s r e^{\frac{\theta}{2}(s^2+r^2)} \psi_H(s, r) ds dr \\ &= \frac{H(2H-1)}{t^2} e^{-\theta t^2} \int_0^t \int_0^t s r e^{\frac{\theta}{2}(s^2+r^2)} (|s-r|^{2H-2} - |s+r|^{2H-2}) \\ &\quad ds dr \rightarrow 0 \end{aligned}$$

for all $\theta > 0$ and $\frac{1}{2} < H < 1$ as t tends to infinity, which implies that Eq. 19 holds in L^2 .

We now check that Eq. 19 holds almost surely as t tends to infinity. By Lemma 3.6, we only need check that Y_t^H converges to zero almost surely as t tends to infinity. We have

$$\begin{aligned} Y_t^H &= \int_0^t [h_\theta(t, s) - h_\theta(s)] dS_s^H \\ &= \left(\int_t^\infty e^{-\frac{1}{2}\theta u^2} du \right) \int_0^t \theta s e^{\frac{\theta}{2}s^2} dS_s^H \sim \frac{1}{t} e^{-\frac{1}{2}\theta t^2} \int_0^t s e^{\frac{\theta}{2}s^2} dS_s^H \end{aligned}$$

for all $\theta > 0$ and $\frac{1}{2} < H < 1$ as t tends to infinity. To obtain the convergence, we define the random sequence

$$Z_{n,k} = Y_{n+\frac{k}{n}}^H, \quad k = 0, 1, 2, \dots, n$$

for every integer $n \geq 1$. Then $\{Z_{n,k}, k = 0, 1, 2, \dots, n\}$ is Gaussian for every integer $n \geq 1$. It follows from Lemma 3.4 that

$$\begin{aligned} \sigma^2(n) &:= E[(Z_{n,k})^2] \sim \frac{1}{\left(n + \frac{k}{n}\right)^2} e^{-\theta \left(n + \frac{k}{n}\right)^2} E \left[\left| \int_0^{n+\frac{k}{n}} s e^{\frac{\theta}{2}s^2} dS_s^H \right|^2 \right] \\ &\leq \frac{1}{\left(n + \frac{k}{n}\right)^2} e^{-\theta \left(n + \frac{k}{n}\right)^2} \int_0^{n+\frac{k}{n}} \int_0^{n+\frac{k}{n}} s r e^{\frac{\theta}{2}(s^2+r^2)} |\psi_H(s, r)| ds dr \sim \frac{C}{n^{2H}} \end{aligned}$$

for every integer $n \geq 1$ and $0 \leq k \leq n$, which implies that

$$\begin{aligned} P(|Z_{n,k}| > \varepsilon) &= \int_\varepsilon^\infty \frac{1}{\sqrt{2\pi\sigma(n)}} e^{-\frac{x^2}{2\sigma^2(n)}} dx \leq \frac{1}{\varepsilon} \int_\varepsilon^\infty \frac{x}{\sqrt{2\pi\sigma(n)}} e^{-\frac{x^2}{2\sigma^2(n)}} dx \\ &= \frac{\sigma(n)}{\varepsilon} \int_{\varepsilon/\sigma(n)}^\infty \frac{y}{\sqrt{2\pi}} e^{-\frac{y^2}{2}} dy \leq \frac{\sigma(n)}{\varepsilon} e^{-\frac{\varepsilon^2}{4\sigma^2(n)}} \int_{\varepsilon/\sigma(n)}^\infty \frac{y}{\sqrt{2\pi}} e^{-\frac{y^2}{2}} dy \\ &\leq \frac{C}{\varepsilon n^H} \exp\{-C_1 \varepsilon^2 n^{2H}\} \end{aligned}$$

for any $\varepsilon > 0$, every integer $n \geq 1$ and $0 \leq k \leq n$.

On the other hand, for every $s \in (0, 1)$, we denote

$$R_s^{n,k} = Y_{n+\frac{k+\varepsilon s}{n}}^H - Y_{n+\frac{k}{n}}^H.$$

Then $\{R_s^{n,k}, 0 \leq s \leq 1\}$ also is Gaussian for every integer $n \geq 1$ and $0 \leq k \leq n$. It follows that

$$E[(R_s^{n,k} - R_{s'}^{n,k})^2] \leq \frac{C}{n^{2H}} E[(S_s^H - S_{s'}^H)^2]$$

for all $s, s' \in [0, 1]$. Thus, for any $\varepsilon > 0$, by Slepian's theorem and Markov's inequality, one can get

$$\begin{aligned} P\left(\sup_{0 \leq s \leq 1} |R_s^{n,k}| > \varepsilon\right) &\leq P\left(\frac{C}{n^H} \sup_{0 \leq s \leq 1} |S_s^H| > \varepsilon\right) \\ &\leq \frac{C}{\varepsilon^6 n^{6H}} E\left[\sup_{0 \leq s \leq 1} |S_s^H|^6\right] \leq \frac{C}{\varepsilon^6 n^{6H}} \end{aligned}$$

for every integer $n \geq 1$ and $0 \leq k \leq n$. Combining this with the Borel-Cantelli lemma and the relationship

$$\left\{ \sup_{n+\frac{k}{n} < t < n+\frac{k+1}{n}} |Y_t^H| > \varepsilon \right\} \subseteq \{|Z_{n,k}| > \varepsilon/2\} \cup \left\{ \sup_{0 \leq s \leq 1} |R_s^{n,k}| > \varepsilon/2 \right\},$$

we show that $Y_t^H \rightarrow 0$ almost surely as t tends to infinity. This completes the proof.

Theorem 4.2. Let $\theta > 0$ and $\frac{1}{2} \leq H < 1$. Then the convergence

$$t^H (X_t^H - X_\infty^H) \rightarrow \mathcal{N}(0, \lambda_{H,\theta}) \quad (21)$$

holds in distribution, where \mathcal{N} is a central normal random variable with its variance

$$\lambda_{H,\theta} = \frac{1}{2} \Gamma(2H+1) \theta^{-2H}.$$

Proof. When $H = \frac{1}{2}$, this result also is unknown. We only consider the case $\frac{1}{2} < H < 1$ and similarly one can prove the convergence for $H = \frac{1}{2}$. By **Eq. 20**, Slutsky's theorem, and Lemma 3.2, we only need to show that

$$t^H \int_t^\infty h_\theta(s) dS_s^H \rightarrow 0 \quad (t \rightarrow \infty) \quad (22)$$

in probability and

$$t^H Y_t^H \rightarrow N(0, \lambda_{H,\theta}) \quad (t \rightarrow \infty). \quad (23)$$

in distribution.

First, **Eq. 22** follows from **Eq. 10** and

$$\begin{aligned} t^{2H} E \left| \int_t^\infty h_\theta(s) dS_s^H \right|^2 &= t^{2H} \int_t^\infty \int_t^\infty h_\theta(s) h_\theta(r) \psi_H(s, r) ds dr \\ &\leq \frac{4t^{2H}}{\theta^2} \int_t^\infty \int_t^\infty \frac{1}{(sr)^2} \psi_H(s, r) ds dr \\ &= \frac{4t^{4H-4}}{\theta^2} \int_1^\infty \int_1^\infty \frac{1}{(xy)^2} \psi_H(x, y) dx dy \rightarrow 0 \end{aligned}$$

for all $\theta > 0$ and $\frac{1}{2} < H < 1$ as t tends to infinity.

We now obtain convergence (23). By the equation

$$\int_t^\infty e^{-\frac{1}{2}\theta u^2} du \sim \frac{1}{\theta t} e^{-\frac{1}{2}\theta t^2},$$

as t tends to infinity and Lemma 3.4, we get

$$\begin{aligned} t^{2H} E |Y_t^H|^2 &= t^{2H} \int_0^t \int_0^t [h_\theta(t, s) - h_\theta(s)] [h_\theta(t, r) - h_\theta(r)] \psi_H(s, r) ds dr \\ &= t^{2H} \left(\int_t^\infty e^{-\frac{1}{2}\theta u^2} du \right)^2 \int_0^t \int_0^t \theta^2 s r e^{\frac{\theta}{2}(s^2+r^2)} \psi_H(s, r) ds dr \\ &\sim \frac{2}{t^{2-2H}} e^{-\theta t^2} \int_0^t \int_0^t s r e^{\frac{\theta}{2}(s^2+r^2)} \psi_H(s, r) ds dr \rightarrow \frac{1}{2} \Gamma(2H+1) \theta^{-2H} \end{aligned}$$

for all $\theta > 0$ and $\frac{1}{2} < H < 1$ as t tends to infinity. Thus, convergence (23) follows from the normality of $t^H Y_t^H$ for all $\frac{1}{2} < H < 1$ and the theorem follows.

At the end of this section, we obtain a law of large numbers. Consider the process Y^H defined by

$$Y_t^H = \int_0^t (X_s^H - X_\infty^H) ds, \quad t \geq 0.$$

Then the self-attracting diffusion X^H satisfies

$$X_t^H = S_t^H - \theta \int_0^t Y_s^H ds + \nu t, \quad t \geq 0 \quad (24)$$

and

$$Y_t^H = t X_t^H - \int_0^t X_s^H ds = \int_0^t s dX_s^H$$

by integration by parts. It follows that

$$dY_t^H = -\theta t Y_t^H dt + t dS_t^H + \nu t dt \quad (25)$$

for all $\frac{1}{2} \leq H < 1$ and $t \geq 0$. By the variation of constant method, we can give the explicit representation of Y^H as follows:

$$Y_t^H = e^{-\frac{1}{2}\theta t^2} \int_0^t s e^{\frac{1}{2}\theta s^2} dS_s^H + \frac{\nu}{\theta} (1 - e^{-\frac{1}{2}\theta t^2}), \quad t \geq 0. \quad (26)$$

Lemma 4.1. Let $\frac{1}{2} \leq H < 1$ and $\theta > 0$. Then we have

$$\frac{1}{T} \int_0^T Y_t^H dt \rightarrow \frac{\nu}{\theta} \quad (27)$$

almost surely and in L^2 as T tends to infinity.

Proof. This lemma follows from **Eq. 24** and the estimates

$$\begin{aligned} E \left(\left| \frac{1}{T} \int_0^T Y_t^H dt - \frac{\nu}{\theta} \right|^2 \right) &= \frac{1}{\theta^2} E \left(\left| \frac{S_T^H}{T} - \frac{X_T^H}{T} \right|^2 \right) \\ &\leq \frac{2}{\theta^2} \left(\frac{E(S_T^H)^2}{T^2} + \frac{E(X_T^H)^2}{T^2} \right) \rightarrow 0, \end{aligned}$$

as T tends to infinity.

Theorem 4.3. Let $\frac{1}{2} \leq H < 1$ and $\theta > 0$. Then we have

$$\frac{1}{T^{3-2H}} \int_0^T (Y_t^H)^2 dt \rightarrow \frac{H}{3-2H} \theta^{-2H} \Gamma(2H) \quad (28)$$

in L^2 as T tends to infinity.

Proof. Given $\frac{1}{2} < H < 1$ and $\theta > 0$,

$$\Delta_t = \frac{\nu}{\theta} (1 - e^{-\frac{1}{2}\theta t^2}), \quad \eta_t^H = e^{-\frac{1}{2}\theta t^2} \int_0^t u e^{\frac{1}{2}\theta u^2} dS_u^H$$

for all $t \geq 0$. Then

$$Y_t^H = \eta_t + \Delta_t$$

for all $t \geq 0$. We now prove the lemma in three steps.

Step I. We claim that

$$\frac{1}{T^{3-2H}} \int_0^T E[(Y_t^H)^2] dt \rightarrow \frac{H}{3-2H} \theta^{-2H} \Gamma(2H), \quad (29)$$

as t tends to infinity. Clearly, we have

$$\lim_{T \rightarrow \infty} \frac{1}{T^{3-2H}} \int_0^T \Delta_t^2 dt = 0.$$

Thus, 29 is equivalent to

$$\frac{1}{T^{3-2H}} \int_0^T E[(\eta_t^H)^2] dt \rightarrow \frac{H}{3-2H} \theta^{-2H} \Gamma(2H). \quad (30)$$

By L'Hôpital's rule and Lemma 3.4, it follows that

$$\begin{aligned} & \lim_{T \rightarrow \infty} \frac{1}{T^{3-2H}} \int_0^T E[(\eta_t^H)^2] dt \\ &= \lim_{T \rightarrow \infty} \frac{1}{T^{3-2H}} \int_0^T e^{-\theta t^2} \left(\int_0^t \int_0^t u v e^{\frac{1}{2}\theta(u^2+v^2)} \psi_H(u, v) du dv \right) dt \\ &= \lim_{T \rightarrow \infty} \frac{e^{-\theta T^2}}{(3-2H)T^{2-2H}} \int_0^T \int_0^T u v e^{\frac{1}{2}\theta(u^2+v^2)} \psi_H(u, v) du dv \\ &= \frac{1}{2(3-2H)} \theta^{-2H} \Gamma(2H+1) = \frac{H}{3-2H} \theta^{-2H} \Gamma(2H) \end{aligned}$$

for all $\frac{1}{2} < H < 1$.

Step II. We claim that

$$\frac{1}{T^{6-4H}} E \left(\int_0^T \Delta_t \eta_t^H dt \right)^2 = \frac{1}{T^{6-4H}} \int_0^T \int_0^T \Delta_t \Delta_s E(\eta_t^H \eta_s^H) ds dt \rightarrow 0, \quad (31)$$

as T tends to infinity. We have that

$$\begin{aligned} E(\eta_t^H \eta_s^H) &= e^{-\frac{1}{2}\theta(t^2+s^2)} E \left(\int_0^t u e^{\frac{1}{2}\theta u^2} dS_u^H \cdot \int_0^s v e^{\frac{1}{2}\theta v^2} dS_v^H \right) \\ &= e^{-\frac{1}{2}\theta(t^2+s^2)} \int_0^t \int_0^s u v e^{\frac{1}{2}\theta(u^2+v^2)} \psi_H(u, v) dv du \\ &= H(2H-1) e^{-\frac{1}{2}\theta(t^2+s^2)} \int_s^t u e^{\frac{1}{2}\theta u^2} \left(\int_0^s v e^{\frac{1}{2}\theta v^2} \{ (u-v)^{2H-2} - (u+v)^{2H-2} \} dv \right) du \\ &\quad + H(2H-1) e^{-\frac{1}{2}\theta(t^2+s^2)} \int_0^s \int_0^s u v e^{\frac{1}{2}\theta(u^2+v^2)} \{ (u-v)^{2H-2} - (u+v)^{2H-2} \} dv du \\ &\equiv H(2H-1) [\Lambda_1(H; t, s) + \Lambda_2(H; t, s)] \end{aligned} \quad (32)$$

for all $t > s > 0$. An elementary calculation may show that

$$\begin{aligned} \Lambda_1(H; t, s) &\leq e^{-\frac{1}{2}\theta(t^2+s^2)} \int_s^t u (u-s)^{2H-2} e^{\frac{1}{2}\theta u^2} \left(\int_0^s v e^{\frac{1}{2}\theta v^2} dv \right) du \\ &\leq \frac{1}{\theta} e^{-\frac{1}{2}\theta(t^2+s^2)} (e^{\frac{1}{2}\theta s^2} - 1) \int_s^t u (u-s)^{2H-2} e^{\frac{1}{2}\theta u^2} du \\ &= \frac{1}{\theta} e^{-\frac{1}{2}\theta(t^2-s^2)} (1 - e^{-\frac{1}{2}\theta s^2}) \int_s^t u (u-s)^{2H-2} e^{\frac{1}{2}\theta(u^2-s^2)} du \\ &\leq \frac{1}{2\theta} e^{-\frac{1}{2}\theta(t^2-s^2)} \int_0^{t^2-s^2} (\sqrt{s^2+x} - s)^{2H-2} e^{\frac{1}{2}\theta x} dx \\ &\leq \frac{1}{2\theta} e^{-\frac{1}{2}\theta(t^2-s^2)} \int_0^{t^2-s^2} x^{2H-2} (\sqrt{s^2+x} + s)^{2-2H} e^{\frac{1}{2}\theta x} dx \\ &\leq \frac{1}{2\theta} (t+s)^{2-2H} e^{-\frac{1}{2}\theta(t^2-s^2)} \int_0^{t^2-s^2} x^{2H-2} e^{\frac{1}{2}\theta x} dx \end{aligned}$$

for all $t > s > 0$. It follows from the equation $\int_0^x y^\beta e^y dy \asymp x^\beta (1 \wedge x) e^x$ with $x \geq 0$ and $\beta > -1$ that

$$\begin{aligned} \Lambda_1(H; t, s) &\leq C(t-s)^{2H-2} (1 \wedge (t^2-s^2)) \\ &\leq C(t-s)^{2H-2} (1 \wedge (t^2-s^2))^\alpha \end{aligned} \quad (33)$$

for all $t > s > 0$ and $0 \leq \alpha \leq 1$. For the term $\Lambda_2(H; t, s)$, by the proof of Lemma 3.4, we find that

$$\begin{aligned} & \lim_{s \rightarrow \infty} \frac{1}{s^{2-2H} e^{\theta s^2}} \int_0^s \int_0^u u v e^{\frac{1}{2}\theta(u^2+v^2)} (u-v)^{2H-2} dv du \\ &= \frac{1}{4} \theta^{-2H} \Gamma(2H+1) \end{aligned}$$

for all $\frac{1}{2} < H < 1$. Combining this with the equation

$$\lim_{s \rightarrow 0} \frac{1}{s^{2+2H} e^{\theta s^2}} \int_0^s \int_0^u u v e^{\frac{1}{2}\theta(u^2+v^2)} (u-v)^{2H-2} dv du = C \in (0, \infty)$$

and the equation $e^{-x} \leq \frac{1}{1+x} \leq \frac{1}{x^\varrho}$ with $x > 0$ and $0 < \varrho < 1$, we get

$$\begin{aligned} \Lambda_2(H; t, s) &= 2e^{-\frac{1}{2}\theta(t^2+s^2)} \int_0^s \int_0^u u v e^{\frac{1}{2}\theta(u^2+v^2)} (u-v)^{2H-2} dv du \\ &\leq C e^{-\frac{1}{2}\theta(t^2+s^2)} (s^{2-2H} (1 \wedge s)^{4H} e^{\theta s^2}) \\ &= C s^{2-2H} (1 \wedge s)^{4H} e^{-\frac{1}{2}\theta(t^2-s^2)} \leq \frac{C s^{2-2H}}{1 + \frac{1}{2}\theta(t^2-s^2)} \\ &\leq \frac{C s^{2-2H}}{(t^2-s^2)^{2-2H-\gamma}} \leq C (t^2-s^2)^\gamma (t-s)^{2H-2} \end{aligned} \quad (34)$$

for all $t > s > 0$, $\frac{1}{2} < H < 1$ and $0 \leq \gamma \leq 2-2H$. Thus, we have showed that the estimate

$$\begin{aligned} E(\eta_t^H \eta_s^H) &\leq C_{H,\theta} (t-s)^{2H-2} (1 \wedge (t^2-s^2))^\alpha \\ &\quad + (t^2-s^2)^\gamma (t-s)^{2H-2}. \end{aligned} \quad (35)$$

holds for all $t > s \geq 0$. In particular, we have

$$E(\eta_t^H \eta_s^H) \leq C_{H,\theta} |t-s|^{2H-2} \quad (36)$$

for all $t, s \geq 0$. As a corollary, we get

$$\begin{aligned} \frac{1}{T^{6-4H}} E \left(\int_0^T \Delta_t \eta_t^H dt \right)^2 &= \frac{1}{T^{6-4H}} \int_0^T \int_0^T \Delta_t \Delta_s E(\eta_t^H \eta_s^H) ds dt \\ &\leq \frac{C_{\theta,H}}{T^{6-4H}} \int_0^T \int_0^T |t-s|^{2H-2} = \frac{C_{\theta,H}}{T^{6-6H}} \rightarrow 0, \end{aligned}$$

as T tends to infinity.

Step III. We claim that

$$\frac{1}{T^{6-4H}} E \left[\left(\int_0^T (Y_t^H)^2 dt \right)^2 \right] \rightarrow \left(\frac{H}{3-2H} \theta^{-2H} \Gamma(2H) \right)^2, \quad (37)$$

as t tends to infinity. By steps I and II, we find that **Eq. 37** is equivalent to

$$\frac{1}{T^{6-4H}} E \left[\left(\int_0^T (\eta_t^H)^2 dt \right)^2 \right] \rightarrow \left(\frac{H}{3-2H} \theta^{-2H} \Gamma(2H) \right)^2, \quad (38)$$

as t tends to infinity. Noting that the equation

$$E((\eta_t^H)^2 (\eta_s^H)^2) = E((\eta_t^H)^2) E((\eta_s^H)^2) + 2(E(\eta_t^H \eta_s^H))^2 \quad (39)$$

for all $t, s > 0$, we further find that convergence (38) also is equivalent to

$$\begin{aligned}\Lambda(H; T) &:= \frac{1}{T^{6-4H}} E \left(\int_0^T ((\eta_t^H)^2 - E(\eta_t^H)^2) dt \right)^2 \\ &= \frac{2}{T^{6-4H}} \int_0^T \int_0^t (E\eta_t^H \eta_s^H)^2 ds dt \rightarrow 0,\end{aligned}\quad (40)$$

as T tends to infinity. We now check that convergence (40) in two cases.

Case 1. Let $\frac{3}{4} < H < 1$. Clearly, by Eq. 36, we have to

$$\begin{aligned}\Lambda(H; T) &\leq C_{\theta, H} \frac{1}{T^{6-4H}} \int_0^T \int_0^t (t-s)^{4H-4} ds dt \\ &\leq C_{\theta, H} T^{8H-8} \rightarrow 0 \quad (T \rightarrow \infty).\end{aligned}\quad (41)$$

Case 2. Let $\frac{1}{2} < H \leq \frac{3}{4}$. By Eq. 36, we have that

$$\begin{aligned}\int_1^T \int_0^{\sqrt{t^2-1}} [E(\eta_t^H \eta_s^H)]^2 ds dt &\leq C_{\theta, H} \int_1^T \int_0^{\sqrt{t^2-1}} (t-s)^{4H-4} ds dt \\ &\leq C_{\theta, H} T^{4H-2}\end{aligned}$$

with $\frac{1}{2} < H < \frac{3}{4}$ and

$$\int_1^T \int_0^{\sqrt{t^2-1}} [E(\eta_t^H \eta_s^H)]^2 ds dt \leq \int_1^T \int_0^{\sqrt{t^2-1}} \frac{1}{t-s} ds dt \leq CT \log T$$

with $H = \frac{3}{4}$ for all $T > 1$. Similarly, by Eq. 35, we also have

$$\begin{aligned}&\int_1^T \int_0^{\sqrt{t^2-1}} [E(\eta_t^H \eta_s^H)]^2 ds dt \\ &\leq C_{\theta, H} \int_1^T \int_0^{\sqrt{t^2-1}} (t-s)^{4H-4+2\alpha} (t+s)^{2\alpha} ds dt \\ &\leq C_{\theta, H} \int_1^T \int_0^{\sqrt{t^2-1}} t^{2\alpha} (t-s)^{4H-4+2\alpha} ds dt \\ &= C_{\theta, H} \int_1^T t^{2\alpha} (t - \sqrt{t^2-1})^{4H-3+2\alpha} dt \\ &= C_{\theta, H} \int_1^T \frac{t^{2\alpha}}{(t + \sqrt{t^2-1})^{4H-3+2\alpha}} dt \leq CT^{4-4H}\end{aligned}$$

for all $T > 1$ and $\frac{3}{2} - 2H < \alpha = \gamma < 2 - 2H$ since $0 < t^2 - s^2 < 1$ for $(s, t) \in \{(s, t) | 1 \leq t \leq T, \sqrt{t^2-1} < s < t\}$. Thus, we have shown that

REFERENCES

- Alós E, Mazet O, Nualart D Stochastic Calculus with Respect to Gaussian Processes. *Ann Probab* (2001) 29:766–801. doi:10.1214/aop/1008956692
- Benaïm M, Ciotir I, Gauthier C-E Self-repelling Diffusions via an Infinite Dimensional Approach. *Stoch Pde: Anal Comp* (2015) 3:506–30. doi:10.1007/s40072-015-0059-5

$$\begin{aligned}\Lambda(H; T) &= \frac{1}{T^{6-4H}} \int_1^T \int_0^{\sqrt{t^2-1}} [E(\eta_t^H \eta_s^H)]^2 ds dt \\ &+ \frac{1}{T^{6-4H}} \int_1^T \int_{\sqrt{t^2-1}}^t [E(\eta_t^H \eta_s^H)]^2 ds dt + \frac{1}{T^{6-4H}} \int_0^1 \int_0^t [E(\eta_t^H \eta_s^H)]^2 ds dt \\ &\leq \frac{C_{\theta, H}}{T^{6-4H}} (T^{4H-2} + T^{4-4H} + 1) \leq \frac{C_{\theta, H}}{T^2} \rightarrow 0\end{aligned}\quad (42)$$

with $\frac{1}{2} < H < \frac{3}{4}$ and

$$\Lambda\left(\frac{3}{4}; T\right) \leq \frac{C_{\theta, H}}{T^3} (T \log T + T + 1) \leq C_{\theta, H} (\log T + 1) \frac{1}{T^2} \rightarrow 0, \quad (43)$$

as T tends to infinity. This shows that convergence (40) holds for all $\frac{1}{2} < H < 1$. Similarly, we can also show the theorem holds for $H = \frac{1}{2}$ and the theorem follows.

Remark 1. By using the Borel–Cantelli lemma and Theorem 4.3, we can check that convergence (28) holds almost surely.

5 SIMULATION

We have applied our results to the following linear self-attracting diffusion driven by a sub-fBm S^H with $\frac{1}{2} < H < 1$ as follows:

$$dX_t^H = dS_t^H - \theta \left(\int_0^t (X_t^H - X_s^H) ds \right) dt + \nu dt, \quad X_0^H = 0,$$

where $\theta > 0$ and $\nu \in \mathbb{R}$ are two parameters. We will simulate the process with $\nu = 0$ in the following cases:

- $H = 0.7$: $\theta = 1$, $\theta = 10$ and $\theta = 100$, respectively (see, **Figures 1–3, Tables 1–3**);
- $H = 0.5$: $\theta = 1$, $\theta = 10$ and $\theta = 100$, respectively (see, **Figures 4–6, Tables 4–6**).

Remark 2. From the following numerical results, we can find that it is important to study the estimates of parameters θ and ν .

DATA AVAILABILITY STATEMENT

The original contributions presented in the study are included in the article/supplementary material; further inquiries can be directed to the corresponding authors.

AUTHOR CONTRIBUTIONS

All authors listed have made a substantial, direct, and intellectual contribution to the work and approved it for publication.

- Benaïm M, Ledoux M, Raimond O Self-interacting Diffusions. *Probab Theor Relat Fields* (2002) 122:1–41. doi:10.1007/s004400100161
- Bojdecki T, Gorostiza LG, Talarczyk A Some Extensions of Fractional Brownian Motion and Sub-fractional Brownian Motion Related to Particle Systems. *Elect Comm Probab* (2007) 12:161–72. doi:10.1214/ecp.v12-1272
- Bojdecki T, Gorostiza LG, Talarczyk A Sub-fractional Brownian Motion and its Relation to Occupation Times. *Stat Probab Lett* (2004) 69:405–19. doi:10.1016/j.spl.2004.06.035

6. Bojdecki T, Gorostiza LG, Talarczyk A Occupation Time Limits of Inhomogeneous Poisson Systems of Independent Particles. *Stochastic Process their Appl* (2008) 118:28–52. doi:10.1016/j.spa.2007.03.008
7. Bojdecki T, Gorostiza LG, Talarczyk A Self-Similar Stable Processes Arising from High-Density Limits of Occupation Times of Particle Systems. *Potential Anal* (2008) 28:71–103. doi:10.1007/s11118-007-9067-z
8. Cranston M, Le Jan Y Self Attracting Diffusions: Two Case Studies. *Math Ann* (1995) 303:87–93. doi:10.1007/bf01460980
9. Cranston M, Mountford TS The strong Law of Large Numbers for a Brownian Polymer. *Ann Probab* (1996) 24:1300–23. doi:10.1214/aop/1065725183
10. Durrett RT, Rogers LCG Asymptotic Behavior of Brownian Polymers. *Probab Th Rel Fields* (1992) 92:337–49. doi:10.1007/bf01300560
11. Gan Y, Yan L Least Squares Estimation for the Linear Self-Repelling Diffusion Driven by Fractional Brownian Motion (In Chinese). *Sci CHINA Math* (2018) 48:1143. doi:10.1360/scm-2017-0387
12. H Gao, R Guo, Y Jin, L Yan, Large Time Behavior on the Linear Self-Interacting Diffusion Driven by Sub-fractional Brownian Motion I: Self-Repelling Case. *Front Phys* (2021) volume 2021. doi:10.3389/fphy.2021.795210
13. Gauthier C-E Self Attracting Diffusions on a Sphere and Application to a Periodic Case. *Electron Commun Probab* (2016) 21(No. 53):1–12. doi:10.1214/16-ecp4547
14. Herrmann S, Roynette B Boundedness and Convergence of Some Self-Attracting Diffusions. *Mathematische Annalen* (2003) 325:81–96. doi:10.1007/s00208-002-0370-0
15. Herrmann S, Scheutzw M Rate of Convergence of Some Self-Attracting Diffusions. *Stochastic Process their Appl* (2004) 111:41–55. doi:10.1016/j.spa.2003.10.012
16. Li M Modified Multifractional Gaussian Noise and its Application. *Phys Scr* (2021) 96(1212):125002. doi:10.1088/1402-4896/ac1cf6
17. Li M Generalized Fractional Gaussian Noise and its Application to Traffic Modeling. *Physica A* (2021) 579:126138. doi:10.1016/j.physa.2021.126138
18. Li M Multi-fractional Generalized Cauchy Process and its Application to Teletraffic. *Physica A: Stat Mech its Appl* (2020) 550(14):123982. doi:10.1016/j.physa.2019.123982
19. Li M Fractal Time Series-A Tutorial Review. *Math Probl Eng* (2010) 2010:1–26. doi:10.1155/2010/157264
20. Mountford T, Tarrés P An Asymptotic Result for Brownian Polymers. *Ann Inst H Poincaré Probab Statist* (2008) 44:29–46. doi:10.1214/07-aihp113
21. Nualart D *Malliavin Calculus and Related Topics*. 2nd ed. New York: Springer (2006).
22. Pemantle R Phase Transition in Reinforced Random Walk and RWRE on Trees. *Ann Probab* (1988) 16:1229–41. doi:10.1214/aop/1176991687
23. Shen G, Yan L An Approximation of Subfractional Brownian Motion. *Commun Stat - Theor Methods* (2014) 43:1873–86. doi:10.1080/03610926.2013.769598
24. Shen G, Yan L Estimators for the Drift of Subfractional Brownian Motion. *Commun Stat - Theor Methods* (2014) 43:1601–12. doi:10.1080/03610926.2012.697243
25. Sun X, Yan L A central Limit Theorem Associated with Sub-fractional Brownian Motion and an Application (In Chinese). *Sci Sin Math* (2017) 47:1055–76. doi:10.1360/scm-2016-0748
26. Sun X, Yan L A Convergence on the Linear Self-Interacting Diffusion Driven by α -stable Motion. *Stochastics* (2021) 93:1186–208. doi:10.1080/17442508.2020.1869239
27. Sun X, Yan L The Laws of Large Numbers Associated with the Linear Self-Attracting Diffusion Driven by Fractional Brownian Motion and Applications, to Appear in. *J Theoret Prob* (2021). Online. doi:10.1007/s10959-021-01126-0
28. Tudor C Some Properties of the Sub-fractional Brownian Motion. *Stochastics* (2007) 79:431–48. doi:10.1080/17442500601100331
29. Tudor C Inner Product Spaces of Integrands Associated to Subfractional Brownian Motion. *Stat Probab Lett* (2008) 78:2201–9. doi:10.1016/j.spl.2008.01.087
30. Tudor C On the Wiener Integral with Respect to a Sub-fractional Brownian Motion on an Interval. *J Math Anal Appl* (2009) 351:456–68. doi:10.1016/j.jmaa.2008.10.041
31. Tudor C Some Aspects of Stochastic Calculus for the Sub-fractional Brownian Motion. *Ann Univ Bucuresti Mathematica* (2008) 24:199–230.
32. Tudor CA. *Analysis of Variations for Self-Similar Processes*. Heidelberg, New York: Springer (2013).
33. Yan L, He K, Chen C The Generalized Bouleau-Yor Identity for a Sub-fractional Brownian Motion. *Sci China Math* (2013) 56:2089–116. doi:10.1007/s11425-013-4604-2
34. Yan L, Sun Y, Lu Y On the Linear Fractional Self-Attracting Diffusion. *J Theor Probab* (2008) 21:502–16. doi:10.1007/s10959-007-0113-y
35. Yan L, Shen G On the Collision Local Time of Sub-fractional Brownian Motions. *Stat Probab Lett* (2010) 80:296–308. doi:10.1016/j.spl.2009.11.003
36. Yan L, Shen G, He K Itô's Formula for the Sub-fractional Brownian Motion. *Comm Stochastic Anal* (2011) 5:135–59. doi:10.31390/cosa.5.1.09

Conflict of Interest: The authors declare that the research was conducted in the absence of any commercial or financial relationships that could be construed as a potential conflict of interest.

Publisher's Note: All claims expressed in this article are solely those of the authors and do not necessarily represent those of their affiliated organizations, or those of the publisher, the editors, and the reviewers. Any product that may be evaluated in this article, or claim that may be made by its manufacturer, is not guaranteed or endorsed by the publisher.

Copyright © 2022 Guo, Gao, Jin and Yan. This is an open-access article distributed under the terms of the Creative Commons Attribution License (CC BY). The use, distribution or reproduction in other forums is permitted, provided the original author(s) and the copyright owner(s) are credited and that the original publication in this journal is cited, in accordance with accepted academic practice. No use, distribution or reproduction is permitted which does not comply with these terms.



Early Warning Signals for Critical Transitions in Sandpile Cellular Automata

Andrey Dmitriev^{1,2*}, Vasily Kornilov³, Victor Dmitriev³ and Nadezda Abbas²

¹Laboratory of Complex Systems Modeling and Control, National Research University Higher School of Economics, Moscow, Russia, ²Cybersecurity Research Center, University of Bernardo O'Higgins, Santiago, Chile, ³Department of Business Informatics, National Research University Higher School of Economics, Moscow, Russia

The sandpile cellular automata, despite the simplicity of their basic rules, are adequate mathematical models of real-world systems, primarily open nonlinear systems capable to self-organize into the critical state. Such systems surround us everywhere. Starting from processes at microscopic distances in the human brain and ending with large-scale water flows in the oceans. The detection of critical transitions precursors in sandpile cellular automata will allow progress significantly in the search for effective early warning signals for critical transitions in complex real systems. The presented paper is devoted to the detection and investigation of such signals based on multifractal analysis of the time series of falls of the cellular automaton cells. We examined cellular automata in square lattice and random graphs using standard and facilitated rules. It has been established that log wavelet leaders cumulant are effective early warning measures of the critical transitions. Common features and differences in the behavior of the log cumulants when cellular automata transit into the self-organized critical state and the self-organized bistability state are also established.

Keywords: early warning signals, sandpile cellular automata, self-organized criticality, selforganized bistability, wavelet leaders method, log-cumulants, multifractal formalism

OPEN ACCESS

Edited by:

Ming Li,
Zhejiang University, China

Reviewed by:

Alexander Shapoval,
University of Łódź, Poland
Victor Popov,
Lomonosov Moscow State University,
Russia

*Correspondence:

Andrey Dmitriev
a.dmitriev@hse.ru

Specialty section:

This article was submitted to
Interdisciplinary Physics,
a section of the journal
Frontiers in Physics

Received: 19 December 2021

Accepted: 10 January 2022

Published: 31 January 2022

Citation:

Dmitriev A, Kornilov V, Dmitriev V and
Abbas N (2022) Early Warning Signals
for Critical Transitions in Sandpile
Cellular Automata.
Front. Phys. 10:839383.
doi: 10.3389/fphy.2022.839383

INTRODUCTION

Open complex systems usually operate in a nonequilibrium state, which can lead to the appearance of fluctuations in them, induced by external influence. When the initial structureless state is lost, which is an extrapolation of the equilibrium state to nonequilibrium conditions, a critical transition occurs in the system, leading to the emergence of new stationary states. In addition to the specified critical transition that occurs as a result of bifurcations (the so-called bifurcation-induced critical transition), noise-induced critical transition and rate-induced critical transition can occur in systems. An important feature of such critical transitions is the fact that such transitions have common features, despite the differences in the details of the elements interactions of each system. Due to this reason, many common (unifying) quantitative and qualitative precursors of critical transitions or early warning signals (EWS) in the critical transitions have been proposed (see the papers [1–5]). Despite this, we assume that there should be differences in the EWS for different types of critical transitions, at least in the neighborhood of the critical transition point. Finding such differences is one of the objectives of our research.

The justification for the use of most early warning measures is associated with an increase in the time that needed to return to a stable state with small disturbances in the neighborhood of the critical

point. These EWS include autocorrelation, variance, skewness and kurtosis, power spectral density, and Hurst exponents. These measures are estimated for the time series characterizing changes in some parameters of the systems. For example, the order parameter can be used as such parameter, if the critical transition is the first or the second order phase transition. Other EWS are recurrence measures such as determinism, laminarity and entropy (see the paper [6]).

Complex systems surround us everywhere. Starting from processes at microscopic distances in the human brain and ending with large-scale water flows in the oceans. In the complex systems, the interaction of individual elements with each other is so complex that the entire system acquires completely new and unexpected properties that cannot be reduced to the properties of individual parts. Controlling such parameters as temperature or magnetization, it is possible to provide a phase transition—a transition through a critical point, which is characterized by power laws. However, there are various examples of processes and systems (see the papers [7–9]), which are characterized by power laws that have arisen without any parameters' tuning: seismic activity with destructive earthquakes, neural and social networks, financial markets, forest fires, etc. P. Bak, C. Tang, and K. Wiesenfeld [8] discovered self-organized criticality (SOC) phenomena in 1987. They built a mechanism that explains how a system reaches the critical state without tuning of any parameters. Their model, called the sandpile or BTW model, is implemented on a square lattice on which grains of sand fall. Sandpile cellular automata have simple rules that lead to complex critical behavior. A detailed description of sandpile models is provided in *Time Series Data Generation using Sandpile Cellular Automata*. The self-organized critical transition corresponds to the second order phase transitions. It was recently found (see the papers [10–13]) that in real complex systems the self-organized bistable (SOB) transition is possible, which corresponds to the first order phase transition. A sandpile cellular automata with facilitated rules has also been proposed (see the paper [13]), which is capable to demonstrate the SOB transition. At this moment, we are not aware of papers that present the results of the study of time series features generated by systems when they approach the SOC state and the SOB state. To close this gap, we conducted a study on discovering the EWS of the critical transitions and the features of the critical transitions for sandpile cellular automata. Our study is based on the results of multifractal time series analysis generated by the automata. Research results are presented in this paper.

The paper is structured as follows. *Methods* provides descriptions of local sandpile cellular automata rules in square lattice and random graphs—time series generators for the number of collapsed cells, and the wavelet leader method for time series analysis. In the *Result and Their Discussion*, the results of EWS detection for the critical transitions and multifractal features of the automata being in the subcritical phase and the critical state are presented and discussed. The *Result and Their Discussion* is devoted to the discussion of obtained results, as well as the discussion of possible practical applications obtained by EWS for detecting critical transitions.

METHODS

This Section describes the rules for the operation of sandpile cellular automata - time series generators for number of the falls ($x_t, t \in \{0\} \cup \mathbb{Z}^+$, where t is the iteration step). The rules of automata capable to self-organize into a critical state and the rules of automata capable to self-organize into a bistable state are considered. A brief description of wavelet leader method in the context of multifractal formalism is presented, as well as the role of log wavelet leaders cumulant in the analysis of multifractal time series.

Time Series Data Generation Using Sandpile Cellular Automata

To date, isotropic sandpile cellular automata (SCA) with a variety of local rules have been developed (see the reviews [14, 15]). To generate the time series data, we used the standard rules of the Bak—Tang—Wiesenfeld (BTW) [8], Feder—Feder (FF) [16] and Manna (M) [17] models. SCA with standard rules (SR) are capable to self-organize into a critical state. We also looked at facilitated sandpile cellular automata or facilitated rules (FR) automata. Such automata are capable to self-organize into a bistable state. A modification of the Manna model as a facilitated SCA model is presented in the paper [13]. Finally, we investigated the dynamics of sand grains not only on square lattice (SL), but also on random networks grown using the Erdos—Renyi (ER) model and the Barabasi—Albert (BA) model (see the papers [18, 19]). The introduced abbreviations will further be used to denote a cellular automaton. For example, FF-ST-BA matches sandpile cellular automata with standard Feder—Feder rules on Barabasi—Albert (BA) network.

The basic operating principle of any SCA is quite simple. Let us describe it in the form of an algorithm, at each step of which the similarities and differences of each of the automata are indicated. First of all, if cellular automata on random graphs are considered, then it is necessary to grow these graphs. A description of cultivation is provided at the end of this Subsection.

Step 1. Randomly selected cells (x, y) of a square lattice or a grown random graph are filled randomly, one particle at a time. As a result, the number of particles in these cells is $z_i(x, y) \rightarrow z_i(x, y) + 1$.

Step 2. The critical value of particles (z_c) is determined for each cell. For square lattices $z_c = 4$, for random graphs z_c is equal to the number of connections of the vertex (x, y) .

Step 3. Collapse of cells and redistribution of particles between cells.

The stability condition for each of the cells of the automaton for a model with standard rules is checked. If $z_i(x, y) \geq z_c$, then the given cell (x, y) crumbles with the distribution of particles into neighboring cells. After the cell is overturned, grains of sand are distributed equally to each neighboring cell in deterministic models (FF- and BTW-model); a grain of sand falls into a randomly selected neighboring cell in the stochastic M-model. On nodes with degree 1 of random graphs, the collapse of a cell (node) can only lead to the escape of particles from these nodes.

For the model with facilitated rules, the stability condition for each of the cells of the automaton is also checked. If $z_i(x, y) \geq z_c$ or $f_{i-1}(x, y) \geq 2$ (f is the number of falls into a cell on the previous move), then cell (x, y) collapses into neighboring cells in accordance with rules of the model. Also, shedding can be deterministic and random.

Step 4. The number of collapsed cells is calculated, which corresponds to the value of the time series at a certain step.

In conservative models (M- and BTW-model) on the SL, when the unstable cell is overturned, the value in it decreases by the value z_c , as a result the number of sand grains is preserved. In such models, sand grains can leave the RSL only through the boundaries of the lattice. In the dissipative FF-model on the RSL, after overturning, the number of sand grains sand in the unstable cell becomes zero. In this case, a supercritical number of sand grains $z(x, y) > z_c$ occurs, which are also capable to leave the system through the lattice.

The sandpile cellular automata on the RSL are very approximate models of real systems, which are characterized by self-organization into a critical and bistable states. First of all, the approximation of the models is associated with a fixed and limited number of nearest neighbors of each node of the automaton. Therefore, the study of critical transitions in SCA on ER- and BA-networks is under particular interest. For example, although the ER model does not reproduce some of the typical properties of real networks, on average, the model is a good model for transportation networks, contagion and diffusion (see the paper [19]). The BA model is a good model for complex networks, and therefore has a much wider application area (see the papers [20, 21]). Random graph $G_{ER}(V, E)$ in the ER model is grown as a result of joining any two vertices v_i and v_j ($v \in V$), using edge $e_{ij} \in E$ with some probability $p \in [0, 1]$ regardless of all other pairs of vertices $e_{km} \in E$, the number of which is $C_n^2 - 1$. In other words, edges are grown according to the standard Bernoulli scheme with a fixed number of vertices equal to n . Random graph $G_{BA}(V, E)$ in the BA model is grown from an initial graph with the number of vertices $n \geq 2$ and degree of vertices $k \geq 1$. Each new vertex i joins the existing vertices with probability $k_i / \sum k_j$. The network built using the BA model is a scale-free network with a power-law probability distribution for the degree of vertices. The total number of the edges for the BA graph and ER graph is the same and equals 2,500. The total number of edges in the square lattice is 4,900.

Below, we consider the formal rules of all studied sandpile cellular automata.

Sandpile Cellular Automata on the Square Lattice

Lets N is the number of the square lattice nodes, K is the number of nearest neighbors of the node, $Ne = (x, y \pm 1; x \pm 1, y)$ denotes the nearest neighbors of the node.

Then the formal rules for BTW-ST-SL automata will take the following form.

$$\begin{aligned} z_c = 4, x, y \in [1, N], z_i(x, y) \geq z_c \\ z_{i+1}(x, y) \rightarrow z_{i+1}(x, y) - z_c \\ z_{i+1}(Ne) \rightarrow z_{i+1}(Ne) + 1 \end{aligned} \quad (1)$$

BTW-FA-SL automata.

$$\begin{aligned} z_c = 4, x, y \in [1, N], z_i(x, y) \geq z_c \vee f_i(x, y) \geq 2 \\ z_i(x, y) \geq z_c: \begin{cases} z_{i+1}(x, y) \rightarrow z_{i+1}(x, y) - z_c \\ z_{i+1}(Ne) \rightarrow z_{i+1}(Ne) + 1 \\ f_{i+1}(Ne) \rightarrow f_{i+1}(Ne) + 1 \end{cases} \\ z_i(x, y) < z_c: \begin{cases} z_{i+1}(x, y) \rightarrow z_{i+1}(x, y) - z_i(x, y) \\ z_{i+1}(Ne) \rightarrow z_{i+1}(Ne) + \delta_k, \sum_{k=1}^K (\delta_k \geq 0) = z_i(x, y) \\ f_{i+1}(Ne) \rightarrow f_{i+1}(Ne) + 1, \delta_k > 0 \end{cases} \end{aligned} \quad (2)$$

FF-ST-SL automata.

$$\begin{aligned} z_c = 4, x, y \in [1, N], z_i(x, y) \geq z_c \\ z_{i+1}(x, y) \rightarrow z_{i+1}(x, y) - z_i(x, y) \\ z_{i+1}(Ne) \rightarrow z_{i+1}(Ne) + 1 \end{aligned} \quad (3)$$

FF-FA-SL automata.

$$\begin{aligned} z_c = 4, x, y \in [1, N], z_i(x, y) \geq z_c \vee f_i(x, y) \geq 2 \\ z_i(x, y) \geq z_c: \begin{cases} z_{i+1}(x, y) \rightarrow z_{i+1}(x, y) - z_i(x, y) \\ z_{i+1}(Ne) \rightarrow z_{i+1}(Ne) + 1 \\ f_{i+1}(Ne) \rightarrow f_{i+1}(Ne) + 1 \end{cases} \\ z_i(x, y) < z_c: \begin{cases} z_{i+1}(x, y) \rightarrow z_{i+1}(x, y) - z_i(x, y) \\ z_{i+1}(Ne) \rightarrow z_{i+1}(Ne) + \delta_k, \sum_{k=1}^{K_n} (\delta_k \geq 0) = z_i(x, y) \\ f_{i+1}(Ne) \rightarrow f_{i+1}(Ne) + 1, \delta_k > 0 \end{cases} \end{aligned} \quad (4)$$

M-ST-SL automata.

$$\begin{aligned} z_c = 4, x, y \in [1, N], z_i(x, y) \geq z_c \\ z_{i+1}(x, y) \rightarrow z_{i+1}(x, y) - z_c \\ z_{i+1}(Ne) \rightarrow z_{i+1}(Ne) + \delta_k, \sum_{k=1}^K (\delta_k \geq 0) = z_c \end{aligned} \quad (5)$$

M-FA-SL automata.

$$\begin{aligned} z_c = 4, x, y \in [1, N], z_i(x, y) \geq z_c \vee f_i(x, y) \geq 2 \\ z_i(x, y) \geq z_c: \begin{cases} z_{i+1}(x, y) \rightarrow z_{i+1}(x, y) - z_c \\ z_{i+1}(Ne) \rightarrow z_{i+1}(Ne) + \delta_k, \sum_{k=1}^K (\delta_k \geq 0) = z_c \\ f_{i+1}(Ne) \rightarrow f_{i+1}(Ne) + 1, \delta_k > 0 \end{cases} \\ z_i(x, y) < z_c: \begin{cases} z_{i+1}(x, y) \rightarrow z_{i+1}(x, y) - z_i(x, y) \\ z_{i+1}(Ne) \rightarrow z_{i+1}(Ne) + \delta_k, \sum_{k=1}^K (\delta_k \geq 0) = z_i(x, y) \\ f_{i+1}(Ne) \rightarrow f_{i+1}(Ne) + 1, \delta_k > 0 \end{cases} \end{aligned} \quad (6)$$

Sandpile Cellular Automata on the Random Graphs

Let K_n is the number of nearest neighbors for each node n of the graph, $Ne = (x, y \pm 1; x \pm 1, y)$ denotes the nearest neighbors of the node.

Then the formal rules for BTW-ST automata will take the following form.

$$\begin{aligned} z_{cn} &= K_n, z_i(n) \geq z_{cn} \\ z_{i+1}(n) &\rightarrow z_{i+1}(n) - z_{cn} \\ z_{i+1}(\text{Ne}) &\rightarrow z_{i+1}(\text{Ne}) + 1, z_{cn} > 1 \end{aligned} \quad (7)$$

BTW-FA automata.

$$\begin{aligned} z_{cn} &= K_n, z_i(n) \geq z_{cn} \vee f_i(n) \geq 2 \\ z_i(n) \geq z_{cn}: &\begin{cases} z_{i+1}(n) \rightarrow z_{i+1}(n) - z_{cn} \\ z_{i+1}(\text{Ne}) \rightarrow z_{i+1}(\text{Ne}) + 1, z_{cn} > 1 \\ f_{i+1}(\text{Ne}) \rightarrow f_{i+1}(\text{Ne}) + 1, z_{cn} > 1 \\ z_{i+1}(n) \rightarrow z_{i+1}(n) - z_i(n) \end{cases} \\ z_i(n) < z_{cn}: &\begin{cases} z_{i+1}(\text{Ne}) \rightarrow z_{i+1}(\text{Ne}) + \delta_k, \sum_{k=1}^{K_n} (\delta_k \geq 0) = z_i(n), z_{cn} > 1 \\ f_{i+1}(\text{Ne}) \rightarrow f_{i+1}(\text{Ne}) + 1, \delta_k > 0, z_{cn} > 1 \end{cases} \end{aligned} \quad (8)$$

FF-ST automata.

$$\begin{aligned} z_{cn} &= K_n, z_i(n) \geq z_{cn} \\ z_{i+1}(n) &\rightarrow z_{i+1}(n) - z_i(n) \\ z_{i+1}(\text{Ne}) &\rightarrow z_{i+1}(\text{Ne}) + 1, z_{cn} > 1 \end{aligned} \quad (9)$$

FF-FA automata.

$$\begin{aligned} z_{cn} &= K_n, z_i(n) \geq z_{cn} \vee f_i(n) \geq 2 \\ z_i(n) \geq z_{cn}: &\begin{cases} z_{i+1}(n) \rightarrow z_{i+1}(n) - z_i(n) \\ z_{i+1}(\text{Ne}) \rightarrow z_{i+1}(\text{Ne}) + 1, z_{cn} > 1 \\ f_{i+1}(\text{Ne}) \rightarrow f_{i+1}(\text{Ne}) + 1, z_{cn} > 1 \\ z_{i+1}(n) \rightarrow z_{i+1}(n) - z_i(n) \end{cases} \\ z_i(n) < z_{cn}: &\begin{cases} z_{i+1}(\text{Ne}) \rightarrow z_{i+1}(\text{Ne}) + \delta_k, \sum_{k=1}^{K_n} (\delta_k \geq 0) = \\ z_i(n), z_{cn} > 1 \\ f_{i+1}(\text{Ne}) \rightarrow f_{i+1}(\text{Ne}) + 1, \delta_k > 0, z_{cn} > 1 \end{cases} \end{aligned} \quad (10)$$

M-ST automata.

$$\begin{aligned} z_{cn} &= K_n, z_i(n) \geq z_{cn} \\ z_{i+1}(n) &\rightarrow z_{i+1}(n) - z_{cn} \\ z_{i+1}(\text{Ne}) &\rightarrow z_{i+1}(\text{Ne}) + \delta_k, \sum_{k=1}^{K_n} (\delta_k \geq 0) = z_{cn}, z_{cn} > 1 \end{aligned} \quad (11)$$

M-FA automata.

$$\begin{aligned} z_{cn} &= K_n, z_i(n) \geq z_{cn} \vee f_i(n) \geq 2 \\ z_i(n) \geq z_{cn}: &\begin{cases} z_{i+1}(n) \rightarrow z_{i+1}(n) - z_{cn} \\ z_{i+1}(\text{Ne}) \rightarrow z_{i+1}(\text{Ne}) + \delta_k, \sum_{k=1}^{K_n} (\delta_k \geq 0) = z_{cn} \\ f_{i+1}(\text{Ne}) \rightarrow f_{i+1}(\text{Ne}) + 1, \delta_k > 0, z_{cn} > 1 \\ z_{i+1}(n) \rightarrow z_{i+1}(n) - z_i(n) \end{cases} \\ z_i(n) < z_{cn}: &\begin{cases} z_{i+1}(\text{Ne}) \rightarrow z_{i+1}(\text{Ne}) + \delta_k, \sum_{k=1}^{K_n} (\delta_k \geq 0) = z_i(n), z_{cn} > 1 \\ f_{i+1}(\text{Ne}) \rightarrow f_{i+1}(\text{Ne}) + 1, \delta_k > 0, z_{cn} > 1 \end{cases} \end{aligned} \quad (12)$$

Wavelet Leaders Multifractal Analysis of Time Series Generated by Self-Organizing Cellular Automata

Multifractal analysis, being a method of local investigation of the temporal structure of a signal, allows to evaluate its correlation properties even with a relatively short signal registration. This is an undoubted advantage of this method (see the papers [22–24]).

There are several methods of multifractal time series analysis, which have their own capabilities and limitations. The most common are multifractal detrended fluctuation analysis (MFDFA) [25, 26], wavelet transform maxima modules (WTMM) [27], and wavelet leader method (WLM) [28, 29], which is the development of the WTMM method. We used the WLM to estimate the multifractal singularity spectrum. One of the obvious advantages of WLM in relation to the MFDFA method is the absence of the need to detrend the initial time series data, because the wavelets are not sensitive to the trend. In addition, the MFDFA method gives good estimates only for positive values of Holder exponents; at the same time, the accuracy of determining the values of $h(q)$ significantly decreases as $h(q) \rightarrow 0$.

Without consideration technical details of WLM, let us consider the main features of the method in the context of the multifractal formalism. A detailed description of the method is presented in the papers [30–32]. After the discrete wavelet transform, the time series is decomposed into discrete wavelet coefficients of different levels, which are presented in the form of a matrix. After that, this matrix is analyzed: the coefficient and its neighbors (right and left) are analyzed at each level. The largest of them is selected. Thus, a set of the largest coefficients is obtained. These are the wavelet leaders defined for each wavelet expansion level.

Next, the standard procedure for multifractal analysis will be considered. Structural functions are found that have the following form:

$$S(j, q) = \frac{1}{n_j} \sum_{k=1}^{n_j} L_x(j, k)^q \approx j^{\zeta(q)}, \quad (13)$$

where j is the scale, q is the moment, $L_x(j, k)$ are the wavelet leaders for the time series x_t , $\zeta(q)$ denotes the scaling exponent, n_j denotes the number of $L_x(j, k)$ available at scale 2^j .

The scaling exponent $\zeta(q)$ usually represented as the following decomposition:

$$\zeta(q) = c_1 + c_2 \frac{q^2}{2} + \dots, \quad (14)$$

where c_i is the i th log-cumulant.

The singularity spectrum $D(h)$ also allows quadratic expansion in the following form:

$$D(h) = d + \frac{c_2}{2!} \left(\frac{h - c_1}{c_2} \right)^2 + \dots, \quad (15)$$

where h is the Holder exponent.

Expressions (14) and (15) allow to represent $\zeta(q)$ and $D(h)$ as a series with degrees of q with coefficients c_p . The first two log-cumulants have the following interpretation. The log cumulant c_1 corresponds to the position of the singularity spectrum maximum $D(h)$, and therefore $c_1 = h(q = 0)$; c_2 characterizes the spectrum width. Indeed, a typical singularity spectrum $D(h)$ has the shape of a bell and is characterized by the width of the spectrum and the position of the maximum. Also, the log cumulant c_1 characterizes the slope of the scaling exponents $\tau(q)$; c_2 characterizes the deviation from linearity $\zeta(q)$.

If $c_1 \neq 0$ at $c_2 \rightarrow 0$, then $\zeta(q)$ is a linear function corresponding to a monofractal time series. For such time series, the spectrum $D(h)$ is narrow and degenerates into a single point in the limit, while the Holder exponent h is equal to the Hurst exponent (H).

Thus, the doublet c_1, c_2 contains the main part of multifractal information obtained from real data.

RESULTS AND THEIR DISCUSSION

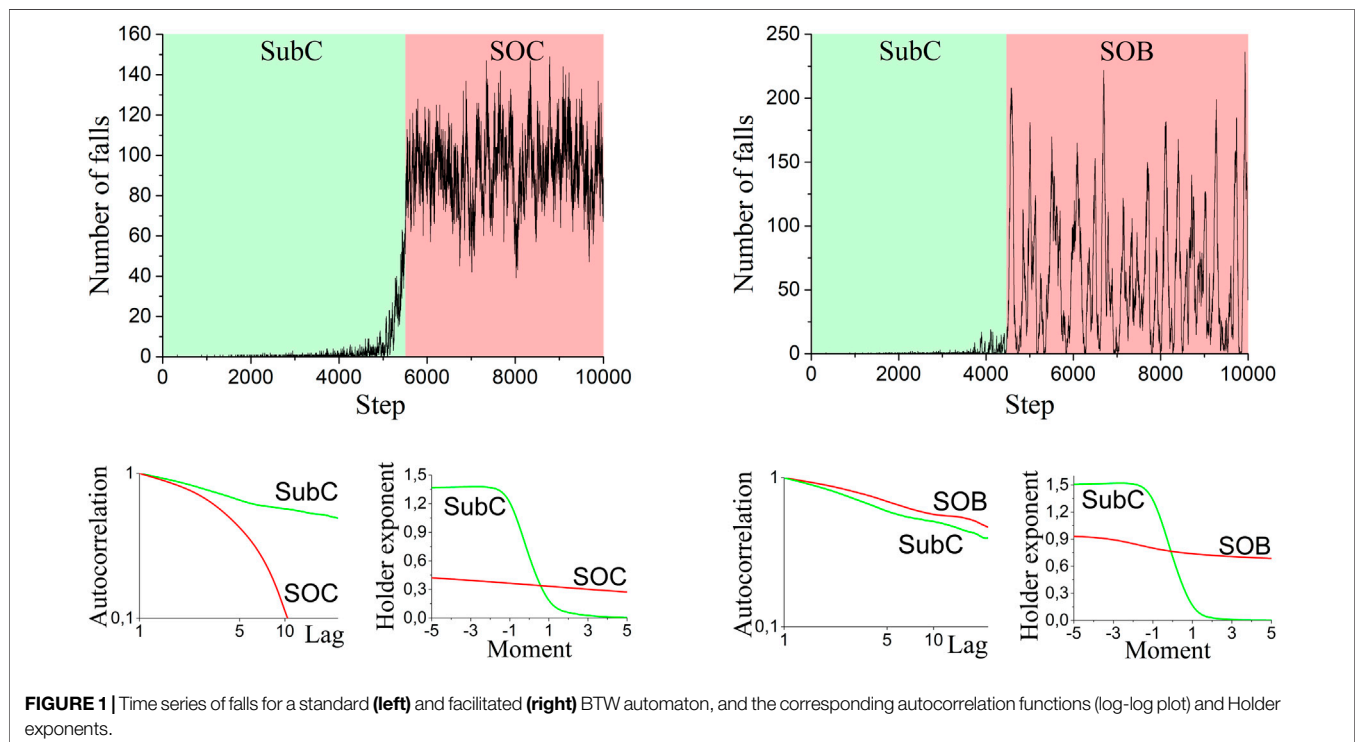
In this Section, we consider the features of the time series for number of falls (x_t)—the presence of long-range dependences and multifractal properties for fragments of time series corresponding to the subcritical (SubC) phase ($t \in [0, t_C]$) and critical state ($t \in [t_C, 10000]$). Here t_C is the time of the cellular automaton reaching the critical state. The results of consideration of the first two log cumulants behavior (c_1, c_2) as early warning identifiers for critical transitions are also presented. We generated fifty time series for each cellular automaton. Thus, we got fifty realizations for each random process. Obtaining such a number of realizations is due to the need to obtain interval estimates, in particular, for log cumulants.

Long-Range Dependence in the Time Series for the Sandpile Cellular Automata

Figure 1 shows the time series x_t , $t \in [0, 10000]$, for the BTW automata on the square lattice. These figures also show the autocorrelation functions and Holder exponents ($h(q)$), corresponding to the SubC phase and the critical state for the sandpile cellular automata on the lattice square. Critical state is

considered either as the self-organized critical state (the SOC state), implemented using standard rules, or as the self-organized bistability state (the SOB state) implemented using facilitated rules. By the SubC phase, we mean the phase in which the cellular automaton occurs until it reaches one of the critical states at the time moment corresponding to the critical iteration step (t_C). The time series for automata on random graphs has a qualitatively similar form, so we limited ourselves to visualizing time series for automata on square lattices. Despite this, in **Supplementary Table S1**, we presented the first two log cumulants (c_1, c_2) for all cellular automata, which are both in the SubC phase, as well as in one of two critical states.

It has been established (**Figure 1**) that for all cellular automata the rate of decrease of the autocorrelation function in the SubC phase ($t \in [0, t_C]$) is much greater than the rate of decrease of the autocorrelation function in the critical phase ($t \in [t_C, 10000]$) for the automata with the standard rules. This phenomenon is typical for all cellular automata, regardless of the graphs' structure. The shape of the curves $h(q)$ indicates that the SubC phase and critical state of cellular automata are characterized by time series x_t with multifractal properties, i.e. are described by a set of exponents $h(q)$ depending on the moment q . A feature of time series corresponding to the SubC phase is the predominant influence of weak fluctuations (at $q < 0$), while at strong fluctuations (at $q > 0$) the values of h are close to zero. First of all, this is due to the presence of a large number of zero values in the time series. In the critical state, the influence of strong fluctuations increases, and the influence of weak fluctuations decreases in comparison with the SubC phase. In the critical state, the stochastic dynamics of falls becomes both anticorrelated (at $h < 0.5$) for strong fluctuations, and correlated (at $h > 0.5$) for weak fluctuations for the automata with the standard rules. Thus, the transition of the standard cellular automaton into the critical state is



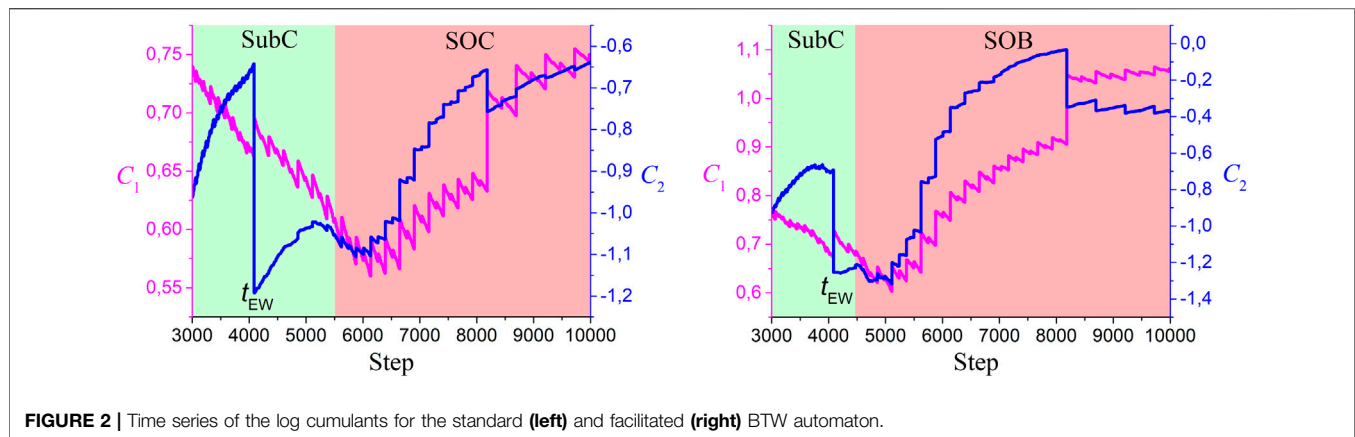


FIGURE 2 | Time series of the log cumulants for the standard (left) and facilitated (right) BTW automaton.

accompanied by a significant decrease of the correlated dynamics corresponding to weak fluctuations, and an insignificant increase in the uncorrelated dynamics corresponding to strong fluctuations. In a critical state, facilitated automata correspond to Holder exponents greater than 0.5.

The value c_1 and its change during a critical transition, presented in **Supplementary Table S1**, indicate an increase in c_1 during the transition of the facilitated cellular automaton from the SubC phase to the critical state.

Thus, the first two log cumulants can be used as precursors of critical transitions in the sandpile cellular automata. The next Subsection is devoted to a discussion of this problem.

Early Detection of Critical Transitions Based on Time Series for Log Wavelet Leaders Cumulant

In a previous Subsection, we showed that c_1 and c_2 can be used as a system of independent quantitative indicators for early detection of critical transitions in the sandpile cellular automata. Indeed, these indicators sufficiently describe the multifractal properties of the time series for the number of falls (x_t). And their change makes it possible to determine the presence or absence of the critical transition in the sandpile cellular automata. If we consider the sandpile cellular automata as time series generators x_t , recorded in real time, then it is quite possible to identify the approach of the automaton to the critical state based on the analysis results of the time series for the log cumulants $c_{1t}(x_t)$ and $c_{2t}(x_t)$. This Subsection is devoted to this analysis.

Figure 2 shows the time series c_{1t} and c_{2t} for cellular automata on square lattices. Time series for automata on random graphs have a similar form. The early warning time (t_{EW}) for the critical transitions is the same for all sandpile cellular automata, except for automaton on the BA graph, and takes the value $t_{EW} = 4087$. Despite this, the time until a decision is made ($\Delta t = t_C - t_{EW}$) depends on the structure and rules of the automaton. Thus, the time $\Delta t = 1413$ for the standard BTW model on the square lattice; the time $\Delta t = 413$ for facilitated BTW model on the square lattice. The Δt values for all cellular automata are presented in **Supplementary Table S2**, from which the following conclusions can be made. The Δt values for automata with Manna stochastic

rules (M-ST-SL, M-FA-SL, M-ST-BA, M-FA-BA, M-ST-ER, and M-FA-ER) less than for other automata. This empirical phenomenon has a simple explanation. In automata with Manna rules, the critical state occurs earlier than in automata with the BTW model and FF model rules. This is because of the Manna model rules are stochastic and, therefore, when some cells overturn, it is possible to quickly bring neighboring cells to an unstable state. Also, Δt for automata with facilitated rules is less than Δt for automata with standard rules. This is due to the fact that automata with facilitated rules transit into the critical state earlier than automata with standard rules. The reason for this is additional stochastic components in facilitated rules.

All cellular automata show the same behavior c_{1t} and c_{2t} , when approaching to t_{EW} (**Figure 2**). A decrease in the value of c_{1t} by the value Δc_1^- is observed, accompanied by a sharp increase by the value Δc_1^+ . For example, for BTW-ST-SL automaton $\Delta c_1^- = 0.0776$ and $\Delta c_1^+ = 0.0343$. An increase in the value of c_{1t} by the value Δc_1^+ is observed, accompanied by a sharp decrease by the value Δc_2^- . For example, for BTW-ST-SL automaton $\Delta c_2^+ = 0.2935$ and $\Delta c_2^- = 0.5586$. Consequently, the approach to t_{EW} is accompanied by an increase in the width of the singularity spectrum, and only at time t_{EW} a sharp decrease in the spectrum occurs. The considered values Δc are presented in **Supplementary Table S2** for all cellular automata. In general, the behavior of the log cumulants is independent of the structure and rules of the automata.

DISCUSSION

This Section presents a discussion of linking of our research results to some recent results from the theory of early warning indicators for critical transitions. Also, a discussion of possible practical applications of proposed early warning measures for detection of critical transitions is presented.

We will start by considering the main similarities and differences in the stochastic dynamics of the number of unstable cells (x_t) of automata located in the SubC phase and in one of the critical states (the SOC state and the SOB state), summarizing the discussions from *Result and Their Discussion*. Common to automata with standard and facilitated rules is the multifractal structure x_t in the SubC phase, and the monofractal (more precisely, a weak multifractal) structure x_t in

the SOC state (for the standard models) and in the SOB state (for the facilitated models). Such a transition into the critical state corresponds to the multifractal-monofractal transition (see the paper [33]). Another common feature is the long-range dependence (LRD) in the time series ($c_1 > 0.5$) for cellular automata in the SubC phase. Therefore, this multifractality is due to the existence of long-term correlations of small and large fluctuations [34]. The only fundamental difference between the SOC state and the SOB state is the presence of the short-range dependence (SRD) in the x_t in the first case ($c_1 < 0.5$), and the presence of the LRD in the x_t in the second case.

As it is shown in the paper [35], the average magnetization time series in the Ising model are multifractal in the SubC phase and in the critical state. Moreover, the structure of the time series is more heterogeneous in the critical state, than in the SubC phase. The increase of the memory in time series as the system approaches the critical point is also shown. In our opinion, a significant difference between the indicated results and those obtained by us lies in the fundamental difference between the rules for the Ising model and the rules for the sandpile cellular automata. In the paper [36], the results of the study of changes in the temporal autocorrelation at lag 1 and the power spectral density (PSD) as the system approaches to the critical point are presented. There was a significant increase in the autocorrelation in the neighborhood of the critical point, which is associated with the critical slowing down, as well as an increase in the parameter β of the power law for PSD ($S(\omega) \propto \omega^{-\beta}$). These results are consistent with our results for the facilitated model. Similar results are presented in [37–39], but obtained using fractal analysis methods. The results we obtained for facilitated models are also fully confirmed by the results presented in the papers [40–43]. However, the results similar to the one obtained by us for the standard models have not been presented yet.

The time series generated by real systems have a more complex structure than the time series generated by the sandpile cellular automata. However, we believe that the main features of c_{1t} and c_{2t} behavior, when the automata approach the critical state, will also be observed for real complex systems (see the papers [44, 45]). Let us take social media as an example. Recent studies have shown that most social networks are capable to self-organize into the critical state (see the papers [7, 46–51]). The mechanisms (local rules) for online social networks (for example, Twitter) for transition into the SOC state are similar to the standard rules of the sandpile cellular automaton on the BA graph. It is known (see the paper [52]) that the graph structure of user interactions in online social networks corresponds to BA graphs. Indeed, the information distribution is carried out by users who are in the state of high-level reflection (unstable state). It manifests itself in the form of reposts to their subscribers (neighboring nodes of the graph). These subscribers, being in the unstable state, send reposts to their subscribers, etc. As a result, starting from the

moment t_C avalanche-like distribution of information in the network is observed. On the contrary, the SubC phase ($t \in [0, t_C]$) of the online social network is characterized by stochastic fluctuations in repost activity with a relatively small amplitude. In most of such situations, it becomes necessary to evaluate t_{EW} , which is of undoubted interest for all specialists in social networks monitoring. Obtaining of such estimates for real time series of retweets relevant to various topics is one of the goals of our further studies.

Finally, we look at the limitations and possible further research in the analysis of critical transition precursors in sandy cellular automata.

We have established only one limitation of the proposed approach associated with the length of the analyzed time series and the large number of zero values in it. To obtain reliable results, the length of the time series must be at least 2000 steps. Otherwise, significant fluctuations in the value of the log cumulants are observed, in which it is impossible to determine their smoothed behavior.

From the point of view of the prospects for further research, in our opinion, one should focus on the interpretation of jumps in the values of log-cumulants, which are characteristic of critical states of all cellular automata. An explanation of this empirical phenomenon is possible by analyzing the time series obtained under various initial conditions and sizes of all investigated cellular automata.

DATA AVAILABILITY STATEMENT

The raw data supporting the conclusions of this article will be made available by the authors, without undue reservation.

AUTHOR CONTRIBUTIONS

AD, VK, and VD designed the research. VK, VD and NA performed the simulations. NA prepared the figures. All authors contributed to writing and reviewing the manuscript.

FUNDING

The work is an output of a research project implemented as part of the Basic Research Program at the National Research University Higher School of Economics (HSE University).

SUPPLEMENTARY MATERIAL

The Supplementary Material for this article can be found online at: <https://www.frontiersin.org/articles/10.3389/fphy.2022.839383/full#supplementary-material>

REFERENCES

- Scheffer M, Carpenter SR, Lenton TM, Bascompte J, Brock W, Dakos V, et al. Anticipating Critical Transitions. *Science* (2012) 338:344–8. doi:10.1126/science.1225244
- Morales IO, Landa E, Angeles CC, Toledo JC, Rivera AL, Temis JM, et al. Behavior of Early Warnings Near the Critical Temperature in the Two-Dimensional Ising Model. *PLoS ONE* (2015) 10:e0130751. doi:10.1371/journal.pone.0130751
- Suweis S, D'Odorico P Early Warning Signs in Social-Ecological Networks. *PLoS ONE* (2014) 9:e01851. doi:10.1371/journal.pone.0101851
- Scheffer M, Bascompte J, Brock WA, Brovkin V, Carpenter SR, Dakos V, et al. Early-warning Signals for Critical Transitions. *Nature* (2009) 461:53–9. doi:10.1038/nature08227
- Dakos V, Carpenter SR, van Nes EH, Scheffer M Resilience Indicators: Prospects and Limitations for Early Warnings of Regime Shifts. *Phil Trans R Soc B* (2015) 370:20130263. doi:10.1098/rstb.2013.0263
- George SV, Kachhara S, Misra R, Ambika G Early Warning Signals Indicate a Critical Transition in Betelgeuse. *A&A* (2020) 640:L21. doi:10.1051/0004-6361/202038785
- Tadić B, Melnik R Self-Organised Critical Dynamics as a Key to Fundamental Features of Complexity in Physical, Biological, and Social Networks. *Dynamics* (2021) 1:181–97. doi:10.3390/dynamics1020011
- Bak P, Tang C, Wiesenfeld K Self-organized Criticality: An Explanation of the 1/f noise. *Phys Rev Lett* (1987) 59:381–4. doi:10.1103/PhysRevLett.59.381
- Shapoval A, Shapoval B, Shnirman M 1/x Power-Law in a Close Proximity of the Bak-Tang-Wiesenfeld Sandpile. *Sci Rep* (2021) 11:18151. doi:10.1038/s41598-021-97592-x
- Buendía V, di Santo S, Bonachela JA, Muñoz MA Feedback Mechanisms for Self-Organization to the Edge of a Phase Transition. *Front Phys* (2020) 8:333. doi:10.3389/fphy.2020.00333
- Cocchi L, Gollo LL, Zalesky A, Breakspear M Criticality in the Brain: A Synthesis of Neurobiology, Models and Cognition. *Prog Neurobiol* (2017) 158:132–52. doi:10.1016/j.pneurobio.2017.07.002
- Buendía V, di Santo S, Villegas P, Burioni R, Muñoz MA Self-organized Bistability and its Possible Relevance for Brain Dynamics. *Phys Rev Res* (2020) 2:013318. doi:10.1103/PhysRevResearch.2.013318
- di Santo S, Burioni R, Vezzani A, Muñoz MA Self-organized Bistability Associated with First-Order Phase Transitions. *Phys Rev Lett* (2016) 116:240601. doi:10.1103/PhysRevLett.116.240601
- Járai AA The Sandpile Cellular Automaton. In: Louis PY Nardi F, editors. *Probabilistic Cellular Automata. Emergence, Complexity and Computation*, Vol. 27 (2018). p. 79–88. doi:10.1007/978-3-319-65558-1_6
- Bak P, Tang C, Wiesenfeld K Self-organized Criticality. *Phys Rev A* (1988) 38:364–74. doi:10.1103/PhysRevA.38.364
- Feder HJS, Feder J Self-organized Criticality in a Stick-Slip Process. *Phys Rev Lett* (1991) 66:2669–72. doi:10.1103/PhysRevLett.66.2669
- Manna SS Two-state Model of Self-Organized Criticality. *J Phys A: Math Gen* (1991) 24:L363–L369. doi:10.1088/0305-4470/24/7/009
- Albert R, Barabási A-L Statistical Mechanics of Complex Networks. *Rev Mod Phys* (2002) 74:47–97. doi:10.1103/RevModPhys.74.47
- Newman MEJ, Strogatz SH, Watts DJ Random Graphs with Arbitrary Degree Distributions and Their Applications. *Phys Rev E* (2001) 64:026118. doi:10.1103/PhysRevE.64.026118
- Buldyrev SV, Parshani R, Paul G, Stanley HE, Havlin S Catastrophic cascade of Failures in Interdependent Networks. *Nature* (2010) 464:1025–8. doi:10.1038/nature08932
- Cannings C, Penman DB Ch. 2. Models of Random Graphs and Their Applications. *Handbook Stat* (2003) 21:51–91. doi:10.1016/S0169-7161(03)21004-X
- Arneodo A, Bacry E, Muzy JF The Thermodynamics of Fractals Revisited with Wavelets. *Physica A: Stat Mech its Appl* (1995) 213:232–75. doi:10.1016/0378-4371(94)00163-N
- Muzy JF, Bacry E, Arneodo A Multifractal Formalism for Fractal Signals: The Structure-Function Approach versus the Wavelet-Transform Modulus-Maxima Method. *Phys Rev E* (1993) 47:875–84. doi:10.1103/PhysRevE.47.875
- Yamamoto M. Fluctuations Observed in Biological Time Series Signals and Their Functional Significance. *Front Med Biol Eng* (1991) 3:135–7.
- Ihlen EAF Introduction to Multifractal Detrended Fluctuation Analysis in Matlab. *Front Physio* (2012) 3:141. doi:10.3389/fphys.2012.00141
- Kantelhardt JW, Zschiegner SA, Koscielny-Bunde E, Havlin S, Bunde A, Stanley HE Multifractal Detrended Fluctuation Analysis of Nonstationary Time Series. *Physica A: Stat Mech its Appl* (2002) 316:87–114. doi:10.1016/S0378-4371(02)01383-3
- Mallat S, Hwang WL Singularity Detection and Processing with Wavelets. *IEEE Trans Inform Theor* (1992) 38:617–43. doi:10.1109/18.119727
- Wendt H, Abry P Multifractality Tests Using Bootstrapped Wavelet Leaders. *IEEE Trans Signal Process* (2007) 55:4811–20. doi:10.1109/TSP.2007.896269
- Jaffard S, Lashermes B, Abry P Wavelet Leaders in Multifractal Analysis. In: Qian T, Vai MI, Yuesheng X, editors. *Wavelet Analysis and Applications* (2006). p. 201–46. doi:10.1007/978-3-7643-7778-6_17
- Wendt H, Roux SG, Abry P Bootstrap for Log Wavelet Leaders Cumulant Based Multifractal Analysis. In: 2006 14th European Signal Processing Conference (2006). p. 1–5.
- Ciuciu P, Abry P, Rabrait C, Wendt H Log Wavelet Leaders Cumulant Based Multifractal Analysis of EVI fMRI Time Series: Evidence of Scaling in Ongoing and Evoked Brain Activity. *IEEE J Sel Top Signal Process* (2008) 2:929–43. doi:10.1109/JSTSP.2008.2006663
- Wendt H *Contributions of Wavelet Leaders and Bootstrap to Multifractal Analysis: Images, Estimation Performance, Dependence Structure and Vanishing Moments. Confidence Intervals and Hypothesis Tests. Signal and Image Processing*. Lyon, France: Ecole normale supérieure de lyon - ENS LYON (2008). Available from: <https://tel.archives-ouvertes.fr/tel-00333599/document> (Accessed December 5, 2021).
- Murcio R, Masucci AP, Arcaute E, Batty M Multifractal to Monofractal Evolution of the London Street Network. *Phys Rev E* (2015) 92. doi:10.1103/PhysRevE.92.062130
- Zhou W-X Finite-size Effect and the Components of Multifractality in Financial Volatility. *Chaos, Solitons & Fractals* (2012) 45:147–55. doi:10.1016/j.chaos.2011.11.004
- Zhao L, Li W, Yang C, Han J, Su Z, Zou Y Multifractality and Network Analysis of Phase Transition. *PLoS ONE* (2017) 12:e0170467. doi:10.1371/journal.pone.0170467
- Morales IO, Landa E, Angeles CC, Toledo JC, Rivera AL, Temis JM, et al. Behavior of Early Warnings Near the Critical Temperature in the Two-Dimensional Ising Model. *PLoS ONE* (2015) 10:e0130751. doi:10.1371/journal.pone.0130751
- Rypdal M Early-Warning Signals for the Onsets of Greenland Interstadials and the Younger Dryas-Preboreal Transition. *J Clim* (2016) 29:4047–56. doi:10.1175/JCLI-D-15-0828.1
- Zhang X, Xu Y, Liu Q, Kurths J, Grebogi C Rate-dependent Tipping and Early Warning in a Thermoacoustic System under Extreme Operating Environment. *Chaos* (2021) 31:113115. doi:10.1063/5.0071977
- Dexing L, Enyuan W, Xiangguo K, Xiaoran W, Chong Z, Haishan J, et al. Fractal Characteristics of Acoustic Emissions from Coal under Multi-Stage True-Triaxial Compression. *J Geophys Eng* (2018) 15:2021–32. doi:10.1088/1742-2140/aac31a
- Dakos V, Carpenter SR, Brock WA, Ellison AM, Guttal V, Ives AR, et al. Methods for Detecting Early Warnings of Critical Transitions in Time Series Illustrated Using Simulated Ecological Data. *PLoS ONE* (2012) 7:e41010. doi:10.1371/journal.pone.0041010
- van der Bolt B, van Nes EH, Scheffer M No Warning for Slow Transitions. *J R Soc Interf* (2021) 18:20200935. doi:10.1098/rsif.2020.0935
- Diks C, Hommes C, Wang J Critical Slowing Down as an Early Warning Signal for Financial Crises? *Empir Econ* (2019) 57:1201–28. doi:10.1007/s00181-018-1527-3
- Zhang Z, Li Y, Hu L, Tang Ca., Zheng H Predicting Rock Failure with the Critical Slowing Down Theory. *Eng Geology* (2021) 280:105960. doi:10.1016/j.enggeo.2020.105960
- Aschwanden MJ, Crosby NB, Dimitropoulou M, Georgoulis MK, Hergarten S, McAtter J, et al. 25 Years of Self-Organized Criticality: Solar and Astrophysics. *Space Sci Rev* (2016) 198:47–166. doi:10.1007/s11214-014-0054-6

45. Lise S, Paczuski M Self-organized Criticality and Universality in a Nonconservative Earthquake Model. *Phys Rev E* (2001) 63:036111. doi:10.1103/PhysRevE.63.036111
46. Zhukov D, Kunavin K, Lyamin S Online Rebellion: Self-Organized Criticality of Contemporary Protest Movements. *SAGE Open* (2020) 10: 215824402092335. doi:10.1177/2158244020923354
47. Tadic B Self-organised Criticality and Emergent Hyperbolic Networks: Blueprint for Complexity in Social Dynamics. *Eur J Phys* (2019) 40:024002. doi:10.1088/1361-6404/aaf144/meta
48. Dmitriev A, Dmitriev V Identification of Self-Organized Critical State on Twitter Based on the Retweets' Time Series Analysis. *Complexity* (2021) 2021: 6612785. doi:10.1155/2021/6612785
49. Dmitriev A, Dmitriev V, Balybin S Self-Organized Criticality on Twitter: Phenomenological Theory and Empirical Investigation Based on Data Analysis Results. *Complexity* (2019) 2019:8750643. doi:10.1155/2019/8750643
50. Wang Y, Fan H, Lin W, Lai Y-C, Wang X Growth, Collapse and Self-Organized Criticality in Complex Networks. *Sci Rep* (2016) 6:24445. doi:10.1038/srep24445
51. Tadić B, Dankulov MM, Melnik R Mechanisms of Self-Organized Criticality in Social Processes of Knowledge Creation. *Phys Rev E* (2017) 96:032307. doi:10.1103/PhysRevE.96.032307
52. Broido AD, Clauset A Scale-free Networks Are Rare. *Nat Commun* (2019) 10: 1017. doi:10.1038/s41467-019-08746-5

Conflict of Interest: The authors declare that the research was conducted in the absence of any commercial or financial relationships that could be construed as a potential conflict of interest.

Publisher's Note: All claims expressed in this article are solely those of the authors and do not necessarily represent those of their affiliated organizations, or those of the publisher, the editors, and the reviewers. Any product that may be evaluated in this article, or claim that may be made by its manufacturer, is not guaranteed or endorsed by the publisher.

Copyright © 2022 Dmitriev, Kornilov, Dmitriev and Abbas. This is an open-access article distributed under the terms of the Creative Commons Attribution License (CC BY). The use, distribution or reproduction in other forums is permitted, provided the original author(s) and the copyright owner(s) are credited and that the original publication in this journal is cited, in accordance with accepted academic practice. No use, distribution or reproduction is permitted which does not comply with these terms.



Dehazing Based on Long-Range Dependence of Foggy Images

Hong Xu Yuan¹, Zhiwu Liao^{1*}, Rui Xin Wang¹, Xinceng Dong¹, Tao Liu¹, Wu Dan Long², Qing Jin Wei¹, Ya Jie Xu¹, Yong Yu³, Peng Chen^{4,5*} and Rong Hou^{4,5*}

¹School of Computer Science, Sichuan Normal University, Chengdu, China, ²School of Computing and Artificial Intelligence, Southwest Jiaotong University, Chengdu, China, ³School of Mathematics and Computer (Big Data Science), Panzhihua University, Panzhihua, China, ⁴Chengdu Research Base of Giant Panda Breeding, Sichuan Key Laboratory of Conservation Biology for Endangered Wildlife, Chengdu, China, ⁵Sichuan Academy of Giant Panda, Chengdu, China

OPEN ACCESS

Edited by:

Ming Li,
Zhejiang University, China

Reviewed by:

Nan Mu,
Michigan Technological University,
United States
Junyu He,
Zhejiang University, China

*Correspondence:

Zhiwu Liao
liaozihiwu@163.com
Peng Chen
capricorncp@163.com
Rong Hou
405536517@qq.com

Specialty section:

This article was submitted to
Interdisciplinary Physics,
a section of the journal
Frontiers in Physics

Received: 04 December 2021

Accepted: 10 January 2022

Published: 16 February 2022

Citation:

Yuan HX, Liao Z, Wang RX, Dong X,
Liu T, Long WD, Wei QJ, Xu YJ, Yu Y,
Chen P and Hou R (2022) Dehazing
Based on Long-Range Dependence of
Foggy Images.
Front. Phys. 10:828804.
doi: 10.3389/fphy.2022.828804

Deep neural networks (DNNs) with long-range dependence (LRD) have attracted more and more attention recently. However, LRD of DNNs is proposed from the view on gradient disappearance in training, which lacks theory analysis. In order to prove LRD of foggy images, the Hurst parameters of over 1,000 foggy images in SOTS are computed and discussed. Then, the Residual Dense Block Group (RDBG), which has additional long skips among two Residual Dense Blocks to fit LRD of foggy images, is proposed. The Residual Dense Block Group can significantly improve the details of dehazing image in dense fog and reduce the artifacts of dehazing image.

Keywords: long-range dependence, residual dense block, residual dense block group, deep neural network, image dehazing, Hurst parameter (H)

INTRODUCTION

The single image dehazing based on deep neural networks (DNNs) refers to restoring an image from a foggy image using DNNs. Although some efforts on dehazing have been proposed recently [1–6], foggy image modeling is still an unsolved problem.

The early image model is Gaussian or Mixture Gaussian [7], but it cannot properly fit with foggy images. In fact, the foggy images seem to show long-range dependence. That is, the gray levels seemed to influence pixels in nearby regions. In our framework, each foggy image with m rows and n columns in SOTS is reshaped as is an $m \times n$ column vector by arranging the elements of the image column by column. Thus, we can fit the images by fractional Gaussian noise (fGn) [8–12] and discuss dependence of an image by its Hurst parameter. The main conclusion of the Hurst parameter of a fGn is as follows.

The auto-correlation function (ACF) of fGn is as follows:

$$C_{fGn}(\tau) = \frac{V_H}{2} \left[(|\tau| + 1)^{2H} + (|\tau| - 1)^{2H} - 2|\tau|^{2H} \right] \quad (1)$$

where

$$V_H = \Gamma(1 - 2H) \frac{\cos \pi H}{\pi H} \quad (2)$$

is the strength of fGn and $0 < H < 1$ is the Hurst parameters [8–10].

If $0.5 < H < 1$, one has the following:

$$\int_0^{\infty} C_{fGn}(\tau) d\tau = \infty \quad (3)$$

Thus, the fGn is of long-range dependency (LRD) when $0.5 < H < 1$.

When $0 < H < 0.5$, one has the following:

$$\int_0^{\infty} C_{fGn}(\tau) d\tau < \infty \quad (4)$$

The above fGn is of short-range dependence (SRD) [8–12].

Recently, some deep neural networks (DNN) with LRD are proposed [4–6, 13], whose motivation is mainly from avoiding gradient disappearance in training. However, the LRD of these DNNs has never been discussed and proven in theory. In this study, the Hurst parameters of test images in SOTS datasets [14] are computed and LRD of foggy images is proven. Motivated by LRD of foggy images, we proposed a new network module, the Residual Dense Block Group (RDBG) composed of two bundled Residual Dense Block Groups (DRBs) proposed in reference [13]. The RDBG has additional long skips between two DRBs to fit LRD of foggy images and can be used to form a new dehazing network. This structure can significantly improve the quality of dehazing images in heavy fog.

The remainder of this article is as follows: the second section introduces the preliminaries of fGn; the third section gives the case study; then a framework based on LRD of foggy images is presented; finally, there are the conclusions and acknowledgments.

PRELIMINARIES

Fractional Brownian Motion

The fBm of Weyl type is defined by [8].

$$B_H(t) - B_H(0) = \frac{1}{\Gamma(H+0.5)} \left\{ \int_{-\infty}^0 [(t-u)^{H-0.5} - (-u)^{H-0.5}] dB(u) + \int_0^t (t-u)^{H-0.5} dB(u) \right\} \quad (5)$$

where $0 < H < 1$, and $B(t)$ is Gaussian.

$$\begin{aligned} \text{fBm has stationary increment: } B_H(t+\tau) - B_H(t) \\ = B_H(\tau) - B_H(0) \end{aligned} \quad (6)$$

$$\text{and self-affinity property: } B_H(at) = a^H B_H(t), a > 0 \quad (7)$$

Fractional Gaussian Noise

Let $x(t)$ be the gray level of the t th pixel of an image and be a fGn [8–12].

$$x(t) = B_H(t) - B_H(0) \quad (8)$$

Its ACF follows Eqs 1, 2.

An approximation of $C_{fGn}(\tau)$ is as follows:

$$C_{fGn}(\tau) \propto |\tau|^{2H-2} \quad (9)$$

CASE STUDY

Data Set

Synthetic data set RESIDE: Li et al. [16] created a large-scale benchmark data set RESIDE composed of composite foggy images and real foggy images.

Synthetic data set: the SOTS test data set is used as the test set. The SOTS test set includes 500 indoor foggy images and 500 outdoor foggy images.

Real data set: it includes 100 real foggy images in the SOTS data set in the RESIDE and the real foggy data collected on the Internet.

Calculate Hurst Parameter

Rescaled range analysis (RRA) [15] for foggy images is closely associated with the Hurst exponent, H , also known as the “index of dependence” or the “index of long-range dependence.” The steps to obtain the Hurst parameter are as follows:

1. Preprocessing: An image with m row and n column is concatenated column by column to form an $m \times n$ column vector. For better understanding, a simple example is presented: the size of the foggy image in Figure 4A is 348×248 , and then it is concatenated column by column to form an 86,304-column vector.
2. Rescale vector: The original vector can be divided equally into several ranges for further RRA, as follows. The first range at the first layer is defined as RS_{11} , representing the original $m \times n$ vector, and then it can be divided into two parts, RS_{21} and RS_{22} , at the second layer, whose dimension equals to $(m \times n/2)$ where $(.)$ represents the floor integer. Repeat the above process until the vector dimensions at a specific layer are less than $(m \times n/2^6)$.

Layer 1. RS_{11} : original $m \times n$ vector.

Layer 2. RS_{21} : $(m \times n/2)$, RS_{22} : $(m \times n/2)$.

Layer 3. RS_{31} : $(m \times n/4)$, RS_{32} : $(m \times n/4)$, RS_{33} : $(m \times n/4)$, RS_{34} : $(m \times n/4)$.

Thus, the dimensions of ranges of the foggy image are as follows:

Layer 1. RS_{11} : 86,304.

Layer 2. RS_{21} : 43,152, RS_{22} : 43,152.

Layer 3. RS_{31} : 21,576, RS_{32} : 21,576, RS_{33} : 21,576, RS_{34} : 21,576.

3. Calculate the mean for each range.

$$m_{ij} = \frac{1}{n_{ij}} \sum_{k_{ij}=1}^{n_{ij}} X_{k_{ij}} \quad (10)$$

where n_{ij} represents the number of the elements in the j th range of the i th layer; $X_{k_{ij}}$ represents the value of the k_{ij} th element in the j th range of the i th layer; m_{ij} represents the mean value of the elements in the j th range of the i th layer.

4. Calculate the deviations of each element in every range. The deviation can be calculated as follows:

TABLE 1 | Some intermediate results of calculating the Hurst parameter of the foggy image in **Figure 5A**.

| Layer | Numbers of ranges in layers | Numbers of data points in ranges (x) | Log(x) | R/S | Log (R/S) | Slope of the fitted straight line (i.e., the value of Hurst parameter) |
|-------|-----------------------------|--------------------------------------|---------|--------|-----------|--|
| 1 | 1 | 86,304 | 10.6725 | 25,754 | 15.3667 | 0.990 |
| 2 | 2 | 43,152 | 9.9793 | 16,445 | 14.9181 | |
| 3 | 4 | 21,576 | 9.2862 | 7,367 | 14.1151 | |
| 4 | 8 | 10,788 | 8.5930 | 3,567 | 13.3899 | |
| 5 | 16 | 5,394 | 7.8999 | 1784 | 12.6969 | |

$$Y_{k_{ij}} = X_{k_{ij}} - m_{ij} \quad (11)$$

where $Y_{k_{ij}}$ represents the deviation of the k_{ij}^{th} element in the j th range of the i th layer.

- Obtain the accumulated deviations for each element in the corresponding range.

$$y_{ij,N} = \sum_{k_{ij}=1}^N Y_{k_{ij}}, \quad N = 1, \dots, n_{ij} \quad (12)$$

where $y_{ij,N}$ represents the accumulated deviation for N elements in the j th range of the i th layer.

- Calculate the widest difference of the deviations in each range.

$$R_{ij} = \max(y_{ij,1}, y_{ij,2}, \dots, y_{ij,N}) - \min(y_{ij,1}, y_{ij,2}, \dots, y_{ij,N}), \quad N = 1, \dots, n_{ij} \quad (13)$$

where R_{ij} represents the widest difference for the j th range of the i th layer.

- Calculate the rescaled range for each range.

$$\text{Rescaled range} = \left(\frac{R}{S}\right)_{ij} = \frac{R_{ij}}{\sigma_{ij}} \quad (14)$$

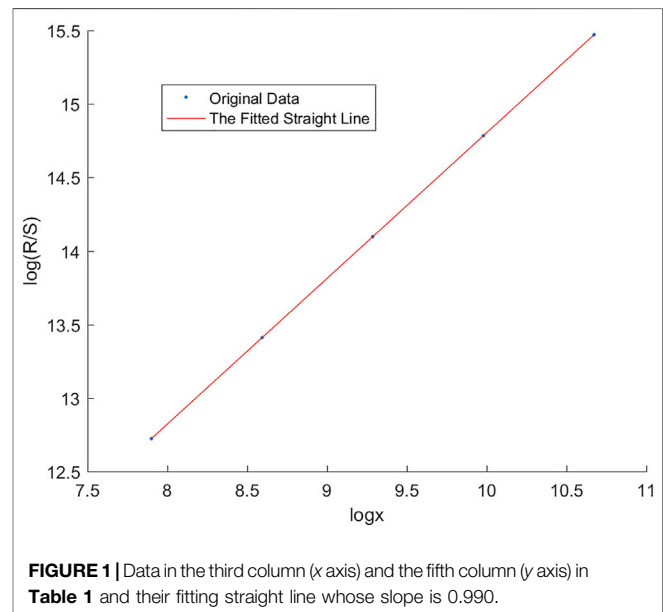
where R/S represents the rescaled range for the j th range of the i th layer, while σ_{ij} represents the standard deviation of the accumulated deviations for the j th range of the i th layer.

- Obtain the averaged rescaled range values for each layer.

$$\left(\frac{R}{S}\right)_i = \frac{1}{2^{l-1}} \sum_{j=1}^{[mxn/2^{l-1}]} \left(\frac{R}{S}\right)_{ij} \quad (15)$$

where l is the layer of the ranges with the identity size. The R/S is calculated using **Eq. 15** and the R/S of the example image is shown in **Table 1**.

- Obtain the Hurst exponent. Plot the logarithm of the size (x axis) of each range in the i th layer versus the logarithm of the average rescaled range of the corresponding layer using **Eq. 15** (y axis) (**Figure 1**), and the slope of the fitted line is regarded as the value of the Hurst exponent, that is, the Hurst parameter.

**FIGURE 1** | Data in the third column (x axis) and the fifth column (y axis) in **Table 1** and their fitting straight line whose slope is 0.990.

Hurst Parameters H of Foggy Images

The plots of four image sets in SOTS, 500 indoor images, 500 outdoor, 1,000 outdoor and indoor images, and 100 real foggy images, are shown in **Figure 2**. The x axis represents the serial numbers of the test images while the y axis is the Hurst parameters of the images. That is, the i th point in **Figure 2** represents the Hurst parameter of the i th image. Thus, we can know the Hurst parameters of over 1,000 foggy images by observing y values of the points in **Figure 2**.

From **Figure 2**, we can observe that the least y values of subfigures in **Figure 2** are 0.6 or 0.65, which means that the Hurst parameters of four image data sets are all above 0.6. Thus the foggy images are of LRD, which can help us design some novel dehazing methods.

Moreover, although the Hurst parameter for each image is a constant, the different images have different Hurst parameters because of their different contents. For example, the Hurst parameter of a complex image with more colors and objects (**Figures 5A,B**) is bigger than a simple image (**Figure 5C**).

Based on the LRD of the foggy images, the Residual Dense Block Group (RDBG) based on RDB is proposed. The RDBG,

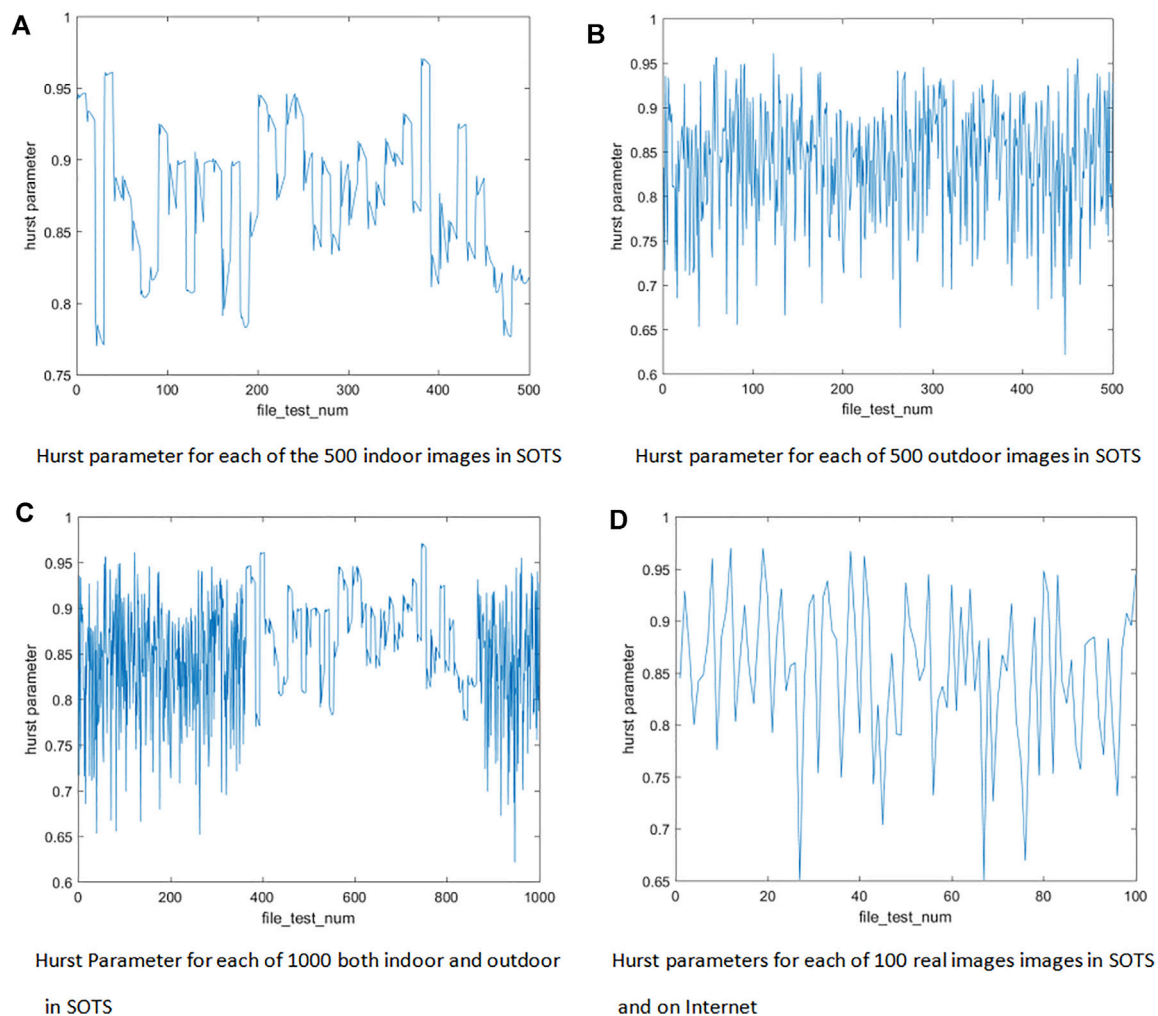


FIGURE 2 | Plots of H of four foggy image datasets.

which has additional long skips between two RDBs to fit LRD of foggy images, can significantly improve the details of dehazing image in dense fog and reduce the artifacts of dehazing image.

DEHAZING BASED ON RESIDUAL DENSE BLOCK GROUP

Dependence in Neural Network

The neural network can be considered as a hierarchical graph model whose nodes are connected by weighted edges. The weights of edges are trained according to some predefined cost functions. Generally, the value of the i th node in the k th layer is decided by the nodes in the $(k-1)$ th layer connected to the i th node [18–24]. That is,

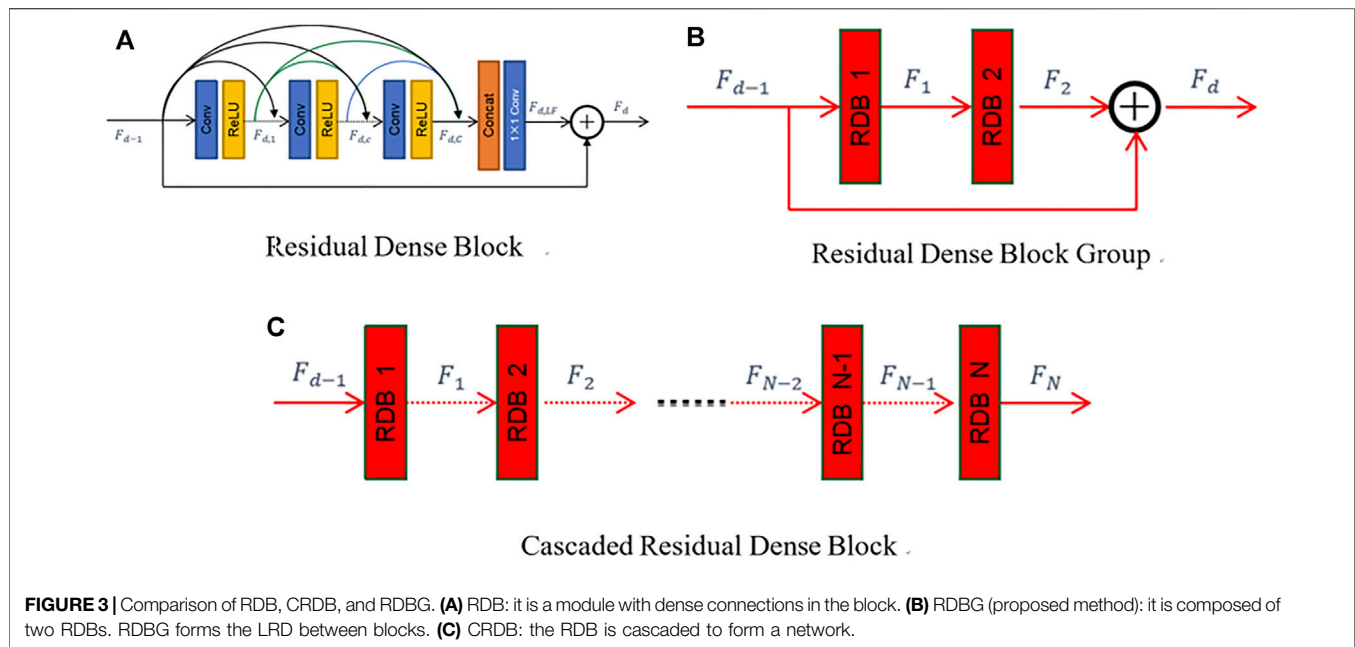
$$x^{(k)}(i) = f(W^{(k-1,k)}(i)x^{(k-1)}(i)) \quad (16)$$

where $x^{(k)}(i)$ is the value of the i th node in the k th layer, f is an activation function, $W^{(k-1,k)}$ is a vector of weights of edges to connect nodes in the $(k-1)$ th layers and the i th node, and $x^{(k-1)}(i)$ are values of nodes in the $(k-1)$ th layers connected to the i th node.

Thus, the value of the i th node is only influenced by its directly connected nodes. This assumption may be correct in some cases, but it is not true in images since we have proved the LRD of foggy images. Thus, we should design a new module of the neural network to fit the LRD of the foggy images.

Residual Dense Block Group

Just as discussed in the above subsection, the most straight method to design a structure fitting LRD of images is to connect a node to nodes with longer distance to it directly. Thus, the information of faraway nodes is introduced to help us to recover the real gray level from foggy observations.



Following this intuitive explanation, the length of a skip (connection edge between two nodes) which is defined as the number of crossing nodes can be used to measure the dependence of a time series approximately.

In this context, motivated by the LRD of foggy images, a new residual module RDBG is proposed by two bundled resident dense blocks (RDBs). As shown in **Figure 3A**, the RDB is a module with dense connections only in the block. In **Figure 3**, the features which are values of nodes in different layers of the RDB form a time series. Thus, an RDB only with dense connections in blocks cannot fit the LRD well, especially in dense fog, while the proposed RDBG which adds an additional long skip from the beginning of the first block to the end of the second block can fit the LRD better than the RDB. In heavy fog, since the RDBG fits LRD of images to utilize more information of images, it can obtain a better dehazing image.

As shown in **Figure 3C**, Yang Aiping [16] et al. and X Liu [17] et al. used consecutive RDBs in a cascade manner. Since connections are also in blocks, in essence, it cannot fit LRD of images well.

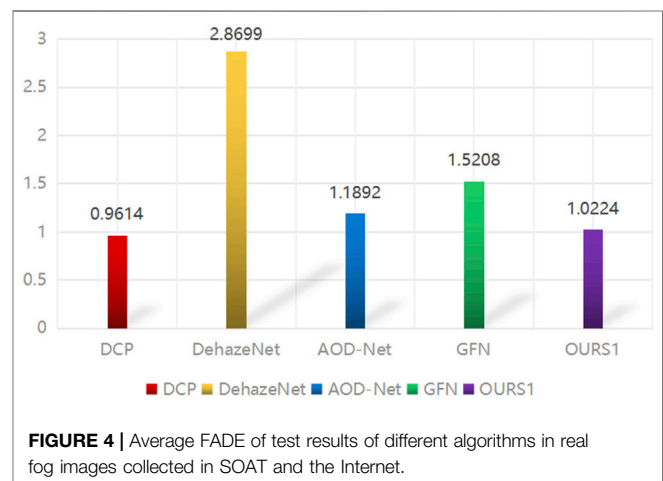
Experimental Results and Discussions

The method proposed in this article will be compared with four state-of-the-art dehazing methods: DehazeNet, AOD-Net, DCP, and GFN.

Three metrics: PSNR, SSIM, and reference-less FADE are used to evaluate the quality of dehazing images. Our proposed method gets the best PSNR and SSIM among all methods (**Table 2**), which means that our method has the largest similarities between the original images and the dehazing images in both image gray levels and image structures. It also has satisfied results in FADE (**Table 2**; **Figure 4**), which means that our method is robust and stable in dehazing.

TABLE 2 | PSNR, SSIM, and FADE between the dehazing results and original images of synthetic image in SOATS. The best results are marked by bold.

| Dataset | Metric | DCP | DehazeNet | AOD-net | GFN | OURS1 |
|---------|--------|---------------|-----------|---------|---------------|---------------|
| Indoor | PSNR | 16.16 | 19.82 | 20.15 | 24.91 | 28.479 |
| | SSIM | 0.8546 | 0.8209 | 0.8162 | 0.9186 | 0.9665 |
| | FADE | 0.7792 | 0.7943 | 0.8052 | 0.5364 | 0.5602 |
| Outdoor | PSNR | 19.14 | 24.75 | 24.14 | 28.29 | 30.033 |
| | SSIM | 0.8605 | 0.9269 | 0.9181 | 0.9621 | 0.9714 |
| | FADE | 0.5941 | 0.7671 | 0.7677 | 0.8238 | 0.7442 |



The dehazing examples are given in **Figures 5, 6**, and their Hurst parameters are given under the foggy images.





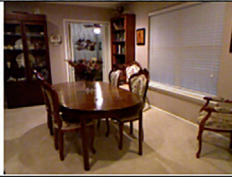

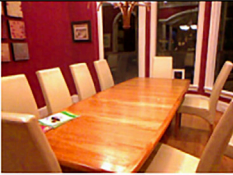


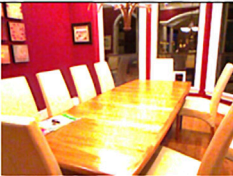
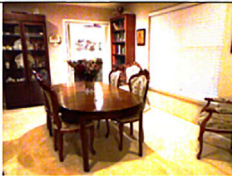

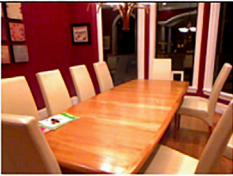
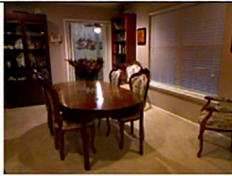

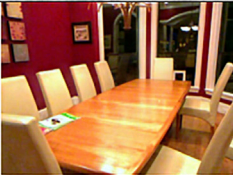
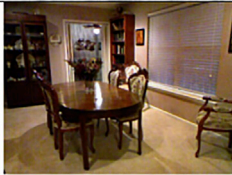

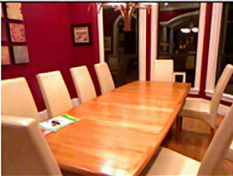
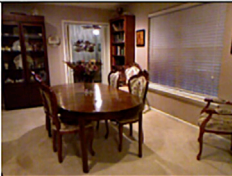

| | A | B | C |
|-----------------|---|---|---|
| Foggy image |  |  |  |
| | H=0.990 | H=0.933 | H=0.876 |
| Original image |  |  |  |
| AOD |  |  |  |
| | PSNR=20.44, SSIM=0.85, FAD=0.80 | PSNR=18.36, SSIM=0.89, FAD=0.78 | PSNR=25.43, SSIM=0.91, FAD=0.76 |
| DCP |  |  |  |
| | PSNR=18.03, SSIM=0.83, FAD=0.78 | PSNR=17.07, SSIM=0.76, FAD=0.79 | PSNR=20.05, SSIM=0.89, FAD=0.59 |
| DehazNet |  |  |  |
| | PSNR=20.84, SSIM=0.85, FAD=0.80 | PSNR=19.16, SSIM=0.90, FAD=0.81 | PSNR=25.33, SSIM=0.94, FAD=0.77 |
| GFN |  |  |  |
| | PSNR=24.51, SSIM=0.92, FAD=0.52 | PSNR=26.96, SSIM=0.96, FAD=0.53 | PSNR=29.73, SSIM=0.95, FAD=0.82 |
| Proposed method |  |  |  |
| | PSNR=30.85, SSIM=0.98, FAD=0.53 | PSNR=30.36, SSIM=0.98, FAD=0.53 | PSNR=30.00, SSIM=0.95, FAD=0.74 |

FIGURE 5 | Some dehazing images and their image quality metrics of synthetic foggy data in SOATS.




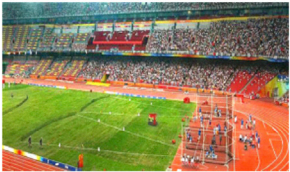














| | A | B | C |
|-----------------|---|---|---|
| Foggy image |  |  |  |
| DCP |  |  |  |
| | FADE=0.99 | FADE=0.99 | FADE=0.94 |
| AOD |  |  |  |
| | FADE=1.33 | FADE=1.41 | FADE=1.05 |
| DehazNet |  |  |  |
| | FADE=2.50 | FADE=2.89 | FADE=1.99 |
| GFN |  |  |  |
| | FADE=1.49 | FADE=1.60 | FADE=1.33 |
| Proposed method |  |  |  |
| | FADE=1.25 | FADE=1.01 | FADE=0.97 |

FIGURE 6 | Some dehazing images and their image quality metrics of real foggy data in SOATS and on the Internet.

CONCLUSION

Assuming the foggy images are of fGn and calculating their Hurst parameters, the LRD of over 1,000 foggy

images are proven by the fact that their Hurst parameters are all more than 0.6. Motivated by the LRD of foggy images, the Residual Dense Block Group (RDBG) with additional long skips between two RDBs is proposed. The

RDBG utilizes information of LRD foggy images well and can obtain satisfied dehazing images.

DATA AVAILABILITY STATEMENT

The original contributions presented in the study are included in the article/Supplementary Material; further inquiries can be directed to the corresponding authors.

REFERENCES

- Cai B, Xu X, Jia K, Qing C, Tao D DehazeNet: An End-To-End System for Single Image Haze Removal. *IEEE Trans Image Process* (2016) 25(11):5187–98. doi:10.1109/tip.2016.2598681
- Li B, Peng X, Wang Z, Xu J, Feng D. AOD-net: All-In-One Dehazing Network [C]. In: Proceeding of the 2017 IEEE International Conference on Computer Vision (ICCV); 22–29 Oct. 2017; Venice, Italy. IEEE (2017). p. 4780–8. doi:10.1109/iccv.2017.511
- Zhang H, Patel VM. Densely Connected Pyramid Dehazing Network[C]. In: Proceeding of the 2018 IEEE/CVF Conference on Computer Vision and Pattern Recognition (CVPR); 18–23 June 2018; Salt Lake City, UT, USA. IEEE (2018). p. 3194–203. doi:10.1109/CVPR.2018.00337
- Hochreiter S, Schmidhuber J Long Short-Term Memory. *Neural Comput* (1997) 9:1735–80. doi:10.1162/neco.1997.9.8.1735
- Zaremba W, Sutskever I, Vinyals O. RECURRENT NEURAL NETWORK REGULARIZATION. In: International Conference on Learning Representations (ICLR) 2015; 2015 May 7–9; San Diego, CA (2014).
- Ren W, Ma L, Zhang J, Pan J, Cao X, Liu W, et al. Gated Fusion Network for Single Image Dehazing [J]. *Proc IEEE Conf Computer Vis Pattern Recognition(CVPR)* (2018), p. 3253–3261. doi:10.1109/CVPR.2018.00343
- Liao Z, Tang YY. Signal Denoising Using Wavelet and Block Hidden Markov Model. *Int J Pattern Recognition Artif Intelligence* (2005) 19(No. 5):681–700. doi:10.1142/s0218001405004265
- Li M Modified Multifractional Gaussian Noise and its Application. *Physica Scripta* (2021) 96(12):125002. doi:10.1088/1402-4896/ac1cf6
- Li M Generalized Fractional Gaussian Noise and its Application to Traffic Modeling. *Physica A* (2021) 579:1236137. doi:10.1016/j.physa.2021.126138
- Li M Multi-fractional Generalized Cauchy Process and its Application to Teletraffic. *Physica A: Stat Mech its Appl* (2020) 550:123982. doi:10.1016/j.physa.2019.123982
- He J, George C, Wu J, Li M, Leng J. Spatiotemporal BME Characterization and Mapping of Sea Surface Chlorophyll in Chesapeake Bay (USA) Using Auxiliary Sea Surface Temperature Data. *Sci Total Environ* (2021) 794:148670. doi:10.1016/j.scitotenv.2021.1016/j.scitotenv.2021
- He J Application of Generalized Cauchy Process on Modeling the Long-Range Dependence and Self-Similarity of Sea Surface Chlorophyll Using 23 Years of Remote Sensing Data. *Front Phys* (2021) 9:750347. doi:10.3389/fphy.2021.750347
- Zhang Y, Tian Y, Kong Y, Zhong B, Fu Y. Residual Dense Network for Image Super-Resolution[J]. *IEEE* (2018).
- Li B, Ren W, Fu D, Tao D, Feng D, Zeng W, et al. Benchmarking Single Image Dehazing and Beyond[J]. *IEEE Trans Image Process* (2017) 28(1):492–505. doi:10.1109/TIP.2018.2867951

AUTHOR CONTRIBUTIONS

All authors listed have made a substantial, direct, and intellectual contribution to the work and approved it for publication.

FUNDING

The Chengdu Research Base of Giant Panda Breeding, Grant/Award Number: 2020CPB-C09, CPB2018-01, 2021CPB-B06, and 2021CPB-C01.

- Hurst HE Long-term Storage Capacity of Reservoirs. *T Am Soc Civ Eng* (1951) 116:770–99. doi:10.1061/taceat.0006518
- Yang A-P, Jin L, Jin-Jia X, Xiao-Xiao L, He Y-Q. Content Feature and Style Feature Fusion Network for Single Image Dehazing. *ACTA Automatica Sinica* (2021) 1–11. [2021-03-25]. doi:10.16383/j.aas.c200217
- Liu X, Ma Y, Shi Z, Chen J. GridDehazeNet: Attention-Based Multi-Scale Network for Image Dehazing [C]. In: Proceeding of the 2019 IEEE/CVF International Conference on Computer Vision (ICCV); Seoul, Korea; 2019 Oct 27–Nov 2. IEEE (2019), p. 7313–7322. doi:10.1109/ICCV.2019.00741
- Girshick R Fast R-CNN. In: IEEE International Conference on Computer Vision (ICCV); 2015 Dec 7–13; Santiago, Chile (2015). p. 1440–1448. doi:10.1109/ICCV.2015.169
- Johnson J, Alahi A, Fei-Fei L. Perceptual Losses for Real-Time Style Transfer and Super-Resolution[J]. *Computer Sci* (2016).
- Russakovsky O, Deng J, Su H, Krause J, Satheesh S, Ma S, et al. ImageNet Large Scale Visual Recognition Challenge. *Int J Comput Vis* (2015) 115(3):211–52. doi:10.1007/s11263-015-0816-y
- Simonyan K, Zisserman A. Very Deep Convolutional Networks for Large-Scale Image Recognition[J]. In International Conference on Learning Representations (ICLR); 2015 May 7–9; San Diego, CA (2014).
- Hu J, Shen L, Albanie S, Sun G, Wu E Squeeze-and-Excitation Networks[J]. *IEEE Trans Pattern Anal Machine Intelligence* (2017).
- Wang Z, Bovik AC, Sheikh HR, Simoncelli EP. Image Quality Assessment: from Error Visibility to Structural Similarity. *IEEE Trans Image Process* (2004) 13(4):600–12. doi:10.1109/tip.2003.819861
- Choi LK, Jaehee You J, Bovik AC Referenceless Prediction of Perceptual Fog Density and Perceptual Image Defogging. *IEEE Trans Image Process* (2015) 24(11):3888–901. doi:10.1109/tip.2015.2456502

Conflict of Interest: The authors declare that the research was conducted in the absence of any commercial or financial relationships that could be construed as a potential conflict of interest.

Publisher's Note: All claims expressed in this article are solely those of the authors and do not necessarily represent those of their affiliated organizations, or those of the publisher, the editors, and the reviewers. Any product that may be evaluated in this article, or claim that may be made by its manufacturer, is not guaranteed or endorsed by the publisher.

Copyright © 2022 Yuan, Liao, Wang, Dong, Liu, Long, Wei, Xu, Yu, Chen and Hou. This is an open-access article distributed under the terms of the Creative Commons Attribution License (CC BY). The use, distribution or reproduction in other forums is permitted, provided the original author(s) and the copyright owner(s) are credited and that the original publication in this journal is cited, in accordance with accepted academic practice. No use, distribution or reproduction is permitted which does not comply with these terms.



Characteristic Sequence Analysis of Giant Panda Voiceprint

Shaoliang Hu¹, Zhiwu Liao², Rong Hou³ and Peng Chen^{3*}

¹School of Automation Engineering, University of Electronic Science and Technology of China, Chengdu, China, ²School of Computer Science, Sichuan Normal University, Chengdu, China, ³Chengdu Research Base of Giant Panda Breeding, Sichuan Key Laboratory of Conservation Biology for Endangered Wildlife, Chengdu, China

By analyzing the voiceprint characteristics of giant panda's voice, this study proposes a giant panda individual recognition method based on the characteristics of the composite Mel composite frequency cepstral coefficient (CMFCC) and proves that the characteristic sequence of the CMFCC has long-range dependent characteristics. First, the MFCC (Mel composite frequency cepstral coefficient) with a low frequency resolution is obtained by the Mel filter bank; then, the inverse Mel frequency cepstral coefficient (IMFCC) features of giant panda calls are extracted. The CMFCC characteristic sequence of giant panda voice composed of the MFCC and IMFCC improves the resolution of high- and low-frequency resolution characteristics of giant panda voice. Finally, the first-order difference characteristic parameters of the MFCC are integrated to obtain the difference characteristics between frames. Through experiments, the improvement of the system recognition effect is verified, and the recognition accuracy meets the theoretical expectation.

Keywords: MFCC, long-range dependent, individual recognition, voiceprint, Gaussian mixture model

OPEN ACCESS

Edited by:

Ming Li,
Zhejiang University, China

Reviewed by:

Jianwei Yang,
Nanjing University of Information
Science and Technology, China
Junyu He,
Zhejiang University, China

*Correspondence:

Peng Chen
capricorncp@163.com

Specialty section:

This article was submitted to
Interdisciplinary Physics,
a section of the journal
Frontiers in Physics

Received: 20 December 2021

Accepted: 14 January 2022

Published: 21 February 2022

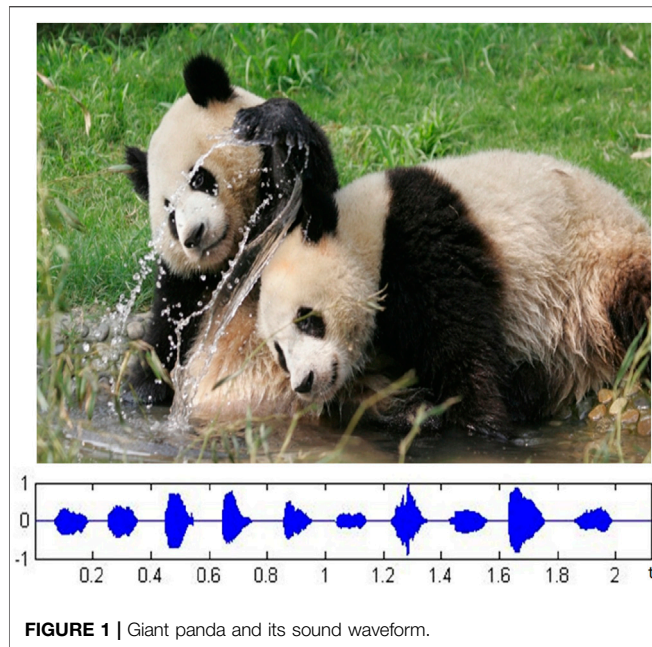
Citation:

Hu S, Liao Z, Hou R and Chen P (2022)
Characteristic Sequence Analysis of
Giant Panda Voiceprint.
Front. Phys. 10:839699.
doi: 10.3389/fphy.2022.839699

1 INTRODUCTION

Voiceprint is a collection of various common acoustic feature maps. It is a sound feature measured by special acoustic instruments. The core of voiceprint recognition is to extract its unique speech features from the collected speech information. The feature template is formed after recognition training. During recognition, the speech used is matched with the data in the template library, and the score is calculated to judge the speaker's identity [1]. Since 1930, there has been a basic research study on speaker recognition [2]. In 1962, the term "voiceprint" officially appeared as a sound texture feature [3]. After that, S. Pruzansky proposed a matching method based on probability value estimation and correlation calculation [4]. At the same time, the focus of recognition has become to select and extract the corresponding feature recognition parameters. Since 1970, voiceprint features such as the short-term average energy feature, linear prediction cepstral coefficient LPC (linear prediction coefficient), and Mel frequency cepstral coefficients MFCC (Mel frequency cepstral coefficients) have emerged. At the same time, some methods have also been used to extract feature parameters by using cepstral coefficients or introducing first- and second-order dynamic differences [5]. After the 1980s, characteristic parameters such as time domain decomposition, frequency domain decomposition, and wavelet packet node energy also gradually appeared and were widely used [6]. Jinxi Guo et al. studied the recognition system in the noise environment [7] and made some achievements and progress.

Voiceprint feature is a key link in human voiceprint recognition technology and related applications. Considering the similarity of the way of sound production between giant pandas



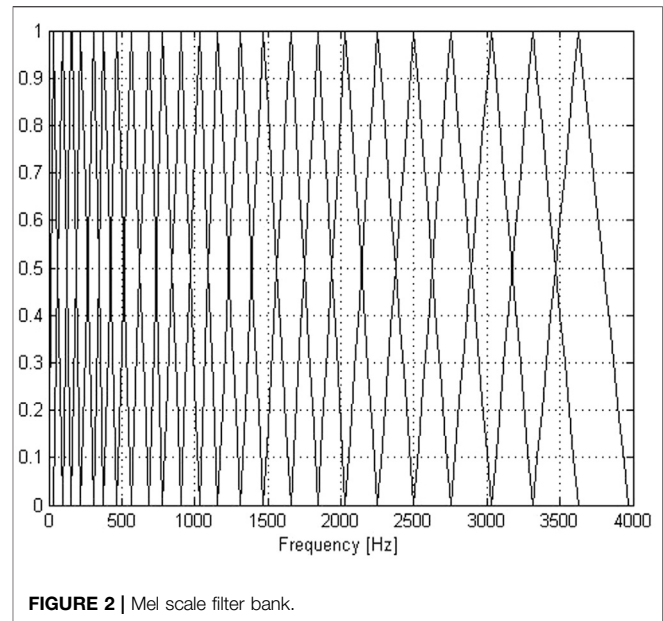
and humans, as well as the universality and wide application of voiceprint recognition technology, the voice of giant pandas can be analyzed and studied. At present, there is no case of research on individual recognition of giant pandas based on voiceprint features, especially because of the precious voice data of giant pandas, and the giant pandas and their call waveforms are shown in **Figure 1**.

Voiceprint feature extraction algorithms mainly include the following [5]: the strong representation ability of the speech signal, good recognition effect, good self-specificity and feature exclusivity, simple operation, and convenient calculation.

In 2021, Li Ming proposed the mmfGn (modified multifractional Gaussian noise) theorem of long-range dependence (LRD) and short-range dependence and used the time-varying Hurst parameter to describe the time-varying sea level of LRD [8]. A new generalized fractional Gaussian noise (gfGn) is introduced. The study uses gfGn to model the actual traffic trace exhibition. The gfGn model is more accurate than the traditional fractional Gaussian noise (fGn) traffic modeling [9].

In 2021, Junyu used the Bayesian maximum entropy (BME) method to represent the internal spatiotemporal dependence of sea surface chlorophyll concentration (SSCC) distribution [10]. The Hurst index value of chlorophyll on the ocean surface ranges from 0.6757 to 0.8431. A high Hurst index value represents strong LRD, which may be a common phenomenon of daily sea surface chlorophyll [11].

This study focuses on the analysis and optimization of the Mel frequency cepstral coefficient of giant panda voice, discusses the long-range-dependent characteristics of feature sequence, analyzes the voiceprint feature sequence suitable for the giant panda individual recognition system,



and realizes the individual recognition algorithm based on the giant panda voiceprint.

2 MEL FREQUENCY CEPSTRAL COEFFICIENTS

Mel frequency cepstral coefficients (MFCCs) are voiceprint features extracted by combining the auditory perception characteristics of human ears with the generation mechanism of speech [12]. The sensitivity of the human ear to sound is not linear, but it changes with the change in frequency. It is more sensitive to low-frequency sound than high-frequency sound. According to the perceptual characteristics of the human auditory system, the Mel cepstral coefficient is widely used in voiceprint recognition.

2.1 Mel Frequency Cepstral Coefficients of Giant Panda

The frequency corresponding to the MFCC is the Mel frequency, which is recorded as f_{mel} , and its functional correspondence with frequency f is as follows:

$$f_{mel} = 2595 \times \log_{10} \left(1 + \frac{f}{700} \right) \quad (2.1)$$

The following is the extraction process of the Mel frequency cepstral coefficient:

- 1) First, the original speech signal $s(n)$ is sampled at the sampling frequency of 44.1 KHz and quantized in the 16bit mode, and then, the background noise and high-frequency noise are eliminated by using a bandpass filter. Finally, the time domain signal $x(n)$ is

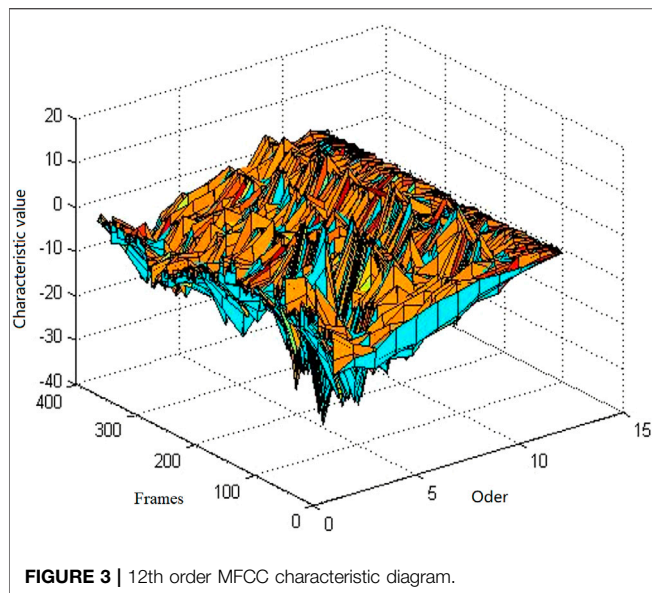


FIGURE 3 | 12th order MFCC characteristic diagram.

obtained by using a pre emphasis technology to compensate the high-frequency loss of sound. Then, it is transformed by formula Eq. 2.2 to obtain the corresponding linear spectrum $X(k)$, where k is the time domain frequency corresponding to each point of the original speech signal.

$$X(k) = \sum_{n=0}^{N-1} x(n)e^{-j2\pi nk/N} \quad (0 \leq n, k \leq N-1) \quad (2.2)$$

- 2) The Mel frequency filter bank composed of a group of triangular filters is used to filter the linear spectrum to obtain the Mel spectrum, and then, its logarithmic energy is calculated to obtain the logarithmic energy $S(m)$ of the original giant panda sound signal.

A group of triangular bandpass filter combinations constitute Mel filter banks, where, $0 \ll m \ll M$, and M is the total number of triangular filters in Mel filter banks. The center frequency of these

filters is $f(m)$. Considering the logarithmic conversion relationship between the Mel frequency and ordinary frequency, it can be seen that the center spectrum of each filter with an equal interval linear distribution in the Mel frequency is dense in the low-frequency band and sparse in the high-frequency band. The schematic diagram of the Mel frequency filter bank is shown in Figure 2.

The transfer function of each bandpass filter is as follows:

$$H_m(k) = \begin{cases} 0 & (k < f(m-1)) \\ \frac{k - f(m-1)}{f(m) - f(m-1)} & (f(m-1) \leq k \leq f(m)) \\ \frac{f(m+1) - k}{f(m+1) - f(m)} & (f(m) < k < f(m+1)) \\ 0 & (k > f(m+1)) \end{cases} \quad (2.3)$$

The formula for obtaining the logarithmic spectrum $S(m)$ is as follows:

$$S(m) = \ln \left(\sum_{k=0}^{N-1} |X(k)|^2 H_m(k) \right), \quad 0 \leq m < M \quad (2.4)$$

- 3) By substituting the above logarithmic energy into the discrete cosine transform (DCT), the Mel cepstral parameters $C(n)$ of order L can be obtained, as shown in Eq. 2.5, where L is the order of MFCC coefficients, usually is 12–16, and M is the number of Mel filters.

$$C(n) = \sum_{m=1}^{M-1} S(m) \cos \left(\frac{\pi(m + \frac{1}{2})}{M} \right), \quad n = 1, 2, \dots, L \quad (2.5)$$

Figure 3 is a 12-order MFCC characteristic diagram of a giant panda voice, in which the X-axis represents the order of the MFCC coefficient, the Y-axis represents the number of frames of voice, and the Z-axis represents the corresponding cepstral parameter value.

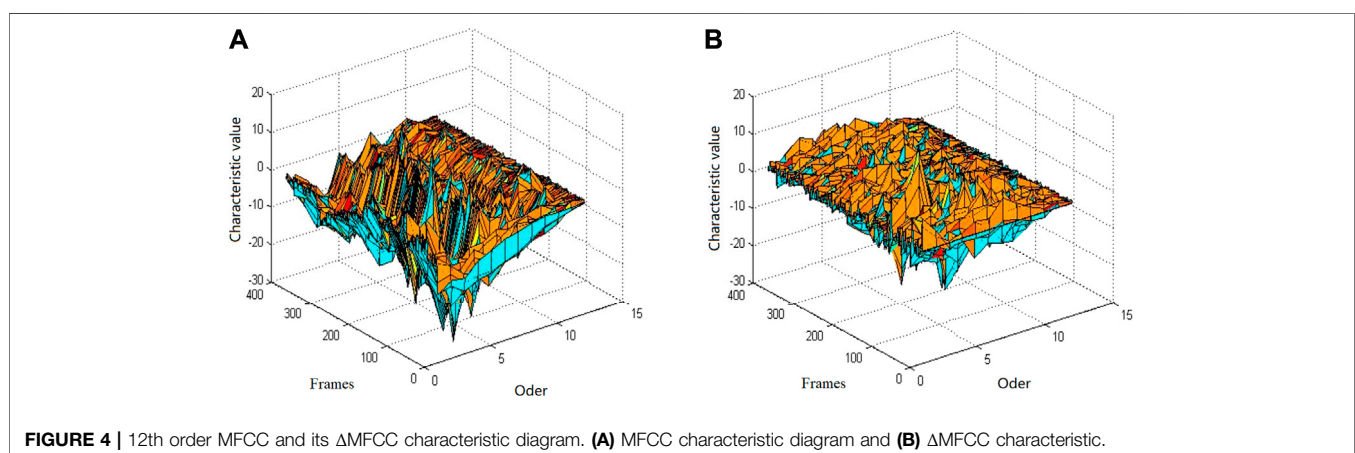


FIGURE 4 | 12th order MFCC and its Δ MFCC characteristic diagram. (A) MFCC characteristic diagram and (B) Δ MFCC characteristic.

2.2 First-Order Differential Mel Frequency Cepstral Coefficients of Giant Panda Sound

The standard MFCC parameters reflect the static characteristics within each frame of speech, while the difference of the MFCC reflects the dynamic characteristics. The Furui experiment shows that adding dynamic characteristics to the features can greatly improve the system performance [13]. The introduction of differential features has a wide range of applications and good results in the field of human voice recognition. Therefore, this method is also first used in the processing of giant panda voice.

After obtaining the MFCC parameters, use Eq. 2.5 to extract the MFCC first-order differential parameter Δ MFCC.

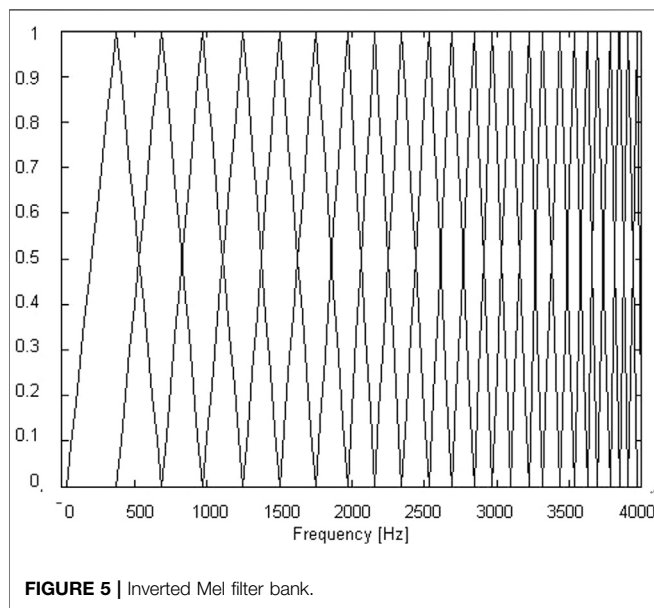


FIGURE 5 | Inverted Mel filter bank.

$$D_t = \begin{cases} C_{t+1} - C_t & t < \theta \\ \sum_{\theta=1}^{\theta} \theta (C_{t+\theta} - C_{t-\theta}) / \left(2 \sum_{\theta=1}^{\theta} \theta^2 \right) & \text{else} \\ C_t - C_{t+1} & t \geq T - \theta \end{cases} \quad (2.6)$$

where D_t represents t -th Δ MFCC, T is the order of the cepstral coefficient, θ is the time difference of the first derivative, and the values of 1 and 2 represent the first cepstral coefficient [14].

Figure 4 shows the characteristics of the MFCC of order 12 and Δ MFCC of order 12 of the same giant panda voice.

3 COMPOUND MEL FREQUENCY CEPSTRAL COEFFICIENT OF GIANT PANDA SOUND

3.1 The Inverse Mel Frequency Cepstral Coefficient

The IMFCC feature can compensate the high-frequency information and improve the system recognition rate through its integration with the traditional MFCC. The structure of the IMFCC filter bank is shown in Figure 5.

Corresponding to the Mel domain of the traditional filter structure, we call this domain as the inverted Mel domain, which is recorded as IMEL, and the corresponding frequency is recorded as F_{imel} . The relationship with the time domain is as follows:

$$F_{imel}(f) = 219.268 - 2595 \log_{10} \left(1 + \frac{4031.25 - f}{700} \right) \quad (3.1)$$

The inverted filter response becomes

$$EH_i(k) = H_{p+i+1} \left(\frac{N}{2} - k + 1 \right) \quad (3.2)$$

where $EH_i(k)$ is the filter response in the MEL domain.

Figure 6 shows the 12th order MFCC and the 12th order IMFCC characteristic diagram of a giant panda sound, in which the X axis represents the order of the MFCC, the Y axis represents

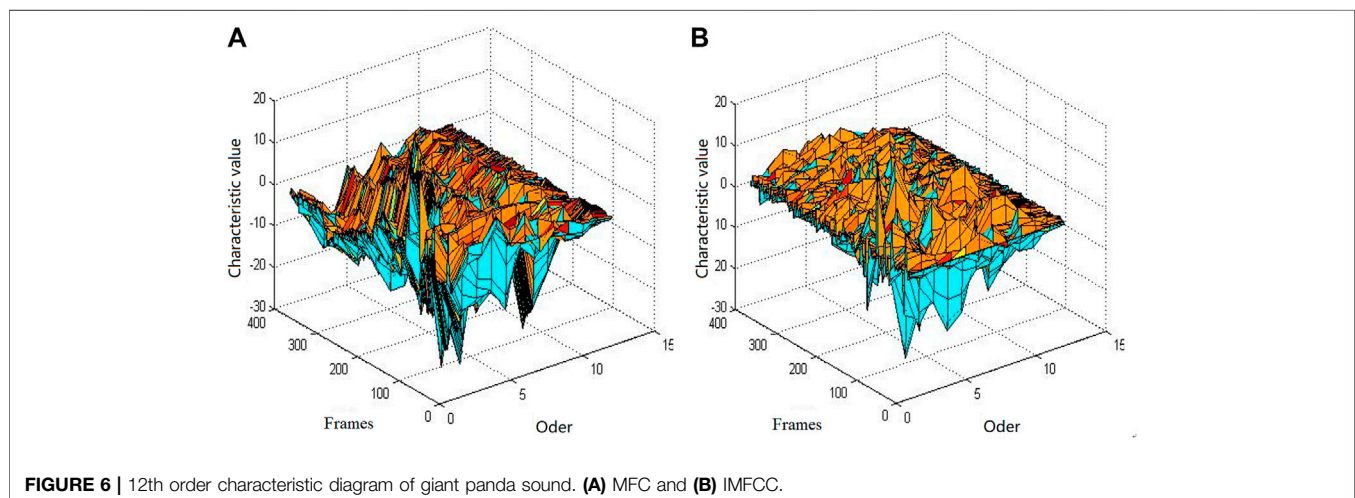


FIGURE 6 | 12th order characteristic diagram of giant panda sound. (A) MFC and (B) IMFCC.

the number of voice frames, and the Z axis represents the corresponding cepstral parameter values.

3.2 Composite Mel Composite Frequency Cepstral Coefficient

MFCC characteristic parameters are obtained through the Mel filter bank and a series of operations. Accordingly, the

characteristic coefficients obtained after a series of operations through the Mel filter bank and composite filter bank of the inverted Mel filter bank are called composite Mel frequency cepstral coefficients, which are recorded as the CMFCC (compound Mel frequency cepstral coefficient).

Therefore, we fuse the 12th order MFCC characteristic diagram and 12th order IMFCC characteristic diagram in **Figure 7** to obtain the corresponding 24th order CMFCC characteristic parameter diagram, as shown in **Figure 8**.

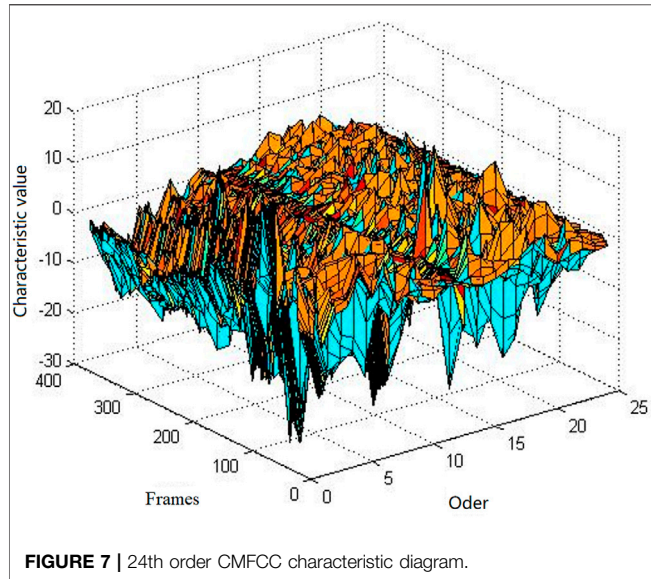


FIGURE 7 | 24th order CMFCC characteristic diagram.

3.3 Hurst Exponent of the Composite Mel Composite Frequency Cepstral Coefficient Feature Sequence

Assuming that the sequence composed of CMFCC features satisfies the fractional Brownian motion distribution, we can calculate H according to the following method [13, 15, 16].

Let n be the number of data of CMFCC-modified multifractional Gaussian noise (mmfGn) [8, 9]. Let $1 < k < N$ be the length of the neighborhood used for estimating the function parameter. We will estimate $H(t)$ only for t in $[\frac{k}{N}, 1 - \frac{k}{N}]$.

Without loss of generality, we assume $m = N/k$ to be an integer. Then, our estimator of $H(i)$ is the following:

$$\hat{H}_i = -\frac{\log\left[\sqrt{\frac{\pi}{2}} S_{k,N}(i)\right]}{\log(N-1)}, \quad (3.3)$$

where

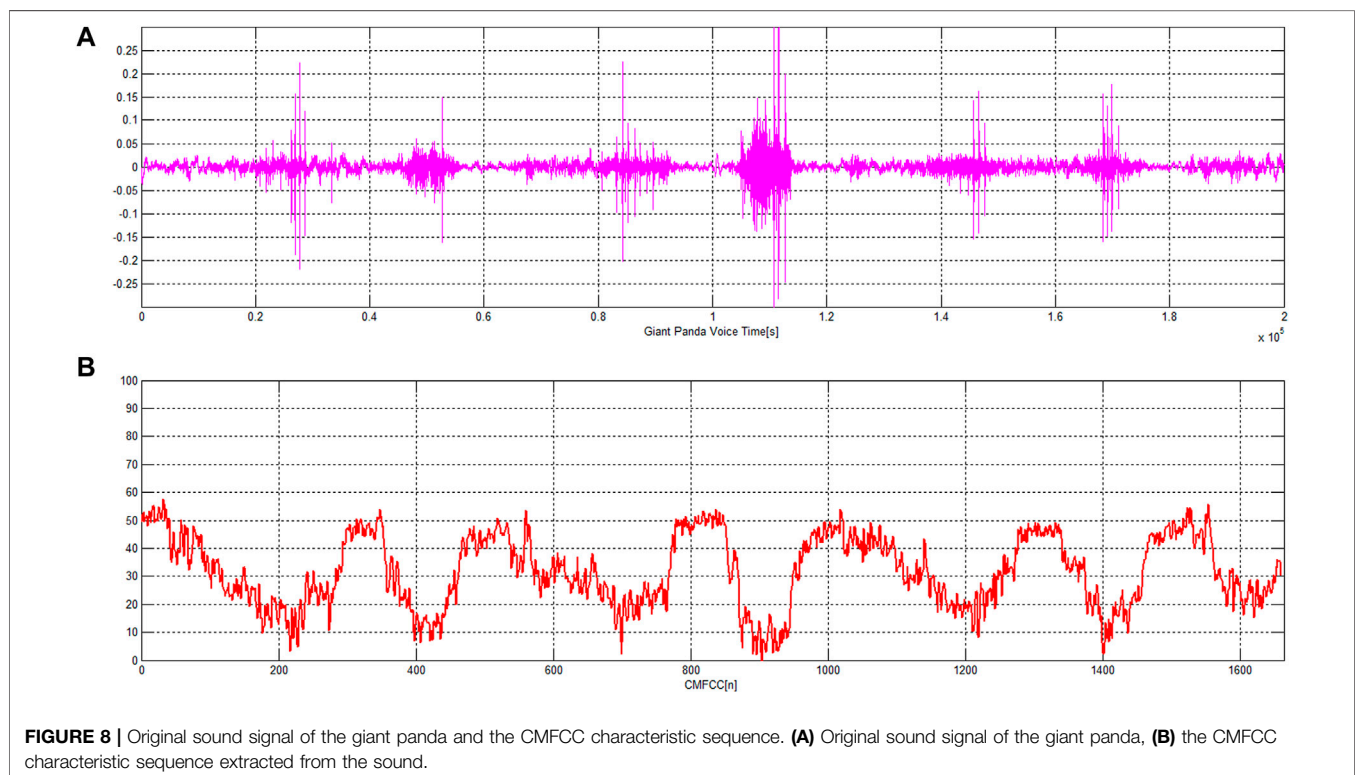


FIGURE 8 | Original sound signal of the giant panda and the CMFCC characteristic sequence. **(A)** Original sound signal of the giant panda, **(B)** the CMFCC characteristic sequence extracted from the sound.

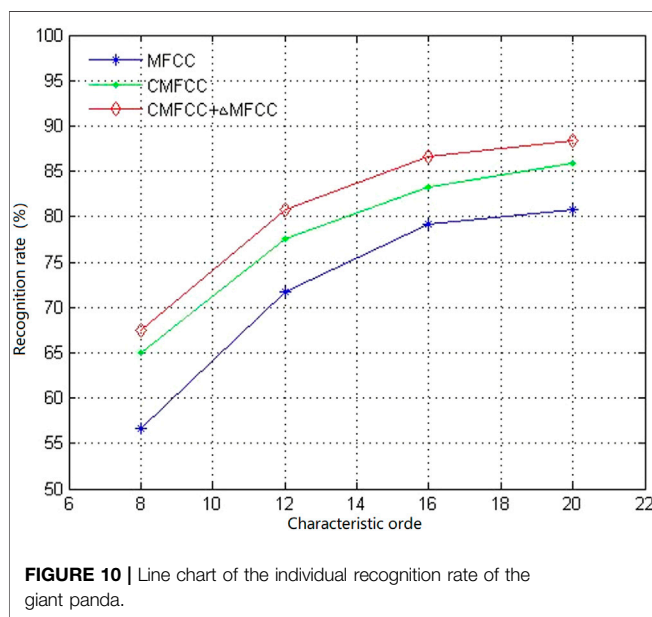
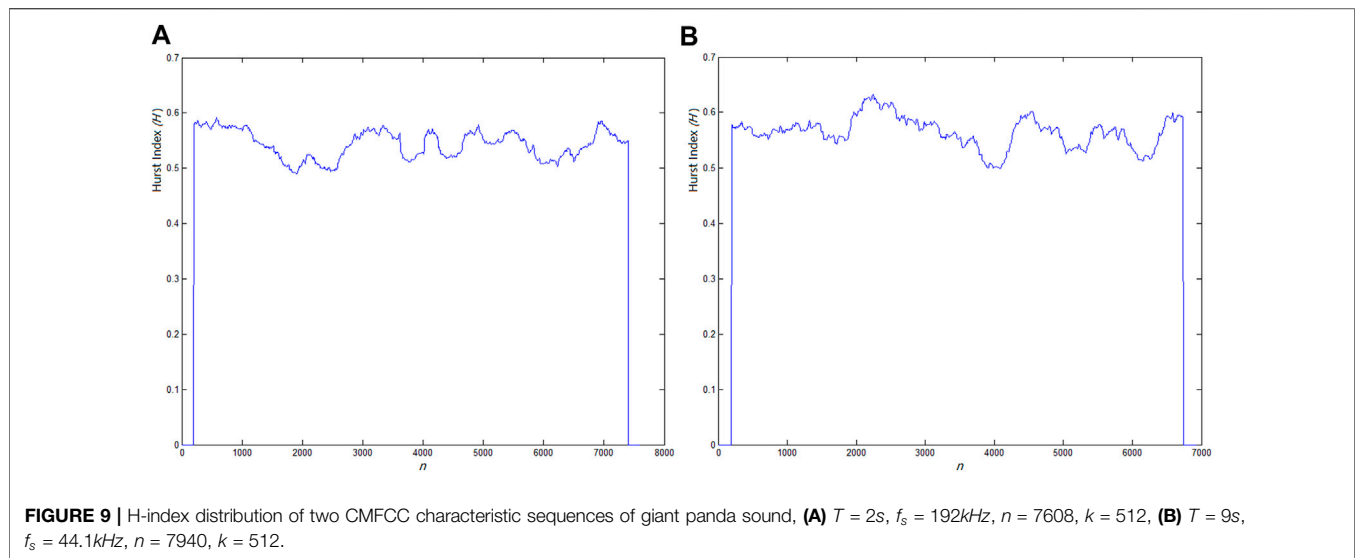


TABLE 1 | Recognition rate of giant panda individual recognition.

| Order\Type | 8 | 12 | 16 | 20 |
|-------------|-----------|-----------|------------|------------|
| MFCC | 56.67(68) | 71.67(86) | 79.17(95) | 80.83(97) |
| CMFCC | 65(78) | 77.5(93) | 83.33(100) | 85.83(103) |
| CMFCC+ΔMFCC | 67.5(81) | 80.83(97) | 86.67(104) | 88.33(106) |

$$S_{k,N}(i) = \frac{m}{N-1} \sum_{j \in \left[i - \frac{k}{2}, i + \frac{k}{2} \right]} |X_{j+1,N} - X_{j,N}| \quad (3.4)$$

Figure 8 shows the original sound signal of giant panda and the CMFCC characteristic sequence. **Figure 9** shows the H-index

distribution of two CMFCC characteristic sequences of the giant panda sound. In **Figure 9A**, the giant panda sound duration time $T = 2s$, sampling frequency $f_s = 192kHz$, $n = 7608$, and $k = 512$. In **Figure 9B**, the giant panda sound duration $T = 9s$, sampling frequency $f_s = 44.1kHz$, $n = 7940$, and $k = 512$. The experimental results show that the CMFCC characteristic sequence of the giant panda voice has long-range dependent characteristics.

4 DISCUSSION

We applied the CMFCC feature sequence with LRD to giant panda individual recognition. Considering that this feature is the feature information obtained within the speech frame, the Δ MFCC of the MFCC feature parameter is introduced. The two features of CMFCC and Δ MFCC are fused to obtain a new feature parameter.

There are 20 individual giant pandas. Each individual has 10s sounds, including 4s for training and 6s for testing. The ratio between the number of correctly recognized test sounds and the total number of test sounds is the correct recognition rate. The final result is the average of the recognition rates of the three experiments, as shown in **Figure 10** and **Table 1**.

The order of CMFCC and MFCC features are 8, 12, 16, and 20, respectively, and the order of Δ MFCC also corresponds to 8, 12, 16, and 20. From **Table 1**, we can see that the higher the order of features, the higher is the recognition rate, indicating that the correlation of feature sequences is also stronger.

The final individual identification of giant panda is shown in **Table 1**. **Figure 10** is a broken line diagram of three feature recognition results.

It can be seen from **Figure 10** and **Table 1** that the characteristic parameters obtained by flipping the Mel filter bank can improve the resolution of the high-frequency part. Therefore, after using CMFCC features, the recognition rate of giant panda individuals is higher than that under the MFCC. At the same time, this is because the Δ MFCC feature considers the difference between frames and improves the feature performance of the CMFCC. Therefore, the recognition rate

of the CMFCC and Δ MFCC combination feature is better, and the theoretical results are consistent with the experimental expectations.

5 CONCLUSION

This study mainly presents the characteristics of the Mel composite cepstral coefficient of giant panda sound (CMFCC) for individual recognition. It is verified that the CMFCC feature sequence conforms to the distribution characteristics of fractional Brownian motion, which has long-range dependence. This feature sequence makes use of the memory characteristics of the giant panda voice in time and can obtain the characteristics of the giant panda sound in low- and high-frequency resolution at the same time. Through experimental verification, it has the best effect on individual recognition of the giant panda and improves the efficiency of the giant panda. The recognition rate has reached the expected effect of individual recognition of the giant panda.

REFERENCES

- Li Y, Gu Z, Liu S. Voiceprint Authentication Technology. *Water conservancy Sci Technol economy* (2005) 11(6):384–6. doi:10.3969/j.issn.1006-7175.2005.06.034
- Wu X. Voiceprint Recognition Auditory Recognition. *Computer World* (2001)(8). doi:10.15949/j.cnki.0371-0025.2001.03.011
- Kersta LG. Voiceprint Identification. *Nature* (1962) 196(4861):1253–7. doi:10.1038/1961253a0
- Pruzansky S. Pattern-Matching Procedure for Automatic Talker Recognition. *The J Acoust Soc America* (1963) 35(3):354–8. doi:10.1121/1.1918467
- Arsikere H, Gupta HA, Alwan A. Speaker Recognition via Fusion of Subglottal Features and MFCCs. *Interspeech* (2014) 1106–10. doi:10.21437/Interspeech.2014-284
- Gong C. *Research on Speaker Recognition of Ear Speech Based on Joint Factor Analysis [D]*. Suzhou, China: Suzhou University (2014).
- Guo J, Yang R. Robust Speaker Identification via Fusion of Subglottal Resonances and Cepstral Features. *IEEE Signal Process.* (2015). doi:10.1121/1.4979841
- Li M. Modified Multifractional Gaussian Noise and its Application. *Physica Scripta* 96(12):202112500212. doi:10.1088/1402-4896
- Li M. Generalized Fractional Gaussian Noise and its Application to Traffic Modeling. *Physica A* 579(22):20211236137. doi:10.1016/j.physa.2021.126138
- He J, George C, Wu J, Li M, Leng J. Spatiotemporal BME Characterization and Mapping of Sea Surface Chlorophyll in Chesapeake Bay (USA) Using Auxiliary Sea Surface Temperature Data. *Sci Total Environ* (2021) 794:148670. doi:10.1016/j.scitotenv.2021
- He J. Application of Generalized Cauchy Process on Modeling the Long-Range Dependence and SelfSimilarity of Sea Surface Chlorophyll Using 23 Years of Remote Sensing Data. *Front Phys* (2021) 9:750347. doi:10.3389/fphy.2021.750347
- Peltier RF, Levy-Vehel J. Multifractional Brownian Motion: Definition and Preliminaries Results. *INRIA TR* (1995) 2645:1995. doi:10.1007/978-1-4471-0873-3_2
- Milner B. Inclusion of Temporal Information into Features for Speech Recognition. *Proc ICSLP* (1996) 96:256269. doi:10.1109/icslp.1996.607093
- Sampson D. System and Method for Pitch Detection and Analysis. *U.S Patent Appl* (2017) 14:883.
- Li M. Fractal Time Series-A Tutorial Review. *Math Probl Eng* 2012 (2010). doi:10.1155/2010/157264
- Wen L. *Research and Design of Speech Recognition System Based on Improved MFCC*. Changsha: Central South University (2011). p. 20–30.

DATA AVAILABILITY STATEMENT

The original contributions presented in the study are included in the article/Supplementary Material, further inquiries can be directed to the corresponding author.

AUTHOR CONTRIBUTIONS

All authors listed have made a substantial, direct, and intellectual contribution to the work and approved it for publication.

FUNDING

This research is supported by the Chengdu Research Base of Giant Panda Breeding (Nos. 2020CPB-C09 and CPB2018-01).

Conflict of Interest: The authors declare that the research was conducted in the absence of any commercial or financial relationships that could be construed as a potential conflict of interest.

Publisher's Note: All claims expressed in this article are solely those of the authors and do not necessarily represent those of their affiliated organizations, or those of the publisher, the editors, and the reviewers. Any product that may be evaluated in this article, or claim that may be made by its manufacturer, is not guaranteed or endorsed by the publisher.

Copyright © 2022 Hu, Liao, Hou and Chen. This is an open-access article distributed under the terms of the Creative Commons Attribution License (CC BY). The use, distribution or reproduction in other forums is permitted, provided the original author(s) and the copyright owner(s) are credited and that the original publication in this journal is cited, in accordance with accepted academic practice. No use, distribution or reproduction is permitted which does not comply with these terms.



Giant Panda Video Image Sequence and Application in 3D Reconstruction

Shaoliang Hu¹, Zhiwu Liao², Rong Hou³ and Peng Chen^{3*}

¹School of Automation Engineering, University of Electronic Science and Technology of China, Chengdu, China, ²School of Computer Science, Sichuan Normal University, Chengdu, China, ³Chengdu Research Base of Giant Panda Breeding, Sichuan Key Laboratory of Conservation Biology for Endangered Wildlife, Chengdu, China

Giant panda 3D reconstruction technology plays an important role in the research of giant panda protection. Through the analysis of giant panda video image sequence (GPVS), we prove that it has the long-range-dependent characteristics. This article proposes an algorithm to accurately reconstruct the giant panda 3D model by using the long-range-dependent characteristics of GPVS. First, the algorithm uses a skinned multi-animal linear model (SMAL) to obtain the initial 3D model of giant panda, and the 3D model of the single-frame giant panda image is reconstructed by controlling shape parameters and attitude parameters; then, we use the coherence information contained in the long-range-dependent characteristics between video sequence images to construct a smooth energy function to correct the error of the 3D model. Through this error, we can judge whether the 3D reconstruction result of the giant panda is consistent with the real structural characteristics of the giant panda. The algorithm solves the problem of low 3D reconstruction accuracy and the problem that 3D reconstruction is easily affected by occlusion or interference. Finally, we realize the accurate reconstruction of the giant panda 3D model.

OPEN ACCESS

Edited by:

Ming Li,
Zhejiang University, China

Reviewed by:

Junyu He,
Zhejiang University, China
Wen-Sheng Chen,
Shenzhen University, China

*Correspondence:

Peng Chen
capricorncp@163.com

Specialty section:

This article was submitted to
Interdisciplinary Physics,
a section of the journal
Frontiers in Physics

Received: 20 December 2021

Accepted: 12 January 2022

Published: 23 February 2022

Citation:

Hu S, Liao Z, Hou R and Chen P (2022)
Giant Panda Video Image Sequence
and Application in 3D Reconstruction.
Front. Phys. 10:839582.
doi: 10.3389/fphy.2022.839582

Keywords: time series, long-range dependent, 3D reconstruction, SMAL, Hurst

1 INTRODUCTION

In recent years, in the field of animal protection, computer three-dimensional reconstruction methods are more and more used in the study of animal morphology. Giant pandas are China's national treasures and first-class protected animals. China has established giant panda breeding research bases in many places for the protection and research of giant pandas. Through the research on the three-dimensional reconstruction of giant pandas, we can not only carry out non-contact body size measurement of giant pandas, including the measurement of giant pandas' body height, body length, chest circumference, and weight, but also the protection workers can better understand the growth status of giant pandas, such as height, obesity, weight gain and loss, and body length increase and decrease, so as to further analyze the living environment and health status of giant pandas and to better protect giant panda species and improve the protection level of giant pandas. At the same time, through flexible and diversified forms such as rapid three-dimensional reconstruction and three-dimensional display, people can have a more intuitive and comprehensive understanding of the species of giant panda and further enhance people's awareness of animal protection. This is not only helpful for animal protection but also beneficial to the whole society.

Since the giant panda is a nonrigid target, the traditional rigid body-based 3D reconstruction algorithm (Structure-from-Motion-SFM [1], etc.) is not suitable for its 3D modeling. NRSFM (non-rigid structure-from-motion) is an extended SFM method. In 2000, Bregler first proposed the



FIGURE 1 | Giant panda video image sequence. (A) First frame, (B) 60th frame, and (C) 1800th frame.

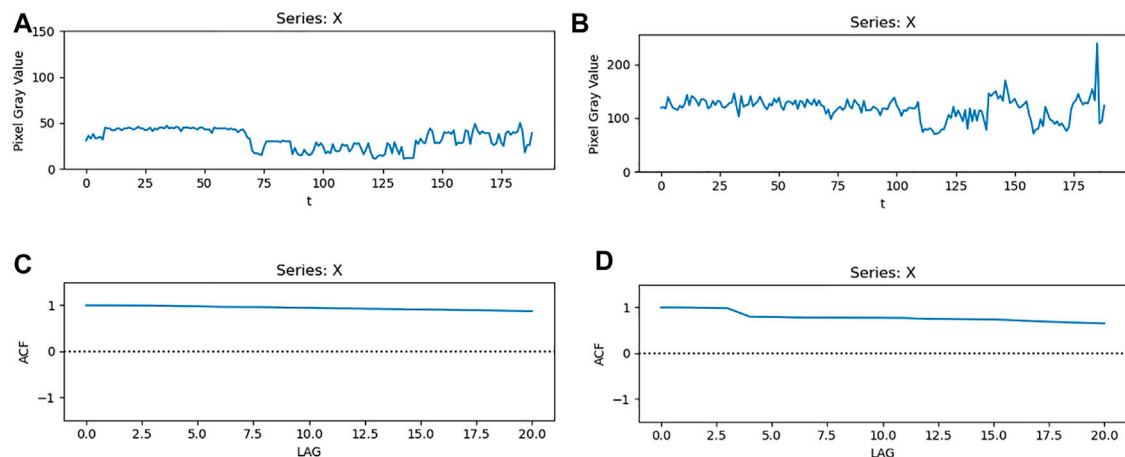


FIGURE 2 | Pixel value and ACF value of GPVS. (A,C) GPVS of (300,400) and (B,D) GPVS of (600,800).

scientific question of how to recover the 3D nonrigid shape model [2] from the video sequence of single view. In 2013, Grag, Ravi, and other scholars used a variant algorithm for dense 3D reconstruction of nonrigid surfaces from monocular video sequences [3], which formulate the nonrigid structure of NRSFM into a global variational energy minimization problem. This method can reconstruct highly deformed smooth surfaces. In reference [4], a method for observing the dynamic motion of nonrigid objects from long monocular video sequences is adopted. This method makes use of the fact that many deformed shapes will repeat over time and simplifies NRSFM to a rigid problem.

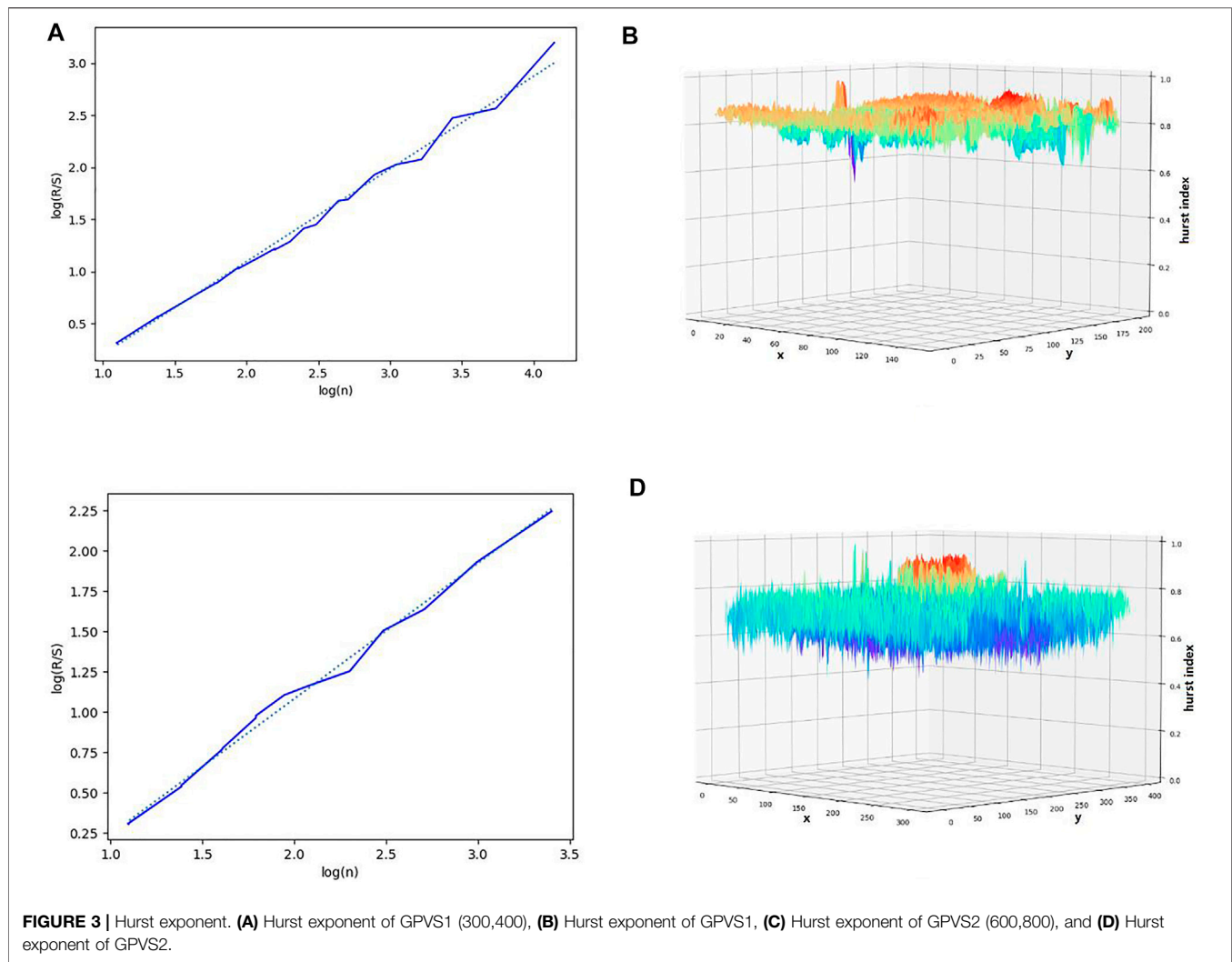
In 2015, Matthew Loper and other scholars proposed a three-dimensional SMPL (skinned multi-person linear) model of human body using human shape and position [5]. In 2018, Angjoo Kanazawa et al. utilized a network framework for recovering a 3D human model from a 2D human image by the end-to-end method [6]. This method directly infers 3D-mesh parameters from image features and combines the 3D reconstruction method with deep learning.

Due to the uncontrollable behavior of giant pandas and other animals, the three-dimensional modeling algorithm suitable for human body cannot obtain high three-dimensional modeling

accuracy. In 2017, Silvia Zuff et al. designed a 3D modeling method of animals based on a single image, using the 3D shape [7] and pose of animals to build the same statistical shape model as SMPL, called SMAL (skinned multi-animal linear model) [8, 9]. At present, the model has achieved satisfactory results in the application of three-dimensional reconstruction of several kinds of quadrupeds, such as three-dimensional reconstruction of dogs, horses, and cattle.

In the study, we found that the accuracy of the 3D giant panda model based on the single image is related to the results of 3D giant panda pose modeling based on the SMAL model. Because the temporal relationship between frames is not considered in the giant panda 3D model of single frame image data, the motion sequence composed of the results of single-frame pose modeling will be uneven and not smooth. Such errors are difficult to be automatically corrected in the single-frame algorithm. Therefore, the 3D reconstruction effect is usually unsatisfactory.

This article is organized as follows: in **Section 2**, we define the autocorrelation coefficient of GPVS (giant panda video image sequence) and discuss the long-range dependent of GPVS by analyzing the H index. In **Section 3**, we propose the giant panda 3D model. In **Section 4**, we took advantage of the new motion smoothing constraint to improve 3D accuracy by using frame-to-frame relationships. In **Section 5**, the experimental



results of 3D modeling are presented, and in **Section 6**, we give the conclusion.

2 LONG-RANGE DEPENDENT OF GPVS

2.1 ACF of GPVS

If the ACF value of a sequence is not zero or has a tailing phenomenon, we believe that the sequence may be long-range-dependent sequence [10].

Theorem: Let $X(i, j)$ be a sequence composed of pixel values at the coordinates of each image (i, j) in GPVS, and let x_t ($t = 1, 2, \dots, n$) is the gray value of the coordinates of frame t picture (i, j) in sequence X , then,

$$acf(k) = \frac{n}{n-k} \times \frac{\sum_{t=k+1}^n (x_t - \mu)(x_{t-k} - \mu)}{\sum_{t=1}^n (x_t - \mu)(x_t - \mu)}, \quad (2.1)$$

where k is the lag order ($k = 0, 1, \dots, n-1$), and μ is the mean of sequence X .

Proof. Let the mean μ of sequence X be:

$$\mu = E(X). \quad (2.2)$$

Let the autocovariance c_k of sequence X be:

$$c_k = \frac{1}{n-k} \sum_{t=k+1}^n (x_t - \mu)(x_{t-k} - \mu), \quad (2.3)$$

where k is the lag order ($k = 0, 1, \dots, n-1$).

The ACF of sequence X is:

$$acf(k) = \frac{c_k}{c_0}. \quad (2.4)$$

Bring Eq. 2.3 into Eq. 2.4, we get

$$acf(k) = \frac{n}{n-k} \times \frac{\sum_{t=k+1}^n (x_t - \mu)(x_{t-k} - \mu)}{\sum_{t=1}^n (x_t - \mu)(x_t - \mu)}. \quad (2.5)$$

This finishes the proof.

Figure 1 is a first frame, a 60th frame, and a 1,800th frame image in the GPVS. **Figure 2** shows that the ACF value of the GPVS is not equal to 0, and the ACF curve has a tailing effect, which indicates that the GPVS may be the long-range-dependent sequence.

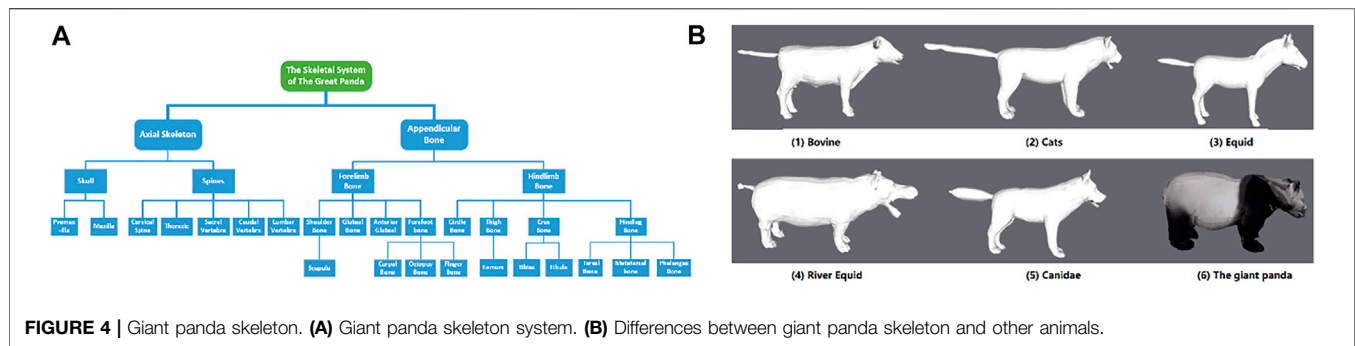


FIGURE 4 | Giant panda skeleton. **(A)** Giant panda skeleton system. **(B)** Differences between giant panda skeleton and other animals.

TABLE 1 | Joint description of the giant panda skeleton.

| Serial number | Joint | Description |
|---------------|--------------|------------------|
| 0 | Root | Roots (pelvis) |
| 1 | Pelvis0 | Pelvis0 |
| 2 | Spine | Spine |
| 3 | Spine0 | Spine 0 |
| 4 | Spine1 | Spine 1 |
| 5 | Spine2 | Spine 2 |
| 6 | Spine3 | Spine 3 |
| 7 | L-Leg1 | Left leg 1 |
| 8 | L-Leg2 | Left leg 2 |
| 9 | L-Leg3 | Left leg 3 |
| 10 | L-Foot | Left foot |
| 11 | R-Leg1 | Right leg 1 |
| 12 | R-Leg2 | Right leg 2 |
| 13 | R-Leg3 | Right leg 3 |
| 14 | R-Foot | Right foot |
| 15 | Neck | Neck |
| 16 | Head | Head |
| 17 | L-Leg-Back1 | Left back leg 1 |
| 18 | L-Leg-Back2 | Left back leg 2 |
| 19 | L-Leg-Back3 | Left back leg 3 |
| 20 | L-Foot--Back | Left back foot |
| 21 | R-Leg-Back1 | Right back leg 1 |
| 22 | R-Leg-Back2 | Right back leg 2 |
| 23 | R-Leg-Back3 | Right back leg 3 |
| 24 | R-Foot-Back | Right back leg |
| 25 | Tail | Tail |
| 26 | Mouth | Mouth |

2.2 Hurst Exponent of GPVS

A Hurst exponent (H) is an index established by H.E. Hurst, a British hydrologist. Its essence is a judgment index, which can be used to judge whether the time series data are a random walk form or a biased random walk process.

When $0.5 < H < 1$, according to the model of fractional Gaussian noise, the time series data has long-range dependent (persistence), indicating that the time series has the characteristics of long-range dependent. If the sequence goes up in the previous period, it will continue to go up in the next period. When the H value is close to 1, this trend is stronger [11, 12].

Through the analysis in Section 2.1, we can see that the GPVS sequence may have long-range-dependent characteristics. Next, we use the H exponent to further judge that the GPVS has long-range-dependent characteristics, and use the H exponent

analysis method of [13] to calculate the H exponent. The calculation process is as follows:

- (1) Divide the sequence X into G groups of nonoverlapping subsequences with length n :

$$x_{11}, x_{12}, \dots, x_{1r}, x_{21}, x_{22}, \dots, x_{2r} \dots x_{g1}, x_{g2}, \dots, x_{gr}.$$

- (2) Calculate the mean value \bar{x}_i of each group of subsequences $x_{g1}, x_{g2}, \dots, x_{gr}$ ($i = 1, 2, \dots, g$).

$$\bar{x}_i = \frac{1}{n} \sum_{j=1}^n x_{ij} \quad i = 1, 2, \dots, g \quad j = 1, 2, \dots, n. \quad (2.6)$$

- (3) Calculated deviation y_{ij} :

$$y_{ij} = x_{ij} - \bar{x}_i \quad i = 1, 2, \dots, g \quad j = 1, 2, \dots, n. \quad (2.7)$$

- (4) Calculate cumulative deviation z_{ij} :

$$z_{ij} = \sum_{k=1}^j y_{ik} \quad i = 1, 2, \dots, g \quad j = 1, 2, \dots, n. \quad (2.8)$$

- (5) Calculate range R_i :

$$R_i = \max(z_{ij}) - \min(z_{ij}) \quad i = 1, 2, \dots, g \quad j = 1, 2, \dots, n. \quad (2.9)$$

- (6) Calculate standard deviation S_i :

$$S_i = \sqrt{\frac{1}{n-1} \sum_{j=1}^n y_{ij}^2} \quad i = 1, 2, \dots, g. \quad (2.10)$$

- (7) Get value RS_i :

$$RS_i = \frac{R_i}{S_i} \quad i = 1, 2, \dots, g. \quad (2.11)$$

The average value \overline{RS} of each subsequence was obtained:

$$\overline{RS} = \frac{1}{g} \sum_{i=1}^g RS_i. \quad (2.12)$$

Finally, $\log \overline{RS}$ as the explained variable Y and $\log n$ as the explanatory variable X , the data pair $(\log n, \log \overline{RS})$ is obtained

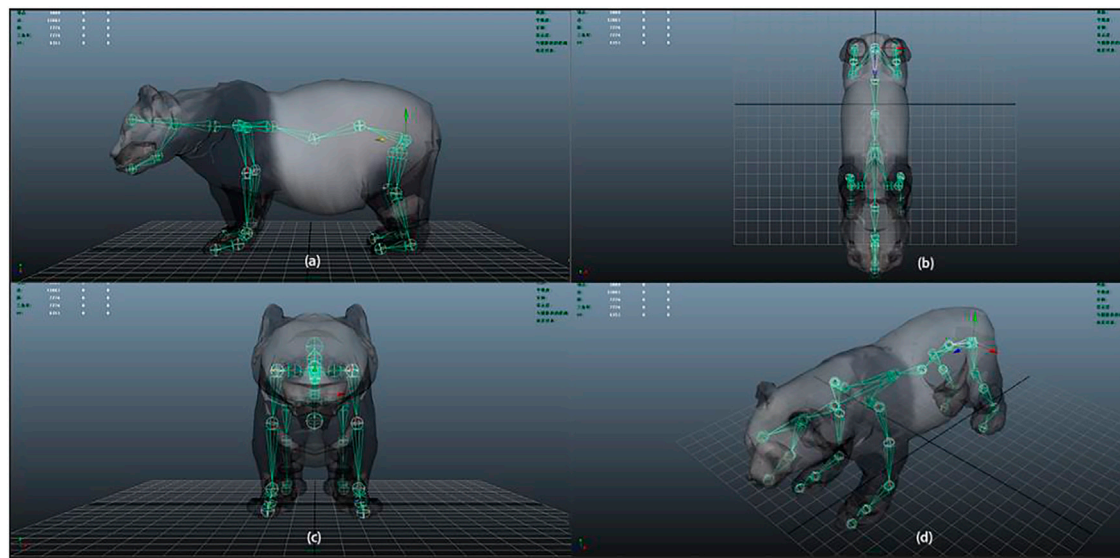


FIGURE 5 | 3D model of a giant panda is bound by a giant panda skeleton. (A) Side view, (B) top view, (C) front view, and (D) oblique view.

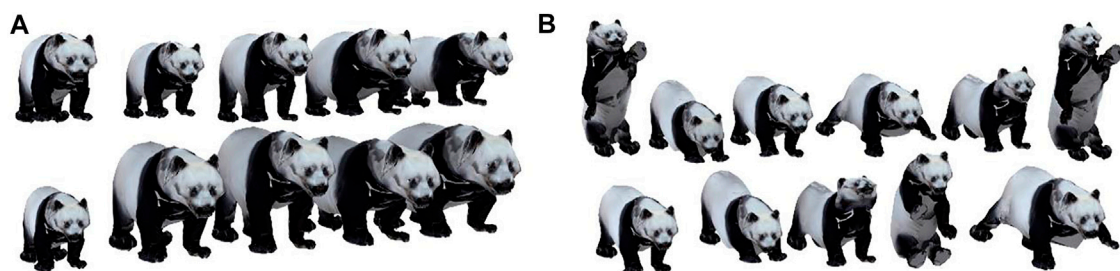


FIGURE 6 | Giant panda SMAL model. (A) Giant panda shapes obtained by SMAL. (B) Panda poses obtained by SMAL.

for each grouping $X_n (k = 1, 2, \dots, m)$, and the slope H is estimated by linear regression, that is, the Hurst index.

Figure 3A shows the sequence H value composed of the values of (300,400) in 190 giant panda video images, $H = 0.906348$. **Figure 3B** shows the H value distribution of all pixels in 190 giant panda video images.

Figure 3C shows the sequence H value composed of the values of (600,800) in 127 giant panda video images, $H = 0.840534$. **Figure 3D** shows the H distribution of all pixels in 127 giant panda video images.

From **Figure 3**, we can see that the H value of the giant panda video image sequence is far greater than 0.5, close to 1, indicating that GPVS has long-range-dependent characteristics.

3 GIANT PANDA 3D MODELING

3.1 Giant Panda Skeleton

The structure formed by a series of joints and bones is called the skeleton. Each joint can correspond to one or more bones and can have multiple subjoints. A correct skeleton structure can ensure that the giant panda has a real and correct motion structure after

three-dimensional modeling, which is one of the important links of the giant panda model.

The selection of bones and joints will affect the deformation of the three-dimensional model of the giant panda. Therefore, the analysis of the skeleton structure of the giant panda plays a very important role in the three-dimensional model of the giant panda. **Figure 4A** shows the detailed skeleton system of the giant panda. In the SMAL model, we usually use 33 joints to represent five kinds of quadrupeds with different attributes, such as cats, dogs, equines, cattle, and hippopotamuses [9, 14]. Compared with these five kinds of quadrupeds, the giant panda has certain similarities, so most of the bones and joints in the whole skeleton can be used for reference, such as head, spine, and leg bone structures.

However, the characteristics of giant panda and other quadrupeds are also different in the skeleton structure, as shown in **Figure 4B**. The tail of the adult giant panda is very short. The body length of the giant panda is about 120–180 cm, while the tail length is only about 10–12 cm. Some tails are shorter than the tail of the rabbit, so we cannot feel the existence of the tail of the giant panda intuitively. In the whole movement structure, we combined the structural characteristics of the giant panda and combined the seven joints of the tail. We used

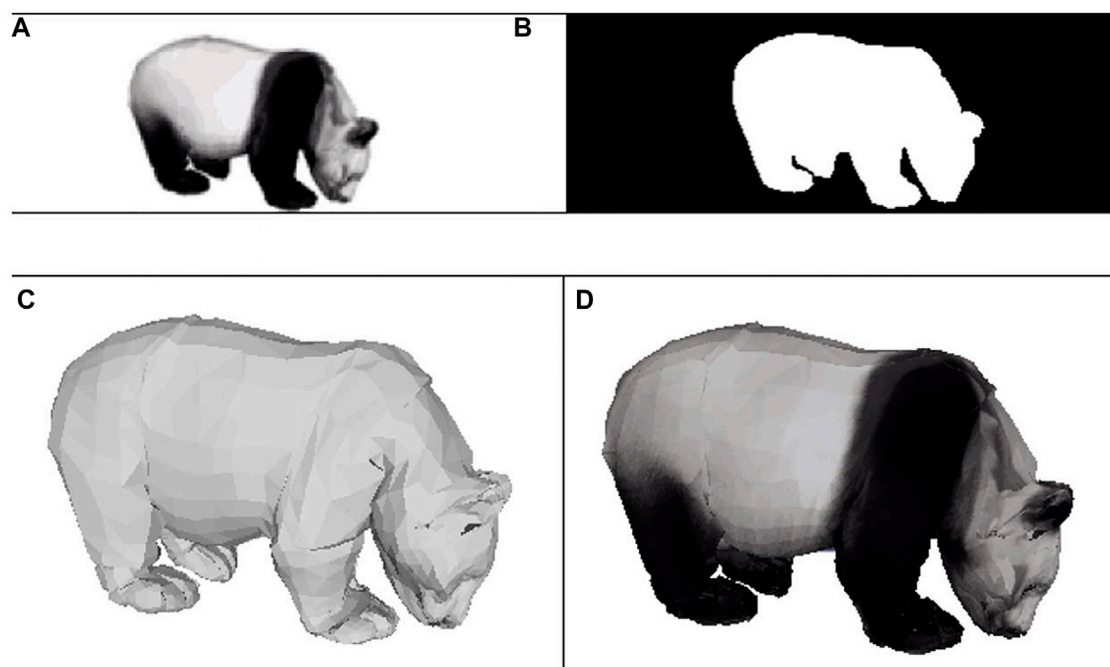


FIGURE 7 | 3D reconstruction of GPVS in frame 10. **(A)** Original image, **(B)** contour silhouette after segmentation, **(C)** reconstruction effect of the 3D model of the giant panda without skin texture, and **(D)** reconstruction effect of the 3D model of the giant panda with skin texture.

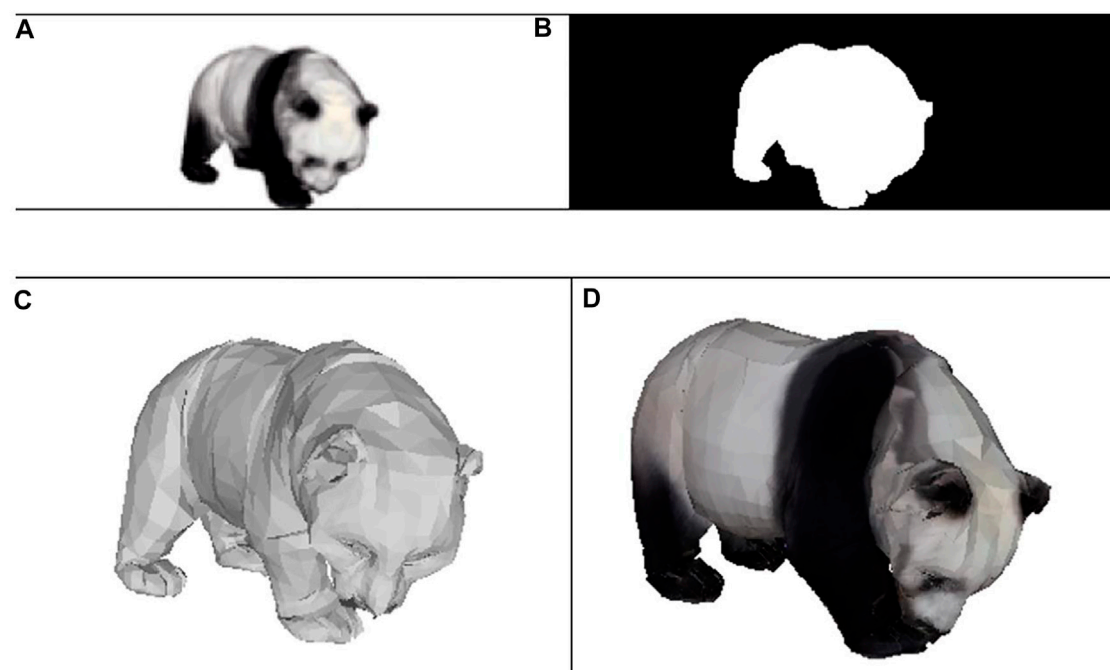


FIGURE 8 | 3D reconstruction of GPVS in frame 30. **(A)** Original image, **(B)** contour silhouette after segmentation, **(C)** reconstruction effect of the 3D model of the giant panda without skin texture, and **(D)** reconstruction effect of the 3D model of the giant panda with skin texture.

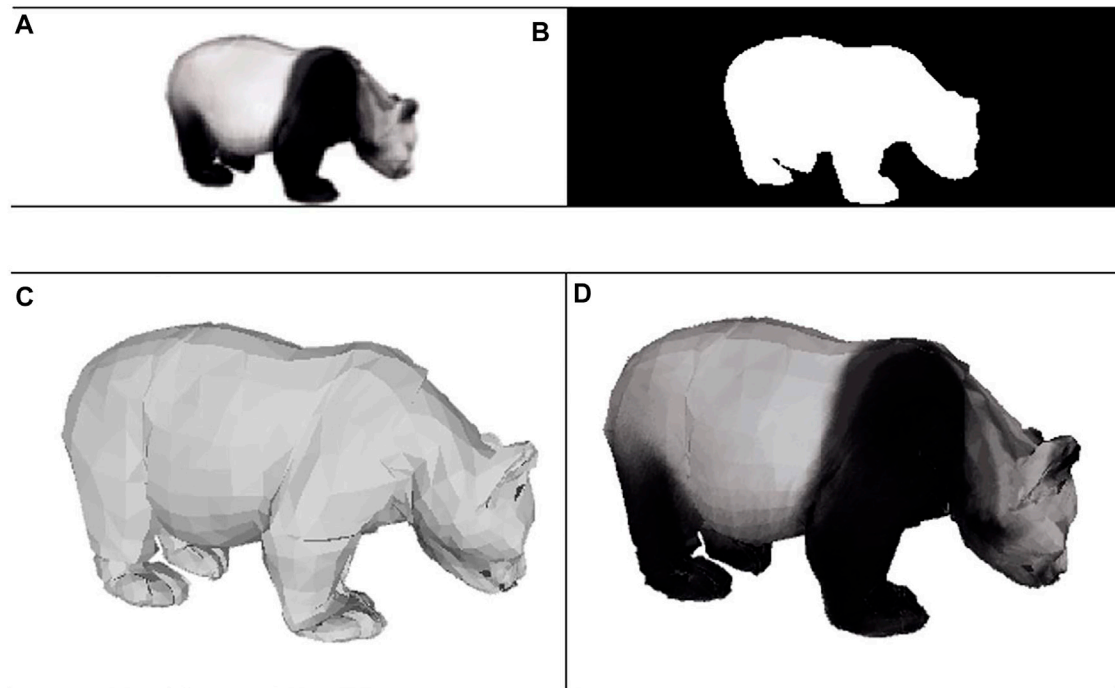


FIGURE 9 | 3D reconstruction of GPVS in frame 60. **(A)** Original image, **(B)** contour silhouette after segmentation, **(C)** reconstruction effect of the 3D model of the giant panda without skin texture, and **(D)** reconstruction effect of the 3D model of the giant panda with skin texture.

27 joints as the basic skeleton structure of the giant panda, as shown in **Table 1**.

3.2 Giant Panda SMAL Model

Since it is impossible to obtain the three-dimensional model of giant panda by scanning the living body of giant panda, this article uses the designed three-dimensional model of giant panda to bind the skeleton [15], as shown in **Figure 5**. The SMAL model is shown in Formula 3.1. Linear blending skinning (LBS) is used to generate giant panda models with different shapes and postures, so as to build the giant panda shape data set and attitude data set, as shown in **Figure 6**.

$$\begin{cases} S(\beta) = \bar{S} + B_s \beta \\ T'_p = \bar{T}_p + B_p(\theta) \end{cases} \quad (3.1)$$

where $S(\beta)$ is the deformation shape parameter of giant panda, \bar{S} is the giant panda average model, β is the shape parameter, and B_s is the shape basis matrix of the eigenvector.

P is a matrix composed of 243 attitude vectors P_i , T'_p is a giant panda posture model, \bar{T}_p is the average posture model, θ is the joint rotation angle, and $B_p(\theta)$ is the vertex offset between the posture model at angle θ and the average attitude model.

4 MOTION SMOOTHING PROCESS

The 3D model of giant panda reconstructed from a single-frame video image does not take into account the time relationship

between frames and the long-range-dependent characteristics of the video image sequence. When the target is obscured or has large noise, there will be relatively large 3D reconstruction errors, such as left leg matching to right leg and right leg matching to left leg. Moreover, the motion sequence composed of the results of single-frame 3D modeling will be not smooth [16].

For video image sequences, the long-distance dependent between data is used to capture the correlation between pixels of distant frames in the sequence, which is more conducive to the recognition and judgment of image information. In **Section 2.2**, we have analyzed that the GPVS has long-distance-dependent characteristics, so we will use the characteristics of the GPVS to improve the giant panda 3D modeling.

In order to improve the accuracy of the single-frame pose modeling algorithm, we fully consider that the RGB video sequence has long-range-dependent characteristics. That is, the movement and limb rotation angle of the giant panda in the video sequence shall not change too much. We use this characteristic to correct the error of 3D modeling results, so as to make the 3D modeling results of giant panda more smooth and accurate.

First, the body shape parameters β and attitude parameters θ of giant pandas in each frame of the video are solved by **Eq. 3.1**. Then, the energy function formula 4.1 is used to construct the time-smoothing term to improve the motion fluency and 3D reconstruction accuracy.

$$E_n(\beta, \theta) = \lambda_{3d} E_{3d}(\beta, \theta) + \lambda_{sm} E_{sm}(\beta, \theta), \quad (4.1)$$

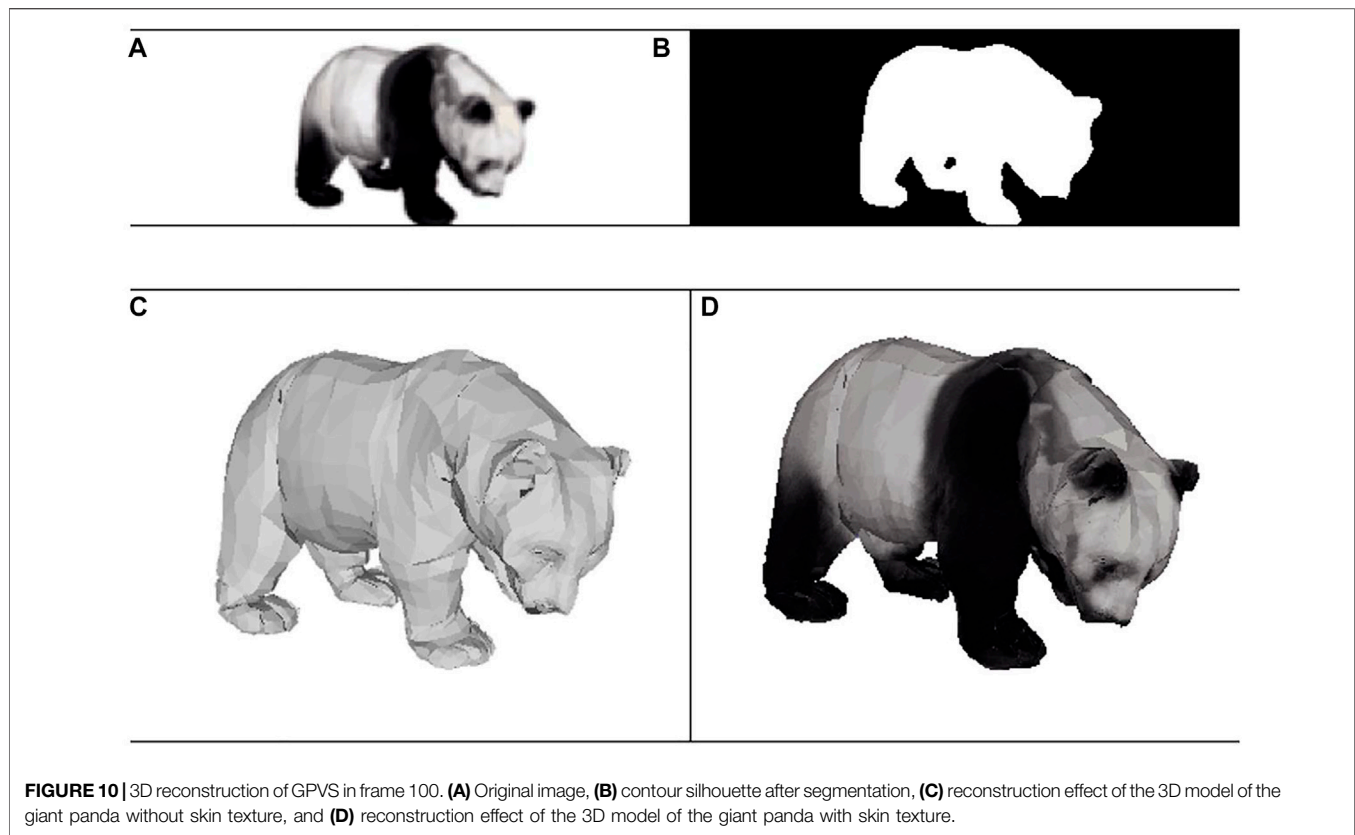


FIGURE 10 | 3D reconstruction of GPVS in frame 100. **(A)** Original image, **(B)** contour silhouette after segmentation, **(C)** reconstruction effect of the 3D model of the giant panda without skin texture, and **(D)** reconstruction effect of the 3D model of the giant panda with skin texture.

TABLE 2 | PCK results table of different thresholds.

| Sample | PCK @0.01 | PCK @0.02 | PCK @0.05 | PCK @0.10 | PCK @0.15 | Number of visible key points |
|--------|--------------|--------------|--------------|--------------|--------------|------------------------------------|
| image1 | 4.32 | 14.13 | 45.01 | 76.17 | 83.16 | 23 |
| image2 | 4.01 | 13.15 | 43.38 | 74.23 | 81.24 | 18 |
| image3 | 3.35 | 10.37 | 38.35 | 70.34 | 77.15 | 16 |

where λ_{3d} λ_{sm} is the weight parameter of the corresponding energy term, E_{3d} is the three-dimensional error energy, and E_{sm} is the motion-smoothing energy.

(1) 3D attitude error

$$\begin{cases} E_{3d} = \sum_n w_n \text{dist}(\theta_n, \hat{\theta}_n) \\ w_n = \exp(-\delta_n) \\ \delta_n = \sum_j C_{nj} \|x_{nj} - \hat{x}_{nj}\|_2^2 \end{cases}, \quad (4.2)$$

where dist is the distance between the SMAL 3D model and the 3D model after rotation. x_{nj} and C_{nj} is the two-dimensional coordinates of the joint in the n th frame of the video and its confidence, and \hat{x}_{nj} is the two-dimensional joint coordinates projected from the three-dimensional joint of the model to the image.

The main function of this item is to slightly adjust the first three-dimensional vector of the attitude parameters of the SMAL model to adjust the rotation angle of the model while maintaining

the consistency between the projection of the three-dimensional attitude of the model and the results of the two-dimensional joint points, so as to improve the accuracy of attitude modeling and restrain some problems of incorrect pose estimation of the model, so as to ensure the accuracy of the attitude modeling algorithm.

(2) Motion smoothing

$$E_{sm} = \sum_n \sum_j \|J_i(\beta_n, \theta) - J_i(\beta_{n+1}, \theta)\|_2^2, \quad (4.3)$$

where J_i is the function of the coordinates of the three-dimensional joint numbered I of the SMAL model given the shape and attitude parameters of the SMAL model.

This item uses the similarity of giant panda actions in adjacent frames of the video to constrain the changes of three-dimensional bone joints of the model. The greater the change of model posture from the previous frame, the greater the energy value of this item. In case of large errors, due to image feature mismatch or over-fitting, this item can be constrained to correct some large errors such as leg exchange or posture inversion.

5 DISCUSSION

Our experimental work is based on the prior information of the giant panda SMAL model. According to two-dimensional images of the giant panda, the algorithm uses Formula 3.1 to obtain the shape, pose, and other parameters of the three-dimensional model of the

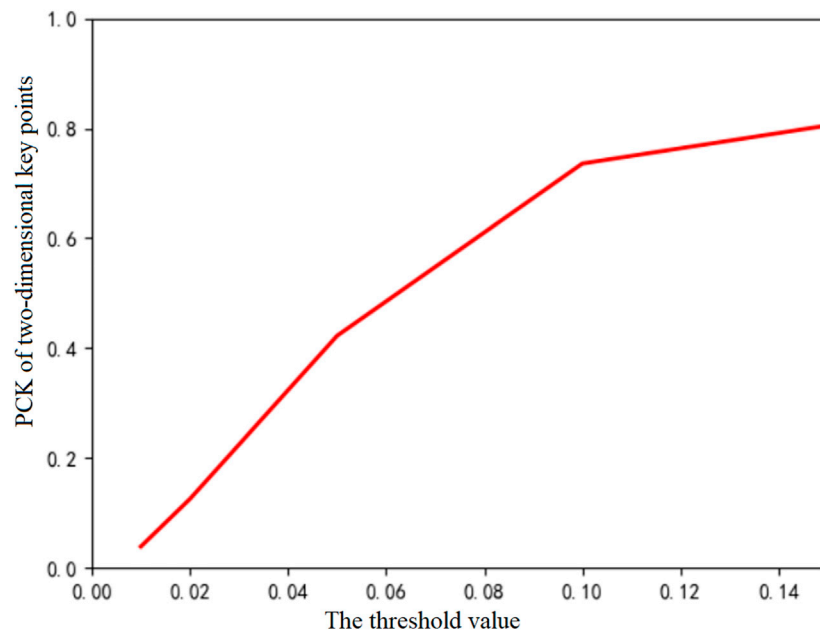


FIGURE 11 | PCK indicators.

giant panda and reconstructs a 3D model of the giant panda. Then, the 3D reconstruction accuracy is improved by **Eq. 4.1**, and the motion fluency of the 3D model is improved, and the 3D reconstruction results of giant panda are shown in **Figures 7–10**.

Figures 7–10 show the experimental results of the algorithm in restoring the SMAL giant panda 3D model from the image. The upper left figure of each group of images is the original image, the upper right figure is the segmented contour silhouette, and the lower left corner and lower right corner are the reconstruction effects of the giant panda 3D model without skin texture and with skin texture, respectively. It is obvious that there is a good fit between the image and the restored three-dimensional model of giant panda.

Table 2 shows the PCK indicators under different thresholds for some image examples. **Figure 11** shows the visualization results of the mean value of the evaluation index PCK between the projection key points obtained after the restoration of the three-dimensional model of the giant panda and the truly marked key points of the input image. When the threshold of key point detection is PCK@0.15 (corresponding to 0.15 times of image pixels), the accuracy can reach 80.51%. Therefore, experiments show that our method can also obtain a 3D model of giant panda with a good reconstruction effect in the presence of occlusion or insufficient key points.

6 CONCLUSION

Through the analysis of GPVS, we prove that it has the long-range-dependent characteristics [17, 18]. We propose a

method to use the coherent information contained in the long-range-dependent characteristics between video sequence images to construct a smooth energy function to correct the 3D model error. Through this error, we can judge that the 3D reconstruction result of giant panda is different from the real structure of giant panda. Finally, the experimental results show that our algorithm can obtain a more accurate 3D reconstruction model of giant panda.

DATA AVAILABILITY STATEMENT

The original contributions presented in the study are included in the article/Supplementary Materials; further inquiries can be directed to the corresponding author.

AUTHOR CONTRIBUTIONS

All authors listed have made a substantial, direct, and intellectual contribution to the work and approved it for publication.

FUNDING

This research is supported by the Chengdu Research Base of Giant Panda Breeding (NOs. 2020CPB-C09 and CPB2018-01).

REFERENCES

- Schönberger JL, Frahm JM. Structure-from-Motion Revisited[C]. In: IEEE Conference on Computer Vision & Pattern Recognition; 2016 Jun 27–30; Las Vegas, Nevada (2016).
- Bregler C, Hertzmann A, Biermann H. Recovering Non-Rigid 3D Shape from Image Streams[C]. In: IEEE Conference on Computer Vision & Pattern Recognition; 2000 Jun 13–15; Hilton Head, SC. IEEE (2000).
- Garg R, Roussos A, Agapito L. Dense Variational Reconstruction of Non-Rigid Surfaces from Monocular Video[C]. In: IEEE Conference on Computer Vision and Pattern Recognition; 2013 Jun 23–28; NW Washington, DC. IEEE (2013).
- Li X, Li H, Joo H, Liu Y, Sheikh Y. *Structure from Recurrent Motion: From Rigidity to Recurrency*[J]. (2018). Salt Lake City, UT: IEEE CVPR.
- Loper M, Mahmood N, Romero J, Black MJ. *SMPL: A Skinned Multi-Person Linear model*[J]. Kobe, Japan: ACM Transactions on Graphics TOG (2015).
- Kanazawa A, Black MJ, Jacobs DW, Malik J. *End-to-end Recovery of Human Shape and Pose*[J]. (2017). Salt Lake City, UT: IEEE CVPR, 2018.
- Zuffi S, Kanazawa A, Jacobs D, Black MJ. 3D Menagerie: Modeling the 3D Shape and Pose of Animals. In: IEEE Conf. on Computer Vision and Pattern Recognition(CVPR); 2017 Jul 21–26; Hawaii Convention Center, Hawaii (2017). doi:10.1109/cvpr.2017.586
- Vicente S, Agapito L. Balloon Shapes: Reconstructing and Deforming Objects with Volume from Images[C]. In: International Conference on 3d Vision-3dv; 2013 Jun 29–Jul 01; Seattle, WA. IEEE (2013).
- Biggs B, Roddick T, Fitzgibbon A, Cipolla R. Creatures Great and SMAL: Recovering the Shape and Motion of Animals from Video. In: Asian Conference on Computer Vision; 2018 Dec 04–06; Perth, Australia (2018).
- Li M. Fractal Time Series—A Tutorial Review. *Math Probl Eng* (2010) 2010: 157264. doi:10.1155/2010/157264
- Li M. Modified Multifractional Gaussian Noise and its Application. *Physica Scripta* (2021) 96(12):125002. doi:10.1088/1402-4896/ac1cf6
- Li M. Generalized Fractional Gaussian Noise and its Application to Traffic Modeling. *Physica A* (2021) 579(22):126138. doi:10.1016/j.physa.2021.126138
- Peltier RF, Levy-Vehel J. Multifractional Brownian Motion: Definition and Preliminaries Results. INRIA TR 2645 (1995).
- Zuffi S, Kanazawa A, Black M. *Lions and Tigers and Bears: Capturing Non-Rigid 3D*. Salt Lake City, UT: Articulated Shape from Images (2018).
- Bogo F, Kanazawa A, Lassner C, Gehler P, Romero J, Black MJ. Keep it SMPL: Automatic Estimation of 3D Human Pose and Shape from a Single Image. In: European Conference on Computer Vision; 2016 Oct 11–14; Amsterdam, Netherlands (2016).
- Zhang H. *Research on 3D Human Modeling and its Application Based on SML Model*. Xian, Shaanxi, China: Shaanxi University of Science & Technology (2020).
- He J, George C, Wu J, Li M, Leng J. Spatiotemporal BME Characterization and Mapping of Sea Surface Chlorophyll in Chesapeake Bay (USA) Using Auxiliary Sea Surface Temperature Data. *Sci Total Environ* (2021) 794(1):148670. doi:10.1016/j.scitotenv.2021
- He J. Application of Generalized Cauchy Process on Modeling the Long-Range Dependence and SelfSimilarity of Sea Surface Chlorophyll Using 23 Years of Remote Sensing Data. *Front Phys* (2021) 9:750347. doi:10.3389/fphy.2021.750347

Conflict of Interest: The authors declare that the research was conducted in the absence of any commercial or financial relationships that could be construed as a potential conflict of interest.

Publisher's Note: All claims expressed in this article are solely those of the authors and do not necessarily represent those of their affiliated organizations, or those of the publisher, the editors, and the reviewers. Any product that may be evaluated in this article, or claim that may be made by its manufacturer, is not guaranteed or endorsed by the publisher.

Copyright © 2022 Hu, Liao, Hou and Chen. This is an open-access article distributed under the terms of the Creative Commons Attribution License (CC BY). The use, distribution or reproduction in other forums is permitted, provided the original author(s) and the copyright owner(s) are credited and that the original publication in this journal is cited, in accordance with accepted academic practice. No use, distribution or reproduction is permitted which does not comply with these terms.



Dependence Research on Multi-Layer Convolutions of Images

Zhiwu Liao^{1*}, Yong Yu² and Shaoxiang Hu^{3*}

¹School of Computer Science, Sichuan Normal University, Chengdu, China, ²School of Mathematics and Computers (Big Data Science), Panzhihua University, Panzhihua, China, ³School of Automation Engineering, University of Electronic Science and Technology of China, Chengdu, China

Convolutions are important structures in deep learning. However, theoretical analysis on the dependence among multi-layer convolutions cannot be found until now. In this paper, the image pixels before, in, and after multi-layer convolutions are of modified multifractional Gaussian noise (mmfGn). Thus, their Hurst parameters are calculated. Based on these, we applied mmfGn model to analyze the dependence of gray levels of multi-layer convolutions of the image pixels and demonstrate their short-range dependence (SRD) or long-range dependence (LRD), which can help researchers to design better network structures and image processing algorithm.

Keywords: fraction Brownian motion, Hurst parameter, time-varying Hurst parameter, long-range dependence (LRD), modified multifractional Gaussian noise, fractional Gaussian noise (fGn)

OPEN ACCESS

Edited by:

Ming Li,
Zhejiang University, China

Reviewed by:

Jianwei Yang,
Nanjing University of Information
Science and Technology, China

Junyu He,
Zhejiang University, China

*Correspondence:

Zhiwu Liao
liaoziwu@163.com
Shaoxiang Hu
hushaox@126.com

Specialty section:

This article was submitted to
Interdisciplinary Physics,
a section of the journal
Frontiers in Physics

Received: 19 December 2021

Accepted: 04 February 2022

Published: 07 March 2022

Citation:

Liao Z, Yu Y and Hu S (2022)
Dependence Research on Multi-Layer
Convolutions of Images.
Front. Phys. 10:839346.
doi: 10.3389/fphy.2022.839346

1 INTRODUCTION

Deep learning models are composed of multiple convolution layers to learn features of images [1, 2]. However, so far, the theoretical analysis on dependence among multi-layer convolutions have not been reported.

Fractional Brownian motion (fBm) is commonly used in modeling fractal time series. The fBm of the Weyl type is defined by [3–5]

$$B_H(t) - B_H(0) = \frac{1}{\Gamma(H+0.5)} \left\{ \int_{-\infty}^0 [(t-u)^{H-0.5} - (-u)^{H-0.5}] dB(u) + \int_0^t (t-u)^{H-0.5} dB(u) \right\} \quad (1)$$

where $0 < H < 1$ is the Hurst parameters.

Its auto-correlation function (ACF) of the Weyl type is

$$C_{fBm}(t, s) = \frac{V_H}{(H+0.5)\Gamma(H+0.5)} [|t|^{2H} + |s|^{2H} - |t-s|^{2H}] \quad (2)$$

where

$$V_H = \Gamma(1-2H) \frac{\cos \pi H}{\pi H} \quad (3)$$

The fBm is nonstationary, but it has a stationary increment. The process fBm reduces to the standard Brownian motion when $H = 0.5$.

Based on the dependence theory, the main contributions of this paper are:

- 1) Discuss dependence of image multi-layer convolutions by assuming that gray levels of multi-layer convolutions of an image pixel are of modified multifractional Gaussian noise (mmfGn).
- 2) Calculate the time-varying Hurst parameters by point-by-point basis to discuss the dependence of different pixels.

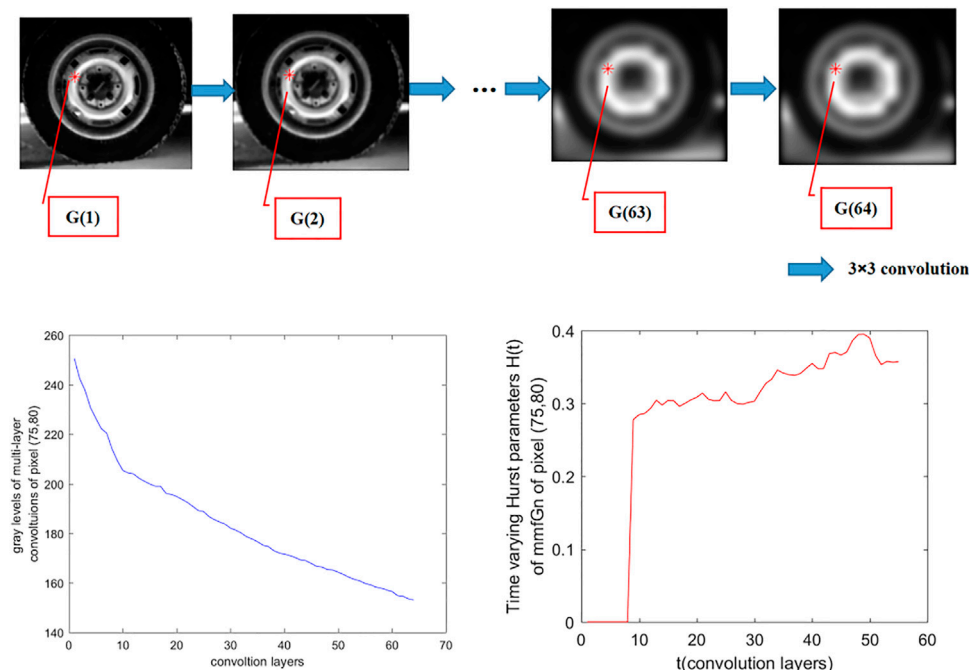


FIGURE 1 | The 64-dimensional column vector $G = [G(1), G(2), \dots, G(63), G(64)]^T$ whose components are the gray levels of multi-layer convolutions on pixel (75, 80). Top: the components of the 64-dimensional column vector on pixel (75, 80). Left bottom: the plot of the 64-dimensional vector whose x-axis represents the convolution layers and y-axis represents the gray levels of convolution layers on pixel (75, 80). Right bottom: time-varying Hurst parameters $H(t)$ of mmfGn of the 64-dimensional column vector of pixel (75, 80) using **Eqs 7 and 8** where $n = 64$, $k = 16$.

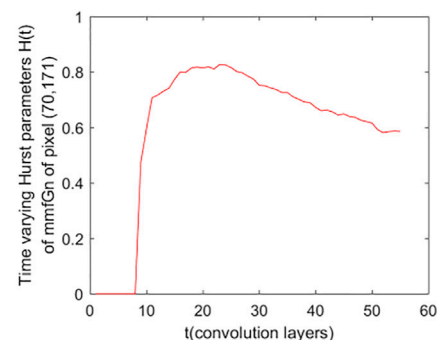


FIGURE 2 | Left: the test image and the selected pixel (70, 171). Right: the time-varying Hurst parameters $H(t)$ of pixel (70, 171).

The remainder of this paper is as follows: the second section introduces the preliminaries on fractional Gaussian noise (fGn) and mmfGn; the third section gives a case study. Finally, the conclusions and acknowledgments are given.

2 PRELIMINARIES

2.1 Fractional Gaussian Noise

The fGn is the derivative of the fBm. Its ACF is:

$$C_{fGn}(\tau) = \frac{V_H}{2} \left[(|\tau| + 1)^{2H} + (|\tau| - 1)^{2H} - 2|\tau|^{2H} \right] \quad (4)$$

where

$$V_H = \Gamma(1 - 2H) \frac{\cos \pi H}{\pi H} \quad (5)$$

fGn is of long-range dependence (LRD) for $0.5 < H < 1$ and is of short-range dependence (SRD) for $0 < H < 0.5$. If $H = 0.5$, fGn reduces to the white noise [5–7].

2.2 Modified Multifractional Gaussian Noise

Let $G(t)$ be the mmfGn. The ACF of mmfGn is [6]

$$C_{mmfGn}(\tau) = \frac{V_{H(t)}}{2} \left[(|\tau| + 1)^{2H(t)} + ||\tau| - 1|^{2H(t)} - 2|\tau|^{2H(t)} \right] \quad (6)$$

The condition of mmfGn to be of LRD is $0.5 < H(t) < 1$, while to be of SRD is $0 < H(t) < 0.5$.

Based on the local growth of the increment process, Peltier and Levy-Vehel gave $H(t)$ estimator in Eqs 7 and 8 [8–11].

Let n be the number of data of a sample mmfGn and $G(i)$ be the i th sample point. Let k ($1 < k < n$) be the length of the neighborhood used for estimating the functional parameter $H(i)$. The $H(i)$ will be estimated only for $i = [k/2] + 1, [k/2] + 2, \dots, n - 1$ where $[k/2]$ is the integral part of $k/2$. Let $m = [n/k]$ be the integral part of n/k . Then the estimator of $H(i)$ is [8]:

$$\hat{H}(i) = -\frac{\log\left[\sqrt{\frac{\pi}{2}} S_k(i)\right]}{\log(n-1)} \quad (7)$$

where

$$S_k(i) = \frac{m}{n-1} \sum_{j=i-[k/2]}^{j=i+[k/2]} |G(j+1) - G(j)| \quad (8)$$

3 CASE STUDY AND DISCUSSION

3.1 Data in Case Study

Tire.tif in matLab is chosen as test data. The image is convoluted 64 times by randomly generated 3×3 masks whose sum is equal to 1. Thus, the normalized gray levels in $[0, 1]$ of multi-layer convolutions on each pixel in the image will form a 64-dimensional column vector $G = [G(1), G(2), \dots, G(63), G(64)]^T$; see top image of **Figure 1**. We will discuss the dependence among the components of each 64-dimensional vector.

3.2 $H(t)$ of mmfGn

We now study the dependence of samples among multi-layer convolution by computing $H(t)$ of mmfGn for each 64-dimensional vector. That is, the 64-dimensional vector is of mmfGn; the time-varying Hurst parameter $H(t)$ of samples should be calculated to feature the local similarity of the vectors.

The $H(t)$ is calculated using Eqs 7 and 8: the sample number $n = 64$, and the length of the neighborhood $k = 16$. Thus, the Hurst parameter $H(t)$ will be estimated only for $t = 9, 10, \dots, 55$. H forms a 55-dimensional vector with 8 zeros on the 1st to 8th positions.

Tire.tif in MatLab is used to discuss the dependence of 64-dimensional vectors of a pixel. Since gray levels of multi-layer convolution of each of image pixel form a 64-dimensional vector whose time-varying Hurst parameter $H(t)$ is a 55-dimensional vector, we can obtain a 3-dimensional matrix to record $H(t)$ of image pixels with $W \times L \times 55$ where W is the width of the image and L is the length of the image.

The condition of mmfGn to be of LRD is $0.5 < H(t) < 1$, while to be of SRD it is $0 < H(t) < 0.5$.

DISCUSSION

In order to discuss the dependence of different pixels of 64-dimensional vector G , two pixels are selected, and their time-varying Hurst parameter $H(t)$ of mmfGn is shown in the bottom right of **Figure 1** and the right of **Figure 2**. In **Figure 1**, the Hurst parameter $H(t)$ of pixel (75, 80) is less than 0.5 for $t = 1, \dots, 55$. Thus, G of pixel (75, 80) is of SRD. But the Hurst parameter $H(t)$ of pixel (70, 171) is larger than 0.5 for $t = 9, \dots, 55$ in **Figure 2**. It is of LRD.

From the above discussion, the dependence of 64-dimensional vectors of some pixel are of LRD, while for other pixels, they are of SRD.

We think the above dependence of image multi-layer convolution coincides with the nature of images and is a very promising character in designing a deep neural network. Maybe, we can design more powerful algorithms and networks with smaller computation cost.

CONCLUSION

The dependence of samples of multi-layer convolutions has been discussed. Based on the model of mmfGn, we found that each pixel with a 64-dimensional vector has the statistical dependence of either LRD or SRD on a pixel-by-pixel basis, relying on the value of $H(t)$ of image pixels.

DATA AVAILABILITY STATEMENT

The original contributions presented in the study are included in the article/supplementary material, further inquiries can be directed to the corresponding authors.

AUTHOR CONTRIBUTIONS

All authors listed have made a substantial, direct, and intellectual contribution to the work and approved it for publication.

REFERENCES

1. LeCun Y, Bengio Y, Hinton G. Deep Learning. *Nature* (2015) 521:436–44. doi:10.1038/nature14539
2. Rahman Minar M, Naher J. Recent Advances in Deep Learning: An Overview, CoRR, abs/1807.08169 (2018). Available from: <http://arxiv.org/abs/1807.08169>, 21 July 2018.
3. Flandrin P. On the Spectrum of Fractional Brownian Motions. *IEEE Trans Inform Theor* (1989) 35(1):197–9. doi:10.1109/18.42195
4. Li M. On the Long-Range Dependence of Fractional Brownian Motion. *Math Probl Eng* (2013) 2013, 5. doi:10.1155/2013/842197
5. Li M. Fractal Time Series—A Tutorial Review. *Math Probl Eng* (2010) 2010, 26. doi:10.1155/2010/157264
6. Li M. Modified Multifractional Gaussian Noise and its Application. *Phys Scr* (2021) 96(12):125002. Dec. 2021. doi:10.1088/1402-4896/ac1cf6
7. Li M. Multi-fractional Generalized Cauchy Process and its Application to Teletraffic. *Physica A: Stat Mech its Appl* (2020) 550:123982. doi:10.1016/j.physa.2019.123982
8. Peltier RF, Levy Vehel J. A New Method for Estimating the Parameter of Fractional Brownian Motion. RR-2396. Paris, France: INRIA (1994). (inria-00074279).
9. Peltier RF, Levy-Vehel J. Multifractional Brownian Motion: Definition and Preliminaries Results. *INRIA TR* (1995) 2645, 43. <https://hal.inria.fr/inria-00074045/document>.
10. He J, George C, Wu J, Li M, Leng J. Spatiotemporal BME Characterization and Mapping of Sea Surface Chlorophyll in Chesapeake Bay (USA) Using Auxiliary Sea Surface Temperature Data. *Sci Total Environ* (2021) 794(1 Nov):148670. doi:10.1016/j.scitotenv.2021.148670
11. He J. Application of Generalized Cauchy Process on Modeling the Long-Range Dependence and Self-Similarity of Sea Surface Chlorophyll Using 23 Years of Remote Sensing Data. *Front Phys* (2021) 9(28 September 2021):750347. doi:10.3389/fphy.2021.750347

Conflict of Interest: The authors declare that the research was conducted in the absence of any commercial or financial relationships that could be construed as a potential conflict of interest.

Publisher's Note: All claims expressed in this article are solely those of the authors and do not necessarily represent those of their affiliated organizations, or those of the publisher, the editors and the reviewers. Any product that may be evaluated in this article, or claim that may be made by its manufacturer, is not guaranteed or endorsed by the publisher.

Copyright © 2022 Liao, Yu and Hu. This is an open-access article distributed under the terms of the Creative Commons Attribution License (CC BY). The use, distribution or reproduction in other forums is permitted, provided the original author(s) and the copyright owner(s) are credited and that the original publication in this journal is cited, in accordance with accepted academic practice. No use, distribution or reproduction is permitted which does not comply with these terms.



Two Novel One-Way Delay Clock Skew Estimators and Their Performances for the Fractional Gaussian Noise/Generalized Fractional Gaussian Noise Environment Applicable for the IEEE 1588v2 (PTP) Case

Yehonatan Avraham and Monika Pinchas*

Department of Electrical and Electronic Engineering, Ariel University, Ariel, Israel

OPEN ACCESS

Edited by:

Ming Li,
Zhejiang University, China

Reviewed by:

Hu Shaoxiang,
University of Electronic Science and
Technology of China, China
Nan Mu,
Michigan Technological University,
United States

*Correspondence:

Monika Pinchas
monika.pinchas@gmail.com

Specialty section:

This article was submitted to
Interdisciplinary Physics,
a section of the journal
Frontiers in Physics

Received: 01 February 2022

Accepted: 14 February 2022

Published: 22 March 2022

Citation:

Avraham Y and Pinchas M (2022) Two
Novel One-Way Delay Clock Skew
Estimators and Their Performances for
the Fractional Gaussian Noise/
Generalized Fractional Gaussian Noise
Environment Applicable for the IEEE
1588v2 (PTP) Case.
Front. Phys. 10:867861.
doi: 10.3389/fphy.2022.867861

Papers in the literature dealing with the Ethernet network characterize packet delay variation (PDV) as a long-range dependence (LRD) process. The fractional Gaussian noise (fGn) or the generalized fractional Gaussian noise (gfGn) belong to the LRD process. The IEEE1588v2 is a two-way delay (TWD) protocol that uses the messages from the Forward (Master to Slave) and the Reverse (Slave to Master) paths. Suppose we have a significant difference between the PDV variances of the Forward and the Reverse paths. Thus, if we can use only the path with the lowest PDV variance (namely, only the one-way delay (OWD) technique), we might get a better clock skew performance from the mean square error (MSE) point of view compared with the traditional TWD method. This paper proposes two OWD clock skew estimators, one for the Forward path and one for the Reverse path applicable for the white-Gaussian, fGn and gfGn environment. Those OWD estimators do not depend on the unknown asymmetry between the fixed delays in the Forward and Reverse paths and nor on the clock offset between the Master and Slave. We also supply two closed-form approximated expressions for the MSE related to our new proposed OWD clock skew estimators. In addition, we supply some conditions, summarized in a table, guiding us whether we should use the OWD clock skew estimator for the Forward path or for the Reverse path, or just use the TWD algorithm. Simulation results confirm that our new proposed OWD clock skew estimators achieve better clock skew performances from the MSE point of view, compared with the TWD clock skew estimator recently proposed by the same authors and compared with two literature known OWD methods (the maximum likelihood and Kalman clock skew estimators).

Keywords: PTP, PDV, LRD, fGn, gfGn, TWD, OWD, IEEE1588V2

1 INTRODUCTION

The Precision Time Protocol (PTP), named also as the IEEE 1588v2 standard [1] is a TWD exchange scheme where the Slave exchanges a series of synchronization packets with its Master so the packet timestamps can be employed to estimate the clock skew relative to the Master. In other words, the PTP as a TWD algorithm uses messages received from the Forward (Master to Slave) and from the Reverse (Slave to Master) paths in order to estimate the clock skew relative to the Master. The synchronization packets can encounter several intermediate switches and routers along the network path between the Master and the Slave [2]. Networks often suffer large unpredictable queuing delays at switches and routers (thus having heavy PDV in the network) due to the presence of background traffic [3]. This background traffic may be a real traffic or one caused by a cyber attack [2] where a malicious intermediate node deliberately delays the transmission of synchronization messages. A heavy PDV can be seen in the Forward path, in the Reverse path or in both paths. Usually, the PDV in the Forward path is different from the PDV in the Reverse path. The problem is that the PDV of the Forward and Reverse paths can significantly hamper the accuracy of the clock skew estimation [3]. A lower PDV will lead to a more accurate clock skew estimation compared to a higher PDV. Thus, if the difference in the PDVs encountered in Forward and Reverse paths is high, the clock skew estimation accuracy obtained with the TWD technique is mainly decreased due to the path with the higher PDV. Thus, if we could use for the clock skew estimation task only the path with the lowest PDV (namely, using the OWD technique), the clock skew performance from the MSE point of view might be improved compared with the case where we have also to consider the path with the higher PDV (the TWD approach). Since the lower PDV path may occur in the Forward path as well as in the Reverse path, two different OWD clock skew estimators are needed (one for the Forward path and the other one associated with the Reverse path). So far we have seen that for the clock skew estimation task, the OWD technique may be more useful compared with the TWD approach in cases where the Forward PDV variance is very different from the Reverse PDV variance. According to [4], PTP (which is a TWD exchange scheme) has more unknown parameters than available equations. Thus, in order to solve the problem, a symmetric path is usually assumed. Namely, the fixed delay in the Forward path is usually assumed to be the same as the fixed delay for the Reverse path. But, in practical scenarios, this is not the case. Thus, for an asymmetrical path, when the symmetric path assumption is applied, a degradation in the clock skew estimation may be obtained when the TWD approach is applied. Now, the OWD technique relies only on one path, on the Reverse path or on the Forward path. Thus, the symmetric assumption is not needed in the OWD technique which can be considered here as an advantage compared with the TWD approach. Suppose for a moment that we have three clock skew estimators applicable for the PTP case. Namely, we have one OWD clock skew estimator for the Forward path, one OWD clock skew estimator for the Reverse path and a TWD clock skew estimator. Next we wish to

know which of the three clock skew estimators should be taken for the clock skew estimation task given a network where different PDV variances are seen on both Forward and Reverse paths but the fixed delay of the Forward path is equal to the fixed delay of the Reverse path. It is quite reasonable to think that when the Forward path PDV variance is equal or close to equal to the Reverse path PDV variance, the TWD clock skew estimator is preferable over the OWD clock skew estimator due to the “averaging” effect of the variances in the TWD clock skew estimator. But, when the PDV variances of the Forward and Reverse paths are different and on the same time the difference in the variances is not very high, it is not clear if the OWD clock skew estimator for the Forward path or the OWD clock skew estimator for the Reverse path or maybe the TWD clock skew estimator should be applied for the clock skew estimation task. Thus, some guiding lines (closed-form expressions, conditions) are needed here, telling us which approach should be applied in order to get the best clock skew performance in the MSE point of view. Namely, which clock skew estimator should be taken: the OWD clock skew estimator for the Forward path or the OWD clock skew estimator for the Reverse path or perhaps the TWD clock skew estimation approach. Recently [4], we proposed a new TWD clock skew estimator for the PTP case that has the best clock skew performance in the MSE point of view compared to the relevant literature known estimators [5–7]. This clock skew estimator [4] is suitable for the white-Gaussian and fGn/gfGn cases and does not depend on the asymmetric fixed delay between the Forward and the Reverse paths, nor on the offset between the Master and the Slave clocks. This paper is a direct continuation of our previous work [4]. Thus, please refer to [4] in order to find a detailed overview of the existing TWD and recently proposed OWD approaches for the PTP case. Please note that the two recently proposed OWD clock skew estimators [6,7], are both OWD clock skew estimators associated with the Forward path. Thus, if the Forward path PDV variance is much higher compared with the Reverse path PDV variance, [6,7] may not get better clock skew performance from the MSE point of view compared with the TWD approach and compared with the OWD clock skew estimator associated with the Reverse path. As already was mentioned, this paper is a direct continuation of our previous work [4] where we proposed a novel TWD clock skew estimator applicable for the PTP case. In this paper we propose:

1. A novel OWD clock skew estimator for the Forward path based on [4], applicable for the white-Gaussian and fGn/gfGn environment.
2. A novel OWD clock skew estimator for the Reverse path based on [4], applicable for the white-Gaussian and fGn/gfGn environment.
3. A closed-form-approximated expression for the clock skew performance (MSE) related to our OWD proposed clock skew estimator for the Forward path.
4. A closed-form-approximated expression for the clock skew performance (MSE) related to our OWD proposed clock skew estimator for the Reverse path.
5. Guiding lines (closed-form expressions, conditions), summarized in a table (please refer to **Table 1**), telling us if

TABLE 1 | Summary of the conditions where the suggested estimator have the possible lower MSE.

| | $Z\sigma_{\omega_1}^2 = \sigma_{\omega_2}^2$ | |
|----------------|--|---|
| | $Z = 1 \quad (\sigma_{\omega_1}^2 = \sigma_{\omega_2}^2 = \sigma^2)$ | $Z \neq 1$ |
| white-Gaussian | <p>if $(\sigma^2 \geq \hat{\sigma}^2)$ then we use OWD in Eq. 62 otherwise, we use TWD in Eq. 60 $\hat{\sigma}^2 = 2 \frac{A}{B} T_{syn}^2$</p> | <p>when $Z > 1$: if $(Z \geq \tilde{Z})$ then we use OWD in Eq. 61 otherwise, we use TWD in Eq. 60 when $Z < 1$: if $(Z \leq \tilde{Z})$ then we use OWD in Eq. 62 otherwise, we use TWD in Eq. 60 $\tilde{Z} = 3(1 + \frac{B}{A} \frac{\sigma_{\omega_1}^2}{T_{syn}^2})$ $\tilde{Z} = \frac{1}{3}(1 + \frac{B}{A} \frac{\sigma_{\omega_1}^2}{T_{syn}^2})$</p> |
| fGn/gfGn | <p>if $(\sigma^2 \geq \hat{\sigma}_{fGn/gfGn}^2)$ then we use OWD in Eq. 62 otherwise, we use TWD in Eq. 60 $\hat{\sigma}_{fGn/gfGn}^2 = 2 \frac{A}{B} \frac{C+D}{C} T_{syn}^2$</p> | <p>when $Z > 1$: if $(Z \geq \tilde{Z}_{fGn/gfGn})$ then we use OWD in Eq. 61 otherwise, we use TWD in Eq. 60 when $Z < 1$: if $(Z \leq \tilde{Z}_{fGn/gfGn})$ then we use OWD in Eq. 62 otherwise, we use TWD in Eq. 60 $\tilde{Z}_{fGn/gfGn} = 3(1 + \frac{C}{C+D} \frac{B}{A} \frac{\sigma_{\omega_1}^2}{T_{syn}^2})$ $\tilde{Z}_{fGn/gfGn} = \frac{1}{3}(1 + \frac{C}{C+D} \frac{B}{A} \frac{\sigma_{\omega_1}^2}{T_{syn}^2})$</p> |

we should use the OWD clock skew estimator for the Forward path or the OWD clock skew estimator for the Reverse path or perhaps the TWD clock skew estimator proposed by [4] in order to get the best clock skew performance from the MSE point of view.

The clock skew performances (MSE) of our new proposed OWD clock skew estimators were compared via simulation with the clock skew performances (MSE) obtained with two TWD clock skew estimators [4,5] and with the literature known OWD clock skew estimators [6,7]. Simulation results will show the advantage in performance (MSE) of our new proposed OWD clock skew estimators compared to [4–7]. Simulation results will also show the effectiveness of our closed-form-approximated expressions for the clock skew performance (MSE) associated to the Forward and Reverse paths as well as the effectiveness of our proposed guiding lines, leading us to the right choice of the clock skew estimator from the MSE point of view.

The paper is organized as follows. **Section 2** briefly introduces the system under consideration and the assumptions we applied for our algorithm. **Section 3** proposes the OWD clock skew estimators for the Forward and Reverse paths. **Section 4** suggests the closed-form approximated expressions for the MSE related to our new proposed OWD clock skew estimators where the PDV is a white-Gaussian process. **Section 5** suggests the closed-form approximated expressions for the MSE related to our new proposed OWD clock skew estimators where the PDV is an fGn/gfGn process. In **Section 6**, we derive some guiding lines (conditions), summarized in **Table 1**, telling us under what condition should we prefer the OWD for the Forward path over the OWD for the Reverse path or should just prefer the TWD clock skew estimator obtained in [4]. **Section 7** presents simulation results, and in **Section 8**, a conclusion is given.

2 SYSTEM DESCRIPTION

As already was mentioned earlier, this paper is a direct continuation of our previous work [4]. Thus, the system description is the same as in [4]. Please refer to [4], for having a detailed description of the message exchange flow between the Master and the Slave. Let us recall **Figure 1** from [4] where based on [8–10] we may write:

$$t_1[j] + d_{ms} + \omega_1[j] = t_2[j](1 + \alpha) + Q \quad (1)$$

$$t_4[j] - d_{sm} - \omega_2[j] = t_3[j](1 + \alpha) + Q \quad (2)$$

where Q is the time difference between the Master and the Slave clocks (offset) and α is the clock skew. The Forward and the Reverse fixed delays are denoted as d_{ms} , d_{sm} respectively. The Forward PDV is denoted as $\omega_1[j]$ and the Reverse PDV is denoted as $\omega_2[j]$. The total number of the Sync messages periods is denoted as J , where $j = 1, 2, 3, \dots, J$. At timestamp t_1 , the Master sends a Sync message to the Slave. The Slave receives this Sync message at timestamp t_2 and sends back to the Master a Delay Req message at timestamp t_3 . The Master receives this Delay Req message at timestamp t_4 . Please note that $t_1[j]$, $t_2[j]$, $t_3[j]$, $t_4[j]$ are the timestamps of t_1 , t_2 , t_3 and t_4 respectively at the j th Sync message period.

We consider two different models for the PDV, as was done in [4]:

1. The PDV is modeled as a white-Gaussian noise with zero mean and the variance $E[\omega_n[j], \omega_n[m]]$ is $\sigma_{\omega_n}^2$ when $j = m$ and zero when $j \neq m$

where $E[.]$ denotes the expectation operator on $(.)$ and $n = 1, 2$.

2. The PDV is modeled as an fGn/gfGn process with zero mean. Based on [11–13] we have:

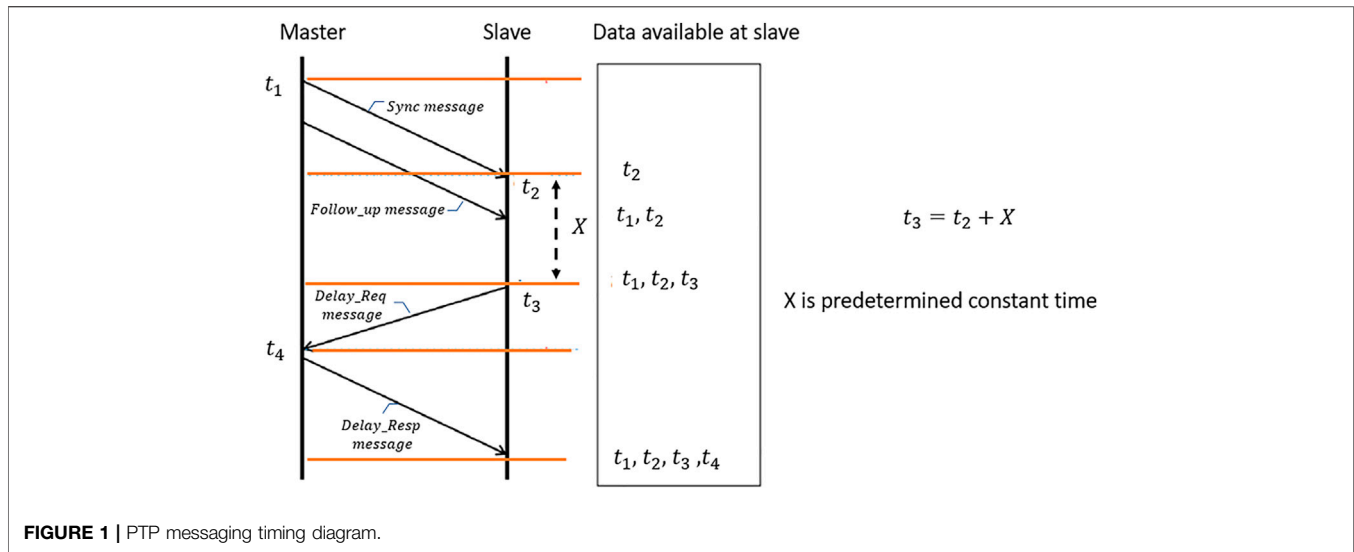


FIGURE 1 | PTP messaging timing diagram.

- When $j = m$: $E[\omega_n[j], \omega_n[m]] = \sigma_{\omega_n}^2$.
- When $j \neq m$: $E[\omega_n[j], \omega_n[m]] = \frac{\sigma_{\omega_n}^2}{2} [|(j-m)^a| - 1]^{2H} - 2(|(j-m)^a|)^{2H} + (|(j-m)^a| + 1)^{2H}$.

where $a = 1$ is the fGn case.

In addition, we use also the same assumptions as were made in [4]:

- The Forward and the Reverse PDVs are independent. Thus, we have: $E[\omega_1[j], \omega_2[m]] = 0 \quad \forall \quad j, m$.
- In the Slave clock the time between $t_2[j]$ to $t_3[j]$ is constant and is denoted as X . Thus, we have: $t_3[j] - t_2[j] = X$.

In this paper we propose two novel OWD clock skew estimators, one for the Forward path and one for the Reverse path. Both OWD clock skew estimators are based on our previously TWD clock skew estimator [4] given by:

$$\hat{\alpha} = \frac{1}{J(J-1)} \sum_{i=1}^{J-1} \sum_{j=1}^{J-i} \left(\frac{T_{1,j}(i)}{T_{2,j}(i)} + \frac{T_{4,j}(i)}{T_{2,j}(i)} \right) - 1 \quad (3)$$

where

$$\begin{aligned} T_{1,j}(i) &= t_1[j+i] - t_1[j], & T_{2,j}(i) &= t_2[j+i] - t_2[j], \\ T_{4,j}(i) &= t_4[j+i] - t_4[j] \end{aligned} \quad (4)$$

3 THE OWD CLOCK SKEW ESTIMATORS

In the following, we present in Theorem 1 our new proposed OWD clock skew estimator for the Forward path and in Theorem 2 our new proposed OWD clock skew estimator for the Reverse path.

3.1 Theorem 1

The clock skew estimator for the OWD in the Forward path (Master to Slave) can be written as:

$$\hat{\alpha}^F = \frac{2}{J(J-1)} \sum_{i=1}^{J-1} \sum_{j=1}^{J-i} \left(\frac{T_{1,j}(i)}{T_{2,j}(i)} \right) - 1 \quad (5)$$

where $\hat{\alpha}^F$ is the clock skew estimator that based only on timestamps from the Forward path.

Proof of Theorem 1

In order to avoid the fixed delay, we can subtract between two timestamps from different Sync periods. Therefore, based on Eq. 1 we have:

$$T_{1,j}(i) + \Omega_{1,j}(i) = T_{2,j}(i)(1 + \alpha_{j,i}^F) \quad (6)$$

where $\alpha_{j,i}^F$ is the clock skew between the $(j+i)$ -th and i th Sync period, and $\Omega_{1,j}(i)$ is:

$$\Omega_{1,j}(i) = \omega_1[j+i] - \omega_1[j] \quad (7)$$

Based on Eq. 6 the clock skew can be written as:

$$\alpha_{j,i}^F = \frac{T_{1,j}(i)}{T_{2,j}(i)} + \frac{\Omega_{1,j}(i)}{T_{2,j}(i)} - 1 \quad (8)$$

The OWD clock skew in the Forward path can be defined as:

$$\alpha^F = \frac{2}{J(J-1)} \sum_{i=1}^{J-1} \sum_{j=1}^{J-i} \alpha_{j,i}^F \quad (9)$$

By putting Eq. 8 into Eq. 9 we define the clock skew in the Forward path as:

$$\begin{aligned} \alpha^F &= \frac{2}{J(J-1)} \sum_{i=1}^{J-1} \sum_{j=1}^{J-i} \left(\left(\frac{T_{1,j}(i)}{T_{2,j}(i)} \right) + \left(\frac{\Omega_{1,j}(i)}{T_{2,j}(i)} \right) \right) - 1 \\ &= \hat{\alpha}^F + \frac{2}{J(J-1)} \sum_{i=1}^{J-1} \sum_{j=1}^{J-i} \left(\frac{\Omega_{1,j}(i)}{T_{2,j}(i)} \right) \end{aligned} \quad (10)$$

This completes our proof.

3.2 Theorem 2

The skew clock estimator for the OWD in the Reverse path (Slave to Master) can be written as:

$$\hat{\alpha}^R = \frac{2}{J(J-1)} \sum_{i=1}^{J-1} \sum_{j=1}^{J-i} \left(\frac{T_{4,j}(i)}{T_{2,j}(i)} \right) - 1 \quad (11)$$

where $\hat{\alpha}^R$ is the clock skew estimator that based only on timestamps from the Reverse path.

Proof of Theorem 2

In order to avoid the fixed delay, we can subtract between two timestamps from different Sync periods. Therefore, based on Eq. 2 we have:

$$T_{4,j}(i) - \Omega_{2,j}(i) = T_{3,j}(i) (1 + \alpha_{j,i}^R) \quad (12)$$

where $\alpha_{j,i}^R$ is the clock skew between the $(j+i)$ -th and i th Sync period, and

$$T_{3,j}(i) = t_3[j+i] - t_3[j] \quad ; \quad \Omega_{2,j}(i) = \omega_2[j+i] - \omega_2[j] \quad (13)$$

Based on the definition that $t_3[j] - t_2[j] = X$, as mentioned in the section of System Description (assumption 2), we can write:

$$T_{3,j}(i) = t_3[j+i] - t_3[j] = t_2[j+i] + X - (t_2[j] + X) = T_{2,j}(i) \quad (14)$$

By using Eq. 14, we can write Eq. 12 as:

$$T_{4,j}(i) - \Omega_{2,j}(i) = T_{2,j}(i) (1 + \alpha_{j,i}^R) \quad (15)$$

Therefore, based on Eq. 15 the clock skew can be written as:

$$\alpha_{j,i}^R = \frac{T_{4,j}(i)}{T_{2,j}(i)} - \frac{\Omega_{2,j}(i)}{T_{2,j}(i)} - 1 \quad (16)$$

The OWD clock skew in the Reverse path can be defined as:

$$\alpha^R = \frac{2}{J(J-1)} \sum_{i=1}^{J-1} \sum_{j=1}^{J-i} \alpha_{j,i}^R \quad (17)$$

By putting Eq. 16 into Eq. 17 we define the clock skew in the Reverse path as:

$$\begin{aligned} \alpha^R &= \frac{2}{J(J-1)} \sum_{i=1}^{J-1} \sum_{j=1}^{J-i} \left(\left(\frac{T_{4,j}(i)}{T_{2,j}(i)} \right) - \left(\frac{\Omega_{2,j}(i)}{T_{2,j}(i)} \right) \right) - 1 \\ &= \hat{\alpha}^R - \frac{2}{J(J-1)} \sum_{i=1}^{J-1} \sum_{j=1}^{J-i} \left(\frac{\Omega_{2,j}(i)}{T_{2,j}(i)} \right) \end{aligned} \quad (18)$$

This completes our proof.

4 THE CLOCK SKEW PERFORMANCE FOR THE WHITE-GAUSSIAN CASE

In the following, Theorems 3 and 4 present the closed-form approximated expressions for the MSE related to our new

proposed OWD clock skew estimator for the Forward path and Reverse path, respectively. According to [4], the MSE for the TWD clock skew estimator for the Gaussian case is given by:

$$E[e^2] \approx \left(\frac{1}{J(J-1)} \right)^2 \left[\frac{(\sigma_{\omega_1}^2 + \sigma_{\omega_2}^2)}{T_{syn}^2} A \left(1 + \frac{1}{P} \right) \right] \quad (19)$$

where P is:

$$P = \frac{A}{B} \left(\frac{\sigma_{\omega_1}^2 + \sigma_{\omega_2}^2}{\sigma_{\omega_1}^4} \right) T_{syn}^2 \quad (20)$$

and A, B are given by:

$$A = \left(2 \sum_{i=1}^{J-1} \frac{J-i}{i^2} + \sum_{i=1}^{J-1} \sum_{j=1}^{J-i} \sum_{\substack{k=1 \\ k \neq i}}^{J-i} \sum_{\substack{m=1 \\ m=j \\ m=j+i-k}}^{J-k} \frac{1}{ik} - \sum_{i=1}^{J-1} \sum_{j=1}^{J-i} \sum_{k=1}^{J-i} \sum_{\substack{m=1 \\ m=j+i \\ m=j-k}}^{J-k} \frac{1}{ik} \right) \quad (21)$$

$$B = \left(12 \sum_{i=1}^{J-1} \frac{J-i}{i^4} + 6 \sum_{i=1}^{J-1} \sum_{j=1}^{J-i} \sum_{\substack{k=1 \\ k \neq i}}^{J-i} \sum_{\substack{m=1 \\ m=j \\ m=j+i-k \\ m=j-i-k}}^{J-k} \frac{1}{(ik)^2} + 4 \sum_{i=1}^{J-1} \sum_{j=1}^{J-i} \sum_{k=1}^{J-i} \sum_{\substack{m=1 \\ m=j+i \\ m=j-k}}^{J-k} \frac{1}{(ik)^2} \right) \quad (22)$$

4.1 Theorem 3

For $\left| \frac{\Omega_{1,j}(i)}{T_{1,j}(i)} \right| \ll 1$, the closed-form-approximated expression for the MSE related to the OWD clock skew estimator (for the Forward path), can be defined as:

$$E[e_F^2] \approx \left(\frac{2}{J(J-1)} \right)^2 \left[\frac{\sigma_{\omega_1}^2}{T_{syn}^2} A \left(1 + \frac{1}{P_F} \right) \right] \quad (23)$$

where P_F is:

$$P_F = \frac{A}{B} \left(\frac{T_{syn}^2}{\sigma_{\omega_1}^2} \right) \quad (24)$$

where A and B are defined in Eq. 21, 22 respectively.

Proof of Theorem 3

Based on Eq. 10 the error of the OWD clock skew estimator (for the Forward path) is:

$$e_F = \alpha_F - \hat{\alpha}_F = \frac{2}{J(J-1)} \sum_{i=1}^{J-1} \sum_{j=1}^{J-i} \left(\frac{\Omega_{1,j}(i)}{T_{2,j}(i)} \right) \quad (25)$$

Now, according to Eq. 6 we can write $T_{2,j}(i)$ as following:

$$T_{2,j}(i) = \frac{T_{1,j}(i) + \Omega_{1,j}(i)}{(1 + \alpha_{j,i}^F)} \quad (26)$$

Based on Eq. 26 we may write the expectation of Eq. 25 as:

$$E[e_F] = \frac{2(1 + \alpha^F)}{(J(J-1))} \sum_{i=1}^{J-1} \sum_{j=1}^{J-i} E\left[\frac{a_{j,i}}{(1 + a_{j,i})}\right] \quad (27)$$

where

$$a_{j,i} = \frac{\Omega_{1,j}(i)}{T_{1,j}(i)} \quad (28)$$

For $|\frac{\Omega_{1,j}(i)}{T_{1,j}(i)}| \ll 1$ we can write **Eq. 27** as:

$$E[e_F] \approx \frac{2(1 + \alpha^F)}{(J(J-1))} \sum_{i=1}^{J-1} \sum_{j=1}^{J-i} [E[a_{j,i}(1 - a_{j,i})]] \quad (29)$$

Based on **Eq. 29** the approximated MSE related to the OWD clock skew estimator (for the Forward path) can be define as:

$$E[e_F^2] \approx \frac{4(1 + \alpha^F)^2}{(J(J-1))^2} \sum_{i=1}^{J-1} \sum_{j=1}^{J-i} \sum_{k=1}^{J-i} \sum_{m=1}^{J-k} [E[a_{j,i}a_{m,k}] - E[a_{j,i}^2a_{m,k}] - E[a_{j,i}a_{m,k}^2] + E[a_{j,i}^2a_{m,k}^2]] \quad (30)$$

According to [4], we can write $T_{1,j}(i)$ and $T_{1,m}(k)$ as:

$$\begin{aligned} T_{1,j}(i) &= t_1[j+i] - t_1[j] = iT_{syn} \\ T_{1,m}(k) &= t_1[m+k] - t_1[m] = kT_{syn} \end{aligned} \quad (31)$$

where T_{syn} is the Sync messages period.

Based on **Eq. 28** and on **Eq. 31** we can simplify the expressions in **Eq. 30**:

$$E[a_{j,i}a_{m,k}] = E\left[\frac{\Omega_{1,j}(i)}{T_{1,j}(i)} \frac{\Omega_{1,m}(k)}{T_{1,m}(k)}\right] = \frac{E[\Omega_{1,j}(i)\Omega_{1,m}(k)]}{ikT_{syn}^2} \quad (32)$$

$$E[a_{j,i}^2a_{m,k}] = E\left[\frac{\Omega_{1,j}^2(i)}{T_{1,j}^2(i)} \frac{\Omega_{1,m}(k)}{T_{1,m}(k)}\right] = \frac{E[\Omega_{1,j}^2(i)\Omega_{1,m}(k)]}{i^2kT_{syn}^3} \quad (33)$$

$$E[a_{j,i}a_{m,k}^2] = E\left[\frac{\Omega_{1,j}(i)}{T_{1,j}(i)} \frac{\Omega_{1,m}^2(k)}{T_{1,m}^2(k)}\right] = \frac{E[\Omega_{1,j}(i)\Omega_{1,m}^2(k)]}{ik^2T_{syn}^3} \quad (34)$$

$$E[a_{j,i}^2a_{m,k}^2] = E\left[\frac{\Omega_{1,j}^2(i)}{T_{1,j}^2(i)} \frac{\Omega_{1,m}^2(k)}{T_{1,m}^2(k)}\right] = \frac{E[\Omega_{1,j}^2(i)\Omega_{1,m}^2(k)]}{i^2k^2T_{syn}^4} \quad (35)$$

Since the PDV has zero mean **Eqs 33** and **34** can be set to zero. Now, by putting **Eqs 32** and **35** into **Eq. 30**, we can write the following expression:

$$E[e_F^2] \approx \left(\frac{2(1 + \alpha^F)}{(J(J-1))T_{syn}}\right)^2 \sum_{i=1}^{J-1} \sum_{j=1}^{J-i} \sum_{k=1}^{J-i} \sum_{m=1}^{J-k} \left[\frac{E[\Omega_{1,j}(i)\Omega_{1,m}(k)]}{ik} + \frac{1}{T_{syn}^2} \frac{E[\Omega_{1,j}^2(i)\Omega_{1,m}^2(k)]}{(ik)^2}\right] \quad (36)$$

Based on [4] we can write the two summation parts in **Eq. 36** as:

$$\begin{aligned} \sum_{i=1}^{J-1} \sum_{j=1}^{J-i} \sum_{k=1}^{J-i} \sum_{m=1}^{J-k} \frac{E[\Omega_{1,j}(i)\Omega_{1,m}(k)]}{ik} &= \sigma_{\omega_1}^2 A \\ \sum_{i=1}^{J-1} \sum_{j=1}^{J-i} \sum_{k=1}^{J-i} \sum_{m=1}^{J-k} \frac{1}{T_{syn}^2} \frac{E[\Omega_{1,j}^2(i)\Omega_{1,m}^2(k)]}{(ik)^2} &= \frac{\sigma_{\omega_1}^4}{T_{syn}^2} B \end{aligned} \quad (37)$$

where A and B are defined in **Eq. 21, 22** respectively.

Based on **Eq. 37** we may write (36) as:

$$E[e_F^2] \approx \left(\frac{2(1 + \alpha^F)}{(J(J-1))T_{syn}}\right)^2 \left(\sigma_{\omega_1}^2 A + \frac{\sigma_{\omega_1}^4}{T_{syn}^2} B\right) \quad (38)$$

For practical systems, the two clocks (Master and Slave) operate at almost the same frequency. Therefore we can write that $(1 + \alpha^F) \approx 1$.

After rearranging **Eq. 38** we can write:

$$E[e_F^2] \approx \left(\frac{2}{(J(J-1))T_{syn}}\right)^2 \sigma_{\omega_1}^2 A \left(1 + \frac{\sigma_{\omega_1}^2}{T_{syn}^2} \frac{B}{A}\right) \quad (39)$$

Now, it can be easily seen that based on **Eq. 39** we can write **Eq. 23**, and this completes our proof.

4.2 Theorem 4

For $|\frac{\Omega_{1,j}(i)}{T_{1,j}(i)}| \ll 1$, the closed-form-approximated expression for the MSE related to the OWD clock skew estimator (for the Reverse path), can be defined as:

$$E[e_R^2] \approx \left(\frac{2}{(J(J-1))}\right)^2 \left[\frac{\sigma_{\omega_2}^2}{T_{syn}^2} A\right] \quad (40)$$

where A is defined in **Eq. 21**.

Proof of Theorem 4

Based on **Eq. 18** the error of the OWD clock skew estimator (for the Reverse path) is:

$$e_R = \alpha^R - \hat{\alpha}^R = \frac{2}{J(J-1)} \sum_{i=1}^{J-1} \sum_{j=1}^{J-i} \left(\frac{-\Omega_{2,j}(i)}{T_{2,j}(i)}\right) \quad (41)$$

Let us recall (26):

$$T_{2,j}(i) = \frac{T_{1,j}(i) + \Omega_{1,j}(i)}{(1 + \alpha_{j,i}^F)}$$

Based on **Eq. 26**, we may write the expectation of **Eq. 41** as:

$$E[e_R] \approx \frac{2(1 + \alpha^F)}{(J(J-1))} \sum_{i=1}^{J-1} \sum_{j=1}^{J-i} \left[-E\left[\frac{b_{j,i}}{(1 + a_{j,i})}\right]\right] \quad (42)$$

where

$$a_{j,i} = \frac{\Omega_{1,j}(i)}{T_{1,j}(i)} \quad b_{j,i} = \frac{\Omega_{2,j}(i)}{T_{1,j}(i)} \quad (43)$$

As mentioned before for practical systems, the two clocks (Master and Slave) operate at almost the same frequency. Therefore, we can write $(1 + \alpha^F) \approx 1$.

For $|\frac{\Omega_{1,j}(i)}{T_{1,j}(i)}| \ll 1$ we can write **Eq. 42** as:

$$E[e_R] \approx \frac{2}{(J(J-1))} \sum_{i=1}^{J-1} \sum_{j=1}^{J-i} [-E[b_{j,i} - a_{j,i}b_{j,i}]] \quad (44)$$

Based on the assumption of independence of the Forward and the Reverse messages (as mentioned in assumption 1 in **section 2**), we may write **Eq. 44** as:

$$E[e_R] \approx \frac{2}{(J(J-1))} \sum_{i=1}^{J-1} \sum_{j=1}^{J-i} [-E[b_{ji}]] \quad (45)$$

Based on **Eq. 45** the closed-form-approximated expression for the MSE related to the OWD clock skew estimator (for the Reverse path) can be define as:

$$E[e_R^2] \approx \frac{4}{(J(J-1))^2} \sum_{i=1}^{J-1} \sum_{j=1}^{J-i} \sum_{k=1}^{J-i} \sum_{m=1}^{J-k} [E[b_{ji}b_{mk}]] \quad (46)$$

Based on **Eq. 43** and on **Eq. 31** we can rewrite the expression $E[b_{ji}b_{mk}]$ as:

$$E[b_{ji}b_{mk}] = E\left[\frac{\Omega_{2,j}(i)}{T_{1,j}(i)} \frac{\Omega_{2,m}(k)}{T_{1,m}(k)}\right] = \frac{E[\Omega_{2,j}(i)\Omega_{2,m}(k)]}{ikT_{syn}^2} \quad (47)$$

Now, based on **Eq. 47** the closed-form-approximated expression for the MSE related to the OWD clock skew estimator (for the Reverse path) is:

$$E[e_R^2] \approx \left(\frac{2}{(J(J-1))T_{syn}}\right)^2 \sum_{i=1}^{J-1} \sum_{j=1}^{J-i} \sum_{k=1}^{J-i} \sum_{m=1}^{J-k} \left[\frac{E[\Omega_{2,j}(i)\Omega_{2,m}(k)]}{ik}\right] \quad (48)$$

According to [4], we can write the summation part in **Eq. 48** as:

$$\sum_{i=1}^{J-1} \sum_{j=1}^{J-i} \sum_{k=1}^{J-i} \sum_{m=1}^{J-k} \left[\frac{E[\Omega_{2,j}(i)\Omega_{2,m}(k)]}{ik}\right] = \sigma_{\omega_2}^2 A \quad (49)$$

where A is defined in **Eq. 21**.

Now, it can be easily seen that by putting **Eq. 49** into **Eq. 48** we get **Eq. 40**, and this completes our proof.

5 THE CLOCK SKEW PERFORMANCE FOR THE LRD CASE

In this section we applied the fGn/gfGn model for the LRD process. This model has the Hurst exponent in the range of $0.5 \leq H < 1$ and the a parameter in the range of $0 < a \leq 1$, where for $a = 1$ we have the fGn case. In the following, Theorems 5 and 6 present the closed-form approximated expressions for the MSE related to our new proposed OWD clock skew estimator for the Forward path and Reverse path, respectively. According to [4] the closed-form-approximated expression for the MSE related to the TWD clock skew estimator [4] is given by:

$$E[e^2] \approx \left(\frac{1}{(J(J-1))}\right)^2 \left(\frac{\sigma_{\omega_1}^2 + \sigma_{\omega_2}^2}{T_{syn}^2}\right) \left(\left(1 + \frac{1}{P}\right)C + D\right) \quad (50)$$

where C and D are given by:

$$C = \sum_{i=1}^{J-1} \frac{J-i}{T^2} (2 - fG_H(i, H)) + \sum_{i=1}^{J-1} \sum_{j=1}^{J-i} \sum_{k=1}^{J-i} \sum_{m=1}^{J-k} \frac{1}{ik} \left(1 + \frac{1}{2} (fG_H^*(i-k, H, a) - fG_H^*(i, H, a) - fG_H^*(k, H, a))\right) - \sum_{i=1}^{J-1} \sum_{j=1}^{J-i} \sum_{k=1}^{J-i} \sum_{m=1}^{J-k} \frac{1}{ik} \left(1 - \frac{1}{2} (fG_H^*(i, H, a) - fG_H^*(k, H, a) + fG_H^*(i+k, H, a))\right) \quad (51)$$

$$D = \sum_{i=1}^{J-1} \sum_{j=1}^{J-i} \sum_{k=1}^{J-i} \sum_{m=1}^{J-k} \frac{1}{2ik} (fG_H^*(j-m, H, a) - fG_H^*(j+i-m, H, a) - fG_H^*(j-m-k, H, a) + fG_H^*(j+i-m-k, H, a)) \quad (52)$$

the function $fG_H^*(.)$ is:

$$fG_H^*(x, H, a) = [||x^a| - 1|^{2H} - 2(|x^a|)^{2H} + (|x^a| + 1)^{2H}] \quad (53)$$

and P is defined in **Eq. 20**.

5.1 Theorem 5

The closed-form approximated expression for the MSE related to our new proposed OWD clock skew estimator (for the Forward path) can be defined as:

$$E[e_F^2] \approx \left(\frac{2}{(J(J-1))}\right)^2 \left(\frac{\sigma_{\omega_1}^2}{T_{syn}^2}\right) \left(\left(1 + \frac{1}{P_F}\right)C + D\right) \quad (54)$$

where C , D and P_F are defined in **Eq. 51**, **52** and **24** respectively.

Proof of Theorem 5

The MSE for the fGn/gfGn case is based on the MSE of the OWD clock skew estimator for the Forward path defined in **Eq. 36**. Based on the fact that $1 + \alpha^F \approx 1$, we can write **Eq. 36** as:

$$E[e_F^2] \approx \left(\frac{2}{(J(J-1))T_{syn}}\right)^2 \sum_{i=1}^{J-1} \sum_{j=1}^{J-i} \sum_{k=1}^{J-i} \sum_{m=1}^{J-k} \left[\frac{E[\Omega_{1,j}(i)\Omega_{1,m}(k)]}{ik} + \frac{1}{T_{syn}^2} \frac{E[\Omega_{1,j}^2(i)\Omega_{1,m}^2(k)]}{(ik)^2}\right] \quad (55)$$

According to [4], we can write the first part in **Eq. 55** as:

$$\sum_{i=1}^{J-1} \sum_{j=1}^{J-i} \sum_{k=1}^{J-i} \sum_{m=1}^{J-k} \left[\frac{E[\Omega_{1,j}(i)\Omega_{1,m}(k)]}{ik}\right] = \sigma_{\omega_1}^2 (C + D) \quad (56)$$

where C and D are defined in **Eq. 51**, **52** respectively.

The calculation of the second expression in **Eq. 55** is quite difficult to carry out for the fGn/gfGn case. Therefore, following [4] we can write:

$$\sum_{i=1}^{J-1} \sum_{j=1}^{J-i} \sum_{k=1}^{J-1} \sum_{m=1}^{J-k} \left[\frac{E[\Omega_{1,j}(i)\Omega_{1,m}(k)]}{ik} + \frac{1}{T_{syn}^2} \frac{E[\Omega_{1,j}^2(i)\Omega_{1,m}^2(k)]}{(ik)^2} \right] = \sigma_{\omega_1}^2 \left(C \left(1 + \frac{1}{P_F} \right) + D \right) \quad (57)$$

Now, by putting Eq. 57 into Eq. 55, we get Eq. 54 and this completes our proof.

5.2 Theorem 6

The closed-form approximated expression for the MSE related to our new proposed OWD clock skew estimator (for the Reverse path) can be defined as:

$$E[e_R^2] \approx \left(\frac{2}{(J(J-1))} \right)^2 \frac{\sigma_{\omega_2}^2}{T_{syn}^2} (C + D) \quad (58)$$

where C and D are defined in Eq. 51, 52.

Proof of Theorem 6

The MSE for the fGn/gfGn case is based on the MSE of the OWD clock skew estimator for the Reverse path defined in Eq. 48. Let us recall Eq. 48:

$$E[e_R^2] \approx \left(\frac{2}{(J(J-1))T_{syn}} \right)^2 \sum_{i=1}^{J-1} \sum_{j=1}^{J-i} \sum_{k=1}^{J-1} \sum_{m=1}^{J-k} \left[\frac{E[\Omega_{2,j}(i)\Omega_{2,m}(k)]}{ik} \right]$$

We can write the summation part in Eq. 48 as was done in [4] as:

$$\sum_{i=1}^{J-1} \sum_{j=1}^{J-i} \sum_{k=1}^{J-1} \sum_{m=1}^{J-k} \left[\frac{E[\Omega_{2,j}(i)\Omega_{2,m}(k)]}{ik} \right] = \sigma_{\omega_2}^2 (C + D) \quad (59)$$

Now, by putting Eq. 59 into Eq. 48, we get Eq. 58 and this completes our proof.

6 THE PREFERRED CLOCK SKEW ESTIMATOR FOR EACH SCENARIO

In this paper we proposed two OWD clock skew estimators (Eqs 5, 11). Thus, we can consider now two OWD clock skew estimators and one TWD clock estimator proposed by [4]. Let us recall the three estimators.

At first, we recall the TWD clock skew estimator from [4]:

$$\hat{\alpha} = \frac{1}{J(J-1)} \sum_{i=1}^{J-1} \sum_{j=1}^{J-i} \left(\frac{T_{1,j}(i)}{T_{2,j}(i)} + \frac{T_{4,j}(i)}{T_{2,j}(i)} \right) - 1 \quad (60)$$

The OWD clock skew estimator for the Forward path is given by Eq. 5:

$$\hat{\alpha}^F = \frac{2}{J(J-1)} \sum_{i=1}^{J-1} \sum_{j=1}^{J-i} \left(\frac{T_{1,j}(i)}{T_{2,j}(i)} \right) - 1 \quad (61)$$

The OWD clock skew estimator for the Reverse path is given by Eq. 11:

$$\hat{\alpha}^R = \frac{2}{J(J-1)} \sum_{i=1}^{J-1} \sum_{j=1}^{J-i} \left(\frac{T_{4,j}(i)}{T_{2,j}(i)} \right) - 1 \quad (62)$$

It would be very helpful for the system designer if he could know which of the above listed clock skew estimators (Eqs 60–62) he should choose in order to achieve the best clock skew performance in the MSE point of view. In this section we will give the system designer guidelines (conditions) that will help him to choose wisely the best clock skew estimator in order to achieve the best clock skew performance from the MSE point of view.

Please note, in this section we define Z as:

$$Z = \frac{\sigma_{\omega_2}^2}{\sigma_{\omega_1}^2} \quad (63)$$

Thus we have:

- when $Z > 1 \rightarrow \sigma_{\omega_1}^2 < \sigma_{\omega_2}^2$,
- when $Z < 1 \rightarrow \sigma_{\omega_1}^2 > \sigma_{\omega_2}^2$,
- when $Z = 1 \rightarrow \sigma_{\omega_1}^2 = \sigma_{\omega_2}^2$.

In the following we have Theorem seven supplying us guidelines for choosing the preferable clock skew estimator from the above listed clock skew estimators (Eqs 60–62) leading to the best clock skew performance from the MSE point of view for the white-Gaussian case. Theorem 8 supplies us guidelines for choosing the preferable clock skew estimator from the above listed clock skew estimators (Eqs 60–62) leading to the best clock skew performance from the MSE point of view for the fGn/gfGn case.

6.1 Theorem 7

For the white-Gaussian process we have the following conditions:

Case a: For $Z > 1$:

If $Z \geq \tilde{Z}$, then we use the OWD clock skew estimator in the Forward path (Eq. 61).

where

$$\tilde{Z} = 3 \left(1 + \frac{B}{A} \frac{\sigma_{\omega_1}^2}{T_{syn}^2} \right) \quad (64)$$

Otherwise, we use the TWD clock skew estimator (Eq. 60).

Case b: For $Z < 1$:

If $Z \leq \bar{Z}$, then we use the OWD clock skew estimator in the Reverse path (Eq. 62),

where

$$\bar{Z} = \frac{1}{3} \left(1 + \frac{B}{A} \frac{\sigma_{\omega_1}^2}{T_{syn}^2} \right) \quad (65)$$

Otherwise, we use the TWD clock skew estimator (Eq. 60).

Case c: For $Z = 1$ ($\sigma_{\omega_1}^2 = \sigma_{\omega_2}^2 = \sigma^2$):

If $\sigma^2 \geq \hat{\sigma}^2$, then we use the OWD clock skew estimator in the Reverse path (Eq. 62),

where

$$\tilde{\sigma}^2 = 2 \frac{A}{B} T_{syn}^2 \quad (66)$$

Otherwise, we use the TWD clock skew estimator (Eq. 60).

Proof of Theorem 7

We rewrite the closed-form-approximated expression for the MSE related to the TWD clock skew estimator (Eq. 19), and the closed-form-approximated expressions for the MSE related to our new proposed OWD clock skew estimators (Eqs 23, 40) with the help of Z (Eq. 63).

The closed-form approximated expressions for the MSE related to the TWD clock skew estimator (Eq. 19) can be written as:

$$E[e^2] \approx \left(\frac{1}{J(J-1)} \right)^2 \left[\frac{\sigma_{\omega_1}^2 (1+Z)}{T_{syn}^2} A \left(1 + \frac{1}{P} \right) \right] \quad (67)$$

The closed-form approximated expression for the MSE related to the OWD clock skew estimator for the Forward path (Eq. 23) can be written as:

$$E[e_F^2] \approx \left(\frac{2}{J(J-1)} \right)^2 \left[\frac{\sigma_{\omega_1}^2}{T_{syn}^2} A \left(1 + \frac{1}{P_F} \right) \right] \quad (68)$$

The closed-form approximated expression for the MSE related to the OWD clock skew estimator for the Reverse path (Eq. 40) can be written as:

$$E[e_R^2] \approx \left(\frac{2}{J(J-1)} \right)^2 \left[\frac{Z \sigma_{\omega_1}^2}{T_{syn}^2} A \right] \quad (69)$$

where A , B , P and P_F are defined in Eqs 21, 22, 20 and 24 respectively.

In the following, we define MSE_G^T , MSE_G^F and MSE_G^R as the MSE of the TWD case (Eq. 67), OWD in the Forward path case (Eq. 68) and OWD in the Reverse path case (Eq. 69) respectively.

For $Z > 1$, we wish to find the value for Z where we have $MSE_G^T \geq MSE_G^F$. Thus, we may write with the help of Eqs 20, 24:

$$\left(\frac{1}{J(J-1)T_{syn}} \right)^2 \left[\sigma_{\omega_1}^2 (1+Z)A + B \frac{\sigma_{\omega_1}^4}{T_{syn}^2} \right] \geq \left(\frac{1}{J(J-1)T_{syn}} \right)^2 \left[\sigma_{\omega_1}^2 A + B \frac{\sigma_{\omega_1}^4}{T_{syn}^2} \right] \quad (70)$$

where Eq. 70 can be written also as:

$$\left[\sigma_{\omega_1}^2 (1+Z)A + B \frac{\sigma_{\omega_1}^4}{T_{syn}^2} \right] \geq 4 \left[\sigma_{\omega_1}^2 A + B \frac{\sigma_{\omega_1}^4}{T_{syn}^2} \right] \quad (71)$$

After rearranging Eq. 71 we can write:

$$Z \sigma_{\omega_1}^2 A \geq 3 \left(\sigma_{\omega_1}^2 A + B \frac{\sigma_{\omega_1}^4}{T_{syn}^2} \right) \quad (72)$$

We can divide Eq. 72 by $A \sigma_{\omega_1}^2$ ($A \sigma_{\omega_1}^2 > 0$) and then we can write:

$$Z \geq \tilde{Z} \quad (73)$$

where \tilde{Z} is defined in Eq. 64.

This completes our proof of Theorem 7, **case a**.

Now, we continue the proof of case b. For $Z < 1$, we wish to find the value for Z where we have $MSE_G^T \geq MSE_G^R$. Thus, with the help of Eq. 20 we may write:

$$\left(\frac{1}{J(J-1)T_{syn}} \right)^2 \left[\sigma_{\omega_1}^2 (1+Z)A + B \frac{\sigma_{\omega_1}^4}{T_{syn}^2} \right] \geq \left(\frac{1}{J(J-1)T_{syn}} \right)^2 \left[4 \left[Z \sigma_{\omega_1}^2 A \right] \right] \quad (74)$$

where Eq. 74 can be written also as:

$$\sigma_{\omega_1}^2 (1+Z)A + B \frac{\sigma_{\omega_1}^4}{T_{syn}^2} \geq 4Z \sigma_{\omega_1}^2 A \quad (75)$$

After rearranging Eq. 75 we can write:

$$\sigma_{\omega_1}^2 \left(A + B \frac{\sigma_{\omega_1}^2}{T_{syn}^2} \right) \geq 3Z \sigma_{\omega_1}^2 A \quad (76)$$

We can divide Eq. 76 by $3A \sigma_{\omega_1}^2$ ($3A \sigma_{\omega_1}^2 > 0$) and then we can write:

$$Z \leq \bar{Z} \quad (77)$$

where \bar{Z} is defined in Eq. 65.

This completes our proof of Theorem 7, **case b**.

Now we can continue the proof of case c of Theorem 7. For $Z = 1$, we defined that $\sigma_{\omega_1}^2 = \sigma_{\omega_2}^2 = \sigma^2$. We wish to find the value for Z where we have $MSE_G^T \geq MSE_G^R$ (please note that for $Z = 1$: $MSE_G^T < MSE_G^F \forall j$, since B has only positive values). Thus, with the help of Eq. 20 we can write:

$$\left(\frac{1}{J(J-1)T_{syn}} \right)^2 \left[2\sigma^2 A + B \frac{\sigma^4}{T_{syn}^2} \right] \geq \left(\frac{1}{J(J-1)T_{syn}} \right)^2 \left[4[\sigma^2 A] \right] \quad (78)$$

where Eq. 78 can be written also as:

$$2\sigma^2 A + B \frac{\sigma^4}{T_{syn}^2} \geq 4\sigma^2 A \quad (79)$$

After rearranging Eq. 79 we can write:

$$\sigma^2 \geq \tilde{\sigma}^2 \quad (80)$$

where $\tilde{\sigma}^2$ is defined in Eq. 66. Now, we have completed our proof of Theorem 7.

6.2 Theorem 8

For the fGn/gfGn process we have the following conditions:

Case a: For $Z > 1$:

If $Z \geq \tilde{Z}_{fGn/gfGn}$, then we use the OWD clock skew estimator in the Forward path (Eq. 61),

where

$$\tilde{Z}_{fGn/gfGn} = 3 \left(1 + \frac{C}{C+D} \frac{B}{A} \frac{\sigma_{\omega_1}^2}{T_{syn}^2} \right) \quad (81)$$

Otherwise, we use the TWD clock skew estimator (Eq. 60).

Case b: For $Z < 1$:

If $Z \leq \bar{Z}_{fGn/gfGn}$, then we use the OWD clock skew estimator in the Reverse path (Eq. 62), where

$$\bar{Z}_{fGn/gfGn} = \frac{1}{3} \left(1 + \frac{C}{C+D} \frac{B}{A} \frac{\sigma_{\omega_1}^2}{T_{syn}^2} \right) \quad (82)$$

Otherwise, we use the TWD clock skew estimator (Eq. 60).

Case c: For $Z = 1$ ($\sigma_{\omega_1}^2 = \sigma_{\omega_2}^2 = \sigma^2$):

If $\sigma^2 \geq \bar{\sigma}_{fGn/gfGn}^2$, then we use the OWD clock skew estimator in the Reverse path (Eq. 62), where

$$\bar{\sigma}_{fGn/gfGn}^2 = 2 \frac{C+D}{C} \frac{A}{B} T_{syn}^2 \quad (83)$$

Otherwise, we use the TWD clock skew estimator (Eq. 60).

Proof of Theorem 8

We rewrite the closed-form-approximated expression for the MSE related to the TWD clock skew estimator (Eq. 50), and the closed-form-approximated expressions for the MSE related to our new proposed OWD clock skew estimators (Eqs 54, 58 with the help of Z (Eq. 63).

The closed-form approximated expressions for the MSE related to the TWD clock skew estimator (Eq. 50) can be written as:

$$E[e^2] \approx \left(\frac{1}{J(J-1)} \right)^2 \left[\frac{\sigma_{\omega_1}^2 (1+Z)}{T_{syn}^2} \left(C \left(1 + \frac{1}{P} \right) + D \right) \right] \quad (84)$$

The closed-form approximated expressions for the MSE related to the OWD clock skew estimator for the Forward path Eq. 54 can be written as:

$$E[e_F^2] \approx \left(\frac{2}{J(J-1)} \right)^2 \left[\frac{\sigma_{\omega_1}^2}{T_{syn}^2} \left(C \left(1 + \frac{1}{P_F} \right) + D \right) \right] \quad (85)$$

The closed-form approximated expressions for the MSE related to the OWD clock skew estimator for the Reverse path Eq. 58 can be written as:

$$E[e_R^2] \approx \left(\frac{2}{J(J-1)} \right)^2 \left[\frac{Z \sigma_{\omega_1}^2}{T_{syn}^2} (C+D) \right] \quad (86)$$

where C , D , P and P_F are defined in Eqs 51, 52, 20 and 24 respectively.

In the following, we define: $MSE_{fGn/gfGn}^T$, $MSE_{fGn/gfGn}^F$ and $MSE_{fGn/gfGn}^R$ as the MSE of the TWD case (Eq. 84), OWD in the Forward path case (Eq. 85) and OWD in the Reverse path case (Eq. 86) respectively.

For $Z > 1$, we wish to find the value for Z where we have $MSE_{fGn/gfGn}^T \geq MSE_{fGn/gfGn}^F$. Thus, we may write:

$$\left(\frac{1}{J(J-1)T_{syn}} \right)^2 \left[\sigma_{\omega_1}^2 (1+Z) \left(\left(1 + \frac{1}{P} \right) C + D \right) \right] \geq \left(\frac{1}{J(J-1)T_{syn}} \right)^2 \left[4(\sigma_{\omega_1}^2) \left(\left(1 + \frac{1}{P_F} \right) C + D \right) \right] \quad (87)$$

where Eq. 87 can be written also as:

$$(1+Z) \left(\left(1 + \frac{1}{P} \right) C + D \right) \geq 4 \left(\left(1 + \frac{1}{P_F} \right) C + D \right) \quad (88)$$

Based on the definition of P and P_F in Eqs 20, 24 respectively, we can write:

$$P = \frac{A}{B} \frac{(1+Z)T_{syn}^2}{\sigma_{\omega_1}^2}, \quad P_F = \frac{A}{B} \frac{T_{syn}^2}{\sigma_{\omega_1}^2} \rightarrow P = P_F (1+Z) \quad (89)$$

Based on Eq. 89 we can write Eq. 88 as:

$$(1+Z) \left(\left(1 + \frac{1}{P_F(1+Z)} \right) C + D \right) \geq 4 \left(\left(1 + \frac{1}{P_F} \right) C + D \right) \quad (90)$$

After rearranging Eq. 90 we can write:

$$Z \geq 3 \left(\frac{\left(1 + \frac{1}{P_F} \right) C + D}{C + D} \right) \quad (91)$$

By putting the definition of P_F Eq. 24 into Eq. 91 we can write:

$$Z \geq 3 \left(\frac{C + D + \frac{BC}{A} \frac{\sigma_{\omega_1}^2}{T_{syn}^2}}{C + D} \right) \rightarrow Z \geq \bar{Z}_{fGn/gfGn} \quad (92)$$

where $\bar{Z}_{fGn/gfGn}$ is defined in Eq. 81.

This completes our proof of Theorem 8, case a.

Now we continue the proof of case b. For $Z < 1$, we wish to find the value for Z where we have $MSE_{fGn/gfGn}^T \geq MSE_{fGn/gfGn}^R$. Thus, we may write:

$$\left(\frac{1}{J(J-1)T_{syn}} \right)^2 \left[\sigma_{\omega_1}^2 (1+Z) \left(\left(1 + \frac{1}{P} \right) C + D \right) \right] \leq \left(\frac{1}{J(J-1)T_{syn}} \right)^2 \left[4(Z\sigma_{\omega_1}^2) (C+D) \right] \quad (93)$$

where Eq. 93 can be written also as:

$$(1+Z) \left(\left(1 + \frac{1}{P} \right) C + D \right) \leq 4Z(C+D) \quad (94)$$

By using the definition of P in Eq. 20 into Eq. 95 we may write:

$$(1+Z) \left(\left(1 + \frac{B}{A} \frac{\sigma_{\omega_1}^2}{(1+Z)T_{syn}^2} \right) C + D \right) \leq 4Z(C+D) \quad (95)$$

After rearranging Eq. 95 we can write:

$$Z \leq \frac{1}{3} \left(\frac{C + D + \frac{CB}{A} \frac{\sigma_{\omega_1}^2}{T_{syn}^2}}{C + D} \right) \rightarrow Z \leq \bar{Z}_{fGn/gfGn} \quad (96)$$

where $\bar{Z}_{fGn/gfGn}$ is defined in Eq. 82.

This completes our proof of Theorem 8, case b.

Now we can continue the proof of case c of Theorem 8. For $Z = 1$, we defined that $\sigma_{\omega_1}^2 = \sigma_{\omega_2}^2 = \sigma^2$. We wish to find the value for Z where we have $MSE_{fGn/gfGn}^T \geq MSE_{fGn/gfGn}^R$. Note that for $Z =$

1 $MSE_{fGn/gfGn}^T < MSE_{fGn/gfGn}^F \forall j$ since, A , B and C have only positive values. Thus, we can write:

$$\left(\frac{1}{J(J-1)T_{syn}}\right)^2 \left[2\sigma^2 \left(C\left(1 + \frac{1}{P}\right) + D\right)\right] \geq \left(\frac{1}{J(J-1)T_{syn}}\right)^2 [4\sigma^2 (C + D)] \quad (97)$$

where Eq. 97 can be written also as:

$$2\sigma^2 \left(C\left(1 + \frac{1}{P}\right) + D\right) \geq 4\sigma^2 (C + D) \quad (98)$$

By using the definition of P in Eq. 20, we may write Eq. 98 as:

$$2\sigma^2 \left(C\left(1 + \frac{B}{A} \frac{\sigma^2}{2T_{syn}^2}\right) + D\right) \geq 4\sigma^2 (C + D) \quad (99)$$

After rearranging Eq. 99 we can write:

$$\sigma^2 \geq \tilde{\sigma}_{fGn/gfGn}^2 \quad (100)$$

where $\tilde{\sigma}_{fGn/gfGn}^2$ is defined in Eq. 83. Now, we have completed our proof of Theorem 8.

7 SIMULATION RESULTS

In this section, we first start to test our guidelines (conditions) from Theorem 8, summarized in Table 1. Figures 2, 3 show the simulated clock skew performance (MSE) comparison between the OWD clock skew estimator for the Forward path (Eq. 61) with the TWD clock skew estimator proposed by Avraham and Pinchas [4] for the fGn case. Figures 4–6 show the simulated clock skew performance (MSE) comparison between the OWD clock skew estimator for the Reverse path (Eq. 62) with the TWD clock skew estimator proposed by Avraham and Pinchas [4] for the fGn case. Figure 7 shows the simulated clock skew performance (MSE) comparison between the OWD clock skew estimator for the Forward path (Eq. 61) with the TWD clock skew estimator proposed by Avraham and Pinchas [4] for the gfGn case. Figure 8 shows the simulated clock skew performance (MSE) comparison between the OWD clock skew estimator for the Reverse path (Eq. 62) with the TWD clock skew estimator proposed by Avraham and Pinchas [4] for the gfGn case. In Figures 2, 3 and Figure 7, the Forward PDV variance was set lower than the Reverse PDV variance ($Z > 1$). Now, according to test case a of Theorem 8, if $Z \geq \tilde{Z}_{fGn/gfGn}$ we should choose the OWD clock skew estimator for the Forward path over the TWD clock skew estimator, else we should choose the TWD clock skew estimator. Namely, if $Z \geq \tilde{Z}_{fGn/gfGn}$, a better clock skew performance from the MSE point of view can be obtained with the OWD clock skew estimator for the Forward path compared with the TWD clock skew estimator proposed by Avraham and Pinchas [4]. In Figure 2 and Figure 7, we have $Z \geq \tilde{Z}_{fGn/gfGn}$ while in Figure 3 we have $Z < \tilde{Z}_{fGn/gfGn}$. Indeed we can see that in Figure 2 and Figure 7 a lower MSE is obtained with the OWD clock skew estimator for the Forward path compared with the TWD clock skew estimator proposed by Avraham and Pinchas [4]

which clearly demonstrates that the OWD clock skew estimator for the Forward path should be chosen for the clock skew estimation task. In Figure 3 a lower MSE is obtained with the TWD clock skew estimator compared with the OWD clock skew estimator for the Forward path which means that the TWD clock skew estimator should be chosen for the clock skew estimation task. Thus, we may say that according to Figures 2, 3 and Figure 7, test case a of Theorem 8 works correctly. In Figures 4, 5 and Figure 8, the Reverse PDV variance was set lower than the Forward PDV variance ($Z < 1$). Now, according to test case b of Theorem 8, if $Z \leq \tilde{Z}_{fGn/gfGn}$ we should choose the OWD clock skew estimator for the Reverse path over the TWD clock skew estimator, else we should choose the TWD clock skew estimator. Namely, if $Z \leq \tilde{Z}_{fGn/gfGn}$ a better clock skew performance from the MSE point of view can be obtained with the OWD clock skew estimator for the Reverse path compared with the TWD clock skew estimator proposed by Avraham and Pinchas [4]. In Figure 4 and Figure 8, we have $Z \leq \tilde{Z}_{fGn/gfGn}$ while in Figure 5 we have $Z > \tilde{Z}_{fGn/gfGn}$. Indeed we can see that in Figure 4 and Figure 8 a lower MSE is obtained with the OWD clock skew estimator for the Reverse path compared with the TWD clock skew estimator proposed by Avraham and Pinchas [4] which clearly demonstrates that the OWD clock skew estimator for the Reverse path should be chosen for the clock skew estimation task. In Figure 5 a lower MSE is obtained with the TWD clock skew estimator compared with the OWD clock skew estimator for the Reverse path which means that the TWD clock skew estimator should be chosen for the clock skew estimation task. Thus, we may say that according to Figures 4, 5 and Figure 8, test case b of Theorem 8 works correctly. In Figure 6, the Reverse PDV variance was set equal to the Forward PDV variance ($Z = 1$). Now, according to test case c of Theorem 8, if $\sigma^2 \geq \tilde{\sigma}_{fGn/gfGn}^2$ we should choose the OWD clock skew estimator for the Reverse path over the TWD clock skew estimator, else we should choose the TWD clock skew estimator. Namely, if $\sigma^2 \geq \tilde{\sigma}_{fGn/gfGn}^2$ a better clock skew performance from the MSE point of view can be obtained with the OWD clock skew estimator for the Reverse path compared with the TWD clock skew estimator proposed by Avraham and Pinchas [4]. According to Figure 6, up to approximately $J = 80$ we have that $\sigma^2 < \tilde{\sigma}_{fGn/gfGn}^2$. Thus, up to approximately $J = 80$ we see according to Figure 6 that a lower MSE is obtained with the TWD clock skew estimator proposed by Avraham and Pinchas [4] compared with the OWD clock skew estimator for the Reverse path. But, for $J > 80$, $\sigma^2 > \tilde{\sigma}_{fGn/gfGn}^2$ thus a lower MSE is obtained with the OWD clock skew estimator for the Reverse path compared with the TWD clock skew estimator proposed by Avraham and Pinchas [4]. Figure 6 clearly demonstrates the effectiveness of test case c of Theorem 8. According to Figures 2–8, our guidelines (conditions) from Theorem 8 indeed may help the system designer to choose wisely the preferred approach among Eqs 60–62 that should be applied for the clock skew estimation task in order to get the best clock skew performance from the MSE point of view. According to Figures 2–8 we can also see the advantage of having two OWD clock skew estimators (one for the Forward path and one associated with the Reverse path) that can supply better clock skew performance from the MSE point of view compared to our recently proposed TWD clock skew estimator Avraham and

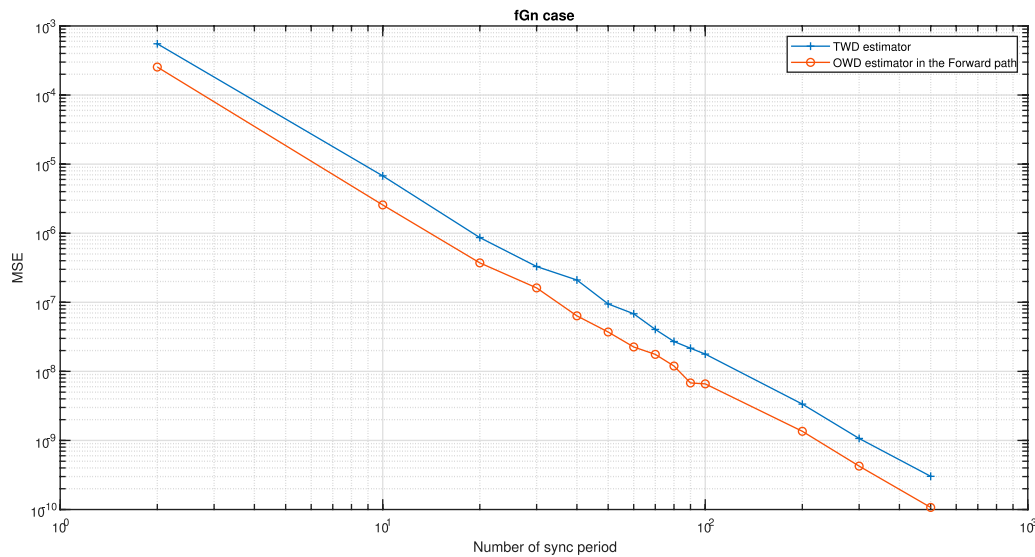


FIGURE 2 | Test **case a** of Theorem 8. Performance (MSE) comparison between the OWD clock skew estimator in the Forward path (Eq. 61) and the TWD clock skew estimator (Eq. 60). The PDV is an fGn process. $\alpha = 50\text{ppm}$, $Q = 5\text{ ms}$, $T_{\text{syn}} = 15.6\text{ ms}$ ($64 \frac{\text{packet}}{\text{sec}}$), $H = 0.7$, $d_{\text{ms}} = 5\text{ ms}$, $d_{\text{sm}} = 5.5\text{ ms}$, $\sigma_{\omega_1}^2 = 4e-8[\text{sec}^2]$, $\sigma_{\omega_2}^2 = 6.4e-7[\text{sec}^2]$, $Z = 16$, $\tilde{Z}_{\text{fGn/gfGn}}(J = 500) = 3.233$ (for $J < 500$, $\tilde{Z}_{\text{fGn/gfGn}} < 3.233$). The results were obtained for 100 Monte-Carlo trails.

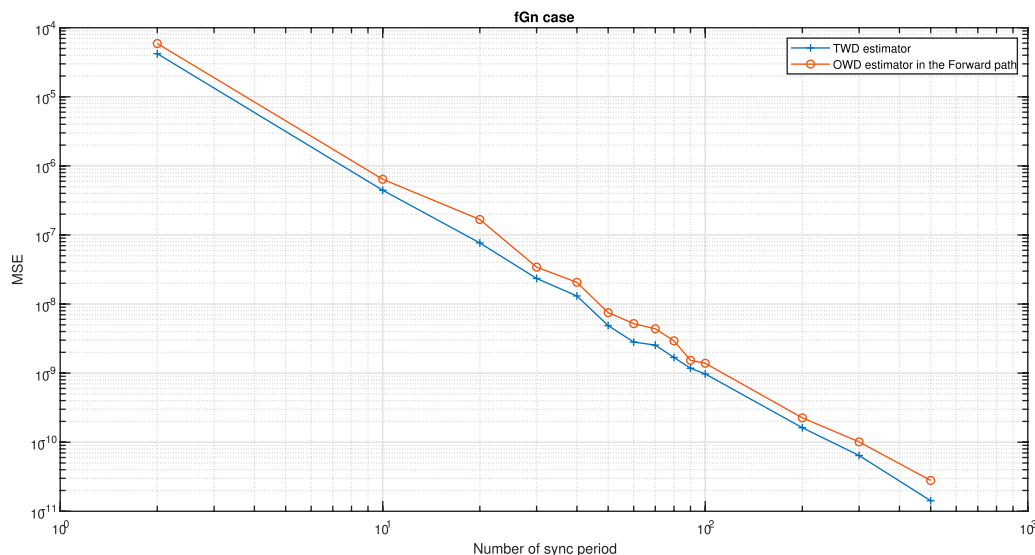


FIGURE 3 | Test **case a** of Theorem 8. Performance (MSE) comparison between the OWD clock skew estimator in the Forward path (Eq. 61) and the TWD clock skew estimator (Eq. 60). The PDV is an fGn process. $\alpha = 50\text{ppm}$, $Q = 5\text{ ms}$, $T_{\text{syn}} = 15.6\text{ ms}$ ($64 \frac{\text{packet}}{\text{sec}}$), $H = 0.7$, $d_{\text{ms}} = 5\text{ ms}$, $d_{\text{sm}} = 5.5\text{ ms}$, $\sigma_{\omega_1}^2 = 1e-8[\text{sec}^2]$, $\sigma_{\omega_2}^2 = 1.44e-8[\text{sec}^2]$, $Z = 1.44$, $\tilde{Z}_{\text{fGn/gfGn}}(J = 500) = 3.058$ (for $J < 500$, $\tilde{Z}_{\text{fGn/gfGn}} < 3.058$, $\tilde{Z}_{\text{fGn/gfGn}}(J = 10) = 3.004$). The results were obtained for 100 Monte-Carlo trails.

Pinchas [4], when complying with our proposed guidelines (conditions) from Theorem 8.

In Figures 9–12 we compared the clock skew performance (MSE) of our new proposed OWD clock skew estimators (Eqs 61, 62) with the clock skew performance (MSE) that is obtained from three clock skew algorithms: a.) TWD clock skew estimator, named as the ML-like estimator (MLLE) proposed by Noh et al. [5], b.)

OWD clock skew estimator, named as the maximum likelihood estimator proposed by Levy and Pinchas [7], c.) OWD clock skew estimator, named as the Kalman estimator proposed by Chaloupka et al. [6]. According to Noh et al. [5] we have:

$$\hat{\beta} = \frac{T_{2,1}(J-1)^2 + T_{3,1}(J-1)^2}{T_{1,1}(J-1)T_{2,1}(J-1) + T_{3,1}(J-1)T_{4,1}(J-1)} - 1 \quad (101)$$

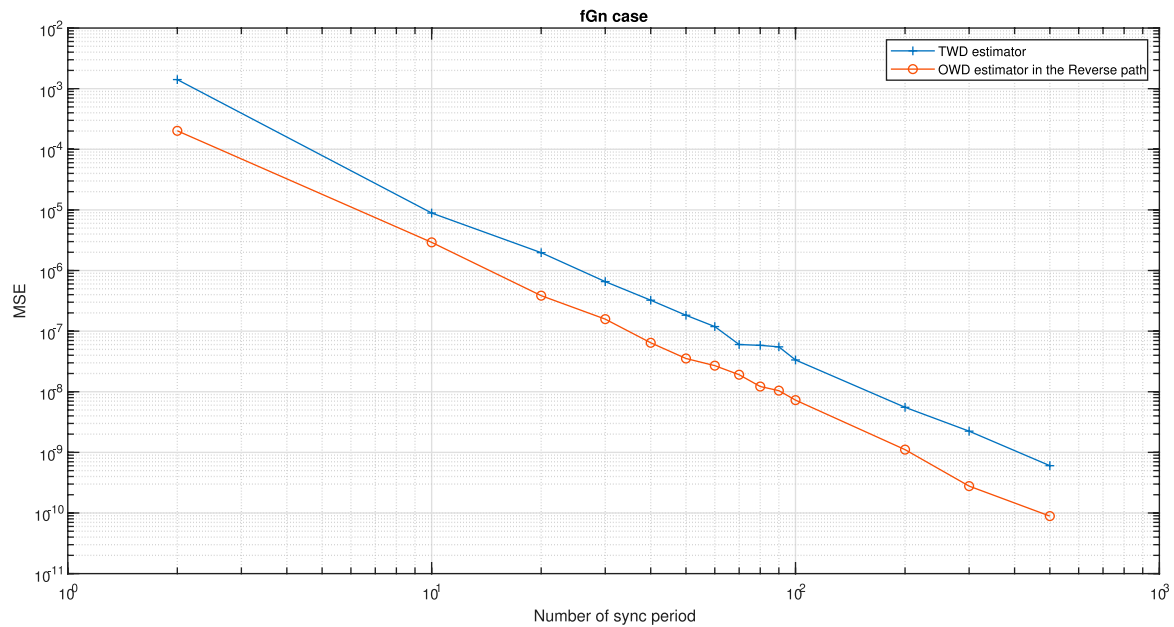


FIGURE 4 | Test **case b** of Theorem 8. Performance (MSE) comparison between the OWD clock skew estimator in the Reverse path (Eq. 62) and the TWD clock skew estimator (Eq. 60). The PDV is an fGn process. $\alpha = 50ppm$, $Q = 5\text{ ms}$, $T_{syn} = 15.6\text{ ms}$ ($64 \frac{\text{packet}}{\text{sec}}$), $H = 0.7$, $d_{ms} = 5\text{ ms}$, $d_{sm} = 5.5\text{ ms}$, $\sigma_{\omega_1}^2 = 6.4e-7[\text{sec}^2]$, $\sigma_{\omega_2}^2 = 4e-8[\text{sec}^2]$, $Z = 0.0625$, $\bar{Z}_{fGn/gfGn}(J = 500) = 0.748$ (for $J < 500$, $\bar{Z}_{fGn/gfGn} < 0.748$, $\bar{Z}_{fGn/gfGn}(J = 10) = 0.36$). The results were obtained for 100 Monte-Carlo trails.

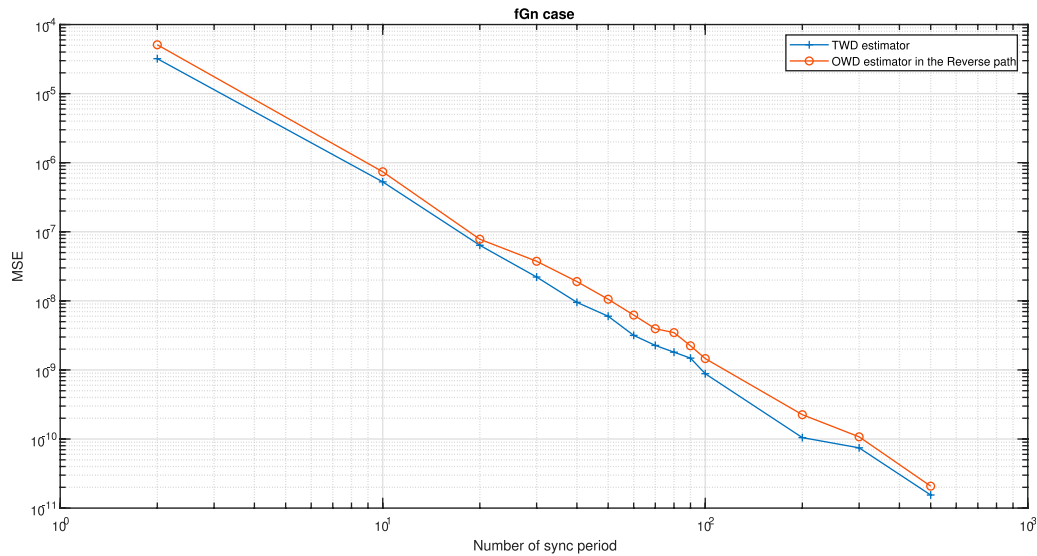


FIGURE 5 | Test **case b** of Theorem 8. Performance (MSE) comparison between the OWD clock skew estimator in the Reverse path (Eq. 62) and the TWD clock skew estimator (Eq. 60). The PDV is an fGn process. $\alpha = 50ppm$, $Q = 5\text{ ms}$, $T_{syn} = 15.6\text{ ms}$ ($64 \frac{\text{packet}}{\text{sec}}$), $H = 0.7$, $d_{ms} = 5\text{ ms}$, $d_{sm} = 5.5\text{ ms}$, $\sigma_{\omega_1}^2 = 1.44e-8[\text{sec}^2]$, $\sigma_{\omega_2}^2 = 1e-8[\text{sec}^2]$, $Z = 0.69$, $\bar{Z}_{fGn/gfGn}(J = 500) = 0.3427$ (for $J < 500$, $\bar{Z}_{fGn/gfGn} < 0.3427$). The results were obtained for 100 Monte-Carlo trails.

where

$$\hat{\beta} = \frac{1}{\hat{\alpha} + 1} - 1 \quad (102)$$

$T_{2,1}(J-1) = t_2[J] - t_2[1]$, $T_{1,j}(i)$, $T_{2,j}(i)$, $T_{3,j}(i)$ and $T_{4,j}(i)$ are defined in Eqs 4, 13.

According to Levy and Pinchas [7] we have:

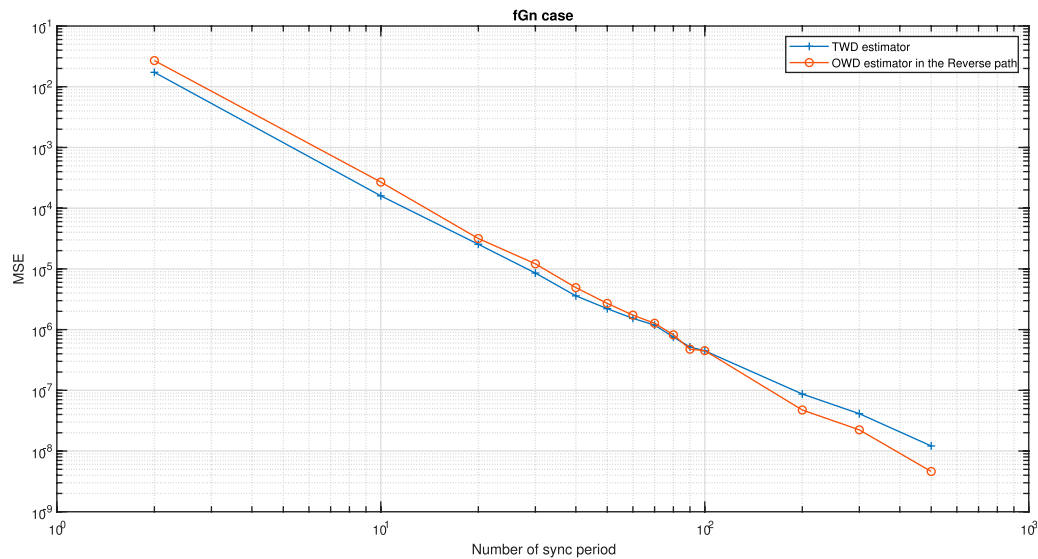


FIGURE 6 | Test **case c** of Theorem 8. Performance (MSE) comparison between the OWD clock skew estimator in the Reverse path (Eq. 62) and the TWD clock skew estimator (Eq. 60). The PDV is an fGn process. $\alpha = 50\text{ppm}$, $Q = 5\text{ ms}$, $T_{\text{syn}} = 15.6\text{ms}$ ($64 \frac{\text{packet}}{\text{sec}^2}$), $H = 0.6$, $d_{\text{ms}} = 2.5\text{ ms}$, $d_{\text{sm}} = 3\text{ ms}$, $\sigma_{\omega_1}^2 = \sigma_{\omega_2}^2 = 4e-6[\text{sec}^2]$, $Z = 1$, $\hat{\sigma}_{fGn/gfGn}^2(J = 500) = 1.03e-6$ (for $J < 500$: $\hat{\sigma}_{fGn/gfGn}^2 > 1.03e-6$, $\hat{\sigma}_{fGn/gfGn}^2(J = 100) = 3e-6$, $\hat{\sigma}_{fGn/gfGn}^2(J = 60) = 4.3e-6$, $\hat{\sigma}_{fGn/gfGn}^2(J = 10) = 1.72e-5$). The results were obtained for 100 Monte-Carlo trails.

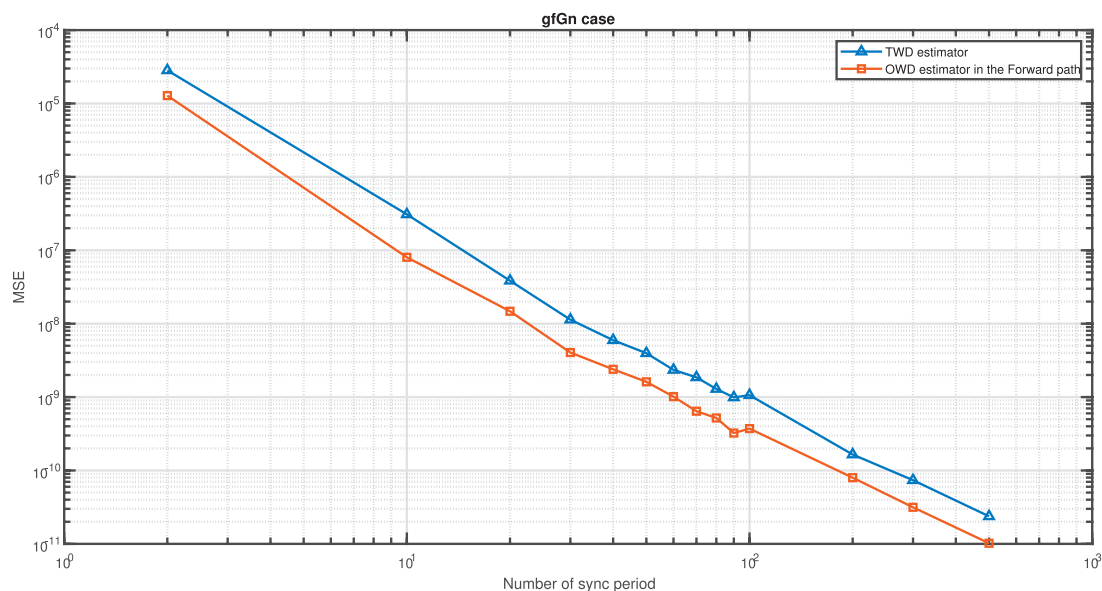


FIGURE 7 | Test **case a** of Theorem 8. Performance (MSE) comparison between the OWD clock skew estimator in the Forward path (Eq. 61) and the TWD clock skew estimator (Eq. 60). The PDV is a gfGn process. $\alpha = 50\text{ppm}$, $Q = 5\text{ ms}$, $T_{\text{syn}} = 15.6\text{ms}$ ($64 \frac{\text{packet}}{\text{sec}^2}$), $H = 0.95$, $a = 0.08$, $d_{\text{ms}} = 5\text{ ms}$, $d_{\text{sm}} = 5.5\text{ ms}$, $\sigma_{\omega_1}^2 = 1e-8[\text{sec}^2]$, $\sigma_{\omega_2}^2 = 9e-8[\text{sec}^2]$, $Z = 9$, $\hat{Z}_{fGn/gfGn}(J = 500) = 3.02$ (for $J < 500$: $\hat{Z}_{fGn/gfGn} < 3.02$). The results were obtained for 100 Monte-Carlo trails.

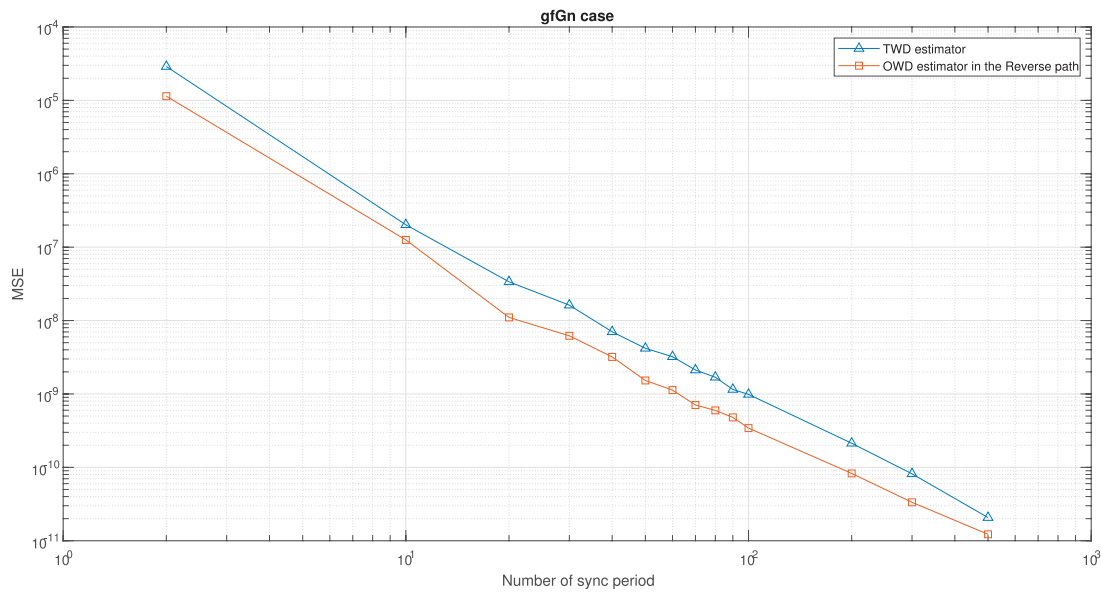


FIGURE 8 | Test **case b** of Theorem 8. Performance (MSE) comparison between the OWD clock skew estimator in the Reverse path (Eq. 62) and the TWD clock skew estimator (Eq. 60). The PDV is an gfGn process. $\alpha = 50\text{ppm}$, $Q = 5\text{ ms}$, $T_{\text{syn}} = 15.6\text{ms}$ ($64 \frac{\text{packet}}{\text{sec}}$), $H = 0.95$, $a = 0.08$, $d_{\text{ms}} = 5\text{ ms}$, $d_{\text{sm}} = 5.5\text{ ms}$, $\sigma_{\omega_1}^2 = 9e-8[\text{sec}^2]$, $\sigma_{\omega_2}^2 = 1e-8[\text{sec}^2]$, $Z = 0.111$, $\hat{Z}_{\text{fGn/gfGn}}(J = 500) = 0.356$ (for $J < 500$, $\hat{Z}_{\text{fGn/gfGn}} < 0.356$, $\hat{Z}_{\text{fGn/gfGn}}(J = 10) = 0.337$). The results were obtained for 100 Monte-Carlo trails.

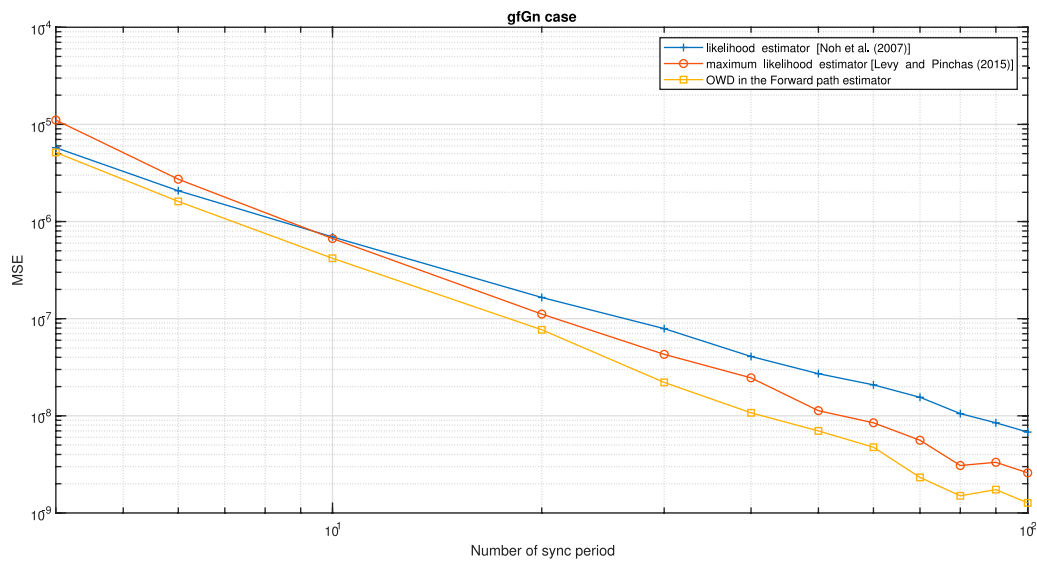


FIGURE 9 | Performance (MSE) comparison between the OWD clock skew estimator for the Forward path (Eq. 61), likelihood clock skew estimator proposed by Noh et al. [5] and maximum likelihood clock skew estimator proposed by Levy and Pinchas [7]. The PDV is an gfGn process. $\alpha = 50\text{ppm}$, $Q = 5\text{ ms}$, $T_{\text{syn}} = 15.6\text{ms}$ ($64 \frac{\text{packet}}{\text{sec}}$), $H = 0.95$, $a = 0.08$, $d_{\text{ms}} = 5.5\text{ ms}$, $d_{\text{sm}} = 5\text{ ms}$, $\sigma_{\omega_1}^2 = 4e-8[\text{sec}^2]$, $\sigma_{\omega_2}^2 = 1.6e-7[\text{sec}^2]$. The results were obtained for 100 Monte-Carlo trails.

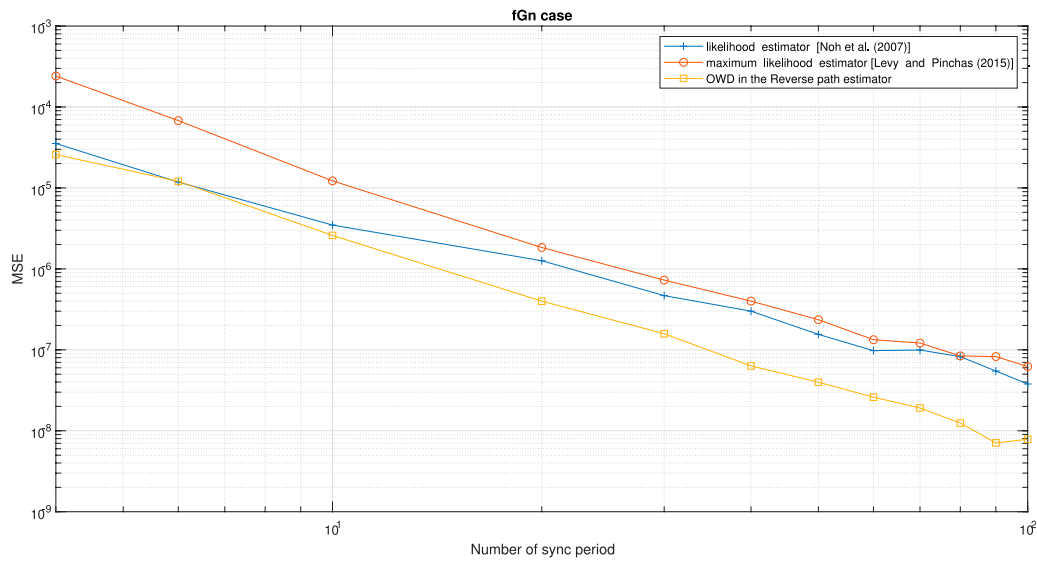


FIGURE 10 | Performance (MSE) comparison between the OWD clock skew estimator for the Reverse path (Eq. 62), likelihood clock skew estimator proposed by Noh et al. [5] and maximum likelihood clock skew estimator proposed by Levy and Pinchas [7]. The PDV is an fGn process. $\alpha = 50ppm$, $Q = 5\text{ ms}$, $T_{syn} = 15.6\text{ms}$ ($64 \frac{\text{packet}}{\text{sec}}$), $H = 0.7$, $d_{ms} = 5.5\text{ ms}$, $d_{sm} = 5\text{ ms}$, $\sigma_{\omega_1}^2 = 1.6e-7[\text{sec}^2]$, $\sigma_{\omega_2}^2 = 4e-8[\text{sec}^2]$. The results were obtained for 100 Monte-Carlo trails.

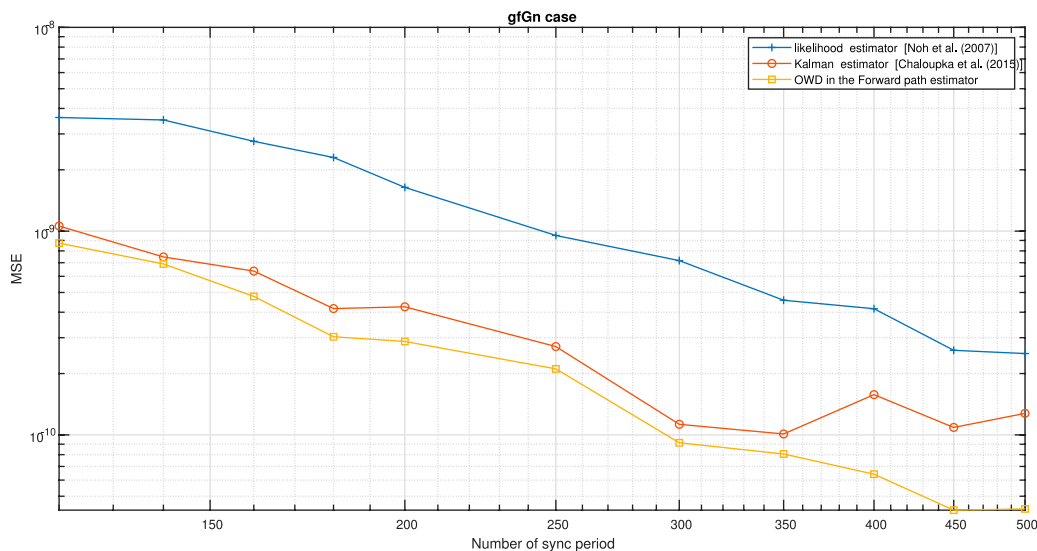


FIGURE 11 | Performance (MSE) comparison between the OWD clock skew estimator for the Forward path (Eq. 61), likelihood clock skew estimator proposed by Noh et al. [5] and Kalman clock skew estimator proposed by Chaloupka et al. [6]. The PDV is an gfGn process. $\alpha = 50ppm$, $Q = 5\text{ ms}$, $T_{syn} = 15.6\text{ms}$ ($64 \frac{\text{packet}}{\text{sec}}$), $H = 0.95$, $a = 0.08$, $d_{ms} = 5.5\text{ ms}$, $d_{sm} = 5\text{ ms}$, $\sigma_{\omega_1}^2 = 4e-8[\text{sec}^2]$, $\sigma_{\omega_2}^2 = 1.3e-7[\text{sec}^2]$, $L = 100$, $Q_{KAL} = 0$, $\delta_\sigma = \delta_\mu = 1e-4$, $\hat{\mu}[1] = 0$. The results were obtained for 100 Monte-Carlo trails.

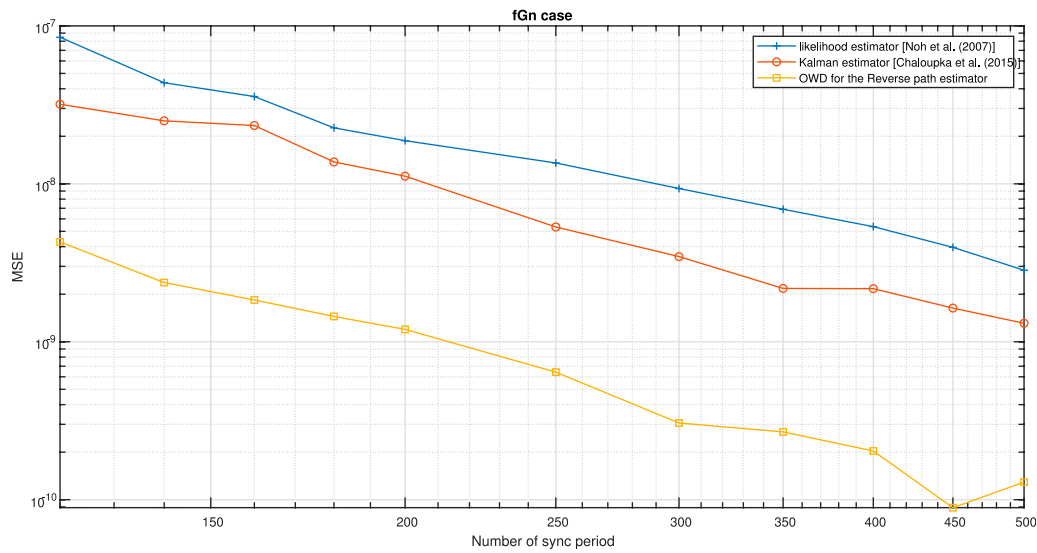


FIGURE 12 | Performance (MSE) comparison between the OWD clock skew estimator for the Reverse path (Eq. 62), likelihood clock skew estimator proposed by Noh et al. [5] and Kalman clock skew estimator proposed by Chaloupka et al. [6]. The PDV is an fGn process. $\alpha = 50\text{ppm}$, $Q = 5\text{ ms}$, $T_{\text{syn}} = 15.6\text{ms}$ ($64 \frac{\text{packet}}{\text{sec}}$), $H = 0.7$, $d_{\text{ms}} = 5.5\text{ ms}$, $d_{\text{sm}} = 5\text{ ms}$, $\sigma_{\omega_1}^2 = 3.6e-7[\text{sec}^2]$, $\sigma_{\omega_2}^2 = 4e-8[\text{sec}^2]$, $L = 100$, $Q_{\text{KAL}} = 0$, $\delta_\sigma = \delta_\mu = 1e-4$, $\hat{\mu}[1] = 0$. The results were obtained for 100 Monte-Carlo trails.

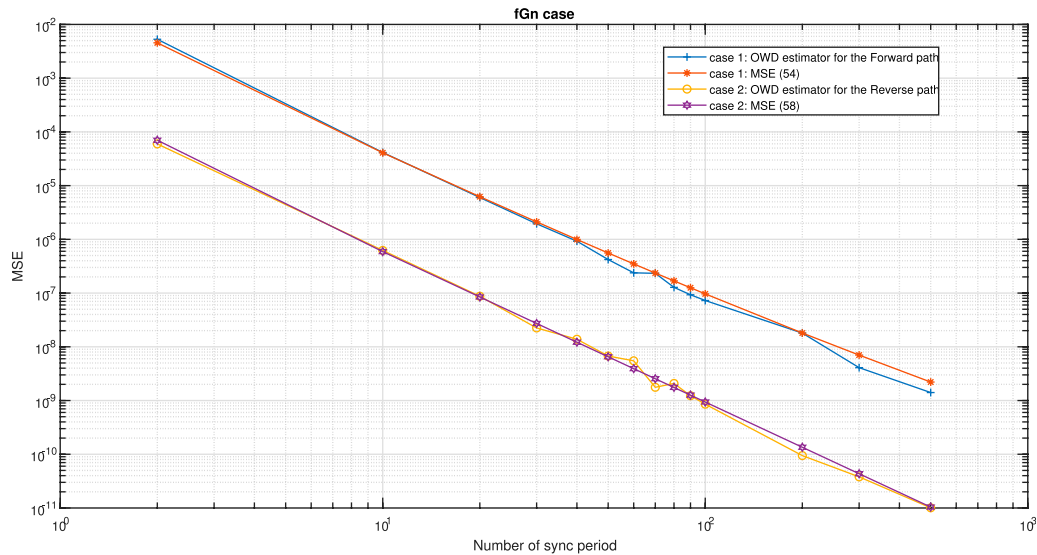


FIGURE 13 | case 1: Performance comparison for the fGn case, between our new proposed clock skew estimator for the Forward path (Eq. 61) with the performance results for our new proposed expression for the MSE (Eq. 54). $\sigma_{\omega_1} = 0.8e-3[\text{sec}]$. **Case 2:** Performance comparison for the fGn case, between our new proposed clock skew estimator for the Reverse path (Eq. 62) with the performance results for our new proposed expression for the MSE (Eq. 58). $\sigma_{\omega_2} = 0.1e-3[\text{sec}]$. For both cases: $\alpha = 50\text{ppm}$, $Q = 5\text{ ms}$, $T_{\text{syn}} = 15.6\text{ms}$ ($64 \frac{\text{packet}}{\text{sec}}$), $H = 0.6$, $d_{\text{ms}} = 5.5\text{ ms}$, $d_{\text{sm}} = 5\text{ ms}$. The results were obtained for 100 Monte-Carlo trails.

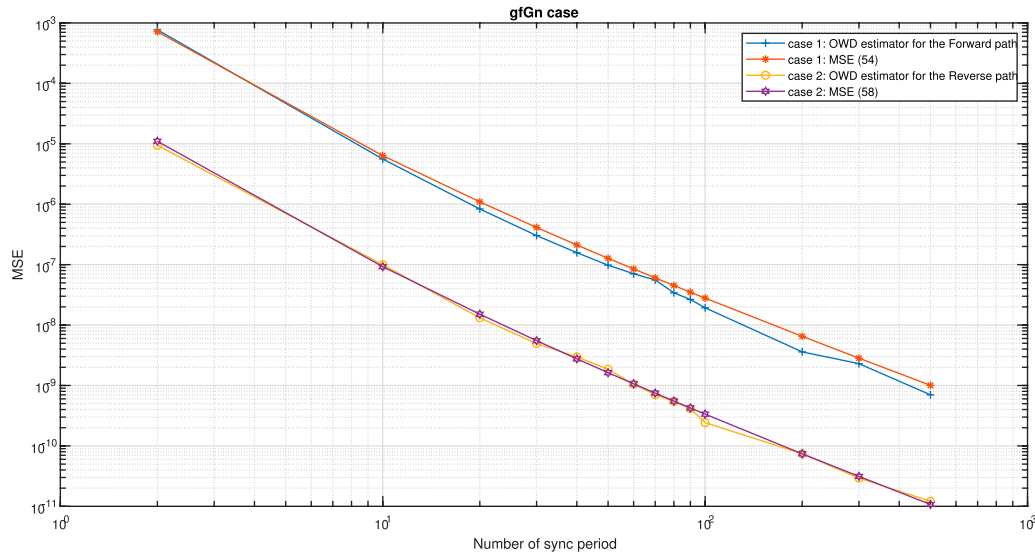


FIGURE 14 | case 1: Performance comparison for the gfGn case, between our new proposed clock skew estimator for the Forward path (Eq. 61) with the performance results for our new proposed expression for the MSE (Eq. 54). $\sigma_{w_1} = 0.8e-3$ [sec]. **Case 2:** Performance comparison for the gfGn case, between our new proposed clock skew estimator for the Reverse path (Eq. 62) with the performance results for our new proposed expression for the MSE (Eq. 58). $\sigma_{w_2} = 0.1e-3$ [sec]. For both cases: $\alpha = 50\text{ppm}$, $Q = 5\text{ ms}$, $T_{syn} = 15.6\text{ms}$ ($64 \frac{\text{packet}}{\text{sec}}$), $H = 0.95$, $a = 0.95$, $d_{ms} = 5.5\text{ ms}$, $d_{sm} = 5\text{ ms}$. The results were obtained for 100 Monte-Carlo trails.

$$\hat{\varepsilon} = \left(2 \sum_{i=1}^J \sum_{j=1}^J \sum_{k=1}^{\min(i,j)-1} [A_{\max}(J, i, j, k, H) (\Delta T_{s1,i} - \Delta T_{s2,i}) (\Delta T_{s1,j} - \Delta T_{s2,j})] \right) \left(\sum_{i=1}^J \sum_{j=1}^J \sum_{k=1}^{\min(i,j)-1} [A_{\max}(J, i, j, k, H) [\Delta T_{m,j} (\Delta T_{s1,i} - \Delta T_{s2,i}) + \Delta T_{m,i} (\Delta T_{s1,j} - \Delta T_{s2,j})]] \right)^{-1} - 1 \quad (103)$$

where $A_{\max}(J, i, j, k, H)$ is:

$$A_{\max}(J, i, j, k, H) = \left[\frac{\Gamma(J)}{\Gamma(-H+0.5)\Gamma(J-H+0.5)} \right]^2 (\Gamma(i-k-H+0.5)) \frac{\Gamma(J-H+0.5-i+k)\Gamma(j-k-H+0.5)\Gamma(J-H+0.5-j+k)}{(\Gamma(J-i+k)\Gamma(J-j+k)\Gamma(i-k)\Gamma(j-k))^{-1}} \left[\frac{1}{(i-k)} \frac{1}{(j-k)} - \frac{1}{(J-i+k)} \frac{1}{(J-j+k)} \right] \quad (104)$$

and $\hat{\varepsilon}$ is:

$$\hat{\varepsilon} = \frac{1}{\hat{\alpha} + 1} - 1 \quad (105)$$

$\Gamma(\cdot)$ denotes the Gamma function, Δ denotes the difference between two consecutive timestamps. $T_{m,i}$ is the timestamp in the i th period when the Master sends the Sync message. $T_{s1,i}$ is the timestamp in the i th period when the dual-Slave receives the Sync message. $T_{s2,i}$ is the timestamp in the i th period when the Slave receives the Sync message.

The Kalman estimator from Chaloupka et al. [6] depends on a predefined parameter L that defines the sliding window's length in the algorithm. The L parameter impacts the performance (MSE). As we increase L , it reduces the MSE. However, L also depends on the total number of sync periods, which we set for the

frequency synchronization task as 500. Therefore, L must be smaller than 500.

According to Chaloupka et al. [6] the Kalman's measurement equation is:

$$T_{1,j}(L) - T_{2,j}(L) = T_{2,j}(L)\alpha[j] + \Omega_{1,j}(L) \quad (106)$$

The Kalman's state equation is:

$$\hat{\alpha}[j+1] = \hat{\alpha}[j] + u[j]. \quad (107)$$

where the variance of $u[j]$ is Q_{KAL} . The estimate of the noise measurement variance is given by Chaloupka et al. [6]:

$$\hat{R}[j] = (1 - \delta_\sigma)\hat{R}[j-1] + \delta_\sigma(x[j] - \hat{\mu}[j])^2 \quad (108)$$

where

$$\hat{\mu}[j] = (1 - \delta_\mu)\hat{\mu}[j-1] + \delta_\mu x[j]; \quad x[j] = T_{1,j}(L) - T_{2,j}(L) \quad (109)$$

δ_μ and δ_σ are smoothing factors which are between zero and one.

According to Figures 9, 10, our new proposed OWD clock skew estimator for the Forward path (Eq. 61) (Figure 9) or for the Reverse path (Eq. 62) (Figure 10) achieves a lower MSE compared to the clock skew estimators proposed by Noh et al. [5] and Levy and Pinchas [7]. Please note that for the simulation results presented in Figure 10, the PDV for the Reverse path was set lower than the PDV for the Forward path. Since the OWD clock skew estimator proposed by Levy and Pinchas [7] is based on the Forward path only, the clock skew accuracy with this estimator Levy and Pinchas [7] is indeed decreased (Figure 10).

According to Figures 11, 12, our new proposed OWD clock skew estimator for the Forward path (Eq. 61) (Figure 11) or for

the Reverse path (Eq. 62) (Figure 12) achieves a lower MSE compared to the clock skew estimators proposed by Noh et al. [5] and Chaloupka et al. [6]. Please note that for the simulation results presented in Figure 12, the PDV for the Reverse path was set lower than the PDV for the Forward path. Since the OWD clock skew estimator proposed by Chaloupka et al. [6] is based on the Forward path only, the clock skew accuracy with this estimator Chaloupka et al. [6] is indeed decreased (Figure 12).

Next we tested our new proposed OWD clock skew estimators' performances (MSE) for the Forward and Reverse paths (Eqs 61, 62) with our closed-form-approximated expressions for the MSE for the LRD case (Eqs 54, 58) for the Forward and Reverse path, respectively. Case 1 in Figures 13, 14 presents the clock skew performance of our new proposed OWD clock skew estimator for the Forward path (Eq. 61) compared with our closed-form-approximated expression for the MSE in Eq. 54. Case 2 in Figures 13, 14 presents the clock skew performance of our new proposed OWD clock skew estimator for the Reverse path (Eq. 62) compared with our closed-form-approximated expression for the MSE in Eq. 58. According to Figures 13, 14 it can be clearly seen that our new closed-form-approximated expressions for the MSE in Eqs 54, 58 supply very close results to the simulated one.

8 CONCLUSION

In this paper we derived two novels OWD clock skew estimators for the Forward and Reverse paths applicable for white-Gaussian process and for the fGn/gfGn environment. Those estimators

do not depend on the unknown fixed paths nor on the clock offset between the Master and Slave. In addition, we derived also closed-form-approximated expressions for the clock skew performance (MSE) for the new proposed OWD clock skew estimators for the Forward and Reverse paths. In order to help the system designer to choose the right clock skew estimator that may get the best clock skew performance from the MSE point of view, some guidelines (conditions) were derived, helping choosing the right clock skew estimator wisely. Simulation results has confirmed that our new OWD clock skew estimators indeed achieve better clock skew performance from the MSE point of view compared to the literature known clock skew estimators. Simulation results have also confirmed that our closed-form-approximated expressions for the MSE related to our new proposed OWD Forward and Reverse estimators are indeed efficient.

DATA AVAILABILITY STATEMENT

The original contributions presented in the study are included in the article/Supplementary Material, further inquiries can be directed to the corresponding author.

AUTHOR CONTRIBUTIONS

All authors listed have made a substantial, direct, and intellectual contribution to the work and approved it for publication.

REFERENCES

- [Dataset] Arnold D. *IEEE 1588-2019-IEEE Standard for a Precision Clock Synchronization Protocol for Networked Measurement and Control Systems* (2019). Available from: <https://standards.ieee.org/standard/1588-2019.html> (Accessed June 17, 2021).
- K.Karthik A, S.Blum R. *Estimation Theory Based Robust Phase Offset Estimation in the Presence of Delay Attacks* (2016). Available from: <https://arxiv.org/pdf/1611.05117.pdf> (Accessed August 10, 2021).
- Guruswamy A, Blum RS, Kishore S, Bordogna M. On the Optimum Design of L-Estimators for Phase Offset Estimation in IEEE 1588. *IEEE Trans Commun* (2015) 63:5101–15. doi:10.1109/TCOMM.2015.2493534
- Avraham Y, Pinchas M. A Novel Clock Skew Estimator and its Performance for the IEEE 1588v2 (PTP) Case in Fractional Gaussian Noise/Generalized Fractional Gaussian Noise Environment. *Front Phys* (2021) 9:1–21. doi:10.3389/fphy.2021.796811
- Noh K-L, Chaudhari QM, Serpedin E, Suter BW. Novel Clock Phase Offset and Skew Estimation Using Two-Way Timing Message Exchanges for Wireless Sensor Networks. *IEEE Trans Commun* (2007) 55:766–77. doi:10.1109/TCOMM.2007.894102
- Chaloupka Z, Alsindi N, Aweya J. Clock Skew Estimation Using Kalman Filter and IEEE 1588v2 PTP for Telecom Networks. *IEEE Commun Lett* (2015) 19:1181–4. doi:10.1109/LCOMM.2015.2427158
- Levy C, Pinchas M. Maximum Likelihood Estimation of Clock Skew in IEEE 1588 with Fractional Gaussian Noise. *Math Probl Eng* (2015) 2015:1. doi:10.1155/2015/174289
- Karthik AK, Blum RS. Robust Clock Skew and Offset Estimation for IEEE 1588 in the Presence of Unexpected Deterministic Path Delay Asymmetries. *IEEE Trans Commun* (2020) 68:5102–19. doi:10.1109/TCOMM.2020.2991212
- Karthik AK, Blum RS. Robust Phase Offset Estimation for IEEE 1588 PTP in Electrical Grid Networks. In: 2018 IEEE Power & Energy Society General Meeting (2018). doi:10.1109/PESGM.2018.8586488
- Karthik AK, Blum RS. Optimum Full Information, Unlimited Complexity, Invariant, and Minimax Clock Skew and Offset Estimators for IEEE 1588. *IEEE Trans Commun* (2019) 67:3624–37. doi:10.1109/TCOMM.2019.2900317
- Li M, Zhao W. On Bandlimitedness and Lag-Limitedness of Fractional Gaussian Noise. *Physica A: Stat Mech its Appl* (2013) 392:1955–61. doi:10.1016/j.physa.2012.12.035
- Cappe O, Moulines E, Pesquet J-C, Petropulu AP, Xueshi Y. Long-range Dependence and Heavy-Tail Modeling for Teletraffic Data. *IEEE Signal Process Mag* (2002) 19:14–27. doi:10.1109/79.998079
- Li M. Generalized Fractional Gaussian Noise and its Application to Traffic Modeling. *Physica A: Stat Mech its Appl* (2021) 579:126138. doi:10.1016/j.physa.2021.126138

Conflict of Interest: The authors declare that the research was conducted in the absence of any commercial or financial relationships that could be construed as a potential conflict of interest.

Publisher's Note: All claims expressed in this article are solely those of the authors and do not necessarily represent those of their affiliated organizations, or those of the publisher, the editors, and the reviewers. Any product that may be evaluated in this article, or claim that may be made by its manufacturer, is not guaranteed or endorsed by the publisher.

Copyright © 2022 Avraham and Pinchas. This is an open-access article distributed under the terms of the Creative Commons Attribution License (CC BY). The use, distribution or reproduction in other forums is permitted, provided the original author(s) and the copyright owner(s) are credited and that the original publication in this journal is cited, in accordance with accepted academic practice. No use, distribution or reproduction is permitted which does not comply with these terms.



OPEN ACCESS

EDITED BY

Víctor M. Eguiluz,
Institute of Interdisciplinary Physics and
Complex Systems, (CSIC), Spain

REVIEWED BY

Sergio Da Silva,
Federal University of Santa Catarina,
Brazil
Haci Mehmet Baskonus,
Harran University, Turkey
Luis Manuel Sánchez Ruiz,
Universitat Politècnica de València,
Spain

*CORRESPONDENCE

Carlo Cattani,
cattani@unitus.it

SPECIALTY SECTION

This article was submitted to
Interdisciplinary Physics,
a section of the journal
Frontiers in Physics

RECEIVED 07 October 2021

ACCEPTED 18 August 2022

PUBLISHED 10 October 2022

CITATION

Deng W, Song W, Cattani C, Chen J and
Chen X (2022), On the fractional
weibull process.
Front. Phys. 10:790791.
doi: 10.3389/fphy.2022.790791

COPYRIGHT

© 2022 Deng, Song, Cattani, Chen and
Chen. This is an open-access article
distributed under the terms of the
[Creative Commons Attribution License](https://creativecommons.org/licenses/by/4.0/)
(CC BY). The use, distribution or
reproduction in other forums is
permitted, provided the original
author(s) and the copyright owner(s) are
credited and that the original
publication in this journal is cited, in
accordance with accepted academic
practice. No use, distribution or
reproduction is permitted which does
not comply with these terms.

On the fractional weibull process

Wujin Deng¹, Wanqing Song¹, Carlo Cattani^{2*}, Jianxue Chen¹
and Xiaolong Chen¹

¹School of Electronic and Electrical Engineering, Shanghai University of Engineering Science, Shanghai, China, ²Engineering School, DEIM, University of Tuscia, Viterbo, Italy

Engineering applications of the fractional Weibull distribution (fWd) are quite limited because a corresponding stochastic process is not yet constituted and completely analyzed of fundamental properties. In order to fill this gap, the fractional Weibull process (fWp) is defined in this paper with the realization algorithm. The self-similarity property as well as long range dependence (LRD) are proven for the future research. The simulation is conducted by the actual data. The fWd is utilized to fit the actual probability distribution and the corresponding process is generated to reflect the stochasticity of the data. The random walk based on the fWp expands the simulation to the planar space.

KEYWORDS

self-similarity, long range dependence, fractional Weibull distribution, fractional Weibull process, random walk

1 Introduction

After the discovery of fractal geometry, there has been recently a growing interest for the application of the fractional dimension processes in several fields. The fractional process is often used in the modeling of the Internet traffic. An abstract model for aggregated connectionless traffic, which is based on the fractional Brownian motion, is presented in [1]. In [2], generalized fractional Gaussian noise is proposed and used in the traffic modelling. The stochastic process with fractional dimension can also be used in the field of remaining useful life prediction for the mechanical parts. The remaining useful life is the remaining time for the mechanical parts before the next failure. The purpose of the remaining useful life prediction is to schedule the maintenance of the system and improve the reliability. The multi-modal fractional Lévy stable motion degradation model is developed to predict the remaining useful life of a blast furnace [3].

The Weibull distribution was originally introduced for modeling the strength data of material by Weibull in 1939, which is inspired by the works of the extreme value distribution, and then extended to several fields [4]. The traditional applications of the Weibull distribution is in the field of mechanical engineering, which is the lifetime prediction. A new extended model is used in the lifetime prediction in [5]. The Weibull distribution is combined with the artificial neural network to form a new predicting model for the prediction of the remaining useful life of the bearing [6]. There are also a lot of

Abbreviations: fWd, Fractional weibull distribution; fWp, fractional Weibull process; LRD, long range dependence; GoF, goodness of fitting; SSE, Sum of squared error; RMSE, Root mean square error.

applications of Weibull distribution in the power system. The combining modified Weibull distribution model is proposed for the forecast of the power system reliability [7]. Based on simple and complex Weibull distributions, a hypothesis of the power system reliability has been confirmed [8]. In [9] the upper-truncated Weibull distribution has been used both for modeling the wind speed data and estimating the wind power density. Weibull distribution is combined with the artificial neural network to establish an advanced wind speed prediction model [10].

The versatility of Weibull distribution raises people's interests on the fractional transformation. In [11] the fWd was proposed for modeling the wind speed data. The researchers find out that the actual wind speed data contains a lot of low wind speed values. By discarding the wind speed data that is close to zero, the wind speed is fitted by the fWd with high accuracy for the speed range suitable for wind power production. The fractal parameter is the fraction of data extracted from the wind speed data to make a better fit. Therefore, the essence of the fWd is to improve the fitting results by an additional fractal parameter.

In [12], the power load is modeled by the Weibull distribution. The power load data resembles the wind speed data because the power load is commonly be zero or approximate to zero. In the power break, the load is zero. At night, the factories are closed, therefore the total power load consumption in the area is close to zero. Therefore, this paper proposes the fWd for the modelling of the power load in wish of a better modelling result.

Probability distribution as fWd describes the time series in the statistical sense. In order to express the temporal characteristics of the time series conforming to fWd, the corresponding stochastic process need to be defined and studied. In this paper, the fWp is defined with respect to fWd. At each of the time point, draw a value randomly from the fWd will constitute the corresponding fWp temporally. If we count the values of the fWp in a long enough time period, the frequency distribution of the counted data will be the corresponding fWd. Therefore, the fWd and fWp are strongly connected mathematically.

As a stochastic process is defined, some fundamental and crucial property for the process need to be studied. Random walk characteristics is a common stochastic behavior for a process, which is beneficial in the optimization and graph machine learning. The random walk can be useful for the optimization to avoid the local maximum and the graph machine learning to simplify the graph. A lot of stochastic time series in the application conveys the properties of the self-similarity and LRD, which is useful for the study. Stochastic process with self-similarity and LRD can be employed in the modeling and prediction of the time series with the same properties. Therefore, in this paper, the random walk characteristics, self-similarity and LRD of the fWd are studied and illustrated to facilitate the future engineering application of the proposed process.

A random walk is known as a random behavior, in which a particle in space takes a succession of random steps to create a trajectory of moving [13]. In each of the step, the direction is random and the step length follows a certain distribution. If the distribution is normal distribution, then the random walk is called Rayleigh flight [14]. The random walk with the probability distribution to be Lévy distribution is called the Lévy flight [15]. In this paper, the random walk based on the fWp is proposed, in which the probability for the step length is the fWd.

Self-similarity means that the partial segment of the stochastic process or distribution resembles the whole stochastic process or distribution [16]. In [17], the Weibull distribution is used in the modelling of the self-similar Internet traffic and the formula of the self-similarity parameter is derived in [18]. The Hurst parameter of the Weibull distribution belongs to (0.5,1), which can be confirmed from the formula in [18]. Moreover, the mathematical definition of self-similarity contains the concept of equality in distribution [19]. Two random variables X and Y are said to be equal in distribution, if they have the same probability distribution function. In [20] a proposition is proven for the equivalent condition of the equality in distribution. In this paper, the proposition is employed to prove the self-similarity of the fWp.

LRD means that the value of the stochastic process is strongly influenced by the previous values of the time series [21]. The autocorrelation function of the long range dependent signal cannot be integrated in the infinity range, instead it diverges to infinity. The reason for the divergence is that the autocorrelation decays to zero very slowly as the power functional speed. In order to make the integration to converge, the autocorrelation need to decay exponentially, which corresponds to the short range dependence.

In [22] the following theorem about the connection between the self-similarity and LRD has been proved so that we can prove the LRD based on self-similarity:

If a process is self-similar with self-similarity parameter belonging to the half unit interval of (0.5, 1) and the second moments exist, then it can be shown that its incremental stochastic process is characterized by LRD.

In this paper, fWp is defined with respect to the fWd and the random walk characteristics is analyzed. The self-similarity property and the existence of the second moments are proved, therefore the incremental process of fWp is characterized by LRD [22]. Furthermore, LRD of the fWp is derived. The simulation is carried out with the real data.

The rest of the paper is arranged as follows: In Section 2, the properties of fWd is elaborated and the corresponding fWp is defined with the realization algorithm. In Section 3 and Section 4, the self-similarity and LRD of the fWp are proven. In Section 5, the simulation of the fWp is carried out with the analysis for the corresponding random walk. The work of this paper is summarized in the conclusion.

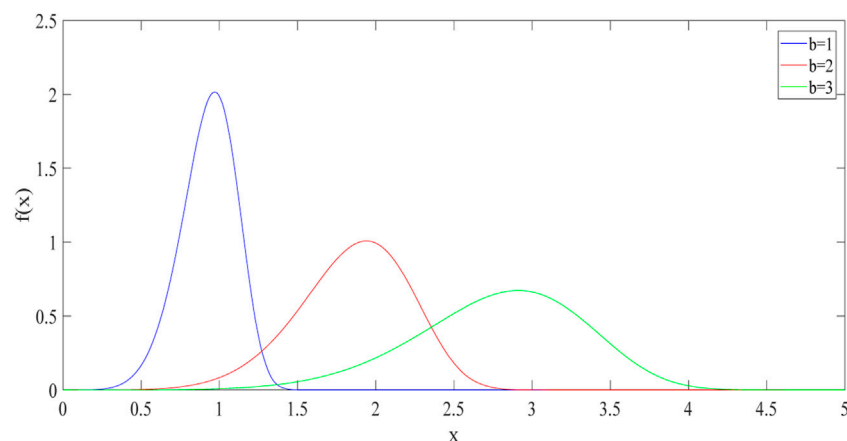


FIGURE 1
The influence of the change of scale parameter.

2 The fWp as well as the corresponding random walk

2.1 Data modeling with the fWd

The density function of the fWd is defined as:

$$f_x(x|a, b, c, \delta) = \frac{c}{b} (1 - \delta) \left(\frac{x-a}{b} \right)^{c-1} \exp \left\{ - \left(\frac{x-a}{b} \right)^c \right\}, x \geq a, \quad (2.1)$$

where δ is the fractal parameter, a is the location parameter, b is the scale parameter and c is the shape parameter.

The location parameter a is the origin where the probability of the physical values is above zero. Changing the value of a will cause a shift of curve horizontally. The shape parameter c is the key parameter of the distribution because it can change the shape of the density function dramatically. The density curve of the fWd is L-shaped when the value of parameter c is not larger than 1. Otherwise, the density curve is single-peaked.

Changing the scale parameter b while the other parameters are hold constants will cause the curve to shift both vertically and horizontally (see e. g., Figure 1). With the increase of the scale parameter, the dispersion of the distribution is larger, and the skewness of the data is smaller.

The skewness is very important for the modeling of the real physical quantities. The maximum and minimum of the data is confined by the application background of the data. Therefore, the data area with high probability is relatively small and the probability for other areas are close to zero. This common phenomenon introduces skewness to the actual density function with its admissible range between zero and positive infinity. The skewness of fWd makes it easier to describe this sort of data distribution.

Comparing with the Weibull density function, the probability density function of the fWd has a scaling factor $(1 - \delta)$ which is smaller than 1 representing the reserved proportion of the data. Therefore, the fWd can be considered as the generalization of the Weibull distribution with an additional fractal parameter. If fractal parameter δ is zero, then the fWd degenerates to Weibull distribution. Changing δ while the other parameters are kept invariant will cause the peak of the curve to move vertically. In Figure 2, some fWds corresponding to different fractal parameters are depicted.

The physical meaning of δ is the discarding rate of the original data. When the ratio of the low value samples is high, a higher fractal parameter can reduce the modeling error. When the fractal parameter is determined to be smaller, there will be less of the original data to be discarded. The value of δ can influence the accuracy of modeling, thus the fractal parameter should be determined through experiment.

2.2 Definition and realization algorithm of the fWp

Definition of the fWp:

The stochastic process is fWp if the following two conditions are satisfied:

$$1. fWp(0) = 0 \quad (2.2)$$

$$2. \text{The increments of the fWp are independent} \quad (2.3)$$

$$3. \text{For given } t > s \geq 0, \text{ the increment satisfies}$$

$$fWp(t) - fWp(s) \sim fWd \quad (2.4)$$

Set s to be 0 and combining Eq. 2.2 and Eq. 2.4, Eq. 2.5 can be reached:

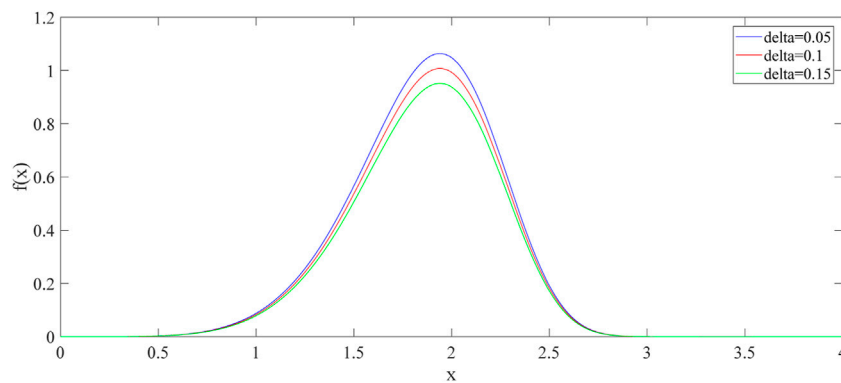


FIGURE 2

The influence of the change of fractal parameter.

$$fWp(t) \sim fWd \quad (2.5)$$

Derivation of the realization algorithm for fWp

Select a minimum calculation step length Δ in the interested definition range of the distribution and then define the discrete argument x_i in the definition range.

$$x_i = i\Delta, \quad (2.6)$$

where the argument i is the total number of the step lengths pertaining to the value of the physical quantities.

Substitute the discrete argument to the density function of the fWd:

$$p(x_i) = p(i\Delta) \\ = (1 - \delta) \frac{c}{b} \left(\frac{i\Delta - a}{b} \right)^{c-1} \exp \left\{ - \left(\frac{i\Delta - a}{b} \right)^c \right\}, i\Delta \geq a \quad (2.7)$$

The definition range of the stochastic time series is limited by the physical law and there is only a proportion of the definition range that can raise people's research interests. Therefore, the maximum value of the argument i , which is i^* , can be defined:

$$i^* = \max i = \left\lceil \frac{\max x}{\Delta} \right\rceil \quad (2.8)$$

The maximum value of i is determined based on the types of the physical values and the applications

Therefore, the finite valued and discretized density function of the fWd:

$$pdf(i\Delta) \sim \begin{bmatrix} 0 & \Delta & i\Delta & i^*\Delta \\ 0 & \frac{p(\Delta)}{\theta} & \frac{p(i\Delta)}{\theta} & \frac{p(i^*\Delta)}{\theta} \end{bmatrix}, i = 0, 1, 2, \dots, i^*, \quad (2.9)$$

where

$$\theta = \sum_{i=1}^{i^*} p(i\Delta), \quad (2.10)$$

The parameter θ is introduced to normalize the values in the random variable. Such that it can meet the basic requirements of a discrete random variable.

Define another discrete random variable X_{i^*}

$$X_{i^*} \sim \begin{Bmatrix} 0 & 1 & i & i^* \\ \frac{1}{i^*} & \frac{1}{i^*} & \frac{1}{i^*} & \frac{1}{i^*} \end{Bmatrix} \quad (2.11)$$

The discrete random variable X_{i^*} means that the integer value i is equally distributed in the range of $[0, i^*]$.

The constitution of the stochastic process can be separated into three steps. The

First step is to draw an integer value of i from the discrete random variable X_{i^*} with the uniform probability. The second step is to calculate the probability value of $pdf(i\Delta)$. The third step is to multiply the probability values of the two steps.

Therefore, we can define the fWp as follows:

$$fWp(t) \sim \begin{Bmatrix} 0 & \Delta & i\Delta & i^*\Delta \\ 0 & \frac{1}{i^*} \frac{p(\Delta)}{\theta\sigma} & \frac{1}{i^*} \frac{p(i\Delta)}{\theta\sigma} & \frac{1}{i^*} \frac{p(i^*\Delta)}{\theta\sigma} \end{Bmatrix}, \quad (2.12)$$

where σ is introduced to meet the basic requirement of the discretized random variable:

$$\sigma = \sum_{i=1}^{i^*} \frac{1}{i^*} p(i\Delta) = \frac{1}{i^*}, \quad (2.13)$$

Substitute the value of σ to the definition of the discrete random variable:

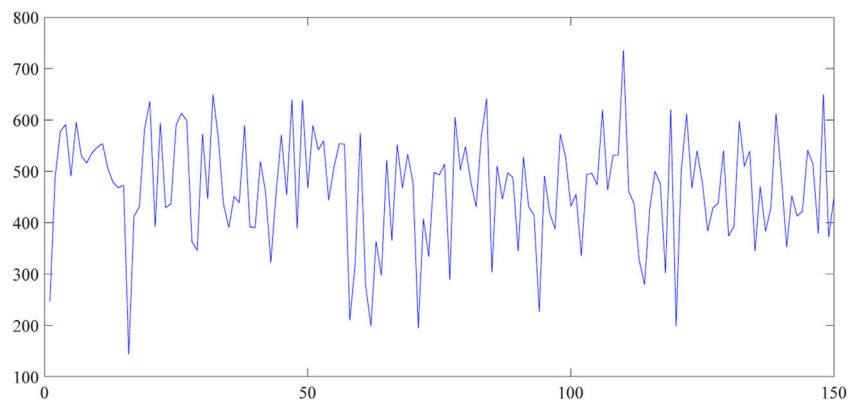


FIGURE 3
An exemplary trajectory of the fWp.

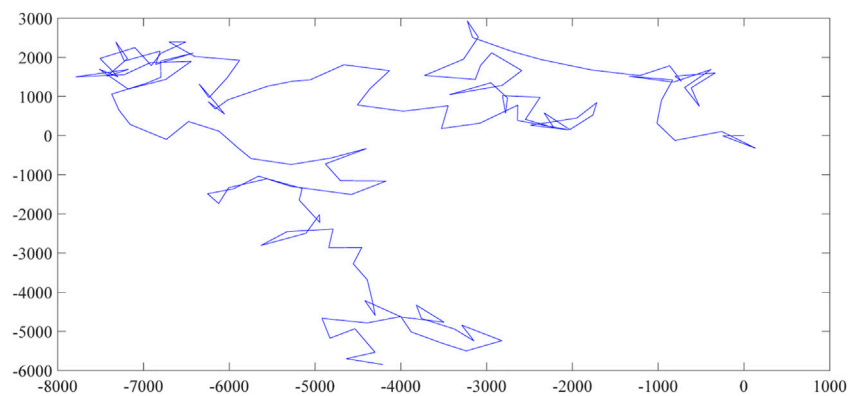


FIGURE 4
An exemplary random walk based on the fWp.

$$fWp(t) \sim \left\{ \begin{array}{ccc} 0 & \Delta & i\Delta \\ 0 & \frac{p(\Delta)}{\theta} & \frac{p(i\Delta)}{\theta} \end{array} \right\}, i = 0, \dots, i^* \quad (2.14)$$

There are six different parameters in the fWp. Four of them are the same as the fWd and are estimated by the actual data. These four parameters can reflect the statistical characteristics of the data. The other two parameters are determined based on the physical background of the data. In this section, a trajectory of the fWp and the corresponding random walk are depicted separately in Figure 3 and Figure 4. The parameters are chosen randomly in this section and in Section 5 the whole procedure for the construction of the fWp as well as the corresponding random walk is provided.

3 Self-similarity property

3.1 Self-similarity criterion for a general stochastic process

Let X_k be a stochastic process, and k is the argument. X_k is self-similar with self-similarity parameter $H \in (0, 1)$ if and only if

$$X(\lambda k) \stackrel{(d)}{=} \lambda^H X(k) \quad \forall \lambda > 0, \quad (3.1)$$

where $\stackrel{(d)}{=}$ denotes equality in distribution, i. e., they have the same probability distribution function.

In [20], the following proposition expressed by Eq. 3.2 and Eq. 3.3 are proved. Equations 3.2 is the general form of the equivalent condition for equality in distribution with respect to

two different random variables. If the random variable is Weibull distribution, then the specialized form is presented as Eq. 3.3.

Given two cumulative distribution functions $F_1(k)$ and $F_2(k)$, and a fixed number m , we have that $F_1(k)$ is equal to $F_2(k)$ in distribution if and only if $g_4(F_2(k), m)$ is equal to $g_4(F_1(k), m)$, where the function $g_4(F(k), m)$ is called the discriminant function and is defined as:

$$g_4(F(k), m) = F^{-1}((F(k) - F(m)) \bmod 1), \quad (3.2)$$

where F^{-1} is the inverse function of the cumulative function and mod is the modular operation.

For the Weibull distribution, we can get the specialized definition for $g_4(F(k), m)$:

$$g_4(F(k), m) = \left(-\log \left[\exp \left\{ -\left(\frac{k-a}{b} \right)^c \right\} - \exp \left\{ -\left(\frac{m-a}{b} \right)^c \right\} \right] \right)^{\frac{1}{c}} \quad (3.3)$$

By combining the self-similarity definition (3.1) with Eq. 3.2, we can get the criterion of the self-similarity for a general stochastic process:

$$g_4(F(\lambda k), m) = g_4(F'(k), m) \quad (3.4)$$

where $F(k)$ is the cumulative distribution function of X_k , $F'(k)$ is the cumulative distribution function of $\lambda^H X_k$.

$$F'(k) = P(\lambda^H X_k \leq k) = P\left(X_k \leq \frac{k}{\lambda^H}\right) = F\left(\frac{k}{\lambda^H}\right) \quad (3.5)$$

Substituting (3.5) into (3.4) we get

$$g_4(F(\lambda k), m) = g_4\left(F\left(\frac{k}{\lambda^H}\right), m\right), \quad (3.6)$$

which is a practical criterion for the self-similarity of a stochastic process

On the left side of Eq. 3.6, it is the discriminant function $g_4(F(k), m)$ with argument λk , while on the right hand side, it is the discriminant function $g_4(F(k), m)$ with argument $\frac{k}{\lambda^H}$.

3.2 The discriminant function for the fWp

In the following, we will derive the discriminant function for the fWp.

The following equations can be derived from the definitions:

$$f^*(k) = (1 - \delta)f(k), \quad (3.7)$$

$$F^*(k) = \int_{-\infty}^k f^*(t) dt = \int_{-\infty}^k (1 - \delta)f(t) dt = (1 - \delta)F(k), \quad (3.8)$$

$$F^{-1*}(k) = \frac{1}{1 - \delta} F^{-1}(k), \quad (3.9)$$

where $f(x)$ and $f^*(x)$ are the density functions of the Weibull distribution and the fWp. $F(x)$ and $F^*(x)$ are the cumulative

density functions of the Weibull distribution and the fWp. $F^{-1}(x)$ and $F^{-1*}(x)$ are the inverse cumulative density functions of the Weibull distribution and the fWp.

From Eq. 3.2, we have:

$$g_4^*(F(k), m) = F^{-1*}((F^*(k) - F^*(m)) \bmod 1) \\ = \frac{1}{1 - \delta} F^{-1}(((1 - \delta)[F(k) - F(m)]) \bmod 1) \quad (3.10)$$

Besides the additional coefficient $\frac{1}{1 - \delta}$, the only change between (3.2) and (3.10) is the difference $F(k) - F(m)$, which is added by a scaling factor $(1 - \delta)$. $F(k) - F(m)$ in Eq. 3.2 results in a $\exp\{-(\frac{k-a}{b})^c\} - \exp\{-(\frac{m-a}{b})^c\}$ proportion of Eq. 3.3 specialized for the Weibull distribution. Thus we can conclude that the discriminant function specialized for the fWp is:

$$g_4^*(F(k), m) = \left(-\log \left[(1 - \delta) \left\{ \exp \left\{ -\left(\frac{k-a}{b} \right)^c \right\} - \exp \left\{ -\left(\frac{m-a}{b} \right)^c \right\} \right\} \right] \right)^{\frac{1}{c}} \quad (3.11)$$

3.3 Self-similarity for the fWp

In this subsection we will show the self-similarity of the fWp.

Theorem 1. The fWp is self-similar

Proof Combining Eq. 3.3 and Eq. 3.6, we can reach Eq. 3.12:

$$g_4'(F(\lambda k), m) = \left(-\log \left[\exp \left\{ -\left(\frac{\lambda k - a}{b} \right)^c \right\} - \exp \left\{ -\left(\frac{m - a}{b} \right)^c \right\} \right] \right)^{\frac{1}{c}} \\ = g_4'\left(F\left(\frac{k}{\lambda^H}\right), m\right) = \left(-\log \left[\exp \left\{ -\left(\frac{\frac{k}{\lambda^H} - a}{b} \right)^c \right\} - \exp \left\{ -\left(\frac{m - a}{b} \right)^c \right\} \right] \right)^{\frac{1}{c}} \quad (3.12)$$

Eq. 3.12 can be simplified to be Eq. 3.13 by removing the minus sign and the power.

$$\log \left[\exp \left\{ -\left(\frac{\lambda k - a}{b} \right)^c \right\} - \exp \left\{ -\left(\frac{m - a}{b} \right)^c \right\} \right] \\ = \log \left[\exp \left\{ -\left(\frac{\frac{k}{\lambda^H} - a}{b} \right)^c \right\} - \exp \left\{ -\left(\frac{m - a}{b} \right)^c \right\} \right] \quad (3.13)$$

By considering the self-similarity condition (3.6) and Eq. 3.11, we have to show that the following Eq. 3.14 and Eq. 3.15 are equal to prove the self-similarity of the fWp.

$$g_4^*(F(\lambda k), m) = \left(-\log \left[(1 - \delta) \left\{ \exp \left\{ -\left(\frac{\lambda k - a}{b} \right)^c \right\} - \exp \left\{ -\left(\frac{m - a}{b} \right)^c \right\} \right\} \right] \right)^{\frac{1}{c}} \quad (3.14)$$

$$g_4^*\left(F\left(\frac{k}{\lambda^H}\right), m\right) = \left(-\log\left[(1-\delta)\left\{\exp\left\{-\left(\frac{k}{\lambda^H}-a\right)^c\right\}-\exp\left\{-\left(\frac{m-a}{b}\right)^c\right\}\right]\right)\right) \quad (3.15)$$

In fact (3.14) and (3.15) can be transformed into (3.16) and (3.17), respectively, as follows.

$$\begin{aligned} & \log\left[(1-\delta)\left\{\exp\left\{-\left(\frac{k}{\lambda^H}-a\right)^c\right\}-\exp\left\{-\left(\frac{m-a}{b}\right)^c\right\}\right]\right] \\ &= \log(1-\delta) + \log\left\{\exp\left\{-\left(\frac{k}{\lambda^H}-a\right)^c\right\}-\exp\left\{-\left(\frac{m-a}{b}\right)^c\right\}\right\} \end{aligned} \quad (3.16)$$

$$\log\left[(1-\delta)\left\{\exp\left\{-\left(\frac{k}{\lambda^H}-a\right)^c\right\}-\exp\left\{-\left(\frac{m-a}{b}\right)^c\right\}\right]\right] \quad (3.17)$$

Therefore, the equality of (3.16) and 3.17 can be transformed into the equality of (3.18) and 3.19:

$$\log\left\{\exp\left\{-\left(\frac{k}{\lambda^H}-a\right)^c\right\}-\exp\left\{-\left(\frac{m-a}{b}\right)^c\right\}\right\} \quad (3.18)$$

$$\log\left\{\exp\left\{-\left(\frac{k}{\lambda^H}-a\right)^c\right\}-\exp\left\{-\left(\frac{m-a}{b}\right)^c\right\}\right\} \quad (3.19)$$

According to Eq. 3.13, the two functions (3.18) and (3.19) are equal if we select the same self-similar parameter with the Weibull distribution. Therefore, the self-similarity of the fWp is proven because there exists a self-similar parameter to make Eq. 3.1 to hold, which is within the interval of (0.5,1).

4 The second moments and LRD property

4.1 The second moments of the fWp exists

For simplicity we give here only one kind of second moment, since the derivation of other moments are similar. The second moment about zero of the fWp can be easily obtained by a direct computation as follows:

$$\begin{aligned} E(fWb(t)^2) &= \int_0^\infty x^2 f_X^*(x|0,1,c)dx = (1-\delta) \int_0^\infty x^2 f_X(x|0,1,c)dx \\ &\xrightarrow{u=x^c} (1-\delta) \int_0^\infty x^2 c x^{c-1} \exp\{-x^c\}dx \\ &= (1-\delta) \int_0^\infty u^{\frac{2}{c}} e^{-u} du = (1-\delta) \Gamma\left(\frac{2}{c}+1\right) \end{aligned} \quad (4.1)$$

Therefore, we have proven that the second moments of the fWp exists.

4.2 The LRD of the fWp

The LRD means the slow decay of the auto-correlation function $\rho(k)$, which also means that the auto-correlation in the process remains strong as the time lag goes to infinity. The

strong auto-correlation means that the value of the process is influenced by other values of the process. With the slow decay of the auto-correlation function, it cannot be integrated in the infinite range.

$$\rho(k) \sim \beta k^{-\alpha} \text{ as } k \rightarrow \infty, \quad (4.2)$$

where

$$\rho(k) = E(X(k)X(k-\tau)) \quad (4.3)$$

$0 < \alpha < 1$ and β is a given non-zero constant.

Eq. 4.2 summarizes the physical meaning of the LRD. The slow decaying rate of the auto-correlation function does not specify the exact decaying rate. By changing the values of constants α and β , the decaying rate of the auto-correlation changes accordingly. The slower the decaying is, the stronger is the LRD. Therefore, the proof of the LRD focuses on the existence of the slow decaying auto-correlation.

Let $X(k)$ be the fWp, then its incremental process $Y(k)$ fulfills:

$$\begin{cases} Y(k) = X(k) - X(k-1) & , \quad k = 1, \dots, n \\ Y(0) \xrightarrow{\text{def}} 0 & , \quad X(0) = 0 \end{cases} \quad (4.4)$$

Based on the theorem in [22], we can show the incremental process $Y(k)$ is of LRD, which means the auto-correlation function of $Y(k)$ decays as a power function. In the following, we can show the fWp is of LRD.

Theorem 2. The fWp is of LRD

Proof: According to the definition (4-4), we can express $X(k)$ by the linear combinations of $Y(k)$, $k = 0, 1, \dots, n$. Moreover, the auto-correlation function of $X(k)$ can be expressed as the linear combination of auto-correlation functions of $Y(k)$, $k = 0, 1, \dots, n$.

$$X(k) = Y(k) + Y(k-1) + \dots + Y(1) + Y(0) \quad (4.5)$$

$$\begin{aligned} \rho(X(k)) &= E(X(k)X(k-\tau)) = E\left(\left(\sum_{i=0}^k Y(i)\right)\left(\sum_{j=0}^{k-\tau} Y(j)\right)\right) \\ &= \sum_{i=0}^k \sum_{j=0}^{k-\tau} E(Y(i)Y(j)) = \sum \rho(Y(k)) \end{aligned} \quad (4.6)$$

From Eq. 4.6 and the law of infinitesimal substitution, there follows that the auto-correlation function of $X(k)$ decays in a multinomial power law way. It also means that the auto-correlation function of $X(k)$ decays at the same speed as the slowest decaying rate among auto-correlation functions of $Y(k)$, $k = 0, 1, \dots, n$. The auto-correlation function of $Y(k)$ that processes the slowest decaying rate is the biggest one, in other words, the one with the smallest power.

$$\rho(X(k)) = \sum \rho(Y(k)) \sim \sum \beta_i k^{a_i} \sim \max(\beta_i k^{a_i}) = \beta_* k^{-\min(a_i)} \quad (4.7)$$

Therefore, we have proven that the auto-correlation function of $X(k)$ is decaying as the power function, which proves the LRD of the fWp.

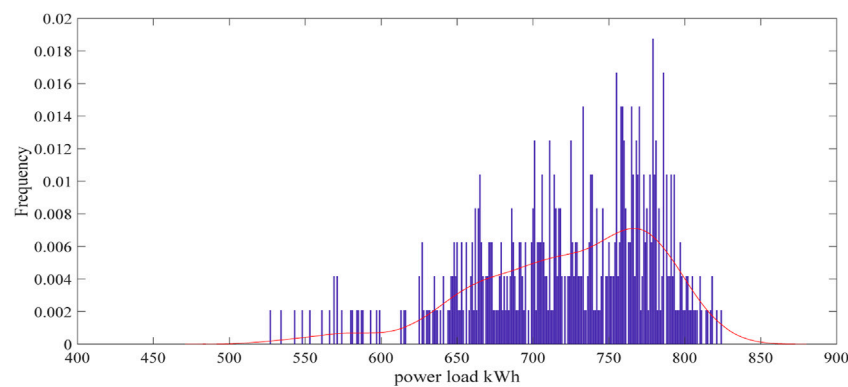


FIGURE 5
The actual power load frequency distribution and density function.

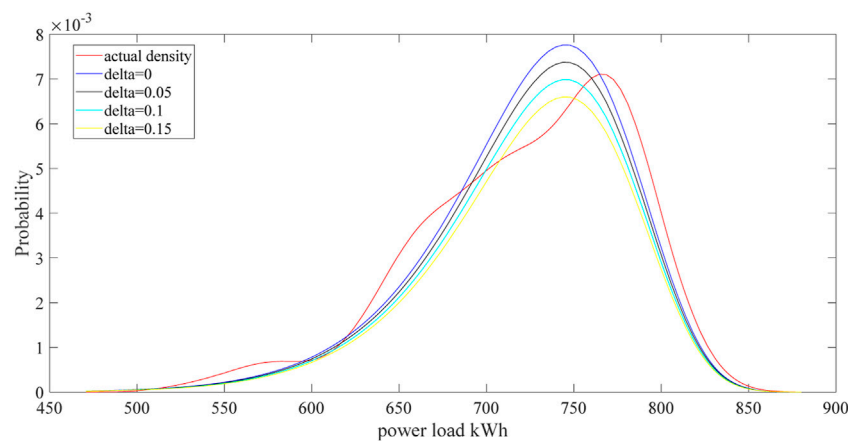


FIGURE 6
The fitting results of fWd with different fractal parameters.

5 Simulation on the fWp

5.1 Time series fitted with the fWd

In this paper, the power load data from the European Network on Intelligent.

Technologies prediction contest is used in the validation of the proposed process. In Figure 5, the actual power load frequency distribution is plotted and the corresponding probability density function is provided numerically

The power load data cannot be negative values, therefore the Gaussian fit is not appropriate. Select fWd to fit the actual power load distribution and can achieve a better fitting result than the Weibull distribution because of the fractal parameter. The location parameter a is set to be zero for the power load are positive and the scale fractal parameter is determined later through experiment. The scale parameter

and shape parameter are estimated by the maximum similarity estimation.

The maximum likelihood function of the fWd:

$$\begin{aligned}
 L(x|b, c) &= \prod_{i=1}^n f_X(x_i|b, c) \\
 &= \prod_{i=1}^n \left[(1 - \delta) \left(\frac{c}{b} \right) \left(\frac{x_i}{b} \right)^{c-1} \exp \left\{ - \left(\frac{x_i}{b} \right)^c \right\} \right] \\
 &= (1 - \delta)^n \left(\frac{c}{b} \right)^n \left(\frac{1}{b} \right)^{n(c-1)} \prod_{i=1}^n x_i^{c-1} \exp \left\{ - \left(\frac{1}{b} \right)^c \sum_{i=1}^n x_i^c \right\}
 \end{aligned} \quad (5.1)$$

The logarithmic maximum likelihood function of the fWd:

$$\begin{aligned}
 \ln L(x|b, c) &= \ln \left[(1 - \delta)^n \left(\frac{c}{b} \right)^n \left(\frac{1}{b} \right)^{n(c-1)} \prod_{i=1}^n (x_i)^{c-1} \exp \left\{ - \left(\frac{1}{b} \right)^c \sum_{i=1}^n x_i^c \right\} \right] \\
 &= n \ln(1 - \delta) + n \ln \left(\frac{c}{b} \right) + n(c-1) \ln \left(\frac{1}{b} \right) + (c-1) \sum_{i=1}^n \ln x_i - \left(\frac{1}{b} \right)^c \sum_{i=1}^n x_i^c
 \end{aligned} \quad (5.2)$$

TABLE 1 The evaluation of fitness for different fractal parameters.

| | delta = 0 | delta = 0.05 | delta = 0.1 | delta = 0.15 |
|------|------------|--------------|-------------|--------------|
| SSE | 0.3812E-04 | 0.3309E-04 | 0.3455E-04 | 0.4250E-04 |
| RMSE | 0.6174E-03 | 0.5753E-03 | 0.5878E-03 | 0.6520E-03 |

Take the partial derivative of the logarithmic maximum likelihood function with respect to the scale parameter b and then make it equal to zero.

$$\frac{\partial \ln L(x|b, c)}{\partial b} = \left(\frac{-n}{b}\right) - n(c-1)\left(\frac{1}{b}\right) + c \sum_{i=1}^n x_i^c \left(\frac{1}{b}\right)^{c+1} = 0 \quad (5.3)$$

Separate the scale parameter b and the shape parameter c :

$$\hat{b} = \left\{ \frac{\sum_{i=1}^n x_i^c}{nc} \right\}^{\frac{1}{c}} \quad (5.4)$$

Take the partial derivative of the logarithmic maximum likelihood function with respect to the shape parameter c and then make it equal to zero.

$$\begin{aligned} \frac{\partial \ln L(x|b, c)}{\partial c} &= n\left(\frac{1}{c}\right) + n \ln\left(\frac{1}{b}\right) + \sum_{i=1}^n \ln x_i - \left[\left(\frac{1}{b}\right)^c \sum_{i=1}^n \frac{\partial x_i^c}{\partial c} \right] \\ &\quad - \left[\sum_{i=1}^n x_i^c \left(\frac{1}{b}\right)^c \ln\left(\frac{1}{b}\right) \right] \\ &= n\left(\frac{1}{c}\right) + n \ln\left(\frac{1}{b}\right) + \sum_{i=1}^n \ln x_i - \left[\left(\frac{1}{b}\right)^c \sum_{i=1}^n x_i^c \ln x_i \right] \\ &\quad - \left[\sum_{i=1}^n x_i^c \left(\frac{1}{b}\right)^c \ln\left(\frac{1}{b}\right) \right] = 0 \end{aligned} \quad (5.5)$$

After performing some algebraic calculation, the equivalent equation can be derived

$$\ln\left(\frac{1}{b}\right) + \frac{1}{n} \sum_{i=1}^n \ln x_i + \frac{c}{n^2} - \left(\frac{1}{b}\right)^c \frac{\sum_{i=1}^n x_i^c \ln\left(\frac{x_i}{b}\right)}{n} = 0 \quad (5.6)$$

Substituting Eq. 5.4 to Eq. 5.6:

$$n^{\frac{1}{c}} c^{\left(\frac{1}{c}+n\right)} \left[\sum_{i=1}^n x_i^c \right]^{\left(\frac{n-1}{n}\right)} \left[\prod_{i=1}^n x_i \right]^{-c} - \frac{e^{\frac{1}{n^2}}}{n \left[\prod_{i=1}^n x_i \right]^{\frac{1}{n^2}}} = 0 \quad (5.7)$$

Therefore, the estimation of the scale parameter b and the shape parameter c is reached. The scale parameter b is estimated to be 748.4289 and the shape parameter c is estimated to be 15.7742.

The fractal parameter needs to be evaluated chosen by the fitting results. The density function of the fWd with

different fractal parameters are depicted in Figure 6 as well as the actual power load density function. The criteria of goodness of fitting (GoF) are the sum of squared error (SSE) and the root mean square error (RMSE) [23]. The formulas are listed below. For both criteria, the smaller value means better fitting results.

$$RMSE = \sqrt{\frac{1}{n} \sum_{i=1}^n (p_i - f_i)^2} \quad (5.8)$$

$$SSE = \sum_{i=1}^n (p_i - f_i)^2 \quad (5.9)$$

The calculations of the SSE and RMSE are listed in Table 1. The density function of fWd with zero fractal parameter is Weibull distribution. As we can see from Table 1, the delta value of 0.05 is chosen in the end because both the values of SSE and RMSE are the smallest.

After the parameter estimation and the experiment, the power load is fitted with the fractional Weibull distribution in Figure 7.

5.2 The construction of the fWp

On the purpose of generating the fWp conveying the stochasticity of the stochastic time series, the other parameters in the fWp need to be calculated.

The step length Δ of the modeling can set to be 1 kWh because the power load data are all positive integers. The maximum value of the power load concerned in the research is 900 kWh. Therefore, the maximum value of the argument i , which is i^* , can be calculated:

$$i^* = \max i = \left\lceil \frac{\max x}{\Delta} \right\rceil = 900 \quad (5.10)$$

where x is the value of the power load series for research and the square bracket represents the integer valued function.

Therefore, the fWp with the stochasticity of the time series is depicted in Figure 8.

5.3 The simulated path for the random walk of the fWp

After the construction of the fWp, the corresponding random walk path can be simulated. As depicted in Figure 9, the particle in the random walk starts from the origin. At each of the iteration, the jump direction is random and the jump length follows the fWd with parameters estimated from the actual data. The simulation path of the random walk expands the dimension of the fWp to a planar space with the same stochasticity coming from the actual data.

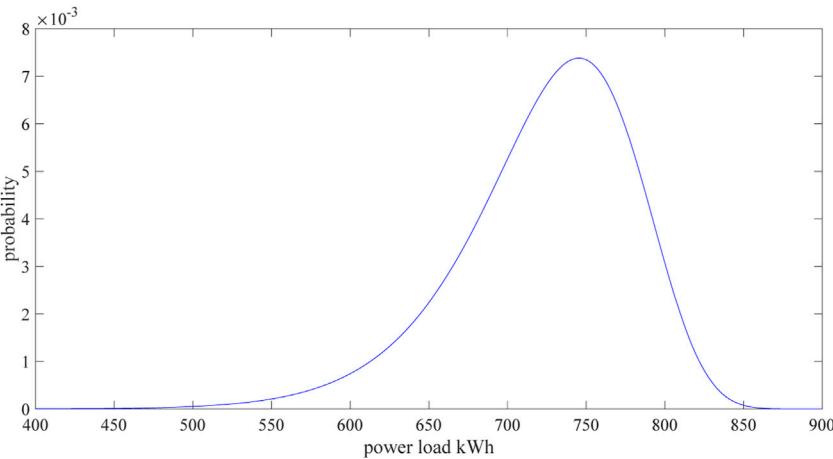


FIGURE 7
The fractional Weibull fit of the data.

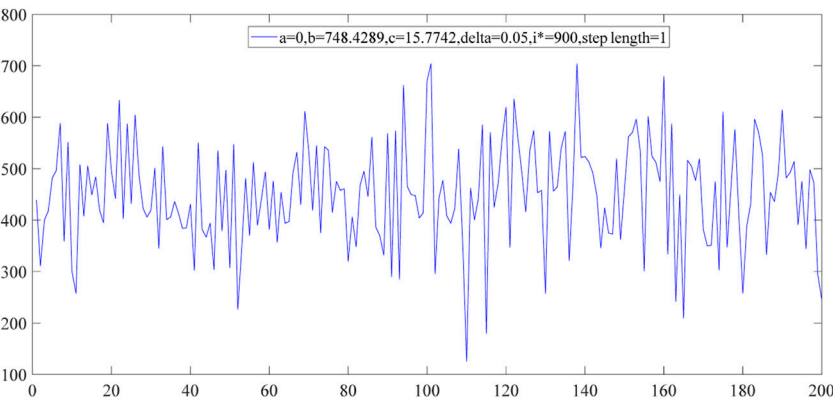


FIGURE 8
The fWp based on the power load series.

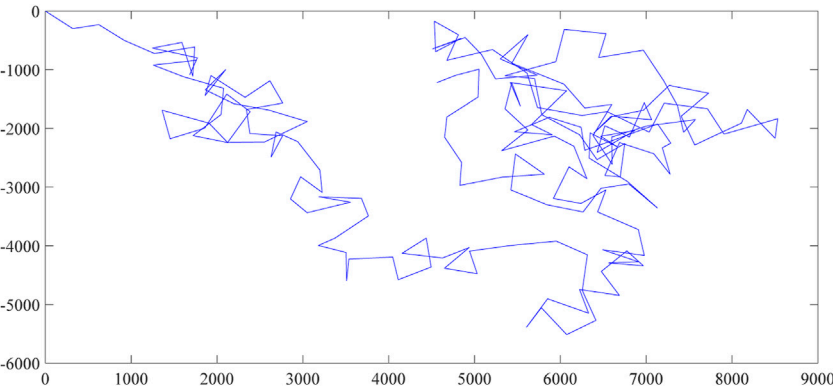


FIGURE 9
The random walk characteristics of the fWp.

6 The potential engineering applications of the fWp

Wind power generation is very unreliable because it relies solely on the wind speed. The historical wind speed data can be used to construct the fWp for representing its stochasticity and the statistical wind speed prediction model can be constructed. Once the wind speed variation tendency is predicted in advance, the wind power generation can be predicted with accuracy and the power system reliability can be improved [24].

The power load prediction is very important for the reliability of the power system. If there is surplus electricity according to the power load prediction results, the maintenance of the power facilities can be scheduled. If the power consumption is difficult to guarantee, the dispatching of electricity need to be carried out [25]. With the fWp conveying the stochasticity of the power load, the power load statistical prediction model can be established and the blackouts caused by the high temperature can be reduced.

7 Conclusion

The fWd can be considered to be the generalization of the Weibull distribution with a non-zero fractal parameter. In this paper, the definition of the fWp is provided and the algorithm of realization is derived. In order to facilitate the future research, the self-similarity and LRD are proven. The actual time series is employed for the simulation of the fWp. The random walk characteristics for the fWp is analyzed in the planar space. The future research can focus on the prediction model for the potential engineering application areas of the fWp.

References

- Norros I. On the use of fractional Brownian motion in the theory of connectionless networks. *IEEE J Sel Areas Commun* (1995) 13:953–62. doi:10.1109/49.400651
- Li M. Generalized fractional Gaussian noise and its application to traffic modeling. *Physica A: Stat Mech its Appl* (2021) 579:126138. doi:10.1016/j.physa.2021.126138
- Shouwu D, Wanqing S, Enrico Z, Carlo C, Ming L. Product technical life prediction based on multi-modes and fractional Lévy stable motion. *Mech Syst Signal Process* (2021) 161:107974. doi:10.1016/j.ymssp.2021.107974
- Hallinan J, Jr. A review of the Weibull distribution. *J Qual Tech* (1993) 25: 85–93. doi:10.1080/00224065.1993.11979431
- Ibrahim E, Mohamed Z, Mahdi R, Ahamed AZ. A new extended Weibull model for lifetime data. *J Appl Probab Stat* (2019) 14:1.
- Jaouher BA, Brigitte CM, Lotfi S, Simon M, Farhat F. Accurate bearing remaining useful life prediction based on Weibull distribution and artificial neural network. *Mech Syst Signal Process* (2015) 56–57:150–72. doi:10.1016/j.ymssp.2014.10.014
- Ming D, Alexandre BN. Combining modified Weibull distribution models for power system reliability forecast. *IEEE T Power Syst* (2019) 34:2. doi:10.1109/TPWRS.2018.2877743
- Kalaba DV, Radakovic ZJ, Dordevic ML, Kirin SD. Determining the theoretical reliability function of thermal power system using simple and complex Weibull Distribution. *Therm Sci* (2014) 18:229–38. doi:10.2298/TSCI120611168K
- Yeliz MK, Ilhan U. Analysis of the upper-truncated Weibull distribution for wind. *Speed Energ Convers Manage* (2015) 81:88. doi:10.1016/j.enconman.2015.02.063
- Athraa AK, Noor IAW, Lshak A, Jasronita J, Ahmed NA. Advanced wind speed prediction model based on a combination of Weibull distribution and an artificial neural network. *Energies* (2017) 10:11. doi:10.3390/en10111744
- Zuwei Y, Akiner T. Fractional Weibull wind speed modeling for wind power production estimation, In proceedings of the International Conference on Sustainable Power Generation and Supply. Nanjing, China (2009), 952–7. doi:10.1109/PES.2009.5275785
- Muhammad UA, Intisar AS, Luigi M. Weibull distribution model for the characterization of aggregate load patterns. In: proceedings of the IEEE international Conference on Environment and Electrical Engineering. Palermo, Italy (2018). p. 1–5. doi:10.1109/EEEIC.2018.8494371

Data availability statement

The original contributions presented in the study are included in the article/Supplementary Material, further inquiries can be directed to the corresponding author.

Author contributions

WD: initial draft, software; WS: concept, validation, revision; CC: revision, language editing; JC: validation, revision; XC: validation, revision.

Acknowledgments

We thank the help from Shanghai university of engineering and science and university in Tuscia. Without the help of them, this work cannot be finished. The diligent work from the reviewers and editor is really helpful for this work.

Conflict of interest

The authors declare that the research was conducted in the absence of any commercial or financial relationships that could be construed as a potential conflict of interest.

Publisher's note

All claims expressed in this article are solely those of the authors and do not necessarily represent those of their affiliated organizations, or those of the publisher, the editors and the reviewers. Any product that may be evaluated in this article, or claim that may be made by its manufacturer, is not guaranteed or endorsed by the publisher.

13. Feng X, Jiaying L, Hansong N, Yonghao F, Liangtian W, Xiangjie K. Random walks: A review of algorithms and applications. *IEEE Trans Emerg Top Comput Intell* (2020) 95:95. doi:10.1109/TETCI.2019.2952908
14. Wilfrid SK. Rayleigh random flights on the Poisson line SIRS. *Electron J Probab* (2020) 1:36. doi:10.1214/20-EJP526
15. Mridul C, Manoj D. Levy flights in metaheuristics optimization algorithms - a review. *Appl Artif Intell* (2018) 9-10:802–21. doi:10.1080/08839514.2018.150.8807
16. Yuantao C, Jin W, Xi C, Mingwei Z, Kai Y, Zhi W, et al. Single-image super-resolution algorithm based on structural self-similarity and deformation block features. *IEEE ACCESS* (2019) 58791:58801. doi:10.1109/ACCESS.2019.291.1.892
17. Popoola J, Ipinyomi RA. Empirical performance of Weibull self-similar tele-traffic model. *Int J Eng Appl Sci* (2017) 8:4.
18. Anatolii L, Yevgenii L. Investigation of simulating methods for self-similar traffic flows the qos-characteristics depend on the type of distribution in self-similar traffic. In: proceedings of the 4th International Scientific-Practical Conference Problems of Infocommunications-Science and Technology(PIC S&T). Ukraine: Khark (2017). p. 410–3. doi:10.1109/INFOCOMMST.2017.8246428
19. Mobaraki H, Hassani A, Kashkalani T, Khalilnejad R, Chimeh EE. Equality in distribution of human resources: The case of Iran's ministry of health and medical education. *Iran J Public Health* (2013) 161:165.
20. Dan K, Eric M, Robert DS. On the equality in distribution of the random variables X and g(X). *Int J Pure Appl Math* (2005).
21. Shaifu G, Dileep AD. Long range dependence in cloud servers: A statistical analysis based on google work load trace. *Computing* (2020) 102:6. doi:10.1007/s00607-019-00779-4
22. Michele P. Self-similarity and long range dependence in teletraffic. In: Proceedings of the 15th international Asian School-Seminar Optimization Problems of Complex Systems (OPCS). Novosibirsk, Russia (2019). p. 125–30. doi:10.1109/OPCS.2019.8880260
23. Haobo Z, Wufeng H, Junhui Z, Jiefeng L, YiYi Z, Shi Z, et al. A normal falling model for wind speed probability distribution of wind farms. *Renew Energ* 91–9. doi:10.1016/j.renene.2021.11.073
24. He L, Wanqing S, Enrico Z. Generalized Cauchy difference iterative forecasting model for wind speed based on fractal time series. *Nonlinear Dynam* (2021) 759–73. doi:10.1007/s11071-020-06150-z
25. Wanqing S, Ming L, Yuanyuan L, Carlo C, Chi-Huang C. Fractional brownian motion: Difference iterative forecasting models. *Chaos Soliton Fract* (2019) 347:355. doi:10.1016/j.chaos.2019.04.021

Advantages of publishing in Frontiers



OPEN ACCESS

Articles are free to read
for greatest visibility
and readership



FAST PUBLICATION

Around 90 days
from submission
to decision



HIGH QUALITY PEER-REVIEW

Rigorous, collaborative,
and constructive
peer-review



TRANSPARENT PEER-REVIEW

Editors and reviewers
acknowledged by name
on published articles

Frontiers

Avenue du Tribunal-Fédéral 34
1005 Lausanne | Switzerland

Visit us: www.frontiersin.org

Contact us: frontiersin.org/about/contact



REPRODUCIBILITY OF RESEARCH

Support open data
and methods to enhance
research reproducibility



DIGITAL PUBLISHING

Articles designed
for optimal readership
across devices



FOLLOW US

@frontiersin



IMPACT METRICS

Advanced article metrics
track visibility across
digital media



EXTENSIVE PROMOTION

Marketing
and promotion
of impactful research



LOOP RESEARCH NETWORK

Our network
increases your
article's readership